

# REPORT DOCUMENTATION PAGE

Form Approved  
OMB No. 0704-0188

The public reporting burden for this collection of information is estimated to average 1 hour per response, including the time for reviewing instructions, searching existing data sources, gathering and maintaining the data needed, and completing and reviewing the collection of information. Send comments regarding this burden estimate or any other aspect of this collection of information, including suggestions for reducing the burden, to Department of Defense, Washington Headquarters Services, Directorate for Information Operations and Reports (0704-0188), 1215 Jefferson Davis Highway, Suite 1204, Arlington, VA 22202-4302. Respondents should be aware that notwithstanding any other provision of law, no person shall be subject to any penalty for failing to comply with a collection of information if it does not display a currently valid OMB control number.

PLEASE DO NOT RETURN YOUR FORM TO THE ABOVE ADDRESS.

|   |             |   |                               |   |   |
|---|-------------|---|-------------------------------|---|---|
| 1. REPORT DATE (DD-MM-YYYY)<br>03/25/13   |             | 2. REPORT TYPE<br>Interim Research Performance Report (Final) |                               | 3. DATES COVERED (From - To)<br>01/01/11 - 12/31/12 |   |
| 4. TITLE AND SUBTITLE<br>The California Central Coast Research Partnership: Building Relationships, Partnerships and Paradigms for University-Industry Collaboration  |             |   |                               | 5a. CONTRACT NUMBER                                 |   |
|   |             |   |                               | 5b. GRANT NUMBER<br>N00014-11-1-0359                |   |
|   |             |   |                               | 5c. PROGRAM ELEMENT NUMBER                          |   |
|   |             |   |                               | 5d. PROJECT NUMBER                                  |   |
| 6. AUTHOR(S)<br>Opava,S; Arens,R; Bellardo, J; Blank, J; Chen, J; Clague, D; Costanzo, P; Derickson, D; Dolan, D; Elghandour, E; Fidopiastis, P; Keller, M; Laiho, L; Lehr, C; Lundquist, T; Nelson, Y; Palandoken, H; Pan, J; Prodanov, V; Qu, B; Rahman, S; Ridgely, J; Rihal, S; Saliklis, E; Sharpe, J; Singh J; Vorst, K; Wood, Z; miscellaneous student authors.  |             |   |                               | 5e. TASK NUMBER                                     |   |
|   |             |   |                               | 5f. WORK UNIT NUMBER                                |   |
| 7. PERFORMING ORGANIZATION NAME(S) AND ADDRESS(ES)<br>Cal Poly Corporation, Sponsored Programs Office<br>Bldg. 38, Rm. 102<br>San Luis Obispo, CA 93407-0830  |             |   |                               | 8. PERFORMING ORGANIZATION<br>REPORT NUMBER         |   |
| 9. SPONSORING/MONITORING AGENCY NAME(S) AND ADDRESS(ES)<br>Cody Reese<br>Office of Naval Research<br>875 Randolph St.<br>Arlington, VA 22203-1995   |             |   |                               | 10. SPONSOR/MONITOR'S ACRONYM(S)<br>ONR             |   |
|   |             |   |                               | 11. SPONSOR/MONITOR'S REPORT<br>NUMBER(S)           |   |
| 12. DISTRIBUTION/AVAILABILITY STATEMENT<br>Available for public release   |             |   |                               |   |   |
| 13. SUPPLEMENTARY NOTES<br><br><div style="text-align: center; font-size: 2em; font-family: cursive;">20130329079</div>   |             |   |                               |   |   |
| 14. ABSTRACT<br>The primary purpose of this project is to carry out applied research and development projects and build research capacity in areas of interest to the Department of Defense and the Office of Naval Research. Research areas include communications, computing, command and control, sensors, coastal monitoring, force protection and performance, new materials and devices, data acquisition, imaging technologies, autonomous vehicles and robots, alternative energy sources and energy efficiency, logistics. |             |   |                               |   |   |
| 15. SUBJECT TERMS<br>aptamer-based clinical diagnostics, water treatment, AUVs, SGDBR lasers, path optimization, biofuels, photobioreactors, wind energy, electric vehicles, batteries, sandwich panels, seismic analysis/design, logistics, injury repair, biomarkers, LEDs, photonics, knowledge management, satellite constellations, RF amplifiers, emergency shelters, blunt impact, thermally responsive binders.   |             |   |                               |   |   |
| 16. SECURITY CLASSIFICATION OF:   |             |   | 17. LIMITATION OF<br>ABSTRACT | 18. NUMBER<br>OF<br>PAGES                           | 19a. NAME OF RESPONSIBLE PERSON<br>Susan C. Opava, Ph.D.  |
| a. REPORT   | b. ABSTRACT | c. THIS PAGE  |                               |   |   |
| U   | U           | U   | UU                            |   | 19b. TELEPHONE NUMBER (Include area code)<br>805-756-1508 |

**The California Central Coast Research Partnership:  
Building Relationships, Partnerships, and Paradigms for  
University-Industry Research Collaboration**

FINAL REPORT  
ONR GRANT NO. N00014-11-1-0359  
January 1, 2011 to December 31, 2012

Principal Investigator:

Susan Opava, Ph.D.  
Dean of Research and Graduate Programs  
California Polytechnic State University  
San Luis Obispo, CA

March 25, 2013

## Table of Contents

|  |           |
|--|-----------|
| <b>I. Title of Project and Principal Investigator</b>  | <b>1</b>  |
| <b>II. Summary of Project</b>  | <b>1</b>  |
| <b>III. Relevance to ONR Objectives</b>  | <b>1</b>  |
| A. Relevant Partners   | 1         |
| B. Relevant R&D Focus  | 2         |
| C. University-Industry-Government Partnership  | 3         |
| D. University Strengths  | 3         |
| <b>IV. Summary of Results During the Period of Performance</b>   | <b>5</b>  |
| A. General   | 5         |
| B. Development of New Research Capacity  | 7         |
| 1. Instrumentation   | 8         |
| 2. Infrastructure  | 13        |
| C. Detailed Research Reports   | 13        |
| 1. Collaborative Agent Design Research Center (CADRC)  | 13        |
| 2. Other Research Projects   | 13        |
| <b>Partnering Enhanced-NLP with Semantic Analysis In Support of Information Extraction (CADRC) . Hisham Assal, Ph.D., Collaborative Agent Design Research Center (CADRC), John Seng, Ph.D., Computer Science, Franz Kurfess, Ph. D. Computer Science</b> | <b>14</b> |
| <b>Alternative energy sources and energy efficiency</b>  | <b>27</b> |
| <b>Hybrid Electric Vehicle Grid Connectivity – Phase I. Dale Dolan, Ph.D., Electrical Engineering</b>  | <b>28</b> |
| <b>Investigation of Floating Tube Heat Exchangers with Applications in Power Generation, Biofuel Growth, and Clean Water. Melinda Keller, Ph.D., Mechanical Engineering</b>  | <b>42</b> |
| <b>Sensors and Controls for Cal Poly Wind Power Research Center. John Ridgely, Ph.D., Mechanical Engineering</b>   | <b>51</b> |
| <b>Overcoming Barriers to Affordable Algae Biofuels: Phase II. Tryg Lundquist, Ph.D., Civil &amp; Environmental Engineering, Yarrow Nelson, Ph.D., Civil and Environmental Engineering, Corinne Lehr, Ph.D., Chemistry and Biochemistry</b>              | <b>70</b> |

|   |            |
|---|------------|
| <b>Human performance</b>  | <b>86</b>  |
| <b>Does ethanol nullify the benefits of exercise in skeletal muscle?</b> Jason Blank, Ph.D., Biological Sciences  | 87         |
| <b>Aptamer-Based Clinical Diagnostics in Nitrocellulose, Paper-Microfluidic Platforms.</b> David S. Clague, Ph.D., Biomedical Engineering   | 96         |
| <b>Investigation, Design, and Testing of Compact “Envelope” Filter for Use with the Cal Poly Waterbag.</b> Tryg Lundquist, Ph.D., Civil & Environmental Engineering   | 109        |
| <b>Force protection in combat and non-combat situations</b>   | <b>125</b> |
| <b>Alkoxyamine Polymers: Versatile Materials For ‘Ever-Sterile’ Surfaces.</b> Hasan Palandoken, Ph.D., Chemistry and Biochemistry   | 126        |
| <b>Development of Thermally Responsive Binders Designed for Insensitive Munitions Applications.</b> Philip Costanzo Ph.D., Chemistry  | 136        |
| <b>Development of a Virtualization Platform for Airway Device Development.</b> Lily Laiho, Ph.D., Biomedical and General Engineering  | 142        |
| <b>Use of Unstiffened Steel Plates to Prevent Progressive Collapse of Existing Steel Building Frames with Simple Beam-to-Column Connections.</b> Bing Qu, Ph.D., Civil and Environmental Engineering                  | 164        |
| <b>Optimal Contamination Monitoring Station Locations in Water Distribution Systems using Heuristic method.</b> Shikha Rahman, Ph. D., Civil & Environmental Engineering  | 173        |
| <b>Blunt Impact Performance Evaluation of Helmet Lining Systems for Military Use.</b> Jay Singh, Ph.D., Industrial Technology   | 186        |
| <b>New technologies with military applications</b>  | <b>201</b> |
| <b>Efficient Point-to-Point Communication Infrastructure for Low Earth Orbit Satellites.</b> John M. Bellardo, Ph.D., Computer Science  | 202        |
| <b>Assessment of Sonic IR for Detection of Subsurface Damage in Composite Panels.</b> John C. Chen, Ph.D., Mechanical Engineering   | 212        |
| <b>1.08 Micron and 1.3 Micron Sampled Grating Distributed Bragg Reflector (SGDBR) lasers for Optical Coherence Tomography (OCT), LADAR, and Sensing Applications.</b> Dennis Derickson, Ph D., Electrical Engineering | 229        |



|   |     |
|---|-----|
|   |     |
| <b>A novel technique for preventing delamination of the composite skin from the core: Sandwich panels with shear keys.</b> Eltahry Elghandour, Ph.D. Civil Engineering  | 238 |
| <b>Developing a Visual Tracking System for Small Marine Animal Research.</b> Pat M. Fidopiastis, Ph.D., Biological Sciences   | 362 |
| <b>Materials and Methods of Interconnections in LED Packaging.</b> John Pan, Ph.D., Industrial & Manufacturing Engineering  | 374 |
| <b>Linear RF Amplifiers.</b> Vladimir I. Prodanov, Ph.D., Electrical Engineering  | 398 |
| <b>Structural Origami Based Deployable Disaster Relief Shelter.</b> Satwant Rihal, Ph.D., Professor Emeritus, Architectural Engineering Department  | 406 |
| <b>Rapidly Assembled Emergency Shelters, Phase II.</b> Robert Arcns, Ph.D., AIA, Department of Architecture   | 412 |
| <b>Implementation of the switchable grating concept.</b> John Sharpe, Ph.D. Physics   | 420 |
| <b>Scientific Visualization of Massive Underwater Science Data Acquired from Underwater Robots.</b> Zoë Wood, Ph.D., Computer Science   | 428 |
| <b>Facile covalent surface functionalization of multiwalled carbon nanotubes with poly (2-hydroxyethyl methacrylate) and interface related studies when incorporated into epoxy composites</b><br>Keith Vorst, Ph.D., College of Business | 441 |
| <b>V. Appendix</b>  |     |
| A. High – Tech Breakfast Forum Agenda   | 464 |
| B. Project Related Thesis and Relevant Publications   | 471 |

## **I. Title of Project and Principal Investigator**

The California Central Coast Research Partnership: Building Relationships, Partnerships and Paradigms for University-Industry Research Collaboration; Susan C. Opava, Ph.D.

## **II. Summary of Project**

The mission of the California Central Coast Research Partnership (C<sup>3</sup>RP) is to facilitate the exchange of technical knowledge and skills between the higher education sector and the private sector in San Luis Obispo County, and to encourage the growth of high-tech companies in the region, thereby enhancing economic development and quality of life. Since its inception, the project has focused on technologies of relevance to the Department of Defense. The partnership is a long-term plan to create a dynamic and self-supporting university-industry-government partnership that capitalizes on the strengths and mutual interests of the educational and technology-based business sectors. The plan recognizes the key role of higher education in preparing a highly skilled workforce and transferring new knowledge to practical uses. The ongoing outcomes of this partnership include a robust and self-sustaining base of University R&D activities; sustenance and growth of existing technology-based businesses and the creation of new ones; and opportunities for job-training and research and development activities for University and Community College students and faculty.

The project has already resulted in the construction (with non-DOD funding) and launch of the Cal Poly Technology Park on the University campus. This facility provides state-of-the-art space for private technology companies engaged in research and development activities, as well as a business incubator for start-up, technology-based companies. The aspect of the program supported by the ONR grant that this report covers was the continued development of a strong base of applied research at Cal Poly, through university-government-industry partnerships designed to optimize the application of the strengths of each of these sectors to problems of mutual interest. The management team, operational since January '02, continues to lead the project and develop the collaborative relationships between the educational and private sectors that are essential to realizing long-term goals and securing the financial base that will allow full-scale project development.

## **III. Relevance to ONR Objectives**

### **A. Relevant partners.**

C<sup>3</sup>RP represents a coalition of educational institutions, local, state and federal government, and private businesses that have worked together in unprecedented fashion to advance the common goals inherent in this university-industry partnership. The current partners in the project and their contributions include:

**California Polytechnic State University**

- committed the land for the Technology Park construction project, valued at ~\$1.5 million
- provided assistance in financial management of the project
- contributed \$90,000 for a pre-feasibility study by Bechtel Corporation
- committed several hundred thousand dollars of in-kind contributions of senior management time and effort over several years and continues to do so
- invested ~\$1,000,000 in efforts to raise additional funds for the project; secured sufficient private and other federal funding (Economic Development Administration and Housing and Urban Development) to construct the first building in the Cal Poly Technology Park

**CENIC** (Corporation for Educational Network Initiatives in California; association of Internet2 universities in CA)

- works with Cal Poly to provide high-bandwidth internet access to support C<sup>3</sup>RP research projects

**City of San Luis Obispo**

- in partnership with Cal Poly developed a carrier-neutral, fiberoptic ring around the city that benefits both Cal Poly and technology-based businesses

**Housing and Urban Development**

- provided funds toward construction of the pilot technology park building.

**Economic Development Administration**

- provided funds toward construction of the pilot technology park building and development of the incubator space in the building.

Efforts are ongoing to secure new industry partners, including:

- Major corporations
- Small technology-based businesses

**B. Relevant R&D focus.**

The research programs that were supported are relevant to seven of the eight “thrust areas” of ONR’s Code 30 Science and Technology Program. The projects involved basic research in these areas, as well as applied research and development leading to more immediate technological applications. The seven areas of relevance and the more specific focus areas to which the research contributed are listed below:

**Command, Control, Computers and Communication (C4):** situational awareness; communications; knowledge management; autonomous systems; data acquisition; reconnaissance.

**Force Protection:** seismic analysis and design; new materials; emergency response shelters; autonomous robots; path-following algorithms and performance optimization; feature selection and boosted classification algorithms for human detection.

**Human Social, Cultural and Behavioral Sciences:**

**Human Performance, Training and Education:** cognitive performance enhancement; physical performance enhancement; sensors; biological stress reactions; biomarkers; injury repair; improved materials and processes for use on military bases and in the field.

**Intelligence, Surveillance and Reconnaissance:** data acquisition; sensors; autonomous vehicles; imaging technologies.

**Logistics:** alternative energy sources; cold-chain packaging and logistics; new technologies and materials.

**Maneuver:** advanced design and materials for vehicles.

**C. University-industry-government partnership.**

The primary focus of this long-term initiative is to forge a strong link between private sector R&D and University applied research to speed the development of new knowledge and the transfer of technology to the public and private sectors. San Luis Obispo has become a draw for technology businesses (with a heavy concentration of software development companies) from both the LA Basin and Silicon Valley. For example, SRI (Stanford Research Institute), International operates a "software center of excellence" in the city. Lockheed-Martin has a research and development group in nearby Santa Maria, and EADS-North America recently established a research and development operation on the campus of Cal Poly, affiliated with C3RP and the Cal Poly Technology Park programs. Two local companies manufactured critical components for the Mars rovers, and other companies, e.g. California Fine Wire, Aeromech, and CDM Technologies are suppliers to the military. Also located on the Central Coast are branches of two major biotechnology companies: Promega Biosciences and Santa Cruz Biotechnology.

**D. University strengths.**

Cal Poly is a State university that has achieved national distinction as a polytechnic university, with engineering and computer science programs ranked among the very best undergraduate programs in the country. Its strengths have led it to orchestrate the research partnership effort and the consortium of partners described herein. Cal Poly also has affiliations with CSA (California Space Authority) and with Vandenberg Air Force Base, where it recently participated in the Glory Mission. In the past, Cal Poly offered an MS in Aerospace Engineering at Vandenberg through distance learning and has the capability to offer other academic programs in remote locations. In particular, through possible collaborative agreements at cable-head locations around the world (including

Asia and Europe) our programs could be made available to military personnel stationed almost anywhere in the world.

In recent years the University has been hiring more research-oriented faculty and promoting applied research and development. With as many as 50-60 new faculty hires per year over several years, the University is positioned to undertake significant R&D projects for government and industry. C<sup>3</sup>RP has provided needed support and infrastructure for many of these faculty, which has enabled them to develop ongoing research programs. **Since 7/1/02 faculty who received research support through C<sup>3</sup>RP have secured >\$7.1 of competitive funding for each \$1 of C<sup>3</sup>RP funding invested in them.**

Cal Poly also has a highly qualified student body with entering credentials comparable to students who attend the highest ranked campuses of the University of California. Our students gain valuable experience working with faculty on externally sponsored research projects.

A hallmark of Cal Poly is its extensive network of industry partners. The President's Cabinet consists of more than 30 major corporate and business leaders. Each college, and each department within the college, has its own industrial advisory board. Until recently these connections were not exploited to attract industry-sponsored R&D to campus; hence, one of the goals of the C<sup>3</sup>RP partnership is to use these existing relationships with industry to garner support for our R&D efforts. Cal Poly's College of Agriculture, Food and Environmental Science has successfully demonstrated this kind of partnership through its Agricultural Research Initiative. Through this initiative, a consortium of four campuses in the CSU garnered \$5 million a year in on-going funding from the State of California to support agricultural research of interest to the State, with a pledge to raise matching funds from industry. This State and private funding has leveraged additional support from the federal government. Similar new CSU-wide initiatives include the Council on Ocean Affairs, Science and Technology (<http://www.calstate.edu/coast>) and the Water Resources and Policy Initiatives.

As will be seen in the remainder of this report, Cal Poly has extraordinary interdisciplinary technical assets that can be brought to bear on the science and technology issues of importance to ONR.

**In summary**, the California Central Coast Research Partnership has taken advantage of a confluence of factors, including existing and potential relationships, fortuitous technological and economic developments in the region, and a meshing of the research and development interests of the University, the Office of Naval Research, and the private sector. C<sup>3</sup>RP is the vehicle for fully realizing the benefits of the common goals and synergies of the partners and their respective resources.

## IV. Summary of Results During the Period of Performance

### A. General.

The C<sup>3</sup>RP program was originally funded through an award from ONR in FY '02. This report covers an award that began on 01/01/2011 and ended on 12/31/2012. General accomplishments are summarized below. Detailed reports are presented later in the document. An overview of accomplishments during this project period follows:

- Research carried out by the **CADRC (Cooperative Agent Design Research Center)**, of particular interest to ONR and the Marine Corps, was again funded. A detailed report on this project is provided in Section IV.C.1 of this report.
- **New research** has been developed and some research has been continued, including projects with industry collaboration. Projects addressed topics highly relevant to defense and national security, such as data acquisition, imaging and analysis, energy efficiency, communications, command and control, reconnaissance, autonomous vehicles, sensors, robotics, logistics and human performance. Detailed reports of the results of these projects are presented in Section IV.C.2 of this report.
- From July 1, 2002 to December 31, 2013 C<sup>3</sup>RP-supported faculty **received ~\$71million in competitive funding from other sources.**
- **New research capacity was developed**, including new instrumentation and enhanced infrastructure (detailed below in Section IV.B).
- **Information technology infrastructure support** was provided. **Internet2** connectivity was initially acquired for the campus in November 2001, to support current and future research efforts. Internet2 membership and connectivity has continued during this grant period.
- A **database of >85 technology-based companies** that are potential partners in the project and potential research collaborators has been updated. A series of on-campus research forums initiated in 2007 was continued. Companies were invited to campus three times each year to learn about specific University research projects and identify potential areas for collaboration (see Appendix A for examples of forum topics). Several collaborative relationships have developed from these interactions.
- The first **research and development company to be located on campus** in anticipation of the construction of the pilot building for the technology park continues to flourish in the campus environment and has developed research collaborations with faculty in several different disciplines and colleges. These have resulted in federal research grants (USDA and NIH).The company, Applied



Biotechnology Institute, Inc., specializes in the use of genetically modified plants to produce non-food products, for example, industrial enzymes, biochemical reagents and oral vaccines. The presence of the company has spurred faculty to develop research in this area and a specialized research greenhouse supports this developing work. Applied Biotechnology Institute has relocated to the new Technology Park (see below).

- **Cooperative relationships** have been established or renewed with technology companies that are potential research collaborators, including: Arroyo Instruments (LED technology), Avaxia Biologics, Inc. (biotechnology) , Biolargo (biotechnology) , C3 Group (agricultural technologies) Cascade Designs (water treatment), Cerulean Pharmaceutical (animal science), Chandler-May (aerospace), Clorox (consumer products), Cree (LED technology) DayOne Response Inc. (water treatment), Digital West (information technology), EADS & EADS-North America (aerospace, Electricore (technology consortium), , Godiva (packaging technology), Freedom Photonics (communication technologies) Hardy Diagnostics (medical devices), InfoGard (security systems), InfoHealthNetwork (medical devices) Lansmont Corporation (force protection) , Maersk (shipping containers), MicroBioEngineering (algae production), Monsanto (agriculture) OneSys (software), Phillips (lighting), , , Rouch Engineering (underwater vehicles), SeeSmart (LED technology), Specialty Silicon Fabricators (medical devices), Vetel Diagnostics (medical diagnostics), Zodiac Aerospace (aerospace).
- Efforts continue to develop industry partners in the area of **alternative energy and energy efficiency** for the purpose of developing research in this field. Jim Dunning, Project Manager, currently serves on a 9-member board of directors for the Green Coast Alliance, a coalition representing Ventura, Santa Barbara, San Luis Obispo, and Monterey Counties. The alliance was formed to create a framework for innovation, entrepreneurship, economic and workforce development around "green technologies". Through this coalition Mr. Dunning will identify opportunities for collaboration between Cal Poly and business/industry in this important market segment by acting as the interface between the university and interested collaborators. Board membership includes representatives from the Institute for Energy Efficiency, UCSB; Ventura County Economic Development Association; the Community Environmental Council; Pacific Coast Business Times; California Central Coast Research Partnership, Cal Poly; California Lutheran University; Monterey County Business Council; and private businesses.
- The project's leaders have continued to work with other private and government partners to attract research collaborators and support, including the Institute for Energy Efficiency and the Mechanical Engineering Department at the University of California, Santa Barbara, and the Naval Facilities Engineering Command at Port Hueneme.

- During this project period, the **Technology Park** construction was completed and 100% of the space was developed, leased and occupied by 11 private companies, two of which were founded by Cal Poly faculty. Criteria for tenant selection include significant R&D activity in areas that complement Cal Poly's research strengths and a commitment to collaboration with faculty. The following list describes the companies currently in the Technology park:
  1. **Applied Technology Associates** - designs, builds, and manufactures oil-industry technology products;
  2. **Applied Biotechnology Institute** - specializes in plant biotechnology, with extensive experience in products targeted for industrial uses, animal and human health and crop-improvement markets;
  3. **Couto Solutions** - specializes in custom design of social networks for enterprise solutions;
  4. **V Laboratories** - delivers innovative package design, market & supply chain expertise and cutting edge contaminant/composition analysis techniques.
  5. **Platinum Performance** - is a leading provider of nutritional supplements and health education products with particular focus on equine health;
  6. **HT Harvey & Associates** - is an ecological consulting firm with an over 40 year tradition of mixing pure research, applied research and ecological consulting;
  7. **Linkpendium (Incubator)** - is a genealogical web-based startup company that already indexes more than 10,000,000 sources of genealogical information.
  8. **Seven Pinnacles (Incubator)** - provides design services for embedded and mobile platforms
  9. **Mentor eData (Incubator)** - a technology company formed to improve driver performance and safety utilizing cost-effective data capture hardware, sophisticated, and patent-pending analysis techniques.
  10. **Software Inventions (Incubator)** – is a custom software solution provider
  11. **Exploration Sciences (Incubator)** - is a Colorado Nonprofit Corporation, created in 2005 to help advance the application of technology to improve both the scientific exploration of Earth, Oceans and Space and the public's understanding of these activities.

#### **B. Development of new research capacity**

One of the goals of the project was to increase the capacity of the organization to carry out state-of-the-art research in the areas of interest. To this end, specialized instrumentation was acquired and infrastructure was developed, as detailed below.

## 1. Instrumentation.

### Major Instrumentation

Over the last several years Cal Poly has been building the **analytical capability** to do both molecular identification and microscopic structural analysis, applied to a range of research areas in physics, chemistry, biochemistry, biology, biomedical engineering and materials engineering. Molecular identification is an area that has recently evolved from individual component purification and identification to complex mixture handling and deconvolution. It is now possible to analyze a mixture of peptides, and determine their identity given the accurate determination of their mass, as well as to identify small molecules or monomer components in polymers. The second area, structural analysis, is heavily dependent on novel technologies such as atomic force microscopy and different optical microscopes based on fluorescence and laser technology. These technologies provide the capability to query the structure of most organic and inorganic structures.

Instrumentation previously acquired to support research in these two areas is listed below. These instruments have supported various research projects in the C<sup>3</sup>RP program.

#### *Molecular identification and proteomics:*

- Typhoon Variable Mode Scanner and Imager - allows the selection of single spots in 2D gels for latter MS identification.
- HPLC-MS/MS (Chip) - allows the identification of many peptides for proteomics, as well as small molecules or monomer components in polymers.

#### *Structural analysis:*

- Atomic Force Microscope
- Laser Scanning Confocal Microscope

During this grant period we provided on-going repair and maintenance of the above referenced instrumentation, as well as the upgrades described below.

**Multi-photon laser system.** This year, our analytical capability was augmented by the addition of upgrades to the **multi-photon laser system**, a component of the Olympus Laser Scanning Confocal Microscope (LSCM). The existing Olympus FV1000 confocal and multi-photon laser scanning microscope, funded by prior ONR grants to C<sup>3</sup>RP, was upgraded to greatly increase the sensitivity of the imaging system and allow for upright imaging capabilities by the addition of external detectors and an objective-inverter system.

The prior multi-photon system allowed for detection of fluorescent dyes but did not have the necessary sensitivity for detection of auto-fluorescence or low fluorescence concentrations. To allow for this imaging, the system was upgraded with the addition of non-descanned detectors. Non-descanned detectors are a critical component of multi-photon imaging. As a technique providing intrinsic optical sectioning, multi-photon imaging does not require photons to be "de-scanned", that is, passed back through the

scanning mirrors and pinhole of the scanning system. Placement of non-descanned detectors closer to the specimen and avoiding the scan-head components provides a dramatic increase in sensitivity of detection and is a standard capability in multi-photon imaging systems. While our current system had the capability of detecting multi-photon emission signals using the main confocal scan-head, in order to fully utilize the capabilities inherent in multi-photon microscopy, including less photo-bleaching and photo-toxicity, an external detector unit was added to our existing FV1000 MPE system. This provided us with the capability to image deeper into thick specimens with less photo-bleaching and phototoxicity.

In addition we upgraded the system to allow for both upright and inverted microscope imaging. Previously only inverted imaging was allowed. The upgrade added the capability to do whole- animal imaging, which needs to be performed on an upright microscope due to clearance issues and other experimental constraints. Also, the imaging of opaque samples (e.g. whole tissues, wafers, semiconductor materials, etc.) is best performed on an upright system. The upright orientation allows for viewing of the entire specimen area without obstruction from the microscope body. Rather than purchasing an entirely new upright microscope, we upgraded our existing system with an objective inverter adapter added on to the existing objective turret of the multi-photon microscope. This effectively converts the microscope objective from an inverted position to an upright one.

### **Other Instrumentation**

Other research instruments/equipment acquired during this grant period is listed below. Minor instrumentation, acquired for use on individual projects, is described in the reports for those projects.

**Marine Science** – One of the most productive applied research groups at Cal Poly is the Marine Science Group. Cal Poly's Center for Coastal Marine Sciences provides students, faculty and staff with the tools needed to complete their research and education goals. Marine Operations maintains the Cal Poly pier, flowing seawater system, and oversees the Scientific Boating and Scientific Diving Programs, in support of the Center for Coastal Marine Sciences. Through the Scientific Boating Program faculty and researchers have a means of conducting research throughout the nearshore waters of Central and Southern California. During this reporting period Cal Poly augmented the research capability of the Marine Science Group with the purchase of a new research vessel, a 26' deep V mono hull manufactured by Radon Commercial Boats in Goleta, California.

The vessel enables the launching and retrieving of remotely operated vehicles, autonomous underwater vehicles, and gliders, and supports diving teams that are required on such missions. The vessel also adds critical capacity to reach coastal and offshore locations, especially in inclement weather, high winds, and large swells common on the Central Coast of California. The vessel is customized for research activities with features including: diving gate, configured to accept both davit and A-frame attachments, pick

points on the boat used to deploy the vessel with a crane from the pier, and navigation electronics (d-GPS plotter, Fathometer, Radar, VHF radio, Autopilot).

**Micro Systems Technology Research Group.** Many multidisciplinary projects are supported by the Microfabrication Lab, a 1,500 ft<sup>2</sup>, Class-1,000 clean room with a complete set of microfabrication equipment for processing 100mm-size wafers. Equipment for depositing, patterning and etching thin films is available, including: dual-cathode RF/DC sputtering; Thermco Mini-Brute furnaces for oxidation & diffusion; Cannon PLA-501FA mask aligner; Laurel spin-coaters; AGS Plasma S17 RIE plasma etcher; wet benches for etching and spin rinse Ambios XP-1 profilometer; Signatone 4-pt probes and prober; Filmetrics F20 reflectometer; FEI Quanta SEM-EDS; Nicolet FTIR; Asylum MFP-3D AFM; Nanosurf STM; Siemens XRD; Innov-X XRF; and the shared Olympus confocal microscope, described above. This year we supported the following two purchases for the Micro Systems Technology Research Group:

- A **physical vapor deposition system** was purchased and now resides within the Microfabrication Laboratory and provides the ability to deposit thin metal films including NiTi, Cr, Al, NiV, Au, ZnO, and Ti, which are critical layers for fabricating micro scale devices.
- A new probe station was procured that will enable researches to make electrical contacts to microscale structures on devices. Actuation and sensing signals can be sent/received to MEMS devices thru these contacts which enable signal analysis to be performed as part of device characterization.

This new instrumentation, along with existing, supports on-going joint research being conducted by Cal Poly and partners on a number of projects, some of which are summarized below:

- Solid State Lighting: White light LEDs
  - Integration of QDs into PDMS layers that yield white light LEDs
- Solar Cell Arrays
  - Array of micro size solar cells that can serve to power sensors
- Quantum Dots
  - Characterization of reactions to form CdSe QDs as bio-tags for cancer cells
  - Design & fabrication of QD chip for synthesizing QDs on the microliter level
- MEMS Sensors & Actuators
  - Fabrication of microfluidic lab-on-a chip-devices
  - ZnO based piezoelectric speaker for hearing aids
  - Design and fabrication of electrostatically actuated optical switch
  - Artificial Muscle Project: dielectric electro-active polymer (PDMS)



**Biofuels.** Cal Poly purchased three major pieces of equipment to support biofuels research campus-wide. The instruments are housed in the Civil and Environmental Engineering Department where extensive research is done on algae biofuels and anaerobic digestion of various wastes substrates. Other departments planning to use this new equipment are Chemistry, Dairy Science, and Biological Sciences.

Anaerobic digestion breaks down organic wastes into methane and carbon dioxide and is an important research and development topic for renewable energy production and greenhouse gas emissions reduction. **Gas Chromatograph.** The purchase of the Trace 1300 gas chromatograph from ThermoFisher allows for analysis of the constituents in biogas. It can measure hydrogen, nitrogen, oxygen, methane, carbon dioxide, hydrogen sulfide, and nitrous oxide. For biogas analysis the determination of hydrogen, methane, and carbon dioxide are important for determining biogas yields and digester productivity. Hydrogen sulfide is an important natural contaminant of biogas that can corrode biogas generators, and determining the concentration is important to determining what biogas per-treatment devices may be needed before combustion in an engine generator or boiler. As the primary atmospheric gases, oxygen or nitrogen in the biogas can indicate significant leaks in an anaerobic system. As a powerful greenhouse gas, the determination of nitrous oxide emissions from aerobic treatment systems can be an important factor in determining net positive or negative effect on greenhouse gas emissions for that treatment system. The Trace 1300 is pictured below:



**Solvent Extractor & Lyophilizer.** For liquid biofuel research, two important pieces of equipment have been purchased: a Dionex ASE 350 automated solvent extractor and Labconco FreeZone 2.5 lyophilizer. These items can serve a multitude of research purposes at Cal Poly, but they go a long way toward expanding biofuel development capabilities in particular. The ASE 350 rapidly extracts oil samples from a wide variety of plant and other materials. Assessing oil production is critical in biofuels and by speeding oil extractions to a fraction of the time required to extract by hand, the ASE will allow Cal Poly researchers to screen many more samples. The consistency of automated extraction means that not only will the ASE increase the volume of data produced, it will improve the quality of the data as well. The ASE is pictured below:





The Labconco FreeZone 2.5 is a lyophilizer used for freeze drying sample materials. Removing water from samples is a requirement of many assays including many types of lipid analysis, protein analysis, genetic analysis, etc. For example, algae biomass samples to be analyzed in the ASE, above, will first be freeze dried in the FreeZone unit. When samples are dried at very low temperatures, heat degradation is eliminated, improving the quality of the data and in many cases, preserving crucial analytes. Freeze dried samples can also be stored and transported much more easily than untreated samples. This means that Cal Poly researchers can store samples without fear of reduced data fidelity, and they can also exchange preserved samples with other research organizations, further increasing the number of analyses available for use and expanding opportunities for collaboration. The base unit of the FreeZone system is pictured below:



Together these three major equipment purchases have greatly expanded Cal Poly's research capabilities in the area of biofuel and other research areas.

## **2. Infrastructure.**

Details are provided in Section IV.C.2.

### **C. Detailed research reports**

The remainder of this report contains detailed individual reports of the technical results of the research projects carried out during this project period. They are presented in the following order:

#### **1. Collaborative Agent Design Research Center (CADRC) project report**

#### **2. Other research project reports**

Representative publications resulting from this work and documents that supplement the reports are included in Appendix B.

**Partnering Enhanced-NLP with Semantic Analysis In Support of  
Information Extraction**

**Collaborative Agent Design Research Center (CADRC)**

Principal Investigators:

**Hisham Assal, Ph.D., Collaborative Agent Design Research Center (CADRC)**

**John Seng, Ph.D., Computer Science**

**Franz Kurfess, Ph. D. Computer Science**

**Emily Schwarz, Master Student Computer Science**

California Polytechnic State University  
San Luis Obispo, CA

## **Executive Summary**

Natural Language Processing (NLP) provides tools to extract explicitly stated information from text documents. These tools include Named Entity Recognition (NER) and Parts-Of-Speech (POS). The extracted information represents discrete entities in the text and some relationships that may exist among them. To perform intelligent analysis on the extracted information a context has to exist, in which this information is placed. The context provides an environment to link information that is extracted from multiple documents and offers a big picture of the domain. Analysis can then be provided by adding inference capabilities to the environment. The ODIX platform provides an environment for bringing together information extraction, ontology and intelligent analysis. The platform design relies on existing NLP tools to provide the information extraction capabilities. It also utilizes a web crawler to collect text documents from the web. The context is provided by a domain ontology that is loaded at run time. The ontology offers limited inference capabilities and external intelligent agents offer more advanced reasoning capabilities. User involvement is key to the success of the analysis process. At every step of the process the user has the opportunity to direct the system, set selection criteria, correct errors, or add additional information.

The ODIX platform was extended in this phase to implement a domain-specific ontology in the area of intelligence analysis with a focus on terrorist organizations and financial institutions and the relationships that may exist between them through participation in common events or direct communication between members of each group. Another extension was the inclusion of agents, which perform inference to expand the knowledge base by running two types of rule sets, internal and external. Internal rules are built into the ontology and help expand the definition of instances and make them more specific. For example, the definition of a person who is a member of a terrorist organization can be specialized into a 'terrorist' to help further inference. External rules relate a group of ontology objects together to perform a more general inference. For example, a communication event between a 'terrorist' and a member of a financial institution can result in suspicions of a terrorist plot in the making. The third enhancement to ODIX was the deployment to remote servers with the ability to run components on multiple servers in multiple locations. The result of this enhancement is the ability to handle larger demand on the system and the ability to configure services to take advantage of the available resources.

## **1. Background**

The use of information extraction technology can provide benefits in processing large volumes of text documents and organize or categorize the information. To provide meaningful use of the extracted information it has to be placed in a larger context, which describes the role of every piece of information in the domain. This domain context can also provide help in extracting information from documents and organizing it. The bidirectional relationship between the domain context and the extraction process is necessary for the accuracy and relevance of the extracted information.

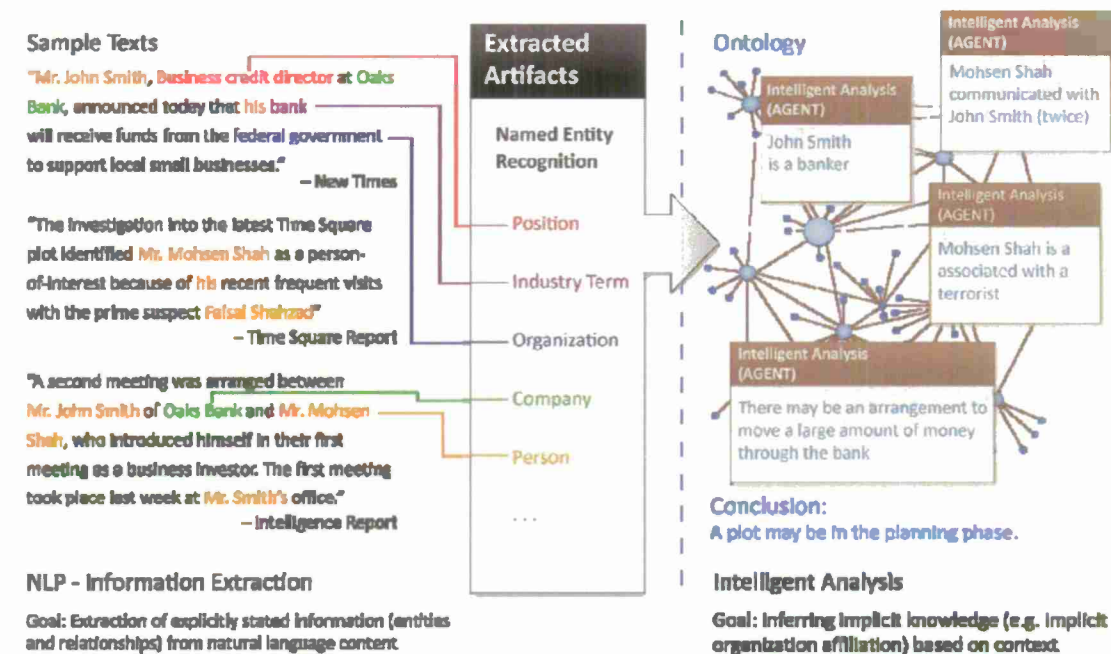


Figure 1: From Text to Ontology

The vision of this research work relies on an ontology to provide the context, i.e. the bigger picture, and to be a medium for performing intelligent analysis. A domain ontology describes the entities in the domain and how they relate. The ontology may also include some rules on how new entities emerge or constraints on the way entities relate to each other. Given this detailed description of the domain in terms of its entities and their behavior, a context now exists for the information coming out of this domain. Figure 1 depicts the intended outcome of the system.

Another aspect of the vision is the ability to process the extracted information in an intelligent way. The sophisticated structures of the ontology, along with the rules that describe their behavior offer an opportunity to perform inference on the existing information, which may lead to producing new information.

The ontology can play a guiding role in the extraction and interpretation of information. The entities in the ontology can serve as a target for the extraction process. The extraction tools can take a set of entity types from the ontology and process the repository documents for entities that fit the description of the ontology entities. This can make the extraction process more efficient and more accurate. The ontology structure provides guidance for the types of other entities that may be connected to any given entity to make the extraction process more comprehensive.

A key aspect of the vision is the user opportunity for involvement in every step of the process from extraction to interpretation, ontology population, inference and request for additional information. The interpretation of textual material in natural language is ambiguous and requires user knowledge of the domain to double check the automated work of the system for accuracy and relevance. The user can also provide guidance to the extraction process in the form of rules of extraction (in rule-based extraction) or for adjusting the results of training data (in statistical approaches).

The processing of extracted information may expose the need for more information, which guides the extraction process to look for specific types of entities. The emergence of new entities in the ontology as a result of inference may also trigger the need for more extractions. This iterative nature of the process, along with user involvement is essential to producing meaningful results and can support the complex analysis work for the user.

The objective of the research is to produce a generic platform, which can be configured with external services and a domain ontology to suit the needs of different types of users. There are existing services that provide some of the needed functionality, such as crawling the web for information that fit given criteria, or extracting generic information from plain text documents. It is important for the success of this system to allow the integration of external services and provide tools to process their results into the domain ontology.

## **2. Previous Work**

The ODIK platform resulted from earlier work under the C3RP grant, which produced a general purpose system that can perform information extraction on a collection of articles from the world-wide web. The system allowed the dynamic loading of ontologies at run-time and offered a set of tools to assist in the interpretation of the extracted information. The focus of the research in the previous work was the system level design and implementation. The natural language processing (NLP) tools were developed and compiled together to provide the NLP service, which is the main information extraction service. The model service was developed to allow the dynamic loading of domain ontology at run-time.

The primary components of the system are architected as services that offer the flexibility and agility inherent in Service-Oriented Architecture (SOA) designs. The decision to architect the information extraction capability in a service-oriented manner was twofold. First, the extraction of information is an activity that is intended to be invoked on a repetitive basis by numerous external users as a part of their larger business processes. As such, it is useful to deploy the information extraction capability as a whole in the form of a discoverable and subsequently invocable service that adheres to applicable web service standards. Second, the designers felt it useful to have the ability to easily exchange select components of what amounts to a multi-faceted capability with alternative solutions in an effort to experiment with effectiveness and performance. As such, it seemed advantageous to carry the service-oriented concept into the internal architecture as well. It was anticipated that doing so would produce a test bed-like environment where internal capabilities were extensively decoupled and primed for potential replacement or partnering with additional, complementary capabilities.

### ***NLP Service***

For our work, we utilize the Unstructured Information Management Architecture (UIMA) document processing framework. This framework handles multiple documents and allows our application to process and annotate several documents during each stage of our information extraction task. The UIMA architecture provides facilities that allow the creation of individual annotators which can be used to perform specific NLP tasks. In our work, we create an annotator to identify if a particular name in a document is the name of a known terrorist.

For the task of information extraction, we utilize the OpenCalais service provided by Thomson Reuters. This service takes individual documents as input and provides an RDF file which labels several various entities and relationships. In our application, we focus on the following entities and relationships provided by OpenCalais: *PersonCareer*,



PersonCommunication, PersonRelation, and FinancialInstitution. PersonCareer defines the relationship that a person was or currently is an employee of a particular institution. PersonCommunication defines the event that two people plan to communicate with each other. PersonRelation declares that a type of relationship exists between two people. FinancialInstitution is an entity that OpenCalais believes is a financial institution.

**1. Al-Qaeda's top commander Osama bin Laden**

**Extraction rule:** (terrorist\_organization + "\s+" + adjectives + "\s+)" + person\_role + "\s+" + person)

**2. Osama bin Laden, the top Al-Qaeda commander**

**Extraction rule:** (person + ",\s+(a|an|the)\s+" + adjectives + "\s+)" + terrorist\_organization + "\s+" + person\_role)

*Figure 2: Extraction example*

Using the extracted entities and relationship that OpenCalais provides for each document, we aggregate the common occurrences across several documents and tabulate the frequency of these occurrences. This information, along with the information extracted from the rule-based UIMA terrorist annotator, shown in figure 2, is combined and an RDF file is created which contains all of the assertions.

## **Model Service**

The Model Service is SOAP web service that hosts the ontology management component of our system. Jena is used as the primary tool for managing and persisting the ontology. Jena's SQL-based storage allows the ontology to be saved over multiple web sessions. This service contains functionality for loading a domain-specific ontology. This ontology forms the heart of the knowledge representation for the system.

The Model Service also contains the translation functionality to both import extractions from the NLP component and export selected knowledge to the user interface. An importation process is necessary because the NLP extractions are built around the OpenCalais rather than the domain-specific ontology. While it may seem like extra work to translate out of the ontology of the NLP, this process enforces flexibility within the system. It is possible for the Model Service to be configured to read multiple NLP extractions with different underlying ontologies. Likewise, this allows a single configuration of the NLP Service to create extractions for several Model Services, all with different domain-specific ontologies.

While Jena provides a number of options for exporting ontologies, it was also necessary to create a separate export functionality for interfacing with the user interface component. This is because the user interface requires a general object based XML format, and will not accept RDF/XML. This is a common problem for interoperability between ontologies and web services and is discussed in [Akhtar, et al. 2008]. Our export solution uses a combination of XML templates and SPARQL queries.

### 3. Platform Enhancements

In this research, the platform was extended in a number of ways to allow for the implementation of the selected use case, which is the identification of potential terrorist plots through the communication between members of terrorist organizations and members of financial institutions. The enhancements include a domain-specific ontology for the selected use case, provenance to keep track of the source of information and assign a certainty level with each source, and intelligent agents to perform the inference. Another enhancement was to deploy the platform to the remote servers at the Knowledge Management Laboratory (KML), to test the validity of running the system in the cloud.

#### *Domain-specific Ontology*

An ontology of organizations, events, and communications was developed to describe the relationships that may exist between organizations. The main types in the ontology included people, organizations, and events. The main types of relationships include membership in organizations and communications among people. The ontology focuses on two types of organizations, terrorist and financial. Other organization types can be used, but the support in the inference mechanisms is only available to those two types of organizations.

#### *Provenance*

Our method for data extraction through NLP can be applied to a variety of textual sources, possibly obtained through the Web. We cannot guarantee the veracity of these sources, so our system must have the capability to record and manage the trustworthiness of the extraction. For our application, provenance is the process of tracking the source or derivation of a fact within the assertion component (ABox) of our ontology.

To establish provenance, all facts imported from the NLP are connected to a source object via RDF reification. The contents of the source object for NLP imported facts include the name of the file and the offset and length of where the extraction occurred. This information could be supplemented with additional facts relating to a measure of the trustworthiness of the source, confidence in the NLP extraction, or other metadata relating to the fact. All facts are RDF reified since facts relating to the same individual do not necessarily come from the same NLP extraction.

During reasoning, additional source objects are asserted to maintain provenance. Rather than having a source article, these source objects relate the new fact to the ABox facts that were used to derive it, as well as the terminology component (TBox) facts that triggered the reasoning. This ensures that an ABox fact always have source information, regardless of whether it was extracted directly or inferred. We achieve this through a modified version of Jena's OWL inference rules by adding the source manipulation and creation components to the rules themselves. This is a highly experimental approach, although it is similar to [Vacura and Svatek 2010]. Unlike their approach, our method restricts provenance to the ABox, and thus requires no additional management outside of a modified rule set. Since RDF reification creates an explosion of additional facts within the ontology, we believe this approach will be best suited to environments that handle named triples without reification, such as BigOWLIM.

Figure 3 shows an example of inference and attached source information.

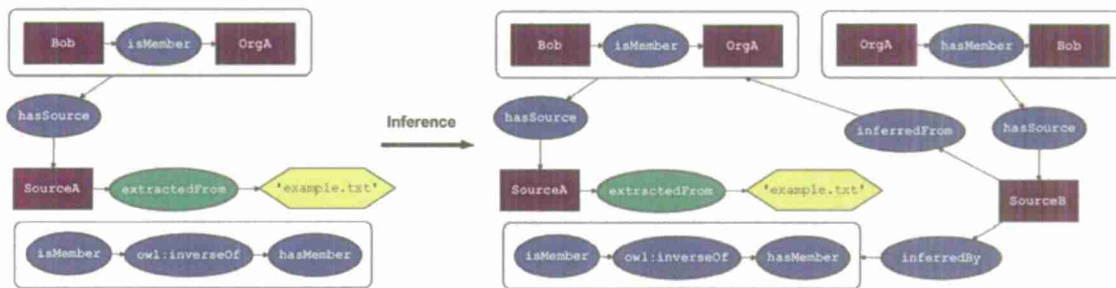


Figure 3: Example Inference

### Intelligent Agents

The ontology in the ODIX platform is built using the OWL environment, which provides inference capabilities, expanding the definitions of ontology objects and allowing re-classification of existing objects. Other inference capabilities were added to the platform by developing external intelligent agents that operated on the OWL model. The use of external agents allows the development of more sophisticated rules, which relate objects of different types in patterns that describe a complex situation. The external rules are loaded through the user interface and many external rule files can be added at run-time.

### Deployment to the cloud

The SOA design of the platform makes possible to deploy the system in a distributed fashion. Running in a 'Cloud' environment offers opportunities to use the platform in different ways. The individual services can be made available to other applications or can be configured in different ways according to the needs of a specific project. The cloud environment offers services that can be shared by many applications, such security, single sign-on, intelligent routing, load balancing and location transparency. The benefits of a cloud environment include high availability and handling large volumes of data.

The ODIX platform was deployed into two environments, locally at Cal Poly on a virtual machine provided by the computer science department, and remotely on KML servers. The KML environment consisted of a number of blade servers hosting virtualization software. The ODIX platform used two virtual machines on the KML environment and were accessed and managed remotely. The configuration of the platform allowed some services to run on Cal Poly servers while others ran on KML servers for the same session.

## 4. Domain Adaptation

The ODIX platform is designed to support the implementation of many domains with the flexibility to provide inference capabilities to any given ontology. The development of a domain-specific system on the ODIX platform requires additional development and configuration tasks.

The first task is to develop a domain ontology, which describes the objects of interest in the given domain and the relationships that exist among them, thus defining the context for the application. The domain ontology may also include basic rules of inference, which determine class membership for objects, or simple property chain inference. An important aspect of the ontology development is to define the types of queries that are needed by the user interface and provide support for fulfilling such queries in a user-friendly manner.

The second task is to develop intelligent agents, which provide the required analysis. Agents operate on ontology objects and need to be aware of the ontology structure. Agent analysis is defined by the requirements for the application.

In addition to development tasks, some configuration may need to take place on the platform. Extraction rules, for example, help classify some of the extracted entities into more specific classes based on the role they play in the text. For example, the role of a person in an organization, or the classification of an organization as a terrorist organization can be defined by extraction rules, which can be added to the platform or even loaded at run-time.

Another configuration element is lists of known entities that may be helpful for the extraction process. For example, in a financial system, a list of known financial institutions and their classification can be added to the platform and used at run-time to identify extracted entities.

Other configuration elements can be added to help fine tune user interaction with the system.

## 5. Published work

The work under this C3RP grant was published and presented in many conferences. The first conference was the ACM Splash conference, 2010. The presentation was made to the 2<sup>nd</sup> International Workshop on Ontology-Driven Software Engineering (ODiSE 2010) at the ACM SPLASH 2010 Conference and the paper was published in the conference proceedings online.

*Hisham Assal, John Seng, Franz Kurfess, Emily Schwarz, and Kym Pohl.*  
2010. Partnering enhanced-NLP with semantic analysis in support of information extraction. In *Ontology-Driven Software Engineering (ODiSE'10)*. ACM, New York, NY, USA, , Article 9 , 7 pages. DOI=10.1145/1937128.1937137  
<http://doi.acm.org/10.1145/1937128.1937137>

The work was then presented to the IEEE Aerospace conference in 2011 and the paper was published in its proceedings.

*Hisham Assal, John Seng, Franz Kurfess, Emily Schwarz, and Kym Pohl.*  
2011. Semantically-enhanced information extraction. In *Proceedings of the 2011 IEEE Aerospace Conference (AERO '11)*. IEEE Computer Society, Washington, DC, USA, 1-14. DOI=10.1109/AERO.2011.5747547  
<http://dx.doi.org/10.1109/AERO.2011.5747547>

In June 2011, Franz Kurfess organized a discussion session and presented a tutorial at the Semantic Technologies conference in San Francisco.

*Kurfess, F. J. (2011a).* Combining ontologies and natural language processing for knowledge retrieval. Discussion session at the 2011 Semantic Technology Conference, San Francisco, CA. [SemanticWeb.com](http://SemanticWeb.com).

*Kurfess, F. J. (2011b).* Computers and knowledge. Tutorial, 2011 Semantic Technology Conference, San Francisco, CA. [SemanticWeb.com](http://SemanticWeb.com).

In August, 2011 the United States Transportation Command (USTRANSCOM) held a summit on Documents and Data. The ODIX platform was presented in this workshop and included in the summit proceedings.



The project team was invited to submit a book chapter on the ODIX platform to the book: '*Advancing Information Management through Semantic Web Concepts and Ontologies*', published in November 2012 by IGI-Global. The chapter title is '*Enhancing Information Extraction with Context and Inference: The ODIX Platform*' <http://www.igi-global.com/chapter/enhancing-information-extraction-context-inference/71857>

## BIBLIOGRAPHY

- Auer S, Lehmann J (01 2010) Creating knowledge out of interlinked data. *Semantic Web* 1(1):97–104
- Banko, M., Cafarella, M. J., Soderland, S., Broadhead, M., & Etzioni, O. (2007). Open Information Extraction From The Web. *IJCAI 07: Proceedings Of The 20th International Joint Conference On Artificial Intelligence* (p. 2670–2676). San Francisco, CA, USA: Morgan Kaufmann Publishers Inc.
- Baeza-Yates, R., & Ribeiro-Neto, B. (2011). *Modern Information Retrieval: The Concepts and Technology behind Search* (2nd Edition) (2nd ed.). Addison-Wesley Professional.
- Belew, R. (2000). *Finding out about: a cognitive perspective on search engine technology and the WWW*. Cambridge U.K. Cambridge University Press.
- Berners-Lee T., Hendler J., Lassila O. (2001) The Semantic Web. *Scientific American* 284(5):34-43
- Bush V. (1945) As We May Think. *The Atlantic Monthly* 176(1):101-108
- Fowler, M. (1997); *Analysis Patterns, Reusable Object Models*; Addison Wesley Longman
- Giarratano J.C., Riley G.D. (2005). *Expert Systems: Principles and Programming*. Pacific Grove, CA, USA: Brooks/Cole Publishing Co..
- Hepp, M., De Leenheer, P., de Moor, A., *Ontology Management: Semantic Web, Semantic Web Services, and Business Applications*, Springer, 2007.
- Lin, T., Etzioni, O., and Fogarty, J. (2009). Identifying Interesting Assertions From The Web. In *CIKM '09: Proceeding of the 18th ACM Conference On Information And Knowledge Management*, pages 1787–1790, New York, NY, USA. 2009.
- Manning, C. D., Raghavan, P., & Schütze, H. (2008). *Introduction to Information Retrieval* (1st ed.). Cambridge University Press.
- Moens, M. *Information Extraction: Algorithms and Prospects in a Retrieval Context*. Springer-Verlag, 2003.
- Vargas-Vera, M., Domingue, J., Motta, E., Buckingham Shum, S. and Lanzoni, M. (2001) Knowledge Extraction by using an Ontology based Annotation Tool, *Proceedings of the Workshop on Knowledge Markup and Semantic Annotation (K CAPA'01)*, Victoria, Canada
- Weikum, G., & Theobald, M. (2010). From information to knowledge: harvesting entities and relationships from web sources. *Proceedings of the twenty-ninth ACM SIGMOD-SIGACT-SIGART symposium on Principles of database systems of data* (p. 65–76). New York, NY, USA: ACM. DOI:<http://doi.acm.org/10.1145/1807085.1807097>
- Pohl K. (2006); '*Perspective Models as a Means for Achieving True Representational Accuracy*'; IEEE Aerospace Conference, Big Sky, Montana, March 4-11.

- Russell S., Norvig P. (2009) *Artificial Intelligence: A Modern Approach* (3rd edition) . Upper Saddle River, NJ, USA: Prentice Hall Press.
- Schmitt, E. (2010).U.S. Tells WikiLeaks to Return Afghan War Logs. New York Times, <http://www.nytimes.com/2010/08/06/world/asia/06wiki.html>; August 5, 2010
- Vacura M. and Svatek V. (2010), *Ontology Based Tracking and Propagation of Provenance NDT 2010*, Part I, CCIS 87, pp. 489–496
- Wang J., Ding Z., Jiang C. (2005) *An Ontology-based Public Transport Query System*. International Conference on Semantics, Knowledge and Grid (SKG 2005), IEEE Computer Society.
- Wikileaks (2010).Afghan War Diary. Wikileaks Organization, [http://wikileaks.org/wiki/Afghan\\_War\\_Diary,\\_2004-2010](http://wikileaks.org/wiki/Afghan_War_Diary,_2004-2010); accessed Aug. 2010
- Wimalasuriya, D. C. and Dou, D. (2010). Ontology-based information extraction: An introduction and a survey of current approaches. *Journal of Information Science* 36(3):306–32.
- Yates, A., Cafarella, M., Banko, M., Etzioni, O., Broadhead, Matthew, &Soderland, S. (2007).TextRunner: Open Information Extraction On The Web. *NAACL 2007: Proceedings of Human Language Technologies: The Annual Conference of the North American Chapter of the Association for Computational Linguistics*. (p. 25–26). Morristown, NJ, USA.

## FURTHER READING

### Ontology

- Alves, A., Antunes, B., Pereira, F. C., & Bento, C. (2009). Semantic enrichment of places: Ontology learning from web. *International Journal of Knowledge-Based and Intelligent Engineering Systems*, 13(1), 19-30.DOI:10.3233/KES-2009-0170
- Cho, W. C., & Richards, D. (2007). Ontology construction and concept reuse with formal concept analysis for improved web document retrieval. *Web Intelligence and Agent Systems*, 5(1), 109-126. Retrieved from <http://iospress.metapress.com/content/187272723XUL1571>
- Janowicz, K. (2010). The role of space and time for knowledge organization on the Semantic Web. *Semantic Web*, 1(1), 25-32.DOI:10.3233/SW-2010-0001
- Ríos, S. A., Velásquez, J. D., Yasuda, H., & Aoki, T. (2006). A hybrid system for concept-based web usage mining. *International Journal of Hybrid Intelligent Systems*, 3(4), 219-235. Retrieved from <http://iospress.metapress.com/content/6JB1PJ9VVF5F0TW0>
- Roberson S., Dicheva D. (2007) *Semi-automatic ontology extraction to create draft topic maps*. In: *Proceedings of the 45th annual southeast regional conference*. New York, NY, USA: ACM. 100–105
- Robinson, E. H. (2010). An ontological analysis of states: Organizations vs. legal persons. *Applied Ontology*, 5(2), 109-125.DOI:10.3233/AO-2010-0077
- Sánchez, D., & Moreno, A. (2006). A methodology for knowledge acquisition from the web. *International Journal of Knowledge-Based and Intelligent Engineering Systems*, 10(6), 453-475. Retrieved from <http://iospress.metapress.com/content/9JKFKC0T84Y8A4KI>
- Spyns, P., Tang, Y., & Meersman, R. (2008). An ontology engineering methodology for DOGMA. *Applied Ontology*, 3(1), 13-39.DOI:10.3233/AO-2008-0047



White R., Roth R. (2008) *Exploratory Search*. Morgan & Claypool Publishers.

Wong, T.-L., Lam, W., & Chen, E. (2005). Automatic Domain Ontology Generation From Web Sites. *Journal of Integrated Design and Process Science*, 9(3), 29-38. Retrieved from <http://iospress.metapress.com/content/EA W8X83GFBQ3FYCQ>

### **Information Extraction**

Bawden, D., & Robinson, L. (2008). The dark side of information: overload, anxiety and other paradoxes and pathologies. *Journal of Information Science*, 35(2), 180-191. DOI:10.1177/0165551508095781

Croft, B., Metzler, D., & Strohmman, T. (2009). *Search Engines: Information Retrieval in Practice* (1st ed.). Addison Wesley.

Dejing Dou. (2010). Ontology-based information extraction: An introduction and a survey of current approaches. *Journal of Information Science*, 36(3), 306–323. DOI:<http://dx.doi.org/10.1177/0165551509360123>

Konchady, M. (2006). *Text Mining Application Programming* (1st ed.). Charles River Media.

Witte, R., Krestel, R., Kappler, T., & Lockemann, P. (2009). Converting a Historical Encyclopedia of Architecture into a Semantic Knowledge Base. *IEEE Intelligent Systems*. DOI:10.1109/MIS.2009.83

Zhu, J., Nie, Z., Liu, X., Zhang, B., & Wen, J.-rong. (2009). StatSnowball: a Statistical Approach to Extracting Entity Relationships. *WWW 2009 MADRID - Track: Data Mining / Session: Statistical Methods*.

### **Natural Language Processing (NLP)**

Durville, P., & Gandon, F. (2009). Filling the Gap between Web 2.0 Technologies and Natural Language Processing Pipelines with Semantic Web. *Advances in Semantic Processing, International Conference on*, 109-112. DOI:<http://doi.ieeecomputersociety.org/10.1109/SEMAPRO.2009.23>

Feldman, R., & Sanger, J. (2006). *The Text Mining Handbook: Advanced Approaches in Analyzing Unstructured Data*. Cambridge University Press.

Li, S.-T., & Tsai, F.-C. (2010). Constructing tree-based knowledge structures from text corpus. *Applied Intelligence*, 1-12. Retrieved from <http://dx.doi.org/10.1007/s10489-010-0243-2>

Marmanis, H., & Babenko, D. (2009). *Algorithms of the Intelligent Web* (1st ed.). Manning Publications.

Polleres, A., Hogan, A., Harth, A., & Decker, S. (2010). Can we ever catch up with the Web? *Semantic Web*, 1(1), 45-52. DOI:10.3233/SW-2010-0016

Preda, N., Kasneci, G., Suchanek, F. M., Neumann, T., Yuan, W., & Weikum, G. (2010). Active knowledge: dynamically enriching RDF knowledge bases by web services. *SIGMOD 2010: Proceedings of the 2010 international conference on Management of data* (p. 399–410). New York, NY, USA: ACM. DOI:<http://doi.acm.org/10.1145/1807167.1807212>

### **Agent-based systems and Multi-agent systems**

Bellifemine, F. L., Caire, G., & Greenwood, D. (2007). *Developing Multi-Agent Systems with JADE*. Wiley.

- Bordini, R. H., Dastani, M., Dix, J., & Seghrouchni, A. E. F. (2006). *Programming Multi-Agent Systems: Third International Workshop, ProMAS 2005, Utrecht, The Netherlands, July 26, 2005, Revised and Invited Papers* (1st ed.). Springer.
- Bordini, R. H., Dastani, M., & Seghrouchni, A. E. F. (2010). *Multi-Agent Programming: Languages, Platforms and Applications* (1st ed.). Springer.
- Buse, D. P., & Wu, Q. (2010). *IP Network-based Multi-agent Systems for Industrial Automation: Information Management, Condition Monitoring and Control of Power Systems* (1st ed.). Springer.
- Carvey, P. M. (1998). *Drug Action in the Central Nervous System* (1st ed.). Oxford University Press, USA.
- Chen, S., Terano, T., & Yamamoto, R. (2011). *Agent-Based Approaches in Economic and Social Complex Systems VI: Post-Proceedings of The AESCS International Workshop 2009* (1st ed.). Springer.
- Choren, R., Garcia, A., Lucena, C., & Romanovsky, A. (2005). *Software Engineering for Multi-Agent Systems III: Research Issues and Practical Applications* (1st ed.). Springer.
- d'Inverno, M., & Luck, M. (2010). *Understanding Agent Systems* (2nd ed.). Springer.
- Dunin-Keplicz, B. M., & Verbrugge, R. (2010). *Teamwork in Multi-Agent Systems: A Formal Approach* (1st ed.). Wiley.
- Edmonds, B., & Moss, S. (2011). *Simulating Social Complexity: A Handbook* (1st ed.). Springer.
- Ferber, J. (1999). *Multi-agent systems: An introduction to distributed artificial intelligence*. Addison-Wesley Professional.
- Kanegsberg, B., & Kanegsberg, E. (2011). *Handbook for Critical Cleaning: Cleaning Agents and Systems, Second Edition* (1st ed.). CRC Press.
- Klusch, M., Ossowski, S., & Shehory, O. (2002). *Cooperative Information Agents VI: 6th International Workshop, CIA 2002, Madrid, Spain, September 18 - 20, 2002. Proceedings (Lecture Notes in Computer ... Notes in Artificial Intelligence)* (1st ed.). Springer.
- Lin, H. (2007). *Architectural Design of Multi-Agent Systems: Technologies and Techniques* (1st ed.). IGI Global.
- Luck, M., Ashri, R., & d'Inverno, M. (2004). *Agent-Based Software Development*. Artech House Publishers.
- Navarro, V. J. B., & Boggino, A. G. (2008). *ANEMONA: A Multi-agent Methodology for Holonic Manufacturing Systems* (1st ed.). Springer.
- Padgham, L., & Winikoff, M. (2004). *Developing Intelligent Agent Systems: A Practical Guide*. Wiley.
- Rehtanz, C. (2010). *Autonomous Systems and Intelligent Agents in Power System Control and Operation* (1st ed.). Springer.
- Shoham, Y., & Leyton-Brown, K. (2008). *Multiagent Systems: Algorithmic, Game-Theoretic, and Logical Foundations*. Cambridge University Press.

- Symeonidis, A. L., & Mitkas, P. A. (2011). *Agent Intelligence Through Data Mining* (1st ed.). Springer.
- Uhrmacher, A. M., & Weyns, D. (2009). *Multi-Agent Systems: Simulation and Applications*. CRC Press.
- Wagner, T. A. (2004). *An Application Science for Multi-Agent Systems* (1st ed.). Springer.
- Weiss, G. (2000). *Multiagent Systems: A Modern Approach to Distributed Artificial Intelligence* (New edition.). The MIT Press.
- Weyns, D. (2010). *Architecture-Based Design of Multi-Agent Systems* (1st ed.). Springer.
- Wooldridge, M. (2009a). *An Introduction to MultiAgent Systems* (2nd ed.). Wiley.
- Zhang, Z., & Zhang, C. (2004). *Agent-Based Hybrid Intelligent Systems: An Agent-Based Framework for Complex Problem Solving* (1st ed.). Springer.

### Key terms and definitions:

**Ontology**: a formal representation of knowledge as a set of concepts within a domain, and the relationships between those concepts. It is used to reason about the entities within that domain, and may be used to describe the domain.

**Agent-Based Systems**: a system of interacting intelligent agents, embedded within an ontology or information model.

**Information Extraction** (IR): the process of extracting entities and relationships from unstructured documents.

**Knowledge Extraction**: the process of extracting information within a given context, which serves to clarify and disambiguate meaning

**Service Oriented Architecture (SOA)**: a software design paradigm, which views software components as a set of interoperable services, which can be packaged, configured and reused in multiple systems.

**Natural Language Processing (NLP)**: The processing of text in natural language with the purpose of extracting information in a structured manner.

**OWL: the Web Ontology Language**. A language to describe ontology for sharing and exchanging knowledge on the web in a machine readable format.

**Provenance**: The property of specifying and tracking the source of information items.

## **Alternative energy sources and energy efficiency Project Reports**

## **Hybrid Electric Vehicle Grid Connectivity – Phase I**

Principal Investigator:

**Dale Dolan, Ph.D., Electrical Engineering**

California Polytechnic State University  
San Luis Obispo, CA

## **1. Abstract**

The commercial availability of hybrid electric vehicles coupled with the need for electric power grid stability and security invite the development of a vehicle to grid interface solution. This project completes Phase I in the development of this interface for the Chevy Volt. The complete project will provide the link between the vehicle and the utility industry and will analyze the effectiveness on such grid connectivity on the stability and economical operation of the power grid. This grid could be the typical centralized utility grid or a localized microgrid, thus leading to the possibility of a 50 kW mobile power source for industrial or military applications. To accomplish this will involve adaptation of the vehicle control system of the Chevy Volt, an advanced series hybrid vehicle with a 50 kW engine/generator set providing power to a 16 kWh lithium ion battery pack. The system as designed powers the 4-passenger car for approximately 35-40 miles before the battery needs to be recharged. Recharge takes place either by starting the engine/generator or by plugging into the grid. This project provides the first steps to add the ability to provide power back to the grid from the battery pack, and therefore also the engine/generator by using the onboard power electronics that have been designed to power the electric propulsion system.

Phase I of the project begins with a technological survey and literature review of the potential topologies. An engineering analysis of the various existing systems will lead to a preliminary design with appropriate requirements and approach that capitalizes on the available resources that reside in the standard Chevy Volt. The system of interfacing with the power grid will be devised using power electronics on board the vehicle and supplemented by advanced designed systems off board of the vehicle. This preliminary design will undergo hardware power electronics simulations. Simulations of the behavior of the grid will be carried out under certain scenarios of power input to and taken from the battery/generator on board the vehicle.

The results of these simulations will lead to the detailed design, which will be the final deliverable of Phase I of the project. Building a Proof of Concept Unit and testing and evaluation of this unit will be the main focus of Phase II of the Hybrid Electric Vehicle Grid Connectivity project.

## **2. Project significance**

The electric grid of the United States has about 650 GW of capacity. The vehicle population is about 200 million. If each vehicle had the power to provide 50 kW of power to the grid on demand, the cumulative power capability of the on-road vehicle population would be 10,000 GW, thus dwarfing the installed electric generating capacity of the utility industry. Up to now this has not been conceivable because electric powered



cars did not exist and if they did exist, they did not have the capability of providing the above power.

Now that advanced hybrid vehicles like the Chevy Volt can provide this power, a very new and significant capability exists. When the population of such vehicles increases due to the increased cost of oil or carbon, the new vehicle population will be a growing resource for the electric grid. In addition, new bio fuels will likely be introduced into the vehicle fleet before being introduced into the utility generating grid, thus providing a vector for the movement of the grid to zero net carbon, fully renewable power generation.

The development of this project has particular relevance to several ONR/DOD interests involved with Logistics and Maneuverability. As the capabilities of the advanced hybrid electric car have increased they are now at the level where they can be used in powerful military equipment, providing increased stealth when running completely on electric power. These vehicles have the potential to provide a source of alternative power when acting as an advanced power plant. As these become more widespread in the military fleet, a source of mobile power plants has the potential to eliminate traditional tow behind generators, thereby making more effective use of available resources. A number of studies and research projects have demonstrated the value of a V2G (vehicle to grid). These will be discussed briefly in the background/prior work section and in attached documents [1]-[4] generated as part of the Phase I project.

### **3. Background/prior work**

The state of the art in this area is still very immature. Pure battery powered electric vehicles (BEV) like the GM EV-1, Toyota RAV-4, Ford Ranger Electric Pickup, and other electric vehicles were driven off the roads in the first years of this century. Pure electric vehicles use lead acid batteries in low performance, low cost applications (e.g. fork lift trucks and golf carts) and nickel metal -hydride batteries in on-road applications. The newer battery technology, the lithium ion battery, is being applied to exotic electric cars by companies such as AC Propulsion and Tesla Motors and the Toyota Prius. Batteries are being developed to serve the hybrid electric vehicle (HEV) market. However, the concept of a plug-in hybrid (PHEV), such as the GM Volt and modified Toyota Prius, is gaining popularity, especially as gasoline prices have risen. Battery test modes for pure electrics and hybrid electrics have been published by the USABC. The Volt will use a lithium ion battery and a number of small companies are offering modified lithium ion batteries for a customer-modified, extended range Prius. Toyota has released the plug-in Prius powered by advanced batteries with smaller capacity than the Chevy Volt. These lithium ion batteries are notorious for high cost and low calendar life, but recent chemical modifications have provided hope for good cycle life. The use of the batteries as sources of power in a V2G (vehicle to grid) mode will require many short charge-discharge cycles to be imposed during the time the vehicle is

parked at the charging station. No one knows and no models exist to predict the effects of such charging on battery durability.

The electric vehicles built to date such as the GM EV-1, Toyota RAV 4, Ford Ranger, and others used chargers for one-way battery charging. AC Propulsion has proposed, and implemented in a converted Toyota Scion (e-Box), a system whereby the power electronics and motors could be adapted to pass power from the vehicle to the grid. AeroVironment has developed battery test equipment that uses similar principles to move discharge power to the grid, thus enabling efficient use of energy in a test environment. General Motors and AeroVironment have demonstrated a battery exchange system that provides effectively limitless electric vehicle range, even with lead acid batteries. Such a system would envision a network of exchange stations with batteries inventoried for quick change. The exchange stations would provide a natural focal point for a resource to provide power to the grid on a high demand basis and might also provide enhanced grid stability in certain situations.

More recently Raser Technologies has produced a military light duty truck which it terms an E-REV (extended range electric vehicle). GM has also adopted this term for the Chevy Volt to distinguish it from the more commonly referred to Hybrid electric vehicle, although they both could still be termed hybrids. The distinction between hybrid and EREV is that in a hybrid both the ICE and battery provide motive power directly. In an EREV the ICE only provides power which is stored in the battery and the battery provides all motive power. It turns out that this is true for the Chevy Volt in most cases but to increase efficiency there is a mode in which the ICE does provide direct power to the propulsion system.

A number of researchers have put forward the idea that economic advantage could be gained if the batteries are connected to the grid so that power can flow in both directions, a so-called vehicle-to-grid (V2G) model [5,6,7,11,12,13,14]. The proposed research has the eventual goal of testing batteries in the V2G model in order to understand if the additional stress imposed by the support of grid ancillary services causes accelerated degradation to the batteries beyond the classical model. The present proposal is part of the much larger economic analysis of batteries and electric vehicles necessary to justify large scale deployment. It is a multidisciplinary problem involving battery technology, charging technology, grid demand profiles, and mechanisms (hardware and controls) to regulate the flow of power.

Although electric power inverters are not new, low cost inverters for widely distributed battery systems such as might be found in electric cars and in battery exchange stations for future electric cars are not available. Advances in power electronics components may make possible the development of such battery-to grid or vehicle to grid interfaces. In this project the focus will be a vehicle to grid interface for the Chevy Volt where the power electronics used for electric propulsion will also be used for the vehicle to grid interface. The combustion engine and electric drive of the Chevy Volt are shown in Figure 1. This project envisions development of the power electronics,

control software, interface communications and utility interfacing to make a vehicle to grid system both practical and economical. It would include analysis of the power electronics and switching architectures, development of a prototype low power unit, scale up criteria (for follow on projects), and schemes for communication to control the flow of power to and from the vehicle.



Fig. 1. Engine compartment of Chevy Volt showing conventional combustion engine on left side and the electric motor and power electronics on the right side. (photo from [http://en.wikipedia.org/wiki/File:Chevy\\_Volt\\_DCA\\_01\\_2010\\_8811.JPG](http://en.wikipedia.org/wiki/File:Chevy_Volt_DCA_01_2010_8811.JPG) )

This project which is phase I of a longer term project vision is of one year duration and stands alone, but did not envision the implementation of a functional prototype in such a short period. Rather, the objectives of the first years' work were to design, build and develop the project to the point where Cal Poly can provide a solid background that will enable a follow on project to look at a complete system on the order of 50-100kW, which would be more appropriate for industrial sized applications.

#### 4. Discussion of Results

Literature review and Proof of Concept V2G Interface Solution have been completed and detailed results/discussion are contained in the following four attached reports:

- [1] Agatep, A., and Ung, M., "Design and Simulation of V2G Bidirectional Inverter and DC-DC converter" Senior Project Report, California Polytechnic State University, 2011
- [2] Aquino, J., "Microcontroller Design of a Bidirectional Three-Level Pulse Width Modulation AC/DC Converter for Vehicle-to-Grid Application" Master's Thesis, California Polytechnic State University, 2012
- [3] Dolan, D., Le, V., and Taufik, "Geographic Variation in Environmental Benefits Achieved by Plug in Electric Vehicles and Electric Vehicles", EVS26 26th International Electric Vehicle Symposium, Los Angeles, CA, May 2012.
- [4] Chhean, R., "Vehicle-to-Grid (V2G) Bidirectional Power Converter Design and Integration for 2011 Chevrolet Volt – Extended Range Electric Vehicle (EREV) Drivetrain" Master's Thesis, California Polytechnic State University, 2012

EVs with V2G functionality benefit both customers (vehicle owners) and the grid (owned by utilities). If the vehicle is connected to the grid for regulation services, annual average income is estimated at \$2,000 per vehicle [17]. Grid support services are only activated when the vehicle is not in use (e.g. parked). On average, vehicle usage in the USA is approximately 1 hour per day [18]. This leaves V2G capable PEVs to be available for grid support 23 hours per day. Grid regulation support not only includes discharging but charging the battery as well. For instance, customers benefit through monetary gain to charge their EVs during down regulation. Customers do not have to worry about low battery levels when the vehicles are needed since on average, there is minimal battery net power loss during regulation services [17]. The utility also benefits by having a more robust, efficient, and responsive grid. In contrast to typical power plants, EVs are directly located at loads, increasing operating transmission efficiency. Currently in the United States, electric power can travel through multiple states before reaching loads. Power plants respond slowly to up/down regulation commands due to inertia of rotating mass and chemical thermal properties. In comparison to power plant response times of 30 seconds to several minutes, V2G power converters can respond at  $1/20^{\text{th}}$  second [17]. This feat is due to the inherent nature of V2G power electronics which do not use rotating masses or chemical thermal properties. The rapid response times of V2G offer faster regulation services such as frequency and voltage regulation. V2G capabilities may offer power quality improvements through peak load shaving and grid ancillary services (e.g. spinning or non-spinning reserve) [19].

Peak load services are extremely beneficial for the electric infrastructure. Examples of a typical daily system load in California suggest load peaks during mid afternoon. The idea of peak shaving is to charge V2G capable PEVs during low load periods and discharge back into the grid during the peak periods. This would result in a lowered peak as seen by the electrical power system infrastructure (e.g. transmission lines). Infrastructure upgrades and design are based on the peak such that if the peak is



lowered, infrastructure requirements would be reduced which is less costly for the electric utility.

Single-stage topologies (Figure 2) have been successfully simulated with V2G capabilities. A modified bidirectional dual active bridge with zero voltage switching (ZVS) was explored in [20]. Unfortunately, the topology requires 12 switches, a resonant tank, and high frequency (HF) transformer. A single-stage solution eliminated the typical full wave rectifier/2-legged half-bridge (HB) combo in [R8]. Rectification and inverter operations were integrated into a modified bidirectional non-inverting buck-boost converter. Both V2G and G2V operations are done via buck-boost mode. The topology has merits with a component count of only 8 switches, 1 inductor, and 1 capacitor. The low component count reduces additional cost, volume, and weight for enabling V2G.

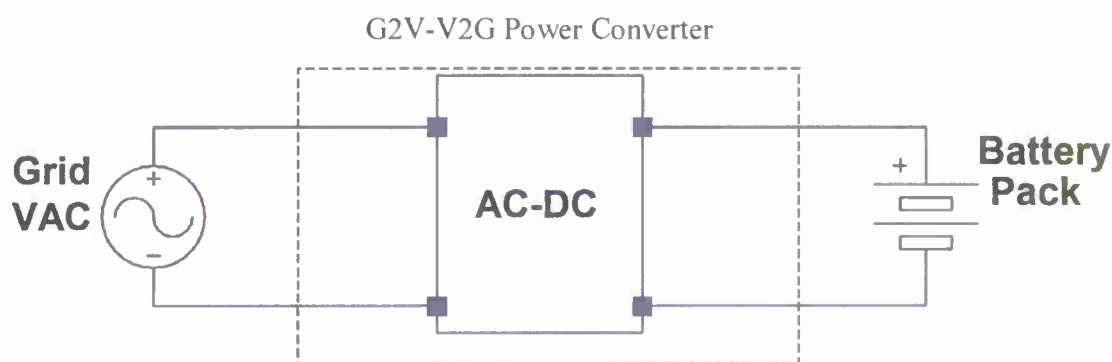


Figure 2. Black box diagram of general G2V-V2G single-stage power converter.

Many different topologies have been used for the AC-DC bidirectional subsystem in a two-stage system (Figure 3). For a single phase connection, the most common bidirectional AC-DC topology is a 2-legged H-bridge with anti-parallel diodes that form a full wave rectifier [22,23,24,25,26]. The 2-legged configuration popularity is due to low component count and simplicity. When a three phase connection is needed, a 3-legged HB with anti-parallel diodes is most prominently proposed [27,28,29,30,31]. It possesses the same advantages of a 2-legged HB, but for a three phase system. Furthermore, 3-legged HB has been proposed for single phase grid-tie inverter operation [16, 32]. The extra leg is connected to the neutral in a North American 240VAC, 60 Hz connection. A 2-legged HB handles such a connection by splitting the DC link capacitors into two series capacitors. The neutral is connected in between the capacitors so the neutral branch always has a current path. Otherwise, there may be a voltage offset. A 3-legged HB uses its neutral leg to eliminate any voltage offset due to unbalanced loads. The neutral leg is pulse width modulated (PWM) at a 50% duty cycle to achieve this [32]. Benefits also include the elimination of DC capacitor voltage balance issues, smaller output filter size, smaller DC bus current ripple, and higher utilization of dc bus voltage [33]. Use of three-level neutral-point-clamped (NPC) or modified versions have been proposed [34,35]. Any benefits from the three-level NPC are mitigated by the switch count of 6 and 8. Both 2- and 3-legged HBs are valid candidates.

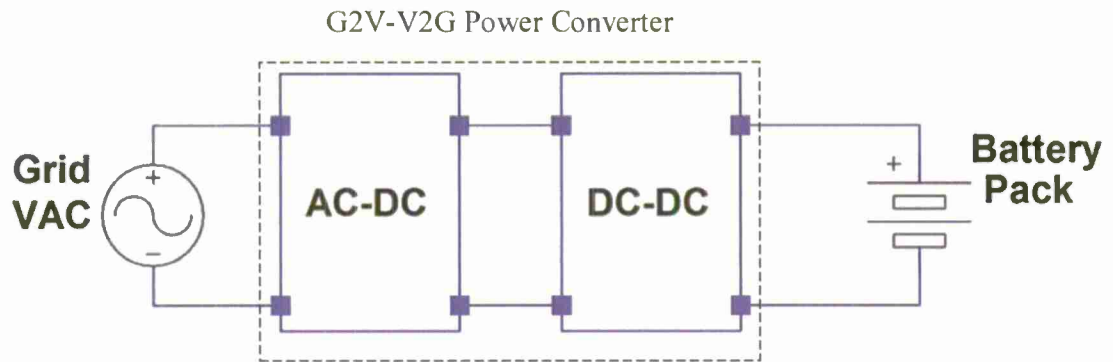


Figure 3. Black box diagram of general G2V-V2G two-stage power converter.

A variety of topologies have been used for the DC-DC bidirectional subsystem in a two-stage system. Many topologies only work if the battery voltage is always greater than the required DC link bus voltage or vice versa. The HB converter topology, also known as a buck or boost, is most popular in literature for G2V-V2G power converters [22,23,24,26,28,29,32,35]. The low component count and simplicity makes it an ideal candidate if a few requirements are met. The battery voltage must always be greater than the DC link bus voltage. As a result, the HB converter charges the battery in boost mode and discharges the battery in buck mode. Otherwise HB converter cannot be used for the DC-DC subsystem. The dual active bridge and such based topologies are utilized in literature [25,27]. The topologies contain a HF transformer for galvanic isolation, but need at least 8 semiconductor switches to operate. The high parts count makes dual active bridge based topologies unattractive candidates unless galvanic isolation is a necessity. An HB converter is an attractive candidate if the battery voltage can be guaranteed to be greater than the DC link bus voltage level.

V2G technologies have motivated researchers since 1997, but more research is required to understand V2G implementations for personal vehicles of the average consumer [36]. Grid support services from V2G EVs have been studied in economics and logistical requirements [16,36,37,38,39,40,41]. There are many technical challenges in V2G design and implementation. A wave of technical V2G designs and implementations have been discussed in literature. These technical designs and discussions include a number of topologies and control methods [16,19,20,21,22,23,24,27,28,29,32,34,35,42,43,44,45,46,47]. Furthermore, V2G systems have been studied in industry since patents exist [30,31].

The proof of concept G2V-V2G power converter is shown in Figure 4. It is composed of a four-switch bidirectional Buck-boost dc-dc converter and 2 legged half bridge inverter/full wave rectifier with an LCL grid filter. It is shown in [4] for 5 generic cases that the topology provides good performance and is able to meet IEEE harmonic standards for most of these cases. For the isolated instances where harmonics slightly exceed standards, an improved LCL grid connection filter should be able to alleviate the problem.



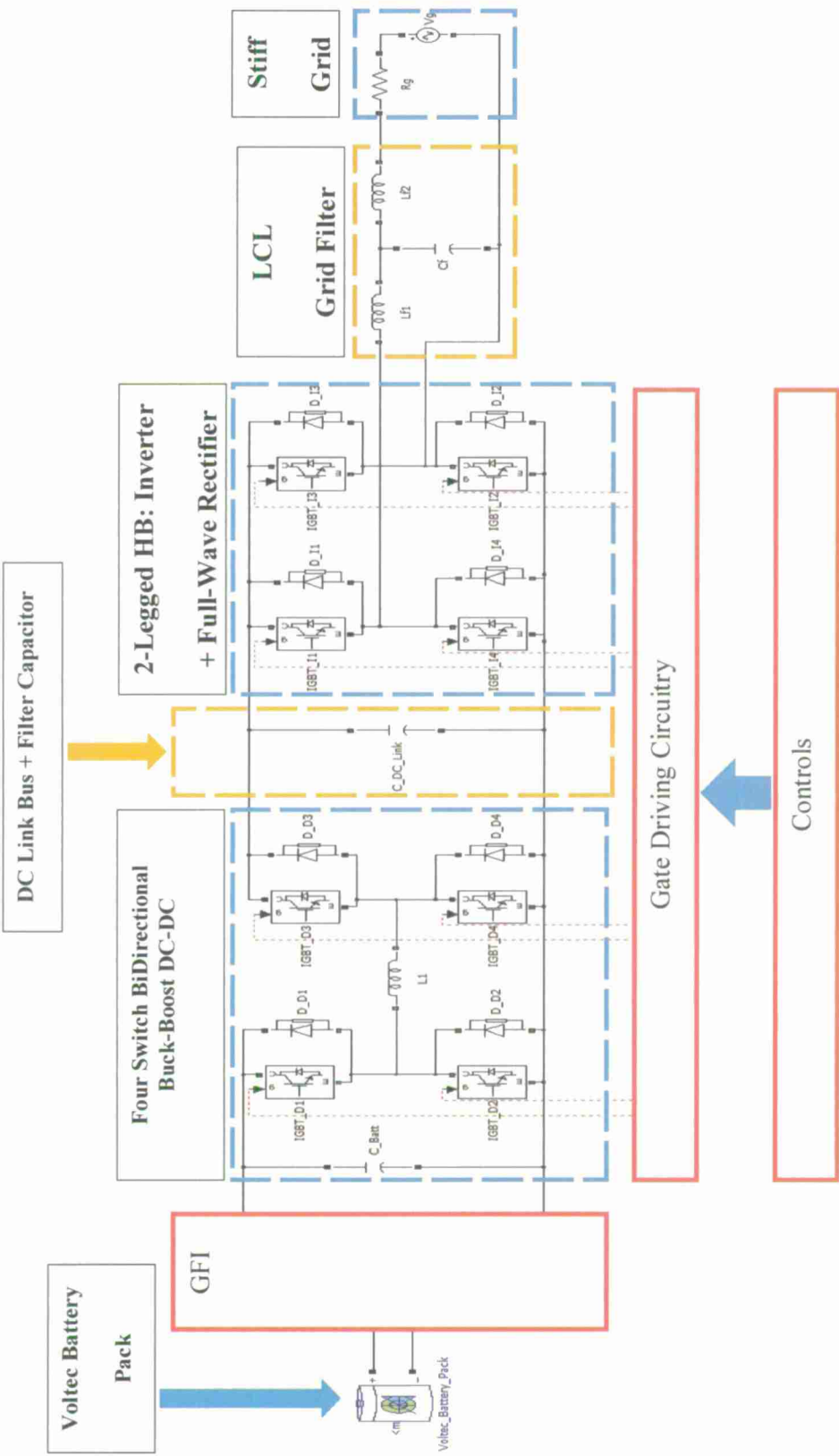


Figure 4. G2V-V2G power converter system layout.

## 5. Future Work Planned

- a) The use of the batteries as sources of power in a V2G (vehicle to grid) mode will require many short charge-discharge cycles to be imposed during the time the vehicle is parked at the charging station. No one knows and no models exist to predict the effects of such charging on battery durability and thus one of the key questions for both V2G viability and electric vehicle practicality and utility in general, is the degradation rate of the batteries in the real world. Future work will use the CAN bus data systems to characterize the changes occurring in effective impedance of battery systems in the Chevy Volt and Nissan Leaf. We will add new analytical and experimental tools to study battery degradation not only in the vehicle but in the laboratory as well and to relate these observations to each other and to physical models (mathematical models) of battery cells under actual use.
- b) The existing vehicle to grid connection in the Chevy Volt is designed for a charge rate of 3.3 kW. However the generation capability of the ICE is 50kW. This presents a large mismatch in V2G capability in terms of the potential available power and the power electronics ratings of the vehicle to grid connection. In order to use the J1772 connector for V2G purposes the vehicle's generation capabilities will be limited. For the concept to be applicable to a mobile power source the full 50 kW power capabilities of the vehicle must be available. This will require alterations to the current connection or a bypass to higher rated components deeper in the vehicle. The current power levels would be suitable for V2G exchange of power over periods of several hours and would assume that power delivery from the vehicle to grid is interrupted once the battery reaches its minimum state of charge and that the ICE is not started to enter charge sustaining mode.
- c) Currently the Chevy Volt can only be operated in charge sustaining mode once the battery has been depleted. The vehicle will not recharge the battery pack using the ICE and generator. It will maintain a particular state of charge such that V2G would still be feasible using the ICE as the power source. In mobile military applications however it would be desirable to have the vehicle fully charged such that when desired it could be run on pure electric to maintain stealth. The modification to allow this to happen will need to be investigated.

## 6. References cited

- [1] Agatep, A., and Ung, M., "Design and Simulation of V2G Bidirectional Inverter and DC-DC converter" Senior Project Report, California Polytechnic State University, 2011
- [2] Aquino, J., "Microcontroller Design of a Bidirectional Three-Level Pulse Width Modulation AC/DC Converter for Vehicle-to-Grid Application" Master's Thesis, California Polytechnic State University, 2012
- [3] Dolan, D., Le, V., and Taufik, "Geographic Variation in Environmental Benefits Achieved by Plug in Electric Vehicles and Electric Vehicles", EVS26 26th International Electric Vehicle Symposium, Los Angeles, CA, May 2012.

- [4] Chhean, R., "Vehicle-to-Grid (V2G) Bidirectional Power Converter Design and Integration for 2011 Chevrolet Volt – Extended Range Electric Vehicle (EREV) Drivetrain" Master's Thesis, California Polytechnic State University, 2012
- [5] AC Propulsion, "An Introduction to AC Propulsion's Split Phase Drive for Brushless Motors," December 20, 2003, [www.acpropulsion.com](http://www.acpropulsion.com)
- [6] Brooks, A., and Thesen, S., "PG&E and Tesla Motors: Vehicle to Grid Demonstration and Evaluation Program," Electric Vehicle Symposium EVS-23, Anaheim CA December, 2007.
- [7] Brooks, A., "Vehicle to Grid Demonstration Project: Grid Regulation Ancillary Service with a Battery Electric Vehicle," Final Report, California Air Resources Board Contract 01-313, December 10, 2002.
- [8] Clement, K., Haesen, E., and Driesen, J., "Stochastic Analysis of the Impact of Plug-in Hybrid Electric Vehicles on the Distribution Grid," IET Conference Publications, 2009
- [9] Gage, T., AC Propulsion, "The ZEV Technology Objective: Transportation Without Petroleum," CARB ZEV Technology Symposium, Sacramento, CA September 26, 2006.
- [10] Gill, J., "Advanced EV/HEV battery pack testing using the ABC-150 power system," Battery Conference on Applications and Advances, 1997., Twelfth Annual , vol., no., pp.127-131, 14-17 Jan 1997
- [11] Guille, C., and Gross, G., "A Conceptual Framework for the Vehicle-to-grid Implementation," Energy Policy ,November 2009.
- [12] Kempton, W., and Tomic, J., "Vehicle –to-Grid Power Fundamentals: Calculating capacity and net revenue," J. Power Sources, vol 144., pp. 268-279., June 2005.
- [13] Kempton, W., and Tomic, J., "Vehicle-to-Grid Power Implementation: From stabilizing the grid to supporting large-scale renewable energy," J. Power Sources, vol 144., pp. 280-294., June 2005.
- [14] Tomic, J., "Vehicle-to Grid (V2G and PHEV)", Alternative Fuels & Vehicle Symposium, Anaheim CA , April 2, 2007
- [15] USABC Battery Test Manual Rev 2, January ,1996
- [16] X. Zhou, S. Lukic, S. Bhattacharya, A. Huang, "Design and Control of Grid-connected Converter in Bidirectional Battery Charger for Plug-in hybrid electric vehicle Application," in *Proc. IEEE Vehicle Power Propulsion Conf.*, 2009, pp. 1716-1721.
- [17] L. J. Beck, in *V2G – 101*, 1<sup>st</sup> ed. Lexington, 2009.
- [18] Tomić, J.; Kempton, W.; "Using fleets of electric-drive vehicles for grid support," in *Journal of Power Sources*, vol. 168, no. 2, pp. 459-468, Jun. 2007.

- [19] W. Kempton, J. Tomić, "Vehicle-to-grid power fundamentals: calculating capacity and net revenue," in *Journal Power Sources*, vol. 144, no. 1, pp. 268–279, Jun. 2005.
- [R6] L. Sanna, "Driving the Solution the Plug-in Hybrid Vehicle," EPRI, 2005.
- [20] S. N. Vaishnav, H. Krishnaswami, "Single-stage isolated bidirectional converter topology using high frequency AC link for charging and V2G applications of PHEV," in *Vehicle Power and Propulsion Conf. (VPPC), 2011 IEEE*, pp.1-4, 6-9 Sept. 2011.
- [21] H. Chen, X. Wang, A. Khaligh, "A single stage integrated bidirectional AC/DC and DC/DC converter for plug-in hybrid electric vehicles," in *Vehicle Power and Propulsion Conf. (VPPC), 2011 IEEE*, pp.1-6, 6-9 Sept. 2011.
- [22] M. C. Kisacikoglu, B. Ozpineci, L. M. Tolbert, "Effects of V2G reactive power compensation on the component selection in an EV or PHEV bidirectional charger," in *Energy Conversion Congr. and Expo. (ECCE), 2010 IEEE*, pp.870-876, 12-16 Sept. 2010.
- [23] M. C. Kisacikoglu, B. Ozpineci, L. M. Tolbert, F. Wang, "Single-phase inverter design for V2G reactive power compensation," in *Applied Power Electronics Conf. and Expo. (APEC), 2011 Twenty-Sixth Annual IEEE*, pp.808-814, 6-11 March 2011.
- [24] M. C. Kisacikoglu, B. Ozpineci, L. M. Tolbert, "Examination of a PHEV bidirectional charger system for V2G reactive power compensation," in *Applied Power Electronics Conf. and Expo. (APEC), 2010 Twenty-Fifth Annual IEEE*, pp.458-465, 21-25 Feb. 2010.
- [25] M. Rosekeit, R. W. De Doncker, "Smoothing power ripple in single phase chargers at minimized dc-link capacitance," in *Power Electronics and ECCE Asia (ICPE & ECCE), 2011 IEEE 8th Int. Conf. on*, pp.2699-2703, May 30 - June 3, 2011.
- [26] B. Bilgin, A. Emadi, and M. Krishnamurthy, "Design considerations for a universal input battery charger circuit for phev applications," in *Industrial Electronics (ISIE), 2010 IEEE Int. Symp. on*, July 2010, pp. 3407–3412.
- [27] N. D. Weise, K. K. Mohapatra, N. Mohan, "Universal utility interface for Plug-in Hybrid electric vehicles with vehicle-to-grid functionality," in *Power and Energy Society General Meeting, 2010 IEEE*, pp.1-8, 25-29 July 2010.
- [28] J. Gallardo-Lozano, M. I. Milanes-Montero, M. A. Guerrero-Martinez, E. Romero-Cadaval, "Three-phase bidirectional battery charger for smart electric vehicles," in *Compatibility and Power Electronics (CPE), 2011 7th Int. Conf.-Workshop*, pp.371-376, 1-3 June 2011.
- [29] X. Wang, P. Yan, L. Yang, W. Yao, G. Shi, "A V2G vector control model of electric car charging and discharging machine," in *Advanced Mechatronic Systems (ICAMechS), 2011 Int. Conf. on*, pp.342-347, 11-13 Aug. 2011.
- [30] W. E. Rippel, "Open Delta Motor Drive with Integrated Recharge," U.S. Patent 0 316 461, issued date Dec. 29, 2011.
- [31] A. G. Cocconi, "Combined Motor Drive and Battery Recharge System," U.S. Patent 5 341 075, issued date Aug. 23, 1994.

- [32] X. Zhou, G. Wang, S. Lukic, S. Bhattacharya, A. Huang, "Multi-function bidirectional battery charger for plug-in hybrid electric vehicle application," in *Energy Conversion Congr. and Expo., 2009. ECCE 2009. IEEE*, pp.3930-3936, 20-24 Sept. 2009.
- [33] J. Wang, F. Z. Peng, J. Anderson, A. Joseph, R. Buffenbarger, "Low cost fuel cell converter system for residential power generation," in *IEEE Trans. Power Electron.*, vol. 19, no.5, pp. 1315-1322, Sep. 2004.
- [34] D. C. Erb, O. C. Onar, A. Khaligh, "An integrated bidirectional power electronic converter with multi-level AC-DC/DC-AC converter and non-inverted buck-boost converter for PHEVs with minimal grid level disruptions," in *Vehicle Power and Propulsion Conf. (VPPC), 2010 IEEE*, pp.1-6, 1-3 Sept. 2010.
- [35] S. Jaganathan, W. Gao, "Battery charging power electronics converter and control for plug-in hybrid electric vehicle," in *Vehicle Power and Propulsion Conf., 2009. VPPC '09. IEEE*, pp.440-447, 7-10 Sept. 2009.
- [36] W. Kempton, A. E. Letendre, "Electric vehicles as a new source for electric utilities," in *Transport. Res. Part D Transport. Envir.*, vol. 2, no 3, pp. 157-175, Sept. 1997.
- [37] W. Kempton, J. Tomić, "Vehicle-to-Grid Power Fundamentals: Calculating Capacity and Net Revenue," in *Journal of Power Sources*, vol. 144, pp. 268-279, 2005.
- [38] W. Kempton, J. Tomić, "Vehicle-to-Grid Power Implementation: From stabilizing the grid to supporting large-scale renewable energy," in *Journal of Power Sources*, vol. 144, pp. 280-294, 2005.
- [39] A. N. Brooks, "Vehicle-to-grid Demonstration Project: Grid Regulation Ancillary Service with a Battery Electric Vehicle," Final report, Contract number 01-313, Prepared for the California Air Resources Board and the California Environmental Protection Agency, Dec. 2002.
- [40] "Bottling electricity: storage as a strategic tool for managing variability and capacity concerns in the modern grid." Electricity advisory committee, December 2008. [Online]. Available: [http://energy.gov/sites/prod/files/oeprod/DocumentsandMedia/final-energy-storage\\_12-16-08.pdf](http://energy.gov/sites/prod/files/oeprod/DocumentsandMedia/final-energy-storage_12-16-08.pdf).
- [41] Z. Wang, X. Sun; L. Liu, "Study on control strategy of V2G in power peaking," in *Power Electronics Systems and Applications (PESA), 2011 4th Int. Conf. on*, pp.1-3, 8-10 June 2011.
- [42] Y. Du, X. Zhou, S. Bai, S. Lukic, A. Huang, "Review of non-isolated bidirectional DC-DC converters for plug-in hybrid electric vehicle charge station application at municipal parking decks," in *Applied Power Electronics Conf. and Expo. (APEC), 2010 Twenty-Fifth Annual IEEE*, pp.1145-1151, 21-25 Feb. 2010.
- [43] I. Cvetkovic, T. Thacker, D. Dong, G. Francis, V. Podosinov, D. Boroyevich, F. Wang, R. Burgos, G. Skutt, J. Lesko, "Future home uninterruptible renewable energy system with vehicle-to-grid technology," in *Energy Conversion Congr. and Expo., 2009. ECCE 2009*.



*IEEE*, pp.2675-2681, 20-24 Sept. 2009.

- [44] G. Choe, J. Kim, B. Lee, C. Won, T. Lee, "A Bidirectional battery charger for electric vehicles using photovoltaic PCS systems," in *Vehicle Power and Propulsion Conf. (VPPC), 2010 IEEE*, pp.1-6, 1-3 Sept. 2010.
- [45] I. Cvetkovic et al., "Future home uninterruptable renewable energy system with vehicle-to-grid technology," in *IEEE Energy Conversion Congr. & Expo. (ECCE'09)*, San Jose, CA, pp. 2675-2681, 20-24 September 2009.
- [46] D. C. Erb, O. C. Onar, A. Khaligh, "Bidirectional charging topologies for plug-in hybrid electric vehicles," in *Proc. IEEE Applied Power Electronics Conf. and Expo.*, Palm Springs, California, pp. 2066-2072, 2010.
- [47] L. Tang, G. J. Su, "A low-cost, digitally-controlled charger for plugin hybrid electric vehicles," in *Energy Conversion Congr. & Expo. (ECCE'09)*, San Jose, CA, 20-24 September 2009.

**Investigation of Floating Tube Heat Exchangers with Applications in  
Power Generation, Biofuel Growth, and Clean Water**

Principal Investigator:

**Melinda Keller, Mechanical Engineering**

California Polytechnic State University  
San Luis Obispo, CA

### 1. Abstract

Inexpensive power, renewable fuel, and clean water are increasingly important both in our country and in developing nations. We are seeking to use inexpensive materials to construct a steam power generator. Side effects of the project are algae and condensation which can be optimized to produce biofuels and potable water. We therefore started a three tiered research project here at Cal Poly that has students working on these three different aspects from majors in engineering such as Mechanical, General, and Bio-resource and Agricultural; different colleges such as Food Science and Biology; and partners from different universities and industry – UCSB and Advanced Laboratory Group.

This project is a floating tube heat exchanger which consists of a 10 m x 3 m rectangular pond approximately 1 m deep. This pond works as a heat exchanger and contains 15 plastic tubes floating on the pond with an inner heat transfer tube simulating a solar reflector (due to budget constraints and IP rights). The main purpose of this floating tube construction is heat transfer and energy efficient cooling. The Mylar in the tubes of the prototype in San Diego reflects sunlight onto a solar collector in order to boil water and power a steam generator. The material for the tubes, Mylar and “sandwich bag” grade plastic, is quite inexpensive. The tubes prevent the evaporation of the pond basin water, which can be used for thermal storage during the day and cooled at night for increased efficiency and almost no water usage. As a secondary effect, the tubes grow algae at a luminescence ideal for biofuel production and, as the condensate forms above the Mylar, there is a tertiary side effect of producing clean water. Figure 1 shows the sun’s rays entering the plastic tubes and bouncing off the Mylar toward the solar collector.

We built and instrumented one of these ponds forming senior projects for 9 students, working with undergraduates and graduates on instructionally related activities, and plan to collaborate with many more students to continue each aspect of the proposed work in the form of capstone projects. So far, we have encountered a great deal of success!

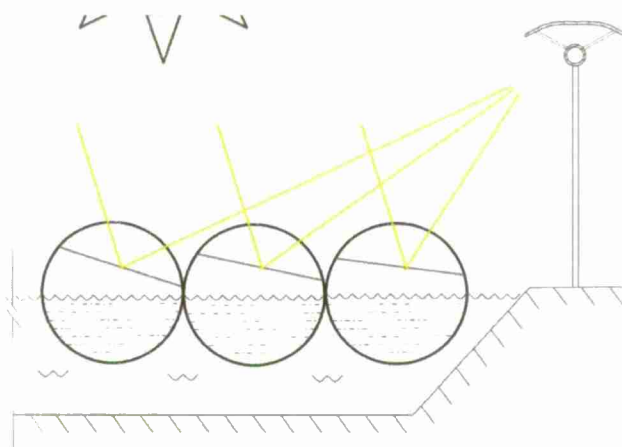


Figure 1: Floating Tubes Reflect Sunlight to Solar Collector

## 2. Project significance

Taking advantage of our natural resources in a way that is sustainable is a significant problem we face today. How do we produce power that is scalable, clean, renewable, and cost competitive with current electricity and fuel production without government subsidies? Our goal is to attempt a system that produces both low cost electricity and algal biomass with a side effect of being able to collect potable water. Figure 2 shows the use of the entire radiation spectrum that will be distributed into optimal biomass production as production of low cost electricity.

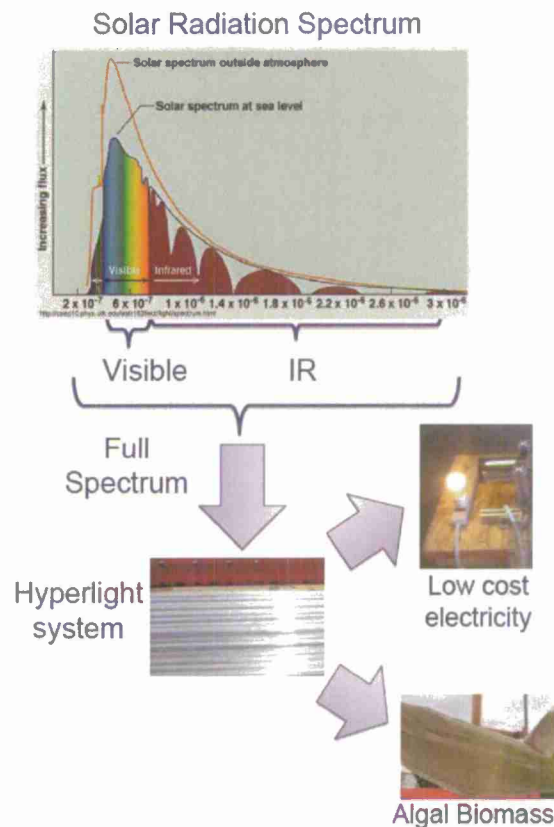


Figure 2: The goal is to convert solar radiation into electricity and biomass

Our solution is to build ponds, and just about any pond will work, with floating tubes set closely together to reflect light onto a solar collector, grow algae, and collect water condensate. Using this proposal, we constructed a small built-up pond, approximately 10m x 3m, filled with 15 tubes. The tubes and pond work as a counter-flow heat exchanger to dissipate stored thermal energy generated by the sun during the day. The tubes are also an ideal place to grow biomass – algae – in a low light, warm environment. As the algae grow, the water condenses in the upper portion of the tubes and can be collected from the inner tube and run to a potable water collector. Shown in figure 3 below is our finished pond which is in the Bonderson Yard at Cal Poly



Figure 3. Photograph of the heat transfer pond designed and built by Extreme Exchangers senior project team in Bonderson Yard.

One of the main problems we began with is in maintaining a cold temperature reservoir and effectively predicting the thermal profile of the system over time. Our first obstacle was to develop an accurate thermal model for an efficient cooling scheme.

The thermal modeling problem is especially interesting because the system contains algae which contribute to the thermal balance in the system in addition to conduction, convection, and radiation heat transfer. Since this system is targeted to be set up in many different environments, accurate performance prediction in varying circumstances will require a significant amount of engineering effort.

We developed a numerical model in ANSYS Workbench and an empirical estimate in EES (Engineering Equation Solver) that could predict transient response of our system.

This project is related to Office of Naval Research (ONR) strategic objectives in that it will enable units to establish water and power in remote and harsh environments for low cost. In a wider setting, if successful, this project could bring clean water and power to many remote and impoverished areas of the world. This technology could save many lives.

The scientific modeling and investigation of both the thermal aspects and algal growth will advance the state of the art. With the materials required for a pond, this project is easily scalable depending upon available funding. Large ponds in a network can be used to produce power on a large scale. One scale model pond can provide valuable data in



thermal geometry predictions. Continued work can advance all tiers of investigation, or just one, if funding is cut. If any of the tiers produces favorable results, the significance of this project will bring attention to Cal Poly and its students.

### 3. Background/prior work

Algae as a potential solution for fuel replacement is not a new idea. The government launched the Aquatic Species Program (ASP) in 1978 which was shut down in 1996.<sup>i</sup>



Figure 4: Typical open pond



Figure 5: Typical photobioreactor.

Other profitable algae growing operations include “Nutraceuticals”<sup>ii</sup> and food for fish farms. Algae as a biofuel, however, have problems with space and water requirements. There are two common design platforms, open ponds and photo bioreactors as shown in figures 4 and 5. Open ponds are cheap, but have poor performance. Photobioreactors (PBR) have higher performance, but are costly. Companies like Seacaps,<sup>iii</sup> Transglobal oil,<sup>iv</sup> and Solix<sup>v</sup> have tackled the first hurdle, cost, by using lightweight plastic film in their bioreactors. The next hurdle is that the best place to build PBRs is where there is a lot of sun. These places are also HOT and in these places water is scarce. The best way to manage the heat is to immerse the PBR in a pond. But replacing the evaporated water from the pond becomes an issue. Our solution is to completely cover the pond surface with floating tubes. This minimizes evaporation and optimizes the use of the lightweight plastic. Now we have a chronic heat problem. Evaporation is one of the easiest ways to dispose of excess heat, but in a closed system, this mechanism is not available. The best way to take advantage of sun for the most hours, but only use the optimum amount of radiation to grow algae is to block the light over most of the algae. We cover our tubes with inexpensive Mylar chords, and produce an optimal growing environment for our algae. At the same time, if we change the angle of the Mylar in each tube, we can bounce the excess radiation onto a solar collector and develop enough heat to boil water and generate electricity.

This Concentrated Solar Power (CSP) idea is not new. Four main configurations are Linear Fresnel Reflectors from Ausra,<sup>vi</sup> the Parabolic Trough from Sunray Energy,<sup>vii</sup> the Stirling Dish from Stirling Energy Systems,<sup>viii</sup> and the Power Tower from eSolar.<sup>ix</sup> The prohibitive cost of CSP, currently at \$4 to \$5 per Watt installed, is keeping it from wide adaptation and commercialization<sup>x</sup>. In comparison, Solar Photovoltaics (PV) are down to \$2 per Watt with subsidies.<sup>xi</sup> The building materials in all of the above configurations are

glass and steel, which contributes \$2/Watt of that cost.<sup>xii</sup> Our project reduces that cost down to \$.20/Watt since our building materials are dirt, water, air, plastic, and Mylar.

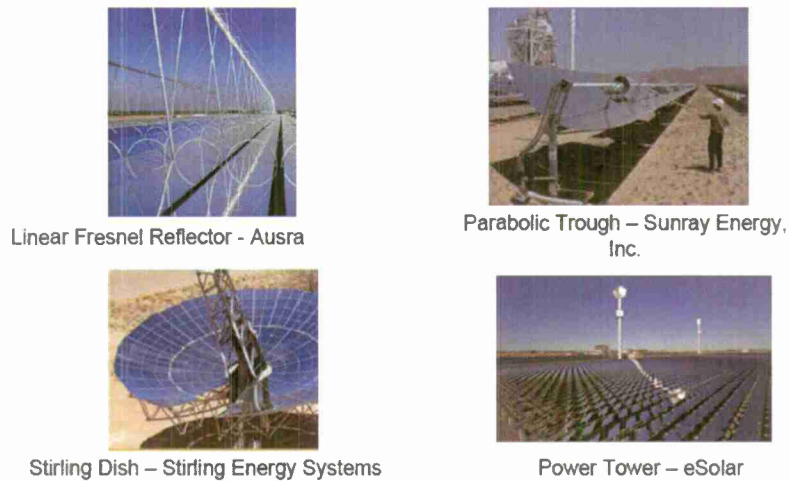


Figure 6: Concentrated Solar Power – four main configurations

Melinda Keller has been a part time lecturer in the Mechanical, Civil, and Aerospace Departments at Cal Poly since 1998. She is currently working on her PhD in Thermo/Fluid Dynamics and moving to a tenure track position in the Mechanical Engineering Department. She wishes to establish herself in the field of renewable energy and hopes to collaborate with professors across CENG and support the international certificate programs currently in development.

Eric Matthys is Melinda Keller's PhD Advisor at University of California at Santa Barbara. His main research areas involve non-Newtonian fluid mechanics and heat transfer, with experimental investigations in biological fluids, such as natural marine polymers among others. Studies on implementation of drag-reducing fluids in industrial applications such as HVAC or fluid transport also have included biological elements.

Combined Power Cooperative (CPC) is an independent, privately backed, research and development cooperative with the goals of developing economically competitive alternatives to fossil fuels and to establish and promote a cooperative venture initiation model for high tech ventures.

We hope that the application of this work will bring people to Cal Poly to learn about our project and has the potential to attract future funding. Dr. Matthys, CPC, and Ms. Keller were awarded \$1,000,000 through PIER to sustain work on this project, and are very thankful for this seed money that got us started.

#### 4. Discussion of Results

This portion of the project established a pond with floating tubes at Cal Poly. The project goals were divided by quarters to facilitate participation by senior project students. We spent Fall Quarter 2010 securing a location and finalizing the design on the pond. Winter Quarter 2011 we started a senior project group with the goal of sizing and instrumenting the pond. Design was completed Winter Quarter and the pond was built Spring and Summer Quarters. Instrumentation began over summer 2011. During Fall, 2011 we were able to propose a second senior project team to start collecting thermal data to optimize the power cycle. This team PolyPond just presented their senior project at an expo 11/27/12 with satisfying results in collecting thermal and pressure data for air and water. We were also able to introduce thermophilic algae to the system and begin our research in biomass cultivation and clean water collection. This senior project will conclude in June 2013.

As a stretch goal, we've also started a senior project team investigating using the power generated by our system to run a Stirling engine that can use either the biofuels produced, the steam generator or be modified to use a more generic gasoline or fuel.

##### Fall Quarter 2010:

We worked with Dennis Elliot, Assistant Director of Sustainability, Energy & Utilities at Cal Poly and Fred DePiero, Associate Dean of Academic Programs for the College of Engineering to find an appropriate location for the pond. Our pond is located at Cal Poly building 197, in the Bonderson Yard

We determined building requirements, constraints, and specifications by working with our industry partner, Combined Power Cooperative (CPC). While doing this, our length changed from the proposed 6 meters to a more useful 10 meters. We increased the depth from 20 cm to 1 meter.

##### Winter 2011:

We submitted a senior project proposal for three mechanical engineering students to begin winter quarter. The first quarter of senior project is generally "Design." These students designed the control system, machine requirements, and instrumentation setup for the pond. CPC has an experimental pond of its own set up in Santee, CA and was able to contribute guidance for the senior project students.

The machine requirements have to do with cooling our system. Students performed pump and fan analysis to choose appropriate flow rates for the thermal cycle. Students also designed a plenum system and had to investigate many health and safety codes.

Thermal modeling and prediction of the pond temperature over time will be a continuing project and we have been collecting thermal throughout the process. Setting up thermal processors and a data acquisition system and storage database has been a project for a mechanical engineering master's student.

#### Spring 2011:

The second quarter of senior project is typically "Build." With plans in place for the pond and its subsystems, we used both Spring and Summer quarters to realize the design. We also traveled to Santee to visit CPC, our industry partner and compared our pond to their setup. We took special note of differences in pond behavior due to climate changes between the two ponds.

#### Fall 2011:

The third quarter of senior project is reserved for "Test." We established baseline conditions for our pond and subsystems and began collecting data. We checked our flow rates and thermal predictions to make sure they match each other. We ascertained that our flow rates and control systems behave as designed. This involved a lot of error checking and modifying the pond by the PolyPond team who took over for the Extreme Exchangers at this time. We have established a solid baseline for system behavior and we are now starting our optimization of each tier: Dry Cooling, Biomass Growth, and Potable Water Production.

### 5. Future Work Planned

Currently, in our project we are able measure air flow and water flow properties for the heat exchanger. The boiler has yet to be installed, though we anticipate installation within the next three weeks at which point our design can be used quantify the heat exchanger system.

Next steps involve integrating the next two senior projects: introduction of thermophilic algae to the tubes, with a senior project team scheduled to start Winter quarter 2013; and combining our project with the Stirling Engine team, in progress and due to complete in June 2013.

Work will continue with testing and verification of the entire thermal model over the next year, culminating in Ms. Keller's PhD dissertation and perhaps continuing to support senior project and master's work in heat transfer, algae growth, and alternative energy applications beyond 2014.

### 6. References cited

- 
- <sup>i</sup> Sheehan, Dunahay, Benemann, Roessler. (1998) NREL/TP-580-24190 A Look Back at the U.S. Department of Energy's Aquatic Species Program: Biodiesel from Algae
  - <sup>ii</sup> Subhadra, Bobban G. (2010) Sustainability of algal biofuel production using integrated renewable energy park (IREP) and algal biorefinery approach. Energy Policy, Volume 38, Issue 10, October 2010, Pages 5892-5901

- 
- <sup>iii</sup> Karine Loubière, Erell Olivo, Gael Bougaran, Jérémy Pruvost, René Robert, Jack Legrand. (18 JUL 2008) A new photobioreactor for continuous microalgal production in hatcheries based on external-loop airlift and swirling flow. *Biotechnology and Bioengineering*, Volume 102, Issue 1, pages 132–147,
- <sup>iv</sup> Wijffels, R. H., Barbosa, M. J. and Eppink, M. H. M. (2010), Microalgae for the production of bulk chemicals and biofuels. *Biofuels, Bioproducts and Biorefining*, 4: 287–295.
- <sup>v</sup> <http://www.solixbiofuels.com/> Accessed 16 Oct. 2010
- <sup>vi</sup> <http://www.ausra.com/technology/> Accessed 16 Oct. 2010
- <sup>vii</sup> [http://www.linvents.com/03\\_solar\\_fuel\\_producer/Images\\_Solar\\_Tech/Solar\\_Technologies\\_Review.htm](http://www.linvents.com/03_solar_fuel_producer/Images_Solar_Tech/Solar_Technologies_Review.htm). Accessed 16 Oct. 2010
- <sup>viii</sup> <http://www.stirlingenergy.com/> Accessed 16 Oct. 2010
- <sup>ix</sup> <http://www.esolar.com/> Accessed 16 Oct. 2010
- <sup>x</sup> Blair, Nate; Short, Walter, Mehos, Mark. (March 2008) Modeling The Impact Of State And Federal Incentives On Concentrating Solar Power Market. 14th Biennial CSP Solar PACES (Solar Power and Chemical Energy Systems) Symposium, 4-7, Las Vegas, Nevada (NREL/CD-550-42709)
- <sup>xi</sup> Patel, Mukund R. (July 15, 2005) *Wind and Solar Power Systems: Design, Analysis, and Operation*, Second Edition. U.S. Merchant Marine Academy, Kings Point, New York, USA
- <sup>xii</sup> Blair, Nate; Short, Walter, Mehos, Mark. (March 2008) Modeling The Impact Of State And Federal Incentives On Concentrating Solar Power Market. 14th Biennial CSP Solar PACES (Solar Power and Chemical Energy Systems) Symposium, 4-7, Las Vegas, Nevada (NREL/CD-550-42709)



**Sensors and Controls for Cal Poly Wind Power Research Center**

Principal Investigator:

**John Ridgely, Mechanical Engineering**

Co-investigator:

**Patrick Lemieux, Mechanical Engineering**

California Polytechnic State University  
San Luis Obispo, CA

## 1. Abstract

In this California Central Coast Research Partnership (C<sup>3</sup>RP) funded project, sensors and a control system have been installed onto the 3 kW capacity wind turbine of the Cal Poly Wind Power Research Center, which is overseen by Professor Patrick Lemieux of Cal Poly Mechanical Engineering. With the installation of the control system, the turbine has been brought to full operation. This wind turbine is used to educate students for careers in the wind energy industry and related professional fields and to conduct research into the application of advanced wind turbine technologies from large turbines onto small turbines. In this project, a control system has been implemented which controls the turbine's operating speed, power output, and yaw (pointing) direction. Several Masters theses, Senior projects, and undergraduate class projects have been undertaken in the course of this project. Ongoing work includes the design and implementation of more sophisticated control systems than the system which is currently operating, and the design of electrical energy management systems which will allow the power output of the turbine to be used to charge a battery and pump water for use in Cal Poly College of Agriculture work. Preparations have been made to deploy a network of wind speed and direction sensors at numerous locations near the Cal Poly campus in order to verify computer models which show that the installation of large utility-grade wind turbines in the area may be viable. Work undertaken during the next several years using the wind turbine and associated sensors will lead to a substantial number of technical publications.

## 2. Project significance

Due to the environmental and political costs of our dependence on fossil fuels, sustainable energy production is an area of growing importance to the competitiveness and security of the United States. There has been long-term growth in the wind energy sector; although the short-term trend since 2011 has seen a decrease in the rate of expansion of the US wind energy industry due to expiring production tax credits and a natural gas glut, installed wind energy capacity has continued to increase<sup>1</sup>. Most energy production industries are typically cyclic, and it can reasonably be expected that the domestic wind energy industry will once again see improved prospects within the next few years. The need for clean, domestically produced energy and well educated engineers to contribute to its production is not going away. Wind power can also serve a useful purpose in generation at remote sites. We therefore consider it wise for Cal Poly to build and maintain an active, long-term program of teaching and research involving wind power.

The technology of large, horizontal-axis utility-scale wind turbines, which typically have capacities of 750kW and higher and sit atop 50 – 80 m high towers, is well developed and utilizes state-of-the-art technology for monitoring, control and power conversion. Such technology has, however, not been adapted in most small-scale (less than 100kW capacity) wind turbines<sup>2</sup>. Most small wind turbine manufacturers must optimize the initial purchase cost of their machines, generally at the expense of energy capture efficiency and reliability, and this increases the cost of energy production using such machines. An opportunity exists for research into the application of large wind turbine technology into small wind turbine design, and Cal Poly is well suited to engage in such research. Cal

Poly owns reasonably large tracts of land with good winds for turbine testing; our faculty and students, from many departments and colleges across campus, are keen to implement our Learn by Doing philosophy through applied research, and the generous support of C<sup>3</sup>RP and other organizations has supplied sufficient seed funding to develop the facilities needed for small wind turbine research.

The educational opportunities of our small-scale wind power projects are extensive. The Cal Poly Wind Power Research Center has been created through a collaboration between the Colleges of Agriculture and Engineering. The capture and distribution of wind energy is an inherently multidisciplinary activity involving mechanical engineering, electrical and computer engineering, materials science, manufacturing, and of course many aspects of business development. Student projects to date have involved undergraduate and graduate students from mechanical, electrical, and computer engineering, and with the major pieces of the wind power center in place, many more projects involving Cal Poly students will be undertaken, preparing these students for careers in many engineering fields as well as other fields of great interest to US industry involving for example energy, aerospace, and transportation. The Cal Poly wind turbine has already had a positive impact on several courses:

- ME 507, Mechanical Control Design – Students designed, built, programmed, and tested circuits such as those shown in Figures 2 and 8
- ME 415, Energy Conversion – Turbine used as example system for study
- ME 329, Design II – Turbine components analyzed by machine design students
- ME 410, Mechanical Measurements – Student projects to measure and model blade vibrations; custom data acquisition systems designed for wind power use applied to many other student projects in this course
- ME 428/429/430, Senior Project – Senior projects

Collaborations have previously been carried out with faculty and students in Civil Engineering to design the tower foundation; students of Electrical Engineering are beginning work on an improved electrical power management system for the turbine; and a Mechanical Engineering senior project team is currently working with the College of Agriculture to implement a water pumping system using energy generated by the turbine. We plan to continue to increase the multidisciplinary involvement of this wind power project in the future.

The project which has been done under the current C<sup>3</sup>RP grant brings benefits in several areas of relevance to ONR. In promoting progress in renewable energy generation, the project helps move the United States towards independence from foreign energy sources. The use of inexpensive but highly capable monitoring and control systems in small energy generation facilities promises to make the logistics associated with remote, renewable energy generation more palatable, reducing the stress on supply chains to provide fuel. Research and education in applications of inexpensive wireless control and monitoring are highly relevant to command, surveillance, and security applications.

### 3. Background/prior work

The Cal Poly Wind Power Research Center field site at Escuela Ranch has been in development since 2008. Ongoing support from C<sup>3</sup>RP has been instrumental in successfully bringing about the reality of a wind power research facility.

A previous C<sup>3</sup>RP grant (52219), which was active from Winter 2009 through Spring 2011 with Professor Patrick Lemieux of Cal Poly Mechanical Engineering as the Principal Investigator, supported the following work:

- Upgrading of wind resource measurement towers at Cal Poly's Escuela Ranch, a roughly 2000 acre facility located approximately 5 miles Northwest of the main Cal Poly campus. Administered by the College of Agriculture, Escuela Ranch is in an area of open space which experiences reliably good wind for the testing of wind turbines, and it is located far enough away from built-up areas that the presence of an operating small wind turbine does not disturb or endanger the public.
- Measurement of the wind resource at the Escuela Ranch site and determination that the wind is sufficient to support a research facility. The wind strength at the proposed wind turbine site has been monitored continuously for over four years, and the wind at turbine height has been found to be, on average, above the minimum speed necessary for the testing of wind turbines.
- Preliminary modeling of the wind at other nearby sites, including open space near the main Cal Poly campus, using Computational Fluid Dynamics (CFD) software calibrated with data from the aforementioned wind sensors. Promising sites for research involving stronger wind and possibly the generation of usable wind energy have been identified and await direct wind resource measurement.
- Design and construction of a tilt-up tower to support the Wind Power Center's wind turbine. This 70-foot tower, designed by a Masters student<sup>3</sup> working with Cal Poly faculty, has a unique combination of characteristics for a small wind turbine which are not present in any commercially available product. It is a monopole design, similar to those used for modern large wind turbines; it takes up less visual and ground space than a tower with guy wires, and it can be safely lowered and raised very quickly – in under ten minutes – allowing the rapid testing of turbine modifications for research purposes and easy access for instructional purposes. This tower's design also allows for a longer lifespan than competing designs. The tower's ferro-concrete foundation was designed by a group of civil engineering students advised by CENVE Professor Rob Moss.
- Design and construction of the wind turbine itself. This 3kW capacity turbine contains several key components, all designed at Cal Poly to support our educational and research mission:
  - The rotor blades, each about 2 meters in length, made of carbon fiber composite. The blades were designed and fabricated by a Cal Poly Masters student<sup>4</sup> and are in use on the turbine.
  - The hub for the blades, designed by a student/faculty team and machined by technician James Gerhardt of Cal Poly ME.
  - The turbine nacelle containing the generator, brake system, and sensing and control components. A first, basic nacelle was designed and built by a

senior project team in 2009; with minor modifications, this nacelle is in use as the heart of the currently operational turbine.

The Cal Poly wind turbine is uniquely designed for its mission of research and teaching. Although small, it incorporates features found in state-of-the-art utility-scale wind turbines; a direct drive generator, an actively controlled disk brake, and composite blades designed and built to industry standards were present before the current project began. The current project adds active computer control and data acquisition, motorized yaw control, a blade balancing method developed in-house, and an electric power conditioning system with battery charge control – all made possible by C<sup>3</sup>RP support – thereby bringing the technological features in the Cal Poly wind turbine in line with those features found in large wind turbines.

Prior to the beginning of work supported by the current C<sup>3</sup>RP grant, the turbine nacelle had been assembled but had not yet been deployed in the field. During the current phase of the project, the turbine has been made fully operational.





#### **4. Discussion of Results**

In the proposal for this project, two main goals were presented: Extending the existing wind measurement network, and adding a monitoring and control system to the wind turbine. The enthusiasm for investment in University research by large wind turbine manufacturers has not been as strong as hoped during the current economic downturn, and the installation of a commercial wind power facility close to campus appears unlikely in the short term. Therefore, the wind measurement goal has been satisfied in the short term through the completion of preparations for wind measurement at multiple sites so that we can deploy an inexpensive and reliable system very quickly to meet such needs as should arise in the future. We have emphasized the second goal of implementing a monitoring and control system in the research wind turbine so as to bring the turbine online as a research and educational platform, and to add further features to the turbine to enhance its viability for research (in particular, active yaw control). The components of the system which have been implemented with the support of the current C<sup>3</sup>RP grant are discussed below.

##### Wind Turbine Control System

In order to minimize the technical risk during development of the wind turbine's control system, this development has been carried out in methodical steps. Each step has allowed for thorough testing and exercise of the turbine's mechanical hardware.

##### PLC Based SCADA

The first control system used with the turbine implements a control scheme using off-the-shelf components to form a simple Supervisory Control And Data Acquisition (SCADA) like system. The goal of the first control system's design has been to allow the turbine to be safely operated for its initial testing period and to allow vibration measurements to be made to validate a blade balancing method for a Master's thesis by Simon<sup>5</sup> which was carried out in 2012. The PLC based system is shown installed in its weatherproof housing at the turbine site in Figure 1.



*Figure 1: Field enclosure with first generation control computer and data logging system. High voltage control electronics are housed in a separate enclosure for safety.*

The original PLC based system uses a simple on/off control scheme to control the rotor angular velocity. In a manner similar to that of a household thermostat, the PLC disconnects the generator from its load when the rotor speed is below a given threshold; it connects the generator to its load, taking power from the rotor and slowing the rotational velocity, when the rotor speed is above a higher threshold. When the difference between the thresholds is small, this on-off control scheme somewhat approximates the action of pulse width modulated (PWM) control, which is the scheme of choice for more sophisticated microcontroller based control systems. The PLC based controller has operated successfully for approximately 20 hours of tests, during which the sensors and power electronics of the turbine have been tested and debugged, and blade balancing vibration data were acquired. Primary data acquisition for the initial tests has been performed using a Squirrel<sup>TM</sup> data logger (the dark gray box at upper right in Figure 1), allowing postprocessing and analysis using generic personal computers.

The sensors with which the control system monitors the turbine's operation and operating environment were developed as part of this project and are listed in Table 1.

| Signal                    | Sensor  |
|---------------------------|---|
| Wind speed                | Anemometer located on a boom attached to the tower a few feet below the turbine. Four additional accelerometers have previously been deployed on a separate tower adjacent to the wind turbine site   |
| Wind direction            | Wind vane with electronic angle sensor located near the anemometer  |
| Nacelle yaw angle         | Angular sensor attached to the bearing on which the turbine pivots to turn into the wind  |
| Rotor rotational velocity | Two sensors are attached to the rotor shaft – one a 60-tooth gear-tooth sensor, the other a single magnet detected by a Hall effect switch. Two redundant sensors are used because rotor speed is a safety critical operating parameter   |
| Generator voltage         | Isolated voltage transducers located both in the nacelle and in the high voltage enclosure on the ground. Nacelle sensor is for control; sensor at ground level is for monitoring and data logging  |
| Generator current         | Isolated current transducers located both in the nacelle and in the high voltage enclosure on the ground. Nacelle sensor is for control; sensor at ground level is for monitoring and data logging  |
| Nacelle vibrations        | Three-axis accelerometer located in the nacelle. During initial testing the accelerometer was used to measure nacelle vibrations caused by rotor imbalance in support of a Masters thesis <sup>5</sup> ; in the future it will be used by the control system as a safety check, applying the brakes if the rotor vibrates excessively |

*Table 1: Sensor systems which have been developed to monitor the operation of the wind turbine and its environmental conditions*

The PLC based control system has been completed and tested. It is currently (November 2012) being prepared for the final phase of PLC-controlled tests, in which the newly attached yaw motor will be put through its initial tests under PLC control. After these tests have been completed, newer microcontroller based control systems will replace the PLC as the primary controller for the wind turbine, and the PLC will be relegated to a role of redundant safety oversight: When the microcontroller based system is in control of the turbine, the PLC will monitor the system for hazardous conditions such as excessive wind speed, rotor over speed or electrical malfunctions and engage the brake if any such hazards are detected.

#### Microcontroller Based Wind Turbine Monitoring and Control System

A microcontroller based controller is a crucial system component for the experiments which will be undertaken over the next 2 to 3 years of the Cal Poly wind turbine's operation. Small, rugged, reliable, and using very little power, a microcontroller

implements the control algorithms which optimally control the turbine. Changing between operating modes – for example, from constant rotor speed control to constant tip speed ratio control – can be accomplished quickly and easily. The microcontroller is responsible for controlling the speed of the turbine rotor as well as for controlling the yaw motor to keep the turbine pointed into the wind). With proper multitasking software, the microcontroller simultaneously measures accelerations and electrical output to ensure that the turbine is operating safely. In the event of a dangerous condition, it applies the brake to stop the turbine. The older PLC based system provides a further layer of redundancy in the unlikely event of microcontroller malfunction.

In order to have efficient and reliable control of small wind turbines, very inexpensive microcontroller based control systems must be designed into those turbines in much the same way that microcontrollers are designed into the engines, transmissions, anti-lock brakes, climate controls, and other subsystems of all modern automobiles. The microcontrollers needed for wind turbine control are less powerful (in terms of computation and energy use) than those in cellular phones or automobile engines, and once development work has been done, such controllers will be manufacturable in modest quantities (100 – 1000) for around \$100 – \$200 each, making them highly economical for use in small turbines. Several prototype controllers have been built by Cal Poly student teams as part of this project and are awaiting testing on the turbine. The designs of the Cal Poly controllers are released under open source licenses and will be available to assist wind turbine manufacturers in developing their own designs. It should be noted that these designs do not in the opinion of the researchers contain innovations worthy of patent protection; rather their designs are implementations of existing prior art in a form which is appropriate for smaller, more inexpensive wind turbines than those in which such sophisticated controls have previously been used.

Students in a graduate-level course on mechatronics system design have designed and built prototype wind turbine control circuits. One student team built a turbine control board in Fall 2011, and two more teams built boards in Fall 2012. Each of the designed boards has a unique combination of Atmel<sup>TM</sup> AVR 8-bit microcontrollers, accelerometer, brake system actuation control, and other components. Each has been tested or will be tested in the laboratory, and each will be tested on the operating wind turbine, with tests expected to begin in early 2013. A CAD image of one student designed controller circuit board is shown in Figure 2. The circuit shown can, in addition to controlling the operation of the turbine, log data to a micro-SD card, transmit operational data via an Xbee-PRO<sup>TM</sup> wireless module to a receiver up to several miles away, and receive operating commands via the wireless module.



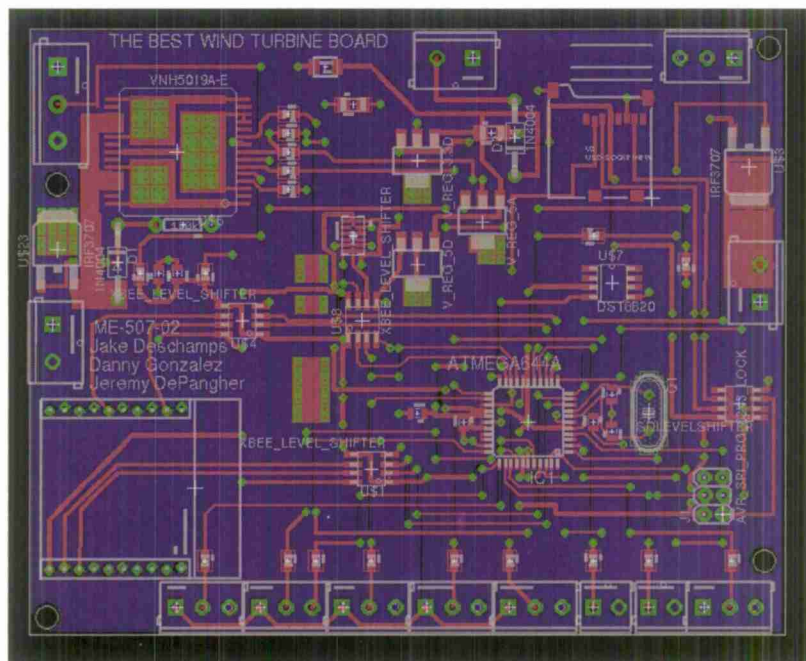


*Figure 2: Example of a wind turbine controller circuit board designed by students in Fall 2012. This board can implement any of the control algorithms discussed in this section.*

### Control Algorithms

One of the research goals of the Cal Poly wind turbine is to investigate the efficacy of several control algorithms for use with small turbines. Several algorithms are under consideration. The simplest are plain PID control schemes which maintain a desired rotor angular velocity. Simulation results suggest that such schemes will provide reasonably accurate and robust control of the turbine under expected operating conditions, but no attempt is made to optimize energy capture using such methods. Algorithms which are expected to be more efficient include control of the turbine's tip speed ratio (TSR). The turbine blades have been designed for optimal aerodynamic performance at a specific TSR; a program of testing will be required to optimize the performance of the system through a range of wind speeds. In order to achieve more precise control and improve energy capture, state feedback control is being investigated. The ability to easily and inexpensively measure most state variables of the turbine system makes this control scheme particularly appealing. Currently, a Master's thesis in which these control schemes are being investigated and compared is nearing completion. Further work will involve testing of these control schemes on the turbine in the field.

### Vibration Monitoring, Blade Balancing, and Condition Based Maintenance

A Master's thesis by Nosti<sup>6</sup> investigating the fatigue behavior of prior art wooden wind turbine blades was completed prior to the current project. In a subsequent thesis by Cheung<sup>7</sup>, work was done to investigate the design of a compact, low power embedded computer with accelerometer which can be installed directly on or in turbine blades to measure their natural frequency of vibration. The hypothesis under investigation is that composite material damage in the blades can be detected through changes in blade



stiffness before such damage leads to failure. The work by Cheung verified that a small, inexpensive, lightweight microcontroller can be used for such work. A future thesis will be done to test this hypothesis further in the laboratory and thereafter in the field.

A Master's thesis by Simon<sup>5</sup> investigated a novel method for blade balancing. Data was acquired through the use of a custom acceleration data logger to verify the efficacy of this method. A photograph of the data logging system installed on the turbine is shown in Figure 3. Results of the blade balancing work have been presented to the American Wind Energy Association (AWEA) at the AWEA Windpower 2012 conference<sup>8,9</sup>. A publication is being prepared for the American Society of Mechanical Engineers' *Journal of Solar Energy Engineering*<sup>10</sup>. An additional, related poster has been presented to *AWEA Windpower 2012* detailing a safety system for wind turbine tower raising and lowering operations.

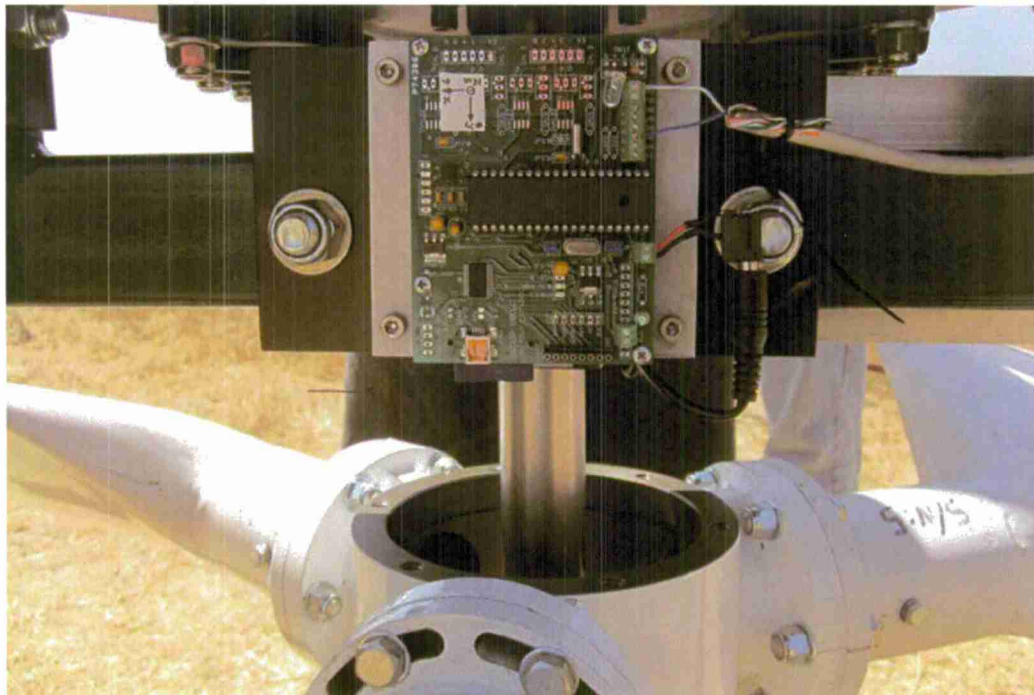


*Figure 3: An acceleration data logger mounted to the wind turbine adjacent to the front rotor bearing. This data logger saves 3-axis acceleration data to an SD card at up to 100 Hz; the frequencies of interest for balancing are close to 5 Hz. The mounting was not made weatherproof because these tests were carried out during a short period of time with the turbine operated under constant supervision.*

#### Load Control

In order to control the rotor speed of the wind turbine, energy extracted by the rotor must be delivered to a load at a controlled rate. In a Senior project which was undertaken before the current work, a load was designed for testing purposes and to take up extra energy when a useful load such as a battery has been filled and cannot accept more energy. This load consists of a set of resistance coils acting as heaters inside barrels filled with water. The heat capacity of the water in the barrels allows a large amount of

energy to be absorbed, with convective heat transfer from the coils to the water allowing a high rate of heat transfer into the water. The area of the barrels allows the full power generated by the turbine to be dissipated into the air at a safe water temperature.



*Figure 4: Resistive load bank for the wind turbine. The two barrels are filled with water and absorb heat from eight resistance coils. The trailer in the distance holds extra water with which the barrels are refilled periodically. The effect of the favorable wind resource at the wind turbine site is visible in the reaction of one of the onlookers.*

Calls for a supply of warm water in remote pastures have been limited. Therefore, as part of the current work, a Senior project has been undertaken to design a power conditioning system for a load which is more useful than a resistive load bank. A team of three senior project students is designing a power regulating system in which the high voltage output of the generator, which in normal operating conditions is on the order of 300 volts DC, is converted by a DC-DC buck converter into 48 volts DC which is useful for charging a battery bank. The energy in the battery bank will be used for pumping water to a higher elevation; this water is needed for animals which are cared for by Cal Poly's College of Agriculture, the administrators of the wind turbine site. Such energy could also be used to serve other needs, of course. As of this writing (November 2012), the senior project team is nearing the completion of their work; their DC-DC converter has been tested at up to 100 volts and several amps, with testing to continue. A second team of students has already been assembled to carry on the work of the first team; the second team is expected to finish their part of the project in the Summer of 2013.

A challenge faced by the designers of the wind turbine control system is that the actuation for the rotor speed controller consists of a resistive load bank and DC-DC conver-

ter/battery charger which are electrically in parallel with one another; in addition, actuation is done by varying the effective resistance of the load rather than by applying a torque to the rotor. The control systems which have been tested to date have used the resistive load bank only; the battery charging system will be tested after it has been successfully tested by the Senior project team. Ongoing Master's thesis work by Ujiie (expected to finish *circa* Summer 2013) has shown that varying the effective resistance of the load should allow for a controller to be implemented which will be stable and robust to changes in operating parameters. The PLC based controllers which have been successfully tested have worked in relatively narrow ranges of operating conditions; more flexible microcontroller based controllers will allow for reliable control over wider ranges of conditions.

Development of a reliable electronic power switch for the wind turbine generator has required extensive development. Power switches for many types of motors, including high voltage motors, are commonplace; the stresses placed on an electronic switch by a permanent magnet DC generator are not as commonly dealt with in most fields. High voltage (2000V and up) surges due to the inductance of the generator cannot be damped through the use of flyback diodes, as is common practice for motors, because of the presence and location of a rectifier bridge in the circuit. The result is that without sufficient protective circuitry, electronic switch elements, be they FET or IGBT based, are quickly destroyed. Development of protective circuitry for the wind turbine power switch entailed the demise of several such switches, but two successful protective circuits were designed and tested. One, designed by Professor Art MacCarley of Cal Poly Electrical Engineering for this project, is based on a MOV surge suppressor with high energy capacity and is very inexpensive but absorbs a non-negligible amount of energy from the turbine power lines. A second design, designed by the author and based on a large high-voltage capacitor, is more expensive but more efficient and is expected to have a longer service life. A combined solution involving elements from both of the aforementioned designs will be used with the battery charging turbine control system.

#### Additional Wind Turbine Physical Enhancements

The implementation of the wind turbine control system developed in this project has required the addition of a substantial amount of new hardware to the turbine. The following is a list of components that were installed into the turbine in the course of the work on this project, and which have not been discussed in previous sections:

- Electric wiring for control signals and power, some of which is shown in Figure 5.
- Sealed boxes for electronics inside the turbine nacelle; one such enclosure is shown in Figure 5. Other boxes house the isolated high voltage and current sensing circuitry and the in-nacelle control computer with its accelerometer.
- A weatherproof, secure enclosure at ground level for the high voltage wiring and components which control the turbine's output power.
- A second weatherproof, secure enclosure at ground level which houses the PLC based control system and the data logger. This enclosure is separate from the high voltage enclosure for safety reasons.



- A 3-axis accelerometer with data logging microcontroller, mounted directly beneath the main rotor bearing nearest the hub. This system was used to measure the vibration of the turbine due to blade imbalances.
- A yaw motor. This motor controls the direction in which the turbine points; in normal use, it points the turbine into the wind. The yaw motor has been configured for initial tests to be operated by the PLC based controller. This admittedly crude initial design will be replaced with a microcontroller based solution after the yaw control system's initial tests have been completed.

The installation of the yaw motor brings two substantial benefits to the wind turbine. First, it allows testing of the response of the turbine rotor to yaw misalignment with the wind direction. Such testing will produce significant and publishable research data. Second, active computer based yaw control is the method used by large utility-scale wind turbines (as opposed passive tail vanes, which are commonly used only in the smallest turbines). Thus the yaw motor enhances the wind turbine's effectiveness as a teaching tool by exposing students to the technology of utility-scale machines.

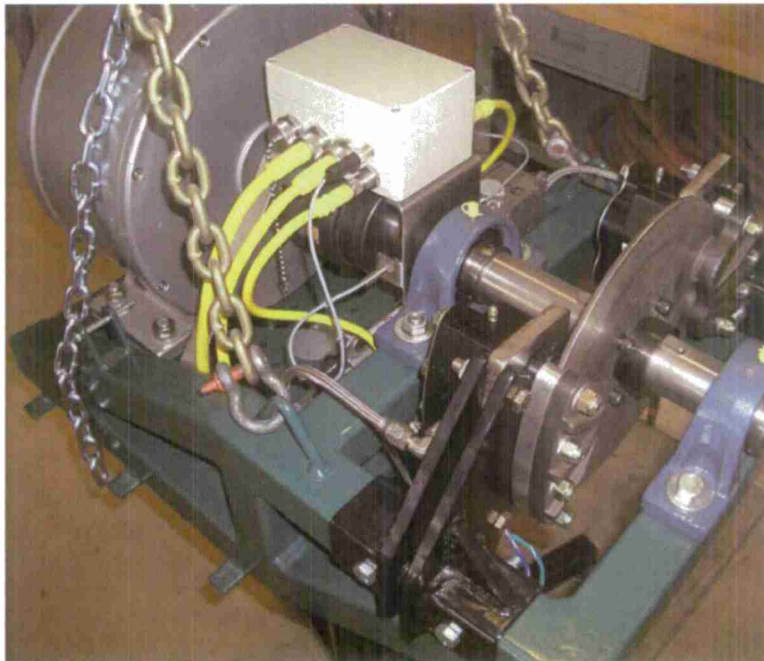


*Figure 5: Wind turbine nacelle with covers removed. The light colored box near center top houses electronic connections. Other enclosures not shown house turbine control computer and high voltage measurement circuitry.*



*Figure 6: The wind turbine nacelle, on the lowered tower, being serviced by the author in the Spring of 2012. The respirator was used to alleviate allergies.*

During the course of the project, most of the wind turbine's components were tested and upgraded, as is normal for any development project during its initial deployment phase. Upgrades have included changes to the venting system for the hydraulic brake to prevent oil spillage as the tower is tilted; alterations to wiring inside the nacelle; and the addition of considerably improved screens on the tower and nacelle to prevent intrusion by rodents, who greatly enjoy chewing on wiring (some rats even climbed into the 70 foot tower at its base, traversed the full length of the tower as it was resting in its horizontal maintenance position, and seriously damaged the wiring inside the top of the tower; the wiring had to be replaced).

#### Wind Turbine Deployment

With the support of C<sup>3</sup>RP, the aforementioned components of the Cal Poly wind turbine have been installed and tested, and the turbine has been brought to operational status

during the Summer and Fall of 2012. So far, the turbine has not been operated unattended, although once the turbine is running, the presence of an operator has been required only as a precaution; once an operational mode is chosen, the turbine operates properly without requiring user input. During operations prior to the writing of this report, maintenance has been performed on the turbine after every few (2 – 5) hours of operation, but such maintenance has been of a preventative nature rather than required to fix problems. The lowering of the tower, removal and replacement of the blades and nacelle covers, and raising of the tower have become routine operations. Typically, it takes approximately 30 minutes to lower the tower, access the turbine and make minor adjustments, and raise the tower again. In addition, the reliability of useful wind at the turbine site has been high, as had been predicted from measurements made over the preceding several years with the anemometer tower located adjacent to the turbine. It is estimated that insufficient wind for testing has been a problem during only about ten percent of the days spent at the site. The efficiency and relative predictability of operations will greatly aid the performance of the research work discussed in Section 5 below.



*Figure 7: Wind turbine tower being raised. Due to the tower's "tilt-up" design, a cycle of lowering the tower, performing minor inspections or maintenance, and raising the tower again can usually be performed in under an hour.*

#### Wind Monitoring Station Design

A goal of this project has been to improve wind monitoring capability with the intention of characterizing the wind resources in the area near the Cal Poly campus and the Escuela



Ranch field site. This information may in the future help with efforts to attract commercial wind turbine manufacturers to site one or more wind turbines in the vicinity of Cal Poly; such efforts have not been successful to date, though discussions have occurred. Unfortunately, the current state of the domestic wind turbine manufacturing industry is one of contraction, and such interest is unlikely in the near term. For this reason, it is felt that a large-scale effort to map the wind resource near campus would not be well justified, and our resources should primarily be concentrated on the development of the wind turbine. However, preparations have been made so that if interest in wind development near campus seems likely, a network of wind measurement stations can be quickly deployed. A set of sensors (anemometers and wind vanes) has been procured, and circuits have been designed which are optimized for wind data collection. These circuits, named "Swoop 3", are improved versions of previous circuits which are currently used for wind measurement and unsurprisingly named Swoop 1 and 2. The new circuits are smaller and less costly than previous versions, and they use more modern radio modules (Xbee-Pro<sup>TM</sup> modules from Digi Corporation) to achieve outdoor ranges up to 10 miles for line of sight connections. Onboard circuitry allows the implementation of a shunt-mode solar panel charge controller without circuitry external to the board. These boards, whose layout is shown in Figure 8, have been designed and tested by a student team in a graduate level course on mechatronics held in Fall 2012. A simple and inexpensive design for 20 foot stayed wind sensor towers has been created; after being fabricated, such towers can each be installed in 2 to 4 hours at remote sites, depending on the local soil conditions. A relatively large number of small towers will provide data that allows a Computational Fluid Dynamics (CFD) based model of the local wind resource which has been developed in a Masters thesis advised by Professor Lemieux to be calibrated so that promising local sites for future turbines can be confidently chosen.

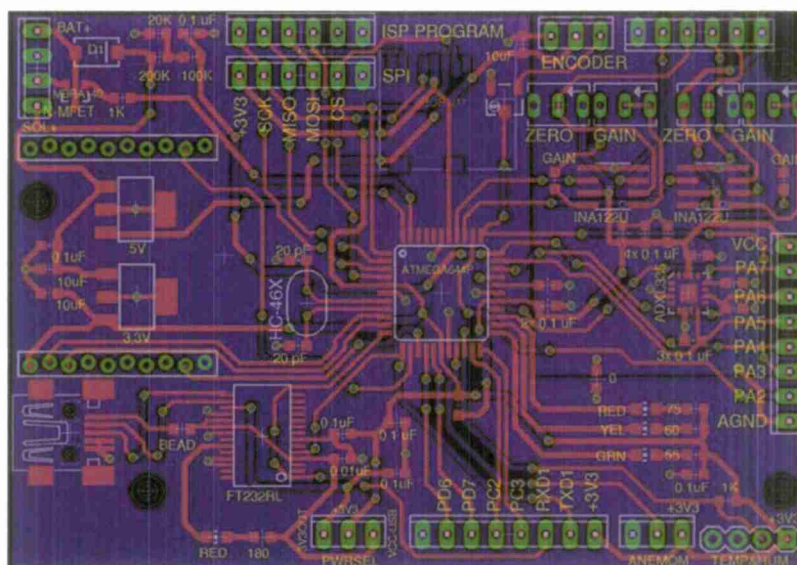


Figure 8: "Swoop 3" weather sensor circuit board layout. The circuit is designed to operate autonomously without requiring maintenance for up to 2 years at a time in remote locations.

## 5. Conclusions and Future Work

With the generous support of ONR and C<sup>3</sup>RP, the Cal Poly Wind Power Center has become fully operational as a unique resource for education and research in wind power and related fields. This facility embodies the Cal Poly philosophy of *Learn by Doing* in a very direct way, having been designed and built almost entirely by Cal Poly students, staff, and faculty. This facility will be used to deliver educational and research benefits to the University and the United States for many years to come.

With the Cal Poly wind turbine operating, a long term program of education and research has been brought fully up to speed; the following projects will be undertaken:

- Development of laboratory exercises for undergraduate courses in wind energy and energy conversion
- Characterization of the turbine's performance over its entire operational envelope
- Blade performance at differing blade pitch angles. Initially, this work will be done by manual pitch control; it is intended that a pitch control system will be designed, built, and installed in the future when funding has been secured
- Analysis of blade loads during operation
- Studies of tower resonances and rotor-tower interactions
- Optimal control of the wind turbine throughout its operational envelope (work began in Spring 2012)
- Condition based maintenance of composite blades (work began in 2011)

Most of these topics are part of the vision for the Wind Power Center which was conceived by Professor Patrick Lemieux as the Center was set up. Each will lead to the

publication of one or more technical papers in the appropriate venues, and all will involve Cal Poly students as an integral part of the work.

#### 6. References cited

1. American Wind Energy Association, [http://www.awea.org/learnabout/industry\\_stats/index.cfm](http://www.awea.org/learnabout/industry_stats/index.cfm), 18 Nov 2012.
2. Lemieux, Patrick, *Final report of C3RP-funded work on the Cal Poly Wind Power Research Center*, 2010.
3. Gwon, Tae Gyun, *Structural Analyses of Wind Turbine Tower for 3 kW Horizontal Axis Wind Turbine*, Cal Poly Masters thesis, 2011, available at <http://digitalcommons.calpoly.edu>.
4. Edwards, Bryan, *Composite Manufacturing Of Small Wind Turbine Blades - Utility Scale Methods Applied To Small Wind*, Cal Poly Masters thesis, 2009, available at <http://digitalcommons.calpoly.edu>.
5. Simon, Derek, *Static Balancing of the Cal Poly Wind Turbine Rotor*, Cal Poly Masters thesis, 2012, available at <http://digitalcommons.calpoly.edu>.
6. Nosti, Chris, *Performance Analysis and Life Prediction for Small Wind Turbine Blades: A Wood Laminate Case Study*, Cal Poly Masters thesis, 2009, available at <http://digitalcommons.calpoly.edu>.
7. Chung, Chun Kau, *Small Wind Turbine Blade Sensor for Condition Based Maintenance*, Cal Poly Masters thesis, 2011, available at <http://digitalcommons.calpoly.edu>.
8. Katsanis, G., Lemieux, P., *Transient Small Wind Turbine Tower Structural Analysis with Coupled Rotor Dynamic Interaction*, poster for American Wind Energy Association *AWEA Windpower 2012*, Atlanta, GA, June 3-6 2012.
9. Simon, D., Lemieux, P., *Static Balancing of Small Composite Turbine Rotors*, presentation to American Wind Energy Association *AWEA Windpower 2012*, Atlanta, GA, June 3-6 2012.
10. Simon, D., Lemieux, P., *Static Balancing of Wind Turbine Rotors*, in preparation for ASME Journal of Solar Energy Engineering.
11. Pastrich, D., Lemieux, P., Owen, F., *Design of a Safety System for Wind Turbine Tower Tilt-Down Operations*, poster for American Wind Energy Association *AWEA Windpower 2012*, Atlanta, GA, June 3-6 2012.

## **Overcoming Barriers to Affordable Algae Biofuels: Phase II**

Principal Investigator:

**Tryg Lundquist, Ph.D., P.E., Civil and Environmental Engineering**

Co-Investigators:

**Yarrow Nelson, Ph.D., Civil and Environmental Engineering**

**Christopher Kitts, Ph.D., Biological Sciences**

**Mark Moline, Ph.D., Biological Sciences**

**Corinne Lehr, Ph.D., Chemistry and Biochemistry**

California Polytechnic State University  
San Luis Obispo, CA

## 1. Abstract

An interdisciplinary team of researchers at Cal Poly has developed a program in microalgal biotechnology research focused on biofuel feedstock production in conjunction with wastewater treatment. The wastewater provides nutrient and water for algae growth, and, in the process of growing algae biofuel feedstock, the algae treat the wastewater. This “co-service” of wastewater treatment could generate revenue and offset a substantial part of the biofuel production cost (Lundquist et al., 2010). In addition, Department of Defense (DOD) has wastewater treatment responsibilities, such as on military bases and in civil administration missions. The wastewater treatment-algae biofuel technology being developed in this project may be preferable to conventional treatment technologies in many of these locations.

Algal biofuel is important because it could contribute to the energy mix of the US military and decrease the overall greenhouse gas footprint of DOD activities. Although algae can produce oil at a much higher rate than conventional crops, the cost of algae production is high due to the need for large ponds and the cost of algae harvesting. The economics of algal biofuel production could be improved most effectively by (1) improving algae production per unit area, (2) increasing the oil content/productivity of the algae, and (3) perfecting low-cost algae harvesting methods.

Previous support from C<sup>3</sup>RP and others was used to develop four 4-m<sup>2</sup> pilot-scale algal production ponds that were operated at the San Luis Obispo wastewater treatment plant during 2007-2011. An additional four ponds were added in 2010 with non- C<sup>3</sup>RP funds. Using information gathered from these ponds, a new larger project was initiated with partial support of the California Energy Commission. In 2011, the new Cal Poly Algae Field Station began operation of new nine 30-m<sup>2</sup> algae ponds growing common algae genera found in wastewater, allowing for extensive replicated research at a meaningful scale. The effluent of the 30-m<sup>2</sup> ponds is pumped to tube settler devices for algae-water separation by gravity. These new ponds successfully demonstrated bioflocculation for low-cost harvesting of algae and nutrient removal on a consistent basis for over a year. We have also conducted successful lipid induction experiments showing up to 50% oil content. Continuing research (supported by DOE) focuses on recycling nutrients and water in algae biofuel systems, while increasing biomass and oil productivity (tons/hectare-year).

## 2. Project significance

Energy alternatives and fuel efficiency are important for DOD missions because these technologies are needed to reduce the military’s reliance on petroleum fuels.

Development of microalgal biofuels is a top priority of the DOD because algal biomass can be produced without competition with food crops, and the areal productivity (g/m<sup>2</sup>/d) of microalgae is among the highest of the photosynthetic organisms (DARPA, 2007; AFOSR, 2008). In addition, algae cultivation can mitigate greenhouse gas emissions by providing carbon-neutral renewable fuels.



Beyond the biofuel/greenhouse (GhG) benefit, the development of a low-cost nutrient removal technology would benefit DOD. Wastewater treatment is one of the vital services supplied by the US military at its bases and in its civil affairs activities. In fiscal year 2003, the US military operated 700 overseas bases and another 6,000 within the US and its territories (DOD, 2003). The Army alone operates over 100 small wastewater treatment plants on bases (Scholze and Zaghloul, 2001). If similar to civilian communities, a substantial proportion of the public works budget of a military base is expended on the wastewater management enterprise.

US civilian needs are also great. The American Society of Civil Engineers estimates that over the next 20 years communities in the US will need to invest \$390 billion to renovate existing wastewater treatment facilities and to build an additional 2,000 treatment facilities (ASCE, 2005). This level of investment has been called an unprecedented financial problem for utilities (WIN, 2000).

### 3. Background/prior work

#### Algal Biofuel Production

The combination of wastewater treatment with algae biofuels production is opportunity to lower the cost of the biofuel by using low cost wastewater nutrients and possibly offsetting some of the fuel cost with treatment fees. Figure 1 shows the standard process diagram for this combined concept.

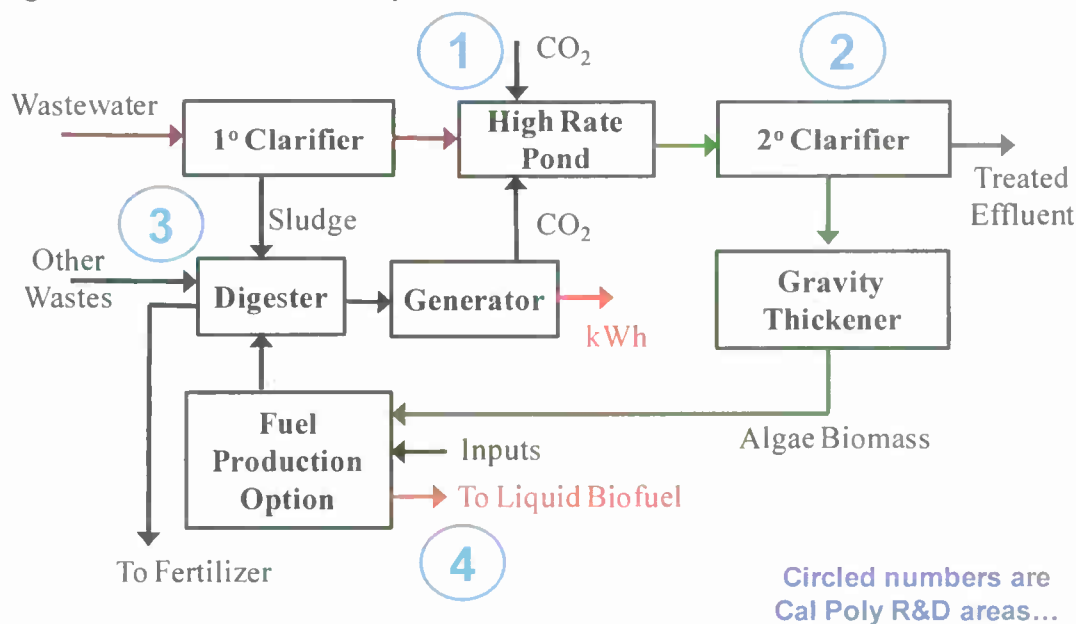


Figure 1: Process flow diagram for an algae wastewater treatment and biofuel system.

In the Figure 1, the primary (1°) clarifier uses gravity to recover wastewater solids for anaerobic digestion. High rate ponds are shallow raceways, mixed by paddle wheels, which are standard devices for algae cultivation. The secondary (2°) clarifier collects settled algae, separating the treated effluent from algae slurry. The algae slurry is thickened and processed for oil extraction, with the non-oil residuals going two anaerobic

digestion. The biogas is combusted to generate electricity and to produce a flue gas enriched with carbon dioxide to promote algae growth.

The Cal Poly Algae Field Station was completed and began operation 2011 (Figure 2). The facility consists of nine 30-m<sup>2</sup> to allow for cultivation research. This facility allows for replicated research on many of the major issues in algae biofuels: (1) cultivation, (2) harvesting, (3) digestion of waste and their recycling, and (4) production of algae oils, in addition to the overall goal of recycling wastewater resources into algae biofuels.



Figure 2: The Cal Poly Algae Field Station used in the current research.

#### **Bioflocculation for Algae Harvesting and Effluent Suspended Solids Control**

Wastewater treatment ponds are notorious for having excessive total suspended solids (TSS) in their effluent, primarily in the form of planktonic algae. Similarly, algae produce for biofuel is planktonic and must be harvested. While pond systems with a series of ponds and long hydraulic residence times are often able to meet local TSS discharge limits, as communities grow, the capacity of the pond systems to settle algae diminishes and increased loading can promote algal blooms of greater concentration, including blue-green algae in the later ponds of a series. A common intervention in these situations is removal of pond TSS by chemical coagulation and clarification (settling or flotation), but these are costly and energy intensive.

Activated sludge is a common wastewater treatment technology. Activated sludge bacteria naturally bioflocculate facilitating settling and harvesting. This phenomenon can also occur in algae cultures. Relatively few studies focusing on bioflocculation of wastewater algae have been conducted since the concept was first introduced (e.g., Gotaas and Golueke 1958, McKinney 1969, Benemann et al. 1980, Hall 1989, Shipin et

al. 1999, Lundquist et al. 2007). The most developed process would seem to be the passage of conventional oxidation pond effluent through an activated sludge plant to trap algae in bacterial flocs (Shipin et al. 1999). The activated sludge plant can also allow for removal of residual nutrients. However, the addition of an activated sludge plant, like addition of coagulation and clarification, diminishes some key advantages of ponds, namely their simplicity, low cost, and low energy consumption.

Another approach to harvesting is in-pond bioflocculation. High rate ponds (HRPs) have mixing intensities similar to water treatment flocculation basins. Bioflocculation in HRPs had been demonstrated previously on large-scale but with only sporadic success (see references above). However, progress has been made at Cal Poly during the C3RP project in achieving continuous bioflocculation, resulting in fairly complete TSS removal in Imhoff cone settling tests and continuous-flow pilot tube settlers.

The regulatory effluent suspended solids concentrations for pond systems varies widely in the US, primarily because pond effluent is often discharged to percolation beds or restricted irrigation allowing more latitude in concentration (e.g., several California pond systems have discharge limits in the range of 40-100 mg/L ). At the Federal level, the USEPA provides for an "equivalent to secondary treatment" standard to trickling filters and ponds, restricting discharge to 45 mg/L (30-day average) and 65 mg/L (7-day average) for both TSS and biochemical oxygen demand (BOD<sub>5</sub>). Further allowances are allowed for ponds (USEPA 2010), but states may, of course, requirement stricter standards. In any case, achieving low effluent TSS is beneficial for slowing the clogging of percolation basins and decreases the chemical costs of coagulation and disinfection in wastewater recycling systems.

At the Cal Poly Algae Field Station, harvesting units were constructed to replicate full scale tube settlers for gravity separation (Figure 3). The individual tube settlers are able to harvest a portion of the effluent from each of the ponds, which is sufficient for pilot testing of the developed bioflocculation techniques.



**Figure 3: Cal Poly Algae Field Station Tube Settlers for algae-water separation.**

#### **Nutrient Removal and Recovery in High Rate Ponds**

Meeting new nutrient removal requirements is another difficulty for full-scale conventional wastewater treatment ponds. For algae biofuel production systems, efficient nutrient recovery is also an important issue. Nutrients can indeed be recovered effectively by algae. Simultaneous nitrogen and phosphorus assimilation by wastewater pond algae has been shown to be virtually complete in benchtop experiments (Fulton, 2009). However, to achieve this effect with most domestic wastewaters, the culture must be sparged with CO<sub>2</sub> to balance the ratio of carbon-to-nutrients (Woertz et al. 2009; Lundquist et al. 2011). The main routes of nitrogen removal in HRPs are (1) assimilation by growing algal cells, followed by their removal from the water by clarifiers; (2) nitrification followed by denitrification during any anoxic periods at night or in sludge deposits; and (3) volatilization of ammonia from the pond surface. For effective nutrient removal, removal of the nutrient-rich suspended solids must be accomplished by sedimentation and, as needed, filtration.

#### **4. Discussion of Results**

The overall project objectives and the related task numbers are the following:

1. Achieve a consistent 90% sedimentation harvesting efficiency of microalgae through control of bioflocculation.
2. Achieve <10 mg/L total ammonia nitrogen (N) year-round.
3. Determine conditions/strains that maximize lipid productivity



### Objective 1: Sedimentation harvesting efficiency results and discussion.

Algae settling efficiencies were measured both by benchtop and at pilot scale in the field. The benchtop method uses an Imhoff cone which replicates a settling tank to test both 2-hr and 24-hr settling. Pilot testing used the Algae Field Station tube settlers (Figure 3) which are continuously fed algae pond water. The supernatants of these tube settlers were monitored on a weekly basis. All nine ponds and their tube settlers were monitored throughout the year. However, we will only discuss two ponds in this report for brevity. The types of algae genera that were grown throughout the year include: *Cyclotella*, *Scenedesmus*, *Chlorella*, *Westella*, Pennate diatoms, and spherical green algae probably *Chlorococcum*.

Benchtop settling results for Ponds 8 and 9, as shown in Figure 4 and Figure 5 respectively, demonstrate 2-hr settling times can achieve a biomass concentration in the supernatant of less than 80 mg/L consistently throughout the year. After 24-hrs of settling the biomass concentration in the supernatant was even lower, below 40 mg/L. These results are a significant demonstration that bioflocculation can be a consistent and an inexpensive technology for harvesting algae.

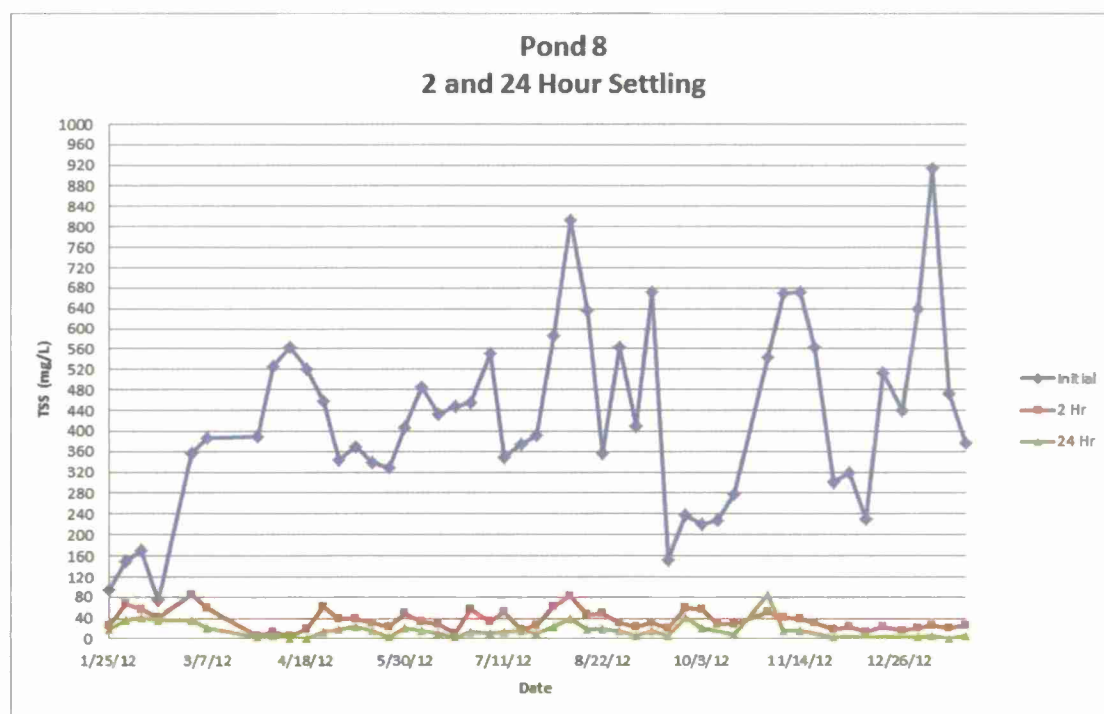


Figure 4: 2-hour and 24-hour settling for Pond 8 for 2012



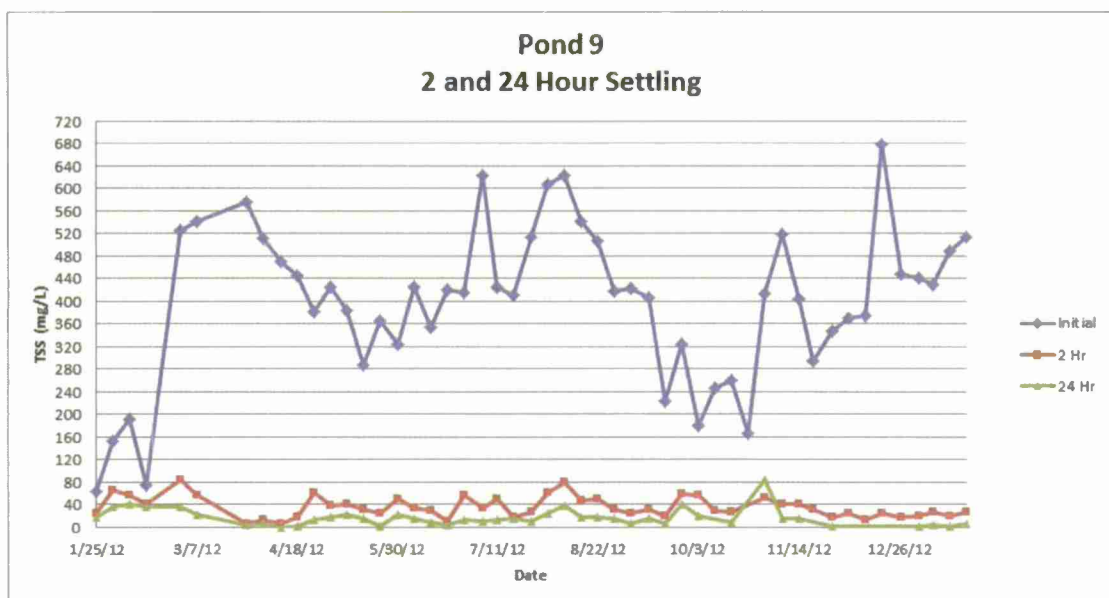


Figure 5: 2-hour and 24-hour settling for Pond 9 for 2012

In-field testing of algae biomass harvesting proved to be as successful as in lab testing (Figure 6 and Figure 7). Results show that concentrations of supernatant TSS from continually operating tube settlers can be held consistently below 40 mg/L. The settled algae biomass concentration was measured to range from 2-5% solids. This biomass concentration is typical to what is found in settled wastewater sludge.

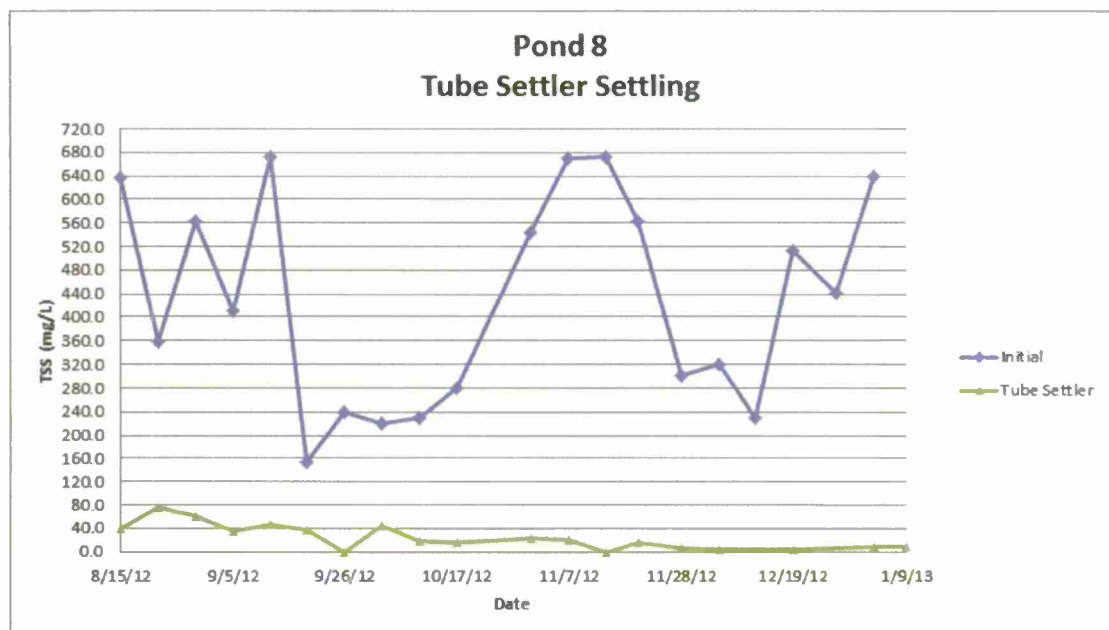


Figure 6: Tube settler influent and supernatant for pond 8

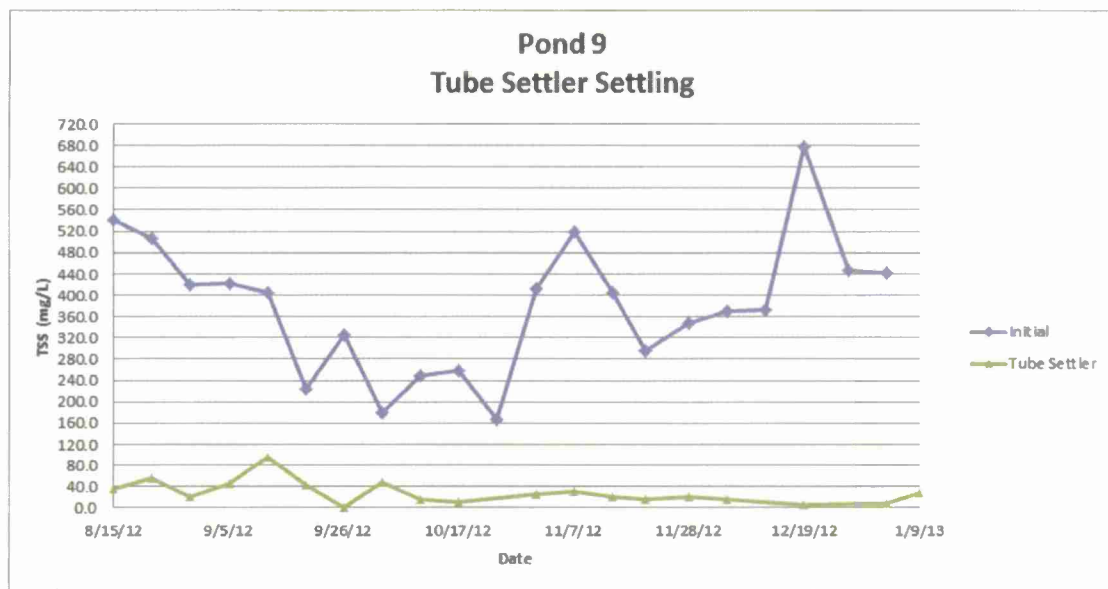


Figure 7: Tube settler influent and supernatant for pond 9

## Objective 2: Achieve <10 mg/L total ammonia nitrogen (N) year-round.

Previous experiments conducted on ammonia nitrogen removal had been successful for the warm parts of the year achieving < 10 mg/L  $\text{NH}_x$ . However, colder winter operation had proven to be difficult to maintain such low concentrations of ammonia. In order to achieve this low of a concentration throughout the year, we operated two sets of triplicates (six ponds in total) in series with algae harvesting after each round. The ponds were operated on a continuous basis with the first round of algae growth operating with hydraulic retention times of 3 days. The second round high rate ponds were operated with retention times of 4 days. In addition, the second round of high rate ponds were supplemented  $\text{CO}_2$  by automatic sparging of gas to maintain a pH of 8.5. The seasonal results are shown below in Figure 8, Figure 9, and Figure 10.

Summer ammonia removal for Round 1 was 90% and Round 2 was >99% (Figure 8). In Fall 2012, ammonia removal dropped to 82%, but Round 2 remained at > 99% (Figure 9). In Winter 2012, ammonia removal in Round 1 dropped to only 73%. However, Round 2 removal decreased slightly to >98%. These results suggest that with two rounds of algae growth in high rate ponds very low ammonia concentrations in wastewater effluent can be maintained throughout the year, even winter. Of course, these results are climate specific and will need to be tested over longer periods, in other locations, and at larger scale.

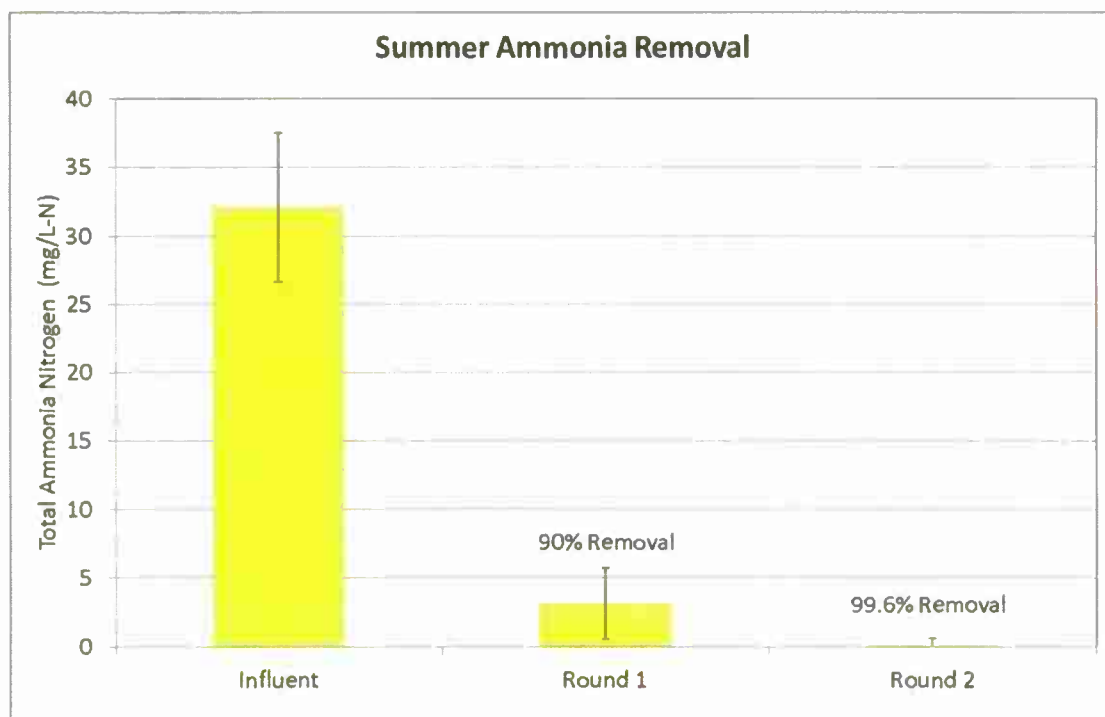


Figure 8: Ammonia removal in Summer of 2012

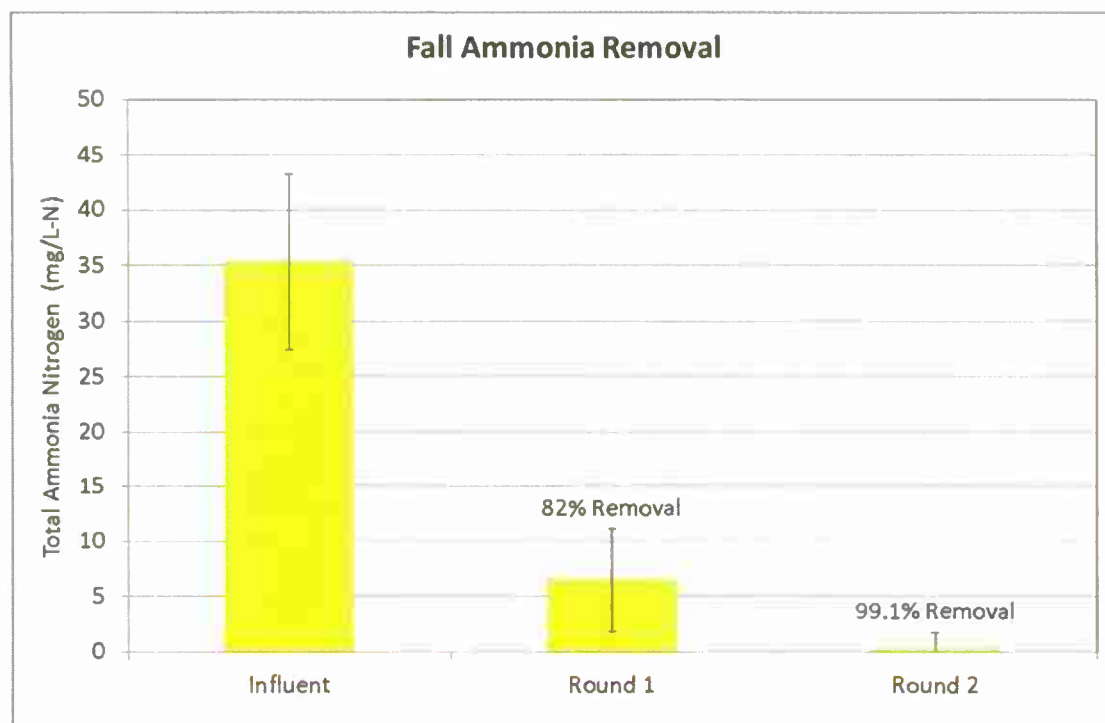


Figure 9: Ammonia removal in Fall 2012

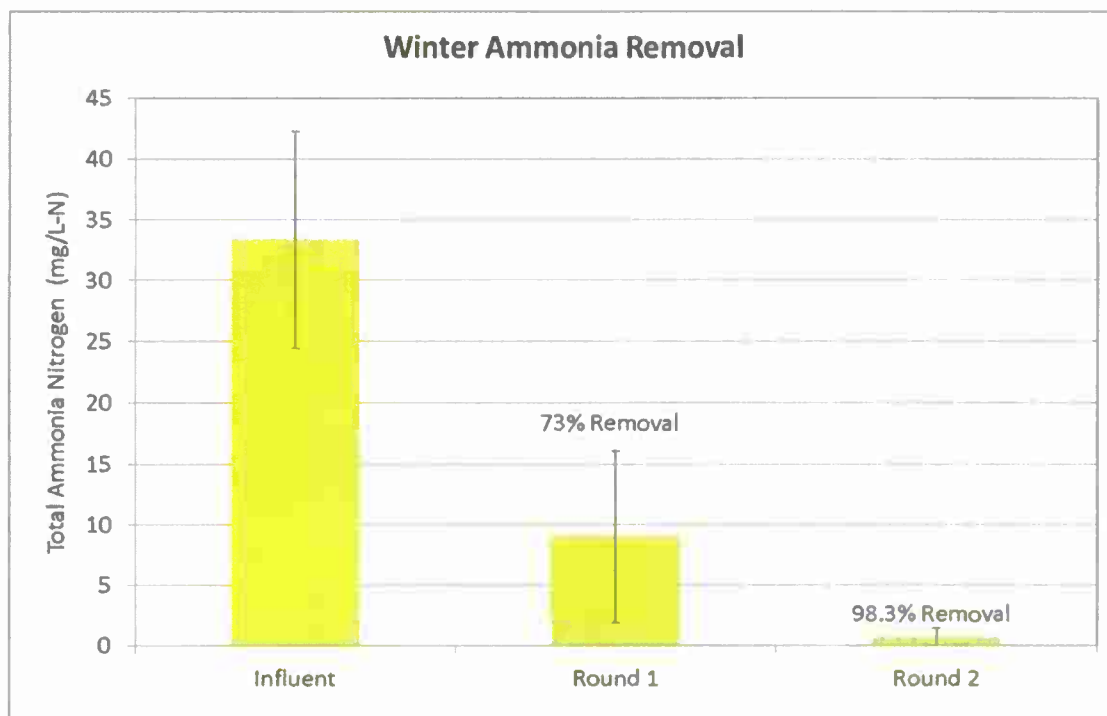


Figure 10: Ammonia removal in Winter 2012

Phosphorus is another nutrient of concern for wastewater treatment as it can lead to eutrophication. Algae assimilation of phosphorus can be an effective way of capturing phosphorus in wastewater. In December of 2012, a phosphorus balance was performed on Pond 2 and its tube settler (Figure 11). Influent phosphorus concentrations of combined particulate and dissolved were just below 4 mg/L. After a round of growth in the high rate pond, the dissolved phosphorus dropped to just above 1 mg/L. The majority of the remaining particulate phosphorus in the pond effluent was assimilated into algae biomass as shown with the tube settler supernatant (settler effluent) phosphorus levels.

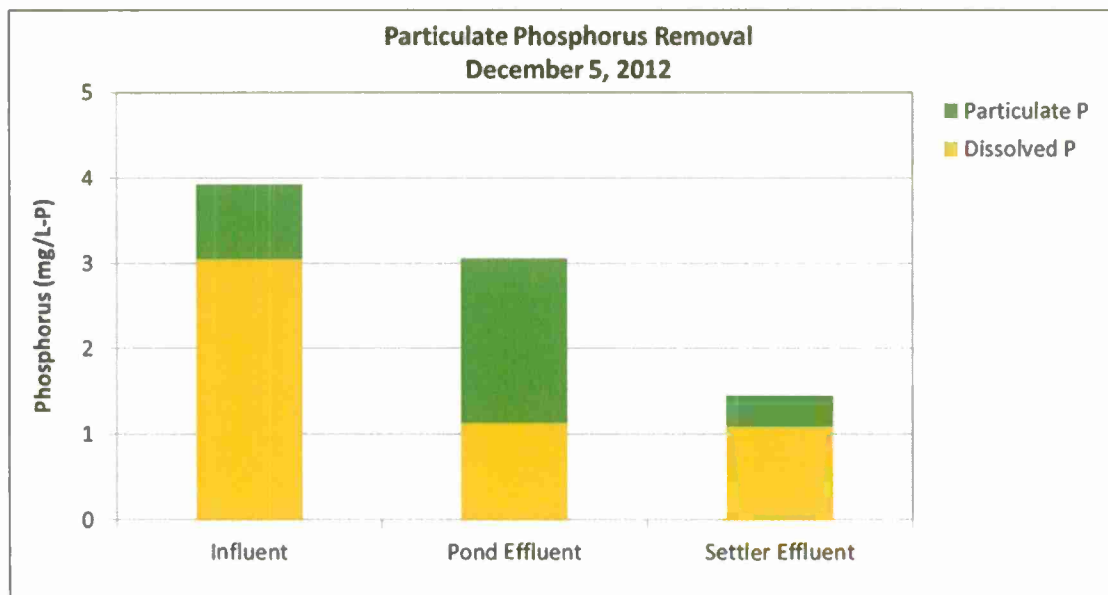


Figure 11: Particulate Phosphorus removal by Pond 2

### Objective 3: Determine conditions/strains that maximize lipid productivity

The most promising lipid optimization results that we have achieved so far are in a lab experiment. In this experiment, a light shift was tested whereby light intensity of grow lights was doubled after nutrients had become limited. It was hypothesized that this stress condition causes algae to increase fatty acid content. This accumulation of lipids was observed to reach up to 50% of the biomass concentration (Figure 12) on day 9 of incubation. The carbon chain length and saturation of these lipids were mainly C16 and C18:1 as measured using a GC-MS. These types of oils are appropriate for conversion to biodiesel or other types of green fuel. Previous in-house experiments have only been able to show lipid concentrations up to ~30% (Woertz et al., 2009). Future experiments hope to decrease the time required to induce this lipid accumulation and to reproduce these findings in the field.



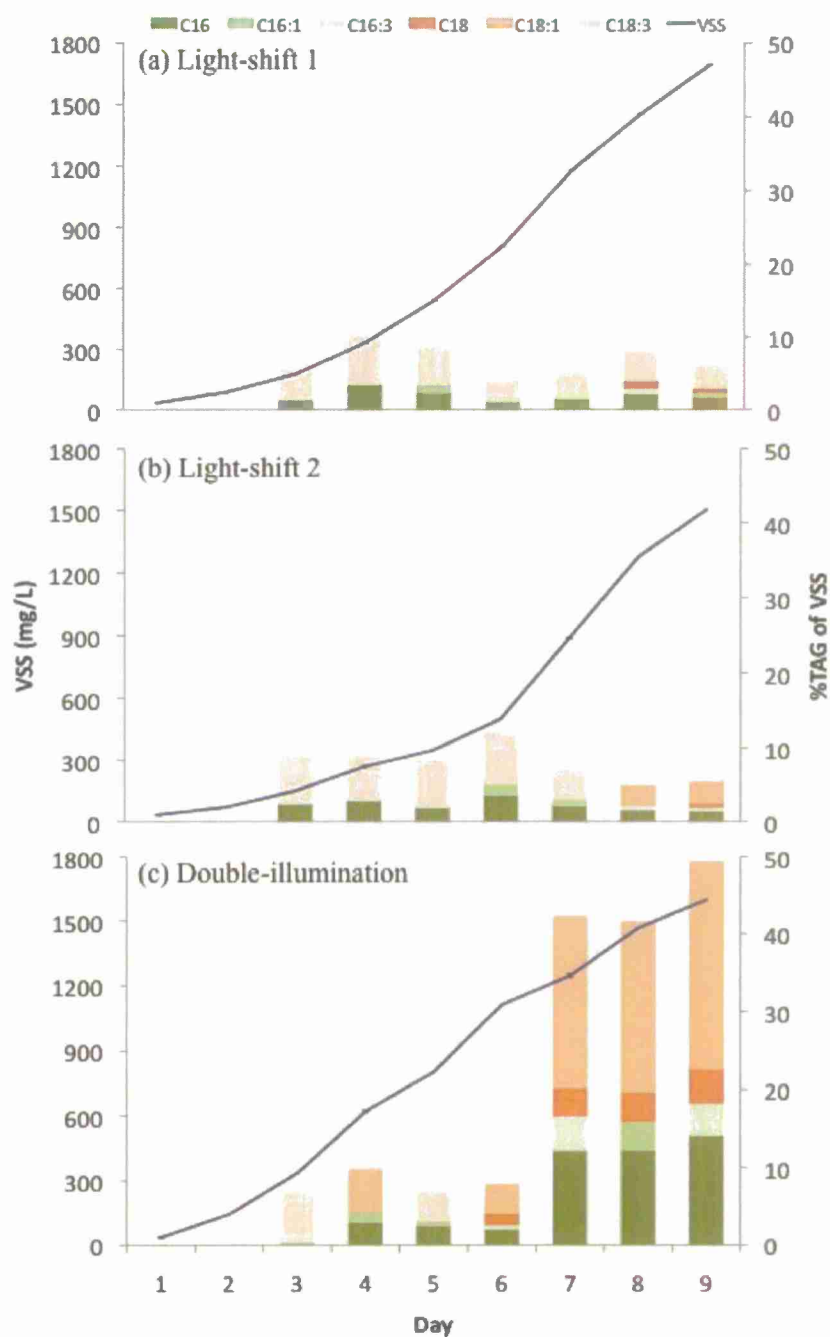


Figure 12: Lipid productivity experiment showing up to 50% lipids

#### Additional Research Conducted

To understand bioflocculation better and control sudden upsets, attempts were made to identify potential bacteria that are contributing to bioflocculation. Samples from Cal Poly Algae Field Station were allowed to settle for two hours in Imhoff cones and total suspended solids (TSS) were measured in the supernatant. Terminal Restriction Fragment

Length Polymorphism (TRFLP) was then used to analyze the bacterial community in both the supernatant and the settled floc. Samples were collected from nine ponds over a three-month period, and TRFLP profiles were compared to TSS values. The relative number of TRF peaks corresponding to the chloroplast of *Chlorella* sp. was negatively correlated to supernatant TSS, indicating that *Chlorella* sp. may enhance flocculation. In additional experiments, samples from paired ponds with high and low TSS were compared. In every case, significant differences were apparent in the bacterial community of both supernatant and floc samples. TRF peaks that were most common in samples with low TSS were used to tentatively identify numerous bacterial contributors to good flocculation. These results indicate there may be specific bacterial contributors to good bioflocculation. Further study is required to confirm their identity and efficacy

## 5. Future Work Planned

Thanks in part to seed money from C3RP Cal Poly has developed an algae program that is considered a leading research organization in the field of algae biofuels. Recently the Department of Energy (DOE) has awarded Cal Poly two separate grants. The first grant for \$1.3 million is to research how nutrients can be recycled for algae production farms. Recycling of nutrients is another way to improve the economics of producing low cost algae biofuels. For example, in most large-scale engineering models the recycling of nutrients and water are a key component to making algae biofuels sustainable and low-cost. There are many unknowns to this process such as the effect of inhibitory compounds that may accumulate in the water after several rounds of algae growth.

The second grant that Cal Poly received recently, as a subcontract from Arizona State University, is part of the U.S. Department of Energy National Algae Biofuel Testbed program, which will build baseline data for algae productivity and culture stability at different geographical locations in the US. Both grants have extensive research plans for the next three years, and the Cal Poly Algae Tech Group has expanded its student and staff numbers to accomplish these goals.

Other future work planned includes scaling up lipid enhancement techniques to pilot testing in-field and continued bioflocculation experiments to prove long term stability, with the ultimate goal of developing more sustainable infrastructure for both fuel production and wastewater reclamation.

## 6. References cited

AFOSR (2008). NREL-AFOSR Workshop on Algae to Biofuels, Seidman Center, February 19-21, Arlington, Virginia.

ASCE (2005). Report card for America's infrastructure, American Society of Civil Engineers, [www.asce.org/reportcard/2005/page.cfm?id=35#one](http://www.asce.org/reportcard/2005/page.cfm?id=35#one), accessed 11/30/05.

Benemann, J.R., B. Koopman, J. Weissman, D. Eisenberg, and R. Gobel (1980). "Development of microalgal harvesting and high-rate pond technologies in California."

In: Algae Biomass (G. Shelef and C.J. Soeder, eds.), Elsevier/North-Holland Biomedical Press, pp. 457-495.

DARPA (2007). "Biofuels–Cellulosic and Algal Feedstocks Program Solicitation Announcement (BAA08-07)," Dr. Douglas Kirkpatrick, Biofuels Program Manager, Algae Biomass Summit, Nov. 15-16, 2007, San Francisco.

DOD (2003). *Base Structure Report*, Fiscal Year 2003, Department of Defense, Office of the Undersecretary of Defense (Installations).

Gotaas, H.B. and C.G. Golueke (1958). "Recovery of Algae from Waste Stabilization Ponds," I.E.R. Series 44, Issue No.7, Sanitary Engineering Research Laboratory, University of California, pp. 154.

Fulton, L.M. (2009). *Nutrient Removal by Algae Grown in CO<sub>2</sub>-Enriched Wastewater over a Range of Nitrogen-to-Phosphorus Ratios*, Master's Thesis, Civil and Environmental Engineering Department, California Polytechnic State University, San Luis Obispo.

Hall, T.W. (1989). *Bioflocculating high-rate algal ponds: Control and implementation of an innovative wastewater treatment technology*, Ph.D. dissertation, Department of Civil and Environmental Engineering, University of California, Berkeley.

Lundquist, T.J., J.R. Benemann, A.S. Feffer, and I. Woertz (2007). "Nutrient Removal and Biofuel Production through Microalgae-Based Wastewater Treatment," presentation to the *First Western Forum on Energy & Water Sustainability*, March 22-23, 2007, University of California, Santa Barbara.

Lundquist, T., I. Woertz, N. Quinn, J. Benemann, (2010). A Realistic Technology and Engineering Assessment of Algae Biofuel Production. Energy Biosciences Inst., U. C. Berkeley, Nov. 2010  
<http://www.energybiosciencesinstitute.org/media/AlgaeReportFINAL.pdf>

Lundquist, T.J., I.C. Woertz, and J.R. Benemann (2011). "Algal high rate ponds with CO<sub>2</sub> addition for energy efficient nutrient recovery," Paper written for the Nutrient Recovery and Management 2011 conference, Water Environment Federation, January 9-12, 2011, Miami, Florida, pp. 14.

McKinney, R.E. (1969). "Waste Treatment," US Patent 3,462,360.

Scholze, R.J., and H.H. Zaghoul (2001). *Assessment of SCADA Technology Applications to Automate U.S. Army Water and Wastewater Sanitary Systems*, Report number: A037893, Engineering Research and Development Center, Champaign, Illinois, pp. 28.

Shipin, O.V., P.G.J. Meiring, M.R. Phaswana, and H. Kluever (1999). "Integrating ponds and activated sludge process in the PETRO concept," *Water Research*, Vol. 33, No. 8, pp. 1767-1774.

USEPA (2010). *National Pollutant Discharge Elimination System (NPDES) Permit Writers' Manual*, EPA-833-K-10-001, September 2010, Water Permits Division, Office of Wastewater Management, United States Environmental Protection Agency Washington, DC.

WIN (2000). *Clean & Safe Water for the 21st Century*, Water Infrastructure Network, Washington, D.C. <http://www.nacwa.org/getfile.cfm?FN=winreport2000.pdf>.

Woertz, I.C., T.J. Lundquist, A.S. Feffer, Y.M. Nelson (2009). "Lipid productivity of algae grown on dairy and municipal wastewaters for biofuel feedstock." *Journal of Environmental Engineering*, American Society of Civil Engineers, Vol. 135, Issue 11, pp. 1115-1122.

# **Human performance**

## **Project Reports**



**Does ethanol nullify the benefits of exercise in skeletal muscle?**

Principal Investigator:

**Jason Blank, Ph.D., Biological Sciences**

California Polytechnic State University  
San Luis Obispo, CA

### 1. Abstract (~250 words)

Alcoholism is widespread in the United States and alcoholic muscle disease afflicts one third to two thirds of chronic alcoholics, resulting in decreased muscle mass and strength. Alcohol/ethanol decreases the size of muscle cells by inhibiting specific steps in the major intracellular signaling pathway that regulates protein turnover and controls cell size. A number of studies have characterized the deficits associated with chronic alcohol consumption and pinpointed the cellular signals blocked by acute ethanol dosage. However, most studies of ethanol effects on muscle have relied on sedentary animals, whereas protein synthesis is highly responsive to muscle activity and exercise. Thus, an important unanswered question is whether exercise can overcome the detrimental effects of ethanol on muscle and/or whether ethanol nullifies the benefits of exercise. This study aimed to assess the interaction of ethanol with exercise training in three experiments in rats. (1) To study resistance training, rats were surgically manipulated to induce growth of hind limb muscles and muscle growth was compared between animals consuming diets with or without ethanol. (2) To study the acute response to endurance exercise, rats ran on a treadmill and received either ethanol or saline injections immediately after exercise. Muscles harvested 3 hours later were analyzed for differences in phosphoprotein composition by proteomic techniques. (3) To study chronic endurance training, rats are run on a treadmill daily for six weeks and receive either ethanol or saline injections immediately after each exercise session. Improvement in running ability and aerobic work capacity ( $VO_2\text{max}$ ) will be compared among groups and activity of aerobic enzymes will be measured in muscle samples.

### 2. Project significance

Alcoholism is the most prevalent form of substance abuse in the United States, with 8.5% of American adults exhibiting either alcohol abuse or alcohol dependence (Grant et al. 2004). Alcoholic myopathy afflicts 45 to 70 % of chronic alcoholics and entails a loss of muscle size and strength and reduction in the diameter of individual muscle fibers, particularly fast-twitch fibers (Preedy et al. 1994, Fernandez-Sola et al. 2007), which has been shown to result from inhibitory effects of ethanol on protein synthesis in muscle cells (Lang et al. 2004, Preedy & Peters 1988).

Ethanol alters muscle protein balance by interfering with intracellular signaling pathways regulating protein synthesis. In particular, ethanol appears to act at the level of the mammalian target of rapamycin (mTOR), where it inhibits the kinase activity of the mTORC1 complex, reducing activation of eIF4E and S6K1 (Lang et al. 2004, 2009). This results in reduced mRNA translation and protein synthesis, as demonstrated in several studies of acute and chronic ethanol administration (Lang et al. 2000, 2009, Preedy & Peters 1988, Reilly 1997).

The protein content of muscle, and hence the overall muscle mass of the body, reflects the dynamic balance of protein synthesis and protein degradation integrated over time (Roy et al. 1991). Rates of both synthesis and breakdown of muscle proteins are regulated by numerous factors including nutritional status, hormonal state, and levels of muscle activity and muscle loading. Protein synthesis increases in response to increased muscle loading and decreases when loading is reduced (Haddad & Adams 2002). The

response to brief bouts of muscular activity can play a particularly important role in determining overall mass balance in muscle (Kim et al. 2008).

As Booth (2006) points out, some daily physical activity is normal, so sedentary humans (or animals) are an inappropriate control group for most studies. Oddly, most previous studies of alcohol effects have ignored the effect of activity on protein turnover in muscle by using only sedentary animals, while few studies have attempted to incorporate exercise with ethanol dosage (Vila et al. 2001, Vingren et al. 2005), with limited results. This focus has permitted the acquisition of detailed knowledge of the molecular mechanisms by which ethanol suppresses muscle protein synthesis, but it has left in question how ethanol might interact with exercise in animals with more complex activity patterns.

In other words, this study proposed to ask, **when ethanol is present during changing loading or activity states, what is the combined effect of ethanol and exercise? Are the effects of ethanol and exercise simply additive? Does ethanol nullify the positive influence of exercise, or does exercise overwhelm the negative effect of ethanol?**

This study aimed to evaluate effects of ethanol on the training response to exercise in the rat. Three distinct experiments were used to 1) assess whether ethanol inhibits muscle hypertrophy in a rodent model of chronic resistance training, 2) test whether post-exercise ethanol inhibits molecular responses to acute endurance exercise, and 3) determine whether ethanol administered following exercise reduces gains in aerobic fitness ( $\text{VO}_{2\text{max}}$ ) due to chronic endurance training.

The results of this study are relevant to ONR human performance goals as a greater understanding of the interaction of acute alcohol consumption and physical training may enable training and/or behavioral strategies that enhance warfighter physical readiness. According to a survey conducted in 2005, 18.5% of US military personnel are self-reported heavy drinkers (i.e. consume more than 5 drinks per occasion at least once a week; Bray 2007) as compared to 15.9% of US adult males, age 18-29 (Dawson, 2004). Thus, physiological effects of alcohol use may have an aggregate impact on force readiness. Rates of heavy drinking among military personnel have remained roughly the same over the last 25 years (Bray 2007); however Reserves/Guard personnel have higher rates of heavy drinking than those on active duty and deployment to combat zones increases post-deployment heavy drinking (Jacobson 2008). These trends suggest that current military demographic trends will only increase the importance of alcohol-related health and readiness issues.

### **3. Background/prior work**

Alcoholic muscle disease (myopathy) has been observed in human alcohol abusers for over 100 years. Horsley and Sturge (1907) remarked on “the fatty metamorphosis undergone by the muscles (and tissues enveloping them) of those who habitually take alcohol.” More recently, alcoholic muscle disease has been characterized as consisting of a reduction in muscle mass and strength caused by selective atrophy of fast-twitch (type II) muscle fibers occurring in one third to two thirds of chronic alcoholics (Preedy et al. 1994, Urbano-Marquez et al. 1989). Controlled studies of chronic ethanol administration in rodents have confirmed this pattern, with ethanol-consuming animals exhibiting reduced muscle mass and muscle protein, particularly in predominantly fast-

twitch muscles (Lang et al. 1999). This phenotype is driven by reduced protein synthesis rates in muscle of ethanol-consuming animals (Preedy & Peters 1988).

Studies of acute ethanol administration in rodents have demonstrated that ethanol inhibits protein synthesis in skeletal muscle by interfering with signaling through the IGF-1 – Akt – mTOR pathway that plays a major role in regulating protein turnover and determining cell size. Specifically, ethanol appears to inhibit the kinase activity of the mTORC1 complex (Lang et al. 2009), reducing phosphorylation of S6K1 (Lang et al. 2004) and activation of eIF4E by phosphorylation of 4EBP1 (Lang et al. 2009) and thereby reducing mRNA translation initiation and protein synthesis. This effect is independent of nutritional status and is not the result of breakdown products of ethanol (Lang et al. 2004).

Relatively few studies have addressed interactions of ethanol with exercise. One previous study (Vila et al. 2001) examined the interaction of endurance exercise training and alcohol ingestion with respect to skeletal muscle, reporting that exercise appeared to ameliorate some effects of ethanol on metabolic enzyme activities and capillary density. However, this study did not measure exercise capacity or  $\text{VO}_2\text{max}$  or test the acute response to exercise. Although muscle capillary density increased with exercise, activities of aerobic enzymes (citrate synthase and  $\beta$ -hydroxyacyl-CoA-dehydrogenase), a hallmark of endurance training, were unchanged by training, even in non-ethanol-dosed animals, suggesting that the training regimen was ineffective. Ethanol was reported to reduce muscle capillary density, however another study reported that a moderate dose of ethanol enhanced expression of angiogenic growth factors following acute treadmill exercise (Gavin & Wagner 2002). A third study of running exercise and ethanol in rats (Reed et al. 2002) focused on bone, but also reported no effect of ethanol on hindlimb muscle weights in either exercised or sedentary animals.

Two previous experiments (Chicco et al. 2006, Vingren et al. 2005) examined the interaction of resistance training and alcohol ingestion. However, these two papers presented limited data on cellular responses in muscle (only androgen receptor content) and relied on a voluntary training protocol that failed to produce significant muscle growth in either the controls or the experimental animals.

#### **4. Discussion of Results**

##### **Aim 1:**

In order to test whether ethanol inhibits the response to resistance training, we removed the gastrocnemius and soleus muscles from the right leg of each rat, leaving the plantaris muscle in place to undergo compensatory growth. The left leg served as a control. Beginning on the second day after surgery, rats in the ethanol group were switched to a liquid diet in which ethanol provided 35% of the total calories. Control rats consumed a calorically equivalent diet containing maltodextrin instead of ethanol. Thirty-five days after surgery, animals were euthanized and the plantaris muscles were removed from each leg, weighed, and preserved for histological, molecular and biochemical analysis.

The experiment was designed to test two null hypotheses:

H<sub>0</sub>A: Ethanol does not reduce muscle hypertrophy resulting from surgical overload

H<sub>0</sub>B: Surgical overload does not prevent reductions in muscle mass in ethanol-treated animals

Results from 20 rats cannot conclusively reject either null hypothesis (Fig. 1). Plantaris muscle hypertrophy (growth) was similar in magnitude in overloaded legs of rats in both groups, suggesting that ethanol does not prevent muscle hypertrophy ( $H_0A$ ). However, a larger sample size might reveal a significant interaction between diet and surgical overload. If so, a lower ratio of overloaded plantaris mass to intact plantaris mass in ethanol-treated animals would indicate that ethanol inhibits muscle hypertrophy. The apparent reduction in muscle mass in each leg in ethanol-treated animals suggests that surgical overload, which mimics resistance exercise, cannot prevent reductions in muscle mass resulting from ethanol consumption ( $H_0B$ ), but the effect of ethanol was not significant. A larger sample size may resolve these uncertainties and further experiments are underway.

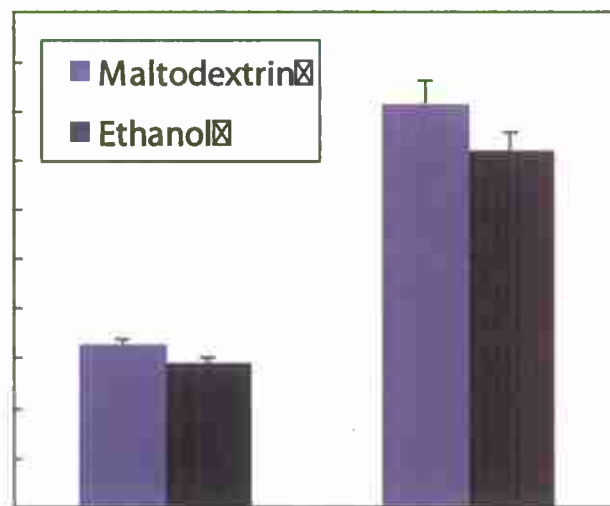


**Figure 1.** Plantaris mass (mean  $\pm$  S.E.M.) of the surgically overloaded right leg and the non-overloaded (intact) left leg. Rats ( $n=10/\text{group}$ ) were fed either a diet in which ethanol provided 35% of calories or a calorically matched control diet in which maltodextrin replaced ethanol. Overload surgery significantly increased muscle mass ( $p<0.001$ ), but diet effects were not significant ( $p=0.168$ ). There was no significant interaction between diet and surgical overload ( $p=0.170$ ). Body mass was similar in maltodextrin ( $306 \pm 7.5$  g) and ethanol-fed animals ( $298 \pm 10.3$  g).

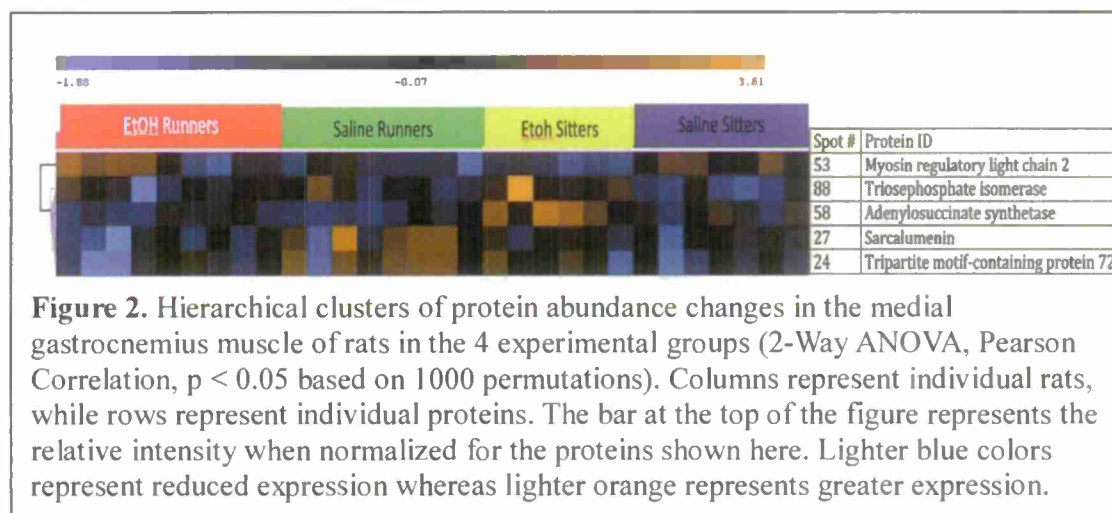
#### Aim 2:

In order to determine whether ethanol alters cellular responses to endurance exercise, rats completed 60 minute interval training sessions on a treadmill and then received injections of either ethanol or a control saline solution. Three hours after completing the exercise session, rats were sacrificed and tissues harvested. Additional rats were not exercised but received injections on the same timetable ( $n=31$  in total).



Proteomic techniques were used to obtain an unbiased assessment of acute changes in signaling pathways and other protein constituents of skeletal muscle following exercise and ethanol treatment.

Two-dimensional gels revealed 375 protein spots. Of these 375 spots, the intensity of 24 spots was significantly affected by ethanol, while 28 were significantly affected by the acute exercise bout. Eighteen protein spots exhibited significant interactions for exercise and ethanol ( $p < 0.02$ ). Thus far, 6 of these proteins have been identified by mass spectrometry (Fig. 2).



## 5. Future Work Planned

### Aim 1:

Synergist ablation surgeries were recently performed on nine additional rats in order to expand the sample size in the resistance exercise experiment. Once these additional animals have completed the experiment, muscle fiber cross-sectional areas will be measured and mRNA levels for markers of muscle hypertrophy and atrophy (eg. IGF-1, collagen 3, MuRF-1, and Atrogin-1) will be measured by qPCR.

### Aim 2:

In order to determine whether ethanol inhibits signaling pathways that lead to formation of additional mitochondria after acute endurance exercise, gastrocnemius muscles from rats subjected to acute running bouts will be chilled in liquid nitrogen and ground into powder prior to homogenization in buffer containing phosphatase inhibitors. Proteins will be separated by SDS-PAGE and Western blots will be used to measure the abundance of signaling factors including PGC-1 $\alpha$  protein and the phosphorylated forms of cyclic AMP response element binding protein (CREB) and p38 MAP-kinase. These factors have been shown to respond to acute exercise and drive mitochondrial biogenesis (eg. Kang et al. 2009), so they can serve as molecular markers of the efficacy of the response in the presence or absence of ethanol.

Quantitative PCR may also be used to measure factors controlling capillary biogenesis (eg. VEGF, HIF-1 $\alpha$  and HIF-1 $\beta$ ) and mRNA encoding mitochondrial proteins

(eg. mRNA for citrate synthase, cytochrome C & UCP3) and other factors which respond rapidly to acute endurance exercise (eg. mono-carboxylate transporter MCT-1, and glucose transporter GLUT-4). Multiple muscles were sampled from both hindlimbs of each animal, providing ample tissue for multiple assays from one animal.

We predict that increases in protein phosphorylation or expression will be smaller in ethanol-treated runners than in saline-treated runners.

### Aim 3:

In order to determine whether ethanol reduces gains in exercise capacity and VO<sub>2</sub>max resulting from endurance training, rats will complete a six-week training regimen while receiving injections of either ethanol or saline solutions following each training session. Sedentary rats will receive injections on the same time schedule in order to measure the response to training and the effect of ethanol on VO<sub>2</sub>max independent of exercise training. VO<sub>2</sub>max testing procedures based on Wisloff et al. (2001) have been tested but no rats have completed the training regimen to date.

## **6. References cited**

- Booth, F.W. and S.J. Lees. 2006. Physically active subjects should be the control group. *Med Sci Sports Exerc* 38: 405-406.
- Bray, R.M and L.L. Hourani. 2007. Substance use trends among active duty military personnel: findings from the United States Department of Defense Health Related Behavior Surveys, 1980–2005. *Addiction* 102: 1092-1101.
- Chicco, A.J., H. McCarty, A.H. Reed, R.R. Story, K.C. Westerlind, R.T. Turner, and R. Hayward. 2006. Resistance exercise training attenuates alcohol-induced cardiac oxidative stress. *Eur J Cardiovasc Prev Rehabil* 13: 74-79.
- Coles, L., J. Litt, H. Hatta, and A. Bonen. 2004. Exercise rapidly increases expression of the monocarboxylate transporters MCT1 and MCT4 in rat muscle. *J Physiol* 561: 253-261.
- Dawson, D.A., B.F. Grant, F.S. Stinson, and P.S. Chou. 2004. Another look at heavy episodic drinking and alcohol use disorders among college and noncollege youth. *J Stud Alcohol* 65: 477-488.
- Fernandez-Solà, J., V.R. Preedy, C.H. Lang, E. Gonzalez-Reimers, M. Arno, J. C. I. Lin, H. Wiseman, S. Zhou, P. W. Emery, T. Nakahara, K. Hashimoto, M. Hirano, F. Santolaria-Fernández, T. González-Hernández, F. Fatjó, E. Sacanella, R. Estruch, J.M. Nicolás, and A. Urbano-Márquez. 2007. Molecular and cellular events in alcohol-induced muscle disease. *Alcohol Clin Exp Res* 31: 1953-1962.
- Gavin, T.P. and P.D. Wagner. 2002. Acute ethanol increases angiogenic growth factor gene expression in rat skeletal muscle. *J Appl Physiol* 92: 1176-1182.
- Grant, B.F., F.S. Stinson, D.A. Dawson, S.P. Chou, M.C. Dufour, W. Compton, R.P. Pickering, K. Kaplan. 2004. Prevalence and Co-Occurrence of Substance Use Disorders and Independent Mood and Anxiety Disorders: Results From the National Epidemiologic Survey on Alcohol and Related Conditions. *Arch Gen Psych* 61: 807-816.
- Haddad, F. and G.R. Adams. 2002. Acute cellular and molecular responses to resistance exercise. *J Appl Physiol* 93: 394-403.

- Horsley, V. and M.D. Sturge. 1907. Alcohol and the human body. p. 142. Macmillan and Co Ltd., New York, NY.
- Jacobson, I.G., M.A.K. Ryan, T.I. Hooper, T.C. Smith, P.J. Amoroso, E.J. Boyko, G.D. Gackstetter, T.S. Wells, and N.S. Bell. 2008. Alcohol use and alcohol-related problems before and after military combat deployment. *JAMA* 300: 663-675.
- Kang, C., K.M. O'Moore, J.R. Dickman, and L.L. Ji. 2009. Exercise activation of muscle peroxisome proliferator-activated receptor- $\gamma$  coactivator-1 $\alpha$  signaling is redox sensitive. *Free Radic Biol Med* 47: 1394-1400.
- Kim, S.J., R.R. Roy, J.A. Kim, H. Zhong, F. Haddad, K.M. Baldwin, and V.R. Edgerton. 2008. Gene expression during inactivity-induced muscle atrophy: effects of brief bouts of a forceful contraction countermeasure. *J Appl Physiol* 105: 1246-1254.
- Lang, C.H., D. Wu, R.A. Frost, L.S. Jefferson, S.R. Kimball, and T.C. Vary. 1999. Inhibition of muscle protein synthesis by alcohol is associated with modulation of eIF2B and eIF4E. *Am J Physiol Endocrinol Metab* 277: E268-E276.
- Lang, C.H., R.A. Frost, V. Kumar, D. Wu, and T.C. Vary. 2000. Impaired protein synthesis induced by acute alcohol intoxication is associated with changes in eIF4E in muscle and eIF2B in liver. *Alcohol Clin Exp Res* 24: 322-331.
- Lang, C.H., A.M. Pruznak, N. Deshpande, M.M. Palopoli, R.A. Frost, and T.C. Vary. 2004. Alcohol intoxication impairs phosphorylation of S6K1 and S6 in skeletal muscle independently of ethanol metabolism. *Alcohol Clin Exp Res* 28: 1758-1767.
- Lang, C.H., A.M. Pruznak, G.J. Nystrom, and T.C. Vary. 2009. Alcohol-induced decrease in muscle protein synthesis associated with increased binding of mTOR and raptor: Comparable effects in young and mature rats. *Nutrition and Metabolism* 6:4.
- Preedy, V.R. and T.J. Peters. 1988. The effect of chronic ethanol ingestion on protein metabolism in type-I- and type-II-fibre-rich skeletal muscles of the rat. *Biochem J* 254: 631-639.
- Preedy, V.R., J.R. Salisbury, and T.J. Peters. 1994. Alcoholic muscle disease: features and mechanisms. *J Pathol* 173: 309-315.
- Reed, A.H., H.L. McCarty, G.L. Evans, R.T. Turner, and K.C. Westerlind. 2002. The effects of chronic alcohol consumption and exercise on the skeleton of adult male rats. *Alcohol Clin Exp Res* 26:1269-1274.
- Reilly, M.E., D. Mantle, P.J. Richardson, J. Salisbury, J. Jones, T.J. Peters, and V.R. Preedy. 1997. Studies on the time-course of ethanol's acute effects on skeletal muscle protein synthesis: comparison with acute changes in proteolytic activity. 1997. *Alcohol Clin Exp Res* 21: 792-798.
- Roy, R.R., K.M. Baldwin, and V.R. Edgerton. 1991. The plasticity of skeletal muscle: effects of neuromuscular activity. *Exerc Sport Sci Rev* 19: 269-312.
- Sola 2007
- Urbano-Márquez, A., R. Estruch, F. Navarro-Lopez, J.M. Grau, L. Mont, and E. Rubin. 1989. The effects of alcoholism on skeletal and cardiac muscle. *N Engl J Med* 320: 409-415.
- Vila, L., A. Ferrando, J. Voces, C. Cabral de Oliveira, J.G. Prieto, and A.I. Alvarez. 2001. Effect of chronic ethanol ingestion and exercise training on skeletal muscle in rat. *Drug Alcohol Dependence* 64: 27-33.

- Vingren, J.L., L.P. Koziris, S.E. Gordon, W.J. Kraemer, R.T. Turner, and K.C. Westerlind. 2005. Chronic alcohol intake, resistance training, and muscle androgen receptor content. *Med Sci Sport Exerc* 37:1842-1848.
- Wisloff, U., J. Helgerud, O.J. Kemi, and O. Ellingsen. 2001. Intensity-controlled treadmill running in rats: VO<sub>2</sub>max and cardiac hypertrophy. *Am J Physiol Heart Circ Physiol* 280: H1301-H1310.

**Aptamer-Based Clinical Diagnostics in Nitrocellulose, Paper-Microfluidic Platforms**

Principal Investigator:

**David S. Clague, Ph.D., Biomedical Engineering**

California Polytechnic State University  
San Luis Obispo, CA



## 1. Abstract (~250 words)

Detection of chemical and biological agents in many environments is of key importance to support our deployed war-fighters, e.g., the temperature can regularly reach ~ 120 °F in Iraq and much higher temperatures on tarmacs. These extreme environs drive detection-device requirements which include: functionality in extreme temperatures, low power requirement, low cost and ease of use and portability. In addition to the above mentioned requirements, the next generation detection technology must be able to detect chemical and biological targets which could be the actual agent or a resultant physiological biomarker. The most suitable technologies that meet these requirements are within the family of lateral flow assays.

In the work presented here, we explored the following: i) creation of three-dimensional paper-microfluidic devices using nitrocellulose membranes, the same material used to make lateral flow assays, ii) comparison between antibodies and complementary DNA Aptamers as capture reagents, and iii) Surface Plasmon Resonance studies to directly compare binding efficiencies of VEGF antibody and VEGF DNA Aptamer.

Three-dimensional nitrocellulose, paper-microfluidic devices were shown to work. Two different approaches to enable wicking between layers were explored. Both antibodies and Aptamers were shown to work on two-dimensional nitrocellulose, paper-microfluidic devices. Surface Plasmon Resonance (SPR) studies revealed that the DNA Aptamers were equal to or greater in effectiveness than complementary antibodies. Furthermore, the SPR experimental techniques led to the use of linker molecules that worked well for inclusion of Aptamers on nitrocellulose.

This work resulted in three MS theses, one poster presentation at an international conference and one invention disclosure.

## 2. Project significance

In remote environments, whether onboard a Naval vessel or in the mountainous regions of Afghanistan, it is very difficult to create the necessary controlled environments suitable for standard diagnostic assays. Such scenarios would require expensive, bulky equipment with significant power requirements. A logical, existing alternative technology would be lateral flow assays. Lateral flow assays are low cost, disposable, storage required, dehydrated reagents on-board, that do not require additional fluid reagents, are designed for pedestrian use, and have no power requirements.

While this appears to be a clear path forward for equipping military personnel to perform clinical diagnostics in the field, a few hurdles need to be overcome; namely, current lateral flow assays make use of antibodies to perform desired detections and lateral flow assays are currently designed to detect just a few target markers per assay. Antibodies function properly only in mild or benign temperature conditions, < 100 °F, e.g., near or at physiological temperatures. The challenges require the discovery or development of temperature robust capture reagents and the ability to create multiplexed lateral flow assays. In this report, experimental results for

exploring the use of paper-microfluidics to create three-dimensional, multiplex assays and the use of DNA Aptamers, which maintain conformational integrity up to DNA melting temperatures,  $\sim 90^\circ\text{C}$ , in place of antibodies in lateral flow assay platforms are presented and discussed.

In addition to military applications, the work discussed here has direct application to i) medicine for the developing world, ii) domestic point-of-care diagnostics for homeland security/first responders.

### **Medicine for the Developing World**

When delivering diagnostic care to a remote location, many times diagnostics need to be airlifted and the landing tarmacs can exceed reagent temperature tolerances. In such circumstances, there are limited to no power sources available on site to enable temperature control. Furthermore, the lack of on-site power also limits the diagnostic instrumentation available to care-givers. As a consequence of excessive temperatures and lack of temperature control, reagents are rendered ineffective. These are just two of the drivers for developing innovative diagnostic capabilities in resource poor locations.[1]

### **Point-Of-Care Diagnostics**

Related to Medicine for the Developing World is domestic Point of Care Diagnostics. Point-of-care (POC) diagnostics is defined as the capability to diagnose a patient's condition at any location – whether that be a diagnosis by a doctor, or by an untrained person at home. The classic example is the home pregnancy test. The gold-standard for diagnosis and treatment traditionally has been a local clinic or central hospital. [2] A central hospital allows for a patient to go to a professionally staffed, well-equipped facility to receive appropriate care on-site in a location that contains advanced technology for the rapid detection and analysis of the sample.

Enabling POC diagnostics requires more innovative work up-front to deliver low cost, easy to use diagnostic capabilities.

### **Homeland Security and First Responders**

In the event of an outbreak of unexplained disease or a known chemical or biological release, First Responders first need to know what they are dealing with and second they need to be able to triage patients on-site without exposing hospital emergency rooms to potential contagions. Samples could range from human biofluids to residues on building walls. The technologies in this instance for assessing the disease state of the public in such a situation have the requirements of little to no training, ease of use, low to no power requirements, and portability. Paper-microfluidic devices used as lateral flow “like” assays immediately come to mind. Once an assay has been done, the results could be transmitted via smart phone (and smart phone image) to a central laboratory for analysis.

These are the main venues where paper-microfluidics coupled with robust reagents becomes an advantageous option for medical diagnostics. It seems clear that advances in this area are of benefit to the military and in other key areas. Owing to the ease of use, paper-microfluidics with robust reagents would be successful in a wide range of locations and with people of most education levels.

### 3. Background/prior work

Aptamers are biological constructs made of ssDNA, ssRNA or peptides that capture target molecules and macromolecules like antibodies. [3, 4, 5, 6] Because Aptamers are similar in size and function to antibodies, they too can be used to perform immunoassays. It should be noted however that Aptamers typically only form one active or capture site while antibodies on the other hand have two capture sites. Furthermore, like antibodies, Aptamers can be developed via the SELECTS process against biological and non-biological targets. [4, 5]

In the work performed here, DNA Aptamers were chosen for their well-known temperature stability up to  $\sim 90^{\circ}\text{C}$ . Shown below in Figure 1 is a DNA Aptamer designed to capture Thrombin.

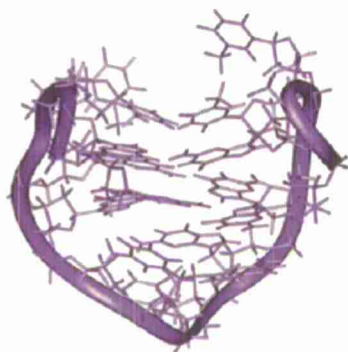


Figure 1. DNA Aptamer-Thrombin Complex. (This image was found via google image search. It is from Professor Ellington's, UT Austin, website <http://aptamer.icmb.utexas.edu/>.)

For this construct, the ssDNA forms desired base-pairing, secondary structures that form an active site that mimics the function of the FAB region of an antibody. As with any DNA structure involving base-pair bonds, it is stable up to  $\sim 90^{\circ}\text{C}$  (or  $\sim 194^{\circ}\text{F}$ ). A key research objective was to successfully tether DNA Aptamers to nitrocellulose membranes for detection on a paper-microfluidic platform.

The complementary breakthrough to inspire the aims of this work and to significantly impact how detection is performed in the field is paper-microfluidics.[Martinez et al.,] Like lateral flow assays, paper-microfluidics, microfluidics in cellulose paper, leverages capillary forces to transport fluids and analytes at predictable rates and in desired directions; however, in paper-microfluidics hydrophobic, and therefore hydrophilic regions, can be patterned

precisely to route fluids. Additionally, because these can be manufactured using the same materials as lateral flow assays, paper-microfluidic devices can naturally be used to perform immunoassays.[4] This new innovation in microfluidics has permitted the manufacture of detection technologies for very low cost, e.g., \$0.003 per square centimeter.[Martinez]

These devices have been demonstrated to be successful in detection of glucose, protein, immunoassay, and sample purification. [8, 9,10] Researchers report good reproducibility. Shown below in Figure 2 is a three-dimensional paper-based microfluidic device developed by Martinez, et al., at Harvard University.[8]

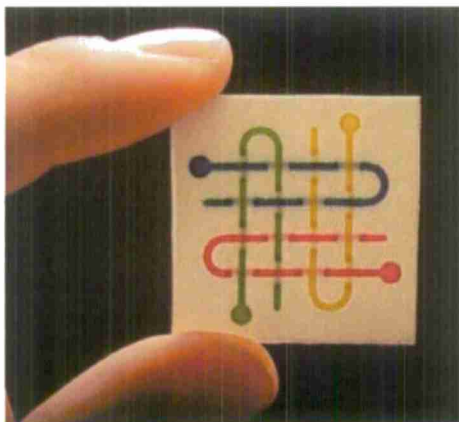


Figure 2. Three dimensional paper-based microfluidic device. The device shown by Martinez et al. has multiple layers and can be used to detect multiple analytes.[8]

Martinez et al. (2008) demonstrated the ability to use chromatography paper to route fluids with fidelity through multiple layers and even transporting over or under other fluid lines without cross-mixing. All fluid and dye transport was accomplished solely through capillary forces, with no power requirement.

The goals of the work discussed in this report were to demonstrate that three-dimensional, paper-microfluidic devices could be constructed using nitrocellulose membranes and that Aptamers could be successful incorporated and used to in an immunoassay.

As mentioned, the specific aims included:

- I. Develop two- and three-dimensional paper-microfluidic devices using nitrocellulose membranes and demonstrate fluid routing
- II. Functionalize nitrocellulose with DNA Aptamers and validate via immunoassay
- III. Compare Aptamer and antibody immunoassay on nitrocellulose membranes
- IV. Quantify binding efficiencies in a head-to-head comparison between VEGF antibodies and DNA Aptamers.

In the section to follow, selected results are shown on Aims I through IV.

#### 4. Discussion of Results

The proposed effort was to develop the ability to incorporate Aptamers on paper-microfluidic platforms, more specifically nitrocellulose platforms. This is a step toward developing robust, low-cost, multiplex assays that work in a wide range of environs. The work was divided in three main efforts:

- I) **Assay Platform Development.** Design and demonstration of two- and three-dimensional, nitrocellulose paper-microfluidic platforms.
- II) **Assay Demonstration.** Inclusion of reagents and demonstration of the use of antibodies and Aptamers as a capture reagent in on-a-chip sandwich, immunoassay.
- III) **SPR Evaluation.** SPR comparison of Vascular Endothelial Growth Factor (VEGF) antibody and Aptamer for binding efficiency

##### Assay Platform Development

Paper-microfluidic platforms were made with Millipore Nitrocellulose membranes. The Millipore membranes can be purchased in 8.5" x 11" sheet form either backed with a clear polyester film or unbacked. It should be noted that these membranes are the standard Millipore product used to make commercial lateral flow assays.

To create hydrophobic regions on the nitrocellulose membranes to direct fluid flow direction, [9, 12] channels and other features were first drawn precisely using AutoCAD® and then printed on nitrocellulose membranes using a Xerox 8570 Color Cube printer, which uses wax ink, see Figure 3 below.



Figure 3. The left panel: Xerox 8570 Color Cube printer. Right panel: backed Millipore Nitrocellulose membrane with channels printed on the surface. The white regions represent regions where wax ink was deposited.



Once the pattern had been printed, then the nitrocellulose membranes were baked in an oven at 150 °C for approximately 3 minutes or until the wax had melted into the membrane. The wax results in hydrophobic regions that define desired channel geometries for fluid routing. Figure 4. shows the oven used to post-process wax printed membranes.



Figure 4. Programmable oven to melt wax patterns into Nitrocellulose membranes.

Once the wax was melted into the membranes, the membranes were allowed to cool to room temperature, and the patterned regions were then cut out and ready for assembly, testing and evaluation. For example, the patterns shown above in Figure 3 were used to experimentally determine the optimal channel widths for the representative channel lengths. The channel widths evaluated were 0.8 mm, 1.6 mm and 2.4 mm. The actual test results are given below in Figure 5.

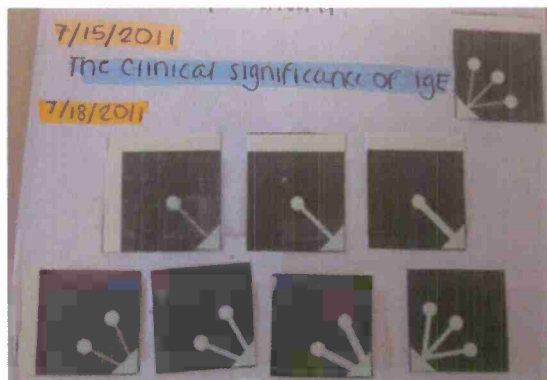


Figure 5. Dye tests to evaluate channel fluid flow continuity.

As shown above, it was found that only the 0.8 mm channel width did not consistently allow fluid to wick the entire length of the channel; therefore, the nitrocellulose, paper-microfluidic platforms that were fabricated for this effort had channel widths between 1.6 to 2.4 mm.

The three-dimensional nitrocellulose platforms were constructed with the goal of creating a paper-microfluidic 4 by 4 microarray of detection regions. To approach this goal, two designs were proposed to illustrate the ability to create flow continuity in a 1 by 4 column of detection regions. One platform was designed for simultaneous development of the detection regions, and the other was designed for 2 wells developing simultaneously at two different times. (In this report, development time is the time it takes a fluid to wick from introduction into the device to reach and fill the detection region).

When constructing a multi-layer paper-microfluidic device, or what is now known as a microPAD [12], the membrane layers need to be aligned and bound together (here we used 3M double-backed tape), and gaps between layers need to be bridged to ensure fluid wicking between layers. Figure 6 shows one of the device designs to illustrate two wells simultaneously developing at successive times.

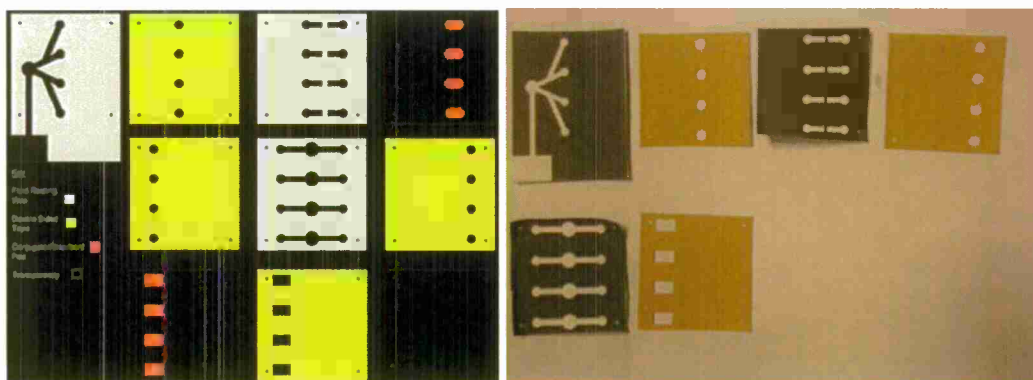


Figure 6. Multiple layers in a 1 by 4 column of detection regions. On the left, the white layers are fluid routing layers. The white color is wax that will be melted into the membrane. The yellow regions represent 3M double back tape, and the red regions represent storage regions for conjugate reagent, top right, and absorbent pads, bottom left. On the right are the actual nitrocellulose layers in black and double-backed tape with tan release paper.

Note in Figure 6 that near the corners of each layer there are four alignment holes. Once the wax regions were melted into the nitrocellulose membrane material, the individual layers were cut out with titanium scissors and the resultant pieces re-assembled, interleaving double-backed tape, to form a cohesive stack. (Note: the double-backed tape layers were laser cut from 8" x 8" sheets.) Once assembled, all devices were tested for fluid continuity using water and dye-laden conjugate reagent pads embedded in between layers. Pure water was introduced to illustrate the resolubilization of the dye and the color was observed to successfully reach the detection region. A resultant dye test for the above AutoCAD® design is illustrated below in Figure 7.

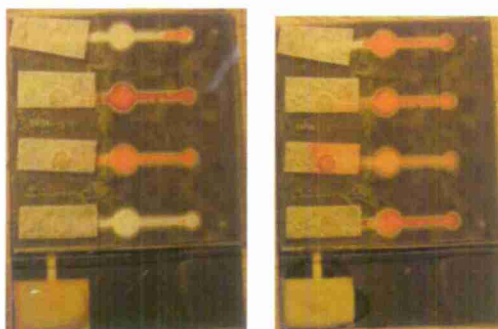


Figure 7. Nitrocellulose, paper-microfluidic microarray column development test. The left panel shows the simultaneous development of the first pair of wells, and the right panel shows the simultaneous development of the second two wells. The pads on the top layer are absorbent pads to ensure sufficient void volume to draw the fluid past the circular detection region.

To ensure flow continuity and reasonable timely development times, the gaps between membrane layers caused by double-backed tape must be filled with porous material to bridge between layers to ensure fluid wicking. In this work, two approaches were employed: i) consistent with Martinez et al (2010) a mulch of nitrocellulose powder was packed in each gap during assembly and ii) whole membrane fragments, e.g., similar to a hole-punch, were introduced into gap regions during stack assembly. Devices made using both approaches had fluid continuity and developed in reasonable times, ~3 to 7 minutes.

### Assay Demonstration

To demonstrate the ability to perform sandwich immunoassays, two-dimensional paper-microfluidic devices were constructed, and the following tests were performed:

Detection of Fluorescein Isothiocyanate (FITC)-labeled anti-IgE with an IgE target and anti-IgE antibody in the detection region, b) Detection of FITC-labeled anti-IgE with an IgE target and anti-IgE DNA Aptamer in the detection region, and c) Detection of 30nm colloidal gold-labeled anti-VEGF with a VEGF target and anti-VEGF DNA Aptamer in the detection region.

The general two-dimensional chip design for the FITC experiments is given in Figure 8.

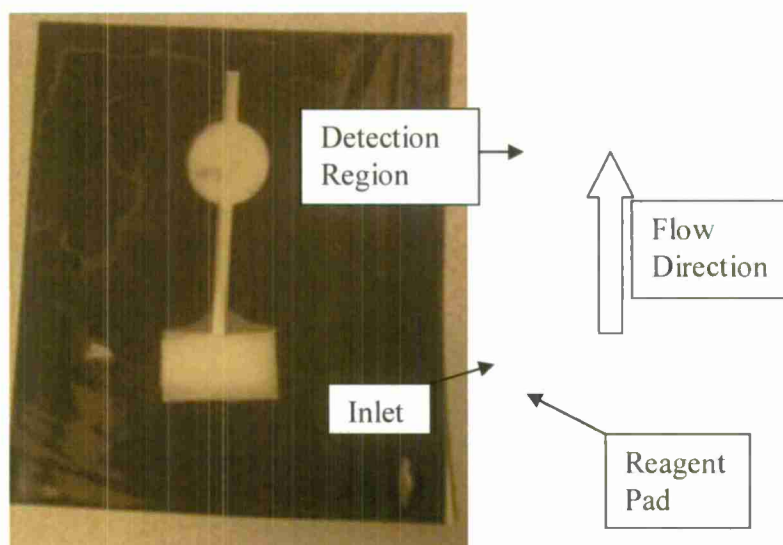


Figure 8. Simple two-dimensional, nitrocellulose device to validate capture reagent efficacy.

In the FITC-labeled antibody experiments, as mentioned above, IgE was the target, and in these experiments the capture reagent was bound to the nitrocellulose membrane by heat treatment, 80 °C for 2 hours. Representative FITC labeled conjugate reagent results are given below. See Figure 9.

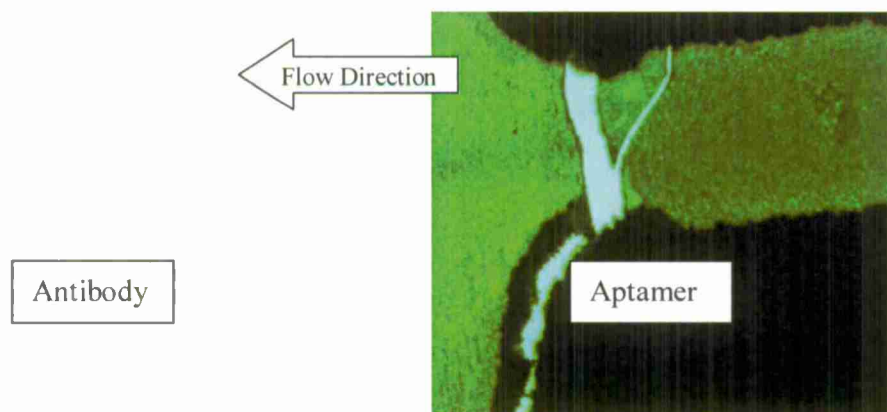


Figure 9. Results for IgE capture in the circular detection region. On the left, the capture reagent was tethered antibody, and on the right the capture reagent is tethered DNA Aptamer. The cracks and channel defects developed after assay completion. The extra bright fluorescent green areas indicate detection.

Most of the IgE, FITC-labeled experiments “worked” for both capture reagents, antibodies and Aptamers. In all there were 10 experiments for each; however, the heat treatment used to induce reagent tethering to the Nitrocellulose membrane also caused damage to the membranes. The combination of reagents and prolonged heat treatment caused the nitrocellulose to eventually crack and appear to dissolve.

An additional device and experiments were performed to illustrate the capability with a different target, VEGF, and a different reporter, colloidal gold. In the experiment to follow, VEGF was detected using an anti-VEGF Aptamer as the capture reagent; however, rather than using heat treatment to tether the Aptamer to the nitrocellulose membrane, the Aptamers were purchased with a linker molecule at the 5' end. This linker molecule enabled Aptamer tethering to the membrane at room temperature and eliminated the heat-induced defects of cracking and dissolution of the wax-laden nitrocellulose. See Figure 10 below.

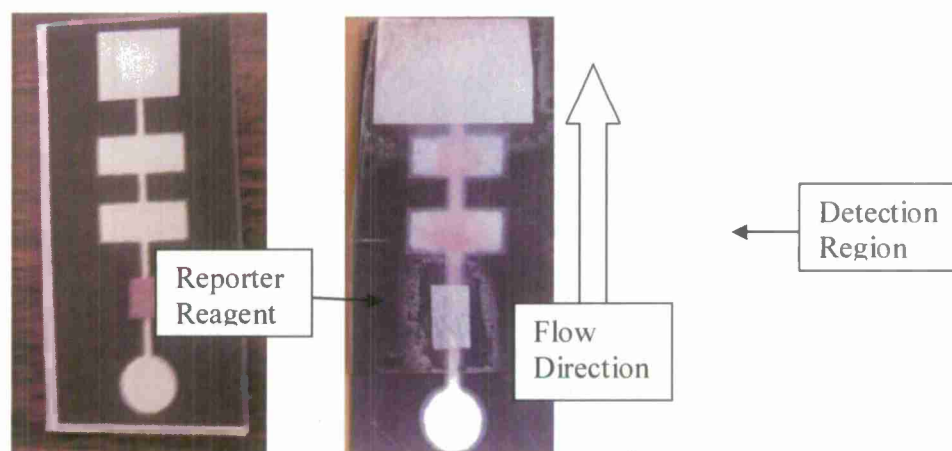


Figure 10. Anti-VEGF detection chip. The left panel shows the chip with dry conjugate, reporter reagent storage pad. The right panel shows a developed assay. The first rectangular region is the detection region.

The ability to tether DNA Aptamers to Nitrocellulose membranes at room temperature is a promising development. Further confirmatory experiments need to be performed to validate the approach.

### SPR Evaluation

Surface Plasmon Resonance experiments were performed to compare binding efficiencies of the anti-VEGF antibody and Aptamer that were used as capture reagents in the experiments above. The VEGF target was actually a portion of the whole growth-factor macromolecule, and therefore, it only had few epitopes available for antibody binding. As a consequence, the anti-VEGF antibody association rate constant was between four and six orders of magnitude less than the complementary Aptamer. For this VEGF fragment the Aptamer clearly had better binding efficiency than the antibody. The SPR studies confirmed the paper-microfluidic findings shown above, that is, that the anti-VEGF Aptamer bound the target as well or better than the complementary antibody.

This work resulted in:



Three Master's theses:

- 1) COMPARING ANTI-VEGF ANTIBODIES AND APTAMERS ON PAPER MICROFLUIDIC-BASED PLATFORMS, **Katherine Clayton, June 2012**
- 2) NITROCELLULOSE PAPER BASED MICROFLUIDIC PLATFORM DEVELOPMENT AND SURFACE FUNCTIONALIZATION WITH ANTI – IGE APTAMERS, **Jennifer Ward, June 2012**
- 3) A KINETIC STUDY OF ANTI-VEGF-A POLYCLONAL ANTIBODIES AND ANTI-VEGF-A ssDNA APTAMERS, **Heather Hedeem, June 2012**

One publication in preparation:

- Aptamer-based detection on nitrocellulose, paper-microfluidic platforms

One conference presentation:

- 3D Nitrocellulose, Microfluidic Assay Platforms: An Assay Comparison. Poster Presentation at the Lab-on-a-Chip World Congress conference, South San Francisco, CA, September 29-30, 2011.

One invention disclosure:

- Title of Invention: Fluid Routing and Reagent Incorporation in Paper Microfluidic, Microarray, 8/10/11

## 5. Future Work Planned

Future plans involve the following: characterization of micro-PAD Limits of Detection using dyes and colloidal gold, electrophoretic separations, and the development of a microarray. In parallel with the continued effort, program development is being pursued with NASA, and the National Laboratory. The PI has already secured a small student grant with NASA.

## 6. References cited

- [1] Private communication Paul LaBarre, PATH Seattle, WA USA
- [2] Paul Yager, G.J.D., John Gerdes, *Point--of--Care Diagnostics for Global Health*. Annual Review of Biomedical Engineering, 2008. **10**: p. 107---144.
- [3] R. Mukhopadhyay, "Aptamers are ready for the spotlight" Amer. Chem Society, 2005, 115A,
- [4] Immunoassay and other bioanalytical techniques, CRC press Chapter 6, page 147,

2007

- [5] M. Famulok, " Oligonucleotide aptamers that recognize small molecules ", *Current Opinion in Structural Biology* 1999, 9:324–329
- [6] P. Ray and R. White , "Aptamers for targeted drug delivery", *Pharmaceuticals*, 2010 3, 1761-1778
- [7] Erin M. Fenton, Monica R. Mascarenas, Gabriel P. Lo'pez, and Scott S. Sibbett, "Multiplex Lateral-Flow Test Strips Fabricated by Two-Dimensional Shaping," *ACS Appl. Mater. Interfaces*, 2009 1 (1), 124-129
- [8] A Martinez, S. Phillips and G. Whitesides, "Three-dimensional microfluidic devices fabricated in layered paper and tape," *PNAS*, 2008 vol. 105, pp. 19606-19611
- [9] Y. Lu, W. Shi, J. Qin and B. Lin, "Fabrication and characterization of paper-based microfluidics prepared in nitrocellulose membranes by wax printing," *Anal Chem*, 2010 82, 329-335
- [10] A Martinez, S. Phillips and G. Whitesides, "Diagnostics for the developing world: microfluidic paper-based analytical devices," *Anal Chem*, 2010, 82, 3-10
- [11] M. Cretich, V. Sadini, F. Damin, M. Pelliccia, L. Sola, Y. and M. Chiari., "Coating of nitrocellulose for colorimetric DNA microarrays," *Analytical Biochemistry*, 2010, 397, pp. 84-88
- [12] E. Carrilho, A. W. Martinez and G. M. Whitesides "Understanding Wax Printing: A Simple Micropatterning Process for Paper-Based Microfluidics, *Anal. Chem.* 2009, 81, 7091-7095

**ENVELOPE FILTER FOR DISASTER RELIEF  
WATER TREATMENT**

Principal Investigator:

**Tryg Lundquist, Ph.D., P.E., Civil and Environmental Engineering**

Primary Author:

**Shasta Billings, Graduate Student, Civil and Environmental Engineering**

California Polytechnic State University  
San Luis Obispo, CA

## 1. Abstract

Humanitarian Assistance and Disaster Relief (HADR) missions by the US military and relief organizations strive to provide drinking water as quickly as possible after a disaster and to as many survivors as possible. However, when transport distances are long or roads are disrupted, days or longer can pass before mechanized water treatment equipment (e.g., filtration, disinfection, reverse osmosis) or bottled water can be brought to affected communities. The Cal Poly Waterbag (now marketed as the DayOne Response Waterbag by DayOne Response, Inc.) is a new low-cost device that responders give survivors so they can make their own clean water from contaminated local sources. The Waterbag is a 10-L bladder with an outlet port attached to a filter. Proctor and Gamble Purifier of Water (PÜR®) sachets are used to pretreat the contaminated water in the Waterbag, which is specially designed to facilitate effective use of PÜR® sachets.

A disadvantage of the Waterbag system for massive disaster response is the high cost (~\$30 each) of the hollow fiber membrane microfilters currently used. The present project sought to develop a new type of filter, which was low-cost (~\$5) and geometrically flat. The low profile would be highly beneficial for decreasing packing and storage volume of Waterbag systems, for example, in pallet bins. When warehouse space and transport capacity are limited, minimizing product volume is important for maximizing the number units delivered to survivors. A filter was developed and a US patent application submitted.

The flat filters developed in this project were termed "envelope filters," reflecting their size and shape. Various envelope filters were constructed of both a 1- $\mu\text{m}$  nominally-rated and 1- $\mu\text{m}$  95% efficiency-rated ("absolute") filter cloths. The cloth was needle-punched, nonwoven polyester filter bag material. The envelope filters constructed and tested included several internal to the Waterbag and several external. Filters were attached to the Waterbag and used to filter water after it had been treated with a PÜR® sachet. PÜR® sachets contain coagulants, flocculants, alkaline agents, and disinfectants in a mixture capable of treated 10-L of contaminated water. Test water used in the experiments to develop the basic envelope filter design consisted of tap water with turbidity increased with a standard dust and salinity increased with ocean salts. Mock U.S. EPA Challenge Water #2 was also prepared in the Cal Poly lab when filters were tested for bacteria and microsphere removal.

After the design and mock challenge experiments were complete, results indicated that the optimal filter design a 2-ply nominal-absolute filter with water flowing through the filter at a 20-mL/min. This filter could meet the turbidity and pathogen removal requirements for emergency drinking water treatment as determined by WHO, The Sphere Project, and the U.S. EPA. However, the success was inconsistent in triplicate testing.

Results indicated that prototype filters met the U.S. EPA Water Purifiers Guidelines for residual turbidity (<5 NTU) and inactivation of viruses (>4-log inactivation). However,

chlorine residual requirements ( $>0.2$  mg/L) were not met in any of the Waterbags, and, in one of the triplicate Waterbags tested, protozoan cyst and *E. coli* removal requirements ( $>3$ -log removal) were not met. PUR<sup>®</sup> sachets do not seem to have sufficient concentrations of oxidants and chlorine overcome the high humic acid dose required in the USEPA Challenge Water #2. More significant was the inability of one of the filters to remove sufficient protozoan cyst surrogates (plastic microspheres) and viruses. This failure may have been due to misplacement or leaking of a hose clamp valve. Further Challenge Tests are needed to validate and improve the envelope filter design.

## 2. Project significance

After large-scale disasters, prevention of water-borne illness in the survivors is important to rescue and recovery. Whether a US war fighter or a displaced survivor in a natural disaster, thirst can quickly force individuals to drink contaminated water, thus clean water must be provided almost immediately. However, in many cases, transport of clean water and/or water treatment devices into disaster zones requires days, and water transport is costly and potentially difficult. Alternatively, compact water treatment methods can be provided, but they can be expensive (hand-pumped filters) or only partially effective (chlorine tablets).

The Cal Poly Waterbag is focused on filling the gap in small-scale, point-of-use, water treatment technologies that can be rapidly deployed during rescue and recovery efforts. Dr. Lundquist and past Cal Poly research teams have investigated, tested, and concluded that a low-cost, compact gravity filter is necessary to complete the Waterbag system package. The potential commercially available options range in price from \$20 to \$100, which is too high for the Waterbag system target price of less than \$20. Any Waterbag filter should consistently produce water that meets World Health Organization, US Environmental Protection Agency (USEPA), and USCHHPM emergency drinking water guidelines (Table 1) for disaster relief efforts, as well as, complement the compact size of the Waterbag bladder.

**Table 1: Water quality objectives for emergency response (World Health Organization, 2006; U.S. Environmental Protection Agency, 1987).**

| Parameter                                | To Demonstrate           |
|--|--------------------------|
| <b>WHO Water Quality Objectives</b>      |                          |
| Turbidity                                | $< 5$ NTU                |
| Chlorine residual                        | 0.2-0.5 mg/L             |
| <i>E. coli</i>                           | $<1$ CFU/100 mL          |
| pH                                       | 6 to 8                   |
| <b>US EPA Purifier Device Objectives</b> |                          |
| Parasitic cysts                          | 3-log removal (99.9%)    |
| Viruses                                  | 4-log removal (99.99%)   |
| Bacteria                                 | 6-log removal (99.9999%) |



Another major disadvantage of current filters is their typically cylindrical shape. The compact Waterbag has the potential to decrease transportation costs and potential logistical obstacles. The earthquake in Haiti shed light on how advantageous a portable lightweight solution for clean drinking water is in the aftermath of a disaster. During the Haiti relief response, the U.S. Agency of International Development (USAID) was readying approximately 100,000 10-liter containers for potable water. However, according to relief workers, the effort was limited by logistical obstacles of transporting large numbers of heavy water containers over wrecked roads or limited by air transport weight. The USAID Field Operation Guide states that a pallet (with dimensions of 48" x 40" x 50") can hold about 600 collapsible 10-liter blow-molded water containers or 32 rigid 5-gallon jerry cans. In contrast, the same pallet could be loaded with 1,300 Waterbags (rolled dimensions 12-in by 2.5-in). In another example, for Haiti relief, a C-17 US military cargo plane carried six pallets of water (36,000 liters). These pallets could have carried 7,800 Waterbags, each with 12 PUR packets, providing the capability to produce 936,000 liters of drinking water. This eliminates tough logistical decisions, for example, about whether to fill a plane with water or medical supplies. The Waterbag allows for both to be provided.

The present project was important for establishing a low-cost, flat filter design as the last piece of the puzzle for producing a complete Waterbag product.

### 3. Background/prior work

Past Cal Poly graduated students who tested and evaluated the Waterbag design (Compas, 2009; Herzog, 2010), concluded that an improved filter housing and filter media needs to be evaluated for improvements including high flow rates and low clogging rates. Compas et al, 2009, developed a clamshell-style filter housing with a one-micron nominal polypropylene filter cloth that improved water quality performance, but due to a leaky housing and potential bypass, did not meet the USEPA challenge water test standards. Additionally, the filter housing was bulky for use with the Waterbag (Figure 1).

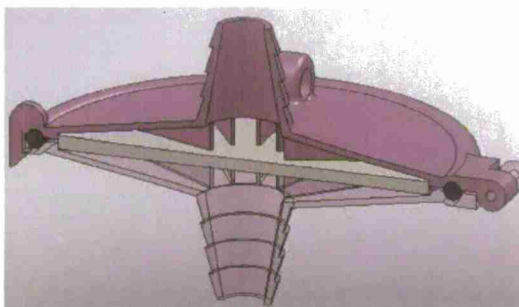


**Figure 1: Filter apparatus shown in SolidWorks with 1-micron polypropylene cloth secured in the apparatus (Compas, 2009). This filter apparatus did not meet drinking water quality due to leaking housing. Full investigation is needed to improve media and filter housing function.**

Additionally, Herzog (2010) tested a variety of off-the-shelf commercially available gravity filters for clogging and filtration performance. Poor performance (flow rates <0.5

L/min and clogging within first 2 liters filtered) indicated that these filters were not suited or designed for the Waterbag system. Thus, further research and development is necessary to create a filter specifically designed to be compatible with the Waterbag in order to produce up to 120 liters of clean drinking water. In an emergency context, this is enough water to sustain a family of four for 10 days until larger scale water treatment systems are established. From a logistical standpoint, a long-life filter that is designed to be compact will enable the Waterbag to maintain its compactness. Different filtration varieties will be designed to evaluate filter performance (e.g., positioned within the bladder of the Waterbag or positioned after the outlet) to determine optimal housing configuration.

#### 4. Discussion of Results

Prior to discussion of the results, an overview of the final filter design and the project experiments conducted will be provided.

After many design and testing iterations, an envelope filter design was finalized. Two plies of nonwoven filter cloth were used—the internal layer was 1-um nominal pore size and the external layer was 1-um absolute pore size (Figures 2 and 3). The cloth plies were encased in a pouch constructed of one sheet of 6-mil low density polyethylene (LDPE) plastic. A hole was punched through the plastic and stretched over the bulkhead fitting protruding from the filter. An additional hole was punched through the plastic outside the edge of the filter to allow for another bulkhead fitting. The exit hole was placed outside the edge of the filter to prevent flow-focusing of effluent. A bulkhead fitting was fit through the second hole in the filter pouch, and the pouch sealed. Plastic stopcock valves were threaded into both the pouch inlet and outlet bulkhead fittings to allow for flow control (Figure 4). The bulky fittings were for the research prototype only. Figure 5 shows the filter with small fitting attached to the Waterbag, which would be the form used for filter manufacturing. The 2-ply nom.-abs. filter was then tested in triplicate with U.S. EPA Challenge Water #2 at BioVir Laboratories, Inc. in Benicia, California (Figure 6).

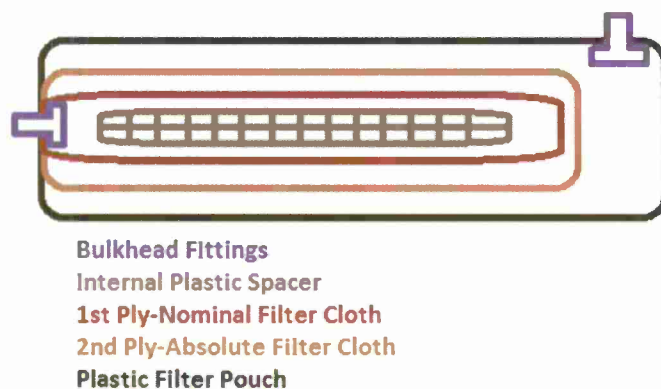
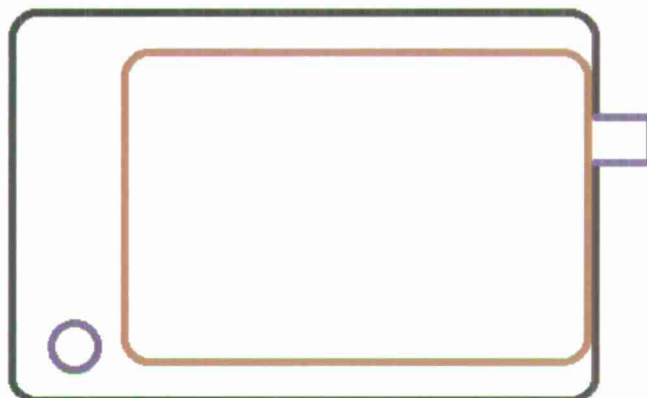


**Figure 2: A cross section of the 2-ply nom.-abs. filter used in experiments H-3 and I-1, as constructed. Water flowed in the bulkhead fitting on the left, through the filter cloth layers, and out the bulkhead fitting on the right.**



**Bulkhead Fittings**  
**2nd Ply of Nom.-Abs. Filter**  
**Plastic Filter Pouch**

Figure 3: Plan view of 2-ply nom.-abs. filter used in experiments H-3 and I-1, shown as attached to the waterbag. Water flowed in the bulkhead fitting on the right, through the filter cloth layers, and out the bulkhead fitting on the left.



Figure 4: 2-ply nom.-abs. filter tested in experiment H-3. Scale: the large diameter bulkhead fitting measures 3.65 cm in diameter.

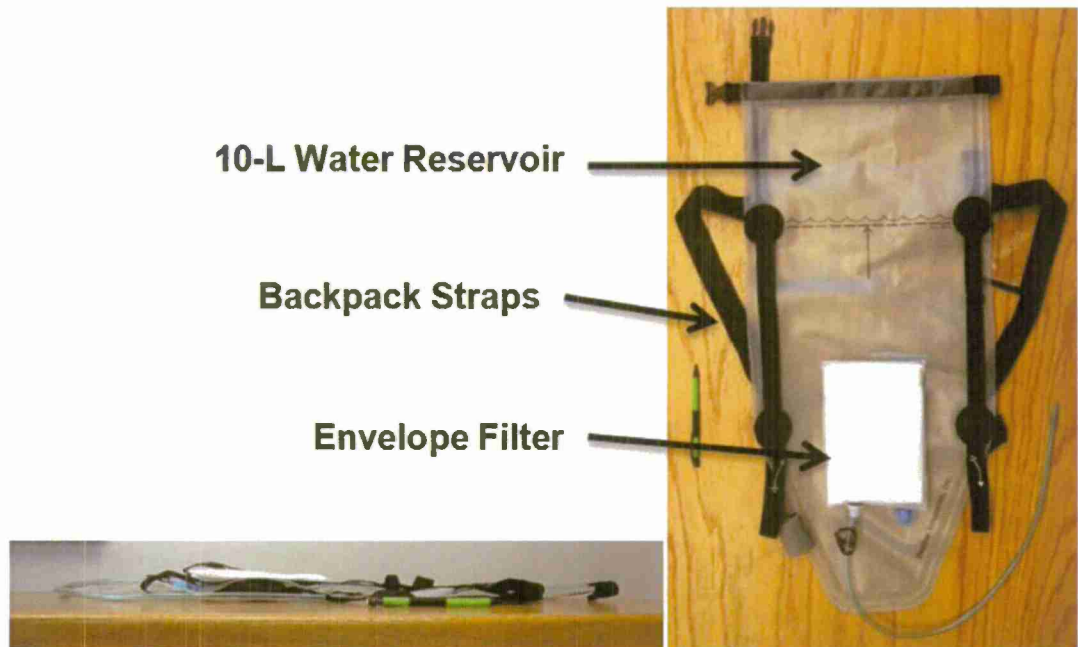


**Figure 5:** A mock-up of an envelope filter attached to a Waterbag. This configuration with small bulkhead fittings would be used for manufacturing. Left: Plan view. Right: Side view. Note the low profile for efficient storage and transport of bulk loads of Waterbags.



**Figure 6:** Testing in triplicate at BioVir Laboratories. Seale: the tubing measures 0.75 cm in diameter. The sandwich bags hanging below the waterbags were taped in place to catch any leaks from an imperfect prototype fitting.

**Experimental Design**

The research performed can be divided into two primary kinds of experiments: (1) design experiments – to determine the most effective and durable filter design as well as the most apt placement of the filter on the waterbag, and (2) U.S. EPA Challenge Water experiments – to test the performance of the filters against the Test Water #2 and to observe the filters' performance regarding bacteria and cyst removal. Experimental objectives, test water preparation, and experimental procedures can be found in the following sections. The experimental plan is detailed in Figure 7.

**Experimental Objectives**

The twenty-two experiments are described herein (Figure 7), each with their purpose. Configuration experiments with both internal and external filters (A-1 through A-3 and B-1 through B-3) were necessary to determine a preferred filter geometry and placement of the filter on the waterbag. Configuration experiments regarding hardware (C-1 and C-2) were performed to determine the preferred bulkhead fittings to be used in filter construction. Configuration experiments regarding flow patterns (D-1 and D-2) were required to determine how water actually flowed through the material. Microsphere removal experiments (E-1, E-2, and F-1 through F-3) helped determine the removal capabilities of various filter designs and over a range of flow rates. Mixing time experiments (G-1 through G-3) were used to optimize treatment prior to filtration. Mock challenge water experiments (H-1 through H-3) were necessary to determine which filter and flow rate was capable of meeting the bacteria and cyst removal requirements of the U.S. EPA Guide Standard and Protocol for Testing Microbiological Water Purifiers. Experiment I-1 was the U.S. EPA Challenge Water #2 trial at BioVir Laboratories using bacterial, viral, and cyst challenges. The experiments and rationale are explained in further detail in the following sections.

**Description and Rationale of Design Experiments**

Design experiments consisted of experiments A-1 through G-3. The filter design evolved throughout testing; once configuration and optimization experiments were complete, a rectangular shaped filter was determined to perform the best. Configuration experiments included experiments A-1 through C-2. Circular filters were tested in experiments A-1 and B-1; square filters were tested in experiments A-2, A-3, B-2, and B-3; and rectangular filters constructed with different bulkhead fittings were tested in experiments C-1 and C-2.

Optimization experiments include experiments D-1 and D-2. A dye study was conducted in these experiments to determine which shape provided the most effective use of available filter area. From these experiments, it was determined that an external rectangular filter provided the best filtration.

Microsphere removal experiments entailed experiments E-1 through F-3. An external rectangular filter manufactured with large diameter bulkheads was used in experiment E-1, and it was determined that one layer of the nominal filter cloth could not provide adequate microsphere removal in order to meet the U.S. EPA Drinking Water Standards.



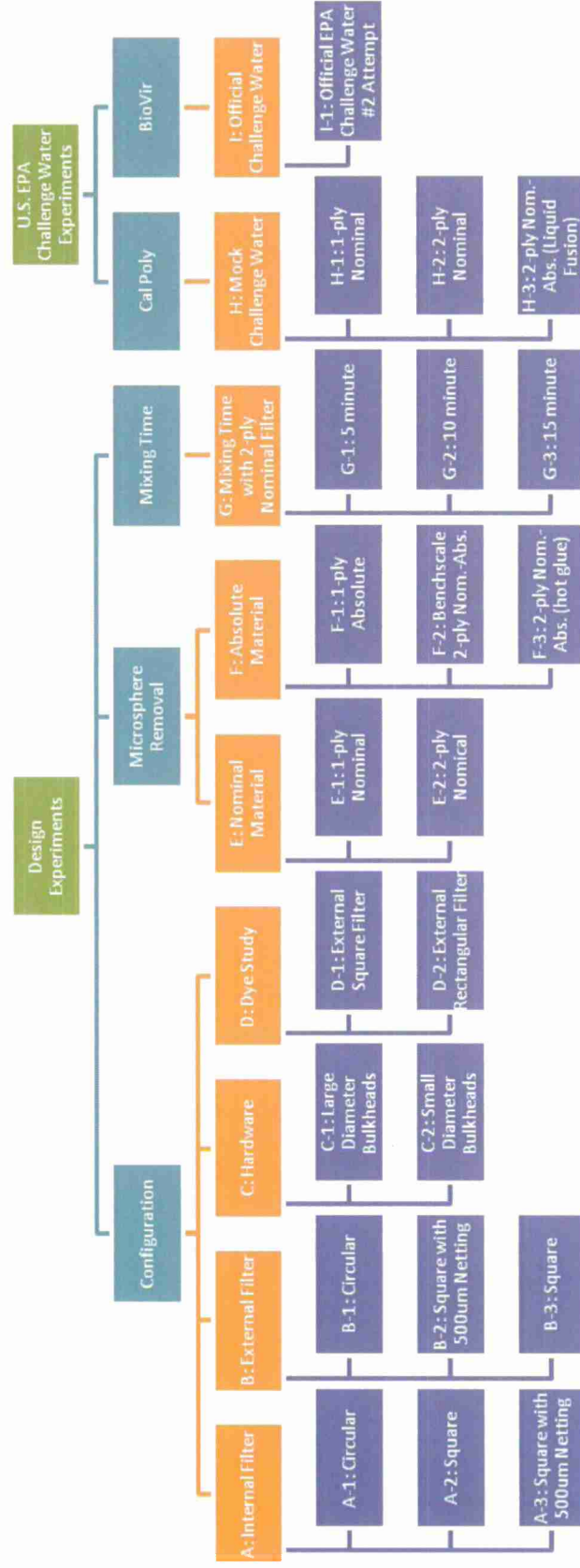


Figure 7: Experiments Performed. Filters for experiments A-1 through D-2 were made of nominal felt material.

Therefore, a 2-ply nominal filter was tested in experiment E-2. This design also proved ineffective at removing microspheres, so the absolute material was used in subsequent filter designs. Initially, a 1-ply absolute filter was tested in experiment F-1. This design required too much head and clogged quickly. Therefore, a 2-ply nom.-abs. filter was designed. The 2-ply nom.-abs. filter consisted of a layer of nominal material inside a layer of the absolute material. A bench-scale model of the 2-ply nom.-abs. filter was tested in experiment F-2. The full-scale 2-ply nom.-abs. filter was tested in experiment F-3. This design also required too much head and clogged quickly.

Various mixing times were tested in experiments G-1, G-2, and G-3. A 2-ply nominal filter was used when comparing 5-min, 10-min, and 15-min times. Experiment G-1 tested the 5-min mixing time, experiment G-2 tested the 10-min mixing time, and experiment G-3 tested the 15-min mixing time. For both the 10-min and 15-min mixing times, a 5-min mix was initially performed followed by a 5-min rest period; this pattern continued until the sought after mixing time was reached. From these experiments, it was determined that the original 5-min mixing time was the most effective.

#### **Description and Rationale of U.S. EPA Challenge Water Experiments**

U.S. EPA Challenge Water experiments included experiments H-1, H-2, H-3, and I-1. Mock challenge water experiments were performed at Cal Poly for experiments H-1, H-2, and H-3. Experiment H-1 tested the 1-ply nominal filter, experiment H-2 tested the 2-ply nominal filter, and experiment H-3 tested the 2-ply nom.-abs. filter. The 2-ply nom.-abs. filter was sealed with Liquid Fusion bonding agent. It was determined that the 2-ply nom.-abs. filter was effective at removing spheres with a 20 mL/min flowrate. This filter was used for experiment I-1, the Challenge Water test at BioVir Laboratories.

### **RESULTS**

The full detail of this project will be available in the MS thesis of Shasta Billings of the Civil and Environmental Engineering Department, Cal Poly. For the sake of brevity, this report will emphasize only the final filter design and the culminating testing at BioVir Laboratories. However, the dye tracer study illustrates how the placement of the inlet port was optimized.

#### **Optimization Experiments D-1 and D-2: Dye Studies**

Dye studies were conducted with both the square filters used in experiment B-3 and the rectangular filters used in experiments C-1 and C-2. Dye studies were performed on both clean and dirty, square and rectangular filters to determine how water flowed through the filter cloth during the usable lifetime of the filter.

Observations during initial dye runs led to a hypothesis that the inlet into the internal chamber of the filter needed to be as high as possible to promote water passage through the largest filter area. The dye study of the square filter also showed the jetting-action of water being forced through the filter cloth upon entry into the internal chamber (Figure 8).

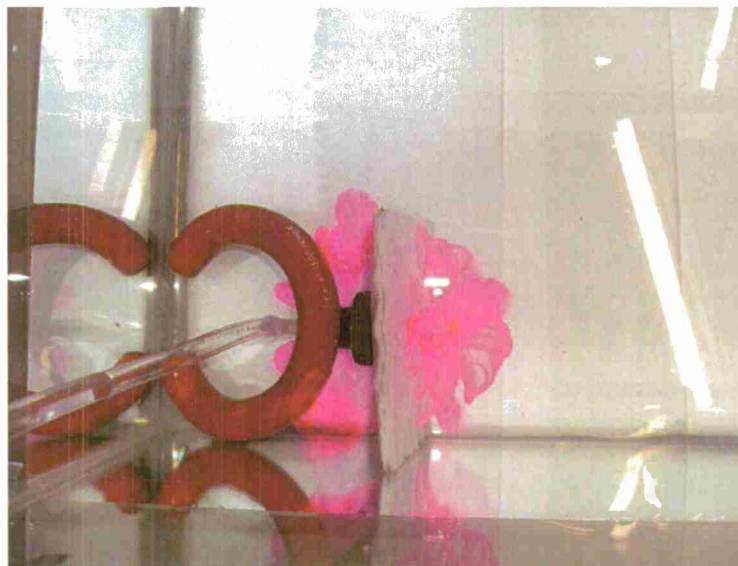


**Figure 8:** Plume of rhodamine dye and water mixture jetting out of the internal chamber of a square filter in experiment D-1. Scale: the large diameter bulkhead on the left side of the filter measures 3.65 cm in diameter.

The jetting of water through the material of the square filters could potentially force microspheres through the filter cloth as well. The inlet port was then reconfigured to flow parallel to the filter cloth. The hope was that the influent would then diffuse slowly through the filter cloth rather than being forced through it in a jet.

Experiment D-2 was performed with both clean and dirty rectangular filters (Figure 9 and 10, respectively). The small diameter bulkhead fitting used on the clean filter shown in Figure 9 was placed as close to the top of the filter as physically possible during filter construction.



**Figure 9:** A clean, rectangular filter with a high bulkhead fitting used in experiment D-2. Scale: the rectangular filter measures 10.2 cm by 15.2 cm.



**Figure 10:** A dirty, previously used rectangular filter with a middle bulkhead fitting used in experiment D-2. Scale: the large diameter bulkhead fitting on the left side of the filter measures 3.65 cm in diameter.

Comparison of Figures 9 and 10 suggested that increasing the height of the inlet bulkhead fitting on the filter increases the filter area used by the water. Experiment D-2 also showed that parallel flow along the filter allowed the water to diffuse through the material as opposed to the jetting observed in perpendicular flow (Figure 11).



**Figure 11:** Thin plume of rhodamine dye and water mixture observed along clean, rectangular filter tested in experiment D-2. Scale: the clear tubing in the upper half of the picture measures 0.75 cm in diameter.

Therefore, it was determined that a rectangular filter with a high-mounted bulkhead fitting and parallel inlet port would be used in all subsequent experiments.

Following the finalization of the filter design, a series of “mock challenge” experiments were run at Cal Poly. These simulated the US EPA Challenge procedure to be conducted at BioVir Laboratories. Through these mock runs, it was determined that a flow of only 20 mL/min allowed for the 3-log microsphere removal required for certification as a U.S. EPA water purifier device. The next section describes the BioVir Laboratories testing results.

#### Experiment I-1: EPA Challenge Water #2 Test at BioVir Laboratories

The 2-ply nom.-abs. filter was tested in triplicate against the U.S. EPA Microbiological Water Purifier Guide Standard and Testing Protocol at BioVir Laboratories on August 17, 2012. The purpose of this test was to prove that the 2-ply nom.-abs. filter could meet the pathogen removal requirements of Test Water #2. The waterbags were filled with tap water first in order to ensure the all valves were set in the appropriate place to throttle the flowrate to 20 mL/min. Once the waterbags were calibrated to the correct flowrate, they were filled with Challenge Test Water #2, dosed with one PÜR<sup>®</sup> sachet, mixed for five minutes at 100 bpm, allowed to settle and disinfect for 25 min, and effluent was filtered and collected in cubitainers for further analysis. Two different effluent samples were collected, an unfiltered sample and a filtered sample, in order to determine removal capabilities of the 2-ply nom.-abs. filter.

*E. coli*, coliphage, and fluorescent microspheres represented the bacteria, virus, and protozoan oo-cyst elements of the Challenge Test (Cooper, 2012). Final removals of all three prototypes are listed in Tables 2, 3, and 4. Note, the flowrate for Bag 3 was the most variable during experiment I-1. This variability could have led to the non-ideal removals reported.

Table 2: *E. coli* (CFU/100 mL) removal results (BioVir, 2012). Bags 1 and 2 met the U.S. EPA Water Purifier device requirements of >6-log removal of *E. coli*.

| Influent          | Bag 1        |                      | Bag 2        |                      | Bag 3             |                      |
|-------------------|--------------|----------------------|--------------|----------------------|-------------------|----------------------|
|                   | Bag Effluent | Post Filter Effluent | Bag Effluent | Post Filter Effluent | Bag Effluent      | Post Filter Effluent |
| $7.3 \times 10^6$ | <1           | <1                   | <1           | <1                   | $1.5 \times 10^4$ | $2.2 \times 10^2$    |
| Log Reduction     |              | >6.7                 |              | >6.7                 | 2.6               | 4.5                  |

Table 3: Coliphage (PFU/mL) removal results (BioVir, 2012). All bags met the U.S. EPA Water Purifier device requirements of >4-log removal of viruses.

| Influent          | Bag 1        |                      | Bag 2        |                      | Bag 3        |                      |
|-------------------|--------------|----------------------|--------------|----------------------|--------------|----------------------|
|                   | Bag Effluent | Post Filter Effluent | Bag Effluent | Post Filter Effluent | Bag Effluent | Post Filter Effluent |
| $1.3 \times 10^5$ | <1           | <1                   | <1           | <1                   | 9            | 4                    |
| Log Reduction     |              | >5.1                 |              | >5.1                 |              | $\geq 4.3$           |



**Table 4: Microsphere (Beads/L) removal results (BioVir, 2012). Bags 1 and 2 met the U.S. EPA Water Purifier device requirements of >3-log removal of protozoan cyst surrogates.**

| Influent          | Bag 1             |                      | Bag 2             |                      | Bag 3             |                      |
|-------------------|-------------------|----------------------|-------------------|----------------------|-------------------|----------------------|
|                   | Bag Effluent      | Post Filter Effluent | Bag Effluent      | Post Filter Effluent | Bag Effluent      | Post Filter Effluent |
| $5.6 \times 10^5$ | $7.7 \times 10^3$ | <50/L                | $7.0 \times 10^3$ | $1.2 \times 10^2$    | $4.4 \times 10^3$ | <10                  |
| Log Reduction     | 1.9               | >4.1                 | 1.9               | 3.7                  | 2.1               | 2.7                  |

Turbidity, pH, and free chlorine residual were also measured on site by Cal Poly researchers. The average initial turbidity value was 39.7 NTU, which satisfies the U.S. EPA Guide Standard and Testing Protocol. Unfiltered post-treatment turbidities varied slightly between Bag 1 and 2 and greatly between Bag 2 and 3 (Figure 12). The pH was 5.7 in Bag 1; pH of samples from Bag 2 and 3 was not measured. The free chlorine residual was 0.03 in Bag 1, 2, and 3. A low free chlorine residual is expected when test waters contain such high organic carbon content as that of U.S. EPA Challenge Water #2.

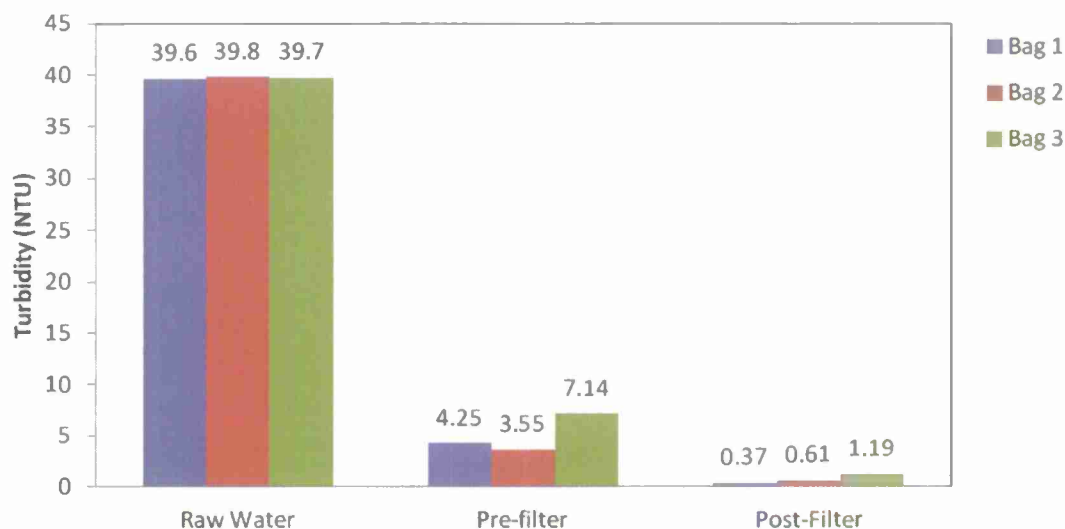


**Figure 12: Turbidity of samples collected by Cal Poly researchers during the 2012 U.S. EPA Challenge Water test from waterbags tested in triplicate.**

When considering the variability in the microsphere results, it was noted that there was a small volume of water between the exit port and the clamp valve that might not get treated to the same extent as the majority of the water in the waterbag. The inconsistency of this volume among the triplicate bags could possibly be the cause of the variable results observed. Dr. Robert Cooper also reported that, given the high concentrations of indicators in the Challenge Water, the lower bacteria log removal observed in Bag 3 could have been due to only 9  $\mu$ L of untreated source water contamination in the effluent cubitainer (Dr. Robert Cooper, personal communication, October, 2012).

The results of the U.S. EPA Challenge Water experiment showed that after treating a contaminated water source with one PÜR<sup>®</sup> sachet in the waterbag, the 2-ply nom.-abs. filter can successfully meet turbidity and pathogen reductions for emergency relief required by the U.S. EPA when used with a 20 mL/min flowrate. However, the success was inconsistent, perhaps due to non-optimal valve location during the BioVir Lab testing or due to leaks or contamination. These passing results with one PUR packet are an improvement over the previous testing at BioVir (Compas, 2009; Herzog, 2011). The 2009 BioVir test found that effective treatment was not obtainable with one PÜR<sup>®</sup> sachet and a filter constructed of one layer of the nominal material (Compas, 2009). The 2010 BioVir test found that effective treatment was obtainable with two PÜR<sup>®</sup> sachets and a filter made of one layer of the nominal material (Herzog, 2011).

## CONCLUSIONS

The twenty-two experiments performed yielded both conclusions as well as possible topics for future research. Both the filter design experiments as well as the U.S. EPA Challenge Water experiments led to conclusions regarding filter design and construction for the Waterbag. From the experiments, it was determined that a 2-ply nom.-abs. filter (sealed with liquid fusion bonding agent) could effectively meet the U.S. EPA Challenge Water #2 bacteria, virus, and cyst removal requirements when the flowrate through the filter was kept no higher than 20-mL/min. However, the results were inconsistent among the triplicate bags tested at the commercial laboratory, with some water quality results not meeting the U.S. EPA requirements. Considering the success of the filter in the Cal Poly Challenge Water tests, it is likely that the commercial lab test had a problem. A small valve leak, contamination, or an excessive volume of water in the bag-to-filter tubing could have caused the incomplete pathogen removals.

## 5. Future Work Planned

Future research on filters for the Waterbag is suggested in order to ensure that the most effective, user-friendly, and cost-effective filter is in place when the Waterbag is distributed commercially.

A focus of future research could include an additional in-depth investigation of available filter cloths and membranes. This scope of this research should be limited to focusing on various microfilter cloths/membranes capable of removing pathogens cysts even with a high flowrate.

An additional focus of future research could include a lifecycle cost assessment of the Gravityworks filter (Cascade Designs, Inc.) currently used on DayOne Response Waterbags. The Gravityworks filter is quite effective and long-lived, but also quite expensive. A lifecycle cost assessment would allow researchers to determine the usable life of the filter and compare that to the cost of producing the 2-ply nom.-abs. filter developed during this research.

## 6. References cited

BioVir Laboratories, Inc. (BioVir) (2012). *Test Report: Polytech Waterbag Challenge, Project #121132*. Benicia, BioVir Laboratories.

- Compas, T. (2009). Point-of-Use Water Treatment Device for Disaster Relief. (Master's thesis). California Polytechnic State University, San Luis Obispo.
- DayOne Response (2012). *Gear for After a Natural Disaster*. Retrieved February 4, 2013, from <http://dayoneresponse.com/press/gear-for-after-the-disaster/>.
- Herzog, M. (2011). Optimization of Point-of-Use Water Treatment Device for Disaster Relief. (Master's thesis). California Polytechnic State University, San Luis Obispo.
- IDEXX (2012). *Colilert®*. Retrieved August 6, 2012, from [http://www.idexx.com/view/xhtml/en\\_us/water/products/colilert.jsf?conversationId=564350](http://www.idexx.com/view/xhtml/en_us/water/products/colilert.jsf?conversationId=564350).
- Procter & Gamble. (2013). PUR packet. *Children's Safe Drinking Water*. Retrieved February 28, 2013, from [http://www.csdw.org/csdw/pur\\_packet.shtml](http://www.csdw.org/csdw/pur_packet.shtml).
- Rosedale Products, Inc. (Rosedale) (2011). Filter Bag Design Details. Retrieved April 13, 2011, from <http://www.rosedaleproducts.com/pdf/126128.pdf>.
- Rosedale Produce, Inc. (Rosedale) (2012). Rosedale High-Efficiency Filter Bags. Retrieved April 20, 2012, from <http://www.rosedaleproducts.com/pdf/153155.pdf>.
- The Sphere Project. (2004). *Humanitarian Charter and Minimum Standards in Disaster Response*. Geneva: The Sphere Project.
- U.S. Environment Protection Agency. (1987). *Guide Standard and Protocol for Testing Microbiological Water Purifiers. Report of Task Force*. U.S. Environmental Protection Agency.
- U.S. Environmental Protection Agency (2013). Microbiological and Chemical Exposure Assessment: *Cryptosporidium* and *Giardia*. Retrieved January 24, 2013, from [http://www.epa.gov/nerlcwww/cpt\\_gda.html](http://www.epa.gov/nerlcwww/cpt_gda.html).
- World Health Organization. (2006). *Guidelines for Drinking-water Quality: incorporating first addendum. Vol. 1 recommendations*, 3<sup>rd</sup> Edition. Geneva: WHO Press.

# **Force protection in combat and non-combat situations**

## **Project Reports**

**Alkoxyamine Polymers: Versatile Materials for 'Ever-Sterile' Surfaces**

Principal Investigator:

**Hasan Palandoken, Ph.D., Chemistry and Biochemistry**

California Polytechnic State University  
San Luis Obispo, CA



## 1. Abstract (~250 words)

The chemoselective condensation between an alkoxyamine ( $\text{RONH}_2$ ) and a ketone or aldehyde affords the robust oxime ethers in near quantitative yields. These simple yet elegant conjugations proceed in aqueous media; and thus are ideal for a variety of applications. The resultant oxime ether bond is very stable and cleaves only after prolonged (e.g., 24 hours) exposure to aqueous strong acid ( $\text{pH} \leq 1$ ) with heat. Furthermore, the oxime ether functionality is prevalent in various pharmaceutical drugs (i.e., antibiotic, anti-cancer). Of particular note, the presence of an oxime ether moiety is known to lead to increased antibiotic activity for penicillin derivatives. The present project seeks to explore the utility of the alkoxyamine functional group in new materials. Alkoxyamines will be installed on polymer side chains as 'molecular anchors' to tether antibiotic compounds on the polymer surface through stable covalent bonds (i.e., oxime ether linkages). An antibiotic drug 'anchored' to a polymer in such a manner is expected to provide a sterile coating that does not require repeated sterilization (e.g., 'ever-sterile' surgical instruments). Existing polymers for similar applications involve additives (e.g., such as an antibacterial compound), which are not attached to the polymer and are thus depleted over time as they leach out of the polymer. The stability of the oxime ether linkages in our polymer systems is expected to circumvent such limitations. The architecture and antibacterial effectiveness of our polymers will be studied. If successful, our alkoxyamine polymers with versatile ligating sites for the attachment of a variety of antibiotic compounds will lead to 'ever-sterile' coatings for a variety of applications.

## 2. Project significance

The present project seeks to explore the utility of the alkoxyamine ( $\text{RONH}_2$ ) functional group in new materials as versatile ligating sites for the attachment of antibiotic compounds on the polymer surface. Specifically, we aim to test the hypothesis that the alkoxyamines located on the proposed new material surfaces can serve as pendant 'molecular anchors' that can tether antibiotic compounds to provide 'ever-sterile' coatings that do not require sterilization (Figure 1).

Immobilization (e.g., tethering) of carbonyl compounds, such as biomolecules (i.e., carbohydrates, proteins), on polymeric surfaces has been an area of intense research [1-3]. The resultant bio-conjugates often display increased stability, bioavailability and activity [2]. The success of the immobilization depends primarily on two factors: (1) polymer architecture; (2) conjugation reaction. The present project addresses both:

**1. Polymer architecture.** End-functionalized poly(ethylene glycol) (PEG) has been the polymer of choice for the preparation of bioconjugates, particularly those of proteins [3]. 'PEGylation' imparts desirable properties such as improved bioavailability. The proposed project will utilize the telechelic 1,3-propylene oxide soft blocks **3** prepared from C(3)-substituted oxetane monomers **1** (Scheme 3) [4]. The PI has extensive experience with C(3)-substituted oxetane monomers and their corresponding polymers

[5]. Unlike the end-functionalized PEG, the hydrophilicity of the proposed polymers is easily modified through the choice of the C(3)-substituents on the oxetane monomers. Copolymerization of the oxetane monomer **2** (Scheme 1) containing the alkoxyamine functionality with other oxetane monomers containing substituents of varying hydrophilicity is expected to allow the facile modification of the polymer hydrophilicity; hence the preparation of surfaces of varying hydrophilicity (i.e., amphiphilic surfaces). Thus, these new alkoxyamine materials will be amenable to surface optimization for the molecular presentation of the antibiotic compounds in the present project.

**2. Conjugation reaction.** Current immobilization techniques rely upon facile (and often chemoselective) reactions that form robust bonds between the polymer surface and the biomolecule under mild conditions. For example, the 1,3-dipolar cycloaddition reaction between an azide and an alkyne affords a triazole but may require a Cu(I) catalyst [1b]. The proposed project will utilize the condensation reaction between an alkoxyamine ( $\text{RONH}_2$ ) and an aldehyde/ketone to immobilize the carbonyl substrate (i.e., antibiotic compound) on the polymer surface (Figure 1). These simple yet elegant chemoselective condensation reactions proceed in aqueous media to afford the robust (see *Background/Prior Work* for the stability of the oxime ether bond) oxime ethers (Figure 2) in near quantitative yields *without the aid of a catalyst*. In fact, the ease with which alkoxyamines condense with aldehydes/ketones has prompted their widespread use in labelling liposome, bacterial and mammalian cell surfaces as well as chemoselectively ligating small molecule 'recognition elements' onto polyfunctional substrates [6].

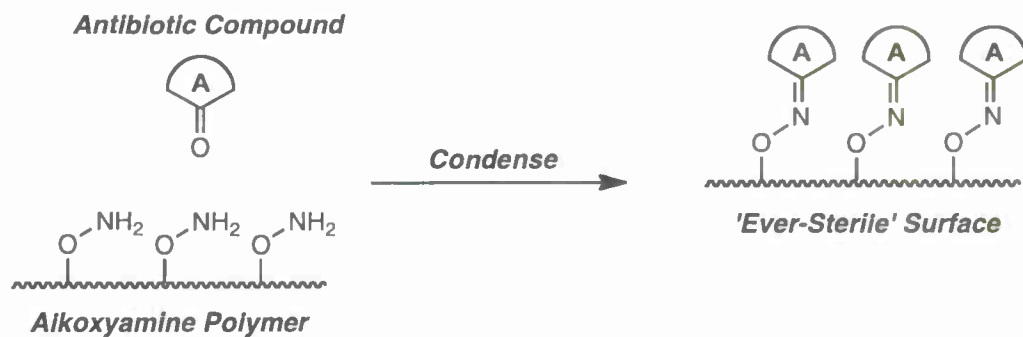


**Figure 1.** Antibiotic tethering on an alkoxyamine polymer surface

The oxime ether functionality (Figure 2) is prevalent in various pharmaceutical drugs, particularly in antibiotic compounds [7]. Figure 3 depicts a representative set of such antibiotic compounds. Of particular note, the presence of an oxime ether moiety leads to increased antibiotic activity in penicillin derivatives relative to unmodified penicillin [7b].

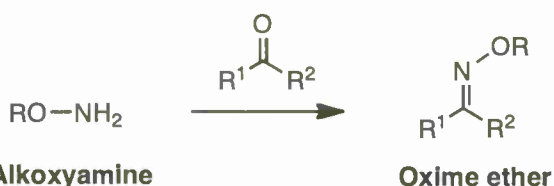


**Figure 2.** Condensation of an alkoxyamine with a carbonyl substrate

Combining the utility of the alkoxyamine functional group and my experiences working with alkoxyamines [8] and polymers [5], I aim to prepare novel polymers with alkoxyamine side chains to create ‘ever-sterile’ surfaces. In the present project, alkoxyamine side chains will be used to permanently ‘anchor’ the antibiotic compound on the polymer surface. For example, an alkoxyamine side chain polymer attached to an antibiotic drug (i.e., penicillin oxime ether derivative in Figure 3) is expected to provide a sterile coating that does not require repeated sterilization. Such a coating has a variety of potential applications, such as surgical instruments that do not require sterilization.

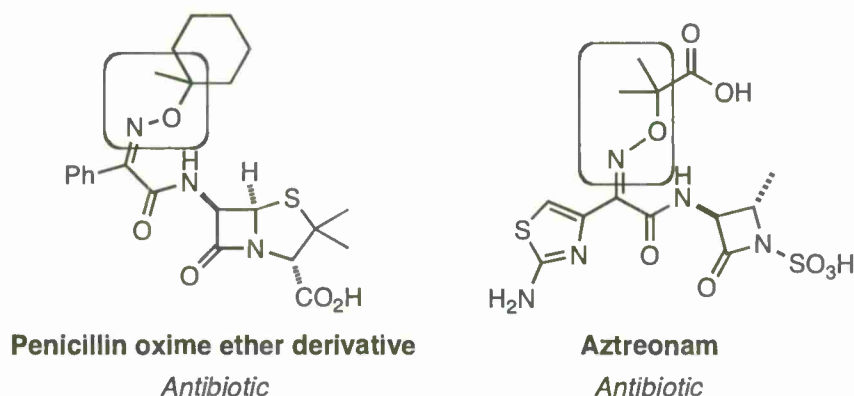


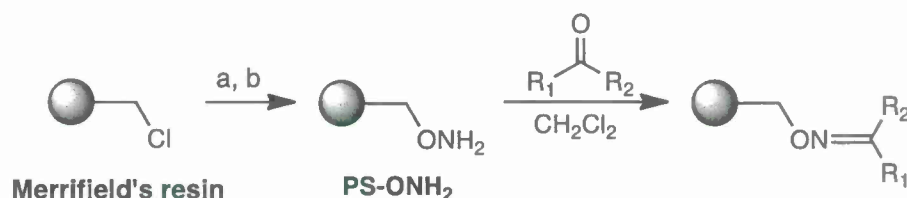
**Figure 3.** Representative oxime ether compounds with antibiotic activity

**Possible relevance to ONR/DOD interests.** If successful, the alkoxyamine polymers of the present project will represent new materials with versatile ligating sites for the immobilization and molecular presentation of antibiotic compounds. An antibiotic drug ‘anchored’ to a polymer surface in such a manner is expected to provide an ‘ever-sterile’ sterile coating (i.e., one that does not require repeated sterilization). Such ‘ever-sterile’ coatings are expected to lead to medical applications such as surgical instruments that do not require sterilization. This would be a vital application on the field or any location where sterilization equipment is not readily available.

### 3. Background/prior work

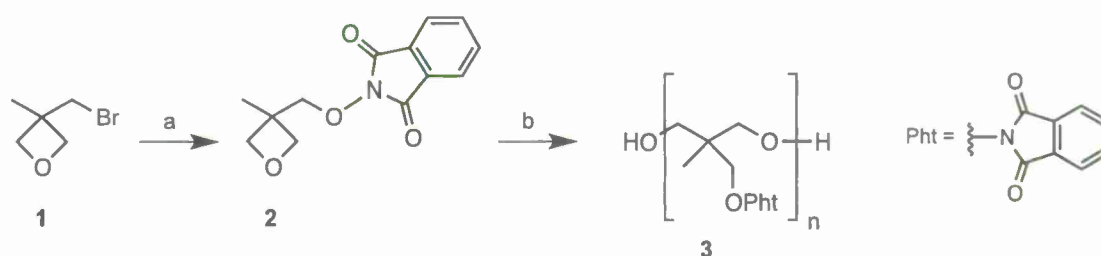
**Conjugation reaction (i.e., carbonyl immobilization on a polymer surface).** We previously demonstrated the feasibility of using alkoxyamines as ‘molecular anchors’ to ‘tether’ carbonyl substrates on polymer surfaces [9]. We installed alkoxyamines on the commercially available Merrifield’s resin to prepare a model polystyrene alkoxyamine

polymer (PS-ONH<sub>2</sub>) (Scheme 1). We were gratified to find that PS-ONH<sub>2</sub> condensed with a variety of carbonyl substrates (i.e., aldehydes or ketones) in organic solutions (e.g., in CH<sub>2</sub>Cl<sub>2</sub>) readily.



**Scheme 1.** Reagents and conditions: (a) *N*-hydroxyphthalimide, Et<sub>3</sub>N, DMF; (b) H<sub>2</sub>NNH<sub>2</sub>•H<sub>2</sub>O, MeOH/CH<sub>2</sub>Cl<sub>2</sub>.

**Polymer architecture.** We recently prepared a C(3)-O-phthalimide (Pht) oxetane monomer **2** from the commercially available 3-bromomethyl-3-methyloxetane **1** (Scheme 2) [10]. A preliminary polymerization reaction indicates that the resultant oxetane monomer **2** provides soft block **3** (as characterized by <sup>1</sup>H/<sup>13</sup>C NMR, IR) quantitatively under Lewis acid catalyzed conditions [10]. However, the degree of polymerization (*n*) requires optimization.



**Scheme 2.** Reagents and conditions: (a) *N*-hydroxyphthalimide, Et<sub>3</sub>N, DMF; (b) 1,4-butanediol, BF<sub>3</sub>•OEt<sub>2</sub>, CH<sub>2</sub>Cl<sub>2</sub>.

**Oxime ether bond stability.** The oxime ether bond has remarkable stability. It is prone to cleavage *only* under forcing and harsh conditions (i.e., acidic conditions such as HCl/HOAc, heat, 24h [12c]) to afford the corresponding carbonyl substrate and the alkoxyamine [12]. In our lab, we confirmed this stability [13]. We have found that the oxime ether bond is stable under neutral (pH 7) and basic conditions (i.e., NaOH pH > 12) with heat for a week. It is important to note that the stability experiments were halted after a week of observing no bond cleavage. The oxime ether bond was cleaved only after treatment with concentrated hydrochloric acid (pH 1) and heat after 24 hours. Furthermore, the oxime ether bond is only partially cleaved when exposed to a strong oxidant (e.g., KMnO<sub>4</sub>) after 24 hours or more.

These indicate that the immobilization (i.e., tethering) of the antibiotic compound on the polymer surface via an oxime ether bond is expected to be a 'permanent' one.

**Antibiotic surfaces.** There have been numerous reports of antibacterial polymer surfaces [14]. In fact, Wynne et al. [14a] utilize polymers based on 1,3-propylene oxide soft blocks as proposed in the present project. The antibacterial agent of choice seems to be tetraalkylammonium salts for most, if not all, of the existing antibacterial surfaces. The tetraalkylammonium salts are either covalently bonded to the polymer surface or simply blended in the polymer formulation. The latter suffers from leaching of the antibacterial agent and limited lifetimes.

The preceding work indicates that the antibacterial compounds can be effective while being bound to a polymer surface. The present project proposes to tether antibiotic compounds covalently to the polymer surface. Furthermore, the proposed synthetic route allows for the tethering of more than one type of antibiotic compound on the same polymer surface, as required.

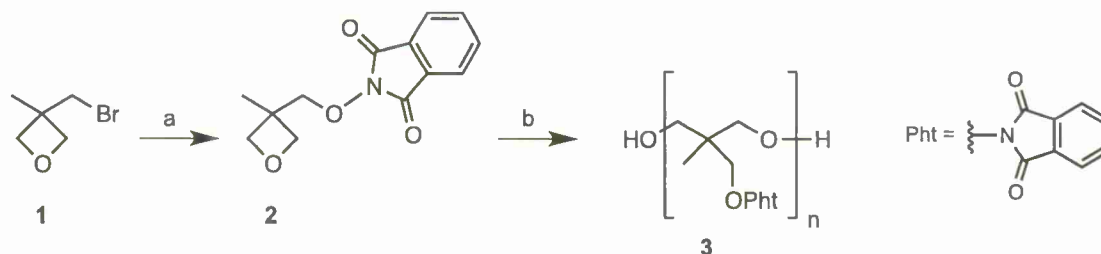
#### 4. Discussion of Results

The present project seeks to study the alkoxyamine ( $\text{RONH}_2$ ) functional group on new polymer surfaces (with adjustable polymer architecture) as 'molecular anchors' to that can immobilize (i.e., tether) antibiotic compounds on the polymer surface (Figure 1).

**Specific objectives.** The objectives for the proposed project can be divided into four categories:

1. Preparation of alkoxyamine polymers;
2. Immobilization of antibiotic drugs to the polymer surface;
3. Characterization and stability evaluation of the resulting polymers;
4. Evaluation of biological activities (i.e., antibiotic) of the resulting polymers.

**Objective #1 Results.** Scheme 3 outlines the synthesis of the telechelic 1,3-propylene oxide soft block **3** bearing 'masked' alkoxyamines (e.g., as *O*-phthalimides) from the C(3)-substituted oxetane monomer **1**. Displacement of the leaving group (Br) in **1** with *N*-hydroxyphthalimide provided the desired C(3)-*O*-phthalimide (Pht) oxetane monomer **2** in 90% yield on a 50 g scale.

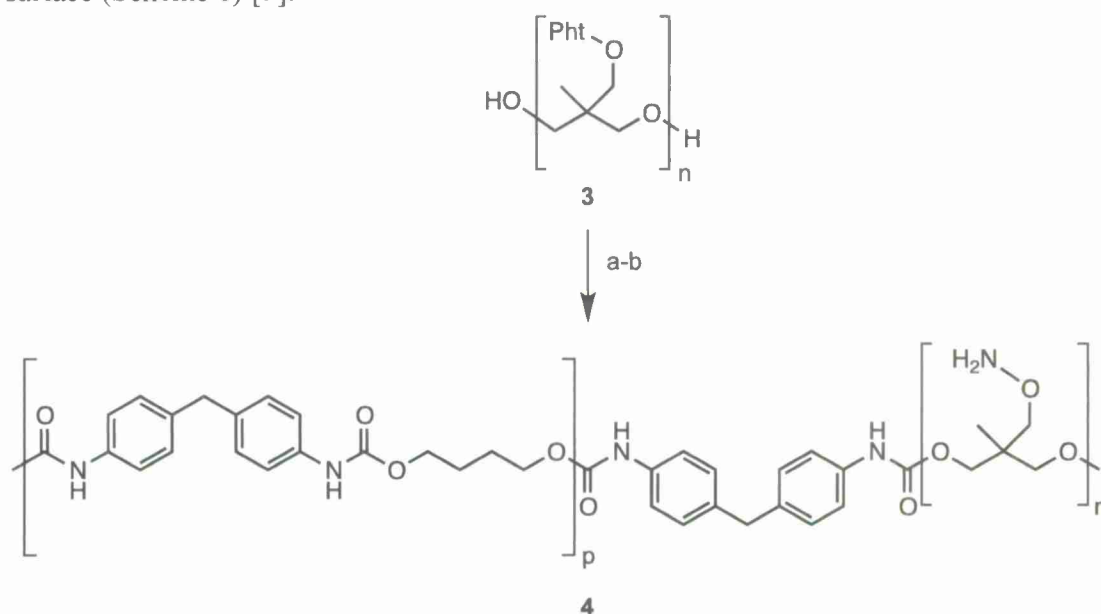


**Scheme 3.** Reagents and conditions: (a) *N*-hydroxyphthalimide,  $\text{Et}_3\text{N}$ , DMF, 80%; (b)  $\text{BF}_3 \cdot \text{OEt}_2$ , PhCl, 130 °C, 70%.



The polymerization conditions were optimized for control over degree of polymerization ( $n$ ) through the Lewis acid selection, solvent and reaction temperature. Polymerization of C(3)-*O*-phthalimide (Pht) oxetane monomer **2** with  $\text{BF}_3 \cdot \text{OEt}_2$  in PhCl at 130 °C (similar to Motoi *et al.* report [11]) provided the telechelic 1,3-propylene oxide soft block **3** (Scheme 3) with good control over the degree of polymerization ( $n$ ). On multiple 10 g scale runs, we achieved an  $n$  of 8-10 with a target  $n$  of 10. Furthermore, the pendant *O*-phthalimide groups in our poly ether **3** survived our cationic polymerization conditions (based on NMR and IR analyses).

Soft block **3** ( $n=9-10$ ) was incorporated into a polyurethane matrix (Scheme 4). Subsequent hydrazinolysis 'unmasked' the pendant alkoxyamines to provide the alkoxyamine polyurethane **4**. We had previously demonstrated this alkoxyamine 'unmasking' approach to prepare a model polystyrene alkoxyamine polymer (PS-ONH<sub>2</sub>) surface (Scheme 1) [9].



**Scheme 4.** Reagents and conditions: (a) 4,4'-Methylenebis(phenyl isocyanate), 1,4-butanediol, dibutyltin dilaurate (cat.); (b)  $\text{H}_2\text{NNH}_2 \cdot \text{H}_2\text{O}$ , MeOH/ $\text{CH}_2\text{Cl}_2$ .

**Objective #2 Results.** The immobilization of three antibiotic compounds containing aldehyde/ketone functional groups (i.e., Ciprofloxacin, Streptomycin and Doxycycline) was tested on our model polystyrene alkoxyamine polymer (PS-ONH<sub>2</sub>) (Scheme 5). These antibiotic compounds are effective in inhibiting *E. coli* growth (see Objective#4 Results). Indeed, all three antibiotic compounds were tethered efficiently onto the PS-ONH<sub>2</sub> surface (as confirmed by IR analyses) to afford PS-ON=A (Scheme 5).



**Scheme 5.** Immobilization of antibiotic compounds on model alkoxyamine polymer, PS-ONH<sub>2</sub>.

Unfortunately, we did not have time to tether the antibiotic compounds on the alkoxyamine polyurethane **4** (Scheme 4) during this study. However, we were able to demonstrate its ability to condense with the model aldehyde, benzaldehyde (PhCHO), as effectively as PS-ONH<sub>2</sub>. Thus, antibiotic compounds containing aldehyde/ketone functional groups (i.e., Ciprofloxacin, Streptomycin and Doxycycline) are expected to tether onto alkoxyamine polyurethane **4**.

**Objective #3 Results.**

**Characterization.** C(3)-*O*-phthalimide (Pht) oxetane monomer **2** and the telechelic 1,3-propylene oxide soft block **3** (Scheme 3) were characterized through <sup>1</sup>H/<sup>13</sup>C NMR and IR spectroscopy. In addition, the degree of polymerization (*n*) in soft block **4** was determined by <sup>1</sup>H NMR (with end group derivatization) [4, 5]. Alkoxyamine polyurethane **4** (Scheme 4) was studied by IR-ATR (attenuated total reflectance) for its surface properties.

**Stability testing.** Oxime ether bound antibiotic polymers, PS-ON=A (Scheme 5), were subjected to highly acidic (pH < 1), highly basic (pH > 12) and physiological pH (*ca.* pH 7.4) media at room temperature and elevated temperatures (i.e., > 75 °C). Upon filtration, the filtered polymer resins and the filtrates were analyzed for antibiotic cleavage. None showed any antibiotic cleavage – consistent with our experience with the oxime ether bond (see 3. *Background/Prior Work*).

**Objective #4 Results.** The three antibiotic compounds, Ciprofloxacin, Streptomycin and Doxycycline, were chosen for this study as:

(1) they contain aldehyde/ketone functional groups required for condensation with the alkoxyamine polymers; (2) they are effective in inhibiting *E. coli* (bacteria used in this study) growth.

The antibiotic activity of our ‘ever-sterile’ polymers, PS-ON=A (Scheme 5), was performed against *E. coli*. Specifically, we observed the *E. coli* growth rate in the presence and absence of PS-ON=A. None of the PS-ON=A resins were effective in inhibiting *E. coli* growth. It is likely that the hydrophobicity of the polystyrene backbone of PS-ON=A prevents the molecular presentation of the antibiotic compounds to *E. coli* in aqueous media.

## 5. Future Work Planned

The three antibiotic compounds, Ciprofloxacin, Streptomycin and Doxycycline, will be tethered on the alkoxyamine polyurethane **4** (Scheme 4). The resulting oxime ether bound antibiotic polymers will be tested for *E. coli* growth inhibition. The increased backbone hydrophilicity of the alkoxyamine polyurethane **4** should allow for a more effective molecular presentation of the antibiotic compounds to *E. coli* in aqueous media.

## 6. References cited

1. For recent, representative examples, see: (a) Laughlin, S. T.; Baskin, J. M.; Amacher, S. L.; Bertozzi, C. R. "In Vivo Imaging of Membrane-Associated Glycans in Developing Zebrafish", *Science*, **2008**, *320*, 664-667; (b) Sun, X.-L.; Stabler, C. L.; Cazalis, C. S.; Chaikof, E. L. "Carbohydrate and Protein Immobilization onto Solid Surfaces by Sequential Diels-Alder and Azide Alkyne Cycloadditions", *Bioconjugate Chem.*, **2006**, *17*, 52-57.
2. Heredia, K. L.; Tolstyka, Z. P.; Maynard, H. D. "Aminooxy End-Functionalized Polymers Synthesized by ATRP for Chemoselective Conjugation to Proteins", *Macromolecules*, **2007**, *40*, 4772-4779 and references therein.
3. Heredia, K. L.; Bontempo, D.; Ly, T.; Byers, J. T.; Halstenberg, S.; Maynard, H. D. "In Situ Preparation of Protein-"Smart" Polymer Conjugates with Retention of Bioactivity", *J. Am. Chem. Soc.*, **2005**, *127*, 16955-16960 and references therein.
4. For a recent example of polymers based on 1,3-propylene oxide, see: Grunzinger, S. J.; Wynne, K. J. "Polyurethanes From Novel 1,3-propyleneoxide Catecholates Having Pendant Hydantoin and Methoxymethyl Groups", *Polymer*, **2006**, *47*, 4230-4237 and references therein.
5. Unpublished research conducted by PI on oxetane monomers & their polymers (specifically polyurethane formulations) at Ampac (formerly Aerojet) Fine Chemicals (1997-2003).
6. For recent examples, see: (a) Marcaurelle, L. A.; Shin, Y.; Goon, S.; Bertozzi, C. R. "Synthesis of Oxime-Linked Mucin Mimics Containing the Tumor-Related TN and Sialyl TN Antigens", *Org. Lett.*, **2001**, *3*, 3691-3694. (b) Perouzel, E.; Jorgensen, M. R.; Keller, M.; Miller, A. D. "Synthesis and Formulation of Neoglycolipids for the Functionalization of Liposomes and Lipoplexes" *Bioconjugate Chem.* **2003**, *14*, 884-898. (c) Sadamoto, R.; Niikura, K.; Ueda, T.; Monde, K.; Fukuhara, N.; Nishimura, S.-I. "Control of Bacteria Adhesion by Cell-Wall Engineering" *J. Am. Chem. Soc.* **2004**, *126*, 3755-3761.
7. (a) *Aztreonam*: Ng, C. *J. Pharm. Sci.* **2004**, *93*, 2535 and references therein; (b) *Antibiotic activity enhancement through oxime ether moiety in penicillin*: Bicknell, A. J.; Gasson, B. C.; Hardy, K. D. EP-386940, 1990.
8. Palandoken, H.; Bocian, C. M.; McCombs, M. R.; Nantz, M. H. "A Facile Synthesis of (*tert*-Alkoxy)amines", *Tetrahedron Lett.*, **2005**, *46*, 6667.

9. Fisher, D. J.; Bratcher, F. B.; Jordan, A. J.; Palandoken, H. "Alkoxyamines: Molecular Hooks To 'Catch And Release' Carbonyl Substrates" presented at the 239th National Meeting Of The American Chemical Society, San Francisco, California, March 2010.
10. Browne, J.; Palandoken, H. *unpublished results from Cal Poly*.
11. Kanoh, S.; Nishimura, T.; Senda, H.; Ogawa, H.; Motoi, M. "Monomer-Isomerization Polymerization of 3-Methyl-3-(phthalimidomethyl)oxetane with Two Different Ring-Opening Courses", *Macromolecules*, **1999**, *32*, 2438-2448 and references therein.
12. For examples of oxime ether hydrolysis under acidic conditions, see: (a) Kalia, J.; Raines, R. T. "Hydrolytic Stability of Hydrazones and Oximes", *Angew. Chem. Int. Ed.* **2008**, *47*, 7523-7526. (b) Carmona, S.; Jorgensen, M. R.; Kolli, S.; Crowther, C.; Salazar, F. H.; Marion, P. L.; Fujino, M.; Natori, Y.; Thanou, M.; Arbuthnot, P.; Miller, A. D. "Controlling HBV Replication *in Vivo* by Intravenous Administration of Triggered PEGylated siRNA-Nanoparticles", *Molecular Pharmaceutics* **2009**, DOI: 10.1021/mp800157x. (c) Hassner, A.; Patchornik, G.; Pradhan, T. K.; Kumareswaran, R. "Intermolecular Electrophilic O-Amination of Alcohols", *J. Org. Chem.* **2007**, *72*, 658-661.
13. Jordan, A. J.; Bratcher, F. B. "Stability Of The Oxime Ether Bond: 'Release Of Carbonyl Substrates'" presented at the Cal Poly College of Science and Mathematics Research Conference, San Luis Obispo, California, May 2010.
14. For recent examples, see: (a) Kurt, P.; Wood, L.; Ohman, D. E.; Wynne, K. J. "Highly Effective Contact Antimicrobial Surfaces via Polymer Surface Modifiers", *Langmuir*, **2007**, *23*, 4719-4723 and references therein; (b) Borman, S. "Surfaces Designed To Kill Bacteria", *Chem. Eng. News*, **2002**, *80*, 36-38 and references therein.

**Development of Thermally Responsive Binders Designed for Insensitive  
Munitions Applications**

Principal Investigator:

**Philip Costanzo Ph.D., Chemistry**

California Polytechnic State University  
San Luis Obispo, CA



## 1. Abstract (~250 words)

The continued development of insensitive munitions remains a critical DoD concern due to potential vulnerabilities arising from various fire and ballistic threats (fast cook-off, slow cook-off, bullet impact, fragment impact, sympathetic detonation, and shaped charge jet impact). This work details our efforts to develop a possible candidate for insensitive munitions binder by modifying existing polymeric binders with Diels-Alder (DA) linkages. DA chemistry was chosen because the retro-DA requires the absorption of thermal energy, which will create a thermodynamic sink that will potentially increase the heat capacity of the binder. In particular, the maleimide/furan DA system has been studied extensively and shown to display a retro-DA at approximately 90 °C, which provides an ideal temperature window for insensitive munitions. Preliminary efforts have prepared different thermally responsive binders, such as thermally responsive hydroxyl-terminated polybutadiene (TR-HTPB) and thermally responsive hydroxyl-terminated polycaprolactone (TR-PCL). The materials were characterized by differential scanning calorimetry (DSC), rheological measurements and thermogravimetric analysis (TGA) and yielded excellent results; however, the initial system was limited due to the formation of irreversible crosslinks associated with the maleimide/furan system. The focus of this project was to develop new DA systems based upon fulvene and electron-deficient dieneophiles. Novel materials will be prepared and characterized in a manner analogous to previously prepared materials, i.e. DSC, rheological measurements and TGA.

## 2. Project significance

The development of insensitive munitions is of particular concern to the Navy for issues with respect to safety and storage of the live materials and potential vulnerabilities due to various fire and ballistic threats (fast cook-off, slow cook-off, bullet impact, fragment impact, sympathetic detonation, and shaped charge jet impact). Our approach for developing insensitive munitions is to modify the prepolymer that is commonly employed as the currently accepted standard binder material with chemical functionality that creates a thermodynamic sink that will potentially improve the insensitivity of the binder to heat. Furthermore, the incorporation of a reversible crosslinking mechanism will allow for the possible development of a venting mechanism. Such a property offers a unique avenue to improve thermal sensitivity and stability. Additionally, simple modification of the base material guarantees the important physical and mechanical properties will be maintained. Finally, by utilizing a commercially available material from an existing commercially accepted propellant formulation, this process should remain scalable and compatible with existing processing conditions.

### 3. Background/prior work

The continued development of insensitive munitions remains a critical DoD concern due to potential vulnerabilities arising from various fire and ballistic threats (fast cook-off, slow cook-off, bullet impact, fragment impact, sympathetic detonation, and shaped charge jet impact). Typical composite explosive and propellant formulations contain a mixture of an oxidizing agent, fuel, and a binder. Additionally, other compounds, such as plasticizers, curing agents, cure catalysts, ballistic catalysts, and other processing aids, can be added to the mixture to optimize final physical properties. Nitramines, such as RDX and HMX, are the most common oxidizing agents. Various metals, such as Al, Zr, Mg, are typical fuels. Finally, many different types of polymers have been utilized for binders; however, poly(urethanes) based upon hydroxyl-terminated polybutadiene (HTPB) or hydroxyl-terminated polycaprolactone (PCL) cured with a multifunctional-isocyanate are the historical binders of choice for the development of insensitive binder applications.<sup>1-3</sup>

Urethane binders based upon HTPB and PCL exhibit physical property characteristics that are critical to the development of insensitive munitions, including adhesion and compatibility with explosives, storage and processing stability, and a tunable pot life. Additionally, there are other properties key to binder applications that are specifically inherent within HTPB/PCL-urethanes, such as excellent low-temperature flexibility, endothermic decomposition under acidic conditions, low cost, and complete curing that does not result in cracking or significant property loss.<sup>2</sup>

Many different strategies have been previously employed for the development of insensitive munitions; in particular, the application of thermally degradable binders is one method of significant interest.<sup>2,3</sup> Henry *et al.* at China Lake developed binders that would undergo controlled thermal degradation, which yielded a material that could be easily removed from the explosive casing for recycling or disposal.<sup>3</sup> These methods were based upon the thermal cleavage of azo-, carbonate-, and amine oxide-linkages within the polymer network of the binder. All binders dissociated into liquid pre-polymers and/or co-monomers upon exposure to elevated temperatures, and some of the binder systems exhibited the capability to re-cure after several days. Preliminary results indicated that the thermally responsive binder approach provided a practical means of disposal and recycling of ordnance. Unfortunately, these binders were unable to compete with HTPB elastomers due to increased synthetic costs and overall performance. Therefore, additional research was not pursued.

These previous results set the stage for the development of an insensitive munitions binder based upon a prepolymer that contains thermally responsive, energy absorbing Diels-Alder (DA) linkages along the polymer backbone. These linkages will create a thermodynamic sink that will potentially increase the heat capacity of the elastomer. Simple modification of commercially available prepolymers guarantees the important physical and mechanical properties will be maintained without adding significant cost to the process.

Diels-Alder chemistry has been studied extensively in the literature and the chemical reaction mechanisms are well understood.<sup>4,5</sup> The formation of the ring structure is temperature dependent and reversible. (Figure 1) Recently, many research groups have exploited the combination of DA chemistry and block copolymers to prepare organic-inorganic polymer hybrids,<sup>6-8</sup> thermoplastic elastomers,<sup>9,10</sup> polyurethanes and foams.<sup>11</sup>

A key aspect of the Diels-Alder reaction that has not been exploited by previous applications is the large endotherm required for cleavage of the Diels-Alder adduct, or retro-DA reaction. In the early 80's, the DOE funded fundamental research for the development of a material that could be utilized for energy storage.<sup>12</sup> Researchers determined that the Diels-Alder adduct had a heat capacity approximately 76% greater than water. In other words, the retro-DA requires the absorption of thermal energy, which is a coveted property for the development of insensitive munitions binders.

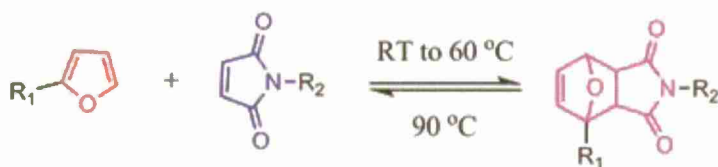


Figure 1. Reversible Diels-Alder adduct (Purple) whose formation is temperature dependent. Red - Diene, Furan. Blue - Dienophile, Maleimide.

Previous efforts from the PI's research group have developed TR-HTPB and TR-PCL binders, and successfully demonstrated the ability to utilize a retro-DA linkage as a thermodynamic sink.<sup>13,14</sup> Preliminary efforts illustrated a simple and scalable system. A variety of DA linkage systems were explored, and several key systems were identified.<sup>13,14</sup> The limitations of the current system were also identified due to the occurrence of unexpected side-reactions. In particular, the initial DA system employed contained a phenolic end-group which caused significant problems in establishing consistent and simple cure times for the prepared elastomers. Additionally, the reaction between the HTPB backbone and the furan-terminated chain ends resulted in the formation of irreversible crosslinks which reduced the effectiveness of the system. Additionally, irreversible crosslinks may have formed due to the cross-polymerization of maleimide functional groups.<sup>15</sup>

#### 4. Discussion of Results

The key result of this project is the incorporation of Diels-Alder linkages within the backbone of a polymer that is ultimately utilized as a binder for propellant applications. Upon application of heat, a retro Diels-Alder reaction is initiated, which results in two important phenomena: 1) absorbance of energy in the retro Diels-Alder, which improves the sensitivity of the propellant, and 2) cleavage of the network to yield oligomers with low viscosity resulting in a de-pressurization of the system, which reduces the severity of detonation.

A multitude of binder formulations were developed. Collaborations with the Army Research Laboratory (ARL) in Aberdeen Proving Grounds, MD and the Naval Research Laboratory (NRL) in Indian Head, MD allowed for live formulations to be prepared via small-batch hand-mixing. It has been found that the stock, thermally-responsive (TR) matrix becomes crystalline after several months, which makes hand mixing extremely difficult. Another significant problem experienced was slow cure times. Many methods have been utilized to improve the properties.

After receiving feedback from ARL and NRL, it was determined that different base pre-polymers, such as poly(caprolactone) (PCL), would be of interest. To date, thermally-responsive poly(caprolactone) (TR-PCL) has been prepared with previously utilized Diels-Alder linkages. Gumstocks were prepared and their thermal properties evaluated. Preliminary testing has shown that replacement of the HTPB backbone with PCL results in significant improvement of the material. An initial batch of ~ 250 g was prepared and sent to Indian Head for live formulation testing. A variety of new diene and dieneophile combinations have been prepared and incorporated within matrix material. Some combinations improved the issues with crystallinity and cure times, but no longer exhibited the retro-Diels-Alder reaction. Current work is aimed at developing new matrix materials and improving their processability.

During the funding period of this award, twelve students worked on this project. The project has resulted in nine presentations at national meetings and four additional presentations in other venues, including five invited speaker requests. During the 2011 Western Coating Symposium in Las Vegas, NV, Greg Strange gave a poster presentation and was awarded the Best Technical Student Poster Award - 1<sup>st</sup> place. At the same conference, Chris Roland gave a poster presentation and was awarded the Best Technical Student Poster Award - 3<sup>rd</sup> place. Undergraduate students gave oral presentations at the 2011 national American Chemical Society (ACS) meeting in Anaheim, CA and the 2012 national ACS in San Diego, CA. At the 2012 meeting, Suzanne Roy was awarded an ACS Undergraduate Travel Award for her presentation.

## 5. Future Work Planned

Future work will be targeted towards the incorporation of Diels-Alder linkages into new matrix and host/guest systems. Additionally, results from this project have been utilized to leverage additional funding from the Army Research Laboratory for a similar project ("Easily processed Host-Guest polymer systems with high-Tg characteristics." Awarded \$47,946 from APR 2011 - AUG 2013) and the National Science Foundation (NSF) ("Preparation of Polymeric Phase Change Materials Based upon Diels-Alder Chemistry." Awarded \$210,000 from SEP 2012 - AUG 2015.)

## 6. References cited

- (1) Amtower, P. K.; Allilant Techsystems: USA, 2003.

- (2) Frisch, K. C.; Young, R. B.; Hillstrom, W. W. *BRL-TR* **1987**, *Contract No. DAAG29-81-0100*, 88.
- (3) Henry, R. A.; Martin, E. C.; Army Research Laboratory: USA, 1980.
- (4) Carruthers, W. *Cycloaddition Reactions in Organic Synthesis* Oxford, U. K., 1990.
- (5) Fringuelli, F.; Taticchi, A. *Dienes in the Diels-Alder Reaction*; John Wiley & Sons: New York, 1990.
- (6) Imai, Y.; Itoh, H.; Naka, K.; Chujo, Y. *Macromolecules* **2000**, *33*, 4343.
- (7) Costanzo, P. J.; Demaree, J. D.; Beyer, F. L. *Langmuir* **2006**, *22*, 10251.
- (8) Costanzo, P. J.; Beyer, F. L. *Macromolecules* **2007**, *40*, 3996.
- (9) Gheneim, R.; Perez-Berumen, C.; Gandini, A. *Macromolecules* **2002**, *35*, 7246.
- (10) Chen, X.; Wudl, F.; Mak, A. K.; Shen, H.; Nutt, S. R. *Macromolecules* **2003**, *36*, 1802.
- (11) Mcelhanon, J. R.; Russick, E. M.; Wheeler, D. R.; Low, D. A.; Aubert, J. H. *J. Appl. Poly. Sci.* **2002**, *85*, 1496.
- (12) Spark, B. G.; Poling, B. E. *AIChE Journal* **1983**, *29*, 534.
- (13) Dirlam, P. T.; Strange, G. A.; Orlicki, J. A.; Wetzol, E. D.; Costanzo, P. J. *Langmuir* **2010**, *26*, 3942.
- (14) Swanson, J. P.; Rozvadovsky, S.; Seppala, J. E.; Mackay, M. E.; Jensen, R. E.; Costanzo, P. J. *Macromolecules* **2010**, *43*, 6135.
- (15) Adzima, B. J.; Aguirre, H. A.; Kloxin, C. J.; Scott, T. F.; Bowman, C. N. *Macromolecules* **2008**, *41*, 9112.



**Development of a Virtualization Platform for Airway Device  
Development**

Principal Investigator:

**Lily Laiho, Ph.D., Biomedical and General Engineering**

California Polytechnic State University  
San Luis Obispo, CA

## **1. Abstract**

Airway device development has historically been dependent on physical modeling, rapid prototyping, and testing in airway simulator mannequins. This method of predicting function and safety is limited by the few mannequin sizes available, i.e. neonate, infant, child, and adult. Also, the airway mannequins that are available represent a “neutral” anatomic configuration for each size that does not reflect the range of anatomic variability in the anatomy of the airway.

The aforementioned assumptions do not serve the development of airway devices and adjuncts for the patient whose airway management is problematic. Patients with issues such as an exceptionally anterior larynx or small mouth opening are most at risk for oxygen deprivation during airway management and are those patients least served by the status quo.

In this project, we created a virtualization platform based on MRI images to simulate a patient’s oral cavity for the development of an airway device. CAD – related techniques and tools, such as 3D scanner (ScanStudio HD), RapidWorks, SolidWorks and Mimics were utilized to create the models used to construct the platform. Validation of the model was performed using an oro-pharyngeal airway (OPA) device to demonstrate the ability of the model assess and modify a new device.

The creation of a virtualization platform enables more cost-effective and efficient development of airway devices that are more likely to solve clinical problems across the spectrum of anatomic variation than is currently possible. In addition, 3D CAD models for airway devices superimposed on the virtualization airway platform will enable modification prior to prototyping and manufacture. This platform may also create a new simulation method for airway management training in both normal and variant/abnormal anatomic situations. Such a platform can be extended to other physiological locations and the other areas of device development.

## **2. Project significance**

Airway management is a crucial aspect of both emergency and elective patient care. Airway management is the process of ensuring that there is an open pathway between a patient’s lungs and the outside world. In nearly all circumstances airway management is the highest priority for clinical care. This is because if there is no airway, there can be no breathing, hence no oxygenation of blood and therefore circulation (and hence all the other vital body processes) will soon cease. Getting oxygen to the lungs is the first step in almost all clinical treatments. The ‘A’ is for ‘airway’ in the ‘ABC’ of cardiopulmonary resuscitation. The most dangerous times for the patient during surgery are before the airway is secured and between the end of surgery, when the airway is again in a transitional state, through the first fifteen minutes in the post-anesthetic recovery room<sup>1</sup>.

In the last decade, the obesity epidemic has led to a 30% increase in airway-related tragedies, despite the greater availability of more sophisticated clinical tools, monitors, and airway management training<sup>2</sup>. Because of the anatomic airway changes during

pregnancy, the obstetric population is at a particularly increased risk, especially when the pregnant state is combined with obesity. More accurate physical airway models are necessary in order to develop tools to help address these areas.

Product development of an airway device, like any other product, requires fit checks, mockups, and prototypes. Unfortunately, this means using the prototype device with either an airway mannequin or cadavers, neither of which is entirely suitable for the work associated with early product development efforts. As a result, the early design optimization of airway devices is often limited. Designs are quite mature by the time they are tested within the context of actual airway geometry, which is clearly not the best way to do product development.

Issues such as an exceptionally anterior larynx or small mouth opening, with or without co-morbidities such as obesity cannot be addressed in airway device development because of the limited sizes and types of physical airway simulators currently available. All currently available simulators reflect anatomy favorable for airway management, such as normal thyromental distance and mouth opening (Figure 1).



Figure 1. (Left to Right) Adult AirSim, Pediatric AirSim, Adult Airsim (original version), and Laerdal Airway Simulators

Contemporary criteria for naso- and oro-pharyngeal airways include low resistance to respiratory gas flow, protection from gastric and nasal contamination of the respiratory tract, tolerance of positive pressure ventilation, and lack of adverse qualities associated with placement, cleaning, and construction materials<sup>3</sup>. The physical models available limit analysis and human factors testing, i.e. ease of insertion and removal as well as other desirable airway attributes such as airway resistance, stability of the device in different head and neck positions, ease of passage of a gastric tube, positioning of the airway over the larynx, suitability for fiberoptic or catheter exchange techniques, and comparisons between new and existing devices<sup>4</sup>.

In order to address the limitations of the current models, a visualization platform is needed which can create computer-aided-design (CAD) models of the airway for studies for product development such as geometry, fit checks, and finite element analysis of performance that accurately simulate the geometry and mechanical properties of the airway during all phases of respiration and over the range of anatomic variability (Figure 2). The visualization platform can subsequently be used to create physical models. Physical models are especially desirable, as they can ultimately be used to aid airway

device development and evaluate new or novel designs. For these benefits to be realized, it is important that the airway be anatomically and mechanically correct. In addition, the airway and superimposed device modeling is the best safety precaution an airway device developer can realistically achieve in order to protect patient safety and improve efficacy.

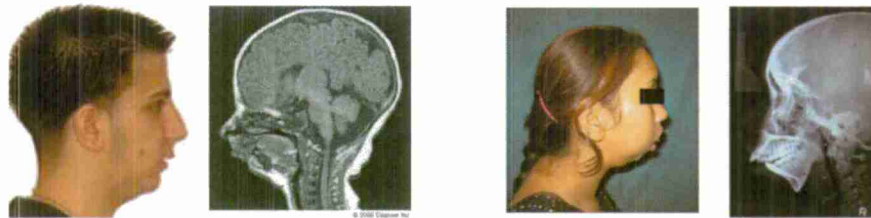


Figure 2. Pictorial examples of abnormal anatomy, i.e. receding chin, that can lead to airway management difficulty, with corresponding MRI and X-ray images

There are currently no virtualization models available for airway device development. Other virtualization models concerning the oropharynx are dedicated to oral surgery and cosmetic work (Figure 3). We will fill the anatomic gap in the tools available to airway device development with this project. Moreover, the virtualization model could also be adapted to training in airway management. Training in airway management is currently limited to solid mannequins of normal anatomy and human subjects, with the attendant risks.

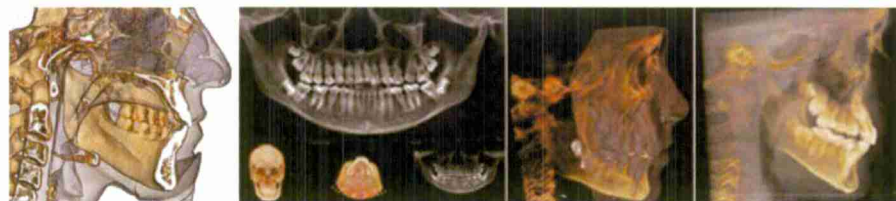


Figure 3. Virtualization images used in oral surgery

### 3. Background/prior work

Oropharyngeal airway, commonly known as oral airway or OPA, is used to prevent airway obstruction in an unconscious patient, as the tongue relaxes, rolls back and blocks the oropharynx, which connects the lower respiratory tract. The oral airway holds the base of the tongue preventing it from obstructing the passage. The device can also be used to facilitate suctioning in an unconscious patient<sup>5</sup>. Use of oral airway is a basic skill which EMTs, nurses and physicians in the United States are trained to use oral airway as for establishing and maintain the breathing air flow<sup>6</sup>. However, it is recommended to be used only on unconscious patients as gag-reflex would cause a conscious patient to vomit and further obstruction of airway<sup>7</sup>.

Typical OPA's, like the Guedel airway shown below in Figure 4, are generally made of hard plastic, and have a semicircular design that conforms to the curvature of the palate. Each oropharyngeal airway has three parts: the flange, the body, and the tip. When properly inserted, the flange rests against the lips, preventing the device from sinking into the pharynx. The body follows the contour of the roof of the mouth and will curve over and rest on top of the tongue. The distal end, or the tip, sits at the base of the tongue. An oral airway will hold the tongue away from the posterior pharynx so air can pass through and around the device<sup>5</sup>.

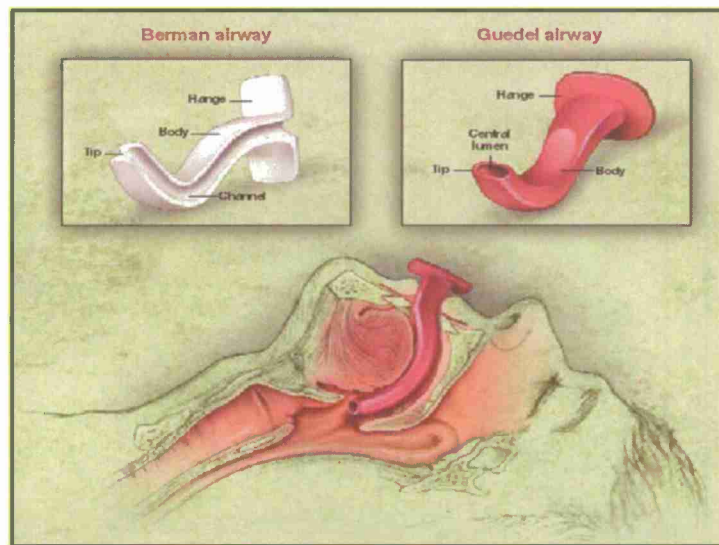


Figure 4. Illustration of the commonly-used oropharyngeal airway (top) and how oral airway is placed inside a patient's oral cavity (bottom)<sup>5</sup>.

Oral airways are often used in an "off-label" fashion by physicians as a bite-block, even though it is recommended to use an actual bite-block to keep the patient's mouth open<sup>5</sup>. During a procedure, a patient who is under general anesthesia is kept unconscious. An endotracheal tube is inserted in the patient's respiratory tract to facilitate air flow. An oral airway is used alongside with the endotracheal tube as a bite-block to keep the incisors from biting on the tube and damaging it. A portion of the airway body at the proximal end is in contact with the incisors, keeping the mouth from closing. However, when the patient regains consciousness after the surgery, anesthesiologists would sometimes remove the airway piece while the patient is biting on it. About 0.01% of the patients who received total anesthesia experience dental injuries, which are reportedly the most common cause of malpractice claims against anesthesia providers<sup>8</sup>.

Although most OPA designs make use of rubber or plastic in order to reduce the risk of damaging the patient's teeth, dental damage still occurs. It is because most designs rely on the straight section between the flange and the curved tube airway to function as a bite-block which receives the patients' jaw clenching force against the incisor. It is shown that the vertical biting force by the patient is enough to fracture incisors<sup>9</sup>. Since the contact surface on an incisor is very small, even though human teeth are about to



withstand axial pressure, it is likely that the clenching force acting on the surface can fracture the incisor.

Validation of our model was performed using a novel hybrid oral airway developed to specifically address the pitfalls of dental injury during anesthesia. Dr. Theodore Burdumy, an anesthesiologist located in Santa Maria, California, invented the Bardo Airway (Figure 5), as a potential solution which addresses the problem previously mentioned. The Bardo airway combines an oral airway portion and a bite-block. The tongue elevator prevents the patient's tongue from blocking the upper airway. The side block portion is designed so the clenching force is now transferred to the molars instead of the incisor. Such design allows the force to be applied on a much larger contact area and thus reduce the axial pressure acting on the teeth. A handle knob extends from the bite block to enable better control during insertion and prevent injury due to a semi-conscious patient's biting<sup>4, 5, 29</sup>.

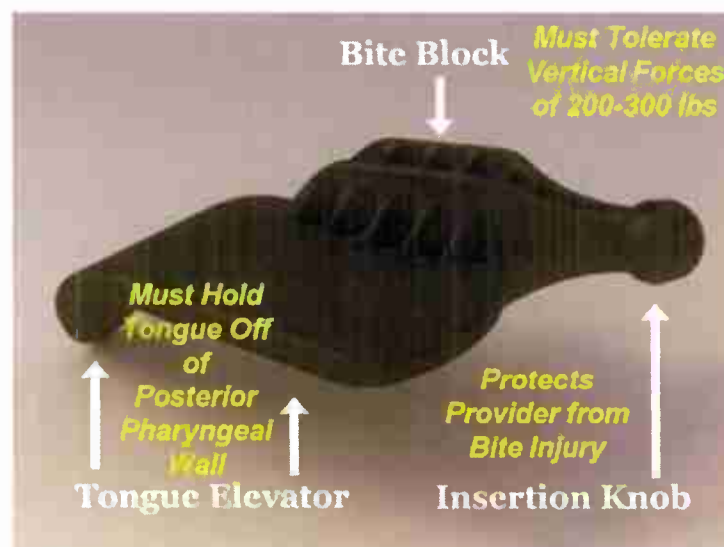


Figure 5. The Bardo airway and its major features

Oral airways are often overlooked yet it is a reliable and essential tool to emergency medical personnel. As the first academic work that provides evaluation of the design for oral airways, it is desired that this project will establish a computerized platform that allow accurate evaluation of oral airways. Using Bardo airway as an example, this project demonstrates what information this evaluation system is able to provide to researchers, and encourages investigation and studies on this valuable device. The deliverables of this project are:

1. Establish an evaluation platform oral airways using CAD techniques;
2. Assess the performance of various OPA devices, including the Bardo Airway, in terms of fit and functionality;
3. Propose modifications that can improve safety and efficacy of the Bardo Airway.

#### 4. Discussion of Results

The first step in creating the hardware of the platform was to build the 3D model of the oral airway to be evaluated. The different OPA's were scanned using ScanStudio HD. The scanner emitted lasers at the object, and the reflections provided surface information of the scanned object. A rough 3D point mesh was created as raw data. The raw 3D point mesh was then imported and repaired using RapidWorks. Using this software the mesh could be repaired, resized, and optimized for further use. The repaired mesh was then imported into SolidWorks to be rebuilt. The mesh by itself, even though it was repaired, was not adequate for accurate simulation. Figure 6 shows the creation of a SolidWorks sketch of an OPA from a mesh. Figure 7 shows the SolidWorks model created as a set of extrusions from the sketch.

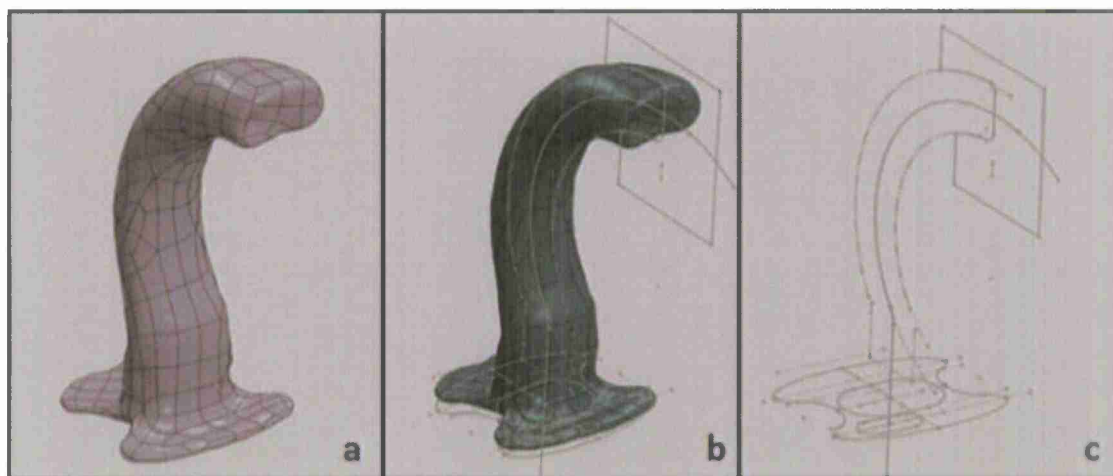


Figure 6. Creation of SolidWorks sketch on an imported mesh from (a) the mesh imported from RapidWorks, (b) sketches drawn to outline key feature of the mesh, and (c) the final make-up of the sketches.

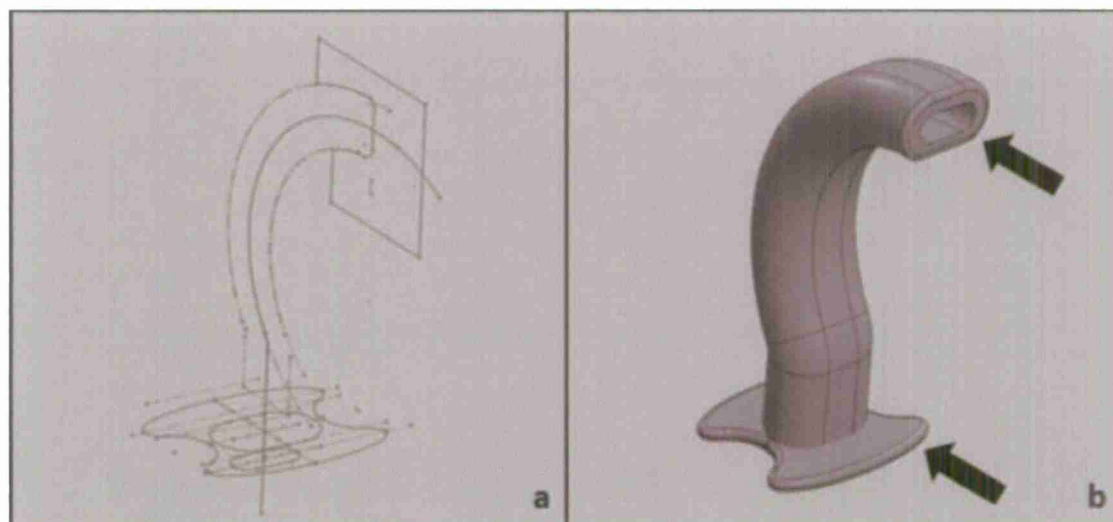


Figure 7. Conversion of an OPA model created from (a) sketches outlining a mesh to (b) an extrusion with filleted corner features (black arrows).

Once the solid model was built using the scan mesh, analysis was performed to estimate the error of the scanning and re-building method. Dimensions of the OPA models were compared against the physical objects. It was found that the error of the length was ranging from -3% to 5%, which is about 1.5-3mm deviation from the physical objects, and which was less than the size difference (10mm) between the different OPA sizes. Thus, it was decided the variations in size were acceptable.

With the OPA models complete, the second part in creating the visualization platform was to create the anatomical model of human head. This was achieved by converting MRI scans into 3D model using Mimics by Materialise. MRI scans of nine patients were provided by San Luis Diagnostics (SLD) Center. The patients had an average age of 59 years old. The SLD Model Set was made by converting head and C-Spine MRI scans of these nine patients into solid models. The conversion process was primarily done using Mimics. One problem arose from the models provided by SLD. The SLD scans were from patients who were all similar in size. To create a larger variation in anatomical models, the models were scaled using information obtained from ANSUR II, an anthropometric database created by the US Army.

The first step for the modeling method was to identify body parts in the MRI images that would be included in the anatomical models. The tongue, throat, face, cheek, maxilla, upper teeth, lower teeth, and mandible parts were identified. In addition, it was necessary to identify the air cavity located posterior to the pharynx. Figures 8 through 12 show the identification of the various body parts.



Figure 8. Identification of the tongue portion of the MRI scans, highlighted in blue.



Figure 9(a)-(c). Identification of the (b) throat and (c) air cavity portion of the MRI scans. The Original image (a) was included for reference.

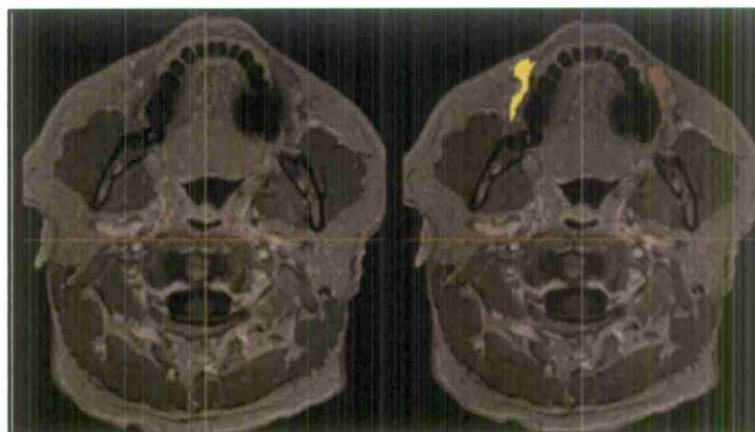


Figure 10. Identification of the *cheek* and the buccinators muscles, highlighted in yellow and brown.



Figure 11. Identification of the maxilla (green), upper teeth (pink), lower teeth (cyan), and mandible (dark blue).





Figure 12. Identification of the face, highlighted in brown and pink.

Once the body parts were identified in the MRI scans, models of the various parts were created in Mimics and then assembled into a single model. The fully assembled head model to be used in evaluation can be seen in Figure 13. The cross-sectional view of the head model can be seen in Figure 14. Models of each individual part can be seen in Figures 15 through 18.



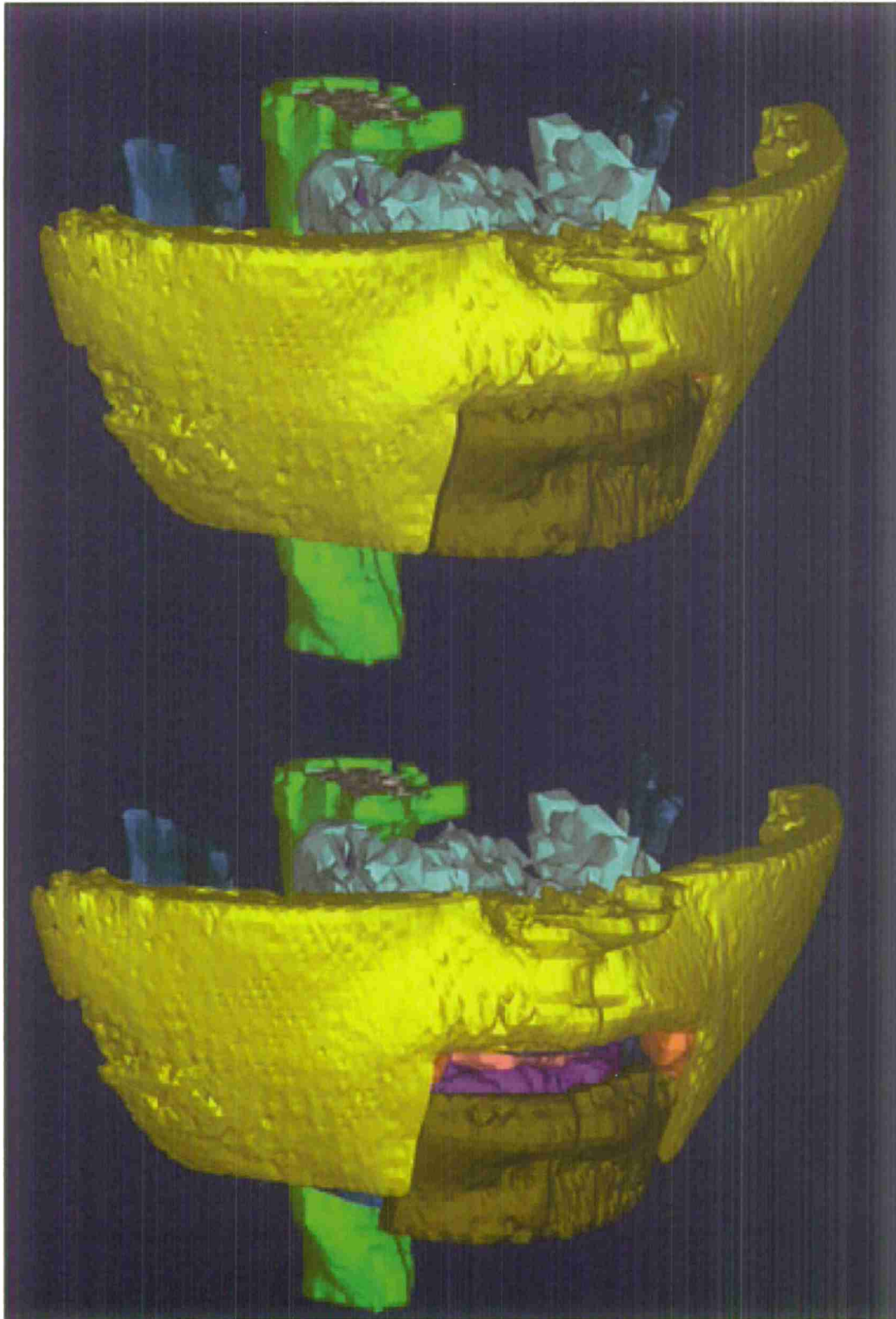


Figure 13. The fully assembled head model used for evaluation.

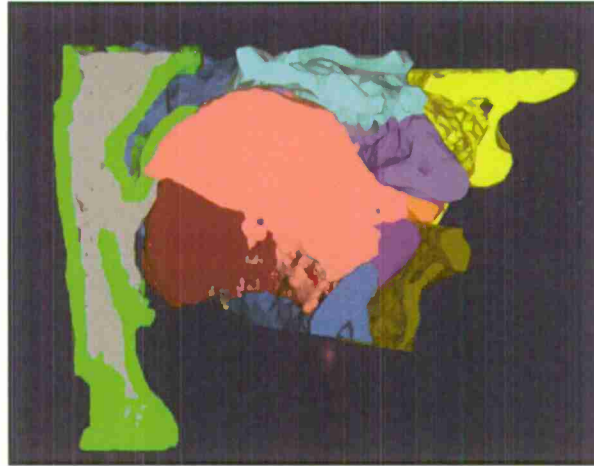


Figure 14. A cross-sectional view of the head model.



Figure 15. The throat (green) and air (grey) models.



Figure 16. The tongue model divided into top (pink) and bottom (red) portions.

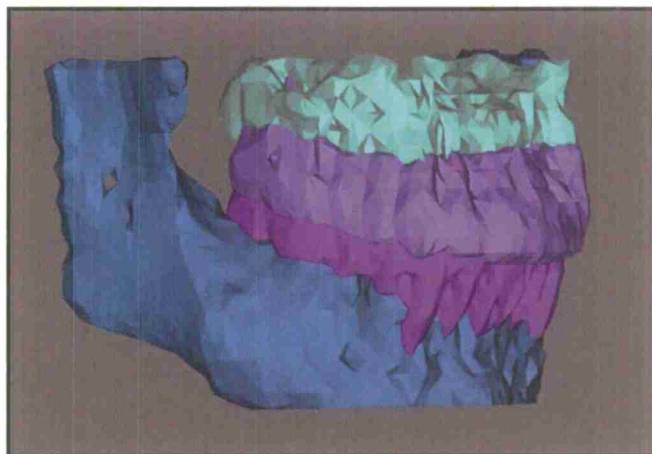


Figure 17. The maxilla, upper teeth, lower teeth and mandible model-parts.

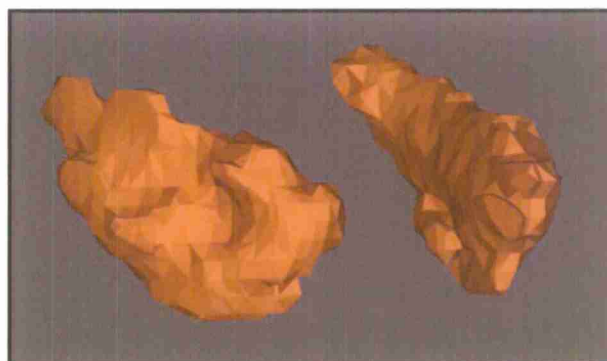


Figure 18. The cheek buccinator model parts.

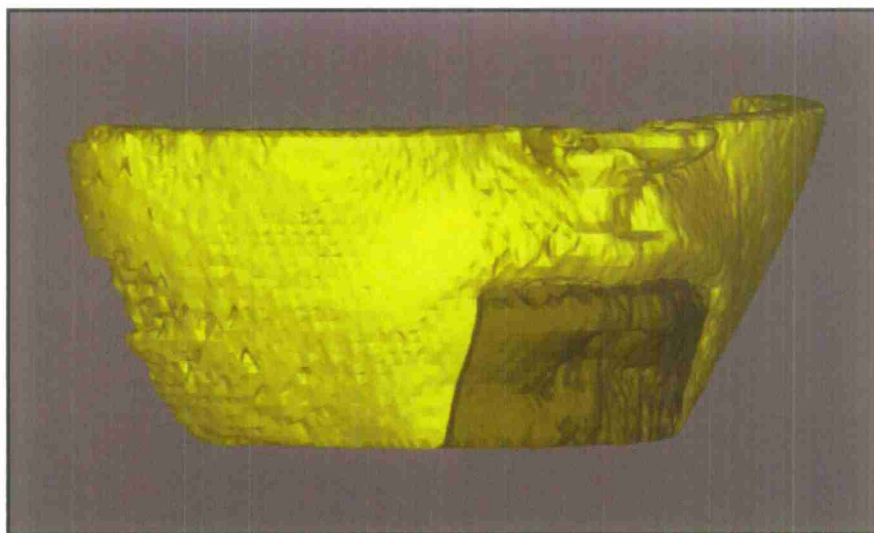


Figure 19. Model of the top portion of the face (yellow) and bottom portion (brown).

The mouth motion of the model, demonstrated in Figure 20, was generated by rotating the lower face, mandible, lower teeth and top tongue together along an axis. A defined point at the top, posterior side of the mandible was picked for each model where the rotational point was placed in the sagittal plane. The point was extended to become the rotational axis in three-dimensional space. When studying the models, several assumptions were made.

1. It was assumed that model-parts representing muscular and skin tissue were elastic.
2. It was assumed that overlapping soft tissue model-parts, being elastic, were compressed when overlapped or protruding from one another.
3. The cut-off representation of model parts, such as the tongue and face, were separated for ease of rotating the model. In actuality, the body parts are connected.



Figure 20(a)-(c). Rotation of the mouth in the head model. Several key points are shown: (a) closed mouth position, (b) the defined point selected as the axis of rotation, (c) open mouth position.

With both the oral airways and anatomical models built, they were put together for evaluation. Each patient's model was fitted with the Berman, Guedel and Bardo Oral Airway. An OPA size was chosen for the patient based on the head size. The OPA was rotated and superimposed on the cross section of the mouth-opened patient model for a visual check for fit, as in Figure 21. Then the position of the OPA was adjusted so it could fit into the oral cavity using the incisor and the throat opening as the reference points. The mouth section of the model-part was then closed to form a closed fit. Then the OPA-fitted model was evaluated by performing a series of measurements at different views to determine the distance of the OPA to the boundary of the oral cavity.





Figure 21 shows a head model fitted with a Bardic OPA.

Measurements of the model were obtained using Mimics. Dimensional measurements obtained from the platform represent the relationship between the OPA and the surrounding soft tissue, and the performance of the OPA for creating air passage. These dimensions were formulated to evaluate the damage of patient's soft tissue during OPA placement and to assess if OPA placement would block the air passage. With the dimensional data of the OPA placement, the fit of the each OPA to the patient was determined by comparing the measurement statistically.

Three dimensions were obtained from the area where the tongue met the throat, which is illustrated in Figure 22, using a Berman OPA. The first dimension measured was tongue compression. Tongue compression is the thickness of the tongue being compressed due to OPA placement. In the model it is the thickness of the tongue model that overlaps with the OPA. It was found that the Guedel OPA created the largest compression at the tongue, while the Berman OPA compressed the least amount of tongue tissue. Bardic's performance in this category was comparable to that of Guedel OPA, as both OPA were assigned to the same group. Berman OPA had a significantly lower average in compressing the tongue.



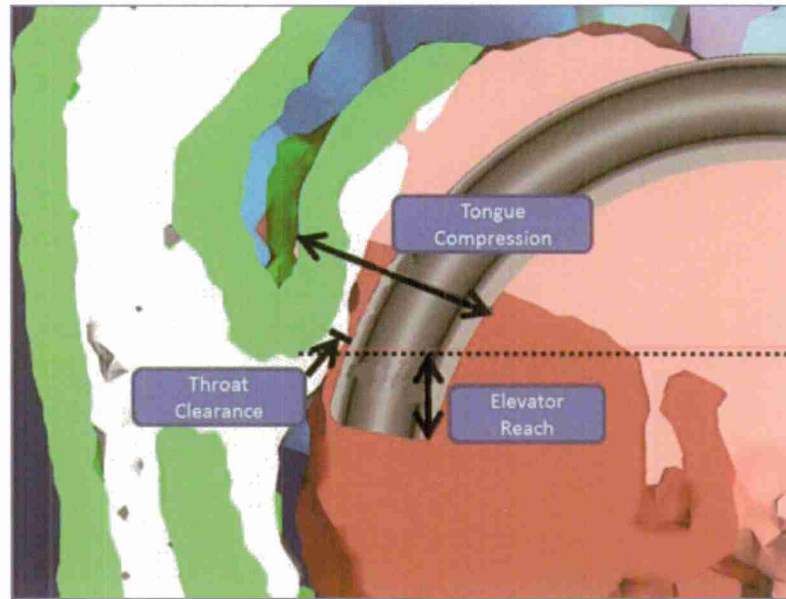


Figure 22. Measurements taken at the posterior part of head with a Berman OPA.

The second dimension measured was throat clearance. Throat Clearance is the vertical distance between the outer surface of the tongue elevator of an OPA and the throat. An OPA with a positive value for the throat clearance indicates there is clearance. From the measurement data and corresponding ANOVA boxplots, there was no significant difference found among the three OPAs.

The third dimension measured was the elevator reach. Elevator Reach is the reach of the OPA tongue elevator at the base of tongue. It represents how much of the tongue an OPA can hold when a patient is unconscious. As shown in Figure 22, only the portion of the elevator below the throat opening, which was indicated by a dashed-line, was counted as the portion holding the tongue. From the measurement data and boxplots of ANOVA analysis, it was found that there was no significant difference between the OPAs' performances.

Another measurement made was the for the mouth opening, which is the shortest distance between the upper and lower incisor. Typically a mouth can be opened from forty to sixty millimeters, which is about the width of two to three fingers. The measurement for the mouth opening is illustrated in Figure 23. The Bardo Airway was significantly different than the traditional designs in that the Bardo had a mouth opening distance more than twice as the Berman and Guedel Airways.

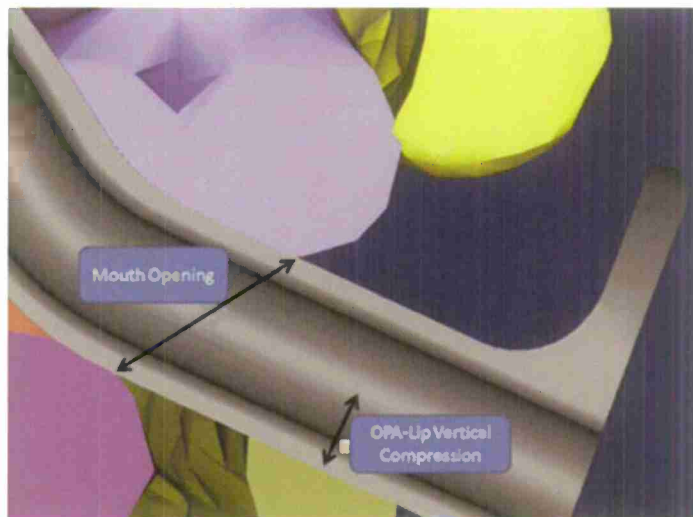


Figure 23. Measurement taken at the anterior part of the head with a Berman OPA.

The compression of the lips by the OPA in the vertical and horizontal distances was measured. The OPA-lip vertical compression is the vertical distance of the lips compressed by a placed OPA. This dimension was slightly different between the traditional airways and the Bardo OPA due to the different OPA designs. The OPA-lip horizontal compression is the compressed (overlapped) distance by the Bardo bite-block to the lip commissure. Due to the unique bite-block design of the Bardo airway, only the Bardo airway was evaluated for this dimension. The dimension was measured for the left side of the mouth, as shown in Figure 24. About three millimeters of lip commissure was compressed.

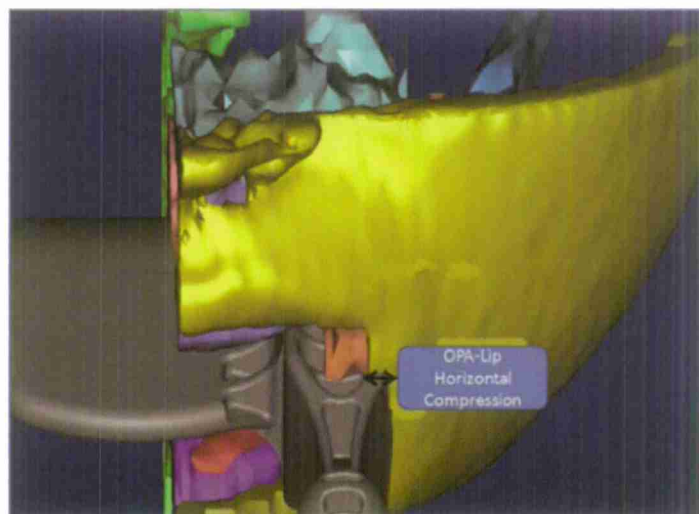


Figure 24. Illustration of OPA - Lip Horizontal Compression with Bardo OPA

The OPAs were placed at an angle to create the “worst-case scenario” of placement of the traditional OPAs, see Figure 25. This placement happens when there is an additional device, such as an optical fiber scope, placed in the oral cavity to aid oral intubation. In such a case, physicians usually placed the OPA sideways to allow for more space for maneuvering the scope. In the simulation, the Berman or Guedel OPA was rotated with the rotating axis placed on the middle of the airway where it meets the throat opening, and then the model was rotated until the side of the OPA was in contact with the right side corner of the mouth. The OPA-cheek horizontal compression was measured for the Berman and Guedel OPA with this configuration. This value was obtained by measuring the distance of the cheek overlapped by the OPA. The three types of OPAs performed similarly to each other.

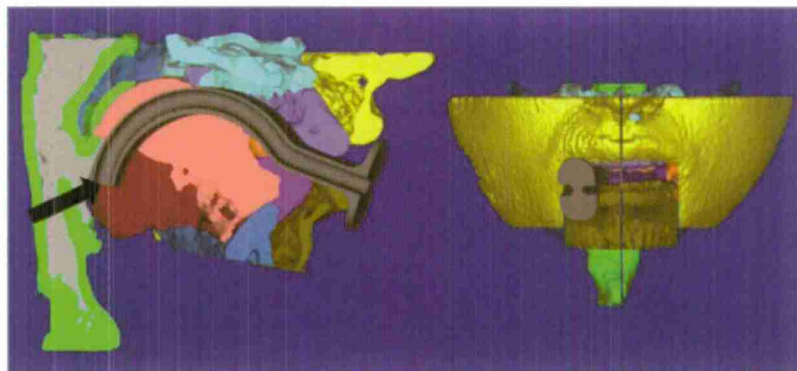


Figure 25. Cross-sectional and front view of the angled placement of an OPA. The arrow indicates where the rotational axis was set.

There were several dimensions critical for the molar-related functions of the Bardo Airway, which can be only evaluated in the top-view perspective. These attributes included the distance between the OPA and molar, as well as the contacting surface area of the bite-block with the molars. The first measurement was the OPA-molar horizontal distance, see Figure 26. This was the lateral distance between the inner side of the molar and the tongue elevator. This distance represented the clearance for the tongue tissue to squeeze into when the elevator was compressing the tongue. The average clearance for the Bardo airway was 6-8.5mm

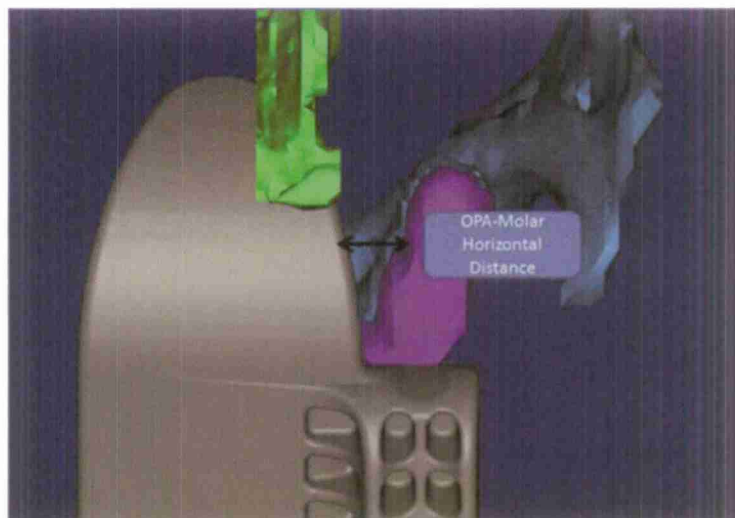


Figure 26. Illustration of the measurement of the OPA-molar horizontal distance.

The last measurement taken was of the number of teeth contacting the slots on the Bardo airway. This measurement denoted the number of slots at the Bardo bite-block in contact with the molar. This value represents the surface area for contact in terms of the slots and only applies to the Bardo airway, due to the non-traditional design. Two values were obtained for this measurement, representing the top and bottom face of the bite-block. From the evaluation, the top surface had more contacting surface than the bottom. This could be observed from the simulation shown in Figure 27(a), showing the bottom surface and Figure 27(b), showing the top surface. This observation was also supported further by the measurement, as the average number of slots at the top surface was about 5 slots and that of the bottom surface was about 2 slots.

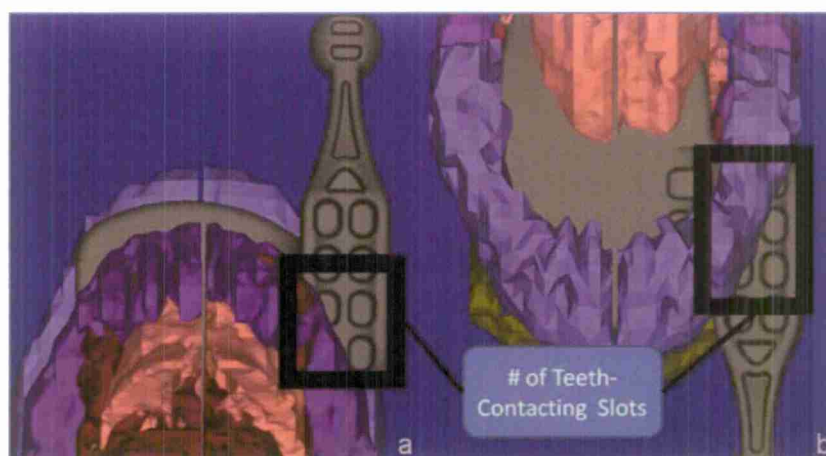


Figure 27(a)-(b). Illustration of the measurement of number of teeth-contacting slots on the bite-block of bardo OPA. The bottom (a) and top (b) sides of the block are illustrated.

From all of the measurements, it was found that all of the head models could be fitted with OPAs of sizes 70 to 90mm, even at the “extreme-case” models, which belong to highest and lowest 10th percentile of the population. The Bardo OPA, which was fitted into the models using similar methods as the traditional OPAs, could fit into all models without incompatibility. It can be concluded that the Bardo airway was comparable to a 70, 80 and 90mm OPA, but it was inconclusive of the limit of the Bardo airway in terms of the OPA sizes. Therefore no modifications for different size of Bardo were recommended.

### 5. Future Work Planned

Although the platform was inconclusive for determining the size limit for the Bardo Airway, there were some observations found which showed potential areas for modification of the Bardo’s unique design. Three aspects of the Bardo airway can be modified, based on the findings of the evaluation, to improve safety and efficacy.

The first recommendation is to reduce the risk of trapping or pinching tongue tissue to inner-side of molars by reducing the width of the tongue elevator. Although not shown in the simulations, when tongue tissue is compressed and raised, it is possible that the tissue would be caught in the gap for prolonged time. Also, the current design of Bardo OPA has rounded edges, which could concentrate the pinching force at a small area. Such small volume of tissue might not withstand the pressure and would cause tissue necrosis.

This problem does not present in any of the traditional OPAs because they have a more slender tongue elevator design. The Bardo OPA has a wider elevator and that can become an issue. The traditional OPAs are good examples for improving the design of the Bardo OPA for this situation. The reduction in width of the tongue elevator, as in Figure 28, could lower the risk of trapping tongue tissue between the side of the OPA and the molars.



Figure 28. Potential design of a Bardo OPA with a narrowed tongue elevator.



The second modification is to increase the bending angle of the tip of the tongue elevator. This creates more bending at the tip of the tongue elevator and increase the area of contact with tongue, thus more effective in holding the tongue. There is a risk that the elevator is not holding the tongue deep enough to prevent it from obstructing the airway. To remedy this situation, the tip of the tongue elevator could be bent so its inner surface has more surface contact with the tongue. Bending the tip would 1) increase the value of elevator reach, and also 2) generate more holding force to the tongue.

The third modification is to trim off unnecessary portions of the bite-block, as seen in Figure 28. The purpose of trimming off unnecessary portions of the bite-block is to decrease the stretching pressure on the mouth commissure and cheek. Most stretching at the mouth commissures and the cheek occur at the same place on the OPA. Eliminating a portion of the bite can ease the contact and stretching forces on the oral cavity.

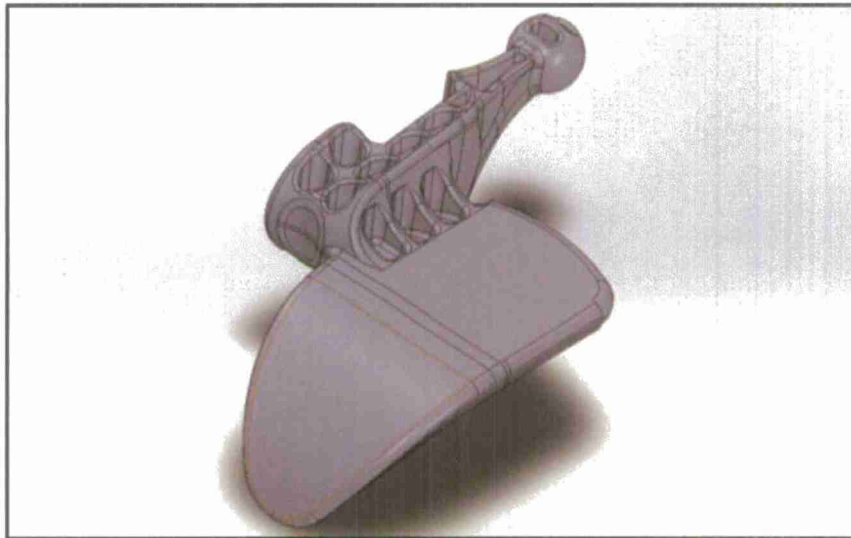


Figure 29. A Bardo Airway with a trimmed bite-block.

Although this project has some pitfalls which affected the results, it nevertheless serves a purpose as the foundation for further studies. Evaluation platform of oral cavity is rare, yet the oral airways are very important in the field of medicine. There is clearly a need for this type of simulation platform for device design. Mannequins commonly used for training are actually far from reality and so simulation generated from real patients can better service the development of devices. The fit of such devices could determine if the devices can be relied on during life-threatening situations. Although there are some limitations to this work, it does demonstrate visualization techniques and methods which would help others with device development in the future.

## 6. References cited

- <sup>1</sup> Presentation at the Society for Airway Management Annual Meeting, September 27, 2009: *What's New in Extubation of the Difficult Airway?* Elizabeth Cordes Behringer M.D. Anesthesiologist-Intensivist, Cardiac Surgical Intensive Care Unit, Department of Anesthesiology, Cedars-Sinai Medical Center, Los Angeles, CA.
- <sup>2</sup> Presentation at the American Society of Anesthesiology Annual Meeting, October, 18, 2009: *Perioperative Considerations for the Morbidly Obese*; Thomas Ebert, M.D., Ph.D., Professor of Anesthesiology, Medical College of Wisconsin, Milwaukee, Wisconsin.
- <sup>3</sup> History of Anesthesia: Oropharyngeal and nasopharyngeal airways : I (1880-1995) Canadian Journal of Anesthesia, 1996/43:6/pp629-35
- <sup>4</sup> Virtual Disaster Medicine Training Center (VDMTC) : Advanced Airway Techniques Part Two - New Generation Supraglottic Ventilatory Devices; 8/16/ 2007
- <sup>5</sup> Beattie S. Placing an oropharyngeal airway. *Modern Medicine*. 2005.
- <sup>6</sup> Warner KJ, Sharar SR, KCopass M, Bulger EM. Prehospital management of the difficult airway: a prospective cohort study. *J Emerg Med*. 2009;36(3):257-265.
- <sup>7</sup> Kovac A. Prevention and Treatment of Postoperative Nausea and Vomiting. *Drugs*. 2000;59(2):213-243.
- <sup>8</sup> Burdumy TJ, Inventor; InfoHealthNetwork, Inc., assignee. Combination bite block, tongue depressor/retractor and airway; 2011.
- <sup>9</sup> Kok PH, Kwan KM, Koay CK. A Case Report of a Fractured Healthy Tooth during Use of Guedel Oropharyngeal Airway. *Singapore Med J*. 2001;42(7):322 - 324.

**Use of Unstiffened Steel Plates to Prevent Progressive Collapse of  
Existing Steel Building Frames with Simple Beam-to-Column  
Connections**

Principal Investigator:

**Bing Qu, Ph.D., P.E., Assistant Professor, Civil and Environmental Engineering**

California Polytechnic State University  
San Luis Obispo, CA

## 1. Abstract

Building structures designed taking into account conventional loads may suffer local damages under the unforeseen abnormal loads (such as vehicle impact, fire, unexpected foundation failure, local impact due to tornadoes, explosions, or terrorist attack). If the damaged structure lacks structural integrity and alternative load transfer path, these initial local failures may spread from member to member resulting in the collapse of an entire structure or a disproportionately large part of it. Such a performance (termed "progressive collapse") is catastrophic and should be avoided from the perspective of national security.

Current design guidelines developed for progressive collapse prevention produce satisfactory solutions for new constructions; however, they are of limited value in retrofit of existing structures where minimum modification and upgrade work are allowed. In addition, many obstacles (such as poor constructability and impractically high cost) impede the widespread acceptance of existing retrofit methodologies. Therefore, an urgent need exists to develop a more practical and economical progressive collapse retrofit strategy.

Inspired by the desirable behavior of steel plate shear walls used in seismic design, this research investigated an innovative retrofit methodology that utilizes unstiffened thin steel plates connected to the boundary building frame to enhance its overall structural integrity and thus prevent progressive collapse of the structure. Based on the extensive finite element numerical simulations in this investigation, it was found the proposed system is valid to minimize the potential of catastrophic outcome from progressive collapse of structures and consequently help improve the national preparedness for abnormal natural and man-made disasters.

## 2. Project significance

Structures designed to support all conventional design loads may suffer local damages from unforeseen extreme events. For example, a multi-story building structure may lose its vertical support (e.g., a column at the ground level which supports gravity of the structure) in the events of vehicle impact, fire, unexpected foundation failure, impact of local effects from very high winds such as those recorded in tornadoes, or blast/explosions caused by gas, industrial liquids or terrorist attack). Generally, these extreme loading scenarios are not considered in conventional structural designs. However, in some cases, local failure in a major structural component caused by the abovementioned abnormal loads may spread from member to member resulting in catastrophic collapse of the entire structure. From the perspective of national security, such progressive collapse failures should be avoided.

Recent terrorist attacks against U.S. Government assets on U.S. soil (such as the one on the Alfred P. Murrah Federal Building in Oklahoma City, 1995) indicate that progressive collapse of building structures is no longer just a possibility. In addition, since the terrorist attacks on the WTC towers and the Pentagon on September 11, 2001, owners of major U.S. buildings including the federal government have emphasized progressive collapse resistance as one of the design requirements (Senate Committee Report 107-57, 2002). Currently, the U.S. General Services Administration (GSA), the Department of Defense (DOD), and the Department of State (DOS) require that their buildings be designed and evaluated for progressive collapse potential.

To achieve the targeted structural integrity, redundancy of the gravity load carrying system takes center stage in tackling the issue of progressive collapse. While this is not explicitly addressed in mainstream building codes, an alternate load path which functions as a protective system is desired in the event one or more columns of a building frame fail due to the extreme scenarios. Properly retrofitted/designed structures should be able to remain stable by redistributing the gravity loads to other members and subsequently to the foundation through an alternate load path, while keeping building damage somewhat proportional to the initial failure.

Current standards for new construction allow architects and engineers to incorporate progressive collapse resistance capabilities at modest increases over routine construction costs. However, retrofit of the existing buildings which vary by design, construction, age, and materials, and were originally designed without any consideration of progressive collapse, are typically difficult and impractically expensive unless specially designed protective systems are installed in the structures.

This research focused on development of a reliable, realistic, and more economical progressive collapse retrofit technology for steel building frames with simple beam-to-column connections which is vulnerable to progressive collapse and one of the most popular structural systems in the United States. The proposed methodology utilizes the thin steel plates attached to the building structural frame. When instantaneous loss of a vertical support member occurs as a result of abnormal loads, these steel plates can buckle in shear and then develop diagonal tension field actions in the building structural frame. Such actions can provide an alternative gravity load transfer mechanism and accordingly prevent progressive collapse of the structure. This research conducted extensive numerical simulations of the retrofitted system. Databases from these analyses form a valuable resource for researchers and practitioners. Understanding that has been developed can minimize the potential of catastrophic outcome from progressive collapse of building structures and consequently improve the national preparedness for abnormal natural and man-made disasters.

### **3. Background/prior work**

Preventing building collapse has been always in a structural engineer's interest. Under the normal loading scenarios, licensed engineers are able to ensure desirable performance and integrity of the structure using their vast knowledge, expertise, and experience on structural design. However, in an unforeseen abnormal loading scenario, localized failures (e.g., loss of loading carrying capacity in columns) are expected to occur in a building structural frame. After that event, depending on the extent of damage and its damage tolerance, the damaged building structure subjected to gravity loads exhibits one of the following two performances: (Performance I) continue to support the gravity loads without fully or partially collapsing; or (Performance II) fail due to collapse of a significant portion or of the entire structure.

If the structure has a reserve capacity to accommodate abnormal loads and remains standing with only relatively insignificant localized damage and no progressive collapse (i.e., Performance I controls), the injuries and damages are limited to those that occurred during the event, and the occupants can be evacuated to safety with the injured ones taken care of by first responders and health care professionals. However, if the abnormal loads cause partial or full collapse of the structure in a domino effect (i.e.,



Performance II controls), a large number of casualties and injuries can be caused as a result of the falling debris of the progressively collapsing structure.

In the past, both Performances I and II were observed in buildings damaged by abnormal loads. A good example of Performance I is the behavior of the north tower of the WTC in the 1993 terrorists attack. In that event, terrorists exploded a car bomb in the basement parking structure near the south-side exterior columns of the tower. Although the explosion resulted in loss of portions of basement floors, the structure was able to carry the gravity load from above even after losing the bracing provided by the girders of the lost floors and only six people were reported perished in this event (Astaneh-Asl, 2007). For Performance II, an example among many tragic cases shown in Figure 1 is the 1995 car-bomb attack on the Murrah Federal Office Building in Oklahoma City where 168 people lost their lives, many of whom are resulted from progressive collapse of more than 70% of the structure (ASCE 2005).



(a) Ronan Point APT- London

(b) Skyline Plaza

(c) Banker's Trust Building-NYC

(d) Murrah Federal Building, Oklahoma City

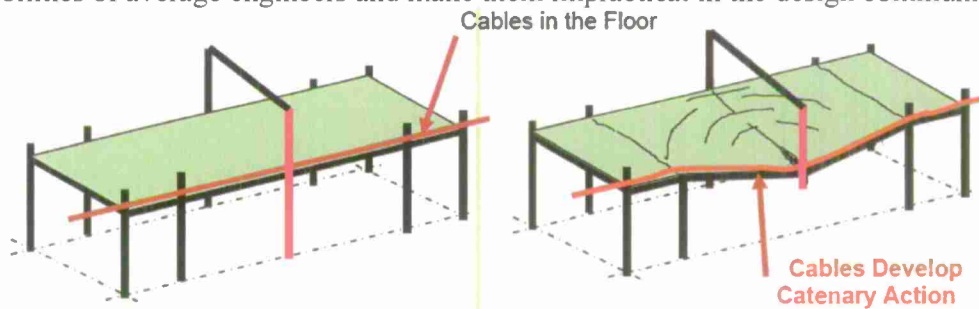
(e) Khobar Towers, Saudi Arabia

Figure 1 Example building damages after abnormal loads (adapted from Lynch 2009)

As progressive collapses in building structures are catastrophic, it becomes imperative for structural engineers to ensure Performance I other than Performance II when abnormal loads are possible. However, abnormal loads are typically unforeseeable and can not be defined precisely like other conventional loads. Accordingly, providing necessary integrity to a structure is a requirement that can not be stated in simple terms.

While significant research progresses in the area of progressive collapse prevention have been made in the past decades (literature review is available in Astaneh-Asl 2007), reliable and cost-effective procedures to substantially enhance the overall building structure integrity within a multi-hazard context that considers both design loads and abnormal loads remain missing. In particular, there is an urgent need to develop practical and economical strategies for permanent or temporary progressive collapse retrofit of existing building structures where only minor changes/upgrades are allowed.

Attempts at alleviating the above problem were recently addressed by the use of catenary cables (Astaneh-Asl 2003) and reinforcement of beam-to-column connections (Crowford 2002) as shown in Figure 2. While these retrofit methodologies help limit the effects of local damages, the following obstacles exist impeding more widespread acceptance of them: (1) they only provide limited increase of structural continuity, redundancy and ductility. For example, strength of the catenary cables may not be sufficient to support the gravity loads in a heavy building structure; (2) significant additional costs in labors can be produced for anchoring the catenary cables to structural frame and for connecting strengthening elements to the beam-to-column connections, and (3) further computational modeling efforts are needed to capture the nonlinear behaviors of catenary cable / strengthened beam-to-column connections which are beyond the capabilities of average engineers and make them impractical in the design community.



(a) Use of catenary cable (Adapted from Astaneh-Asl 2003)



(b) Reinforcement of beam-to-column connections: original vs. retrofitted (from Crawford 2002)

Figure 2 Existing retrofit strategies for progressive collapse prevention

This research seeks an alternative and more reliable and economical strategy to prevent progressive collapse of existing building structural frames subjected to sudden column loss caused by abnormal loads. The proposed methodology utilizes unstiffened thin steel plates connected to the boundary building frame to enhance the overall structural integrity, transfer the gravity loads and thus prevent progressive collapse.

The advantages of infill steel plates attached to boundary frames have long been

recognized in seismic design and continue to find applications (Sabelli and Bruneau 2007). Under the seismic loads in horizontal direction, the slender unstiffened infill steel panels are allowed to buckle in shear at low deflection levels and subsequently provide resistance and load transfer through the formation of diagonal tension field actions. Such a system has been termed steel plate shear walls (SPSWs) and proposed to seismic design community by the Canadian Standard S16 on "Limit states design of steel structures" (CSA 2003) and by the AISC Seismic Provisions for Structural Steel Buildings (AISC 2005). Past monotonic, quasi-static, pseudo-dynamic, and shake table tests on SPSWs in the United States, Canada, Japan, Taiwan, and other countries have shown that this system can exhibit high initial stiffness, behave in a ductile manner, and dissipate significant amounts of energy. These desirable performances along with the ease of installation and architectural flexibility make it an excellent candidate in seismic design of building structures (extensive literature reviews are available in Berman and Bruneau 2003, Sabelli and Bruneau 2007, Qu et al. 2008, to name a few). Analytical research on SPSWs has also validated useful models for the design and analysis of this seismic system (Thorburn et al. 1983; Driver et al. 1997; Berman and Bruneau 2003, Qu and Bruneau 2008).

For the steel plates considered in this research (i.e., those installed in the building frame for prevention of progressive collapse), their behavior is envisioned to be similar to those in seismically designed SPSWs. As such, analytical models, testing data and design procedures obtained from seismic research of SPSWs provides the basic building blocks necessary for a better understanding of progressive collapse performance of the proposed system. Figure 3 illustrates the behaviors of steel plates installed in building frames respectively for seismic design and progressive collapse prevention purposes.

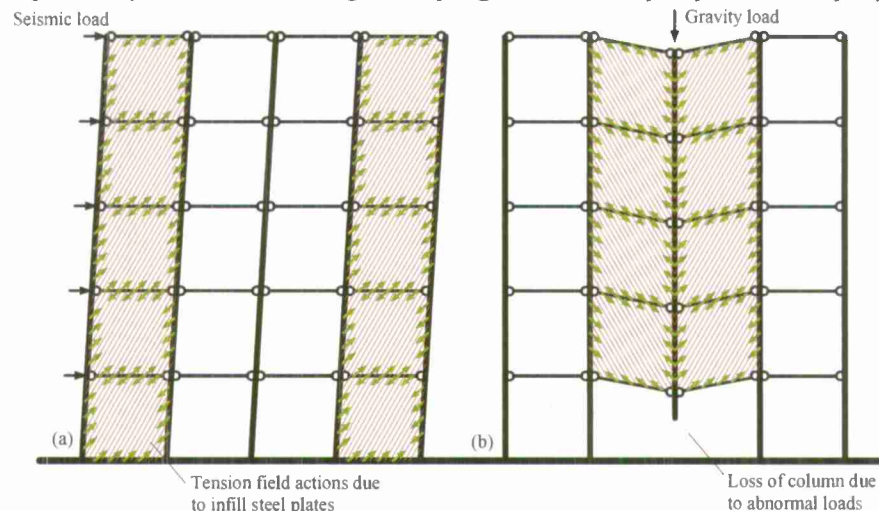


Figure 3 Use of infill steel plates for retrofit of building structures: (a) seismic case (b) progressive collapse case

Performance of the proposed retrofitted system can be optimized by properly selecting thickness of the infill panels, by adjusting the layout of infill steel plates in the building structural frames, and by modifying the arrangements of infill-plate-to-boundary-frame connections (i.e., controlling the length and spacing of the welds). The proposed system can provide a more cost-effective alternative to the existing retrofit methodologies for progressive collapse prevention, with faster construction time and



lesser disturbance on the existing structure. As a result, combined with its recognized excellent seismic resistances, the proposed system will allow to make a major stride along the path of integrated multi-hazard solutions (itself, a new paradigm in structural engineering).

#### 4. Discussion of Results

As the key component of this project, a series of building frame were retrofitted with the proposed infill plates and were subjected to removal of an interior or exterior columns (to simulate the triggering event of a progressive collapse). Different boundary conditions which allow and/or inhibit the horizontal displacements in the considered building frames were considered as shown in Figure 4.

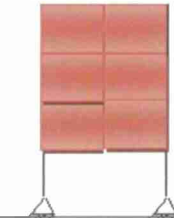
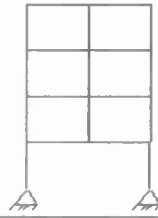
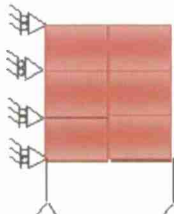
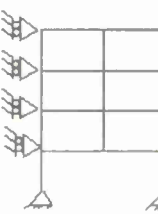
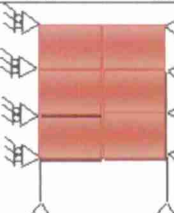
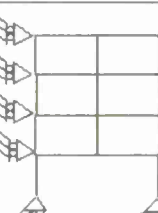
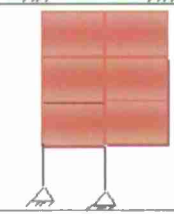
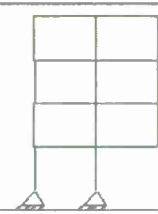
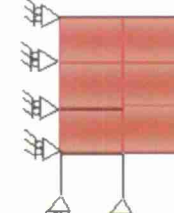
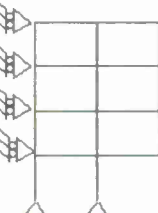
| Boundary Condition | Proposed System   | Description   | Boundary Frame  |
|--------------------|---|---|---|
| #1                 |    | Sidesway uninhibited under interior column removal  |    |
| #2                 |   | Sidesway inhibited on the left side and uninhibited on the right side under interior column removal |   |
| #3                 |  | Sidesway inhibited under interior column removal  |  |
| #4                 |  | Sidesway uninhibited under exterior column removal  |  |
| #5                 |  | Sidesway inhibited on the left side under exterior column removal                                   |  |

Figure 4: Considered boundary conditions and column removal scenarios

A complete result discussion can be found in the attached technical report. Generally, it was found from all considered cases that the proposed technology is valid to provide an alternative load transfer path, significantly increase the vertical resistance of the system, and hence minimize the potential of collapse of the system. For example, Figures 5 (a) to (c) respectively illustrate one of the considered boundary conditions, the corresponding finite element model, and the progressive collapse resistance enhancement when different lateral displacement restraints are applied at the floor levels.

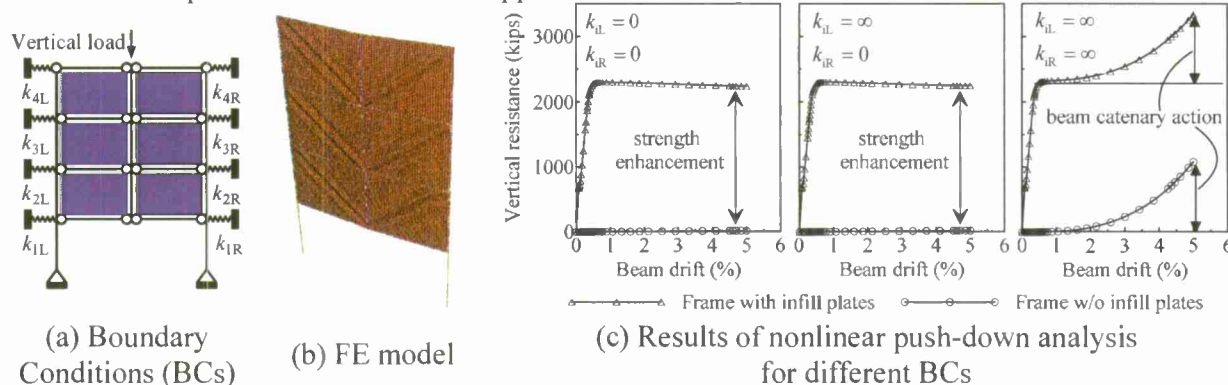


Fig. 5 Preliminary results developed by the research team.

## 5. Future Work Planned

Based on the discoveries from this project, a series of analytical and experimental investigations have been planned to further expand the application of the proposed technology. Specifically, the future work listed on the PI's research agenda includes 1) quasi-static test full-scale framing assemblies to experimentally verify the proposed technology; 2) hybrid testing of full-scale framing assemblies to experimentally investigate interaction of the infill plates and other portions of a building frames that are seismically and non-seismically designed; and 3) investigation of optimum infill plates configurations through extensive parametric studies. To secure external research funding for the future work, the PI has developed the following two research proposals:

Title: *Development of A Low-cost and Practical Solution for Steel Building Frames Vulnerable to Progressive Collapse*

Funding Agency: American Institute of Steel Construction

PI: Bing Qu; co-PI: Rakesh Goel

Status: under review

Title: *Collaborative Research: A Resilient Solution for Steel Gravity Framing Systems Vulnerable to Disproportionate Collapse*

Funding Agency: National Science Foundation-Hazard Mitigation and Structural Engineering Program (NSF-HMSE)

Lead PI: Bing Qu; PI: Wei Song from the University of Alabama

Status: under review



## 6. References cited

- American Institute of Steel Construction (2005), "Seismic Provisions for Structural Steel Buildings." American Institute of Steel Construction, Chicago, Illinois.
- ASCE (2005) "Minimum Design Loads for Building and Other Structures" Reston, VA: ASCE Standard No. ASCE/SEI 7-05
- Astaneh-Asl, A. (2003). "Progressive Collapse Prevention in New and Existing Buildings" The 9<sup>th</sup> Arab Structural Engineering conference, Abu Dhabi, UAE.
- Astaneh-Asl, A. (2007), "Progressive Collapse Prevention of Steel Frames with Shear Connections", Steel Technical Information and Product Services (Steel TIPS) report, Structural Steel Education Council (SSEC), Moraga, CA.
- Berman, J. W. and Bruneau, M. (2003), "Experimental Investigation of Light-Gauge Steel Plate Shear Walls for the Seismic Retrofit of Buildings.", Technical Report MCEER-03-0001, Multidisciplinary Center for Earthquake Engineering Research, Buffalo, N.Y., May 2, 2003.
- Canadian Standards Association (CSA). (2003), "Limit States Design of Steel Structures." CAN/CSA S16-01. Willowdale, Ontario, Canada.
- Driver, R. G., Kulak, G. L., Kennedy, D. J. L., and Elwi, A. E. (1997), "Seismic Behavior of Steel Plate Shear Walls. " Structural Engineering Report 215, University of Alberta, Department of Civil and Environmental Engineering, February 1997.
- Crawford, J.E. (2002). "Retrofit Measures to Mitigate Progressive Collapse," NIST/NIBS, Multihazard Mitigation Council National Workshop on Prevention of Progressive Collapse, Chicago, IL, July 2002.
- Government Printing Office (2002) Senate Committee Report 107-57 available online at <http://www.access.gpo.gov/congress/legislation/02appro.html>
- Lynch, J., (2009) "Naval Facilities Engineering Command" NAVFAC Atlantic Industry Forum.
- Qu, B., Bruneau, M., Lin, C.H., and Tsai, K.C. (2008). "Experimental Investigation of Full-Scale Two-Story Steel Plate Shear Walls with Reduced Beam Section Connections." Technical Report MCEER-08-0010, Multidisciplinary Center for Earthquake Engineering Research, Buffalo, New York.
- Qu, B., and Bruneau, M. (2008). "Seismic Behavior and Design of Boundary Frame Members of Steel Plate Shear Walls.", Technical Report MCEER-08-0012, Multidisciplinary Center for Earthquake Engineering Research, Buffalo, New York.
- Sabelli, R., and Bruneau, M. (2007), "Steel Plate Shear Walls (AISC Design Guide).", American Institute of Steel Construction, Chicago, Illinois.
- Thorburn, L. Jane, Kulak, G. L., and Montgomery, C. J. (1983), "Analysis of Steel Plate Shear Walls." Structural Engineering Report No. 107, Department of Civil Engineering, The University of Alberta, Edmonton, Alberta, May 1983.

**Optimal Contamination Monitoring Station Locations in Water  
Distribution Systems using Heuristic method**

Principal Investigator:

**Shikha Rahman, Ph. D., Civil & Environmental Engineering**

California Polytechnic State University  
San Luis Obispo, CA

## **1. Abstract (~250 words)**

In recent years Civil Engineers have been challenged to develop solutions to protect public infrastructures from intentional attacks. Water distribution system, valued approximately \$675 billion, is identified as one of the eight key infrastructures by the President's Commission on Critical Infrastructure Protection (PPD 63, 1998). Protection of public water distribution systems from intentional contaminations that deal with releasing life-threatening chemical and biological agents into the water systems has been recognized to be vital in the recent years following September 11, 2001. Spatial and temporal variations of water demand as well as the nonlinear nature of the hydraulic analysis of the water distribution system makes determination of the efficient locations of contamination sampling points difficult. This difficulty is compounded by the fact that contamination can occur at any point and at any time within the water distribution system. The present study uses a methodology adapted from Chastain (2004) to identify strategic locations of critical detection points within the water distribution systems thus making the systems more resilient to contamination events. The objective of the research is to employ a quantitative method for identification of an optimal network of monitoring locations to provide efficient coverage of water systems using hydraulic simulation model WaterCAD/WaterGEMS and a new heuristic algorithm. The heuristic methodology uses computer simulations to create a database of water system response to contamination at every node in the system. The optimal locations of the monitoring locations are identified systematically after considering concentration thresholds and time since injection variables. This study analyzes a contamination spread for a California city with a population of approximately 30,000 to 40,000 residents in an attempt to locate the optimal monitoring locations in the water distribution system. Current study focuses on methods to make the water distribution systems, particularly small to mid-sized WDS, more resilient to chemical and biological attacks. The results of the analysis are grouped into zones of significance which contain a cluster of optimal points for placing sensor technology. These zones of significance are to be taken as a guide for improving the resilience of the distribution component as well as for mitigating potential terrorist initiated events on the water distribution system.

## **2. Project significance**

In recent years Civil Engineers are faced with a unique challenge of protecting public infrastructures from intentional attacks. Eight key infrastructures that are "lifelines" to our society are identified by the President's Commission on Critical Infrastructure Protection (PPD 63, 1998). One of these key infrastructures is water supply system - damage, disruption or inadequate capacity of which jeopardizes our economy and social well being significantly.

The water infrastructure system in USA is a major national asset valued at approximately \$675 billion (Grigg, 1999). The USEPA (2003a) has reported that about 170,000 public water systems provide water for more than 250 million Americans. Water distribution systems are vulnerable to intentional/ terrorist attacks because they are extensive, easily accessible, relatively unprotected, and often isolated (USEPA 2002, 2003b, Grayman, 2002; Mays, 2004).

Intentional attacks on water distribution systems (WDS) can be classified as (i) physical, (ii) cyber, and (iii) chemical/biological. Physical attacks aim at destroying or damaging the water distribution networks by targeting the components such as pipes, pumping stations, water tanks and other facilities. Cyber attacks are aimed at damaging and corrupting the information

management system for water infrastructure – Supervisory Control and Data Acquisition (SCADA) system, while the chemical/biological attacks deal with releasing life-threatening chemical and biological agents into the water systems. While a number of factors are important in vulnerability assessment of a certain water distribution system, none is more important than maintaining an acceptable water quality as consumers are most susceptible to contamination events whether accidental or intentional.

Protection of water distribution system involves the capability to effectively monitor the water for constituents that could harm consumers. Obviously, without the ability to detect and quantify a contamination event, the ability to avert or effectively respond to it is severely constrained. The objective of the study is to delineate and examine a heuristic methodology which will help effective placement of water quality monitoring stations within water distribution systems.

### **3. Background/prior work**

As for any other critical infrastructures, in recent years the government has promoted risk and vulnerability assessment, emergency response, training of water facility personnel, and research towards detecting and mitigating attacks. To date most of the research on vulnerability assessment and mitigation of water systems are qualitative or based on subjective judgments from security experts. All water systems that service over 3,300 people are mandated by the Section 1433 of the Public Health Security and Bioterrorism Preparedness and Response Act of 2002 to perform vulnerability assessment. Widely used methods in industry – 2001 AWWA (M19) Vulnerability Assessment (4th Edition), the Vulnerability Assessment Tool (VSAT<sup>TM</sup> –WATER) and the Risk Assessment Methodologies for Water Utilities (RAM-W<sup>SM</sup>), are all based on subjective scoring systems from surveys of water personnel. A more quantitative approach for probabilistic risk assessment to the SCADA system using expenditure, certainty, and flow reduction as performance measures as presented by Ezell (1998). This method was applied to chemical attacks on water tanks in small water systems (Ezell, 2000a, b) as well.

Literature review indicates surprisingly little research or studies relevant to water distribution system monitoring, characterization and protection from a water quality perspective. Quantitative studies, particularly in development of effective layouts and design of contaminant monitoring stations for early detection and identification of a contamination event (either accidental or intentional), is sparse in the literature.

In the past decade, chemical and biological attack scenarios were addressed by a few researchers (Lee and Deininger, 1992; Kumar et al, 1997; Kumar et al., 1999; Bahadur et al., 2001; Woo et al., 2001; Al-Zahrani and Moied, 2001; Bahadur et al., 2003; Van Bloemen Waanders et al., 2003; Ostfeld and Salomons, 2004; Berry et al., 2004; Laird et al., 2004) who developed quantitative approaches to provide some guidance on efficient layout of contaminant monitoring stations.

Lee & Deininger (1992) employed a method using pathway analysis coupled with integer programming to identify nodes with maximum coverage of the distribution system. Kumar, Kansal, & Arora (1997) refined the process of Lee et al. (1992) by re-ranking the pathway matrix thus simplifying and increasing the usability of the methodology. These two studies present methodology applicable to continuous, steady contamination. This approach does not yield reliable results in case of intermittent or rapidly variable water quality fluctuations that might be encountered in a terrorist event or accidental release.

A novel approach was presented by Kessler, Ostfeld & Sinai (1998) where the hydraulics of the distribution system is used as the basis of an “all shortest paths” algorithm to find the minimum propagation times from any source node to other points in the system. Contamination was assumed to be continuous, conservative, and dependent only on water movement. Also, any water passing through a contaminated node is considered contaminated regardless of the concentration. Non- contaminants are not covered under this approach.

Ostfeld and Salomons (2003) built upon the methodology of Kessler et al. (1998) using a genetic algorithm to search the optimal layout of monitoring stations based on defined concentration hazard levels. Berry, Fleisher, Hart & Phillips (2003) presented a mixed integer programming solution for high risk points using probability distributions of coupled population-weighted flows and contamination points.

Bahadur et al. (2001, 2003) developed PipelineNet Model through the integration of ArcView and EPANET that stimulates contaminant transport in water distribution systems. Using a hierarchical approach water system nodes are scored on the basis of a distribution system component scoring matrix, population density and critical infrastructure matrix. Nodes are then ranked and related to the GIS map to identify the most effective locations to minimize system vulnerability.

As none of the studies cited above capitalizes on the power and flexibility of the extended period water quality models currently available, each of these approaches has limitations on applicability due to extensive assumptions. Consequently, past methodologies are based on a limited number of contamination actualizations. In addition, these approaches are mathematically complex and the programs and concepts are out of reach of real life WDS managers.

#### **4. Discussion of Results**

Water distribution data availability was also a concern for this research. Most water utility operators, whether at the city or county levels, are hesitant to release data on the geophysical properties of their water delivery systems. There are obvious security risks for this hesitancy which serve as the main deterrent for releasing water distribution data. This poses a problem for researchers looking to analyze various threat scenarios in order to improve upon water system security. With the data being held back from most utilities, research cannot be done on real systems. For the research conducted in this paper, a real system was obtained from a California city which serves a community of 30,000 to 40,000 residents. For simplicity, the California city will be referred to as “the CITY” for the remainder of this paper. The geophysical properties and name of this system will remain anonymous throughout this paper in an attempt to protect both the operators and the users of the system.

The process by which the optimal operating points will be identified will begin with first assessing the model given by the city and calibrating it, if required, to more accurately represent the hydraulics of the city’s water distribution system (WDS). A constituent analysis will then be performed under various scenarios which are outlined in the later sections of this thesis. The results of this constituent analysis will then be imported into excel in order to determine which nodes detected the highest number of contaminations over a selected duration of time. The node with the highest number of detections would be considered the most efficient node for a particular scenario. Summary tables and figures will be provided, outlining and explaining the resulting trends from the analysis. One of the primary canons of this research is to make the process as simple as possible in order to make the process and method more accessible for small to mid-sized water distribution systems. That is not to imply that this method would not be applicable to



a larger distribution system. It is simply assumed that a larger WDS would have the funding and resources available to them to perform these types of studies using more complicated methods, whereas the smaller systems would not have these resources readily available.

The contaminant that was selected for application to the CITY was cryptosporidium. Cryptosporidium is a single celled parasite that is commonly found in rivers and lakes, especially when raw sewage or animal fecal material is being discharged into the water source. Cryptosporidium is highly resistant to chlorine residuals and is notoriously difficult to disinfect. This resistance is due to the outer shell that accompanies the parasite, allowing it to survive for long periods of time outside of a host body. According to the Center for Disease Control (CDC) crypto is one of the most frequent waterborne diseases among humans in the United States. This makes cryptosporidium a prime contaminant of choice as the vast majority of distribution systems would be vulnerable to its introduction. This can seem counterintuitive due to the fact that many other contaminants, such as Botulinus Toxin A, are considered to be of a much higher risk and therefore have much lower Lethal Dose (LD50) values. However, these types of contaminants are eliminated with a properly maintained chlorine residual in the distribution system and are therefore less of a concern to most water distributors who use chlorine residuals.

The release is assumed to be a quantity of 300,000 mg/L at a rate of 50gpm for one hour. These values were chosen based on the assumptions of Chastain (2004). These properties were then applied to each tank in the contamination analysis in WaterCAD® through the use of a flow paced booster in the contamination alternatives manager. It was assumed for the purpose of this analysis that the most likely point of contamination would be through the tanks of the system. This is due to the ease of accessibility of most water distribution tanks compared to that of pumping system connections.

The WDS is analyzed for the scenarios below:

#### **Scenario 1: Individual Tanks**

For the individual tank analysis the following data scenarios were input into WaterCAD® via the alternative and scenario managers. The analysis duration was 24 hours.

| Tank | Initial Concentration (mg/L) | Injection Method   | Mass Flow Rate (mg/s) | Simulation Start Time |
|------|------------------------------|--------------------|-----------------------|-----------------------|
| 1    | 300,000                      | Flow Paced Booster | 50                    | 5:00AM                |
| 2    | 300,000                      | Flow Paced Booster | 50                    | 5:00AM                |
| 4    | 300,000                      | Flow Paced Booster | 50                    | 5:00AM                |
| 4    | 300,000                      | Flow Paced Booster | 50                    | 5:00AM                |
| 5    | 300,000                      | Flow Paced Booster | 50                    | 4:00AM                |
| 6    | 300,000                      | Flow Paced Booster | 50                    | 5:00AM                |
| 7    | 300,000                      | Flow Paced Booster | 50                    | 4:00PM                |

#### **Scenario 2: Individual Tanks, Half of the Initial Contaminant Concentration**

This scenario was to test the sensitivity of how changing the initial concentration of the contaminant would affect the results for optimal sensor locations. All other inputs were kept the

same as the previous scenario with the full concentration. The alternative and scenario inputs are outlined in Table below.

| Tank | Initial Concentration (mg/L) | Injection Method   | Mass Flow Rate (mg/s) | Simulation Start Time |
|------|------------------------------|--------------------|-----------------------|-----------------------|
| 3    | 150,000                      | Flow Paced Booster | 50                    | 5:00AM                |
| 2    | 150,000                      | Flow Paced Booster | 50                    | 5:00AM                |
| 3    | 150,000                      | Flow Paced Booster | 50                    | 5:00AM                |
| 3    | 150,000                      | Flow Paced Booster | 50                    | 5:00AM                |
| 5    | 150,000                      | Flow Paced Booster | 50                    | 4:00AM                |
| 6    | 150,000                      | Flow Paced Booster | 50                    | 5:00AM                |
| 7    | 150,000                      | Flow Paced Booster | 50                    | 4:00PM                |

### Scenario 3: Tank Combinations based on boost schedules

This scenario looks at multiple tank contamination spreads based on the tank operation schedule. By combining the tanks which operate on the same schedule, a clearer depiction of real world contamination spreads should be observed in the results. Based on the tank boosting schedules, the following tank combinations will be analyzed:

- Tanks 1 and 3
- Tanks 2 and 4
- Tanks 5, 6 and 7

### Scenario 4: (All Tanks Considered)

The last scenario looks at the absolute worst case where all tanks are contaminated and all are operating on the same day. This is less likely to occur in reality, given that the pumping schedules are not likely to change dramatically. However, the results should indicate the most efficient points in the system where the pumping schemes to be compromised, causing a full scale contamination of each tank.

All of the following graphics are color coded depicting the nodes with the highest number of contamination detections in the analysis and will follow the general legend shown in figure 1a. This indicates that nodes color coded red detected a contaminant more times than any other node in the system during the 24 hour duration. Nodes which do not have color coding either did not detect a contamination during the analysis or were deemed to be below the threshold for significant contamination counts. The number of color coded nodes depended on the scenario. Enough nodes were color coded to show the significant zones in the system where optimal nodes could be located.



**Figure 1a: Frequency of detected contaminations above the minimum threshold at a particular node**

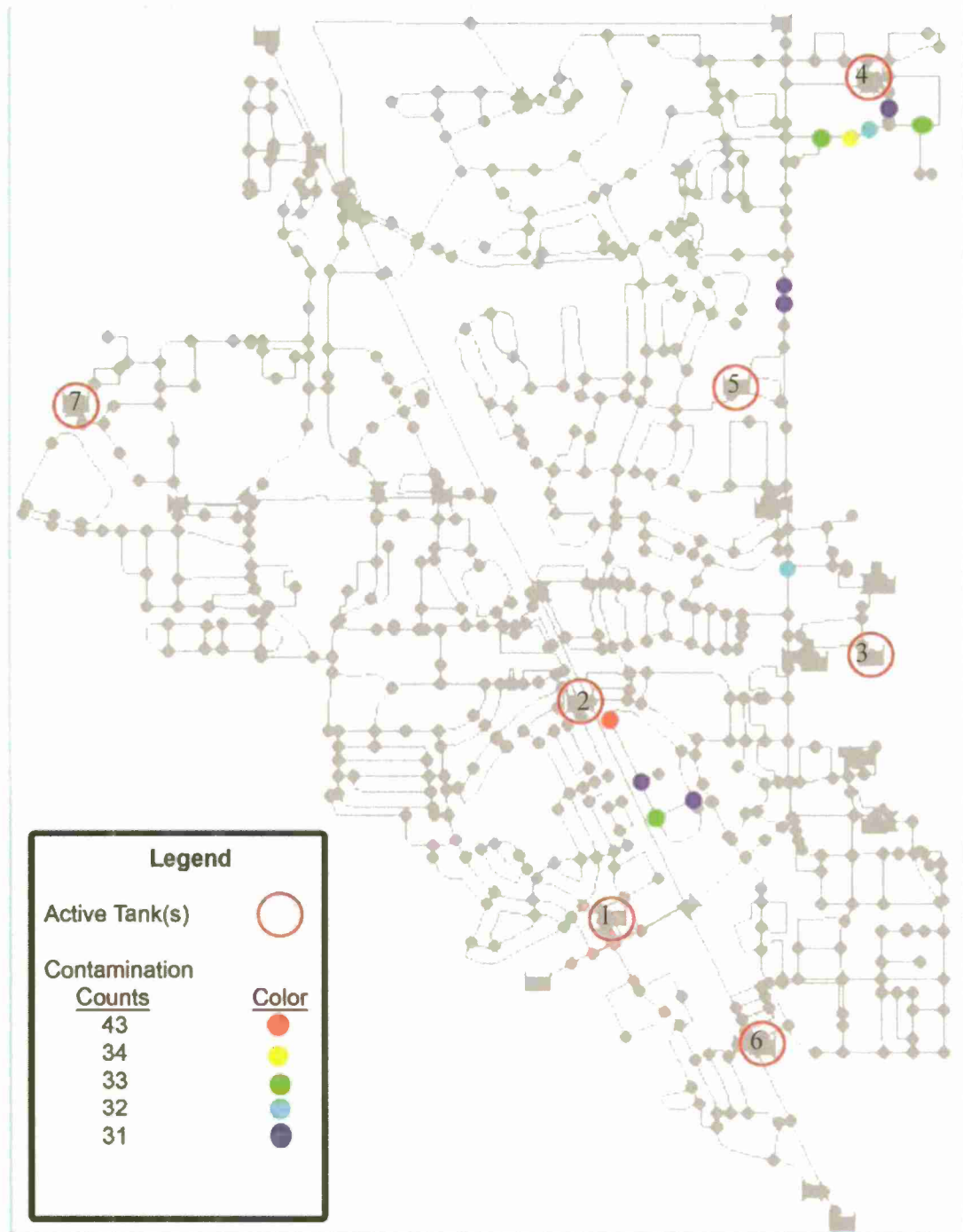


*Figure 1b: Layout of the Water Distribution System (WDS) of THE CITY showing the active tanks*

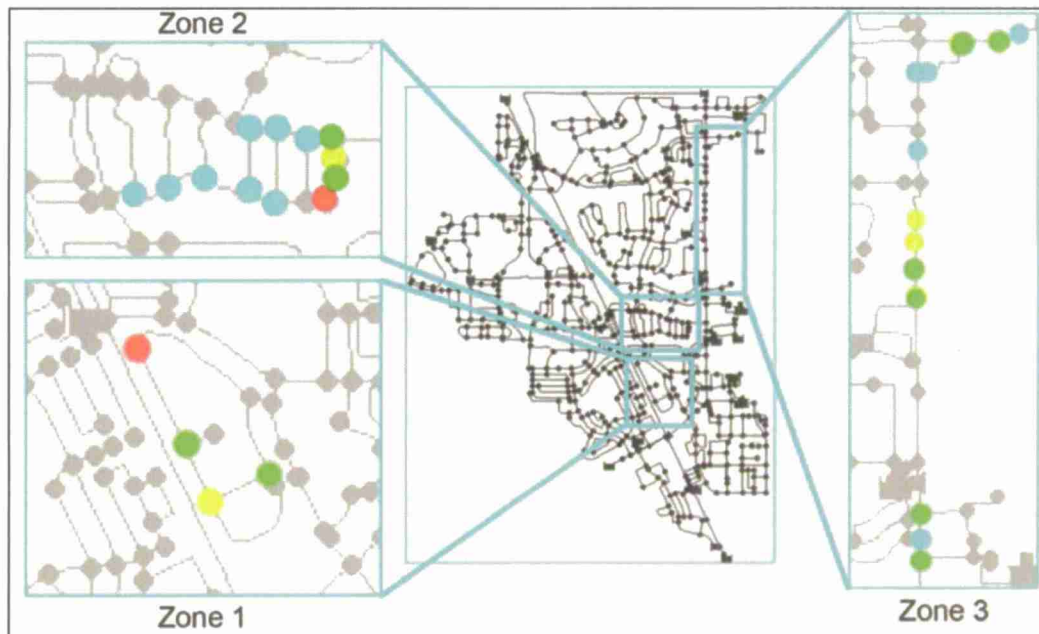


*Figure 2: High Priority Zones for the CITY to implement Monitoring Stations (Scenario 4)*

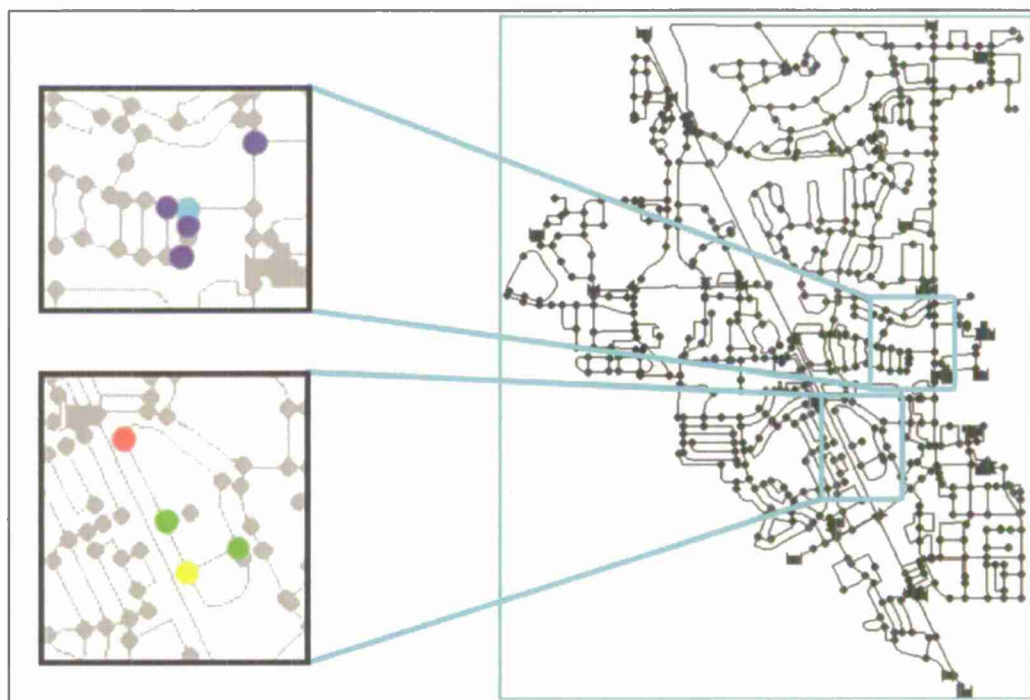


*Figure 3: Optimal Sensor Points for Tanks 1 and 3 combined (Full Concentration)*



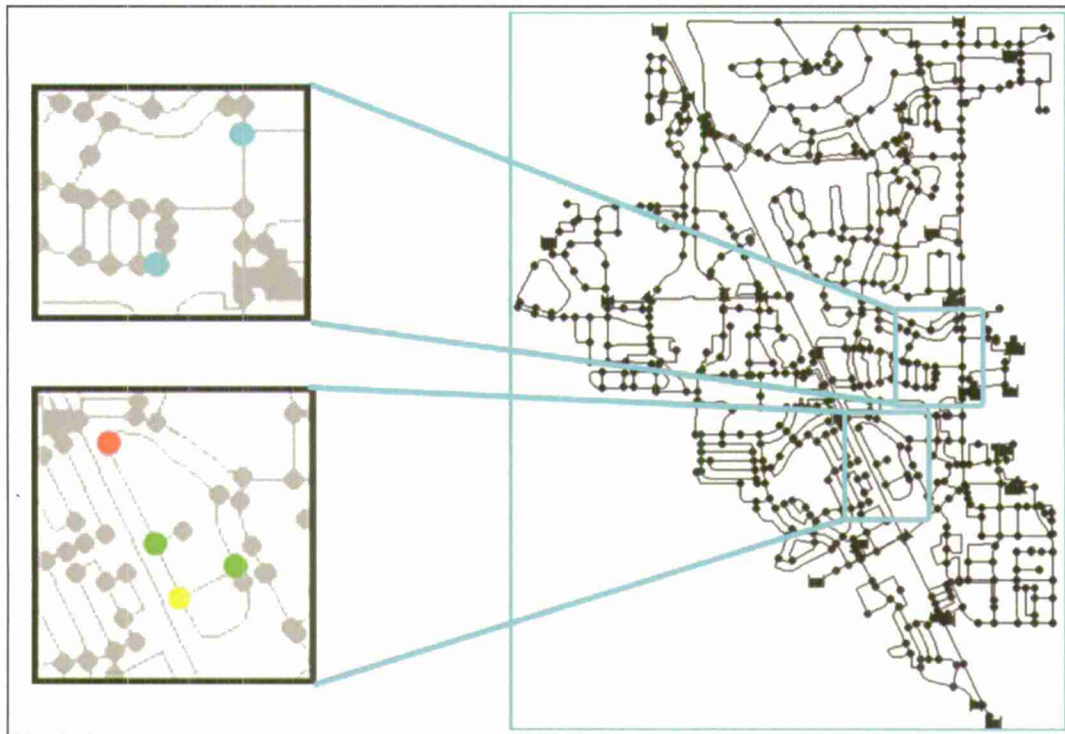


*Figure 4: Optimal Sensor Points for Tanks 1 and 3 combined (Half Concentration)*

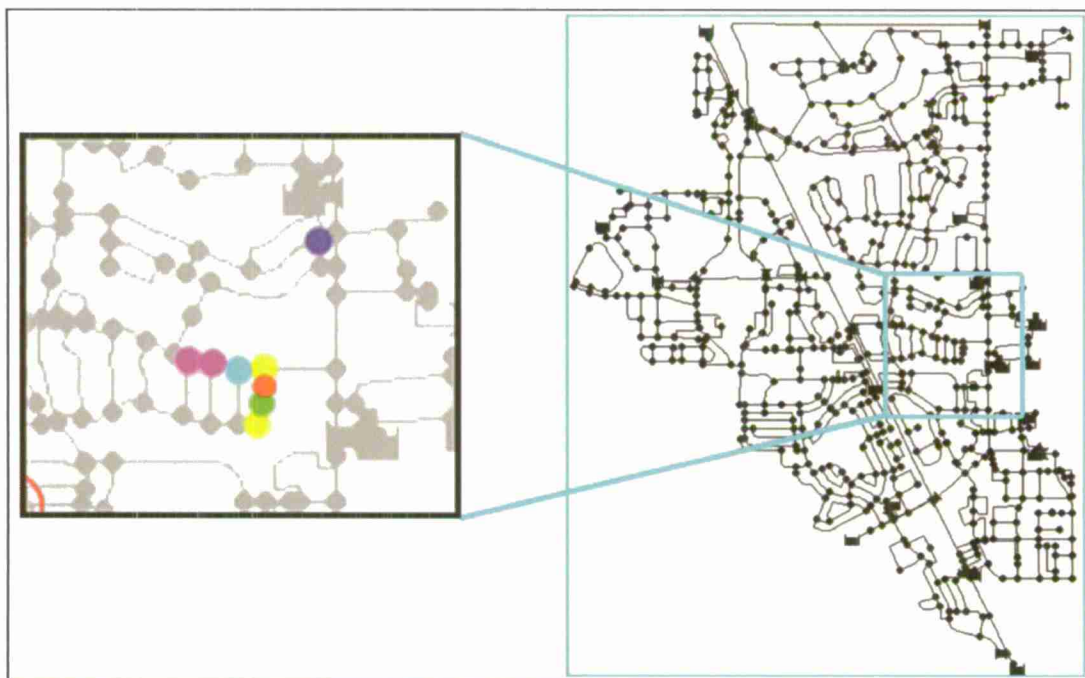


*Figure 5: Optimal Sensor Points for Tanks 2 and 4 combined (Full Concentration)*





*Figure 6: Optimal Sensor Points for Tanks 2 and 4 combined (Half Concentration)*

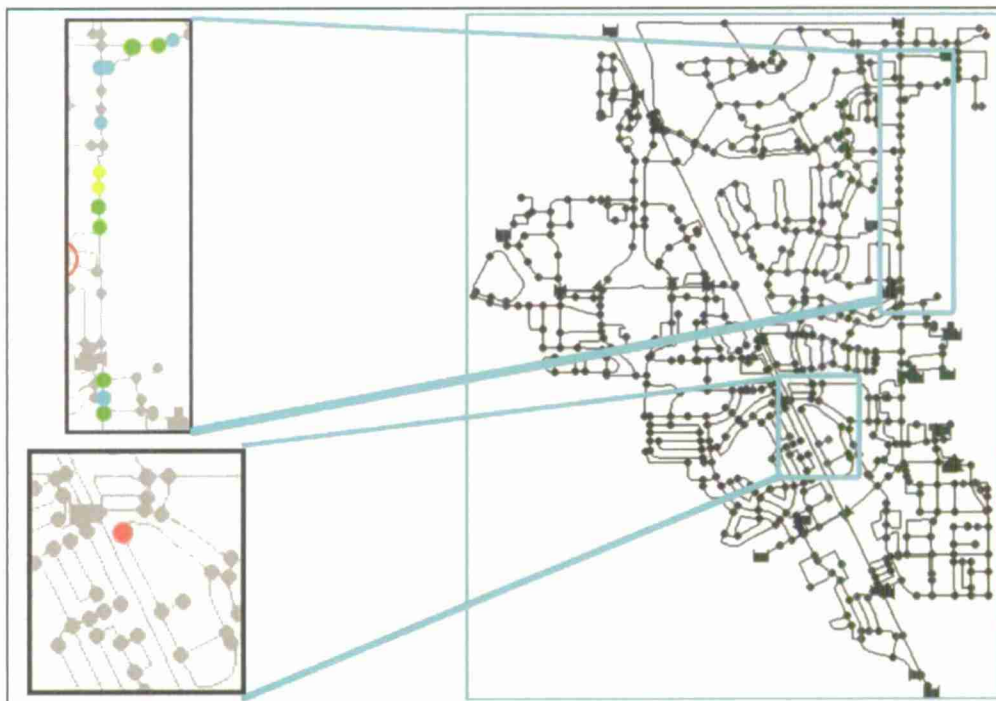


*Figure 7: Optimal Sensor Points for Tanks 5, 6 and 7 combined (Full Concentration)*

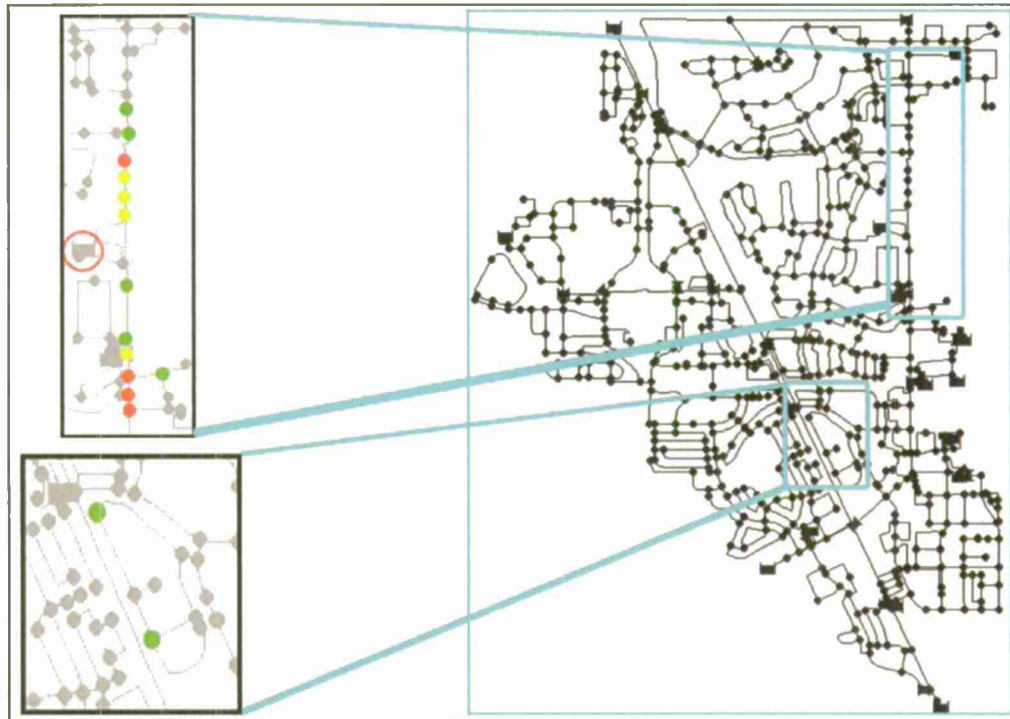


**Figure 7: Optimal Sensor Points for Tanks 5, 6 and 7 combined (Half Concentration)**

As we can see from the results, the change in the injection concentration amount did not have a significant effect on the optimal sensor locations. The effect, if any, was that for a few scenarios the optimal node would change depending on the decrease in injection concentration. The new optimal node would come from the same pool of efficient nodes. In other words, the zones where the clusters of nodes were identified did not change in any scenario when the injection concentration was halved. Figure 2 is the most telling of the overall results as it shows the three zones of significance which contained optimal sensor locations in a majority of the contamination scenarios. Of the twenty two scenarios, only four had a majority of their optimal sensor locations outside of the zones of significance shown in Figure 2. These were:

- Tank 4 (Full Concentration)
- Tank 4 (Half Concentration)
- Tank 7 (Full Concentration)
- Tank 7 (Half Concentration)

The potential reasons for these deviations are as follows: For the two Tank 4 scenarios, the reason the optimal sensor points deviate is because the extent of the Tank 4's influence on the system is relatively small. Tank 7's range of influence on the system is similar and tends to remain along the western portion of the CITY. This is due to the configuration of the distribution system and is highly influenced by the major highway which runs northwest through the center of the system. This effectively isolates the western and eastern portions of the distribution from each other. More importantly, the hydraulics of the system also isolates the spread of the contaminant by containing it in the western portion of the system. This phenomenon occurs in all scenarios, but seems more prominent for the Tank 4 and Tank 7 scenarios.

A single optimal point for the system is not feasible to identify because of the vast amount of variables involved. However, the zones of significance which are outlined for each scenario

dictate the cluster of optimal nodes which would provide robust coverage of the system in regards to monitoring. Figures similar to the sample ones provided should therefore be used as guides for the optimal placement of sensors in the WDS. As previously identified, the quantity of sensors will ultimately drive the location of placement. This will depend on the economic feasibility of using multiple monitoring sensors. For more detail results please see the M. Sc. Thesis "Application of a Heuristic Method to A Water Distribution System for Determining Optimal Water Quality Monitoring Locations" by Lawrence David Johnson, June 2012.  
<http://digitalcommons.calpoly.edu/theses/792/>

## 5. Future Work Planned

Although the given model was calibrated for the hydraulics of the system by changing the fixed grade elevations of the tanks, a calibration could also be performed for the constituent transport. Other contaminant forms will also be explored in future research. Another facet of additional contamination research would include identifying properties of various constituents within pressurized water lines. Identifying properties such as diffusivity and improved decay rates would be highly advantages in modeling approaches. For the zones of significance identified in this study, further exploration of the node importance will be undertaken to gauge which nodes would serve as the ideal location for sensors. The importance of a node can fluctuate based on the outflow use or water demands.

## 6. References cited

- Al-Zahrani, M. A. & Moied, K. (2001), Locating optimum water quality monitoring stations in water distribution system, in *Proceedings of ASCE EWRI World Water and Environmental Resources Congress*, ASCE, Reston, VA, on CDROM.
- Bahadur, R., Pickus, J., Amstutz, D., & Samuels, W.B. (2001), A GIS based water distribution model for Salt Lake City, UT, in *Proceedings of the 21st Annual ESRI Users Conference*, Environmental Systems Research Institute, Redlands, CA, on CD-ROM.
- Bahadur, R., Samuels, W. B., Grayman, W., Amstutz, D., & Pickus, J. (2003), PipelineNet: A model for monitoring introduced contaminations in a distribution system, in *Proceedings of ASCE World Water & Environmental Resources Congress 2003*, ASCE, Reston, VA, on CD-ROM.
- Berry, J., Hart, W. E., Phillips, C. A., & Uber, J. (2004), Sensor placement in municipal water networks, in *Proceedings of ASCE EWRI World Water & Environmental Resources Congress*, Philadelphia, June 23–26, on CD-ROM.
- Chastain, James R., *A heuristic methodology for locating monitoring stations to detect contamination events in potable water distribution systems*. (2004). Theses and Dissertations. Paper 988.
- Ezell, B. C. (1998), Risks of cyber attack to supervisory control and data acquisition for water supply, M.S.Thesis, University of Virginia, Charlottesville, VA.
- Ezell, B. C., Farr, J. V. & Wiese, I. (2000a), Infrastructure risk analysis model, *Journal of Infrastructure Systems*, ASCE, 6(3), 114–17.
- Ezell, B. C., Farr, J. V. & Wiese, I. (2000b), Infrastructure risk analysis of municipal water distribution system, *Journal of Infrastructure Systems*, ASCE, 6(3), 118–22.
- Grayman, W. M., R. A. Deninger, and R. M. Clark. (2002), Vulnerability of water supply to terrorist activities. *CE News* 14:34-38.
- Grigg, N. S. (1999), A systematic approach to sustain and civilize urban water systems, presented at the EPA Conference on Futures of Urban Water Systems, Austin, TX.

- Kumar, A., Kansal, M. L., & Arora, G. (1999), Discussion of 'detecting accidental contamination in municipal water networks' by A. Kessler and A. Ostfeld, *Journal of Water Resources Planning and Management*, 125(5), 308-310.
- Kumar, A., Kansal, M. L., & Arora, G. (1997), Identification of monitoring stations in water distribution system, *Journal of Environmental Engineering*, ASCE, 123(8), 746– 52.
- Laird, C. D., Biegler, L. T., Van Bloemen Waanders, B. G., & Bartlett, R. A. (2004), Time dependent contamination source determination: A network subdomain approach for very large networks, *EWRI ASCE World Water & Environmental Resources Congress 2004*, Salt lake City, UT, on CDROM.
- Lawrence D. Johnson (2012), "Application of a Heuristic Method to A Water Distribution System for Determining Optimal Water Quality Monitoring Locations," M. Sc. Thesis, CalPoly at SLO, June 2012.
- Lee, B. H., & Deininger, R. A. (1992), Optimal locations of monitoring stations in water distribution system, *Journal of Environmental Engineering*, ASCE, 118(1), 4–16.
- Mays, L. W. (2004), Water supply security: an introduction. Pages 1.1- 1.12 in Larry W Mays (ed.) *Water supply systems security*. New York, NY: The McGraw-Hill Companies.
- Ostfeld, A., & Salomons, E. (2003), An early warning detection system (EWDS) for drinking water distribution systems security, in *Proceedings of ASCE EWRI World Water and Environmental Resources Congress*, ASCE, Philadelphia, PA.
- Ostfeld, A. & Salomons, E. (2004), Optimal layout of early warning detection stations for water distribution systems security, *Journal of Water Resources Planning and Management*, 130(5), 377–85.
- PDD 63 (Presidential Decision Directive 63) (1998), The Clinton administration's policy on critical infrastructure protection: Presidential decision directive 63. Available at: <http://www.terrorism.com/homeland/pdd63.htm>.
- U. S. Environmental Protection Agency (2003a), Instructions to Assist Community Water Systems in Complying with the Public Health Security and Bioterrorism Preparedness and Response Act of 2002 Office of Water, EPA 810-B-02-001, Washington, DC.
- U. S. Environmental Protection Agency (2002), Baseline threat information for vulnerability assessments of community water systems, Washington, DC.
- U. S. Environmental Protection Agency (2003b), Planning for and responding to drinking water contamination threats and incidents. Washington, DC.
- Van Bloemen Waanders, G. G., Bartlett, R. A., Biegler, L. T., & Laird, C. D. (2003), Nonlinear programming strategies for source detection of municipal water networks, in *Proceedings of ASCE EWRI World Water & Environmental Resources Congress*, Philadelphia, PA, June 23–26, on CDROM.
- Walski, Thomas M., Donald V. Chase, Dragan A. Savic, Walter Grayman, Stephen Beckwith, Edmundo Koelle (2005), *Advanced Water Distribution Modeling and Management*, Bentley Institute Press.
- Woo, H.-M., Yoon, J. H., & Choi, D. Y. (2001), Optimal monitoring sites based on water quality and quantity in water distribution systems, in *Proceedings of ASCE EWRI World Water and Environmental Resources Congress*, on CD-ROM.

## **Blunt Impact Performance Evaluation of Helmet Lining Systems for Military Use**

Principal Investigator:

**Jay Singh, Ph.D., Industrial Technology**

California Polytechnic State University  
San Luis Obispo, CA



## 1. Abstract

Combat soldiers perform under a varied range of operational environments and injury threats. Military headgear serves as an excellent example for the basis of any protective device. Traditionally, combat helmet design has focused on improving ballistic (penetrating trauma) protection, but there has been recent interest in providing better protection from blunt impacts as well. In the military environment, three head impact threat conditions are easily recognized: motor vehicle accident, trip and fall while maneuvering by foot and the airborne environment. Protection from blunt force depends largely on the dissipation of energy by the helmet, rather than by the wearer's head and brain. This project aimed at evaluating blunt impact performance characteristics of the Advanced Combat Helmet (ACH) focusing primarily on various energy absorbing materials used for padding. This helmet along with approximately five of the standard and non-standard issue padding materials were tested according to the Federal Motor Vehicles Safety Standard (FMVSS) 218 (US DOT). Transmitted acceleration was measured using triaxial accelerometers located at the center of gravity of the headform (conforming to the standard) and the helmet-pad systems were tested at two environmental conditions: ambient and tropical. This research allowed for the padding materials to be evaluated for their suitability towards blunt force protection. It also provided the seed funding to allow us to seek future state/federal grants for military and civilian helmet evaluation and protective padding system design as well as penetrating head trauma related research.

## 2. Project significance

The basis for any protective device, military or civilian, has two goals: there must be the perception of risk and there must also be the perception that the device somehow attenuates that risk. Since its inception, protective headgear has succeeded whenever both these perceptions are present and disappeared whenever either perception is questioned. This basis is particularly true for trauma protective headgear. Combat helmets provide an excellent illustration.

Protecting the soldier's head from injury is critically imperative to individual survivability and mission success. In peacetime, most head injury in the military results from accidental exposure to blunt force and is non-penetrating. In wartime, there is the additional hazard of penetrating head trauma resulting from high speed projectiles. In the past, helmets designed for use in combat have focused on protecting the wearer from penetrating head trauma, with little attention paid to insulating the head and brain from blunt force trauma [1].

The most basic founding theory underlying modern protective cranial helmets of all types involves two principal tenets: a crushable shell that reduces the moment-of-inertia forces encountered by the wearer on first impact and a semi rigid cushioning inner layer that both helps absorb and disperse the secondary crash forces that act upon the head and

brain in an impact. Protection from blunt force depends largely on the dissipation of energy by the helmet, rather than by the wearer's head and brain.

In considering the Army operational environments, three head impact threat conditions are easily recognized. The first is involvement in a motor vehicle accident. If the infantry helmet possesses impact attenuation capabilities, head injury mitigation could be realized during motor vehicle accidents. The second condition is tripping and falling while maneuvering by foot. A simple slip or fall can lead to a head impact. The last condition is the parachutist, or airborne environment. Airborne operations regularly expose paratroopers to risk of head impact during flight (unexpected turbulence or evasive maneuvers), aircraft exit (impact with the door frame or fuselage), descent (riser slap or collision with other jumpers), the parachute landing fall, and after landing (obstacle strikes during dragging in high winds).

Davison (1990) conducted an epidemiological review of paratrooper injuries reported on DA Form 285 "U.S. Army investigation accident report" for the period of 1985 to 1989 [2]. During this period, 277 paratroopers suffered head injuries that resulted in at least one lost work day and four died as a result of their injuries. Most injuries occurred during the landing phase (77.8%) and 89.4% involved concussion or brain contusion. Craig and Morgan (1997) reviewed paratrooper injuries occurring at Fort Bragg, NC, between May 1993 and December 1994 and recorded an overall military parachute injury rate of 8 injuries per 1000 aircraft exits, with head injuries accounting for 18.4% of the casualties [3].

Regardless of the operational environment, even relatively mild head impacts, while not life threatening, can cause short-term impairment from dizziness, headaches, memory loss, lack of ability to concentrate, and irritation. Given the necessity for speed, aggressiveness, and responsiveness on the battlefield, these symptoms become militarily significant, no matter how temporary, by seriously jeopardizing soldier survivability and the success of the unit's mission. There is an obvious need to protect the individual soldier and reduce the injury rate to a minimum, primarily to preserve the efficiency of the fighting unit for combat, but also because a high injury rate would have a detrimental effect on morale, recruiting, etc. [2].

Combat helmets have evolved to counter the threats posed to soldiers in an ever evolving battlefield due to consistently exceeding amount of research and development. The head represents approximately 9% of the body area exposed in combat yet receives approximately 20% of all "hits." The desirability of protecting this vital structure would appear self-evident. Helmet design is a complex issue. Factors that designers of United States Army helmets thoughtfully consider include weight, ballistic qualities of the construction material, balance, helmet-to-person interface (comfort), maintenance of vision and hearing, equipment and weapon compatibility, ease of modification, available materials and manufacturing techniques, durability, ease of decontamination, disposability, and cost [4]. This poses a dynamic challenge to the military forces towards meeting test standards. A recent decision by the Army to recall 44,000 Advanced Combat

Helmets (ACH) issued to soldiers in Iraq and Afghanistan due to incompiancy serves as an example of the constant supervision and monitoring required [5].

The military is constantly improving the protective headgear used by its soldiers. As an example, the sling suspension based Personnel Armor System for Ground Troops (PASGT) helmet used until 2002 by the Army and Marine Corps were replaced by the seven-pad suspension system based ACH helmets due to their ability to provide tested levels of blunt impact protection through a pad suspension system. These helmets are shown in the figure below [6].



**Figure 1: ACH and PASGT Helmets**

The padding systems (energy absorbing materials) used for attenuating blunt force trauma offers a variety of options and include expanded polystyrene (EPS), aluminum foams, polypropylene foams and polyurethane foams amongst several others. British Army's standard issue combat helmets have recently upgraded its liner to incorporate a shock absorbing material called D30. This nanotechnology based gel works on the shear dependent viscosity principle and the molecules of the gel "snag and lock together", i.e. become solid, upon impact [7].

The military is aware of unapproved pad use by soldiers and marines, though the extent and impact of this is unknown. Such unapproved use has been found to occur through purchase of pads by military personnel from the General Services Administration catalogue, which lists an assortment of pads intended for use by a variety of federal agencies and through the procurement of pads by individuals or their friends or family members from commercial sources. In an effort to spur industry to design a more effective pad system, the Army issued a request for information (RFI) in 2007 seeking an off-the-shelf technology solution that could increase blunt impact protection over the current performance standard [6]. This RFI requires the commercial pad system to provide increased non-ballistic protection to 150 g ( $g$  = acceleration due to gravity) maximum at an impact velocity of 17.3 feet per second (objective) or 14.1 feet per second (threshold).

This project falls under the "Application of interest to ONR's Code 30 Science and Technology – force protection (improved protection for the individual, smart materials and injury mitigation)" as described in the request for proposals. This project conducted

an unbiased evaluation of blunt impact performance characteristics for the ACH in conjunction with several currently available (standard and non-standard issue) padding systems. It also provides the seed funding to seek future state/federal grants for civilian helmet evaluation as well as penetrating head trauma related research.

### **3. Background/prior work**

The P.I. has extensive education, knowledge and experience in the field of packaging dynamics. His graduate degrees and subsequent research (~100 projects) over the past 17 years have focused on dynamic cushion characteristics, mechanical property evaluation, fragility testing, dynamic testing to predict performance and distribution environment measurement and simulation. He is also familiar with standard test procedures established by American Society for Testing and Materials (ASTM), Department of Transportation (DOT), Federal Aviation Administration (FAA), International Safe Transit Association (ISTA), International Standards Organization (ISO) and Technical Association of the Pulp and Paper Industry (TAPPI). He has 80 peer reviewed publications in this field, has served as the Division 1 Chair for committee D10.18 of ASTM and currently serves on the Global Board of Directors for ISTA.

The P.I. has investigated the dynamic cushion characteristics of a variety of traditional and bio-based expanded foam materials (open and closed cell). He has also conducted numerous studies related to shock measurement using single and triaxis accelerometers. His recent publication "*Evaluation of the Stress-Energy Methodology to Predict Transmitted Shock through Expanded Foam Cushions*" (Journal of Testing and Evaluation, ASTM) investigated an alternate stress-energy based methodology recommending a considerable reduction in the number of drop tests while providing the ability to predict transmitted shock for any drop height, static loading as well as cushion thickness.

### **4. Materials and Methodology**

There are several performance testing standards available for testing military and civilian use helmets. For blunt impact testing, the Military typically relies on the test procedure prescribed by the Federal Motor Vehicles Safety Standard (FMVSS) 218 (U.S. Department of Transportation). FMVSS 218 describes the test fixture, headforms and impact surfaces and the data collection standard, Society of Automotive Engineers (SAE) Standard J211. This standard establishes minimum performance requirements for helmets. The headforms equipped with triaxis accelerometers are fitted with the helmet to be tested and this combination is then tested in various orientations for impact testing.

It is important to realize that a lot of product type testing like helmet testing does not seek to precisely reproduce real life situations; rather it attempts to define a set of requirements that is analogous to the types of situations that might be encountered while engaged in a prescribed activity. Helmet tests are designed to be repeatable, measurable and include a fixed range of situations a helmet might reasonably encounter. At this point the concerns of helmet testing do not include responses of the neck or body as they react with the head

during a crash. It is strictly a measurement of how a helmet reacts during an event to protect the wearer's brain.

This project had the goals to evaluate the blunt impact attenuation performance of cushioning pads for Advanced Combat Helmet (ACH).

#### **4.1. Materials**

The following materials, fixtures and instrumentation were acquired for this project. The equipment was placed in the Packaging Dynamics lab in the Industrial Technology area.

- Medium sized Advanced Combat Helmets (10, Figure 2)
- Medium drop tower headform (shown in Figure 3)
- Flat steel anvil (impact device that a helmet comes into contact with during an impact test, Figure 4)
- Guide wire free fall drop tower - fabricated per FMVSS 218 standard (Figure 5)
- Five currently available (standard and non-standard issue) helmet liner systems (12 each, Figure 6)
- Piezoelectric accelerometers (PCB 340A50, tri-axial, Figure 7)



**Figure 2: Gentex Advanced Combat Helmet**

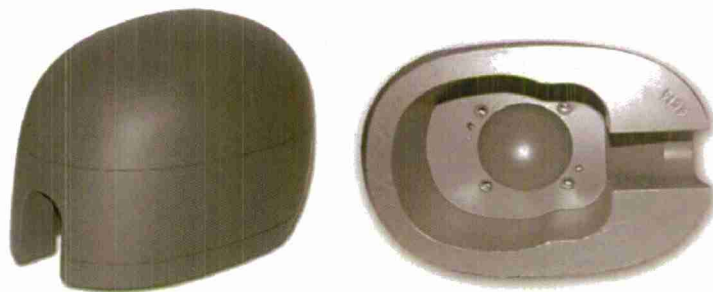


**Figure 3: Drop Tower Headforms**



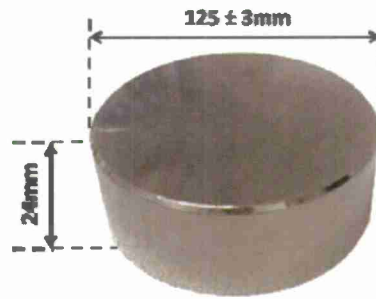


Figure 4: Flat Steel Anvil

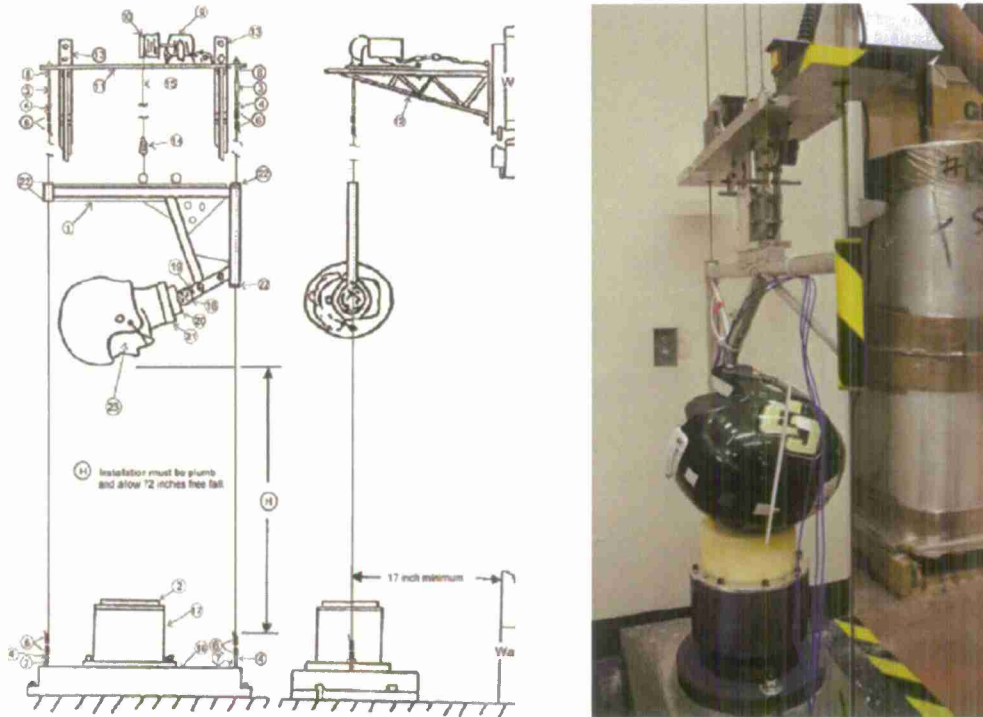


Figure 5: Guided Free Fall Drop Tower  
(a football helmet shown in the picture on the right)

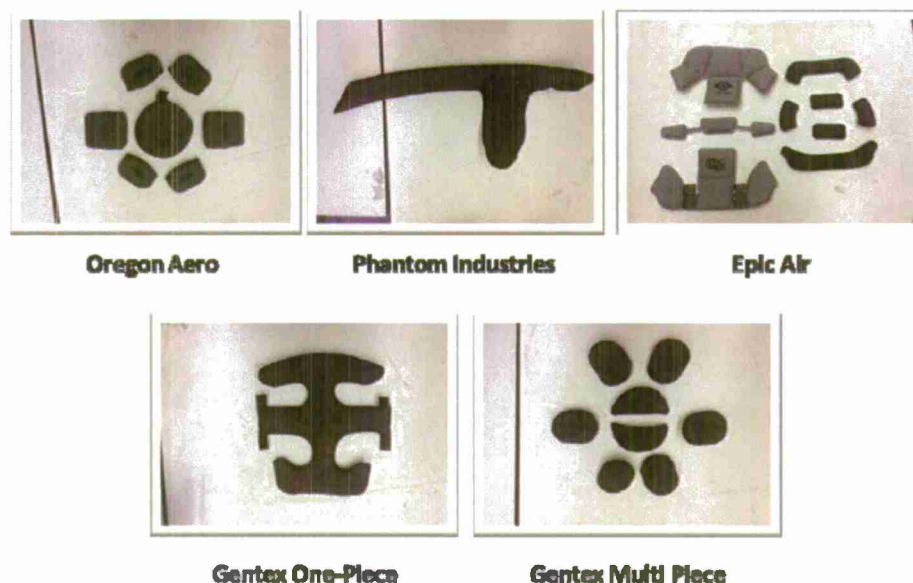


Figure 6: Helmet Liner Systems



Figure 7: PCB 340A50 Piezoelectric Accelerometer

#### 1.1.1 Test Method

The helmets were fitted with the padding systems and mounted on the headform. The headform was instrumented with the accelerometer. Each helmet with pads was tested at an impact velocity of  $14.14 (\pm 3\%)$  feet per second, two environmental conditions (ambient:  $70^\circ \pm 5^\circ\text{F}$  and tropical:  $130^\circ \pm 5^\circ\text{F}$ , Figure 8), at seven different locations (front, back, left side, right side, lower left nape, lower right nape and the crown, Figure 9) and with two successive impacts. Two replicates for each padded helmet was conducted.



Figure 8: Conditioning of Helmet Systems

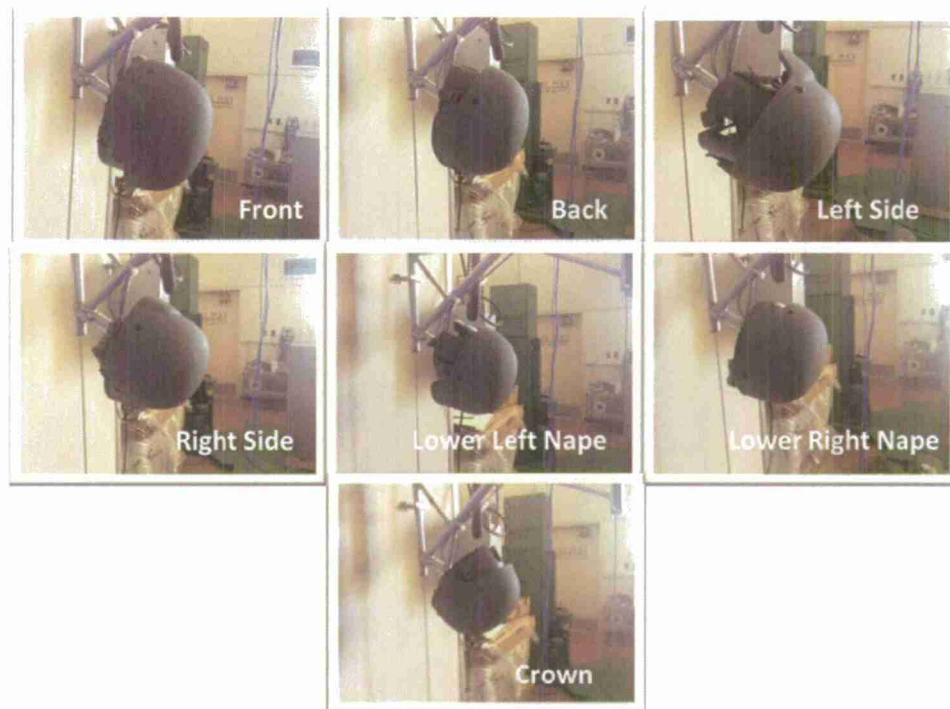


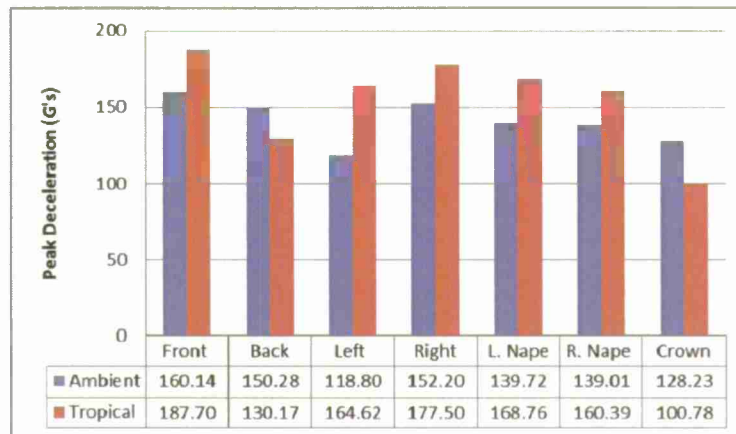
**Figure 9: Helmet Impact Locations**

Each liner was tested in all seven orientations and was exposed to two consecutive drops in each orientation for a total of 14 drops for each helmet at each environmental condition. When testing for the ambient conditions, all 14 drops were conducted while one helmet setup is mounted the apparatus. However, when testing under high the temperature and humidity conditions, the helmets were switched out because conditioned helmets cannot be out of the chamber for longer than 5 minutes before it starts to return to ambient conditions. This resulted in 2 orientations (or 4 total drops) tested before switching to a different helmet with the same type of liner in it.

## **5. Results & Discussion**

The results are shown as:

- a. Performance of individual liners for environmental conditions & impact orientations (Figure 10)
- b. Comparative performance of liners for environmental conditions and impact orientations (Figure 11)
- c. Comparative performance of liners for environmental conditions (Figure 12)
- d. Overall performance of liners (Figure 13)



(a) Oregon Aero



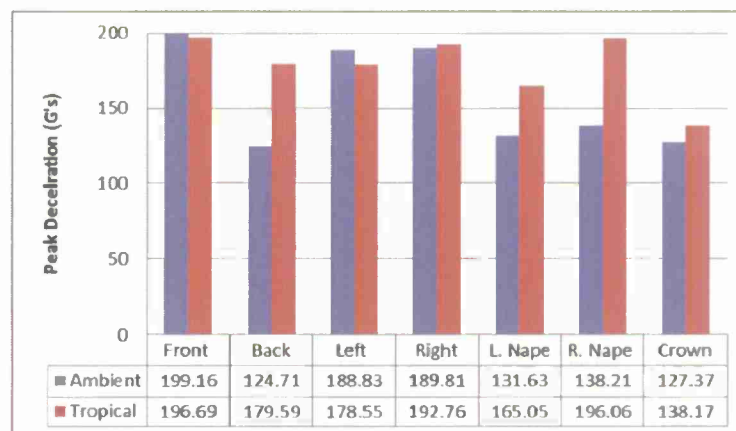
(b) Phantom Industries



(c) Epic Air



(d) Gentex 1-Piece

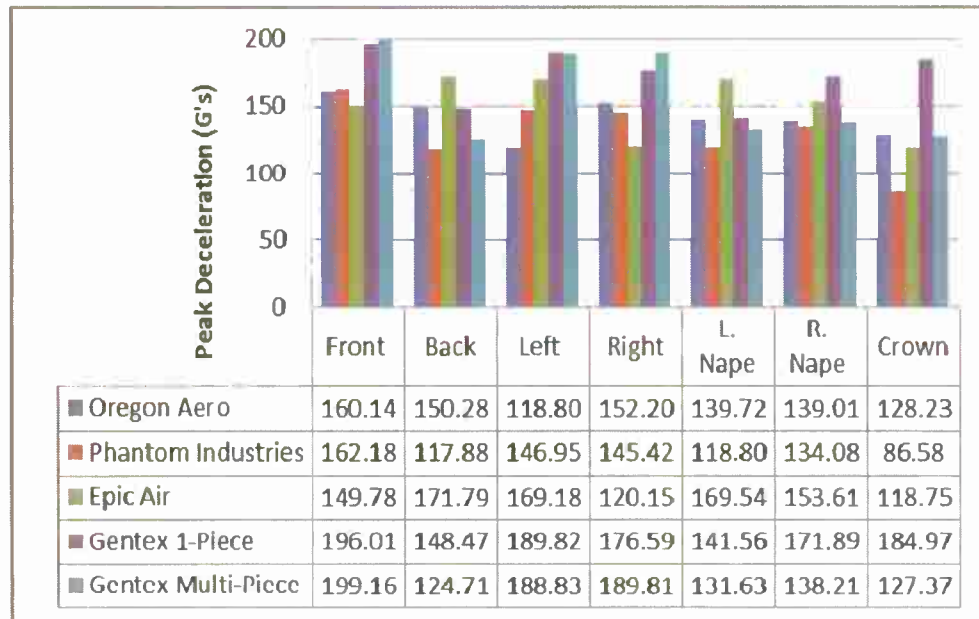


(e) Gentex Multi-Piece

**Figure 10: Performance of Individual Liners for Environmental Conditions & Impact Orientations**

It was observed that the highest shocks for the ambient condition were recorded during the front impacts, except for the Epic Air lining system (left). For the tropical conditions, the exception to the highest shock in the front impacts were for Gentex 1-Piece (right nape) and Phantom (left) liners. Maximum transmitted shocks of 199.16 g's and 196.68 g's respectively for ambient and tropical conditions, were observed for the Gentex Multi-Piece liners. The lowest shock of 86.58 g's was observed (for both conditions) was for the crown impact when using the Phantom Industries liner.



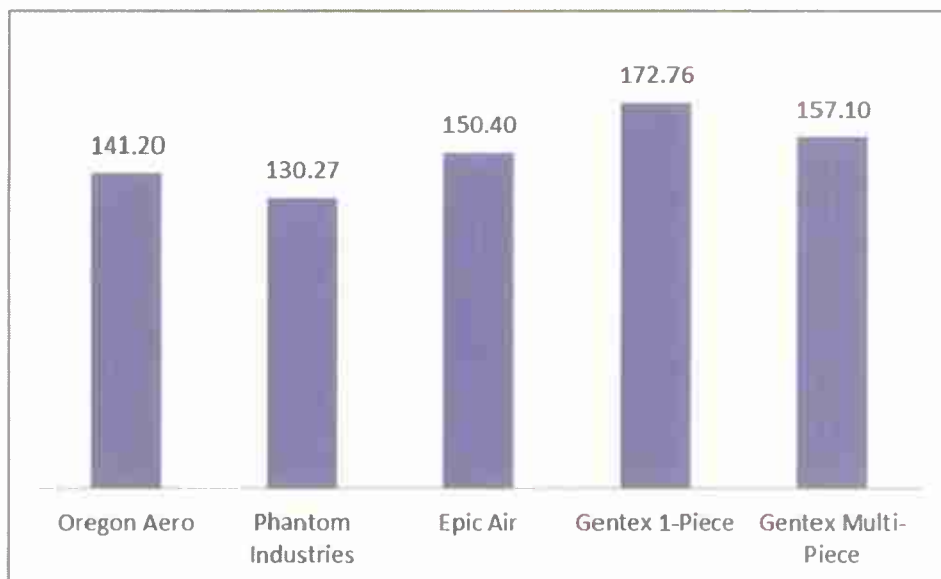


(a) Ambient Conditions

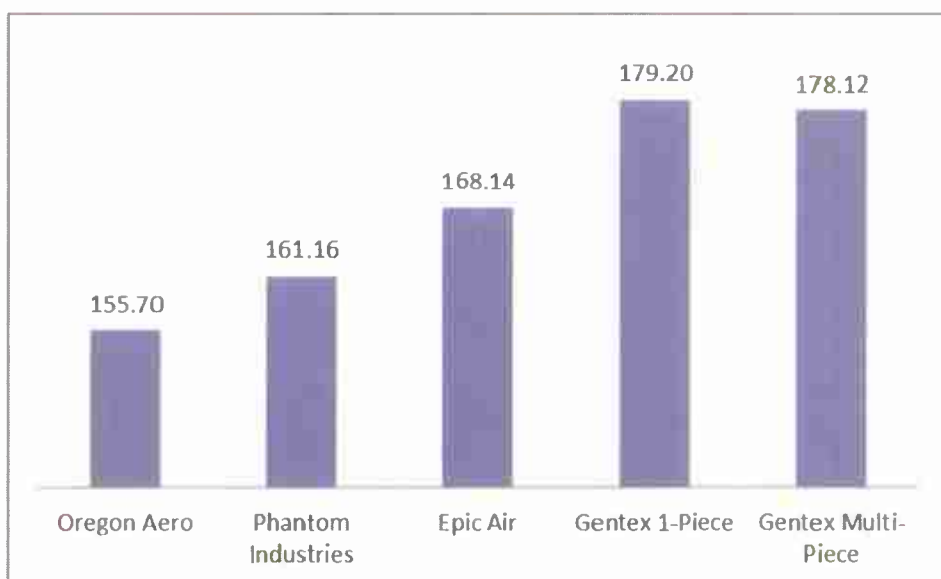


(b) Tropical Conditions

**Figure 11: Comparative Performance of Liners for Environmental Conditions & Impact Orientations**



(a) Ambient Conditions



(b) Tropical Conditions

**Figure 12: Comparative Performance of Liners for Environmental Conditions**

When comparing the average transmitted shock for all seven impact orientations:

*Ambient conditions:* Gentex 1-Piece liner was recorded as the highest (172.76 g's), while the Phantom Industries liner system produced the lowest shock (130.27 g's)

*Tropical conditions:* Gentex 1-Piece liner was recorded as the highest (179.20 g's), while the Oregon Aero liner system produced the lowest shock (155.70 g's). The tropical shock values were also noted to be higher than those for the ambient conditions.

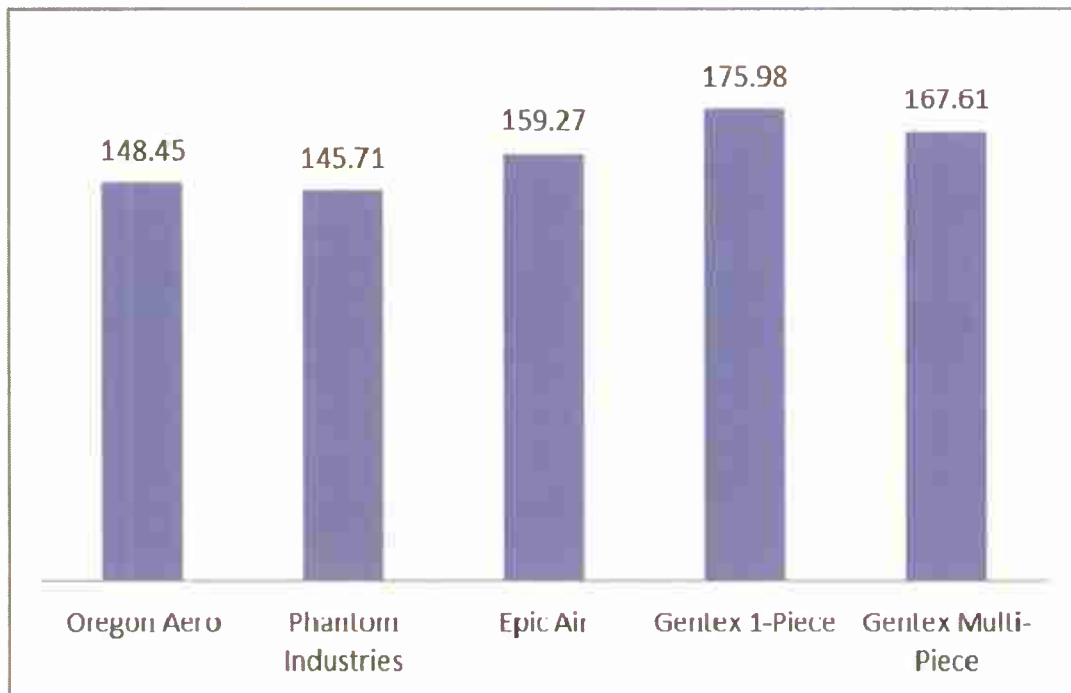


**Figure 13: Overall Performance of Liners**

Overall, the Phantom Industries liner system is rated as the best performing due to the lowest transmitted shock value (145.71 g's). The poorest performer was the Gentex 1-Piece liner system with the highest transmitted shock value of 175.98 g's.

## **6. Future Work Planned**

This grant has provided the resources to fabricate a standardized guided free fall drop tower to allow conducting helmet testing at Cal Poly. Following are some new future plans related to the experiences and findings of this grant work:

- a. The PI will be presenting a paper titled "*Blunt Impact Performance Evaluation of Helmet Lining Systems for Military Use*" at the The National Institute of Packaging, Handling, and Logistics Engineers' (NIPHLE) Training Symposium, March 10-15, 2013 at Williamsburg, Virginia. NIPHLE membership includes Government, Military and Industry. The theme of the symposium is "*Transitioning to the Future: Innovations that Support the Warfighter*".
- b. The research findings are planned to be submitted towards peer review publications in the Journal of Testing and Evaluation (ASTM) or a suitable military journal
- c. Promote the new capabilities (equipment and expertise) towards soliciting proprietary and competitively funded projects

## 7. References cited

1. Brozoski, F. T., McEntire, B. J., Crowley, J. S. and Padgett, K. L. Enhancing Injury Protection Capabilities of Army Combat Helmets. U.S. Army Aeromedical Research Laboratory Report. Available at <http://www.dtic.mil/cgi-bin/GetTRDoc?Location=U2&doc=GetTRDoc.pdf&AD=ADA481713>, Accessed June 7, 2012
2. Davison, D.J. 1990. A review of parachuting injuries. *Injury*. 90:21; 314-316
3. Craig, S.C. and Morgan, J. Parachuting injury surveillance. Fort Bragg, NC. May 1993 to December 1994. *Mil. Med.* 1997; 162-4.
4. Carey, M. E., Herz, M., Corner, B., McEntire, J., Malabarba, D., Paquette, S. and Sampson, J. B. Ballistic helmets and aspects of their design. *Neurosurgery*. 2000 Sep; 47(3):678-88; discussion 688-9
5. Cox, M. Army Recalls 44,000 Helmets. *ArmyTimes.com*, Available at: [http://www.armytimes.com/news/2010/05/army\\_helmet\\_recall\\_051410w/](http://www.armytimes.com/news/2010/05/army_helmet_recall_051410w/), Accessed June 12, 2012
6. U.S. Government Accountability Office. GAO-09-768R Warfighter Support, Report to the Congressional Committees. July 28, 2009. Available at: <http://www.gao.gov/htext/d09768r.html>. Accessed November 26, 2012
7. Hickley, M. Introducing the gel-filled army helmet that will crush bullets as they penetrate it. *MailOnline.com*. Available at <http://www.dailymail.co.uk/sciencetech/article-1156544/Introducing-gel-filled-army-helmet-crush-bullets-penetrate-it.html>. Accessed October 21, 2012

# **New technologies with military applications**

## **Project Reports**



**Efficient Point-to-Point Communication Infrastructure for Low Earth  
Orbit Satellites**

Principal Investigator:

**John M. Bellardo, Ph.D., Computer Science**  
California Polytechnic State University  
San Luis Obispo, CA

**1. Abstract (~250 words)**

Cal Poly's PolySat program has designed, built, flown, and operated a number of low earth orbit satellites. The communication architecture was shared across a number of different satellites. In practice it could not achieve 10% utilization of the radio link between earth and the satellite. The design also lacked the flexibility to quickly adapt to new missions. Based on operational experiences and feedback from external collaborators it became evident that this was a major impediment to expanded scientific collaboration and research.

The reported work addressed these shortcomings in three steps. The communication architecture was redesigned to leverage existing standard protocols and designs, so as to result in a much more adaptable architecture. A performance monitoring and analysis infrastructure was developed and will be used to gather data and gain a detailed understanding of the specific communication challenges facing low earth orbit satellites. Protocol and architecture changes were proposed and evaluated based on the improved understanding provided by the measurement infrastructure.

**2. Project significance**

This project explored communication architectures, related software, and protocol designs for increasing the usable bandwidth between a low earth orbit satellite and its corresponding earth station. This project is significant because communication capacity was a major constraining factor for PolySat missions, limiting both the science and research capability of the spacecraft.

The severity of this problem was demonstrated with a simple analysis of satellite operations. With the prior communication architecture, satellite operators were able to send one small piece of data, called a packet, from the ground station to the satellite and back once every 3 seconds. The theoretical limit of the system, however, was approximately one packet every 0.3 seconds. While it is unreasonable to expect the network to operate at the theoretical limit, only realizing 10% of the available performance is unacceptable and greatly limited the scientific payload that could be flown in these satellites, as most payloads require more communication capacity to send their observations back to earth. Limiting payloads placed limits on the types of missions and external collaboration opportunities available to the PolySat program.

The other major limitation of the communication architecture was its software design. The system was created without incorporating well known design patterns and without using existing, understood communication protocols. As a result the system was not flexible. New missions required invasive changes to the communication protocol, which artificially limited the types of missions available to the PolySat program. For instance, it prevented the platform from being used to gather operational results in support of advanced satellite-to-satellite communication research, such as that underway by the P.I. of this project [1].

At the time this project was proposed, PolySat was collaborating on a scientific mission with industry partners. During discussions and design reviews with them, one of the primary misgivings expressed was the ability for PolySats to transfer enough data back to earth to be useful. In addition to industry feedback, the P.I. has received feedback from government funding agencies that optimizing the current communication channel is a required precursor to introducing the more advanced satellite-to-satellite communication technologies proposed in [1].

This project directly relates to ONR's code 30 "Command and control, computers, communication" topic. The work makes significant indirect contribution in the areas of national security, force protection, and intelligence, surveillance, and reconnaissance.

### **3. Background/prior work**

The prior PolySat communication performance was extremely poor, not more than 10% of optimal, as described previously. There are a number of possible explanations for this. One explanation that is easy to understand is that students designed the current protocols without direction from someone experienced in that area of communications. There is a more detailed set of explanations that requires a deep understanding of the nuances of the current communication protocols. Such knowledge of the protocol is difficult to attain.

This difficulty has two main causes. The majority of the protocols used in the PolySats were designed from scratch despite there being well-known protocols with similar functionality. One big benefit of using standardized protocols is that they have been extensively studied. Their shortcomings and performance enhancements are well known. It would take decades of rigorous research to reach the same level of understanding for the current PolySat protocol suite.

The other impediment to understanding the existing communication protocol is a lack of measurement infrastructure. Thus, when a packet doesn't reach the satellite there is no additional information available to determine *why* it didn't make it. Ideally the communication protocol would be designed by combining the appropriate set of primitives to create the best protocol for low earth orbit communication. It is virtually impossible to do this without understanding the probable causes of packet loss and inefficiency. CubeSat communication issues are new enough that they have not received the research scrutiny afforded to other communication applications.

Communication networks are typically composed of multiple independent layers. One of the layers, the MAC or data link layer [9], is responsible for behaviors specific to the radio link between earth and the satellite. These behaviors include determining which device gets to transmit the next packet, which packet to transmit, when to transmit it, and how to recover from lost or corrupted packets. MAC protocols vary depending on the specific application. The CubeSat communication application is new enough that it hasn't been well studied in existing research literature. One important aspect of this project is further research into the appropriate MAC protocol.

CubeSat communications have historically used slow, half duplex radios. Speeds typically range from 1200 bits per seconds to 9600 bps. In a half duplex system, a radio can either be in transmit mode or receive mode, but not both at the same time. When the radio is transmitting it cannot receive data. These limitations have led to a very simplistic communication paradigm.

Current missions send a single command to the satellite and wait for a response before moving on to the next command. This resolves the half duplex problem because the ground station explicitly waits in receive mode for either a response or a timeout, after which it is assumed the response won't be heard. This also introduces a substantial inefficiency in communication. As the ground station is waiting for a response, nothing is being transmitted over the radio link. This dead air time is a substantial loss because the communication opportunities with the satellites are few and short in duration.

Another big problem with prior systems is the use of custom command formats. Most satellites eschew standard network protocols in favor of custom designed command formats. This has a number of downsides. Due to time constraints, these custom designs tend to be very sparse on features and lightly tested. They make interoperability between different ground stations difficult at best. Finally, they eliminate the possibility of using preexisting, open-source communication solutions.

#### **4. Discussion of Results**

##### **New Architecture**

This next-generation CubeSat communications architecture was designed specifically to address the previous shortcomings. The hardware limitations haven't changed. That is, this work still assumes slow, half-duplex radio communication. This work focuses on working within those constraints to get better radio utilization.

An additional goal of this work was to maintain compatibility with the amateur radio community. This community is very supportive of CubeSats, including providing frequency allocations and extra ground monitoring opportunities. Damaging this relationship, even for the sake of efficiency, isn't in anyone's best interest.

The high-level summary of the protocol is straightforward, and primarily relies on preexisting network standards. HDLC framing is used at layer 1 for compatibility with amateur radio. At layer 2, we support both AX.25 for compatibility and a new protocol, CPL2, for efficiency. Layers 3 and above are a standard IP networking stack. We also support optional header compression to minimize the impact of large IP headers.

The next few sections go into more detail on each of the previous points.

## *HDLC*

HDLC framing is required for compatibility with the amateur radio community; however HDLC doesn't specify how to share the half-duplex link. Most of the layer 2 effort was spent determining how to manage the half-duplex link.

HDLC has two main places it adds overhead. First, individual packets are surrounded with special start and stop bytes. These bytes are required per-packet overhead. The second source of overhead is a long synchronization code at the start of a burst of packets. Since this byte sequence is sent only once for a burst it can be amortized across all the packets in a burst. Therefore the longer the burst the less synchronization overhead is incurred.

The last missing piece from HDLC is some way to share the half duplex wireless medium. This is important when the radios are active close to 100% of the time. If the transmitter and receiver aren't in sync all the packets can be lost. The solution to this problem is to force the transmitter back to receive mode after a short amount of time, even if the transmitter has more data to send. After another short period of time the receiver can begin transmitting again. For perspective, a radio will normally transmit for approximately 1 second and then pause in receive mode for 50ms. In addition to allowing the other end an opportunity to transmit, this provides a window of time where the radio frequency can be changed with a low likelihood of dropping packets. Changing the frequency is required to correct for Doppler shift from the fast moving satellite. The exact amount of time spent transmitting, and then waiting in receive mode, presents a tradeoff between overhead and latency. Note that the radio software performs a form of carrier detection before transmitting. If the software detects another packet being received it will defer transmission until the other end stops transmitting.

## *Layer 2*

AX.25 is the layer 2 standard supported by all amateur radio equipment. The satellite supports using this protocol to ensure backwards compatibility. While AX.25 is serviceable, it isn't very desirable. In its smallest format, it requires 16 bytes but has the potential to grow much larger. Of all these bytes only one or two are actually important to the communication. This unneeded overhead, combined with AX.25 limiting packets to 256 bytes in length, motivated the development of an alternative layer 2 protocol.

The alternative protocol, named Cal Poly Layer 2, or CPL2 for short, retains only the critical information from the AX.25 header. CPL2 removes all but two bytes of the layer 2 header. To accomplish this CPL2 uses the unnumbered frames from the HDLC standard. The address byte in these frames is 0xCB. The control byte determines the type of layer 3 payload. There are currently two defined types, 0x0B for IPv4 and 0x8B for ROHC. It is worth noting that the particular values were chosen to enable AX.25 and CPL2 to be used interchangeably. This enables us to simultaneously support amateur radio stations and the more efficient protocol. In fact, the satellite tracks the type of L2 protocol used on a per-connection basis and responds using the same type. So if the Cal



Poly ground station sends CPL2 packets it receives CPL2 packets in response. There is no satellite-side setting necessary to enable or disable this protocol.

### *Layers 3 and 4*

Layer 3 provides the most opportunity to adopt standards-based networking in CubeSats. In fact, there is only one serious option that meets the design requirements: the Internet Protocol version 4 (IPv4). Along with using IPv4 at layer 3, the Internet network stack includes common layer 4 protocols such as Transmission Control Protocol (TCP) and User Datagram Protocol (UDP). These protocols form the core of the Internet that hundreds of millions of computers and smartphones already use. The biggest downside of this protocol stack is overhead. It wasn't designed with exceedingly slow links in mind. The smallest IP + UDP header is 32 bytes and the smallest IP + TCP header requires 40 bytes. This is a substantial percentage of the AX.25 imposed limit of 256 bytes per packet.

One technique for reducing this overhead is using layer 3 and 4 header compression. It is worth noting that the compression and decompression are done immediately before transmission and after reception, respectively. This means none of the software running on the satellite, including the kernel, hardware drivers, and all related processes, know that compression is being used. They simply interact with the network like they would with any other IP-based network. This preserves the standards-focused architecture.

There are two readily available standards for IP header compression, Von Jacobson and Robust Header Compression (ROHC). ROHC was specifically designed because Von Jacobson was shown to perform poorly when packets were dropped. Since both of these compression techniques are stateful, that is, they require some information from a previous packet to decompress the next packet, they can be very sensitive to packet loss.

We incorporated support for both uncompressed IPv4 headers and ROHC compressed IPv4 headers into our CubeSat communication protocol. A type field present in the previously mentioned layer 2 header allows the satellite to differentiate and freely intermix these two header compression schemes.

Supporting both schemes provides two major benefits. First, ROHC support is not widespread in the amateur radio community. If we only used ROHC we would be drastically limiting amateur radio operators. Second, the correct level of compression depends on the exact amount of packet loss experienced. We cannot accurately predict packet loss because we have no actual flight data with these radios. Supporting both ROHC and uncompressed headers helps us hedge our bets. If there is minimal loss we can use ROHC. If there is a high loss rate we can use uncompressed headers. The satellite remembers which layer 3 headers are used on a per-connection basis and always matches what the earth station is transmitting. This is similar to the layer 2 mechanism described above.

### *Layer 7*

By design, layer 7 contains the commands that are specific to a single process or task. Due to our standard-compliant communication stack, we support some of the more common layer 7 protocols, including ssh, telnet, and ftp. There are also a number of custom protocols defined to interact with our custom processes. Optimizing these layer 7 protocols is outside the scope of this work.

### **Performance**

The communication architecture, as described above, was implemented using the current generation of PolySat hardware and tested in the lab. Identical radios were used on both ends of the radio link. One end consisted of a flight-like electronics stack (the satellite end of the link), and the other consisted of development boards (the ground station). It is worth noting that since the software is based on Linux, all the support for receiving and processing asynchronous commands above the radio link already exists.

Two fundamental tradeoffs were discovered during testing, one with the medium sharing protocol and one with header compression. When sharing the medium, there is a tradeoff between lower overhead with higher efficiency, and higher overhead with lower latency (e.g., response time). This tradeoff comes directly from the amount of time a radio will transmit before resetting to receive mode, and then how long it will wait before returning to transmit mode. In a responsive, low latency system a radio might only transmit for 10ms before listening for a response. This is a very responsive 50% duty cycle (10ms TX, 10ms RX). The other communicating party gets a chance to respond every 10ms. However, this has very high overhead.

Recall that HDLC framing stipulates roughly 30 bytes of synchronization code at the beginning of a packet burst. A 10ms TX time will effectively limit each burst to a single packet, resulting in an extra 30 bytes of overhead per packet. A longer TX time, such as 500ms, permits multiple packets to be transmitted in the same burst, but dramatically increases the time it takes for the receiver to transmit a response. The values for TX and RX time that minimize overhead depend heavily on the communication workload. For example, if 95% of the time is spent downlinking data from the satellite, a TX-lopsided value is the optimum choice. Experiments performed with an artificial workload showed a HDLC overhead ranging from a low of 10% to a high of 60%, depending on the exact TX and RX values. The 60% end of the spectrum resulted in responsive command handling. The 10% end resulted in much faster data downloads.

The second fundamental tradeoff is between stateful compression and packet loss. Due to the inter-packet dependencies created by stateful compression, loss of a single packet may render the subsequent packets useless. In this scenario it is better to not compress the packets. However, given a relatively low loss rate, stateful compression can reduce the 32 byte IP + UDP header down to less than 3 bytes. This is a huge increase in efficiency.

The radio communication protocols were tested in our lab by transferring 100kb files from the satellite to the earth station. Without any of the optimizations developed in this work, we saw approximately 30% effective utilization. So, for our 9600 bits-per-second link, we were transferring about 2880 bits-per-second of the 100kb file. With all the performance options enabled, including header compression and optimum RX & TX timing, we saw 85% efficiency. It is worth noting that there was not any noticeable packet loss in these experiments. On orbit performance is expected to have additional loss not seen in the lab.

### *In-Flight Radio Reconfiguration*

A key feature of this new communication system is the ability to reconfigure the radio parameters after the satellite has been launched. The radio parameters include options like bitrate, modulation, encoding, and frequency. This creates the potential to match the data rate to the environment, instead of using a predetermined, conservative number.

Changing the radio parameters is dangerous. If the satellite and ground station aren't using the same values all communication is lost and recovery is unlikely. A new radio parameter negotiation protocol was developed to ensure the change is made safely. There are a number of steps to this protocol:

1. The ground station flushes its transmit buffer and stops transmitting packets. Packets are still received like they would be in normal operation.
2. Two safety parameters are picked, the total duration (D) and the giveup time (G). The ground station begins transmitting a parameter change request packet (REQ) to the satellite. This packet includes the new radio parameters, D, and G. This packet is transmitted once a second until the satellite acknowledges it or G/2 seconds have passed.
3. The satellite, upon receipt of a REQ, flushes its current transmit buffer and pauses the normal transmission process. After the buffer is empty, the satellite acknowledges the REQ packet by transmitting a REQ\_ACK in triplicate at 200ms intervals. Three copies are sent in case there is packet loss. After the 3<sup>rd</sup> packet the satellite applies the new parameters to its radio. The satellite then transmits a COMMIT packet once per second. The new parameters stay in effect until either G seconds have elapsed or the commit packet is acknowledged with a COMMIT\_ACK. If G seconds elapse before the receipt of a COMMIT\_ACK, it is assumed the radio parameters aren't working and the radio is automatically reverted back to the original parameters.
4. The ground station, upon receipt of a COMMIT packet, sends three copies of the COMMIT\_ACK packet spaced 200ms apart. It continues sending one COMMIT\_ACK per second until it hears a valid data packet from the satellite or G seconds have elapsed. If G seconds elapse without hearing a valid packet, the radio parameters revert back to their original value. If a data packet is received before G seconds elapse, the transmission queue is resumed and the radio values revert back to their original value after D seconds.

5. When the satellite receives a COMMIT\_ACK packet it resumes processing the data in it's transmit queue. In the event the queue is empty, the satellite ensures that it sends 1 packet per second until it receives a valid data packet from the ground.

### *On-Orbit Performance Optimizations*

The biggest unknown is the amount of packet loss the radio link is going to experience. Since this hardware hasn't flown before, we have no data on which to make an educated guess. The loss rate is important because the ROHC compression scheme is sensitive to loss. For instance, the first few packets establish the compression state for the remainder of the data flow. If those get lost, the compression state at both ends of the link is inconsistent, resulting in complete packet loss. The communication system has been implemented to permit enabling and disabling ROHC on a per-flow basis without any interaction with the satellite. This provides the flexibility to use when the link is found to be low loss, and disable it in other circumstances.

Another area ripe for performance optimizations is communication bitrate. These radios run exceptionally slow relative to the communication speeds we have become accustomed to on our computers. A small increase, say by 9600bps, will nearly double the effective performance of the radio link. The biggest deterrent to increasing the link speed is the free space path loss of the radio signal. Low earth orbits (LEO) can be highly elliptical. For example, they can range from 350km above the earth to 850km in one 90-minute orbit. Obviously there is more free space path loss when the satellite is 850km away. Historically the communication bitrate is set conservatively. The maximum distance in the orbit is used, with margin, to determine the mission's bitrate. The ability to change bitrates in orbit opens up a new performance optimization. The optimum bitrate can be selected for the actual distance and actual environmental characteristics, and can be changed every few minutes as the satellite progresses in its orbit. This has the potential to substantially increase the amount of data we can transfer from the satellite in a single pass.

### **5. Future Work Planned**

The ground station infrastructure currently supports a single earth station communicating with a single satellite. There are plans to grow and automate this substantially. We plan to operate multiple concurrent earth stations at Cal Poly. Designing and implementing a ground station architecture to support distributed earth stations is an important piece of future work. Such a geographically diverse network would increase the communication opportunities and substantially increase the amount of data we could receive from the satellite.

## 6. References cited

- [1] – Trevor Koritza and John M. Bellardo, Increasing CubeSat Downlink Capacity with Store-and-Forward Routing and Data Mules, In *Proceedings of Wireless Communications 2010*, Banff, Canada, July 2010.
- [2] – OSI model; [http://en.wikipedia.org/wiki/OSI\\_model](http://en.wikipedia.org/wiki/OSI_model)
- [3] – Internet Protocol; RFC 791; <http://rfc-ref.org/RFC-TEXTS/791/index.html>
- [4] – User Datagram Protocol; RFC 768; <http://rfc-ref.org/RFC-TEXTS/768/index.html>
- [5] – Transmission Control Protocol; RFC 793; <http://rfc-ref.org/RFC-TEXTS/793/index.html>
- [6] – Compressing TCP/IP Headers for Low-Speed Serial Links; RFC 1144; <http://rfc-ref.org/RFC-TEXTS/1144/index.html>
- [7] – RObust Header Compression (ROHC): A Compression Profile for IP; RFC 3843; <http://rfc-ref.org/RFC-TEXTS/3843/index.html>
- [8] – RObust Header Compression (ROHC): Profiles for User Datagram Protocol (UDP) Lite; RFC 4019; <http://rfc-ref.org/RFC-TEXTS/4019/index.html>
- [9] – Data Link Layer; [http://en.wikipedia.org/wiki/Data\\_Link\\_Layer](http://en.wikipedia.org/wiki/Data_Link_Layer)



**Assessment of Sonic IR for Detection of Subsurface Damage in Composite Panels**

Principal Investigators:

**John C. Chen, Ph.D., Mechanical Engineering**  
**Joseph D. Mello, Ph.D., Mechanical Engineering**

California Polytechnic State University  
San Luis Obispo, CA

## 1. Abstract

Sonic IR, also known as thermosonics, thermal acoustic, and vibrothermography, is a nondestructive inspection technique that is in current development for use with metallic components. It is efficacious in such applications for detecting, for example, fatigue cracks and corrosion. In this study we examine sonic IR's effectiveness for detecting impact damage and delamination in carbon-fiber reinforced polymer (CFRP) composite panels. This material is gaining popularity in engineering applications due to its favorable performance characteristics. Its main weakness, however, is its susceptibility to hard-to-detect damage due to a low-energy, normally oriented impact. Such damage, when undetected and corrected, eventually leads to catastrophic component failure. It is critical, therefore, to develop reliable, effective and efficient methods of inspection for CFRP. The results show that sonic IR is well suited for detecting even low-level impact damage and simulated delaminations in CFRP panels. This project has led to three conference presentations and one conference publication, and it is expected to lead to one future journal publication and one patent.

## 2. Project significance

Composite materials are engineered materials made from two or more ingredients that, when combined, possess significantly different physical properties than the original materials and offer superior performance. Examples of composites include plywood (wood panels and glue) and concrete (sand, cement and stone). The focus of this project will be on high-performance composites such as carbon-fiber reinforced polymer (CFRP), which are extremely strong and have superior strength-to-weight ratio. Because of these characteristics and the fact that their manufacturing costs have reduced, these composites are finding wide application in the aerospace and automotive industries. The benefits of designing with composites include weight and fuel savings and the ease of manufacture of the finished product in its end-use shape. For example, Boeing's next commercial aircraft, the 787 Dreamliner, will be the first aircraft to use mostly composite materials for its primary structure – including the fuselage and wings [i, ii].

One significant disadvantage of high-performance composites is impact damage due to, for example, a tool drop or debris impact on a structural member. Such impacts often result in little or no visible damage at the impact site but can cause significant structural flexure due to the thin 'sandwich-like' construction of CFRP composites. When significantly flexed, sandwich composites often develop internal delamination between the sandwich layers that greatly reduce the strength of the material around the defect. If not found and repaired, such damage can lead to catastrophic failure of the component, as was the case in the crash of American Airlines Flight 587 after takeoff in New York City in November 2001. The crash was attributed to a failed composite component in the tail section. The challenge to finding these defects is that they are subsurface to the examinable external surface and are often not marked by easily identifiable markings that indicate a possible (hidden) damage site.

Our ultimate project goal is to develop an instrument that is capable of nondestructively inspecting CFRP components for impact damage quickly and at relatively low cost. This would represent a significant advantage over other methods being considered such as ultrasound inspection. Furthermore, our technique of using heat to reveal internal damage in composites is the only one that is capable of inspecting a large area at once, which represents another advantage over other methods. This is possible because the method utilizes a thermal-imaging camera to view the entire inspection area, as opposed to the need to sequentially scan the same area, such as necessary with ultrasound.

High performance composites require sophisticated techniques and specialized equipment for their manufacture. Fortunately, the Mechanical Engineering Department at California Polytechnic State University (Cal Poly) has both the facilities and the expertise for this. Dr. Joe Mello, Professor of Mechanical Engineering, has extensive experience with composites manufacturing and is a co-PI on this project. Furthermore, the Composites Laboratory (Building 192-135) has the needed equipment and materials to produce finished samples for testing. (The needed raw materials for producing finished test specimens have been donated by various companies.) The Composites Laboratory is also able to conduct material testing using tension and torsion testers to measure the strength of the samples produced.

### **3. Background/prior work**

Sonic IR (infrared) is a relatively new thermal-based, nondestructive evaluation (NDE) method described by Thomas and colleagues in 2000 [iii, iv]. The method was based on original research by Mignogna et al. [v] in 1981. This thermal NDE method is unique compared to other thermal methods since the active energy source is not a heat source, but a sonic one. This method utilizes an ultrasonic gun, commercially available and designed for welding plastics, which vibrates at a frequency of 20 or 40 kHz and can deliver acoustical power up to 1 kW. The gun is made up of a piezoelectric stack coupled to a catenoidal horn. The horn tip makes direct contact with the component being inspected. A short burst of high power acoustical energy, which manifests as mechanical vibration of the horn, is 'injected' into the component and various types of defects such as cracks and corrosion patches heat up due to frictional heating from the induced vibrations. The slight increase in temperature – as low as 0.5°C – at the defect sites is detected using a thermal imaging camera that operates in the infrared portion of the electromagnetic spectrum (hence the name 'sonic IR'). This inspection technique is very fast, taking only a few seconds for the entire inspection process. It is also relatively simple in terms of hardware setup and software requirements. Both of these features represent major advances over the aviation-industry's standard technique of fluorescent dye penetrant inspection, which also has serious environmental and health impacts and are prone to inspector errors [vi].

Figure 1 below shows a typical image from a sonic IR inspection of an aluminum test specimen in which a crack has been synthesized under controlled conditions. Note that the crack is not visible to the naked eye under visual inspection (because of its size and

its tightness) and that the image being viewed represents a 'temperature map' of the specimen surface. The heating arises from the frictional heating due to vibrations, and the maximum temperature rise in this example is only 9°C. In CFRP composite sandwich panels that are the focus of this project, heating will be generated by the induced vibrations *within* the sandwich layers, and the heat will then conduct to the outer surface that is monitored by the thermal-imaging camera.

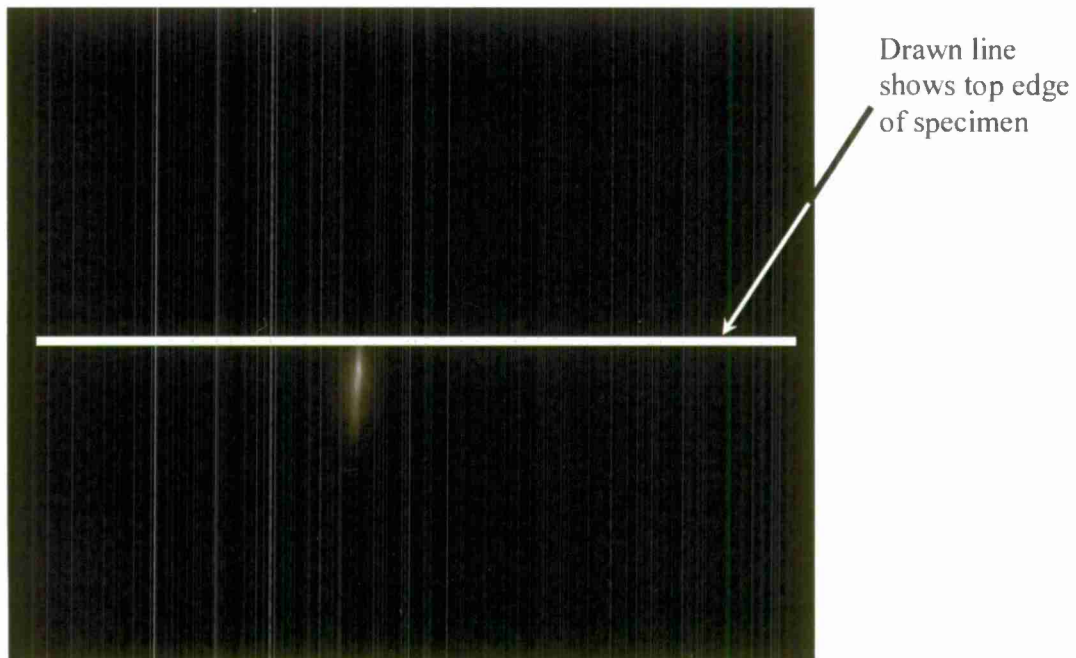


Fig. 1: Typical image from the thermal-imaging camera viewing an aluminum test specimen with a 12-mm long crack. The crack is made visible due to frictional heating. The drawn line in the figure indicates the top edge of the specimen.

Figure 2 below shows the typical sonic IR setup. Only two major components are required: an ultrasonic gun and an infrared camera (not shown in Fig. 2). Supporting components include a computer for the camera control and image acquisition, various parts to support the gun and bring it into contact with the part, and a rigid part holder. We possess all of the necessary equipment to conduct sonic IR experiments and have extensive experience with the technique [vii, viii], although this project is our first experience in applying sonic IR to CFRP composites.

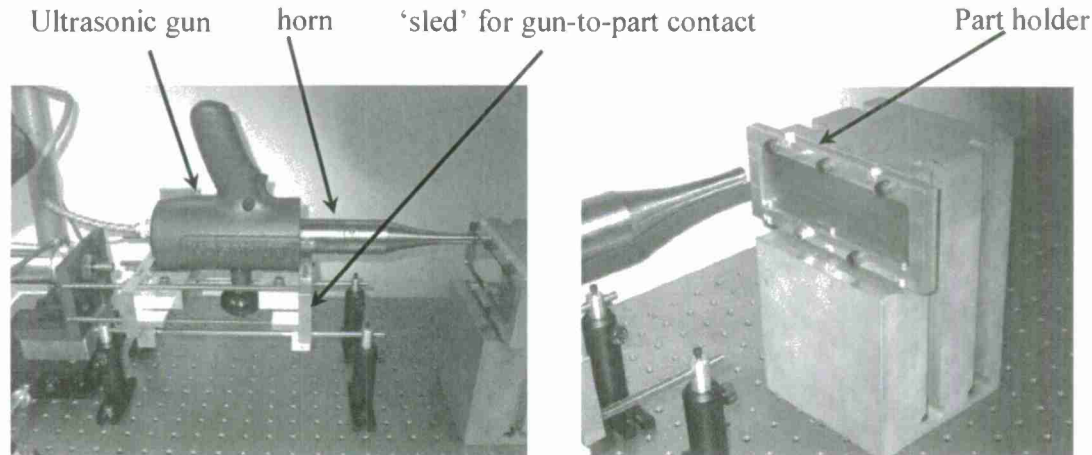


Fig. 2: (left) Photograph showing a typical sonic IR setup. (right) View of the part holder and the horn tip.

#### 4. Discussion of Results

##### A. Sample Manufacture

Two types of CFRP, preimpregnated with an uncured resin (forming what is commonly known as “prepreg”), were the main focus of this study. One type was formed of unidirectional fibers while the other was formed of fiber bundles weaved into a “cloth.” The unidirectional-fiber CFRP was laid up in a quasi-isotropic fashion to form either a 8- or 12-layer final sample for final testing. The weaved cloth was laid up with either the weaves of each layer lined up together or oriented  $45^\circ$  off from the previous layer in a quasi-isotropic fashion. In either case, the raw starting materials were cured in an autoclave to form the final test samples.

##### B. Creation of Impact Damaged Samples and Simulated Delaminations

Figure 3 below shows the Dynatup 8250, which was used to impart controlled impact damage to the CFRP samples. The machine consists of a known mass that traveled vertically on two rails. The mass was raised to a specified height before being dropped onto a sample held by a pneumatically actuated sample holder. The instrumentation included a calibrated load sensor in the impactor head to record the force-time history, and a system for measuring the mass’s speed just prior to impact to determine the energy of the impact.



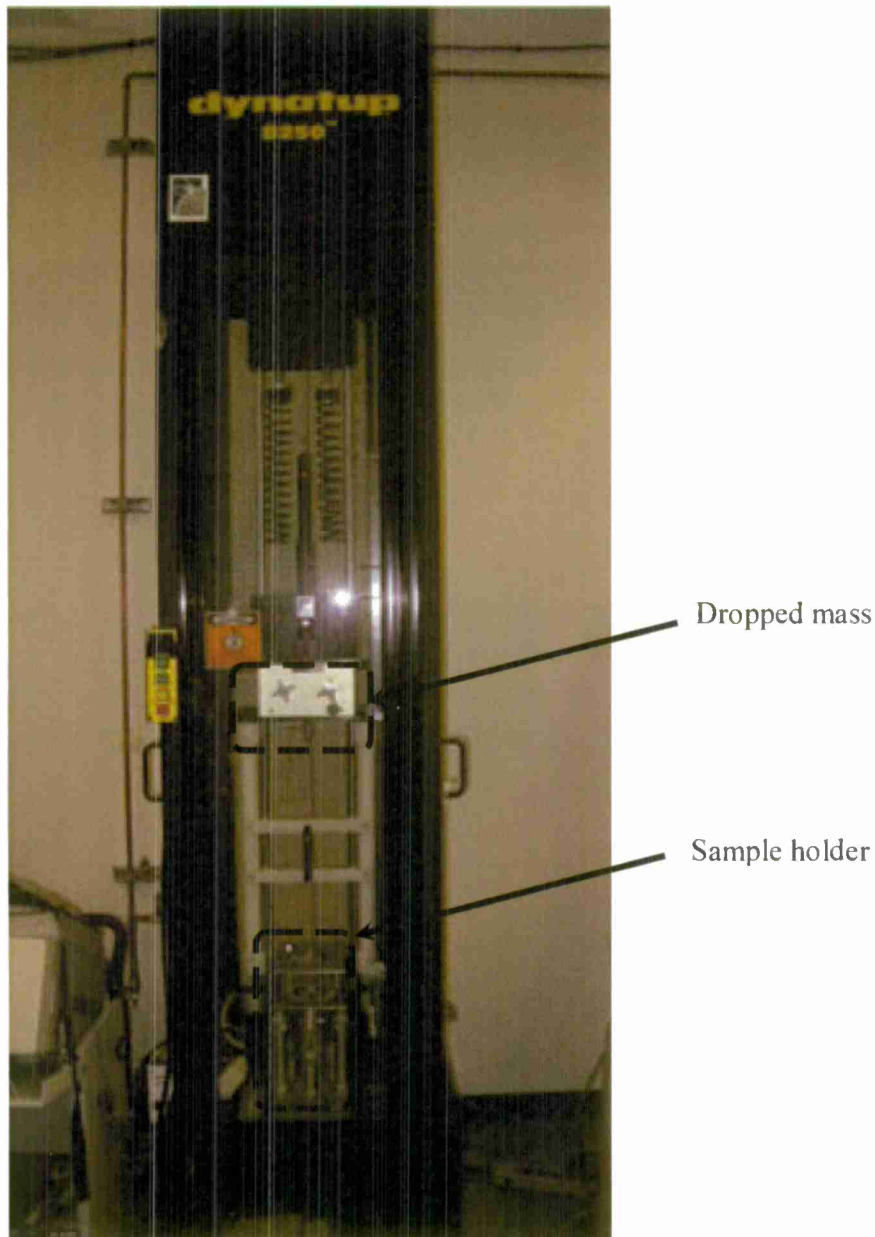


Fig. 3: Photograph of the Dynatup 8250, used to impart controlled impact damage on the samples.

It is well established that impacted CFRP sustain multiple damages, including fiber breakage, delamination, commonly multiple ones, between the laminae of the materials, and matrix cracking that often bridge the delaminations. Since delaminations are the major result of impact damage and could also be a manufacturing defect, we decided to create samples with artificial delaminations for study.

Typically, in studies with laminated composites, artificial delaminations are created by inserting a small patch of thin Teflon between two layers of material. The sample is then cured as usual, but since the resin does not bond to the Teflon, it is thought that the two carbon fiber/resin-Teflon interfaces do not adhere and therefore represents a good proxy for a real delamination. We examine this hypothesis by creating a series of different delaminations, as described later in this report, and conclude that how the artificial delamination is created has a strong effect on the test results, at least for the specific inspection technique used in this study. We strongly believe, however, that it will also affect other thermal-based nondestructive inspection techniques. Our experience in creating artificial delaminations led to the major breakthrough of this project: the development of a novel process to create an artificial delamination that closely resembles an actual delamination. We are currently seeking a patent for this invention, as described in the attachment of invention disclosure.

### C. Test Results

The experiment as shown in Fig. 2 was slightly modified for testing CFRP samples in this project. The part holder was replaced with a stainless steel frame designed specifically to support flat CFRP panels of the sizes and shapes of this project. We describe here the results obtained for impact-damaged samples and for samples containing artificial delaminations.

#### **1. Impact damage**

Figure 4 shows a unidirectional CFRP sample with a 1.0-J impact damage. Figure 4(a) shows the sample on the impact side. Figure 4(b) shows the opposite surface of the sample; note that the texture seen on this surface results from the release film on which the sample is placed during the curing process. Finally, Fig. 4(c) shows a close-up view of Fig. 4(b).

It is clear from Fig. 4(a) that, even for this relatively low-energy impact, a dimple and fiber breakage (perpendicular to the fiber direction) on the surface are visible on the impacted surface. On the opposite surface, Fig. 4(b), the damage is less obvious but a slight bump can be seen. Closer inspection of this site (Fig. 4(c)) reveals that there is fiber breakage across the strands.

Figure 5 shows select frames from a sonic IR test of the above sample. The ultrasonic horn tip is just visible on the left side of the image, and the white rectangular shape is a piece of tape used as a buffer between the horn tip and sample. It is seen that sonic IR can easily identify the damage site and the fiber breaks on either surface, although because the damage on the opposite (non-impact) surface is usually more severe, it is usually more easily identified. In practice, however, the CFRP application may be such that the non-impacted surface is interior to a structure and may not be accessible for inspection. Figure 5(c), which is a frame shot from late in the video sequence, shows an oval-shaped area that may be caused by a subsurface delamination. Since delaminations result in subsurface heat generation, it takes a longer time for this heat to diffuse to the

surface to be detected, and this is consistent with the late appearance of the image in Fig. 5(c).

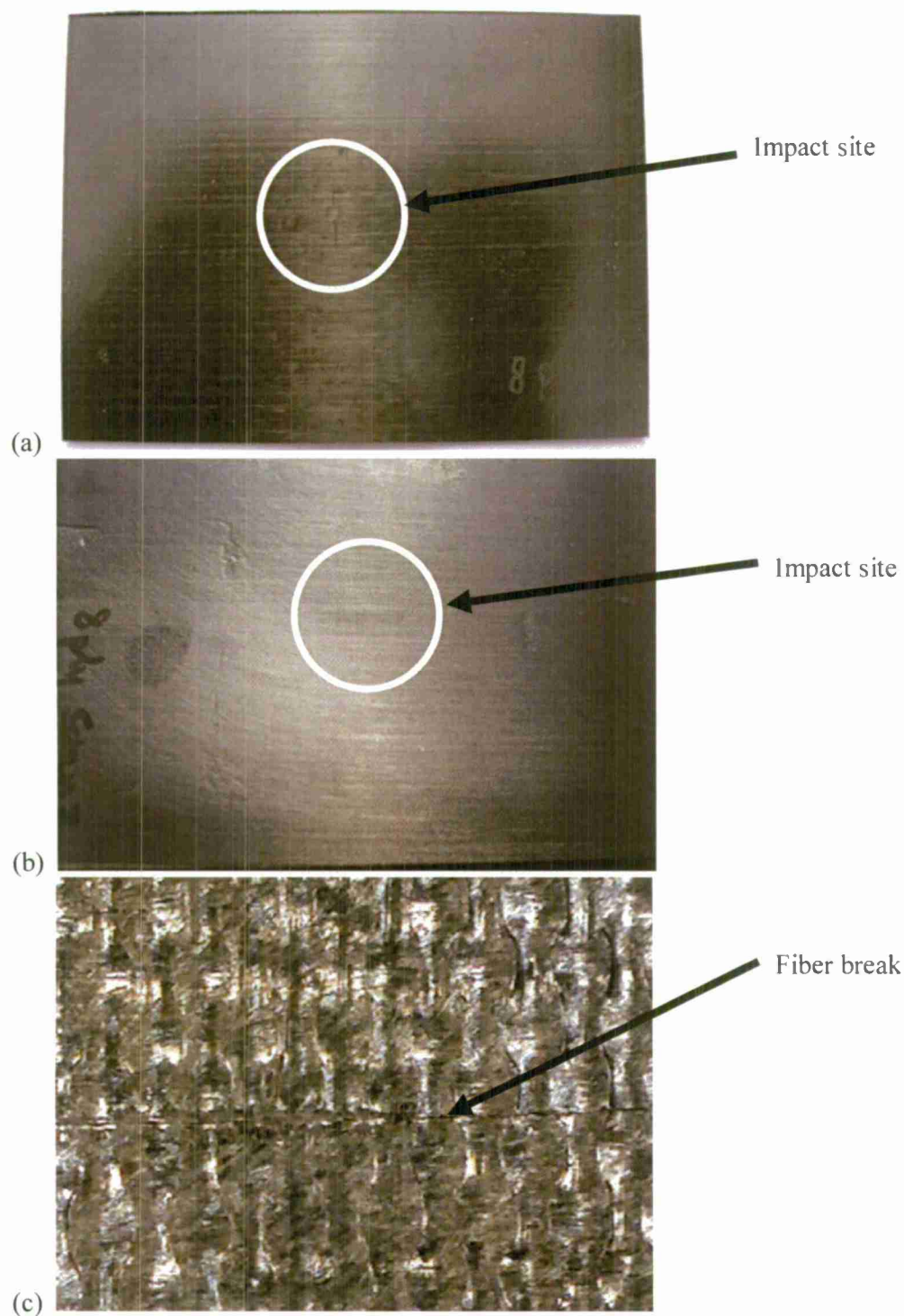


Fig. 4: 8-ply unidirectional quasi-isotropic sample, 2.4-mm thick, 1.0-J impact. (a) Impact surface; (b) opposite surface; (c) close-up of opposite surface.



Fig. 5: Frames from video sequence of sonic IR tests. (a) Frame from early in the test of the impacted surface; (b) frame from early in the test of the non-impacted surface; and (c) frame late in the video of the impacted surface, showing a possible delamination.



Figure 6 shows an 8-ply, 1.6-mm thick, weaved-cloth CFRP sample with a  $0^{\circ}/45^{\circ}$  layup. It was impacted at an energy of 0.76 J, and is a good example of the difficulty of inspecting CFRP for impact damage. Figure 6(a) shows the impact side of the sample, and the impact site is very difficult to locate by visible and tactile inspection. Even a close-up visual inspection (Fig. 6(b)) is difficult for identifying the impact site and there is no visible fiber breakage. The non-impact side, Fig. 6(c), does show fiber breakage and a slight bump.

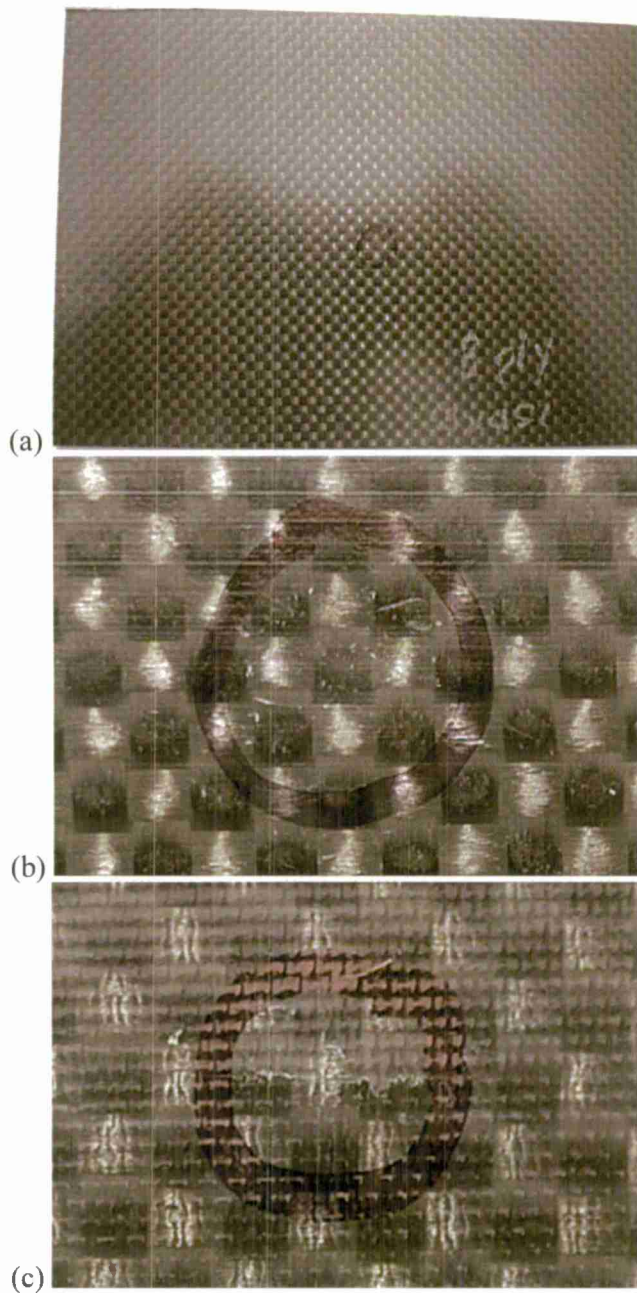


Fig. 6: Impact damage of a weaved-cloth sample, with ink mark highlighting impact site. (a) Impacted side; (b) close-up image of impact site; and (c) non-impact side.



Figure 7(a) is a video frame from early in the sonic IR test, and it shows that there is no surface damage (e.g., fiber breakage). A frame from late in the same test (Fig. 7(b)), however, shows clearly that there is a subsurface delamination, most likely close to the impacted surface. Finally, the more severe damage incurred on the non-impacted side of the sample is easily detected by sonic IR (Fig. 7(c)).

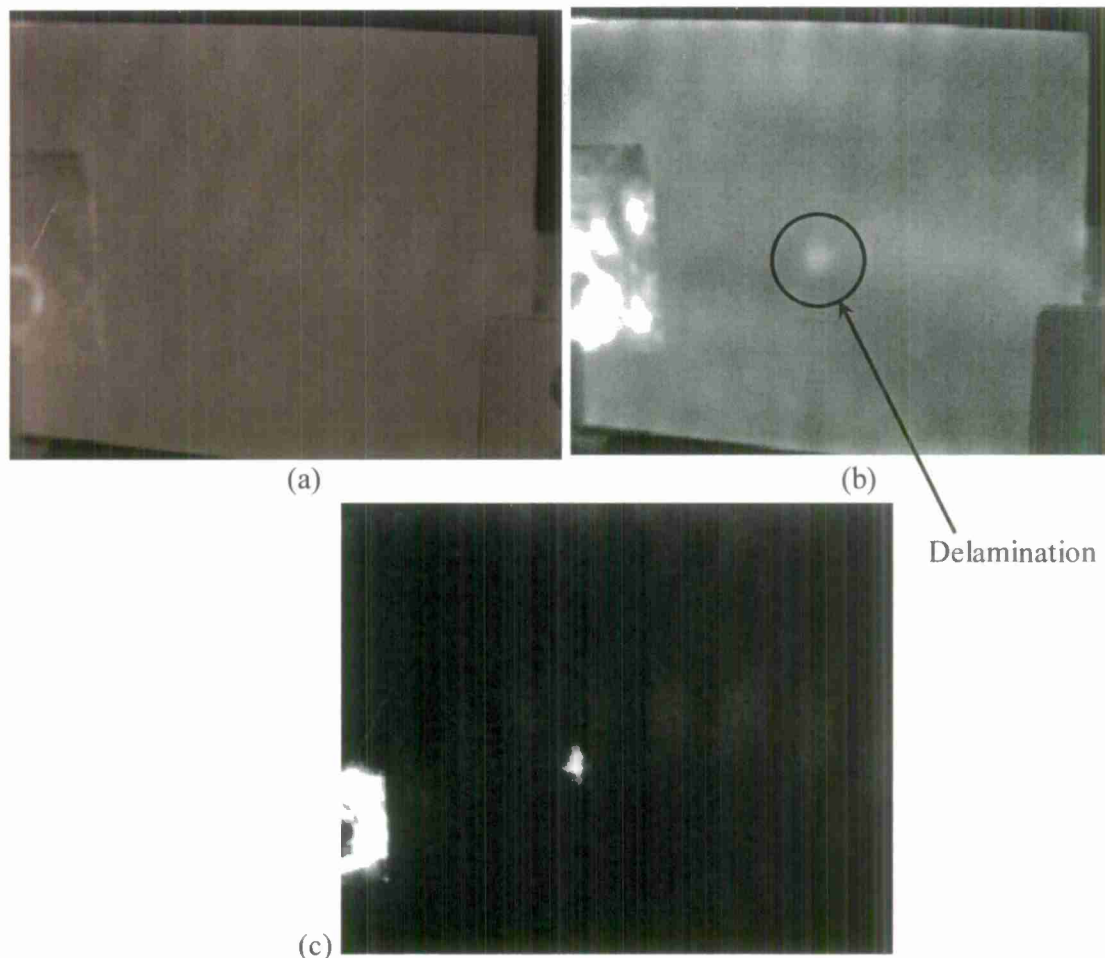


Fig. 7: Frame shots from two sonic IR tests looking at the impact side of the sample. Fig. 7(a) is early in test and 7(b) is late during test, and 7(c) the non-impact side.

## 2. Artificial delaminations

In nearly all previous studies to examine the efficacy of a nondestructive inspection technique in finding delaminations, the defect was created by the inclusion of a thin Teflon insert in between two plies of the laminated composite. While this serves adequately as a proxy for a delamination with certain nondestructive inspection techniques, such as x-ray or ultrasound, this method is suspect for thermal-based techniques such as sonic IR for two reasons. First, sonic IR relies on the diffusion of the internally generated heat from the sample interior to the inspected exterior surface, so any artificial delamination that affects the heat transfer characteristics of the sample will

likely affect its response to sonic IR. Certainly the heat transfer characteristics of a Teflon insert will be very different from an actual delamination, in which two plies of a multi-ply laminate become debonded and a contact resistance is created. The second reason for the unsuitability of a Teflon insert as an artificial delamination is due to the likely mechanism of heat generation in sonic IR. In prior studies of the heat-generation mechanisms in fiber-based laminated composites [ix, x], it was surmised that plastic deformation around the defect is the main cause of heat generation. This is in contrast to cracks and corrosion in metallic components, in which friction due to relative motion is the main heat-generation mechanism [xi].

In this part of the project, we created a variety of artificial delaminations and compared the results of sonic IR testing with each sample type. Specifically, we created traditional, Teflon-insert delaminations, stainless steel-insert delamination, and what we call an air-gap delamination.

Figure 8 below shows two frames from a video sequence of a sonic IR test using Teflon inserts in a 12-ply, 3.5 mm-thick, unidirectional CFRP panel in a quasi-isotropic layup. The samples were 25 mm-wide by 125 mm-long, and each included a 0.051 mm-thick Teflon insert. In Fig. 8(a), the insert is between the 2<sup>nd</sup> and 3<sup>rd</sup> plies of the sample while in Fig. 8(b) it is between the 4<sup>th</sup> and 5<sup>th</sup> plies. The ultrasonic horn tip is at the left in each image, making contact with the sample through a buffer material.

Figure 8 clearly shows that the insert closer to the inspected surface produces a higher contrast image and is therefore more readily detectable. In order to quantify this difference in detectability, we developed a code to first determine an area of analysis defined as the area within the image that is at a signal value of 50% of the maximum signal. This area is shown in Fig. 8(c) by the black-lined oval. The average pixel value within this area of analysis is then calculated for each sample using the video frame corresponding to the maximum heating for the sample. The results comparing the signal levels measured for a Teflon insert located at various depths within an otherwise identical CFRP samples are shown in Fig. 9.

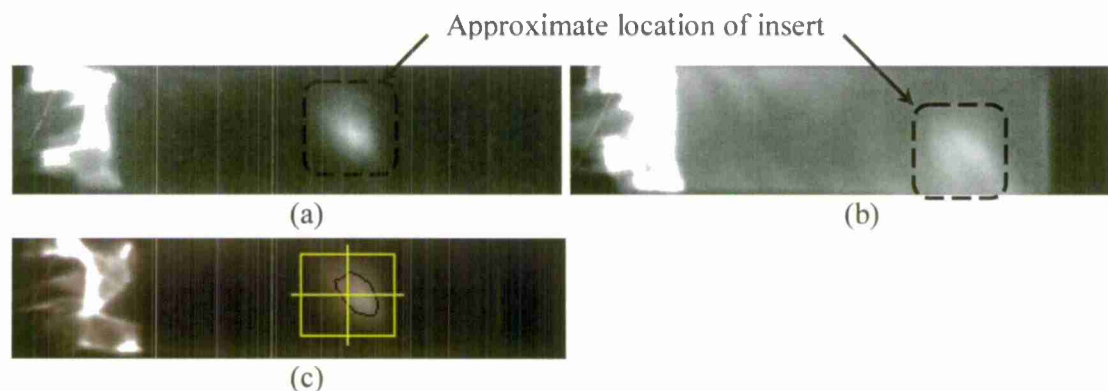


Fig. 8: CFRP samples with Teflon inserts between the (a) 2<sup>nd</sup> and 3<sup>rd</sup> plies, and (b) 4<sup>th</sup> and 5<sup>th</sup> plies. (c) Image of the sample from (a) after segmentation algorithm is applied, showing the area of analysis used to calculate an “average pixel value” for comparison between samples.

Figure 9 shows clearly that a Teflon insert located closer to the inspected surface is more readily detected, as expected, since the heat generated diffuses to the surface with less loss due to lateral diffusion. Figure 9 represents repeated tests of three samples, each with the insert at a different depth. Each sample was loaded into the experiment, tested, unloaded, and then the process was repeated for subsequent tests. Generally, the signals are reproducible from run to run, with the exception of the sample with the insert between the 2<sup>nd</sup> and 3<sup>rd</sup> plies. We cannot explain its large test-to-test variance compared with the other samples at this point.

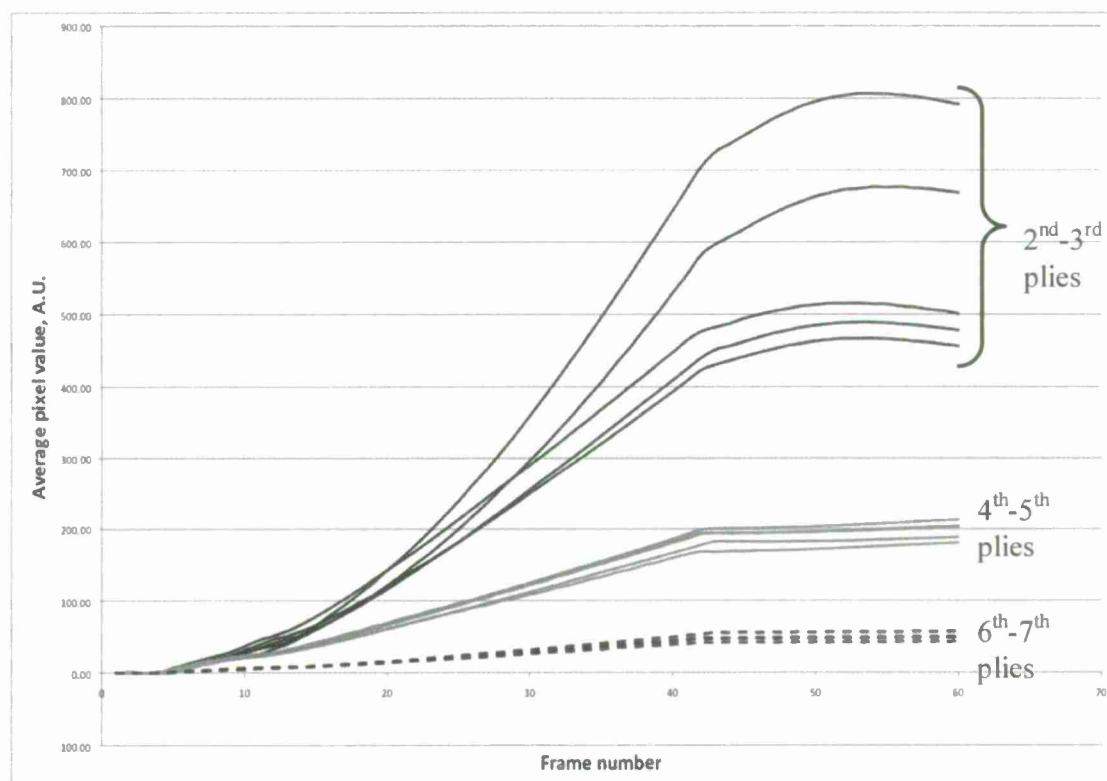


Fig. 9: Tests comparing signal levels measured for 12.5 mm square Teflon inserts located at different depths within a CFRP sample.

Figure 10 shows the results from testing with different sizes of Teflon inserts implanted between the 2<sup>nd</sup> and 3<sup>rd</sup> plies. While the inserts used in Fig. 9 were nominally 12.5 mm squares, the samples here were varied to determine the effect of this parameter on the detectability of the defects. The figure shows that interestingly the largest insert does not lead to the highest signal levels, which suggests that the heat generation in this case is not due solely to plastic deformation around the periphery of the defect, but that one or more other mechanisms may be at play.

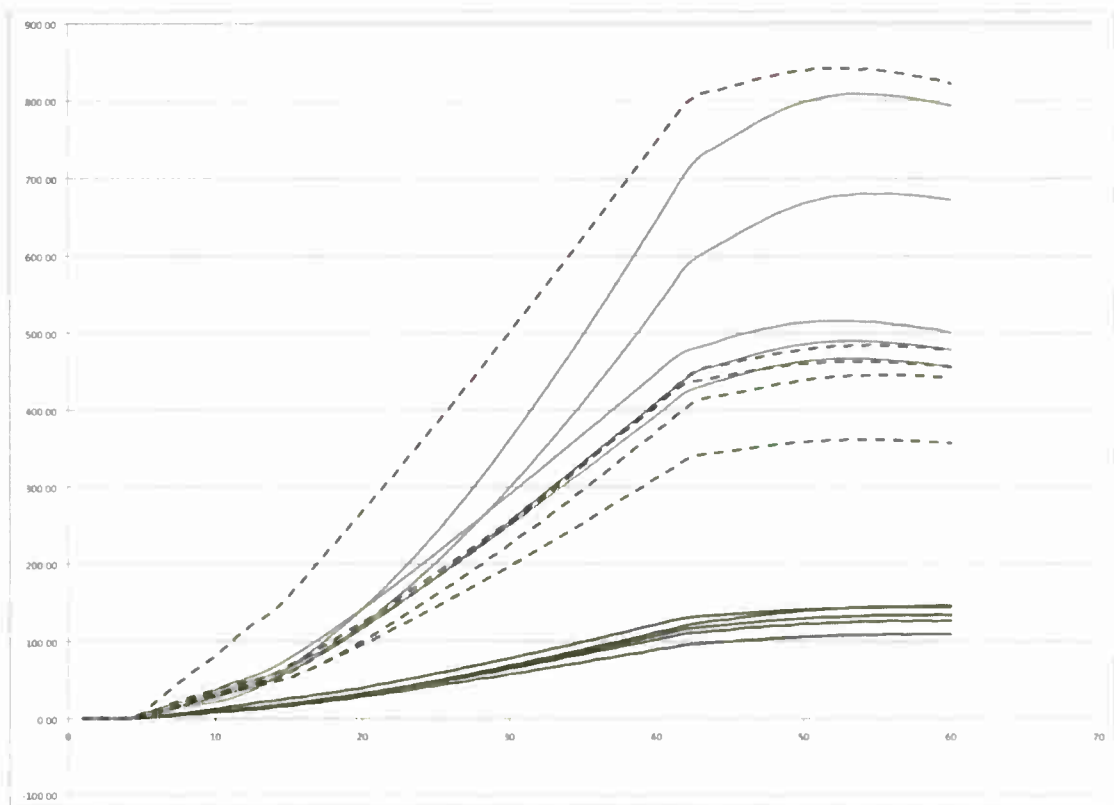


Fig. 10: Repeated tests to determine the effect of the Teflon insert size on average signal value. The light solid lines correspond to an insert of 12.5 mm square, the dashed lines correspond to 18.8 mm square, and the black solid lines correspond to 6.25 mm square.

Finally, we looked into alternative means of creating artificial delaminations in CFRP samples. First, we created delaminations by replacing the Teflon insert with one made from stainless steel of the same thickness (Fig. 11(a)). In a second method, an air gap was created by pulling out the stainless steel insert after inserting it and curing the sample as usual (Fig. 11(b)). We then tested these two samples and compared the results with the Teflon insert (Fig. 12).

The results shown in Fig. 12 demonstrate clearly that the nature of the delamination strongly influences the efficacy of the sonic IR test in a complicated way. The Teflon insert shows a 30% increase in peak signal level over the stainless steel insert, which in turn shows a 30% increase in peak signal level over the air gap sample. These results led us to the conclusion that there is a need to create a more realistic proxy for actual delaminations in CFRP samples. A major part of the effort in the final months of this project was dedicated to finding a means to create this artificial delamination, and we believe we have succeeded. As described earlier, we are currently in the process of filing a U.S. patent for the process.

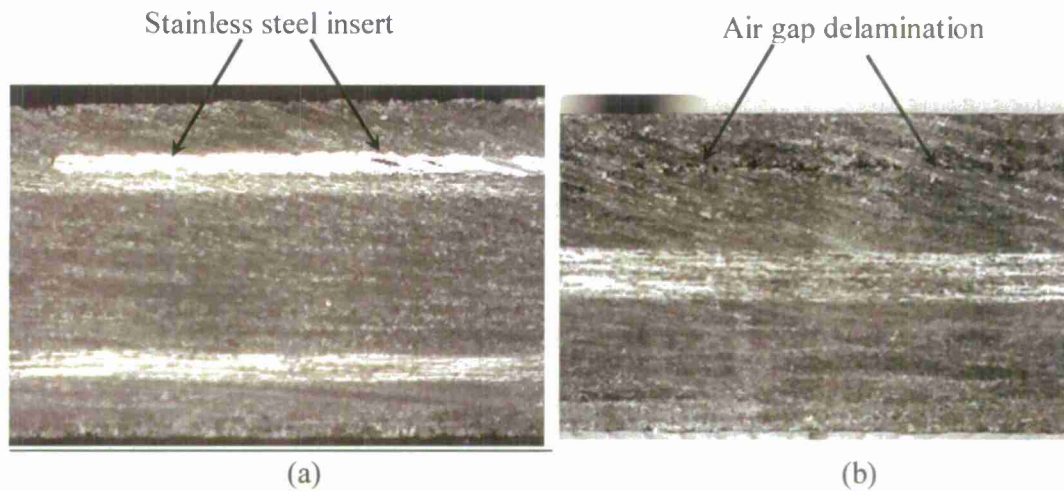


Fig. 11: Artificial delaminations created by using a stainless steel insert (a), and an air gap created by pulling out a stainless steel insert after manufacture.

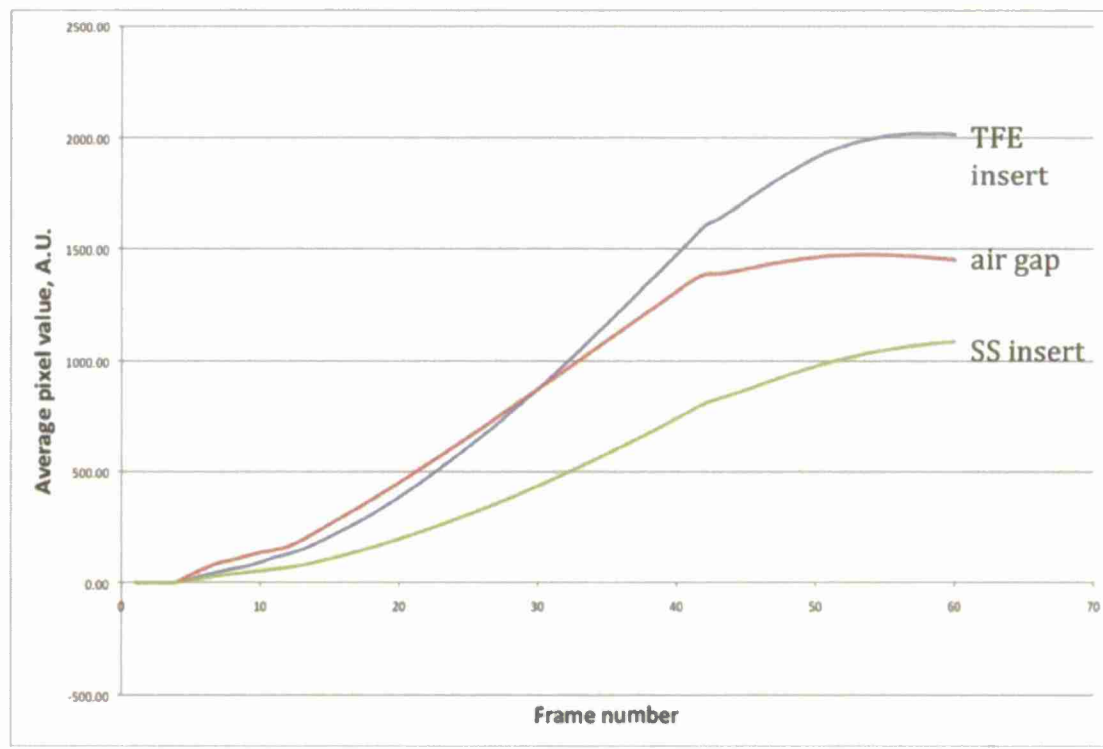


Fig. 12: Test results comparing various artificial delaminations.

#### D. Conference Presentations and Publication

This project has resulted in three conference presentations [xii, xiii, xiv] and one conference publication [xiv]. Please note that the conference referenced in [xiv] takes place in May 2013.



## 5. Future Work Planned

In the short term, we have begun the process of applying for a U.S. patent for the process (developed through this project) of creating artificial delaminations in CFRP and other laminated composite materials. This patent is described in a separate attachment to this report. In addition, we are preparing a journal publication to describe the findings from this project and to compare the results with other thermal-based nondestructive inspection techniques such as lock-in thermography, and pulse-heating thermography. We expect this to be completed and submitted for review in early 2013.

Based on the encouraging results of this project, we will seek additional funding through research grants or contracts for future projects to further develop sonic IR as an inspection tool for CFRP composites. We envision a future project to investigate the fundamental mechanisms of heat generation in CFRP, as this is currently poorly understood, and a second project to focus on developing an inspection instrument that can be put into field use. For the latter project, we will seek industry partners, such as a CFRP end user or a CFRP manufacturer, for collaboration.

## 6. References cited

- i. Norris, G., Thomas, G., Wagner, M. and Forbes Smith, C. , "Boeing 787 Dreamliner - Flying Redefined," *Aerospace Technical Publications International*, 2005.
- ii. <http://www.boeing.com/commercial/787family/background.html>, accessed Nov. 29, 2012.
- iii. L.D Favro, X. Han, Z. Ouyang, G. Sun, H. Sui, and R.L. Thomas "Infrared imaging of defects heated by a sonic pulse", *Review of Scientific Instruments*, Vol. 71, pp. 2418-2421, June 2000.
- iv. R.L. Thomas, L.D. Favro, X. Han, Z. Ouyang, H. Sui, G. Sun, *Infrared Imaging of Ultrasonically Excited Subsurface Defects in Materials*. U.S. Patent 6,236,049. May 22, 2001.
- v. R.B. Mignogna, R.E. Green, J.C. Duke, E.G. Henneke, and K.L. Reifsnider, "Thermographic investigation of high-power ultrasonic heating in materials," *Ultrasonics*, Vol. 19, pp. 159-163, 1981.
- vi. D. Galella (private communication), Inspection Systems R&D, FAA William J. Hughes Technical Center, Airworthiness Assurance Branch, 2005.
- vii. J.C. Chen, J. Kephart, and W.T. Riddell, "A Parametric Study of Crack Propagation during Sonic IR Inspection," *Review of Quantitative Nondestructive Evaluation*, Vol. 25, D.O. Thompson and D.E. Chimenti, eds., American Institute of Physics, 2006.
- viii. Chen, J.C., Kephart, J., Lick, K., and Riddell, W., "Crack Growth Induced by Sonic IR Inspection," *Nondestructive Testing and Evaluation*, 22(2), 83-92, 2007.
- ix. Russell, S.S., "An Investigation of the Excitation Frequency Dependent Behavior of Fiber Reinforced Epoxy Composites during Vibrothermographic Inspection," Ph.D.

Dissertation, Virginia Polytechnic Institute and State University, Blacksburg, VA, USA, November 1982.

- x. Lin, S.S., "Frequency Dependent Heat Generation during Vibrothermographic Testing of Composite Materials," Ph.D. Dissertation, Virginia Polytechnic Institute and State University, Blacksburg, VA, USA, March 1987.
- xi. Renshaw, J., Chen, J.C., Holland, S.D., and Thompson, R.B., "The Sources of Heat Generation in Vibrothermography," *NDT&E International*, 44(8), 736-739 (2011).
- xii. Gomez, L., Valdez, R., Mello, J., and Chen, J., "Characterizing Impact Damage and Simulated Delamination in Carbon Fiber Composites using Sonic IR," ASNT 21<sup>st</sup> Annual Research Symposium and Spring Conference, Dallas, TX, USA, March 2012.
- xiii. Gomez, L., Valdez, R., Ng, C., Mello, J., and Chen, J., "Evaluation of Vibrothermography for Impact Damage and Delamination in Carbon Fiber Composites," Review of Progress in Quantitative Nondestructive Evaluation, Denver, CO, USA, July 2012.
- xiv. Gomez, L., Valdez, R., Ng, C., Botello, R., Mello, J., and Chen, J., "A Comparison of Vibrothermography and Lock-In Thermography for Assessing Defects in CFRP," SAMPE 2013 Conference, Long Beach, CA, USA, May 2013.

**1.08 Micron and 1.3 Micron Sampled Grating Distributed Bragg Reflector (SGDBR) lasers for Optical Coherence Tomography (OCT), LADAR, and Sensing Applications**

Project Subtitle:

**Long Coherence Length and Linear Sweep without an External Optical K-Clock in a Monolithic Semiconductor Laser for Inexpensive Optical Coherence Tomography**

Principal Investigator:

**Dennis Derickson, Ph.D., Electrical Engineering**

Co-Investigators:

**Chris Chiccone and Manuel Velasco, Graduate Students**

California Polytechnic State University  
San Luis Obispo, CA

## 1. ABSTRACT

We demonstrate a new swept-wavelength laser for optical coherence tomography using a monolithic semiconductor device with no moving parts. The laser is based on a Vernier-Tuned Distributed Bragg Reflector (VTDBR) structure. We show highly-linear sweeps at 200 kHz sweep repetition rates, with peak output power of 20 mW. Using a test interferometer, we demonstrate point-spread functions with 45-55 dB dynamic range. The source provides long coherence length ( $> 40\text{mm}$ ) at up to 200 kHz sweep rates. The laser system has sufficient linearity in optical frequency and stability over time to provide an electronic sample trigger clock (an Electronic K-Clock) that denotes equal optical frequency intervals during the sweep. The laser tuning mechanism is all-electronic, easily adjustable and programmable. We demonstrate both flat and Gaussian power vs. wavelength profiles, programmable sweep rates with the same device, and an adjustable duty cycle of up to 85% at full speed. Because the laser is a monolithic semiconductor structure based on reliable, wafer-scale processes, the manufacturing cost of the laser will decrease rapidly in volume production.

**Keywords:** Distributed Bragg reflector diode lasers, swept laser, tunable laser, optical coherence tomography, OCT, swept-source OCT, SS-OCT, VT-DBR, OFDR.

## 2. PROJECT SIGNIFICANCE / BACKGROUND / PRIOR WORK

One of the ongoing challenges facing commercial development of OCT is the development of affordable yet high-performance swept wavelength sources [1]. Monolithic semiconductor tunable lasers based on Distributed Bragg Reflector (DBR) structures are strong candidates. Previous work demonstrated that the coherence length and tuning range of DBR tunable lasers are very attractive for Optical Frequency Domain Reflectometry (OFDR) and OCT [2], [3], including OCT dental imaging [4]. In our previous work, we showed that a single-chip Distributed Bragg Reflector (DBR) wavelength-tunable laser is capable of 100 kHz repetition rate, continuous wavelength ramps that may be made linear in time [5]. We also demonstrated that two DBR laser devices may be concatenated together in a high-speed sweep that spans 100nm [6]. Additionally, monolithic laser structures are robust, stable and inexpensive to produce in volume with wafer-scale fabrication. OCT is basically FM-CW radar applied to biomedical applications. The experimental results described in this report are also applicable to Light Detection and Ranging applications.

In the present work we demonstrate several properties of a VTDBR-based tunable laser that can provide important features for laboratory and commercial OCT systems. First, we show that the sweep of a VTDBR laser may be used to produce a high-quality point spread function at sweep rates up to 200 kHz, based upon a novel electronic clocking scheme unique to the VTDBR laser. Second, we illustrate the flexibility and programmability of these sources by demonstrating a device that produces both flat and Gaussian power spectral profiles, at adjustable scan rates of a few microHz up to 100's of kHz. Third, we demonstrate that the single-longitudinal mode operation of the VTDBR laser provides a long coherence length that is useful for OCT applications.

### 3. DESCRIPTION OF THE EXPERIMENTS

For the experiments reported here, we used two configurations ("alpha" and "beta") of the laser drive system to sweep the VTDBR lasers. In the early alpha configuration, we built upon the laser system described previously [5] using commercially available arbitrary waveform generators. A computer programs the current waveform generators (CWGs) that drive the control currents in the VTDBR source (Figure 1). Spectral calibration of the drive currents to optical frequency (using an Optical Spectrum Analyzer, not shown), produces tunable light emission with a linear sweep of optical frequency versus time. Light from the laser is connected to a 1x2 fiber optic coupler that divides the light between a power-monitoring photodiode and a fiber Mach-Zehnder interferometer (MZI). Optical interference at the output of the MZI is detected with a balanced detector (Thor Labs PDB 430C). The analog signal from the detector is acquired by a 10 MS/sec analog-to-digital converter card (National Instruments PCI-6115). The acquisition is triggered by the Electronic K-Clock signal: a digital clock signal generated by a waveform generator that is synchronized with the sweep of the VTDBR.

In the alpha configuration, through a manual calibration of the Electronic K-Clock to optical frequency, clock edges occur at time points in the sweep that are separated by equal intervals of optical frequency. Interference fringe data collected by the ADC are Fourier Transformed in the computer for generation of the point-spread function (PSF). We demonstrate in these experiments, the fidelity of this clocking scheme is accurate and stable over multi-hour time periods.

The alpha configuration has limitations. First, the calibration and optimization of the sweep and Electronic K-Clock is performed manually by a skilled operator. Second, in this particular alpha test configuration the relatively low bandwidth of the CWGs and of the data acquisition system limit the maximum sweep repetition rates with the Electronic K-Clock to less than 200Hz.

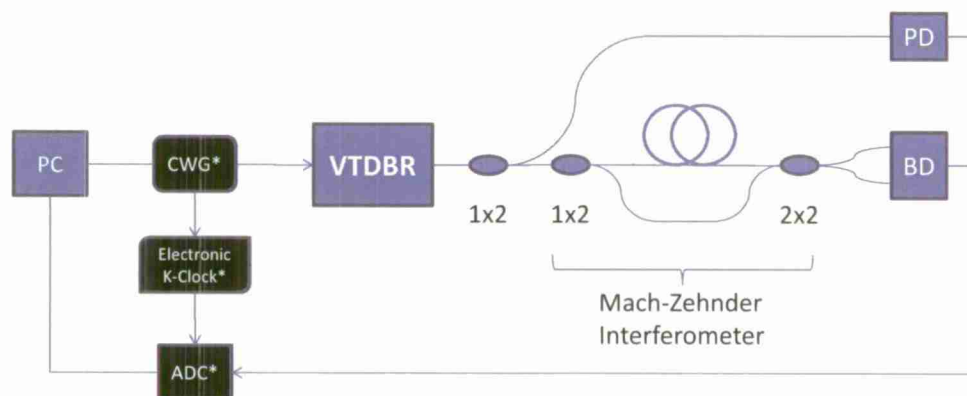


Figure 1: Schematic of the experiment. PC = computer, CWG = current waveform generator, ADC = analog-to-digital converter card, VTDBR = Vernier-Tuned DBR laser, PD = photodiode, BD = balanced detector. Items marked with \* indicate changes between the alpha and beta configurations.



To overcome limitations of the alpha configuration, we improved the CWGs and data acquisition systems in a second beta configuration. In the beta configuration we customized the drive electronics to provide substantially greater drive bandwidths (clocked at 400 MS/sec) and using an AlazarTech 500 MS/sec analog-to-digital converter card (ATS9350). In addition, we codified the manual optimization of the alpha configuration into a systematic software algorithm for laser sweep optimization. This algorithm allows the user to adjust the laser current waveforms automatically for environmental factors such as temperature change; aging of the drive electronics or semiconductor device; and user adjustable variables that can alter the operating conditions of the semiconductor in the laser: sweep speed; changes in average output power and power vs. time profile.

For both alpha and beta configurations, we use either a "C" band laser covering a wavelength range of 1525 – 1565 nm or an "L" band laser covering a wavelength range of 1565 – 1615 nm. Our electrical drive architecture for the CWGs is independent of the wavelength range, and so the same electronics may drive VTDBR laser devices at other wavelengths of interest to OCT such as 1310 nm or 1060 nm.

#### 4A. RESULTS - MEASUREMENTS OF THE POINT SPREAD FUNCTION

Figure 2 shows the measurement of interference fringes from an all-fiber MZI using the C-band tunable laser in the alpha configuration. The free spectral range (FSR) of the MZI is 39 GHz and the frequency step of the Electronic K-Clock is set to 7.1 GHz. The sweep repetition rate is approximately 177 Hz. For simplicity, we operate only a single VTDBR chip, which can sweep approximately 50nm. Previously, we have demonstrated that we can concatenate two single-chip devices that span 100nm at high sweep repetition rate [6]. The sweep range of the laser in the alpha configuration is 47 nm. The duty cycle was variable, but typically set to 85%. As the laser tuning is entirely electrical, with no mechanical tuning mechanism, there is no delay time for flyback or resetting.

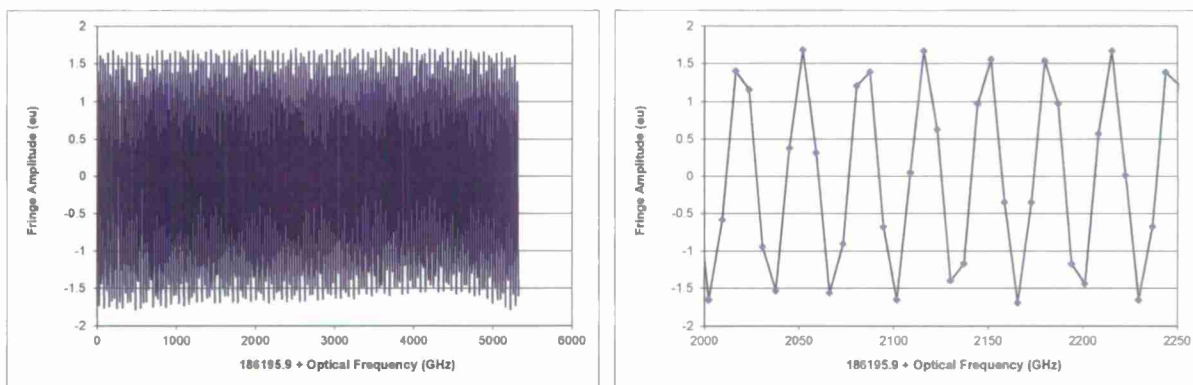


Figure 2: Fringes from the Mach-Zehnder interferometer versus optical frequency in the Alpha configuration. The right plot is a close-up of the fringes on the left.

Figure 2 also shows that we have flattened the power versus wavelength profile of the sweep. Prior to the MZI, we couple a small amount of light to another detector to measure the laser power. Using the Semiconductor Optical Amplifier (SOA) that is monolithically integrated into the laser, we apply an algorithm to adjust the power until it agrees with a target power value at each point of the sweep. Using this power-shaping algorithm we have produced flat profiles within 1% RMS of the target power level. Improvements to the current drive stability should further reduce the amplitude noise. The existing deviations from a flat fringe envelope are due to two reasons. First, the fringes are sparsely sampled, leading to small variations from fringe-to-fringe. Second, wavelength dependence of the split ratio of the coupler,

used to sample the power, appears in the MZI path. The SOA control of the output power in the VTDBR also enables programmatic control over customized power spectral profiles. We further explore this aspect using the Beta configuration.

The point spread function (PSF) of the fringes in Figure 2 is shown in Figure 3. The data were processed with a Blackman window prior to the Fourier transform, and all amplitudes are relative to the peak of the central feature. The dynamic range of the PSF is 45 dB from the peak to the pedestal near the primary feature, and 60 dB in the wings. Once the Electronic K-Clock is calibrated to the sweep, the PSF is repeatable and stable over hours of measurement. We observed that we can leave the system overnight, for approximately 12 hours, and still measure substantially similar PSF quality in the morning. Under normal operating conditions, the laser's sweep may be re-optimized more frequently as needed. The stability of the laser allows the re-optimization to be scheduled between periods of measurement required by a user.

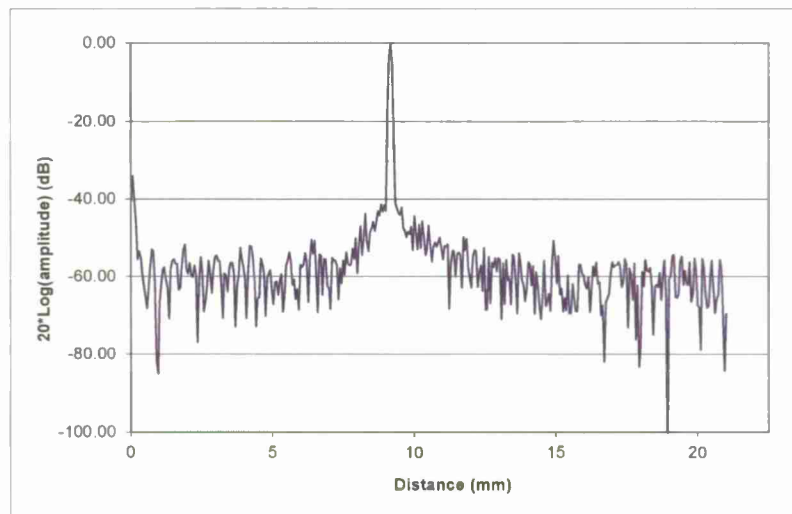


Figure 3: A typical PSF for a fiber Mach-Zehnder Interferometer (FSR = 39 GHz) sampled every 7.1GHz, at a sweep speed of 187 Hz using the Alpha drive configuration. The distance axis assumes refractive index = 1.

In the Beta configuration, we are able to sweep and acquire measurements over a range of substantially higher speeds, with programmatic control. A portion of a typical interferometer measurement, recorded at a 4 kHz sweep rate, is shown Figure 4. Although the data we show for the Beta configuration uses sweeps that are increasing in wavelength no performance difference is observed whether the sweeps are increasing or decreasing in wavelength. In Figure 5 we show PSFs for 4 kHz sweep repetition rate. To change between different sweep rates, a software command changes the laser current drive profile and an algorithm automatically re-optimizes the drive currents to linearize the sweep of optical frequency vs. time. At 4 kHz sweep rates, the algorithm is relatively robust and produces PSFs up to 50dB in dynamic range. As shown in Figure 5, artifacts observed at 0 and 14mm pathlength difference are believed to be due to electrical noise on the drive currents. After switching to 200 kHz, we note that the PSF height decreases and the width increases. We attribute the degradation in the PSF to the greater difficulty in linearizing the laser sweep at higher sweep rate, and synchronizing these steps with the Electronic K-Clock. Through a combination of lower noise, higher bandwidth electronics and more robust linearization algorithms, the sweep linearity and PSF quality can be substantially improved.

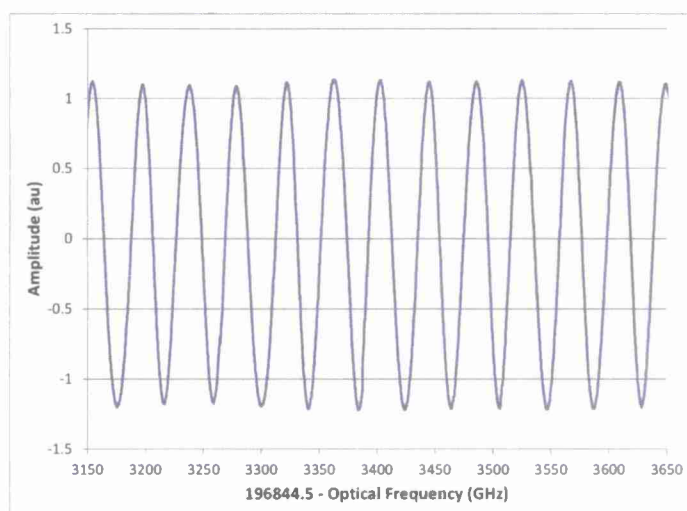


Figure 4: MZI fringes for a 4 kHz sweep

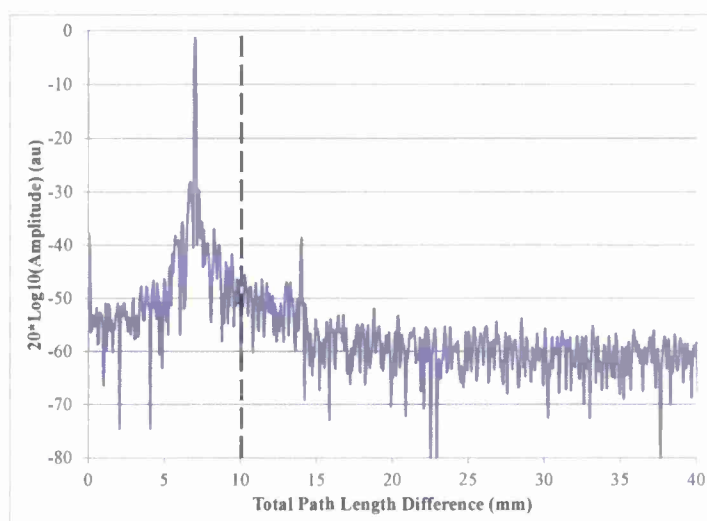


Figure 5: PSFs for a 4 kHz sweep rate of the laser using the Beta configuration. The dashed vertical line indicates a depth of 10mm, for reference.

The programmability of the VTDBR laser sweeps creates opportunities for controlling sweeps in unique ways, such as shaping the power vs. optical frequency profile. For example, in Figure 6 we show flat and Gaussian power spectral profile. The power spectral profile is switched between Gaussian and flat by toggling a software option and allowing the algorithm to adjust the currents to the internal SOA of the VTDBR. In both profiles we observe small transient errors in the amplitude, due to limitations in the electronics and the control algorithm. Improvements in electronics and in the power-shaping algorithm will further reduce the amplitude errors in the power profile.

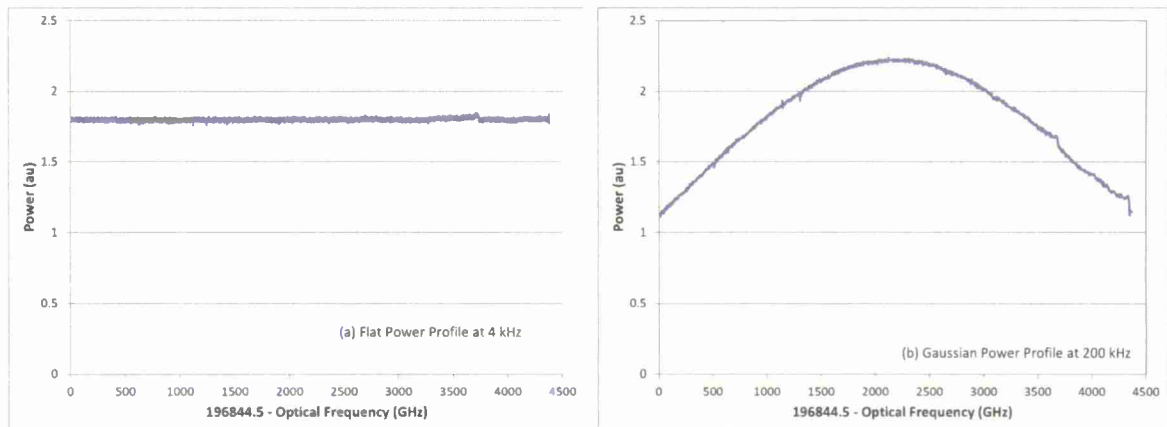


Figure 6: Power vs. Sweep Profiles for the VTDBR laser in the Beta configuration, with (a) flat profile swept at 4 kHz and (b) Gaussian profile at 200 kHz. The amplitude transients are due to small errors in the laser calibration for this device.

#### 4B. RESULTS - COHERENCE LENGTH MEASUREMENTS

Figure 7 shows coherence length measurements of the VTDBR laser swept at a repetition rate of 200kHz. We measured the instantaneous coherence length of the lasers using a Michelson interferometer with variable path length difference. By measuring the fringe amplitude vs. path length delay we determine the single-pass coherence length as where the fringe amplitude is reduced by 3dB. From the recorded data (Figure 7), the 3dB coherence length is at least 40mm. We believe this measurement is a lower limit, as the bandwidth of the photodetector limited the path length range of the measurement.

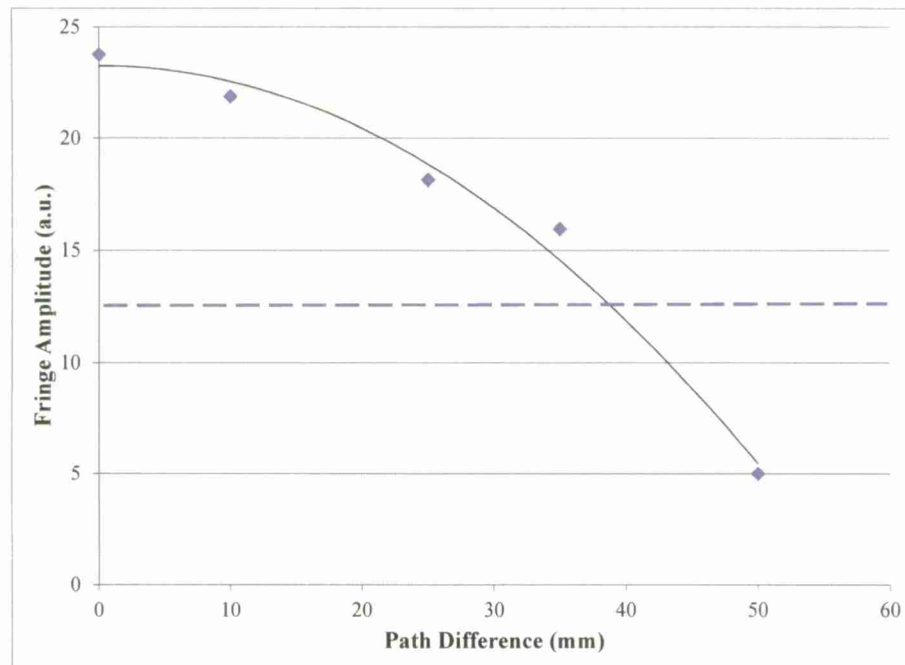


Figure 7: Fringe Amplitude vs. Variable Path Length Difference in a Michelson Interferometer at 200kHz. The curve is meant to guide the eye. The dashed line indicates the -3dB level, which is reached at approximately 40mm.



#### 4C. RESULTS - SUMMARY

In this work we have shown that VTDBR lasers can be configured to provide highly linear sweeps of optical frequency vs. time using calibrated current drive waveforms and a synchronized Electronic K-Clock to trigger data acquisition. The wavelength calibration and stability of the VTDBR lasers allow for repeatable PSFs for many hours of operation. The VTDBR laser is controlled and swept with programmable currents, enabling a flexible and adaptable platform for swept-source OCT. We have shown the ability to control the power vs. wavelength profile and adjust the scan rate easily with the same device. The fundamental single-mode operation of the laser also provides extremely long coherence lengths for OCT applications.

The VTDBR laser provides a versatile and cost-effective platform to integrate OCT measurements with the source [7]. An OCT source/measurement module comprises the laser, laser driver circuitry, detectors (e.g. dual-balanced), data acquisition, and computing/processing elements. An advantage of the VTDBR laser system is that the Electronic K-Clock obviates the need for separate k-clock hardware and software. A second advantage is that the VTDBR laser system already includes data acquisition hardware for laser sweep optimization. Since sweep optimization is performed infrequently, the same acquisition hardware may be dual-purposed as the data acquisition for the OCT system, considerably reducing the total cost of the OCT system. Additional balanced detection for the OCT measurement may be added at low cost using the low noise power supplies of the internal laser. Another potential cost savings could come from utilizing the integrated processing core of the VTDBR laser, allowing some OCT systems to eliminate the need for a separate data processor.

We are presently adapting the Beta laser system with the VTDBR into commercial units. The commercial system will improve the laser sweep optimization and the speed of the laser drive electronics, allowing elimination of transients in sweeps and improvement of the dynamic range and resolution of point-spread functions generated by the laser. The same InGaAs/InP semiconductor material system used to create the C-L band lasers is also being extended into the 1310 nm band, which is clinically-important for a number of OCT applications. We are also investigating VTDBR lasers centered at 1060 nm. The same drive electronics and control systems in this work will operate with 1310 nm and 1060 nm laser devices, thereby allowing us to build a laser capable of 100 nm sweeps centered at 1310 nm or 1060 nm, with long coherence lengths (40mm) at a sweep repetition rate of 200 kHz. As we enter the production of these devices, the semiconductor platform for the VTDBR laser will allow us to rapidly drive-down the cost these devices through wafer-scale fabrication. The performance and flexibility of the VTDBR laser can enable a wide range of OCT applications that are increasingly cost-sensitive.

#### 5. FUTURE WORK

The first 1310 nm VTBR lasers were received at Cal Poly in November 2012. They were fabricated by Freedom Photonics in Goleta, Ca. I have a new graduate student, Desmond Talkington who has started evaluation of these "fresh from the fab" devices. We will go through the same experimental sequence as shown in the earlier part of the report to contrast with our 1550 nm experiments. We will then need to start a robustness and reliability investigation on the 1300 nm VTBR lasers parts to make sure there are not any hidden issues with these parts as the group moves toward a commercial solution.



## 6. REFERENCES

---

- [1] Chinn, S. R., Swanson, E. A., and Fujimoto, H. G., "Optical coherence tomography using a frequency-tunable optical source," *Opt. Lett.* 22, 340-342 (1997).
- [2] Amano, T., Hiro-Oka, H., Choi, D., Furukawa, H., Kano, F., Takeda, M., Nakanishi, M., Shimizu, K., and Ohbayashi, K., "Optical frequency-domain reflectometry with a rapid wavelength-scanning superstructure-grating distributed Bragg reflector laser", *Applied Optics* 44(5), 808-816 (2005).
- [3] Fujiwara, N. Yoshimura, R. Kato, K. Ishii, H. Kano, F. Kawaguchi, Y. Kondo, Y. Ohbayashi, K. Oohashi, H., "140-nm Quasi Continuous Fast Sweep Using SSG-DBR Lasers", *Photonics Technology Letters*, 18, 1015-1017 (2008).
- [4] Kakuma, H., Ohbayashi, K. and Arakawa, Y., "Optical imaging of hard and soft dental tissues using discretely swept optical frequency domain reflectometry optical coherence tomography at wavelengths from 1560 to 1600 nm", *J. Biomedical Optics* 13(1), 0140121-0140126 (2008).
- [5] O'Connor, S., Bernacil, M. A. and Derickson, D., "Generation of High Speed, Linear Wavelength Sweeps Using Sampled Grating Distributed Bragg Reflector Lasers" *Proc. IEEE LEOS*, 147-148 (2008).
- [6] George, B. and Dennis Derickson, D., "High-Speed Concatenation of Frequency Ramps Using Sampled Grating Distributed Bragg Reflector Laser Diode Sources for OCT Resolution Enhancement," *Proc. SPIE* 7554, 96-107 (2010).
- [7] Minneman, M. P., Ensher, J., Crawford, M. and Derickson, D., "All-semiconductor high-speed akinetic swept-source for OCT", *Proc. SPIE* 8311, 16-25 (2011).

**A novel technique for preventing delamination of the composite skin from the core: Sandwich panels with shear keys.**

**Principal Investigators:**

**Eltahry Elghandour, Ph.D., Civil Engineering**

**Eric Kasper, Ph.D., P.E., Civil Engineering**

**California Polytechnic State University**

**San Luis Obispo, CA**

**Research Team**

Faculty: Eltahry Elghandour, Ph.D.  
Eric Kasper, Ph.D.

Graduate Students: Ahmad Amini  
Dominic Surano  
Eugene Eswonia  
Richard Davis  
Richard Balatbat  
Tony Tran  
Thomas Woo

Undergraduate Students: Michael Jacobson  
Matt Ales  
Danny Nunes

Staff: Cody Thompson

**Acknowledgement**

The composites research team would like to thank the Aerospace Department, the Aerospace Student Fee Committee, and C<sup>3</sup>RP for their funding and support of this project. Without their assistance in materials and lab upgrades it would not be possible to conduct the research.

## Abstract

This report presents the investigation of experimental and finite element analysis of composite sandwich structured laminated materials in three different applications using an arrestment shear key to test its effectiveness on the strength of the composite sandwich and its ability to prevent delamination growth. The applications involve composite sandwich skins made of fiber glass/carbon fiber with a core containing closed-cell PVC foam. This introduces the designer to a preventive alternative in repairing the composite sandwich structure.

In the first two applications, an initial delamination is introduced into the composite sandwich structures during the manufacturing process to investigate the effect of delamination size and location on the mechanical characteristics under static and fatigue loading. The first application investigates the effect of the static and fatigue loading on open delamination with and without shear key on mechanical behavior. Also, the second application studies the effect of arrestment keys with initial delamination in a composite sandwich structure under buckling loading. The delamination arrestment keys are semi-circular cross-sections made of fiberglass/epoxy strands. The shear key locations were also varied and their effects noted. The fixed rate under static tests behavior was determined. The fatigue life and behavior were determined for composite sandwich structures with and without initial delamination and shear key.

The third application involves a parametric study on the effects of how a damage arrestment device application interacts with a fastener in a composite sandwich panel. The composite damage arrestment devices are inserted under the face sheet to increase the overall structural strength of the panel and to prevent the propagation of failure along the hole. The damage arrestment devices' thickness was varied and tested under both monotonic and fatigue loading.

A numerical analysis was performed using Finite Element Method (FEM) Software to observe the monotonic behavior of the test specimens with and without delamination. The correlation between FEM and experimental data was accurate enough in predicting the trends of the composite sandwich panels.

The first open delamination showed the shear key to have no significant effect. The second application yielded results that showed that the introduction of a continuous arrestment key parallel to the in-plane loading provided a significant increase in loading and buckling capabilities.

## Nomenclature

ASTM

CNC

E

F

FEA

g

h

in.

kg

kN

l

 $b_f$ 

m

N

Pre-preg

psi

PVC

U

S

sec

t

w

 $\Omega$ 

°

### Subscripts

amp

max

min

mean

ult

y

1

2

3

American Standard for Testing  
Materials

Computer numeric control

Young's Modulus (—)

Force ( $lb_f$ )

Finite element analysis

Grams

height (in.)

Inches

Kilograms

Kilonewtons

length (in.)

Pounds force

Meters

Number of cycles

Pre-impregnated

—

Polyvinyl chloride

Displacement

Stress (—)

Seconds

Time

width (in.)

Resistance (ohms)

Degrees

Amplitude

Maximum

Minimum

Mean

Ultimate

Yield

X

Y

Z



## Chapter 1- Introduction

A brief discussion on composite materials is essential to familiarize the reader on the subject matter ahead. Composites will be defined in this section in terms of their materials, on how they are manufactured, and their advantages and disadvantages. The purpose of the research pertaining to composite sandwich panels will be discussed.

### 1.1 Overview of Composites

Composite materials have been used since the beginning of human history. The earliest recorded use of composites was in ancient Egypt where they created bricks from mud and straw to build their buildings. They also achieved higher strength and better resistance to thermal expansions to their bricks by adding plywood to it. Swords and armor were created with different layers of materials to improve strength during Medieval Europe.

A composite is defined as a material that contains two or more constituents that are combined on a macroscopic scale to form a new material. Composites exhibit the best qualities of their constituents and often some qualities that neither possesses. Some of the properties improved by composite materials include strength, stiffness, corrosion resistance, wear resistance, attractiveness, weight, fatigue life, temperature-dependent behavior, thermal insulation, thermal conductivity, and acoustical insulation. Creating a composite material does not improve all of the properties. The designer can choose which properties to improve by choosing the right pieces to combine. Laminated composites are used to combine the best aspects of the constituent layer in order to achieve a more useful material.

There are three types of composites: fibrous, laminated and particulate composites. All three types are made out of two constituents, the actual composite material and the binding agent or the matrix. The composite material can be a type of metal or a fiber. The binding agent or the matrix can be another type of metal or some type of adhesive material. The two constituent materials are combined with another to create a hybrid material that is much stronger and stiffer.

Fibrous composites consist of fibers in a matrix; this can be seen in Figure 1. Fibers in fibrous composites are much stiffer and stronger than the same material in its bulk form. The geometry of the fiber is crucial to its strength and must be considered in structural applications. The difference between the strength of a fiber and the strength of its bulk material is due to the crystal alignment along the fiber axis. There are also fewer defects in fibers than its respective bulk material.

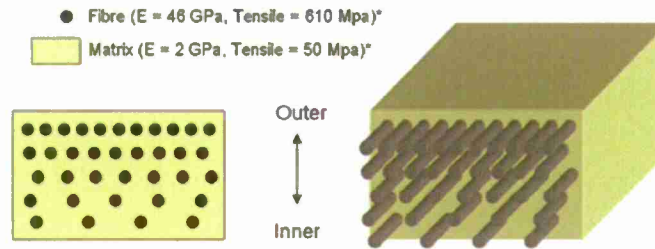


**Figure 1 - Fibrous Composite**

The purpose of the matrix is to support, protect, and transfer the stresses along the fibers. The matrix has a lower density, stiffness, and strength than the fibers. The combination of the fibers and the matrix can create a very strong and stiff material while still maintaining a low density.

A laminated composite can consist of layers of at least two different materials bound to one another; this can be seen in Figure 2. Some classes of laminated composites are bimetal, clad metals, laminated glass; plastic based laminates, and laminated fibrous composites. Bimetals are laminates of two different metals with significantly different coefficients of thermal expansion. Clad metals are the cladding or sheathing of one metal with another, which is done to obtain with the best properties of both metals. An example is high-strength aluminum alloy covered with a corrosion-resistant aluminum alloy. This is a composite material with unique and attractive advantages over regular aluminum which is very corrosive. Plastic based laminates are materials that are saturated with various plastics to improve its material property. Laminated fibrous composites are a hybrid of composites involving both fibrous composites and lamination techniques; this is also known as laminated fiber-reinforced composites. Layers of fiber-reinforced material are built with the fiber directions of each layer typically oriented in different directions to give different strengths and stiffness in various directions.

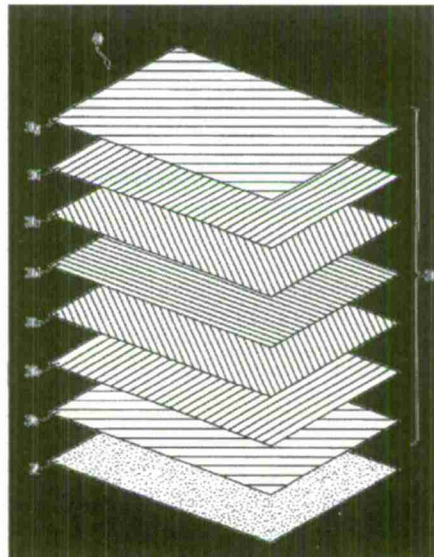


**Figure 2 - Laminated Composite (Courtesy of Picses EU)**

Particulate composites are composed of particles in a matrix; this can be seen in Figure 3. Particles are non-fibrous and generally have no long dimension. The particles and the matrix can be either metallic or nonmetallic. The choice of a particular combination depends upon the desired properties of the final material. The most common example for a particulate composite is concrete. Concrete consists of small sand and rock particles bonded together by a mixture of cement and water that chemically reacts and hardens. The strength of the concrete is comparable to rock.

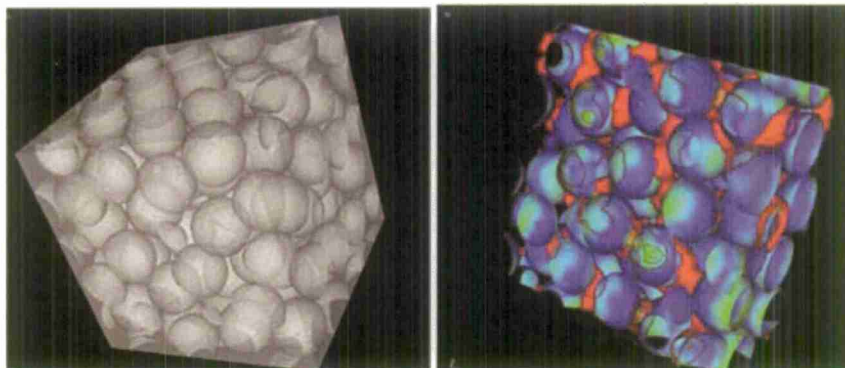


**Figure 3** - Particle Composite (University of Illinois Engineering)

Composites have two major advantages: improved strength and stiffness, especially when compared with other materials on a unit weight basis. The best way of showing the effectiveness of strength or stiffness of a material is the weight per unit volume, as seen in Figure 4. It shows a comparison of the strength and stiffness of several types of advanced composite materials and contemporary metals. The most desired material in the figure is located in the upper right hand corner of the figure, which represents a material with high strength and stiffness. It shows that composite materials are stronger and stiffer than common metals such as aluminum, steel, and titanium, while being lighter than those metals.

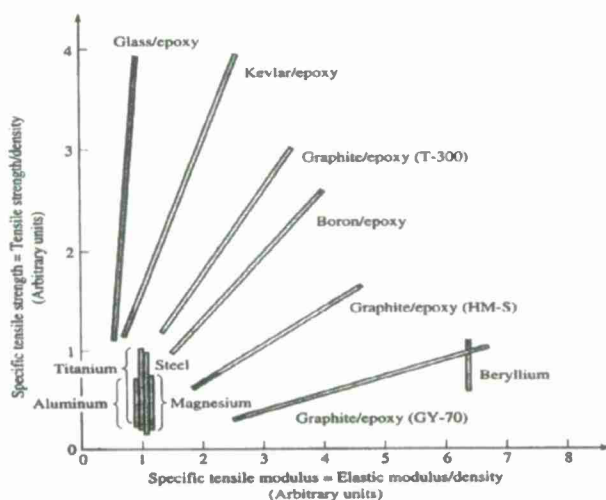


**Figure 4** - Strength and Stiffness of Advanced Composite Materials

The properties of composites are strongly influenced by the properties of the materials they're composed of, the material distribution, and the interaction between the materials. Properties of the composite are mainly dependent on the geometry of the re-enforcement of the composite material such as shape, size, and orientation. Size and distribution control of the material determines the interaction between the fiber and the matrix.

Materials are stronger and stiffer in the fibrous form as in its bulk material form. A high fiber aspect ratio permits very effective transfer of load via matrix materials to the fibers, making a very effective reinforcement material. There are several types of fibers used in composites including glass, carbon, graphite, aramid, boron, and ceramic. Glass fibers are the most common fiber used for composite materials because of their low cost and high strength. Carbon and graphite fibers are mostly high-strength, high-modulus fibers that are used for high-performance composites. Aramid fibers, or Kevlar, are a type of fiber that can change its material property depending on how the material is created. Kevlar fibers have higher tensile strength and modulus, but have a lower fiber elongation than glass or carbon fibers. Boron fibers have a higher tensile strength than carbon fibers, but the fibers are more expensive to produce than other fibers. Ceramic fibers were created because of the need for high temperature fibers. Ceramic fibers combine high strength and elastic modulus with higher temperature capability than other types of fiber materials.

The matrix of a composite material binds the fibers together, transfers loads between them, and protects them against environmental degradation and damage due to handling. The matrix has a great influence on the composite material because it defines several material properties such as shear, compression, transverse modulus, and strength properties. It also limits a material's temperature property by defining the maximum operational temperature the composite material can work in. Polymers or plastics are the most widely used matrix material for fiber composites because of their low cost, ease of production, chemical resistance, and low specific gravity. One of the main disadvantages of polymers is their low strength, low modulus, and low operating temperature. The most common polymers used for a composite matrix are polyester resin and epoxy resins. Metals can also be used as a matrix material for composites. Metals have a high strength, high modulus, high toughness, impact resistance, and its insensitivity to temperature changes over polymers. The main problems associated with use of metals as a matrix is their high density, high processing temperatures, reactivity with fibers, and corrosiveness.

There are three different common types of layup processes used for creating composite pieces. The simplest of these layup processes is the "wet layup" technique; this can be seen in Figure 5. This technique involves the least amount of materials and preparation time out of the three methods, but comes at the cost of the quality of the part. A wet layup is one in which the resin is pushed through the fibers by hand, and then placed inside a vacuum sealed bag and allowed to cure. Major advantages for this layup include low cost relative to the other layup processes, no special materials or additional equipment is required, the part is normally capable of curing at room temperatures, and the method is basic so that almost anyone can use it. Some disadvantages

associated with this method include restricted work time (based on the resin), inconsistencies in resin to fiber ratio or the part, as well as destroying fiber integrity while working resin through the fibers.



**Figure 5 - "Wet Layup" Technique**

Another method typically used is called a resin infusion process or a vacuum resin infusion (VRI) process; this can be seen in Figure 6. This method has the most variation from person to person since each individual typically uses a slightly different setup and process. However, the main idea behind this method is that a vacuum is used to pull resin through the part. The advantage to this is a more consistent resin to fiber ratio throughout the whole part similar to that of the pre-impregnated carbon fiber but at a greatly reduced cost. However it does not require a complex cure cycle nor do the materials need to be stored to preserve a "shelf life" like the pre-preg. It is also a preferred method for repeated experiments over a wet layup since the parts are reproducible and provide more consistent results. However this process does require more knowledge or the materials being used. Work time is dependent on the viscosity of the resin as well as the strength of the pump. The size of the part must also be taken into account since the resin may start to cure before reaching the other side of a larger part. VRI requires more materials and preparation time than either of the other two methods. A flow media is needed in order to allow resin to flow across the part, a peel-ply is placed under this flow media in order to remove it from the part, and additional tubing is required for the resin to be sucked through. This makes this method more costly than the wet layup, but allows the fabricator to avoid tampering with the fibers and causing misalignments in the part.





**Figure 6 - VRI Layup**

The final method used in industry involves the use of pre-impregnated fibers also known as “pre-preg”; this can be seen in Figure 7. This method is ideal for almost any application in which money is not an issue. The extreme advantage with the pre-preg is that it already has the ideal resin to fiber ratio giving the part the maximum strength to weight ratio. The method gives the best consistency and higher quality in fabrication of the parts due to the premade resin to fiber ratio. Another advantage of pre-preg is the work time which is significantly longer than the wet layup technique, which starts to cure when the hardener and the epoxy are mixed. However, the disadvantage of this is that the manufacturer specifies the work time for pre-preg, and also, after the specified “shelf life” has expired, the material is no longer usable. Due to the “shelf life”, a freezer is needed to store the pre-preg in order to prevent it from losing “shelf life” when it is not being used. Pre-preg requires a heating cycle in order for the part to cure; meaning some type of machine has to be used to create the heating cycle. This includes autoclaves and heat presses to cure the pre-preg composite.

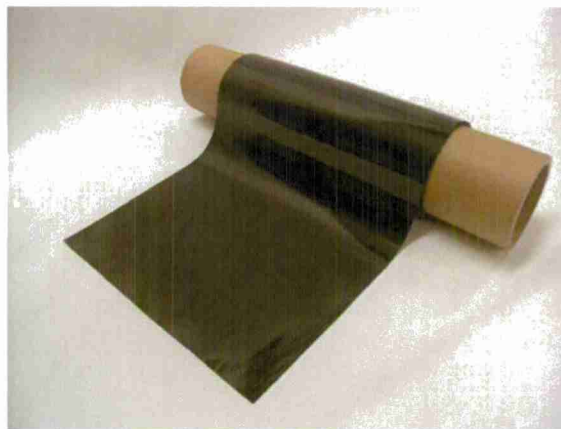


**Figure 7 - Pre-preg Layup (Courtesy of Composite World)**

Composite structures are any structures that contain a fibrous or laminated composite. The most common types of composite structures that will be researched are sandwich composite panels. They are widely used in several industries such as the marine, aerospace, and automotive industries; this can be seen in Figure 8. For application in the aerospace industry, fuselage hulls are made from panels of a foam core sandwiched

between layers of carbon fiber. There are major advantages of sandwich composite panels such as decrease in weight and an increase in structural strength. Some of the major drawbacks are low shear strength and delamination of the composite skin from the core. The sandwich composite panels are susceptible to in-plane shear which is resisted primarily by the core, core compression failure, indentation of face-sheet subjected to impact loading, global buckling and wrinkling instability, and delamination of the face sheet from the core. In a delaminated structures subjected to compression, the face sheet in the delaminated region may buckle allowing the delamination to propagate through the panel causing a global structural failure. The shortcomings of fiber-reinforced plastics are that they have low mechanical properties and are susceptible to failure by impact loading. Low velocity impact on a sandwich structure can induce damage to the facings, the core, and the face-core interface. According to Castaings, there are five different failure modes: core crushing, delamination in the impacted face sheet, core cracking, matrix cracking, and fiber breakage in the facings. Damage of a composite panel is dependent on the properties and interaction of the core material and the facing of the plates.

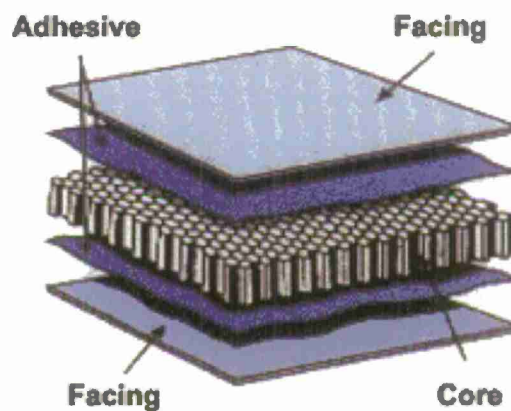


**Figure 8 - Example of Sandwich Composites (Courtesy of Engineer Materials Inc)**

There are accepted testing standards that allow results to be compared with other research by following guidelines on experimental testing. One of these standards is the American Standard for Testing and Materials (ASTM). It is an internationally recognized organization that develops and publishes consensus technical standards for materials, products, systems, and services. Most standards that pertain to composite testing are for the compression of composite sandwich structures and for testing of composite laminates with fasteners. The standards give a full detailed account on how to dimension the test specimens, set-up the testing apparatus, and how to analyze the results of the testing to be comparable to previous work. Since there are few definite or accepted standards to test composite sandwich panels with a fastener, a variation or evolution of some of the standards would be used for the experimental testing to require the desired or predicted results of the research; this will be further discussed later in this report.

Composite sandwich structures are becoming more heavily integrated into everyday applications ranging from marine to aerospace. A composite sandwich structure consists of two composite skins on each

side of a core material. Core materials are generally lightweight materials such as balsa wood, honeycomb structure, or foam. A sandwich structure with an aluminum honeycomb core and an open celled foam core are shown in Figure 9. Composite sandwich structures offer high strength-to-weight ratios when compared to traditional metals. Using composites allow designers more flexibility in being able to tailor the material properties of their part based on the orientation of the composite. However, composite sandwich structures also have disadvantages such as water intrusion and impact, which can cause the composite skin to delaminate from the core. A delaminated sandwich structure significantly loses its structural strength and can approach the point of catastrophic failure.

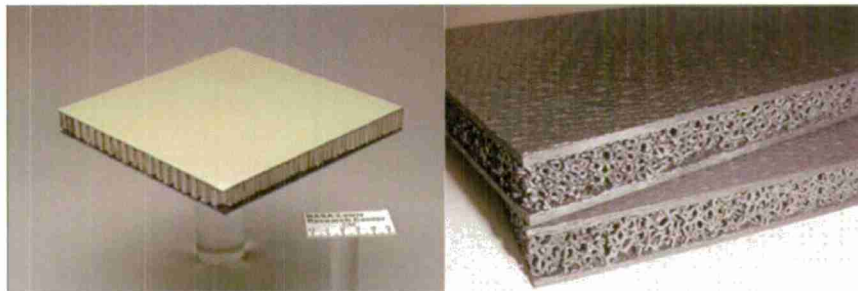


**Figure 9** - Examples of sandwich structures<sup>1,2</sup>

Thus far, only three techniques have been discovered to help stop a composite skin from separating once it has begun to delaminate from the core. The three research methods studied involve buffer strips, peel stoppers, and shear keys. Buffer strips<sup>3</sup> are used to increase the strength of a composite plate that already has cracks or defects. Buffer strips are additional layers of composite strips that are added to the defective regions or to regions where it is anticipated that cracks will occur. Figure 10 shows a general schematic of a buffer strip added to the defective regions a composite panel containing cracks. Under fatigue loading, after additional Kevlar or structural fiberglass strips were added to carbon fiber composite panels, the buffer strips arrested the crack growth and increased the panel's residual strength<sup>3</sup>.

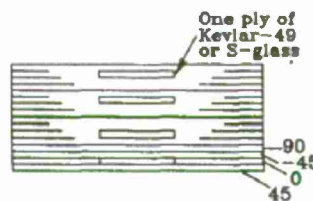


**Figure 10** - Schematic of buffer strips<sup>3</sup>

Another method used for stopping composite face sheet delamination involves a marine peel stopper, developed by Christopher Wonderly and Joachim Grenestedt at Leigh University. A schematic of a peel stopper is shown Figure 11. A peel stopper essentially divides the composite sandwich structure into different regions,

preventing a delaminated skin from traveling into consecutive regions. The peel stopper causes the delaminated face sheet to separate away from the structure and leave the remaining composite intact. The upper part of Figure 12 shows a delaminated skin and the lower part of Figure 12 shows the outer skin breaking away from the structure. Peel stoppers have shown promising performance in stopping delamination, are relatively simple and easy to manufacture, and cost effective. Preliminary tests that were performed have shown that peel stoppers possess good quasi-static in-plane strength<sup>3</sup>.

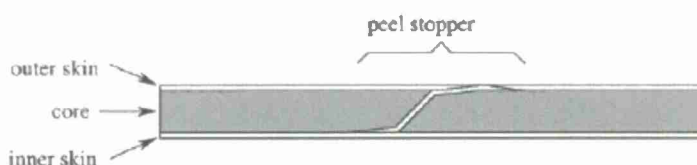


**Figure 11-** General schematic of a peel stopper<sup>3</sup>

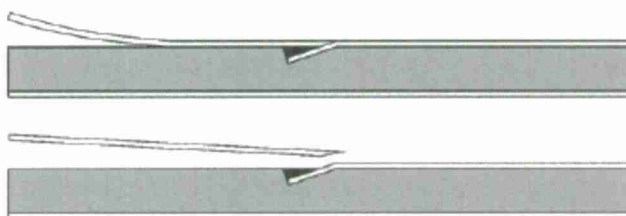


**Figure 12 -** Peel stopper ending delamination<sup>3</sup>

In 2008, Dr. Nilanjan Mitra, Dr. Eltahry Elghandour, and Dr. Eric Kasper began researching another cost effective solution to increasing the shear strength of a composite sandwich<sup>4</sup> structure at California Polytechnic State University in San Luis Obispo. The research was conducted under the sponsorship of the C3RP-ONR grant. The sandwich structures selected consisted of fiberglass face sheets surrounding a closed cell PVC foam core. Fiberglass rods, called shear keys, were incorporated into the foam to increase the shear strength. The shear keys were semicircular fiberglass rods manufactured out of intertwined strands of fiberglass. The left side of Figure 13 shows the shear key rods and the right side shows milled out grooves in the foam where the shear keys will be placed.



**Figure 13 -** Shear key rods and grooves milled into foam core



Dr. Mitra's, Dr. Elghandour's, and Dr. Kasper's research focused on the size, shape, and the location of the shear keys. Triangular shaped shear keys are shown in the right side of Figure 14. Under shear loading conditions, the non-staggered triangular shear keys showed little increase in shear strength, attributed to the stress concentrations introduced at the tips of the triangles. The large circular shear keys as shown on the left side of Figure 14, but in a non-staggered configuration were then tested. Although it was determined that the large circular shear keys were stronger than the triangular shear keys, failure often occurred in the foam between the shear keys because there was less core material present. To address the problem circular shear keys were placed in a staggered manner helping to provide increased shear strength. Shrinking the radius of the shear keys provided the best results because less of the foam was removed.

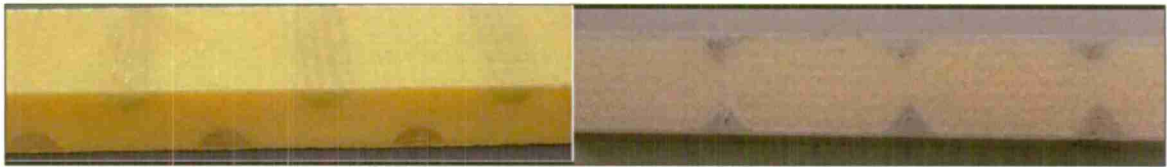


**Figure 14** - Shear key size and location research<sup>4</sup>

Figure 15 - Composite sandwich structures under shear testing (ASTM C273) shows a sandwich structures being tested under shear loading conditions. After the sandwich structures were tested under shear loading, and maximum shear strengths were determined, some researcher looking into how the shear keys could aid in preventing composite delamination due to peeling. The goal of the research was to investigate how delamination length and shear key location affected the monotonic failure characteristics of the composite sandwich structure<sup>6</sup>. The initial results gathered from the delamination testing were inconclusive because many test specimens failed prematurely and therefore only a small sample of tested specimens could be used. This project research will continue on with the shear key work that Dr. Dr. Mitra's, Dr. Elghandour's, and Dr. Kasper's started but will focus primarily on the response of the shear keys in preventing delamination peeling.

This project will exemplify the experimental and numerical analysis of composite sandwich structures under monotonic, buckling, and fatigue loading. This will be done with the use of three different applications experiments involving sandwich composite panels.



**Figure 15** - Composite sandwich structures under shear testing (ASTM C273)



## Chapter 2- Methods of Design and Specimen Manufacture

### 2.1-Sandwich Structure Design

In the first two applications, the materials selected for this research involved using composite materials for the face sheets which were woven roving fiberglass and chopped strand fiberglass mats, or bi-weave carbon fiber. The chopped strand mat consists of 3 inch length fibers that are randomly oriented. The intent of the chopped strand mat is to give the composite sandwich structure more isotropic properties. Woven roving is a fiberglass bi-weave with fibers oriented at angles of  $0^\circ$  and  $90^\circ$ , similar to the weave of the carbon fiber except larger groups of fibers were placed together in the fiberglass. These composite sandwich structures' strength mainly comes from the bi-directional woven plies in the face sheets. Figure 16 shows chopped strand mat on the left and woven roving mat on the right.



**Figure 16** - Chopped strand mat and woven roving fiberglass

The core material used was Divinycell's H 100 PVC foam with a thickness of 20 mm and a density of  $100 \text{ kg/m}^3$  for the monotonic tension and cyclic tensile cases containing fiberglass face sheets. This closed cell foam has a high strength-to-weight ratio as well as excellent ductile qualities. The purpose of the PVC foam core is to increase the sandwich structure's bending and torsional stiffness while only slightly increasing the weight of the test specimens. A stack of different Divinycell foams are shown in Figure 17.

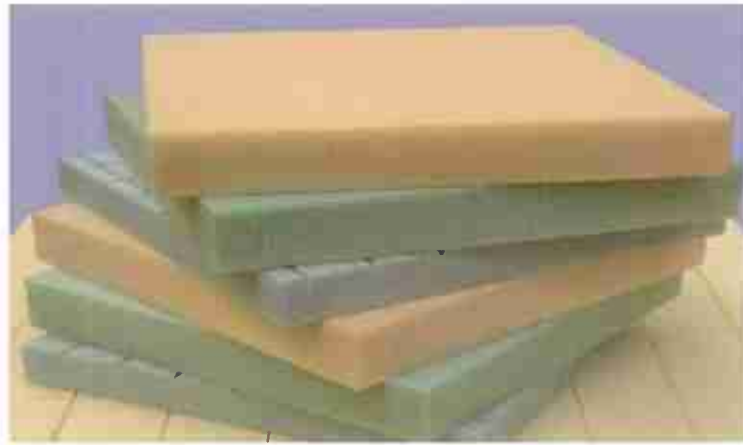


**Figure 17 - Divinycell foam core<sup>13</sup>**

For the rest of the tests, carbon fiber composite sandwiches as well as the compression buckling tests used a different core material. A foam core material was chosen to match what is currently being used in the boating and aerospace industries of today. The foam core used for this part of the project was a LAST-A-FOAM FR-6710 foam material purchased from General Plastics Manufacturing Company. According to General Plastics, the foam is a CFC-free, closed-cell, and a flame-retardant polyurethane material with a density of 10 pounds per cubic foot. This particular foam differs from the one H100 Divinycell PVC foam, but provides the necessary properties to produce the proper results from the buckled structure along with the heating requirements used in the carbon fiber tests.

The composite lay-up used to manufacture the sandwich structures consisted of four layers of fiberglass on either side of the foam core. The stacking sequence of the skin, starting from the outer most layer was: woven roving, chopped strand mat, woven, chopped, core, chopped, woven, chopped, woven.

Six different fiberglass composite sandwich structure configurations were manufactured and tested under monotonic tension loading as well as a cyclic tensile loading, which are listed below:

1. No Initial Delamination
2. 0.5 inch Initial Delamination
3. 1.0 inch Initial Delamination
4. 1.0 inch Initial Delamination with 0 inch shear key
5. 1.0 inch Initial Delamination with 0.5 inch shear key
6. 1.0 inch Initial Delamination with 1.0 inch shear key

Figure 18, Figure 19 - Test specimen schematic for initial delamination and Figure 20 below show schematics of the six different configurations with important components and dimensions labeled. All of the test specimens have the following dimensions: 6 in. x 1.5 in. x 0.787 in.

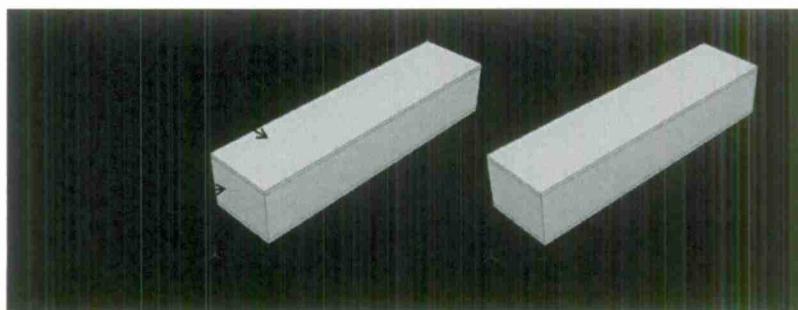


**Figure 18** - Test specimen schematic for no initial delamination

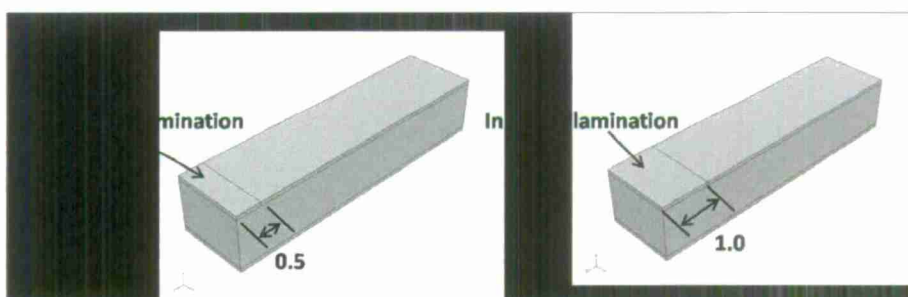


**Figure 19** - Test specimen schematic for initial delamination

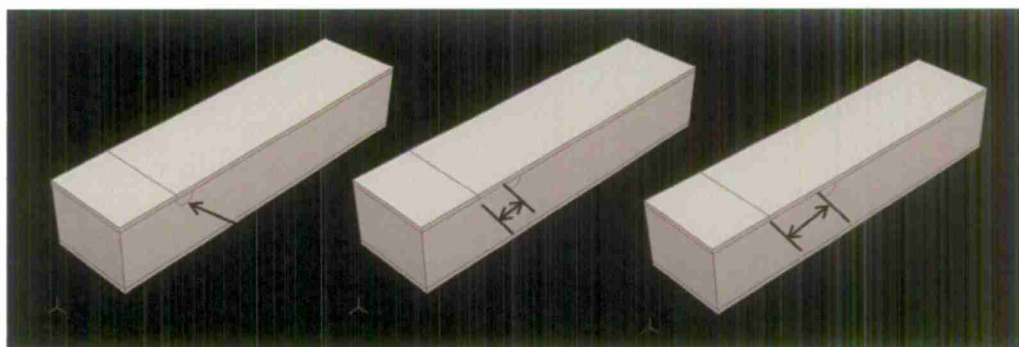


**Figure 20** - Test specimen schematic for initial delamination with shear keys

Fourteen different fiberglass composite sandwich structures were manufactured and tested under a compression buckling load, which are listed below:

1. No delamination
2. 1 inch long delamination placed in the middle
3. 2 inch long delamination placed in the middle
4. Vertical shear key along specimen, no delamination
5. Vertical shear key along specimen, 1 inch long delamination placed in the middle
6. Vertical shear key along specimen, 2 inch long delamination placed in the middle

7. Vertical shear key outside of delamination, 1 inch long delamination placed in the middle
8. Vertical shear key outside of delamination, 2inch long delamination placed in the middle
9. Horizontal shear key, no delamination
10. Horizontal shear key 1 inch away from delamination, 1.0 inch delamination in the middle
11. Horizontal shear key 1 inch away from delamination, 2.0 inch delamination in the middle
12. Horizontal shear key, no delamination
13. Horizontal shear key 2 inches away from delamination, 1.0 inch delamination in the middle
14. Horizontal shear key 2 inches away from delamination, 2.0 inch delamination in the middle

Eight different carbon fiber composite sandwich structures were manufactured and tested under a monotonic and cyclic compression loading, which are listed below:

1. No shear key
2. 1 Layer (2x3/4in strip) shear key
3. 2 Layer (2x3/4in strip) shear key
4. 3 Layer (2x3/4in strip) shear key
5. 4 Layer (2x3/4in strip) shear key
6. 5 Layer (2x3/4in strip) shear key
7. 6 Layer (2x3/4in strip) shear key
8. 7 Layer (2x3/4in strip) shear key

These composite sandwich structures were manufactured using the vacuum assisted resin transfer method (VaRTM).

### 2.1-1 Material Preparation - No Initial Delamination

Figure 21 below shows some of the materials required to manufacture a part using a VaRTM lay-up. All of the materials used to manufacture the composite sandwich structures are listed below.



**Figure 21 - VaRTM specific materials<sup>21</sup>**

**Table 1 – Table of Materials**

| <b>List A of Materials:</b>   | <b>List B of Materials:</b>  |
|---|--|
| <ul style="list-style-type: none"> <li>• Woven roving fiberglass</li> <li>• Chopped strand fiberglass mat</li> <li>• Divinycell H 100 foam / LAST-A-FOAM FR-6710</li> <li>• Peel ply release cloth</li> <li>• Flow media</li> <li>• Vacuum bag</li> <li>• Chromate tacky tape</li> <li>• Spiral tubing</li> <li>• T-fittings</li> <li>• Plastic tubing</li> <li>• Epoxy/Hardener</li> <li>• Mixing cups</li> <li>• Mixing sticks</li> </ul> | <ul style="list-style-type: none"> <li>• Pre-preg Carbon Fiber</li> <li>• LAST-A-FOAM FR-6710</li> <li>• Peel ply release cloth</li> <li>• Flow media</li> <li>• Vacuum bag</li> <li>• Chromate tacky tape</li> <li>• Spiral tubing</li> <li>• T-fittings</li> <li>• Plastic tubing</li> <li>• Epoxy/Hardener</li> <li>• Mixing cups</li> <li>• Mixing sticks</li> </ul> |

During the material preparation phase, large Divinycell PVC foam sheets were obtained and cut into 13 x 10 inch squares using a jigsaw. 13 x 10 inch dimensions were selected to provide 12 test specimens from each lay-up batch.

Four layers of chopped strand mat and woven roving layers were then cut into 13 x 10 inch square sheets. The composite layers were weighed and used to determine the amount of resin and hardener needed to be mixed. The flow media was cut approximately 1 inch longer than the composite layers but with the same width. The peel ply release cloth was cut approximately 2 inch larger on all side than the flow media. The vacuum bag was cut approximately 2 inch longer on all sides than the peel ply release cloth. Two 15 inch segments of plastic tubing were cut and were used to aid the resin flow through the composite sandwich structure. One t-fitting and a segment of spiral tubing were cut to the width of the sandwich structure (10 inch). The spiral tubing was used to dispense the resin's flow through the structure from the t-fittings. Figure 22 shows the spiral tubing, vacuum tubing, and the t-fittings used for the lay-up and Figure 23 shows how the three items are used in the lay-up.



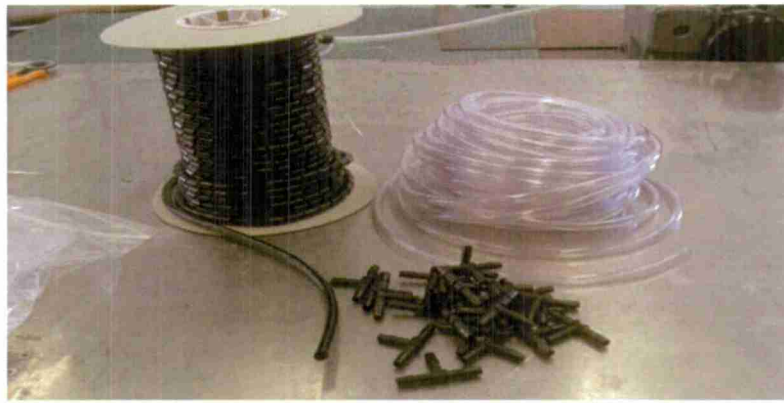


**Figure 22** - T-fitting, spiral and vacuum tubing

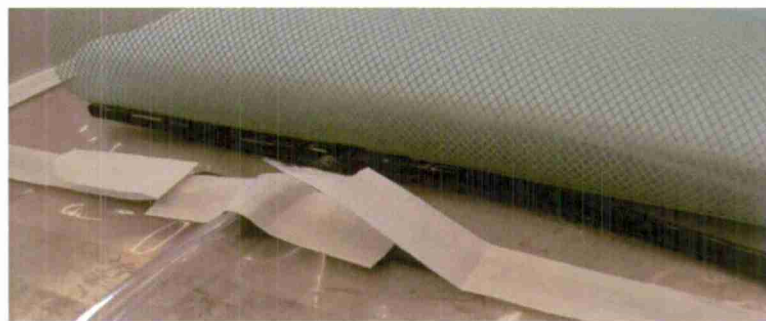


**Figure 23** - Spiral tubing and t-fitting set-up

### **2.1-2 Material Preparation - Test Specimen with Initial Delamination**

The composite sandwich structures with an initial delamination were manufactured in a similar manner compared to the test specimens without delamination but with one difference. A strip of non-porous Teflon material was added to the top of the foam which prevented the composite layer from bonding to the foam core (shown in Figure 24). The strip of non-porous Teflon paper was cut to approximately 0.25 – 0.33 inches. Although extra length was added to the Teflon, the margins were lost when the composite sandwich structure were cut to appropriate dimensions.

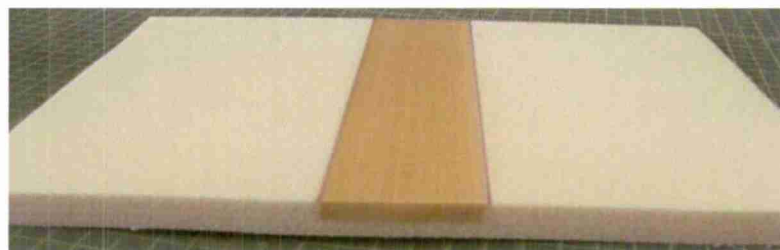


**Figure 24** - Foam core with non-porous Teflon strip added

### 2.1-3 Material Preparation - Test Specimen with Initial Delamination and Shear Keys

The same fiberglass woven roving is used during the prep work for the arrestment shear key. Instead of cutting it down to form sheets, the fiberglass strands are pulled off of the weave and grouped together into a bundle of 17 strands. The 17 strand count are derived from how many of these strands can fit into the grooves on the mold and be manually capable of maintaining the cross-sectional shape of the arrestment key throughout the layup. The length of the strands has to be a bit longer than 12 inches to provide excess length for trimming and fitting perfectly into the composite sandwich structure. The fiberglass strands pulled off the weave can be seen in Figure 25.

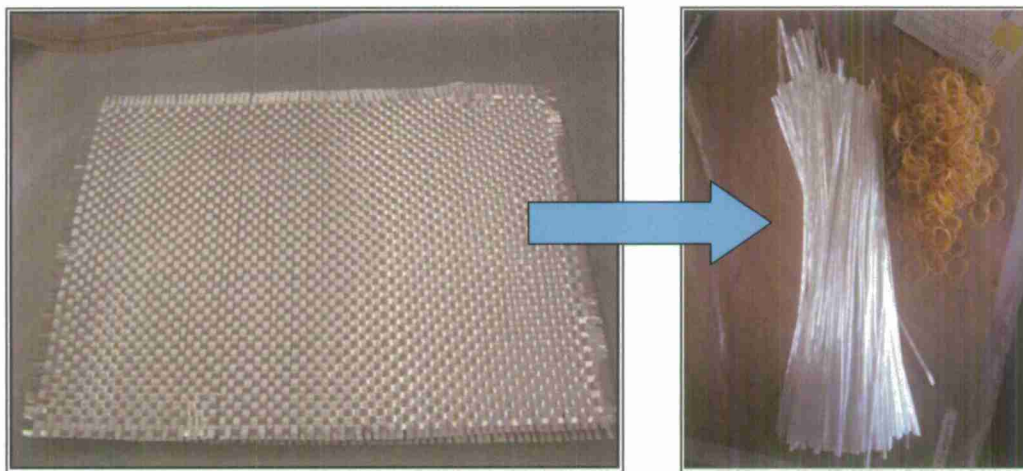


**Figure 25 - Obtaining the Fiberglass Strands**

Once the fiberglass strands are grouped in a set of 17 strands, the strands are held together with a rubber band on one end. It does not need to be a rubber band; it can be anything that holds the strands together and not impact the mechanical properties of the keys. This bundling process can be seen in Figure 26.



**Figure 26 - Bundling of the Fiberglass Strands**

With a cup of 5 to 1 ratio of the West System 105/205 epoxy, the sets of fiberglass strands are then infused manually to where there is an excess amount dripping when holding the set up vertically. The excess epoxy will later be removed per pressurized vacuumed system. It is important to have enough epoxy rather than end up with dry fiberglass in the delamination arrestment key. Make sure that all parts of the sets are wetted with the epoxy. Once the set of fiberglass strands have enough epoxy, it is placed into the grooves on the mold. The mold is first coated with a non-stick wax and is made of Aluminum AL 2024. The surfaces and grooves of the mold are clean before every use to avoid any contaminates getting into the keys during the manufacturing process. The infused set of strands placed on the mold can be seen in Figure 27.



**Figure 27 - Placing into the Mold**

After all the sets of fiberglass strands are put in place, the whole mold with the premature keys is then placed into a vacuum bag and sealed. The vacuum bag has only one output to pull to create the necessary pressure on the keys and remove any unused epoxy in the vacuumed environment. This is displayed in Figure 28.



**Figure 28 - The Vacuumed Mold and Premature Keys**

To add additional support for the shape of the delamination arrestment keys, a uniform plate and 200 pounds of additional weight is placed on top of the vacuumed structure. This is done because the pressure in the vacuumed environment would otherwise leave a thin layer of epoxy through the part. In order to help remove the excess epoxy, the weights are added and also provide a flat backing for the shape of the keys. Figure 29 provides a better look into how the weights are placed.



**Figure 29 - Weights used on Mold**

After the curing of the keys is completed, the structure is then taken out of the mold. At this point, the rubber band section of the layup is later cut off to remove what does not belong in the composite sandwich structure. The keys are cut down along its length to reduce most of the excess materials before being placed back into the mold where the keys are then sanded down to the correct dimensions. A picture of the sanding process is displayed in Figure 30.



**Figure 30 - Sanding of the Keys**

The keys would look something like Figure 31 and Figure 32 – Shear key mold and CAD drawing used in production of actual shear keys. after the sanding and cleaning of the keys is completed. The cleaning of the



key is done with water and nothing else. All residues on the exterior of the keys are removed, and the keys are stored in a clean environment.

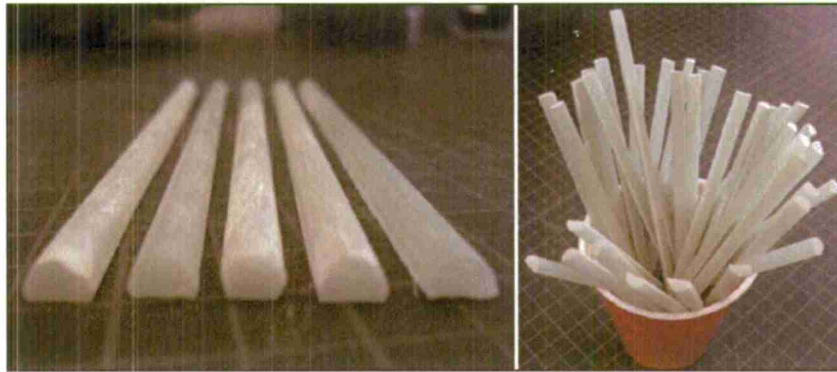


**Figure 31** - The Keys Completed

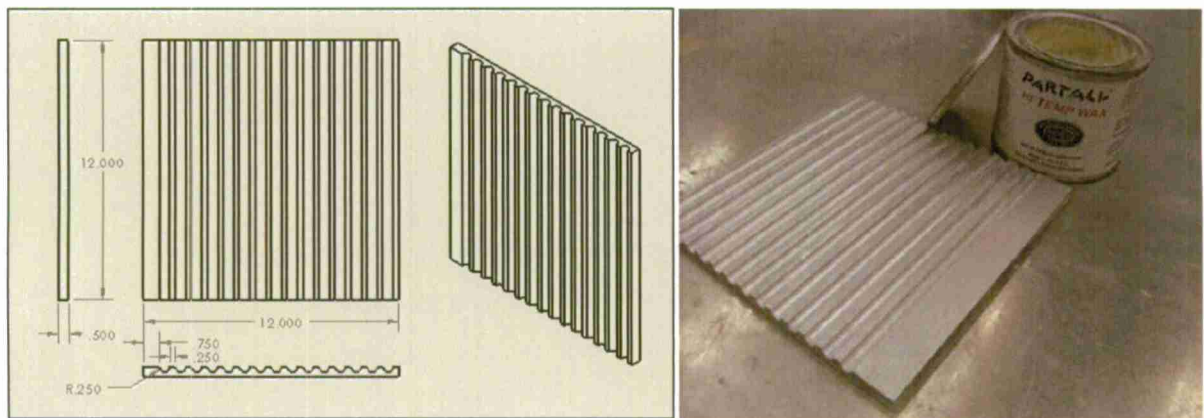


**Figure 32** – Shear key mold and CAD drawing used in production of actual shear keys.

The sandwich structures with shear keys were manufactured in a similar manner to the test specimens with an initial delamination. A piece of foam with the same dimensions used for the previous lay-ups had 4 mm radius grooves milled out using a manual mill. Then a strip of non-porous Teflon film was added in between the shear keys on the foam just like the test specimens with an initial delamination. As before all of the vacuum bagging materials were gathered and set-up to the point right before the vacuum bag was sealed. A small amount of epoxy was mixed (approximately 30 g) which was used to bond the shear keys to the foam. After the epoxy was adequately mixed then the epoxy was applied to the milled out foam regions using a wooden popsicle stick. Finally the shear keys were inserted into the grooves and the upper skin of fiberglass was stacked on top and the bag was sealed up for the resin to flow through.

#### **2.1-4 Material Preparation - Buckling Test Specimen**

Due to the needed pinned-pinned boundaries, the test specimens needed to be manufactured with a stronger material at the boundary. This required a stiffer material that is able to bond with the fiberglass skin and has the same dimension as the foam core. The material used for the boundary is oak wood and is used in the



composite sandwich structure that supports the boundaries of the structure under in-plane displacement. The oak wood core was also chosen to provide enough stiffness to maintain the integrity of the hole's boundary locations. If the holes were manufactured into the foam core, it would saw through the test specimen.

The oak wood was the best choice for its stiffness and its significantly high loading capacity. One note that was considered during the manufacturing process was the grain direction of the oak wood material; hence the direction of how to manufacture the wood core into composite sandwich structure matters. In the layup of the composite structure, the wood grain direction would be laid up parallel to the load vectors.

The wood core design was used to determine the elastic modulus in two different directions where one direction has the grain parallel to the load vector and the other direction is perpendicular to the same vector. From how the oak wood arrived in the lab, the raw material would be cut down into small blocks that were used during testing. The design of the specimen has the following dimensions where the length of the specimen is parallel to the grain:

**Table 1** - Wood Core Design Dimensions for Compressive Properties

| Width (in) | Overall Length (in) | Thickness (in) |
|------------|---------------------|----------------|
| 1.0        | 1.5                 | 0.5            |

The delamination within the specimens was created in the same way as the specimens created for the tensile loading. These designed test specimens would later be placed on the tee shaped jig and compressed to get the load and vertical extension in order to determine the compressive elastic modulus with the given geometry.

### 2.1-5 VaRTM Lay-up

This lay-up procedure was used for the tensile loading and compression buckling fiberglass pieces. Once all of the materials had been cut and prepared the materials were stacked in the lay-up level. The vacuum bag was laid out on a flat surface and the flow media was placed on top of it followed by the release cloth. Components of the composite lay-up were assembled in their appropriate lay-up level and stacked on top starting with the woven roving and the chopped strand mat. Another layer of woven roving and chopped strand mat were added followed by the foam core. Two additional layers of chopped strand mat and woven roving were placed on top of the foam core in an alternating fashion. Chromate sealant tape was used to surround the perimeter of the sandwich structure lay-up in order to seal the vacuum bag later. Segments of plastic tubing were placed at either ends of the sandwich structure to aid in the direction of resin flow from the vacuum pump. A small piece of cotton was added to the tubing closest to the vacuum to increase the bag pressure. The peel ply, flow media, and vacuum bag were then folded over to envelope the entire sandwich structure shown in Figure 33.



**Figure 33** - Stacked VaRTM lay-up before vacuum bagging

The vacuum bag was sealed off using the Chromate sealant tape that was applied to the perimeter of the vacuum bag. Care was taken while sealing the vacuum bag to minimize air leaks. The vacuum end of the tubing was connected to the resin trap and sealed off using another thin strip of sealant tape. A leak check was performed prior to running the resin through the part. To check for leaks, a piece of sealant tape was applied to the resin side of the tube and the vacuum was turned on. If leaks were discovered, then the remaining leaks were sealed off with additional Chromate sealant tape. Caution was also taken to correctly line-up the composite fabric sheets. If the sheets were not correctly placed, the applied vacuum pressure would cause the contents of the bag to shift around. After double checking the placement of the composite sheets and leaks, the sealant tape on the resin side of the tube was removed and the tube was closed off using vice grip pliers (shown in Figure 34).



**Figure 34** - Vacuum bagged composite sandwich structure after lay-up

West System's 105 Epoxy System and 206 Slow Hardener were used as the matrix for the composite sandwich structure lay-up (shown in Figure 35). The amount of resin and hardener used were determined based upon the weight of the dry fibers. The total weight of the dry fibers was multiplied by 1.5 which allowed

extra epoxy to ensure that the fibers were properly saturated. From earlier lay-up experiments it was determined that the total amount of epoxy should be divided into two separate mixing cups in order to prevent the epoxy from curing before it had the chance to travel the entire length of the part. The resin-to-hardener ratio for the resin system used was approximately 3 to 1.



**Figure 35** - West System resin and hardener used for lay-up

The resin and hardener were measured out into two separate cups using a scale. When ready, the two were combined and stirred until fully mixed. The pliers were removed from the resin side of the tubing and the end of tube was placed in the resin cup. Figure 36 shows the resin flowing from the cup through the tubing to the vacuum sealed composite sandwich structure. The pressure from the vacuum pulls the resin across the sandwich structure and through the flow media. The second cup of mixed resin was poured into the 1<sup>st</sup> resin cup when it was almost empty. After all of the resin had flowed across the sandwich structure then vice grips were used to close off the resin side of the tubing to ensure that the part remains under constant vacuum pressure. Then a flat sheet was placed on top of the sandwich structure and weights were added to evenly distribute additional pressure. The part is left under vacuum pressure overnight for approximately 12 hours.



**Figure 36** - VaRTM composite lay-ups resin flow

Figure 37 below shows an exploded view of a VaRTM with all of the materials labeled.

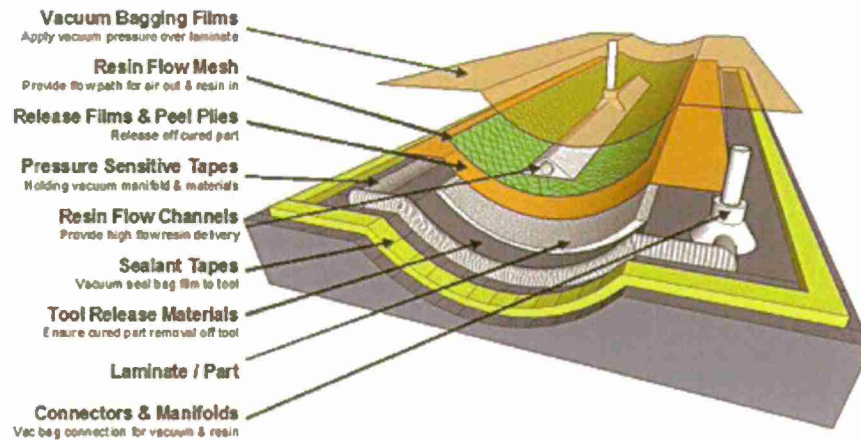


Figure 37 - Composite materials stacked before lay-up<sup>22</sup>

## 2.2 Pre-Preg Lay-Up

In the third application, the composite sandwich panel consisted of the foam core, 4 sheets of LTM45 (2 layers on each side), and two sheets of film adhesive. The dimensions for all the materials were 12" x 12". Two layers or two sheets of non-porous material were used between the composite sandwich panel and the metal plates for the press. The purpose of non-porous material for the lay-up was to absorb any excess resin from the plates and prevent it from curing on the plates and causing dimples on the face sheet. It acts like a protective barrier for the composite sandwich panels. The lay-up process used for manufacturing the composite sandwich panels can be seen in Figure 38.

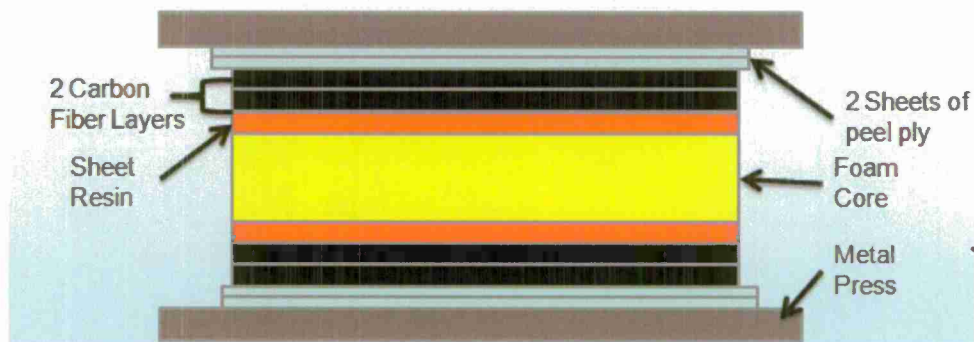


Figure 38 - Schematic for Lay-up of Composite Sandwich Panels

The first step of manufacturing the composite sandwich panels is to sand and wax the press metal plates to ensure smoothness of the face sheets; this can be seen in Figure 39. The plates are sanded down by using a high grit sandpaper to remove any resin that was cured on the metal plate. High grit sandpaper was used to prevent the removable of the magnetic coating on the plate. After the plate was sanded, a wax was used to



smooth any divots on the metal plate. The wax was applied by hand and a buffer tool attached to a motorized drill was used to smooth out the wax that was on the plate.



**Figure 39 - Sanding and Waxing of Press**

With all the materials prepped and ready, the materials are laid-up the way shown in Figure 38. The composite sandwich panel was placed into the press. The manufacture of LTM45 has a specific curing cycle, which is curing the composite by applying heat and pressure on it for a specific amount of time. The manufacturer's curing cycle can be seen in Figure 40. The cycle first starts out with applying a constant load of 1000 lbs on the composite sandwich with the temperature increasing 2 °F per min until the temperature reaches 150 °F. The press then stays on for 16 hours at the temperature and the same force. After the time elapses, the temperature decreases 2 °F per min until the temperature reaches 75 °F with a constant force of 1000 lbs. After the machine reaches room temperature the machine runs for another 2 hours with 1000 lbs of force to end the cycle. According to the manufacturer, the composite would be 98% fully cured after the LTM45 has gone through the cure cycle. The plate would then be removed from the press and cut to dimensions of the test specimens, which will be further discussed.

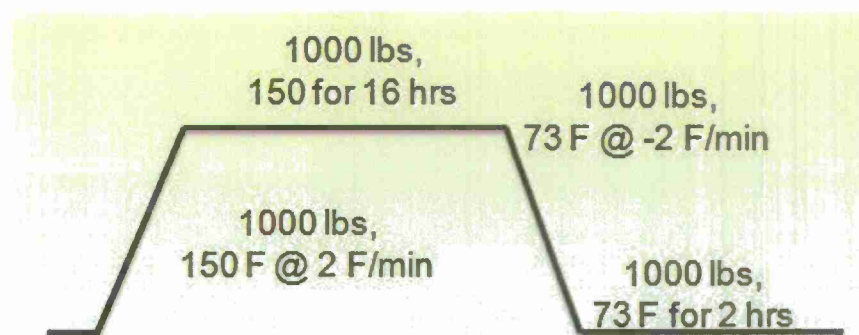


**Figure 40 - Curing Cycle for LTM45**



### 2.2-1 Damage Arrestment Device Prep (DAD)

Composite sandwich panels with DADs were manufactured first with milling the slots on the foam; this can be seen in Figure 41. A CNC end mill was used to mill the foam with a 0.75" four-flute straight end mill. A CAD model of the foam was made and was placed into CAMWORKS to create a CNC code to make the machine mill the foam to provide a better accuracy on the depth and alignment of the slots. Special care of the foam is vital for milling the slots to prevent the foam from being destroyed since it is flimsy. A vice grip cannot be used on the foam to keep it in place because it would leave mark and divots on the foam. To keep the foam in place, six toe clamps were used with three rulers going horizontally across the foam. The toe clamps and the rulers would be placed around the slots to prevent the machine milling any of it out. The foam was milled on one side and flipped around to mill the other side, making sure that the milled out cuts would be aligned on both sides of the foam. The mill depth of the foam was set to 0.039" which is the thickness of three layer of LTM.



**Figure 41** - Milling of foam for DADs

With the foam milled, the DADs would be created using LTM45 cut into strips of 12" x 0.75". A 12" x 12" sheet of LTM45 is marked with dimensions of the DAD strips and is cut using a Rotatrim to have a clean cut; this can be seen in Figure 42. The marking of the sheet was done using a Sharpie and a ruler. This process is repeated until 24 strips are cut to for one 12" x 12" foam plate, having 3 layer DADs per slot.

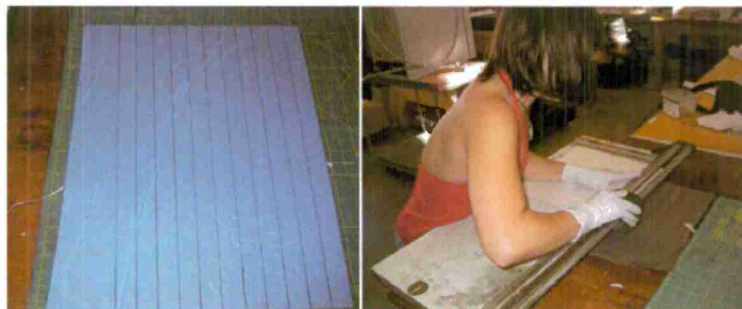


**Figure 42** - Cutting of the DAD strips

With the strips cut, the strips would be set into eight piles of three strips. The protective papers of the strips were removed and laid into the milled out slots of the foam one at a time; this can be seen in Figure 43 - DADs being inserted into foam slots.



**Figure 43** - DADs being inserted into foam slots

The rest of the manufacturing of the plate is the same as the regular test specimens. It would consist of four sheets of LTM45 (two layers on each side), and two sheets of film adhesive, and 4 sheets of non-porous material (two sheets on each side). The panel would go through the same curing cycle as before; the final product can be seen in Figure 44.



**Figure 44** - Finish specimen with DADs

The plates were then removed from the press and were prepped into the final specimen dimensions.

## Chapter 3- Experimental Procedure and Testing

### 3.1- Monotonic and Cyclic Tensile Loading

The experimental testing of the composite sandwich structures were performed in the Cal Poly Aerospace Structures and Composites Lab. Both the static (monotonic) and dynamic (fatigue) testing were performed using an Instron 8801 machine. Two different machine configurations were used specific to either the high load or low load case. The high load cases utilized a 100 kN load cell which was used to test composite sandwich structures with no initial delamination. The high load Instron configuration is shown in Figure 45 - 100 kN load cell Instron grip configuration.



**Figure 45** - 100 kN load cell Instron grip configuration



**Figure 46** - 1 kN load cell configuration and back edge jig

The low force cases used a 1 kN load cell to test specimens with an initial delamination and shear keys. The 1 kN load cell configuration with its appropriate Instron grips is shown in Figure 46 - 1 kN load cell configuration and back edge jig. The aluminum tabs on the test specimens were secured into place by closing the Instron grips. The test specimens were also held into place at the back end using a jig as shown in Figure 46 - 1 kN load cell configuration and back edge jig.

### 3.1-1 Monotonic Testing

Static tests (monotonic testing) were performed on the six different types of test specimens to determine the ultimate loads and failure behavior for each case. The failure loads were required inputs to perform the dynamic (fatigue) testing because the fatigue loading is a function of the monotonic failure. From the previous delamination research the loading rate was investigated under speeds of 0.5, 1.0 and 2.0 mm/min. It was discovered that slower loading rates introduced difficulties with the delaminated test specimens<sup>5</sup>. For that reason a loading rate of 2.0 mm/min was selected. The program used for the monotonic testing was Merlin provided by the Instron. Merlin's failure criteria for testing, was that the loading rate for the tested needed to drop by 50% in order for the tests to stop. Figure 47 - Inputs for monotonic testing shows a screenshot of Merlin before testing, when the inputs are specified Figure 48- Merlin screen during testing shows Merlin during a test.

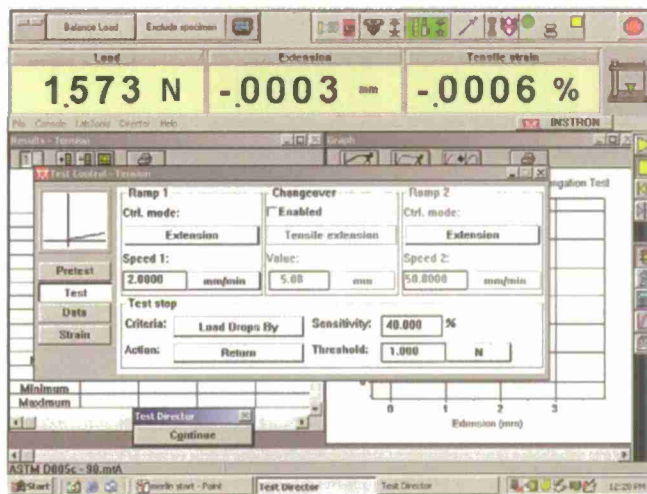


Figure 47 - Inputs for monotonic testing

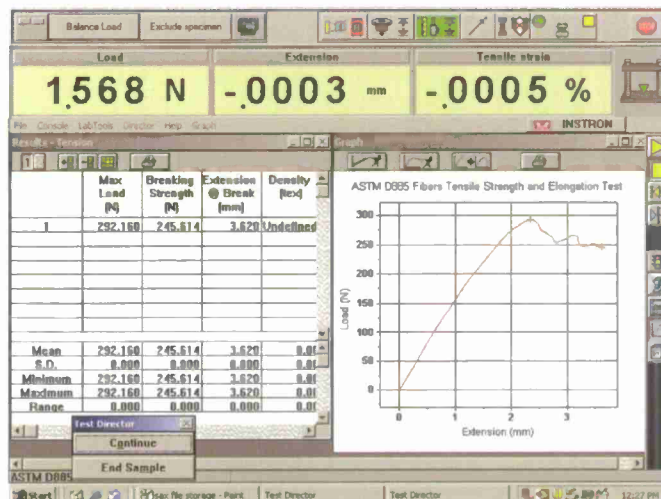


Figure 48- Merlin screen during testing



### 3.1-2 Fatigue Testing

The dynamic testing was performed on the composite sandwich structures to determine the fatigue behavior. The overall goal of the fatigue testing was to construct a stress vs. number of cycles to failure (S-N) curve for the following three sandwich structure configurations:

- No initial delamination
- 0.5 inch initial delamination
- 0.5 inch initial delamination with shear key

The fatigue testing was performed using the Instron program Single Axis MAX (SAX). A sinusoidal cyclic loading was applied to the test specimen from the Instron machine. SAX can either be driven by inputting force or displacement conditions. Force inputs were selected since the monotonic failure characteristics of the sandwich structures were defined in terms of force. The four important parameters that were required inputs into SAX were: frequency, sample rate, mean force, and force amplitude. Figure 49 - SAX input parameters shows a screenshot of SAX and the input parameters required for testing.

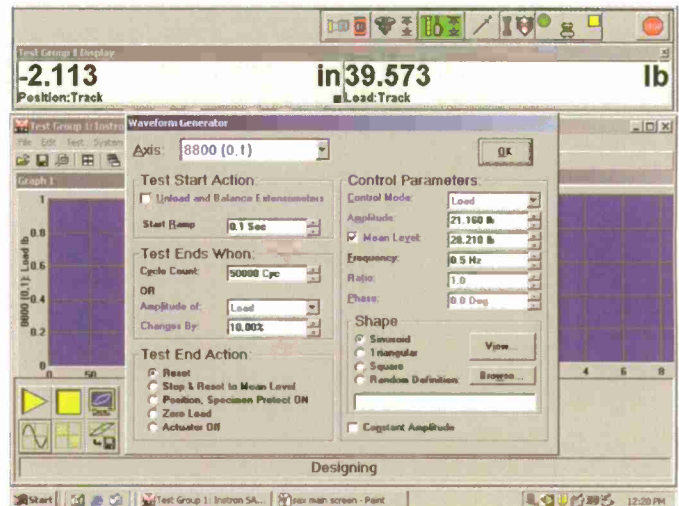
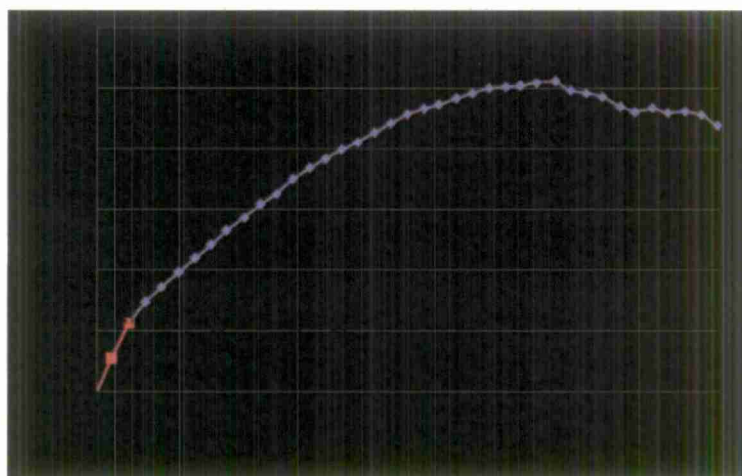


Figure 49 - SAX input parameters

Two important inputs were the force amplitude and mean, which fully defined the sinusoidal wave. Preliminary tests revealed that using the 100 kN load cell put a minimum amplitude requirement of 100 lb<sub>f</sub> for the sin wave to correctly track the input force equal to the output force. This was most likely attributed to the notion that the large load cell has a much smaller force tolerance compared to the 1 kN load cell. This requirement was a driving constraint for determining the force amplitude and mean. From the monotonic testing it was determined that only the test specimens with no initial delamination could be tested using the 100 kN load cell. For the dynamic testing the ratio of the mean force was kept constant for each of the three different composite sandwich structures. Since the non-delaminated test specimens were tested first they dictated the testing parameters for the delamination and shear key test specimens. A mean force of 40% of the max failure load was selected because it allowed for a large number of testing loads to be performed using the 100 kN load cell. Figure 50 - Monotonic force definitions shows an example monotonic force vs. deflection curve and how the ultimate force was selected from the curve.





**Figure 50** - Monotonic force definitions

Figure 51 - SAX input definitions shows an arbitrary sin wave force similar to the one applied for the fatigue testing. To construct the stress vs. number cycles to failure curves (S-N) the specimens were tested at the following percentages of the ultimate monotonic failure forces: 70, 65, 60, 55, and 50. The mean force in Figure 51 - SAX input definitions is represented by the dashed line and was always equal to 40% of the ultimate monotonic failure force. The force amplitude was varied throughout the testing for the different failure force percentages listed above. Example force inputs for an arbitrary case are shown in Table 2 below.

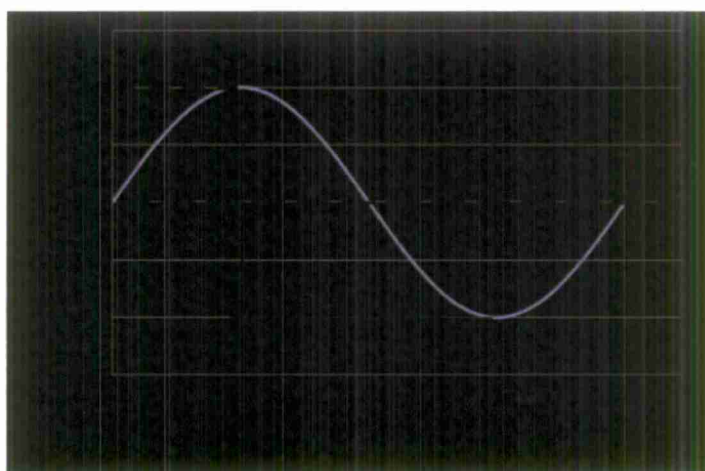


**Figure 51** - SAX input definitions

**Table 2** - Example input forces

| $F_{ULT}$ (lbf) | $F_{MEAN}$ (lbf) | Testing % | $F_{MAX}$ (lbf) | $F_{AMP}$ (lbf) |
|-----------------|------------------|-----------|-----------------|-----------------|
| 550             | 220              | 0.7       | 385             | 330             |

The two other inputs into SAX are the frequency that the machine operates at and also the sampling rate. A frequency of 10 Hz was chosen in an effort to speed up the testing process since fatigue and particularly low force fatigue takes a considerable amount of testing time. The chosen frequency was deemed "not too unrealistically high" to adversely affect the results to the point they would be irrelevant. During the initial testing and calibration phase of the fatigue research, the sample rate was varied. The sample rate not only had an effect on the number of data points stored, but it also affected how the sin wave was applied to the test specimens. A small sample rate had the advantage of data storage but the sin wave would correctly track input equal to output. A sample rate of 0.1 kHz was selected because it was the minimum sample rate that allowed for a correct and smooth sin wave to be input.

To mitigate manufacturing defects on data scatter it was determined that the monotonic failure loads would be determined from each sandwich structure made. Each manufactured sandwich structure yielded 12 test specimens so 2 test specimens were used to determine the failure loads for that particular lay-up batch. This method was used to provide more reasonable test results and present a distinct trend in the data.

### **3-2 Monotonic and Cyclic Compression Loading**

#### **3.2.1 Strain Rate Testing Selection**

A strain rate, according to testing standards, is important for monotonic testing of composites. Since each composite structure is greatly different from one another, one type of strain rate for one structure would be bad for another. A quick strain rate would distort failure results by moving the failure of the fastener/panel interaction quickly from bearing to shear or even to a complete failure of the panel. A slow strain rate would give good results but would take too long to test each specimen. For the strain rate selection, 5 strain rates would be tested ranging from 0.5 mm/min to 1.5 mm/min with 10 specimens per test case and a variance of 0.25 mm/min between the strain rates. The standard for testing metal pieces is a strain rate of 1 mm/min. Since there is no set standard for strain rate for composites, the speeds that were chosen is reasonable to test two rates above and below it for the composite sandwich panel. A failure criterion of a 30% load drop was chosen as the end of test for the monotonic testing. This means that when a total failure drop of 30% for the most maximum load would stop the machine.

All specimens were tested and analyzed; this would be discussed later in detail in Strain Rate/Control Group Results and will be briefly discussed in this section to choose a strain rate for all static testing. A summary of the results are shown in Table 12 in Strain Rate/Control Group Results. The results showed that all five strain rates had similar failure load varying from 890 lbs to 1,011 lbs and had similar elastic modulus varying from 45,170 psi to 50,250 psi. The results show that the strain rate did not greatly affect the characteristics of the panel, but it did show a variance in standard deviation for each case. The table shows that the slowest rate, 0.5 mm/min had the lowest standard deviation for both failure load and elastic modulus. This

rate would be used for all static testing because it gives the best standard deviations compared to the other rates translating a better accuracy to future tests.

### 3.2-2 Static Testing Design

From the detailed literature review, all of the fastener/panel interaction testing was conducted under a tension loading. A compression loading was chosen because a compressive loading would produce a more important failure mode to the panel due to buckling being seen during the testing. A buckling failure would be more of a catastrophic failure for a panel rather than a tear or crack propagating from a tension load. The static testing portion of the experiment would consist of finding the optimum strain rate for testing pieces under monotonic loading and to find the trend of how increasing the thickness of the DADs affect the fastener/composite panel interaction.

From the previous section it was decided that for all static testing the strain rate for the machine to run test would be 0.5 mm/min or 0.0197 in/min. The DAD thickness would be varied from 0 layers to 7 layers. Each case would have a total of 10 specimens to be able to observe the interaction regardless whatever the standard deviation for the case is. A small standard deviation is not necessary since a proof of concept is the purpose of the research and it is assumed that it would have an adequate enough standard deviation from the results shown in the previous section. A failure criterion of a 30% load drop was chosen as the end of test for the monotonic testing. This means that when a total failure drop of 30% for the most maximum load would stop the machine.

### 3.2-3 Fatigue Testing Design

Fatigue testing is when a part is loaded to certain value, usually below the yield stress of the material, and is applied a load amplitude to be cycled. This would show when the material or case would fail over time from normal loading. This is helpful with designers because knowing how the material fails would help design how and when the overall system fails. The load amplitude is usually a sinusoidal wave with its load value varying a percent difference from the yield stress; this can be seen in Figure 52 - Fatigue Cycle. The test is first ramped to half the yield stress. From the detailed literature review and ASTM standards, the yield stress is defined as where the first drop on the stress-strain curve; this is seen in Figure 53 - Yield Stress and Failure Criteria for Fatigue Testing. The stress would be converted to load by the geometry of each test piece, which becomes the force yield. The amplitude, or A, is a dependent on the fatigue testing and what the researcher is investigating with. One fatigue cycle is equivalent to one cycle of the sinusoidal wave. The frequency of the wave is arbitrarily chosen by the researcher. Once the test reaches its failure criterion the test stops and ramps the load back to zero. The criterion is dependent on the researcher. There are two ways to define the failure criterion, a drastic load drop or a drastic change in position of the test specimen.

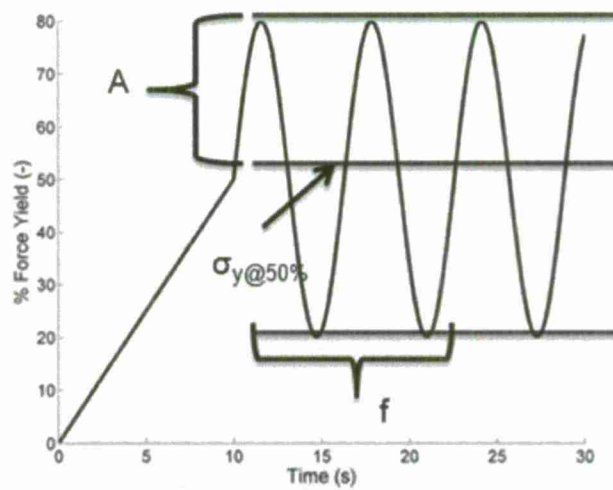


Figure 52 - Fatigue Cycle

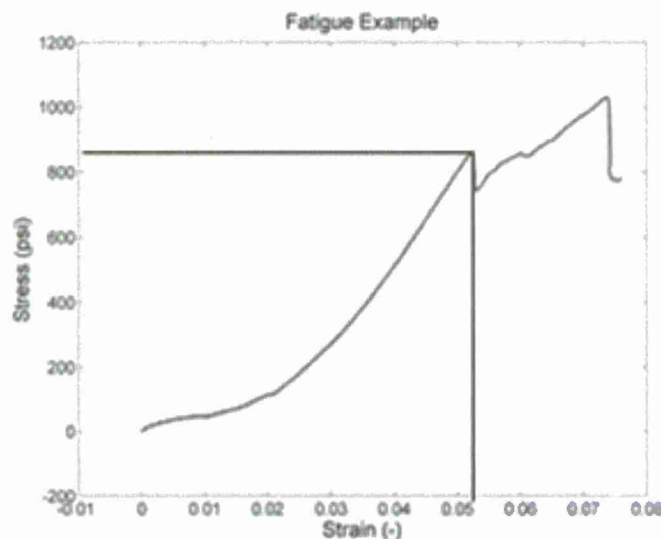


Figure 53 - Yield Stress and Failure Criteria for Fatigue

Two selections were made to fatigue testing for the experiment. The first selection was to choose the failure criterion for the testing. Since the yield stress was chosen as the maximum for the amplitude, the strain at that stress on the stress-strain curve was chosen as the failure criterion. The strain, like the stress, was converted to extension based of each test specimen's geometry and was used as the position failure for the test. Once the test specimen moved by the amount of the extension, the specimen was defined to reach failure. This was also supported from preliminary testing by having a bearing failure around the holes; this would be further discussed.

The second selection for fatigue testing was choosing the frequency to run the testing on. A too high frequency would give inaccurate results because it would be applying too many cycles per second on the

specimen. A low frequency would give more accurate results but would take too long per specimen to run. Two frequencies were investigated to see which one to use for fatigue testing, 5 and 10 Hz. Both test cases were tested with 10 specimens each. The number of cycles of failure and its standard deviation for the two frequencies is shown in Table 3. The results show a drastic difference between the two frequencies, the lower frequency has a lower number of failure cycles while the higher frequency has a higher number of failure cycles. For standard deviation, both have the same similar trend. Since both have high standard deviations, the higher frequency was chosen because it seemed that it would produce a higher average number of cycle failure. It also gives a decent run time, especially if the specimens reach the hundreds of thousands of cycles, which would take hours to run one specimen.

**Table 3 - Summary of Fatigue Frequency Testing Results**

| Frequency | Avg # of Cycles | Std Dev |
|-----------|-----------------|---------|
| (Hz)      | (-)             | (-)     |
| 5         | 5555            | 69.46%  |
| 10        | 7032            | 87.41%  |

For the fatigue testing for the research, two case groups would be run to compare the effects of the DADs on the composite sandwich specimens. The first group would be the control group, no DADs in the specimens, and the other group would only have one type of DAD thickness in each specimen. The trend of how the number of failures increases as the fatigue amplitude decreases would be observed and analyzed for both case groups. The trends would show how the DADs affect the overall lifespan of a composite sandwich panel and how the failure around the fastener happens. It will be assumed that different DAD thicknesses would have similar trends but would be shifted along the graph. The amplitude for each case group would be varied from 90% yield stress to 65% yield stress with 5% spacing, having a total of six test cases. Each test case would have a total of 10 pieces.

The thickness of the DADs for the other case group would be 3 layers. This was chosen because a too thick of a DAD would affect the core/face sheet interaction. The ratio of the total thickness of the DAD over the thickness of the core was set to less than 0.2. The ratio value because it assumes that the insert thickness is still within the infinite range, similar to the ratio value for the hole diameter and the width of the specimen. The 3 layer DADs is the closest to the ration without passing the value, making it the best choice.

### 3.2-4 Static/Fatigue Testing Set-up

The static/fatigue testing of the specimens is pretty simple and straight forward. The specimens are installed on the jig and the software for each respective testing is conducted. The testing specimens are first measured and recorded. The width, length, and thickness of the specimens are measured using a calulator. The



measurements are recorded on Goggle Docs for easy access anywhere; an example of the recording of measurements can be seen in Figure 54 - Example of recording measurements in Google Docs

| Test Specimen | Test Date | Test Type                  | Length | Width | Thickness | Max Load |
|---------------|-----------|----------------------------|--------|-------|-----------|----------|
| 1000-01       | 4/10/2010 | 1 Layer Bond Lay up Method | 1.95   | 1.95  | 1.95      | 1.95     |
| 1000-02       | 4/10/2010 | 1 Layer Bond Lay up Method | 1.95   | 1.95  | 1.95      | 1.95     |
| 1000-03       | 4/10/2010 | 1 Layer Bond Lay up Method | 1.95   | 1.95  | 1.95      | 1.95     |
| 1000-04       | 4/10/2010 | 1 Layer Bond Lay up Method | 1.95   | 1.95  | 1.95      | 1.95     |
| 1000-05       | 4/10/2010 | 1 Layer Bond Lay up Method | 1.95   | 1.95  | 1.95      | 1.95     |
| 1000-06       | 4/10/2010 | 1 Layer Bond Lay up Method | 1.95   | 1.95  | 1.95      | 1.95     |
| 1000-07       | 4/10/2010 | 1 Layer Bond Lay up Method | 1.95   | 1.95  | 1.95      | 1.95     |
| 1000-08       | 4/10/2010 | 1 Layer Bond Lay up Method | 1.95   | 1.95  | 1.95      | 1.95     |
| 1000-09       | 4/10/2010 | 1 Layer Bond Lay up Method | 1.95   | 1.95  | 1.95      | 1.95     |
| 1000-10       | 4/10/2010 | 1 Layer Bond Lay up Method | 1.95   | 1.95  | 1.95      | 1.95     |
| 1000-11       | 4/10/2010 | 1 Layer Bond Lay up Method | 1.95   | 1.95  | 1.95      | 1.95     |
| 1000-12       | 4/10/2010 | 1 Layer Bond Lay up Method | 1.95   | 1.95  | 1.95      | 1.95     |
| 1000-13       | 4/10/2010 | 1 Layer Bond Lay up Method | 1.95   | 1.95  | 1.95      | 1.95     |
| 1000-14       | 4/10/2010 | 1 Layer Bond Lay up Method | 1.95   | 1.95  | 1.95      | 1.95     |
| 1000-15       | 4/10/2010 | 1 Layer Bond Lay up Method | 1.95   | 1.95  | 1.95      | 1.95     |
| 1000-16       | 4/10/2010 | 1 Layer Bond Lay up Method | 1.95   | 1.95  | 1.95      | 1.95     |
| 1000-17       | 4/10/2010 | 1 Layer Bond Lay up Method | 1.95   | 1.95  | 1.95      | 1.95     |
| 1000-18       | 4/10/2010 | 1 Layer Bond Lay up Method | 1.95   | 1.95  | 1.95      | 1.95     |
| 1000-19       | 4/10/2010 | 1 Layer Bond Lay up Method | 1.95   | 1.95  | 1.95      | 1.95     |
| 1000-20       | 4/10/2010 | 1 Layer Bond Lay up Method | 1.95   | 1.95  | 1.95      | 1.95     |

**Figure 54** - Example of recording measurements in Google Docs

Specimens are then taken to the machine and attached to the jig; this can be seen in Figure 55 - Testing Set-up. Bushings are placed inside the hole and are lined up with the holes on the jig. The bolts would contain two washers, placed on the outside of the jigs so the bolt and nut heads aren't touching the jigs. The bolt will be tightened until resistance is made with the jig. The software would then be run until the specimens reach the failure criteria. For static testing, the failure criterion is when the load drops more than 30%. For fatigue testing, the failure criterion is when the position of the test specimens moves a certain amount. For specimens without DADs, the failure criterion is 0.0544" and for specimens with DADs, the failure criterion is 0.0597". All values were calculated from experimental testing. Once the specimens reach the failure criterion, the specimens are removed from the testing apparatus and pictures were taken to document the failure for each specimen. The load failure is recorded on Goggle Docs for future analysis. The specimens are stored for later use and analysis.



**Figure 55** - Testing Set-up

### 3.3 Monotonic Compression Buckling Load

#### 3.3-1 Testing for Mechanical Behaviors under Buckling using Pinned-Pinned Boundary

According to ASTM C-364 standard method, the quasi-static strain rate is 0.2-inch per minute. The setup of the test jig is mounted directly to the displacement unit and the load cell of the Instron 8800 displacement machine. Instron LVDT Displacement Gauge is placed perpendicular to the test specimen and the load vector in order to get the horizontal displacement the specimen is seeing. The test setup can be seen in Figure 56 - Pinned-Pinned Boundary Set Up.



**Figure 56** - Pinned-Pinned Boundary Set Up

The test specimen is placed into the pinned-pinned boundary with aircraft grade bolts, and fastened to avoid any horizontal play. This restricts the specimen to vertical and horizontal movement with rotation capabilities around the hole location. The displacement gauge is lean again the test specimen at its center and measures its displacement. The specimen is loaded digitally using Bluehill 2 software can be seen in Figure 57 - Testing Using Pinned-Pinned Boundary and all raw data is recorded for future processing.



**Figure 57** - Testing Using Pinned-Pinned Boundary

## Chapter 4- Experimental Analysis

The following section is an overview of the experimental results of the three applications being considered: The monotonic loading and fatigue case, the delamination arrestment mechanism case, and damage arrestment device case. To view the full experimental results of each project, see the individual project thesis.

### 4.1- Monotonic Loading and Fatigue Case

#### 4.1-1 Monotonic Failure Analysis

The test specimen stiffness — , was used to compare the monotonic test results for the 6 different test specimen configurations. The fracture mode of the specimens was also of importance because it varied depending on the sandwich structure configuration. The composite sandwich structures had three main material elements where failure may have initiated from: the matrix, the fibers, and/or the foam. From a mechanics point of view, the failure should occur in the weakest of the three materials under constant loading conditions. In all three cases, the failures were caused by the development of cracks in one of the three materials.

##### *No Initial Delamination-Cracks in the Foam*

Most of the test specimens with no initial delamination failed due to the formation of cracks in the foam. Figure 58 - Monotonic failure of specimens with no initial delamination below shows three pictures of a test specimen with no initial delamination and how they failed under monotonic loading. Cracks in the foam normally originated near the upper or lower surfaces as shown on the left hand side of Figure 58 - Monotonic failure of specimens with no initial delamination. Cracks then traveled through the foam at an angle, as shown in the middle and right side of Figure 58 - Monotonic failure of specimens with no initial delamination. The crack stops propagating through the foam when the failure criterion in the Instron machine is reached. These test specimens did not have a symmetric failure on both sides of the foam because the crack traveled across the width of the part as opposed to through the length. It was expected that cracks would initiate in the foam for correctly manufactured test specimens because it was considered the weakest of the three elements.



**Figure 58** - Monotonic failure of specimens with no initial delamination

***No Initial Delamination – Cracks in the Matrix***

The second primary mode of failure in the test specimens was caused by cracks originating in the matrix. Figure 59- Monotonic failure of test specimens without initial delamination shows test specimens that failed due to cracks in the matrix. The picture on the left side shows a crack that started at the top of the test specimen and the picture on the bottom shows a crack that originated on the bottom of the specimen. The majority of the cracks in the matrix originated between the bottom layer of chopped strand mat and the foam. When the specimen failed, the chopped strand mat would delaminate from the foam. The delamination was not smooth because some of the chopped strand mat would remain bonded to the foam. Cracks in the matrix signified the composite sandwich structure was not properly manufactured because the laminate is a stiffer material than the foam. A possible explanation for the cracks could be traced back to the resin/hardener ratio used during the manufacturing process. The resin/hardener ratio could cause the composite to cure as the resin was running through the part, leaving some of the regions of the lay-up with dry fibers.



**Figure 59-** Monotonic failure of test specimens without initial delamination

***0.5 inch Initial Delamination – Cracks in the Foam***

All of the test specimens with a 0.5 inch delamination failed due to the propagation of cracks through the foam core. Figure 60 - Monotonic failure of test specimens with 0.5 inch initial delamination shows 4 pictures of test specimens with a 0.5 inch delamination that have failed. In all of the specimens tested, the cracks originated at the edge of the delamination and then continued to progress through the foam at various angles. The angles at which the cracks traveled through the foam was the only difference between the failures in the test specimens. Both pictures on the upper portion of Figure 60 - Monotonic failure of test specimens with 0.5 inch initial delamination failed due to a crack traveling approximately at 0° from the edge of the delamination. In the two pictures on the bottom of Figure 60 - Monotonic failure of test specimens with 0.5 inch initial delamination traveled down through the foam at angles of approximately 45° and 30°. The failures through the foam signified a good bond between the laminate and the foam core. This was also somewhat unexpected because it was predicted that a delaminated piece would exhibit a peeling effect, causing the delamination to separate the laminate from the foam.



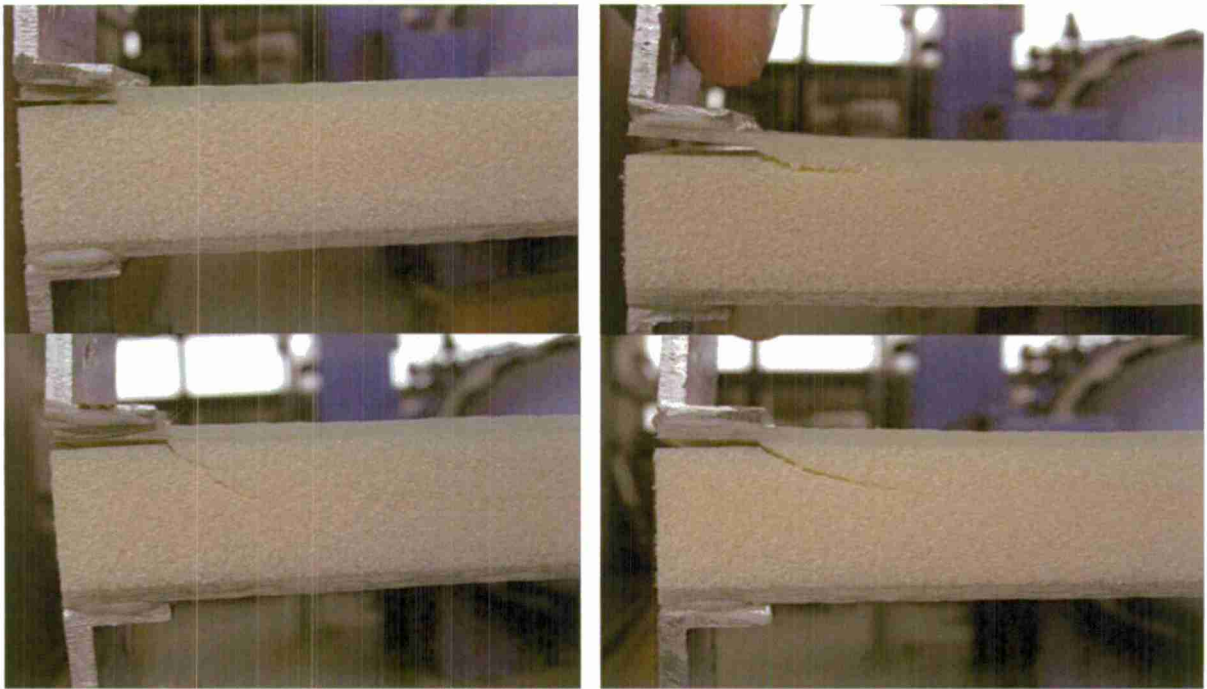


**Figure 60** - Monotonic failure of test specimens with 0.5 inch initial delamination

***1 inch Initial Delamination – Cracks in the Foam***

The majority of the test specimens containing a 1 inch delamination failed due to cracks originating in the foam. Figure 61 - Monotonic failure of test specimens with 1.0 inch initial delamination shows two test specimens that failed due to cracks in the foam core. The 1 inch delaminated test specimens failed in a similar fashion compared to the test specimens with a 0.5 inch delamination. Cracks originated at the edge of the delamination and then traveled downward through the foam, as shown in the upper part of Figure 61 - Monotonic failure of test specimens with 1.0 inch initial delamination. The lower part of Figure 61 - Monotonic failure of test specimens with 1.0 inch initial delamination shows a test specimen where the crack in the foam initially travels downwards but began to travel back through the foam towards the composite skin. The top picture shows a smooth material transition because the crack travels at a relatively constant angle through the foam. The jagged edges of the crack could possibly represent a test specimen that did not receive a good load transfer from the Instron machine.





**Figure 61** - Monotonic failure of test specimens with 1.0 inch initial delamination

#### ***Shear Key Delamination from Foam***

Figure 62 - Monotonic failure shear key delamination shows a side view of the shear key delaminating from the foam. When the deflection of the laminate got too high, it released the shear key free from the foam and the laminate continued to separate from the foam. When this type of failure was first discovered, the validity of the shear key monotonic test data was called into question. Since the shear keys were delaminated from the foam it appeared that there was not a good bond between the foam and the shear keys. It was later determined that there may have been too much wax applied to the shear key mold and the shear keys didn't have enough surface roughness to achieve a good bond to the foam. Future shear key tests implemented these changes, increasing the strength of the test specimens containing shear keys.



**Figure 62** - Monotonic failure shear key delamination

#### ***Shear key crack propagating through foam***

The majority of the test specimens that produced good data failed due to cracks propagating through the foam. Figure 63 - Monotonic shear key failure due to cracks in foam shows a shear key specimen that failed due to a propagating crack. This mode of failure was similar to the failure of the delaminated test specimens with no

shear key. The crack originated at the edge of the delamination and then travels through the foam at a slanted angle.



**Figure 63** - Monotonic shear key failure due to cracks in foam

#### ***0.5 inch Shear Key***

The failure models for the sandwich structures with a shear key 0.5 placed inch behind the delamination edge experienced modes of failure similar to the 0 inch shear keys. The primary mode of failure was the origination of a crack at the edge of the delaminated region that travels through the foam. Figure 64 - Monotonic shear key failure (0.5 inch shear key) shows the failure caused by cracks in the foam. The image on the right side of Figure 64 - Monotonic shear key failure (0.5 inch shear key) shows a crack traveling at approximately a 45° angle which continues through the entire thickness of the foam. This type of crack propagation was the most frequently encountered failure. A secondary type of failure through the foam is shown in the left hand side of Figure 64 - Monotonic shear key failure (0.5 inch shear key). The crack initially travels at an angle less than 30° and then around the shear key as opposed to continuing through the thickness of the foam. This mode of failure was expected with the introduction of shear keys into the sandwich structure test specimens. It was predicted that the shear key would act as a stronger material than the foam, which would drive the crack around the shear key.



**Figure 64** - Monotonic shear key failure (0.5 inch shear key)

#### ***Monotonic Failure Analysis – 1.0 inch Shear Key***

The test specimens with shear keys placed 1.0 inch behind the delamination failed in a similar manner to the 0 and 0.5 inch shear keys. The most common failures occurred in the foam and some failures occurred in

the matrix. Figure 65 - Monotonic shear key failure through matrix (1.0 inch shear key) shows a failure caused by cracks originating in the matrix. Cracks in the matrix caused the delamination to propagate along the upper edge, making the upper composite layer separate from the foam core. The shear key had very little effect on these matrix failures because it was located too far away from the failure region.



**Figure 65** - Monotonic shear key failure through matrix (1.0 inch shear key)

The more common failure for the 1.0 inch shear keys was failure due to cracks in the foam and is shown in Figure 66 - Monotonic shear key failure cracks in foam (1.0 inch shear key) below. The failure for these test specimens was slightly different than the other shear key specimens that failed through the foam. Here the crack starts at a shallow angle of approximately 10-20° and goes down through about 1/10 inch through the foam. Then the crack turns slightly and travels at approximately 180° towards the shear key. Figure 66 - Monotonic shear key failure cracks in foam (1.0 inch shear key) shows two failures caused by shallow cracks in the foam.

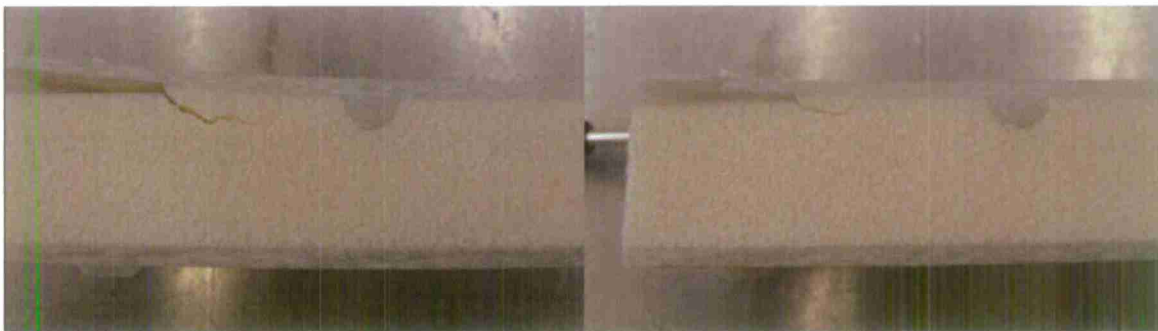


**Figure 66** - Monotonic shear key failure cracks in foam (1.0 inch shear key)

The less common type of foam failure in the 1.0 inch shear keys is shown in Figure 67 - Monotonic shear key failure type II (1.0 inch shear key). The failure starts out the same way as the test specimens depicted in Figure 66 - Monotonic shear key failure cracks in foam (1.0 inch shear key) except the crack travels a different path. The crack travels back up through the foam towards the composite layer and stops at the edge of the shear key. These results seemed somewhat counter intuitive because the intent of the shear keys was to drive the crack away from the upper skin to help stop the delamination.



**Figure 67** - Monotonic shear key failure type II (1.0 inch shear key)

#### **4.1-2 Fatigue Testing**

##### ***1.0 inch Initial Delamination Failure Analysis***

The fatigue failures for the test specimens with a 1.0 inch delamination failed very similarly to the specimens tested under monotonic loading with failure. The majority of the test specimens failed due to cracks originating in the foam. A few test specimens failed due to cracks in the matrix. The main difference between the two types of failures was the speed at which the cracks propagated.

Figure 68 - 1.0 inch delamination fatigue crack propagation through foam and Figure 69 - 1.0 inch delamination fatigue crack propagation type II through foam show the crack propagation of one of the test specimens being subjected to an input of 50% of the — . A 50% load case was selected because it would provide the best representation of the crack propagation because the loading was low, and the crack should move relatively slowly. The left hand side of Figure 68 - 1.0 inch delamination fatigue crack propagation through foam shows the test specimen after 307 cycles, the point at which it was noted the applied force started to drop from the input force. This signified that a microscopic crack had begun to develop even though it was not visible. The right hand side of Figure 69 - 1.0 inch delamination fatigue crack propagation type II through foam shows the same test specimen after 999 cycles where a small crack is clearly visible near the edge of the delaminated region. The angle that the crack begins to travel was similar to the 1.0 inch delaminated test specimens tested monotonically.



**Figure 68** - 1.0 inch delamination fatigue crack propagation through foam



The left side of Figure 69 - 1.0 inch delamination fatigue crack propagation type II through foam shows that after 1385 cycles the crack continued to travel through the foam at approximately the same angle that it began. The right side of Figure 69 - 1.0 inch delamination fatigue crack propagation type II through foam shows the test specimen after 1963 cycles, which was the point the 10% load drop failure criteria was met. It is uncertain whether or not the crack would continue to travel through the foam at the same angle. In most test the cracks appeared to progress down towards the lower fiberglass skin. This type of failure was similar to the results obtained from the test specimens with shear keys placed 1.0 inch behind the back edge of the delamination.



**Figure 69** - 1.0 inch delamination fatigue crack propagation type II through foam

The other type of fatigue failure observed for the test specimens with an initial delamination of 1.0 inch was cracks in the matrix, characterized by a delamination that caused the fiberglass skin to separate from the foam core. Figure 70 - 1.0 inch delamination fatigue crack propagation through matrix shows the fatigue crack propagation when failure was caused by cracks in the matrix. The test specimen here was subjected to a loading rate of 55% of the — and an easily visible crack was expected, but that did not turn out to be the case. The left side of Figure 70 - 1.0 inch delamination fatigue crack propagation through matrix shows that the skin started to peel away from the foam after only 123 cycles. The same test specimen quickly reached the failure criteria after only 381 cycles. Based on the data obtained from the 50% loading rate it was determined that this was a premature failure because the crack should have initiated in the foam because the epoxy is a stronger material than the foam. The stiffness of the epoxy is 5 times greater than that of the foam. For the test specimens with an initial delamination of 1.0 inch fatigue failure caused by a crack in the matrix signified a premature failure that was attributed to defects introduced during the manufacturing process.



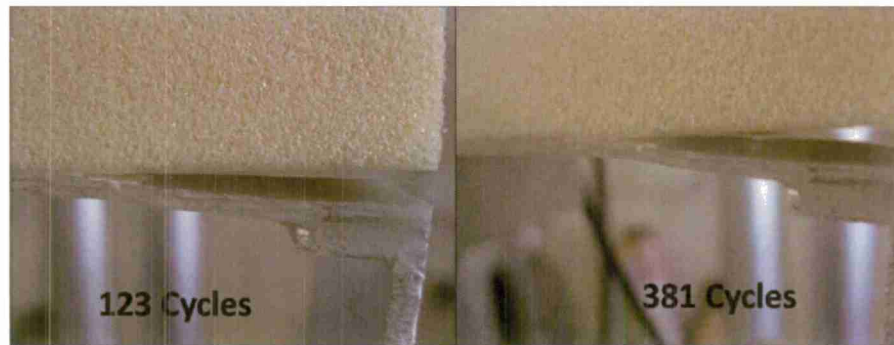


**Figure 70** - 1.0 inch delamination fatigue crack propagation through matrix

#### **1.0 inch Shear Key Failure Analysis**

All of the fatigue failures for the shear key test specimens were caused by cracks in the matrix Figure 71 - Shear key fatigue failure analysis shows a shear key test specimen subjected to 65% loading with a crack propagating along the upper fiberglass skin. The image on the left of Figure 71 - Shear key fatigue failure analysis shows the initiation of the crack and the image on the right of Figure 71 - Shear key fatigue failure analysis shows the final failure.

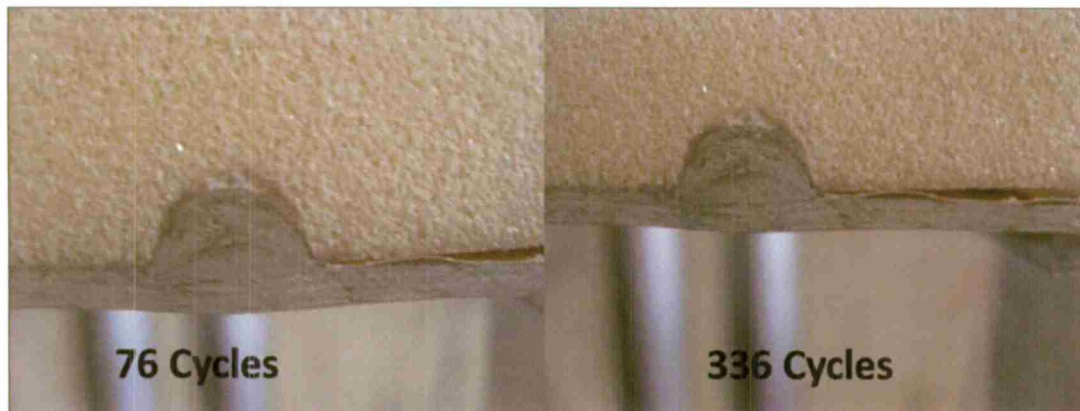


**Figure 71** - Shear key fatigue failure analysis

#### **4.1-3 Monotonic Results Comparison**

Figure 72 - Monotonic experimental results comparison (delamination) shows the monotonic force vs. displacement results for the test specimens with an initial delamination of 0.5 and 1.0 inch. Although both delamination lengths reach a similar ultimate — of approximately 100 — the two curves are very different. The 0.5 inch delamination test specimen only reached a maximum displacement of approximately 0.04 inches where as the 1.0 inch delamination specimens reached a maximum displacement of approximately 0.08 inches.

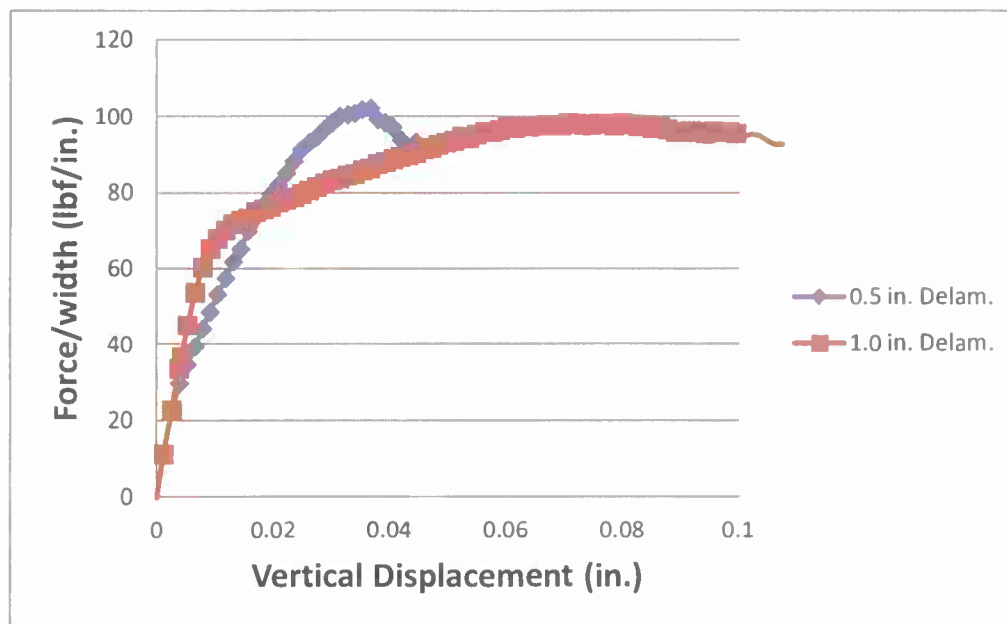


**Figure 72 - Monotonic experimental results comparison (delamination)**

The large differences can be attributed to the L-shaped aluminum brackets used to apply the load to the specimen from the Instron machine. The brackets had leg lengths of 0.5 inches that was bonded to the upper skin of the sandwich structures. The combination of the 0.5 inch delamination and aluminum bracket create almost a purely vertical pull-up force. The 1.0 inch delamination test specimens are not purely a vertical force because half of the delamination length is not bonded to the aluminum tab. At the free delamination area a moment is created there which causes the 1.0 inch delamination test specimens to require more force to initiate the onset of plastic deformation. This can be seen in Figure 73 - Experimental monotonic results (shear keys and delamination) because the red curve has a much larger elastic region (up to approximately 70 —) than the 0.5 inch delamination pieces which only remains elastic up to approximately 20 —. For the 1.0 inch delamination test specimen to deform plastically a larger force is needed because the applied forces not only created a pull-up force, but also a moment due to the delamination length that was not directly under the aluminum tab.

Figure 73 - Experimental monotonic results (shear keys and delamination) shows the monotonic test results for the three different shear key configurations as well as the 1.0 delamination case. All four configurations had very similar elastic and plastic deformation. The shear key configurations were characterized by an elastic response up to approximately 55 — and afterwards followed by plastic deformation until the ultimate force was reached. The 0 inch shear key reached the highest ultimate force/width value of approximately 100 — followed by the 0.5 inch shear key at 98 — and the 1.0 inch shear key at 95 —. The

1.0 inch delamination test specimen had a slightly higher ultimate stiffness of approximately 102 — and similar elastic response. Figure 73 - Experimental monotonic results (shear keys and delamination) shows the shear keys had virtually no positive effect for increasing the monotonic failure strength of initially delaminated test specimens which is not entirely unexpected.

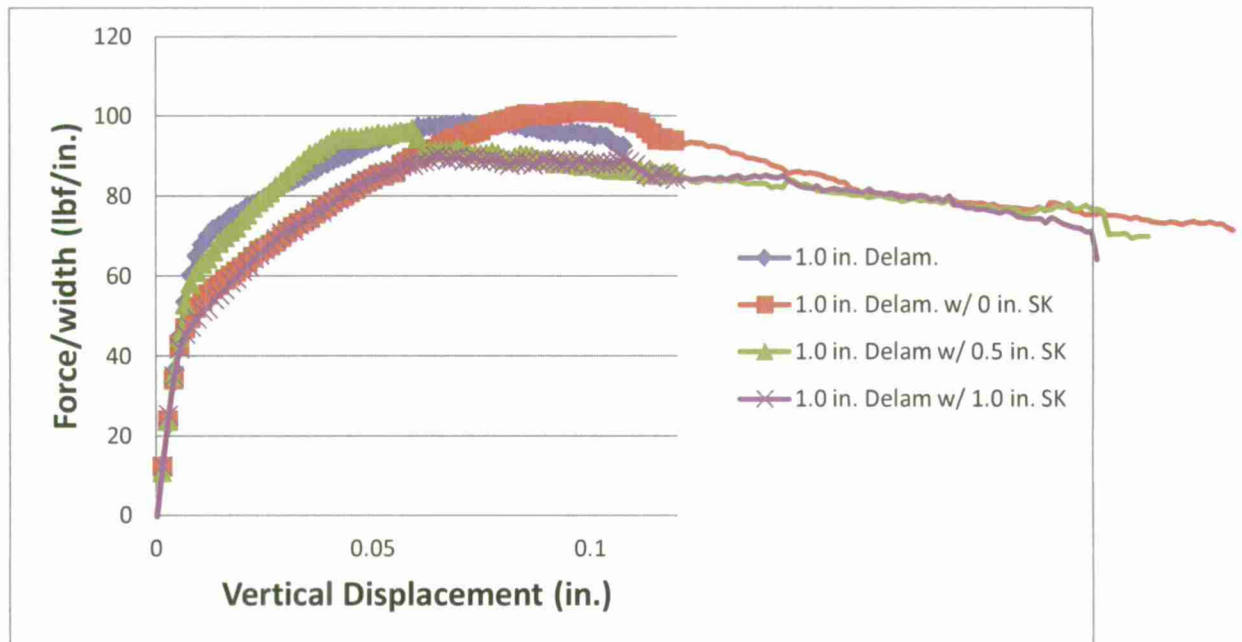


**Figure 73** - Experimental monotonic results (shear keys and delamination)

Adding shear keys to initially delaminated test specimens seemed to only add a stress concentration to the test specimens which does nothing to increase the strength of the parts. The stress concentrations do not have a major effect on the test specimen with a 0 inch shear key but as the shear keys get moved further away from the back edge of the delamination the test specimens slowly get weaker. A possible explanation for this is that shear keys are simply additional defects added to the structure. Just as an initial delamination causes the test specimens to fail much sooner than a part without an initial delamination the shear keys have the same effect. By placing the shear key at the back edge of the delamination it essentially combined the two defects together into one which was why the 0 inch shear key specimens were only slightly weaker than the test specimen with only an initial delamination. As the shear keys moved away from the edge of the delamination this created another defect in the part. This explains why the 0.5 and 1.0 inch shear key specimens were weaker than both the 0 inch shear key and the test specimen with only an initial delamination.

#### 4.1-4 Data Summary

Table 4 is a summary of the three sets of monotonic test data values obtained from the sandwich structures without shear keys. All three test sets have relatively similar elastic stiffness values, with the exception of the 1 inch delaminated specimens being a little less. The yield stiffness value of the 0.5 inch initial

delamination specimens was significantly less compared to the other two sandwich structure types. One would expect a smaller delamination would correspond to a stronger part, with a higher ultimate stiffness, but that was not the case for the yield stiffness. A possible explanation for the weaker yield stiffness for the 0.5 inch delaminated test specimens could be that the 0.5 specimens had a different load path than the 1 inch delaminated specimens. The aluminum tabs used to transfer the load from the Instron machine to the test specimens had a 0.5 inch leg length that got bonded to the upper and lower surface of the specimens. For the 1 inch delaminated pieces the load was not being applied directly axially because the extra 0.5 inch that was not connected to the aluminum tab created a moment. Adding a moment makes the loading conditions no longer purely axial, causing the loading conditions to be mixed modes (Modes I and II). Both the 0.5 inch and non-delaminated pieces had the load applied almost entirely axially applied (Mode I). The different loading conditions could also account for the slight differences in the elastic stiffness.

**Table 4 - Monotonic test data summary**

| Test Type               | Elastic Stiffness — | Yield Stiffness — | Ult. Stiffness — |
|-------------------------|---------------------|-------------------|------------------|
| No Initial Delamination | 8676                | 310.35            | 396.02           |
| 0.5 in. Delamination    | 8777                | 22.69             | 102.21           |
| 1 in. Delamination      | 7832                | 60.32             | 98.34            |

## 4.2 Delamination Arrest Mechanism Under Buckling

### 4.2-1 Control Groups

The control groups, as discussed, are used to provide comparable results between control groups and their experimental group counterparts. The groups include investigating where there is no delamination or an embedded key, test specimens with initial delamination only, and test specimens with an embedded key only.

### 4.2-2 Control Group: No Delamination and No Embedded Arrestment Key

The '11 inches' configuration was retrieved from the buckling length research discussed earlier and is displayed in Table 5.

**Table 5 - '11 inches' Configuration**

| Case      | Slenderness Ratio | Max Vertical Extension | Ultimate Load | Max Horizontal Extension |
|-----------|-------------------|------------------------|---------------|--------------------------|
| -         | -                 | in                     | lbf           | in                       |
| 11 inches | 65.39673          | 0.11083                | 685.60279     | 0.42417                  |

From the Figure 74 - '11 inches' – Load versus Vertical Extension the graph shows a gradual climb in load and then begins to round off at the top of the load versus vertical extension until the test specimen experiences a failure. This configuration is built where no additional components in the structure are so that the bonding between the skin and cores is not disturbed.

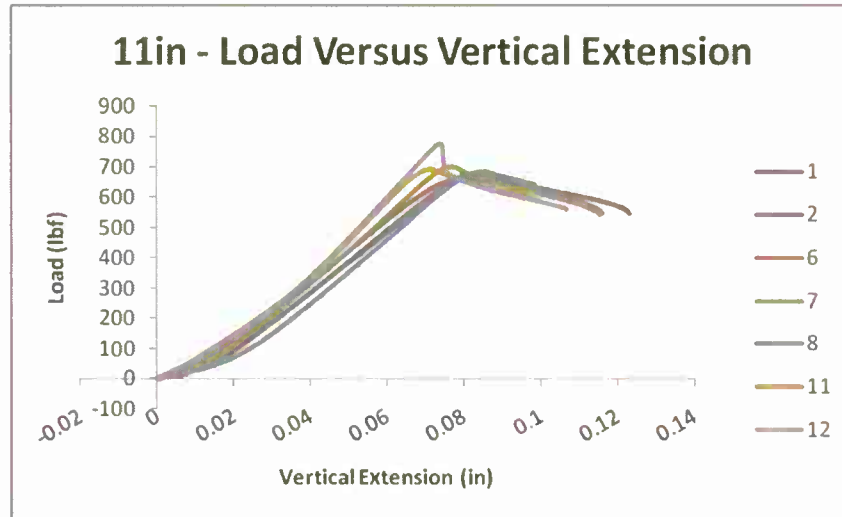


**Figure 74 - '11 inches' – Load versus Vertical Extension**

Figure 74 - '11 inches' – Load versus Vertical Extension is quite similar to Figure 75 - '11 inches' – Load versus Vertical Extension because the vertical displacement transitioned a displacement in the horizontal direction. This transition is due to the pinned boundaries on the test specimen as it rotates to create a deflection with the maximum extension located at the center. It starts off with a slow increase in horizontal displacement per given loading then begins to exponentially displace.

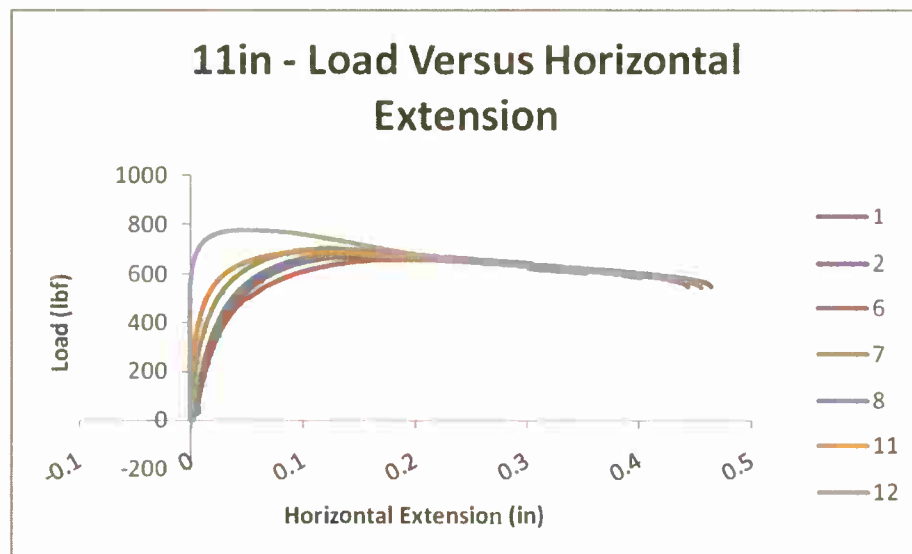


**Figure 75 - '11 inches' – Load versus Vertical Extension**



With the combination of the horizontal extension data and the vertical extension data seen in Figure 76 - '11 inches' – Load versus Vertical Extension the graph shows an increased horizontal displacement when the load is applied. This means that the test specimens began to rotate around the pinned points and buckle.

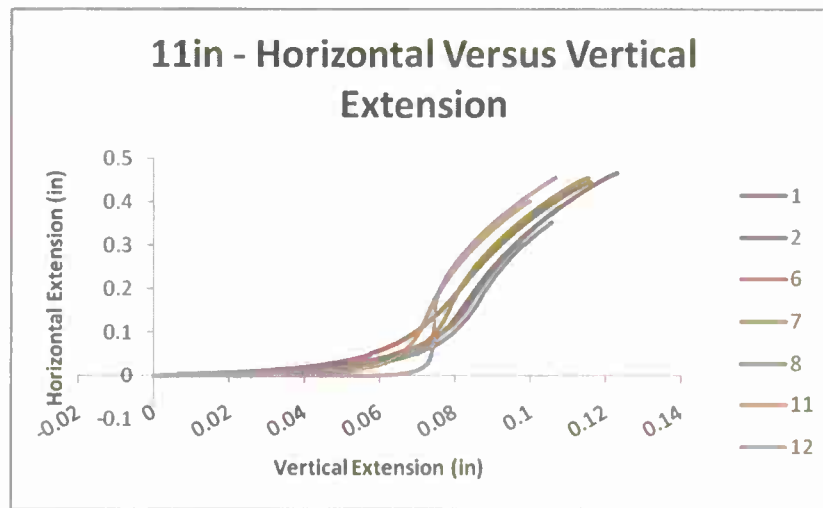


Figure 76 - '11 inches' – Load versus Vertical Extension

#### 4.2-3 Control Group: Initial Delamination with No Embedded Arrestment Key

The second control group that was studied was test specimens that were introduced with a delamination before they were tested. The introduction of the initial delamination is done with non-porous material that is thin and inserted before the skin and the core materials. This non-porous material does not change the material properties of the composite sandwich structure but only create the delamination used in this section. The delamination region extends the width of the structure and varies in height between half-inch to 2 inches in length per half-inch increment. For this group, the delamination length and the term 'ID' denote the different cases after; an example of this is '1.0 ID'. The resultant data is shown in Table 6:

Table 6 - 'ID' Initial Delamination Configuration

| Case # | Case      | Slenderness Ratio | Max Vertical Extension in | Ultimate Load lbf | Max Horizontal Extension in |
|--------|-----------|-------------------|---------------------------|-------------------|-----------------------------|
| 0      | 11 inches | 65.39673          | 0.11083                   | 685.60279         | 0.42417                     |
| 1      | 0.5 ID    | 66.06927          | 0.05020                   | 479.36398         | 0.02274                     |
| 2      | 1.0 ID    | 65.69982          | 0.03675                   | 267.32638         | 0.00986                     |
| 3      | 1.5 ID    | 66.21160          | 0.02963                   | 158.26181         | 0.02399                     |
| 4      | 2.0 ID    | 65.89214          | 0.04118                   | 132.60860         | 0.04519                     |

From the table, it shows that the delamination in the composite sandwich structure dramatically decreases the loading capability of the test specimens. The loading capability drops approximately 35% for the half an inch delamination, denoted by 0.5 ID, and continues to drop per each increase of the delamination's area size. This is why most structures will require repairs before the delamination can affect the structural integrity and needs frequent inspection. Otherwise, the structure can easily become an expensive piece of scrap.

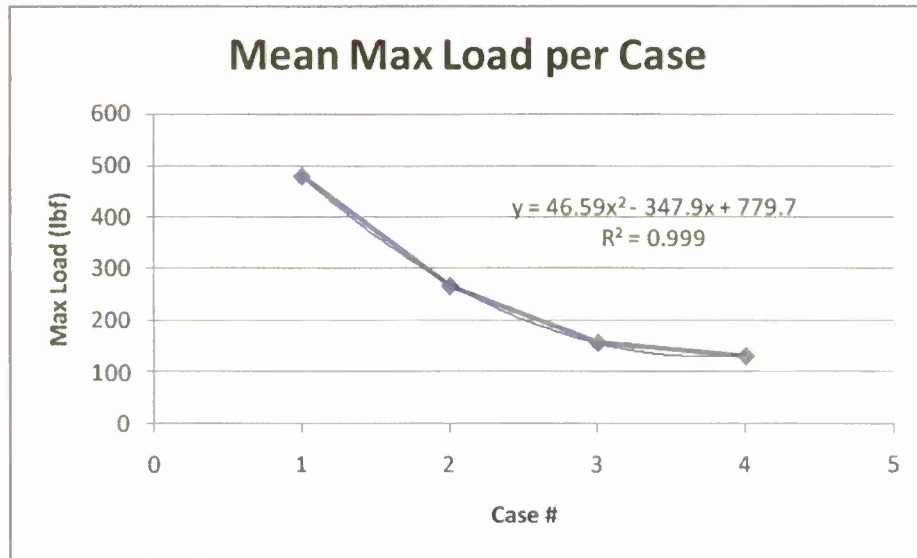


Figure 77 - Mean Ultimate Load per Case

Using the data from Table 6, the graph shows decrease in the load capacity as the delamination region increases. This is a typical trend for most composite metals. One thing to note about Figure HJ is that it fits a parabolic trend line and seems to become asymptotic as the size of the delamination increases. As for Figure 77 - Mean Ultimate Load per Case, it shows a similar trend as Figure 78 - Mean Ultimate Stress per Case but the difference is the geometry factor.

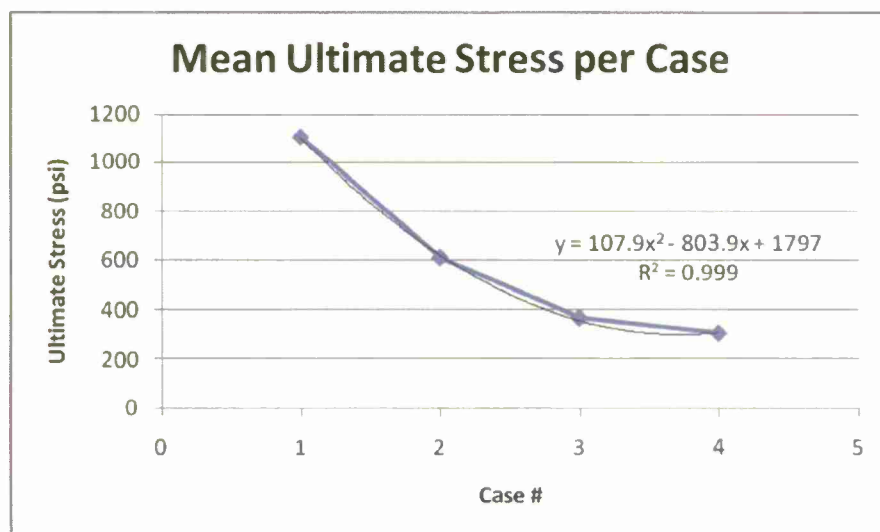
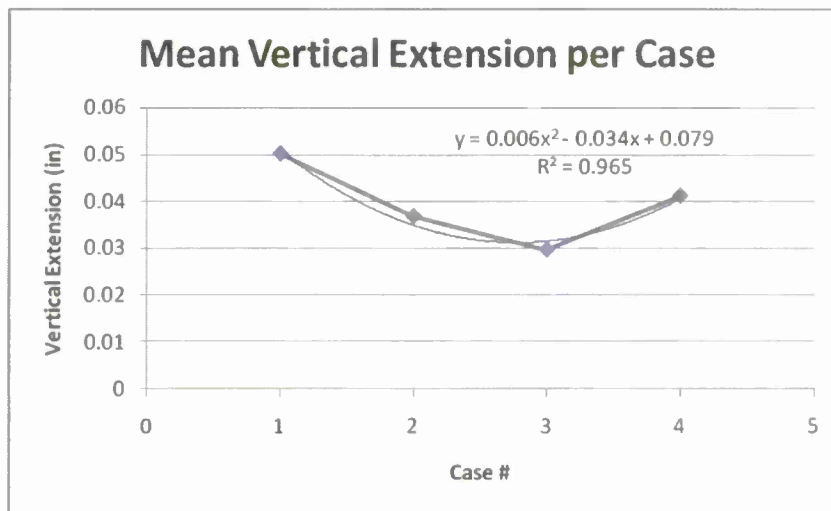
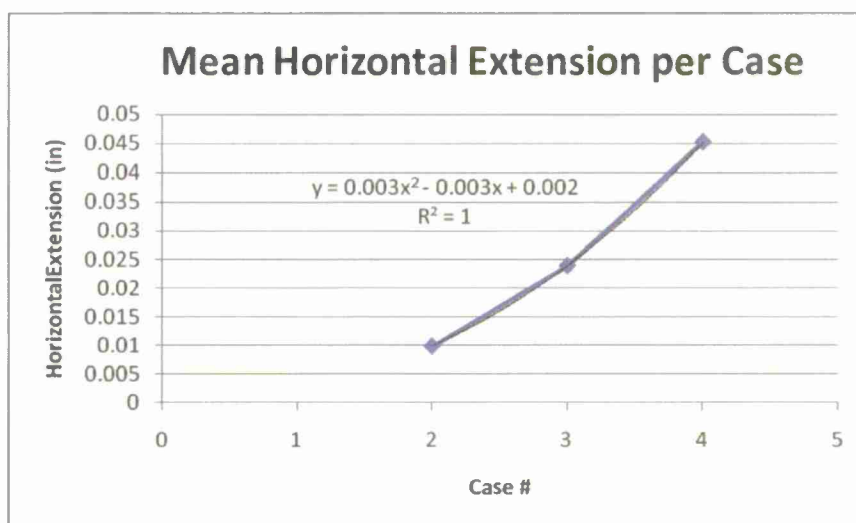


Figure 78 - Mean Ultimate Stress per Case



**Figure 79 - Mean of Maximum Vertical Extension per Case**

The maximum vertical extension per each of the initial delamination cases is shown in Figure 79 - Mean of Maximum Vertical Extension per Case. The data shows that the extension is greatest with the 0.5- inch delamination and bottoms out at the 1.5-inch delamination test specimen. From this parabolic trend line, the increase in the size of the delamination means a decrease in vertical extension until the curve bottoms out and becomes asymptotic. The reason for the decrease in vertical extension with the increase in delamination size is because the composite sandwich structure fails much earlier. The 2.0-inch case was removed from the graph because the vertical extension during the data acquisition was not properly set up. As the vertical extension decreases, the horizontal extension increases due to the structural incapacity to resist the flexure as the structure is loaded. Figure 80 - Mean of Maximum Vertical Extension per Case details the results of the horizontal extension per each case. The case regarding the 0.5-inch delamination was removed from the graph due to its high standard deviation. This high standard deviation can be attributed to the data acquisition setup process.

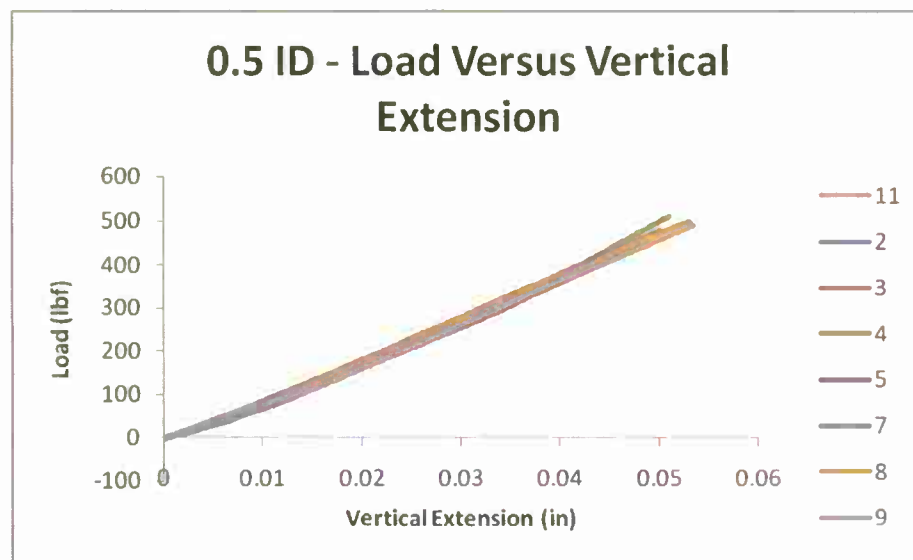


**Figure 80 - Mean of Maximum Vertical Extension per Case**

Note that the following subsections show individual cases with the various delamination sizes. The test specimens in these subsections have the same geometry and same manufactured process except for the delamination sizes. The buckling of these test specimens is only measured on the side with the delamination region. The issue with the buckling of the structure and face sheet is that it requires two different extensometers to measure the extensions on both sides of the test specimens. With the limitations in resources, one extensometer was used and placed on the delamination region side of the test specimens.

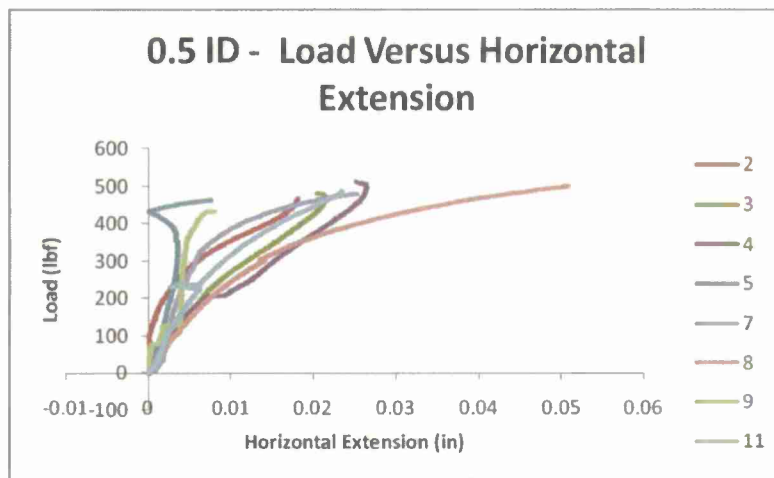
#### 4.2-4 Half-Inch Initial Delamination

The first delamination set of data comes from the test specimens that have an initial delamination that extends the width dimension and the 0.5-inch length at the center of the test specimen. The test specimens remain elastic in nature until they fracture. This is detailed in Figure 81 - 0.5 ID – Load Vs. Vertical Extension where the test specimens are introduced to in-plane loading and remain in the elastic region. The main reason for the brittleness of the structure comes from the materials chosen. The foam core is quite brittle in nature and is reinforced with fiberglass skin.



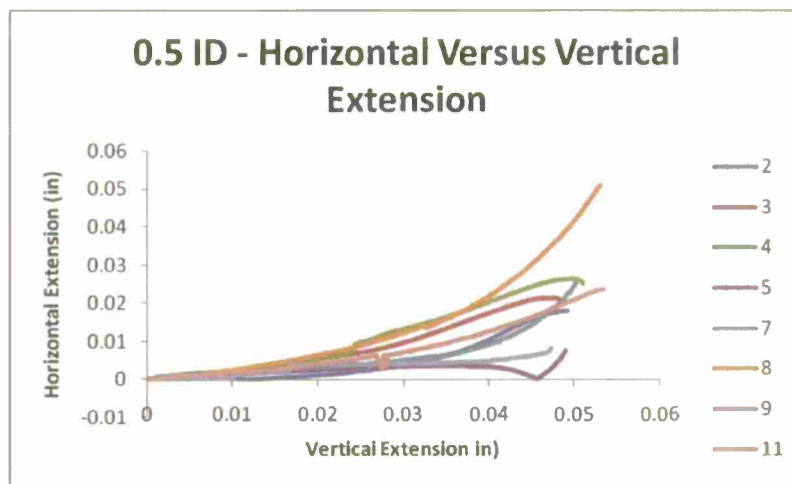
**Figure 81** - 0.5 ID – Load Vs. Vertical Extension

Figure 82 - 0.5 ID – Load Vs. Horizontal Extension shows the test specimens extending horizontally and the buckling of the face sheet before it fractures. This reflects how well the test specimens can hold the load conditions. The smaller the delamination region, the higher loading capacity of the test specimen becomes. This is due to less localized stresses on the part. Figure 82 - 0.5 ID – Load Vs. Horizontal Extension looks odd due to the limitation of the extensometer causing the higher fluctuation.



**Figure 82** - 0.5 ID – Load Vs. Horizontal Extension

Figure 83 - 0.5 ID – Horizontal Extension Vs. Vertical Extension represents the relationship between the horizontal extension and vertical extension and shows a progressive increase in horizontal extension as the vertical extension is being displaced. There is much more vertical displacement than horizontal displacement hence the low profile curves in the Figure 83 - 0.5 ID – Horizontal Extension Vs. Vertical Extension. This is seen as the little spike at the end of the linear plot.



**Figure 83** - 0.5 ID – Horizontal Extension Vs. Vertical Extension





**Figure 84 - 0.5 ID – Experimental Testing Before and After Failure**



What can be seen from

Figure 84 - 0.5 ID – Experimental Testing Before and After Failure was that the experimental testing before failure shows very little horizontal extension and as the strain energy releases, the crack propagates very quicker through the test specimen as seen on the right image.

#### **4.2-5 1-Inch Initial Delamination**

The second data set comes from the 1.0-inch delamination test specimens that were tested under in-plane loading. What differs in Figure 85 - 1.0 ID – Load Vs. Vertical Extension in comparison to the 0.5-inch delamination is that the test specimens fail a bit earlier thus the reason for the shorter vertical extension. The test specimens still exhibit the same elastic properties, but begin to transition near the end of life before they fracture as seen in Figure 83 - 0.5 ID – Horizontal Extension Vs. Vertical Extension.

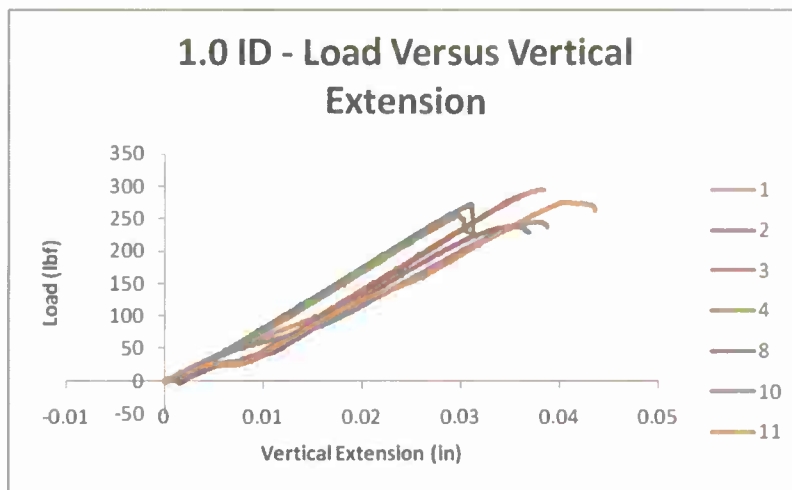


**Figure 85 - 1.0 ID – Load Vs. Vertical Extension**

In Figure 86 - 1.0 ID – Load Vs. Horizontal Extension, it shows a trend that deviates and transitions from the vertical extension where the test specimens would see a slight buckling occurrence of the face sheet when the loading is closer to the ultimate. As discussed earlier in '0.5 ID' configuration section, the limitation of the extensometer dramatically affects the deviation of the horizontal displacement. What can be extracted from the graph is that the test specimens require less loading when increased in delamination length.

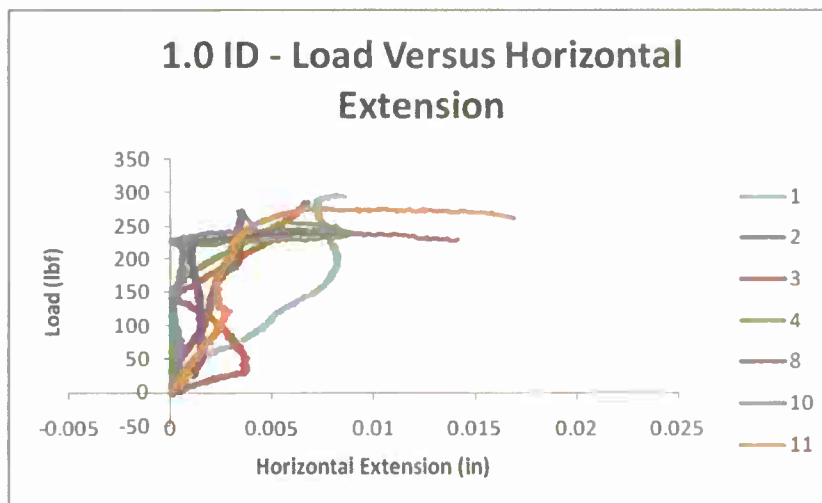


**Figure 86 - 1.0 ID – Load Vs. Horizontal Extension**

From the combination of the vertical extension with the horizontal extension data, it does show that the skin begins to buckle but the structure would fail before the initial delamination could do more damage. This is shown in Figure 87 - 1.0 ID – Horizontal Extension Vs. Vertical Extension.

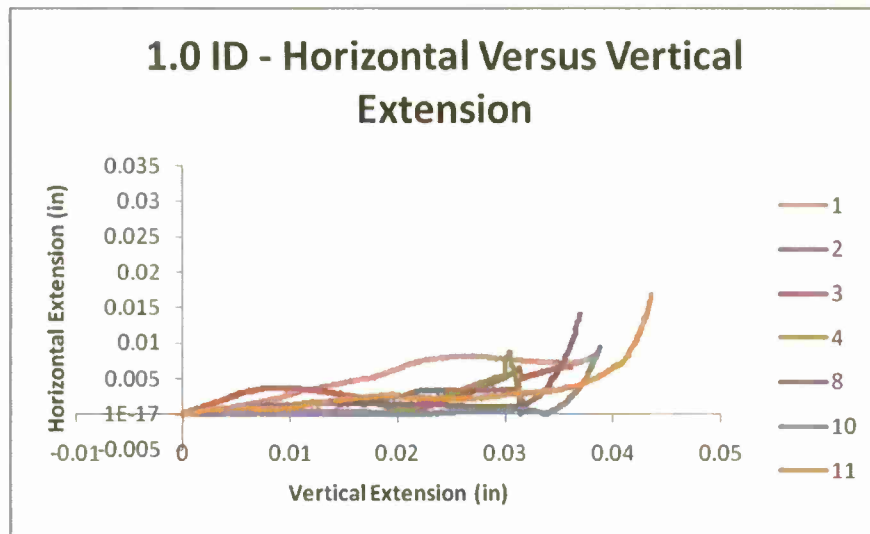


**Figure 87 - 1.0 ID – Horizontal Extension Vs. Vertical Extension**

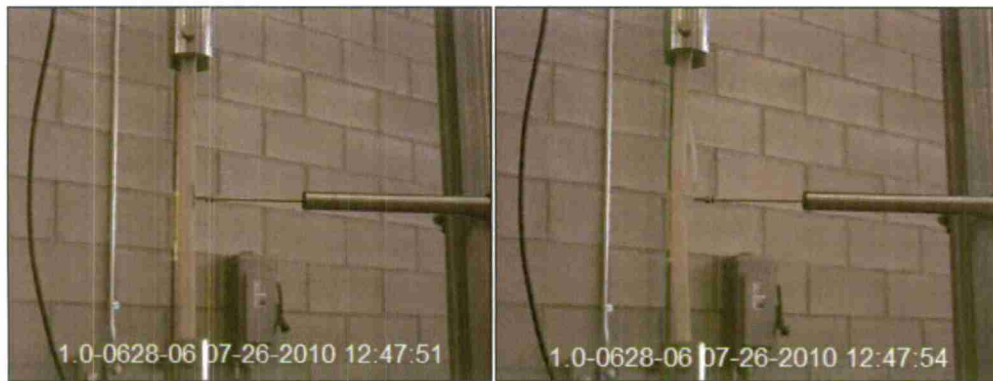


**Figure 88 - 1.0 ID – Experimental Testing Before and After Failure**

Similar to what was seen for the '0.5 ID' configuration, the '1.0 ID' configuration differed by having a slightly larger extension. The strain energy also propagated the crack and caused the failure of the test specimen. This can be seen in Figure 88 - 1.0 ID – Experimental Testing Before and After Failure.

#### **4.2-6 1.5-Inch Delamination**

As for the 1.5-inch delamination test specimens, the delamination of these test specimens is buckling more than the previous two delamination cases. The buckling occurred because the delamination region is much larger and the edge of the delamination region, or the crack, propagates between the skin and core under in-plane loading. The Instron displacement machine will stop the test when the test specimens exhibit a 40% load drops from the ultimate loading. This is why Figure 89 - 1.5 ID – Load Vs. Vertical Extension shows a failure point at the largest vertical extension. Also, another thing to note is how the load versus vertical extension is curved. The curvatures show a displacement that requires less loading, which is exhibiting instability in the composite sandwich structure.

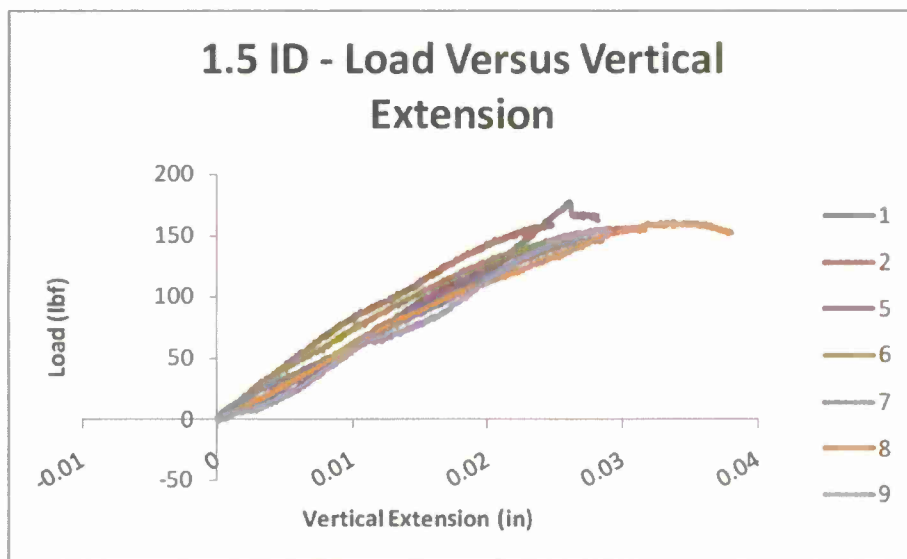


**Figure 89 - 1.5 ID – Load Vs. Vertical Extension**

As seen in Figure 90 - 1.5 ID – Load Vs. Horizontal Extension, the load versus horizontal extension transitioned from Figure 89 - 1.5 ID – Load Vs. Vertical Extension. The vertical extension is transitioned to the horizontal direction where it slows displacement in the horizontal direction with the increase in loading. The curvature in each of the curves details the test specimen's buckling of the whole structure in one direction. Then the hook in the curves details the horizontal extension of the face sheet in the opposite direction.

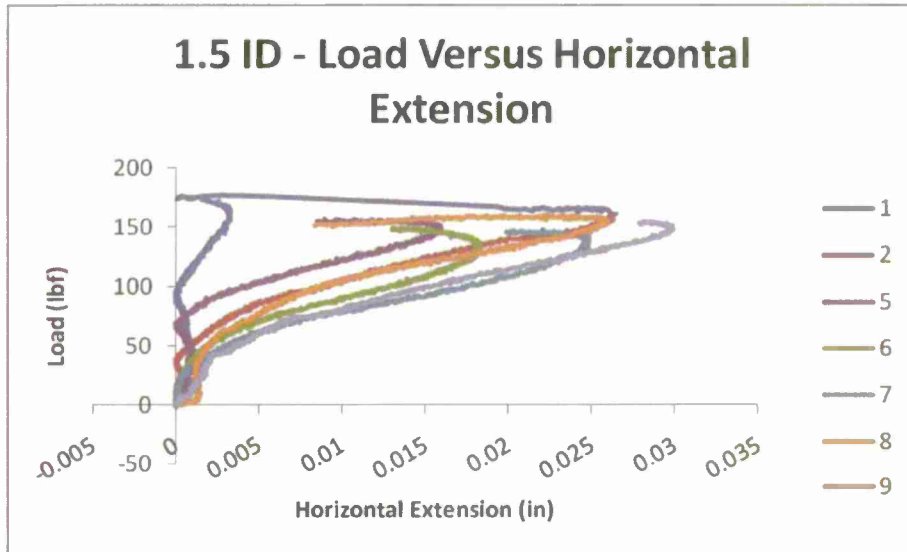


**Figure 90 - 1.5 ID – Load Vs. Horizontal Extension**

The combination of the two extensions, which are the vertical and horizontal extensions, shows a great amount of horizontal extension as the vertical extension increases. Same as what has been discussed; the face sheet delamination buckles more with the increase size of the delamination. This Figure 91 - 1.5 ID – Load Vs. Horizontal Extension below details that quite well.

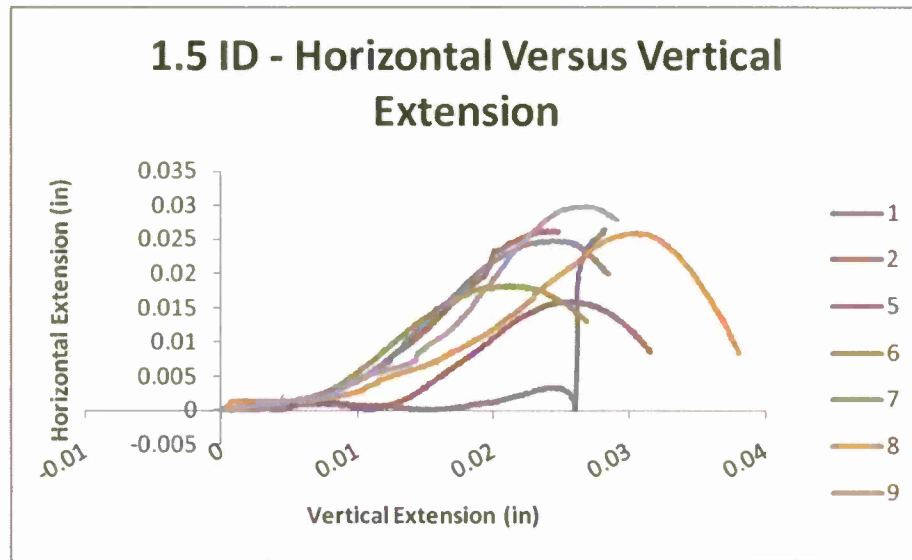


**Figure 91 - 1.5 ID – Load Vs. Horizontal Extension**



**Figure 92 - 1.5 ID – Experimental Testing Before and After Failure**

As the initial delamination size starts to increase, the face sheet delamination becomes more visible and can be seen in Figure 92 - 1.5 ID – Experimental Testing Before and After Failure on the left. The right image shows the failure of the test specimen and because of the larger delamination size. There is less strain energy causing the crack propagation to not spike as high along the seam between the foam and fiberglass skin.

#### **4.2-7 2-Inch Delamination**

Similar to all the other subsections discussing the transition of the composite sandwich structures to the increased experience of a buckling feature; Figure 93 - 2.0 ID – Load Vs. Vertical Extension the 2-inch delamination region experiences this most and much earlier due to the delamination size and the ease of propagation.



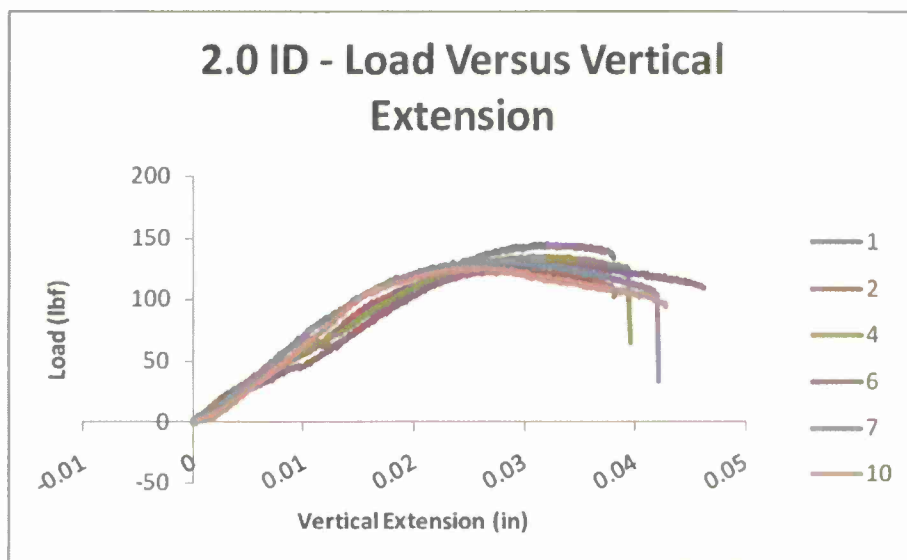


**Figure 93 - 2.0 ID – Load Vs. Vertical Extension**

Similar to what was discussed for '1.0 ID' configuration regarding the load versus the horizontal extension, this stands true for the '2.0 ID' configuration as well. The only difference shown in Figure 94 - 2.0 ID – Load Vs. Horizontal Extension is the increase how much the face sheet is displaced as the vertical displacement is applied. These two graphs show a lot of similarities where the structure buckles in one direction as the face sheet buckles in the other direction.

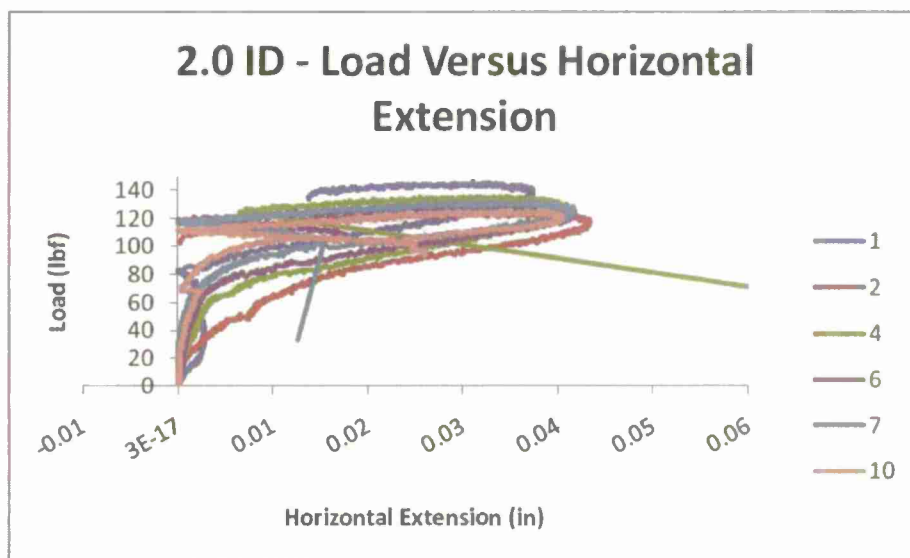


**Figure 94 - 2.0 ID – Load Vs. Horizontal Extension**

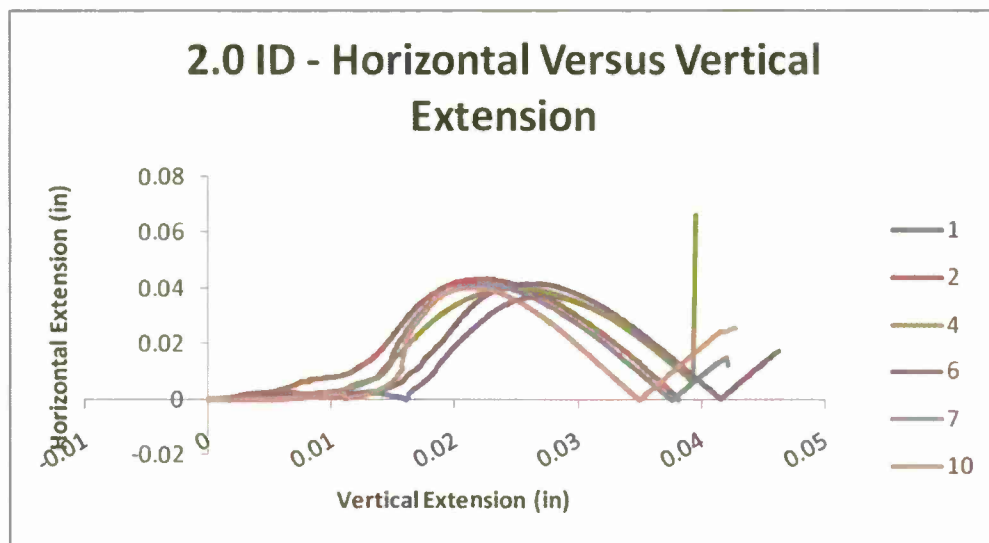


**Figure 95 - 2.0 ID – Horizontal Extension Vs. Vertical Extension**

In Figure 95 - 2.0 ID – Horizontal Extension Vs. Vertical Extension, the trend is a bit different because the structure buckles much more before the face sheet begins to buckle. This is seen in the graph where the horizontal begins to climb then recedes as the vertical extension increases. The spikes at the end of the curves in Figure 95 - 2.0 ID – Horizontal Extension Vs. Vertical Extension are the points of failure.

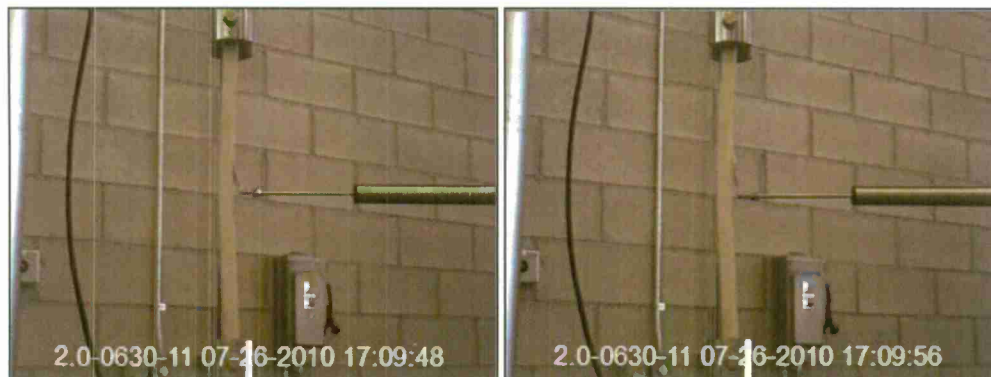


**Figure 96 - 2.0 ID – Experimental Testing Before and After Failure**

Figure 96 - 2.0 ID – Experimental Testing Before and After Failure shows a longer horizontal extension because of the initial delamination size placed under loading. This later transitioned to a small burst of energy causing the edge of the initial delamination to propagate a bit more. The larger delamination size also shows a larger decrease in loading capacity.

### 4.3 Damage Arrestment Devices

All experimental testing and results would be discussed in this chapter in detail. The mechanical characteristics of the material were tested, such as the volume fraction of the face sheets and the material characteristics of the core, the face sheet, and the overall composite sandwich panels. The effects and trends of

changing the DADs thickness on the failure characteristics of the composite sandwich panel would be discussed. Lastly the fatigue characteristics and trends of the DADs on the composite sandwich panel.

#### 4.3-1 Mechanical Characteristics of Material/Specimen

##### Volume Fraction of Face Sheets

The volume fraction of the face sheets with and without a film adhesive was tested and analyzed. The specimen procedure and manufacturing was discussed. The results from the burn test for both test groups can be seen in Table 7. Six specimens were tested for each group and the results were averaged for further analysis. From the results, it can be seen that adding the film adhesive increases the resin content of the laminate by 6% from 54.8% to 61.1% in weight of the specimens.

**Table 7 - Results from Volume Fraction Testing**

| Specimen | Without Film Adhesive |                     | With Film Adhesive |                     |
|----------|-----------------------|---------------------|--------------------|---------------------|
|          | W <sub>t</sub> (g)    | W <sub>if</sub> (g) | W <sub>t</sub> (g) | W <sub>if</sub> (g) |
| 1        | 1.4                   | 0.8                 | 0.9                | 0.5                 |
| 2        | 1.4                   | 0.8                 | 0.9                | 0.5                 |
| 3        | 1.6                   | 0.8                 | 0.9                | 0.6                 |
| 4        | 1.4                   | 0.8                 | 0.9                | 0.5                 |
| 5        | 1.2                   | 0.6                 | 0.9                | 0.6                 |
| 6        | 1.4                   | 0.8                 | 0.9                | 0.6                 |
| Average  | 1.4                   | 0.767               | 0.9                | 0.55                |

These values aren't really that helpful until it converted to its volume fractions. The averaged weights of the fiber and the matrix, with the use of the average dimensions, the volume fractions were calculated. The densities of the materials were obtained by using the dimensions of the specimens and the weights of the materials for the densities. The densities for the case the film adhesive of the composites were 6.57 g/cm<sup>3</sup>, for the LTM45 was 5.60 g/cm<sup>3</sup>, and for the matrix were 1.24g/cm<sup>3</sup>. The volume fractions were then calculated; this can be seen in Table 8. The volume fraction shows that the matrix content drops by 7.5%, opposite from the 6% increase in weight. This could be due to the accuracy of the volume fraction because it's based off of the densities and the volumes used for the calculations. A constant volume obtained from the test specimen was used for both the fiber and matrix volumes. The table also shows the critical volume fraction for the fiber of the LTM45. The obtained volume fraction for the fiber was found to be 68.5%. The volume fraction of the composite without a film adhesive is within this value while the volume fraction of the composite with a film adhesive is 3.2% above the value. This means that the composite has exceeded the strain hardening and plastic flow of the matrix. This makes the composite more brittle than the optimum conditions that it was manufactured

for. Since the research is to study the effects between the fastener and hole of the composite sandwich panel, the volume fraction of the fiber is suitable for testing.

**Table 8 - Volume Fractions with and without the film adhesive**

|                         |       |
|-------------------------|-------|
| $V_f$ w/o Film Adhesive | 64.2% |
| $V_m$ w/o Film Adhesive | 35.7% |
| $V_f$ w/ Film Adhesive  | 71.7% |
| $V_m$ w/ Film Adhesive  | 28.3% |
| $V_{crit}$              | 68.5% |

### Material Properties

The material properties of the composite sandwich panel was tested and analyzed. The first material property that was tested was the Elastic Modulus and the Poisson's Ratio of the core, FR-6710, and the face sheet, LTM45. The core was tested by cutting the specimens of the core into dimensions of 2" x 2" x 0.5". The face sheet was tested by following ASTM standards on calculating the material properties of the composite, ASTM D3410.

The material properties of the core, FR-6710 was tested and analyzed. The test apparatus can be seen in Figure 98 - Foam Material Property Testing. The Elastic Modulus and the Poisson's Ratio of the material were calculated from the stress/strain curve of the test specimens; this can be seen from Figure 97 - Load/Extension for Last-A-Foam FR-6710 The figure shows that the five test specimens have similar slopes, showing that the Elastic Modulus for the foam is consistent with one another. The Poisson's Ratio was calculated by adding a strain gage on the horizontal direction to calculate the value. The results can be seen in Table 9.

**Table 9 - Material Characteristics of Last-A-Foam FR-6710**

|                      | Compressive Strength (psi) | Percent Difference (-) | Elastic Modulus (psi) | Percent Difference (-) | Poisson's Ratio (-) | Percent Difference (-) |
|----------------------|----------------------------|------------------------|-----------------------|------------------------|---------------------|------------------------|
| Manufacturer         | 340                        | -20.6%                 | 11,240                | -34.8%                 | 0.30                | -63.3%                 |
| Experimental Testing | 270                        |                        | 7,330                 |                        | 0.11                |                        |

The property of the foam was analyzed and it decreased by 20.6% for the compressive strength and about 34.8% for the elastic modulus for the material. The decrease in compressive strength and elastic modulus could be due to the way the specimens were tested. The testing procedure for the foam can be different to how the manufacturer tested the foam causing the significant difference in material characteristics. The decrease in material property can also be due to the degradation of the material from being stored too long after purchasing and receiving the material. Being stored in an uncontrolled environment can affect the material characteristics of

the foam, for example, storing the foam in the sun would make it susceptible to UV degradation. For comparison with the FEM, the experimental results of the material characteristics would be used for comparison between experimental and numerical solution.

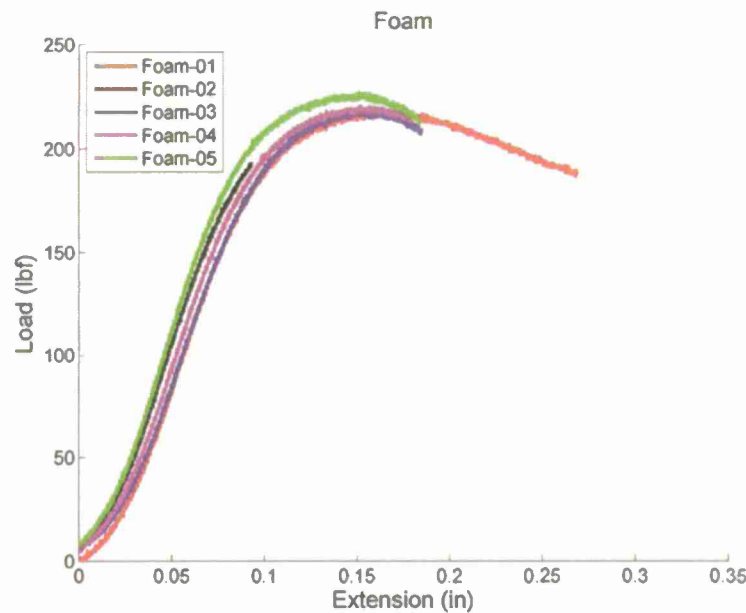


**Figure 97** - Load/Extension for Last-A-Foam FR-6710



**Figure 98** - Foam Material Property Testing

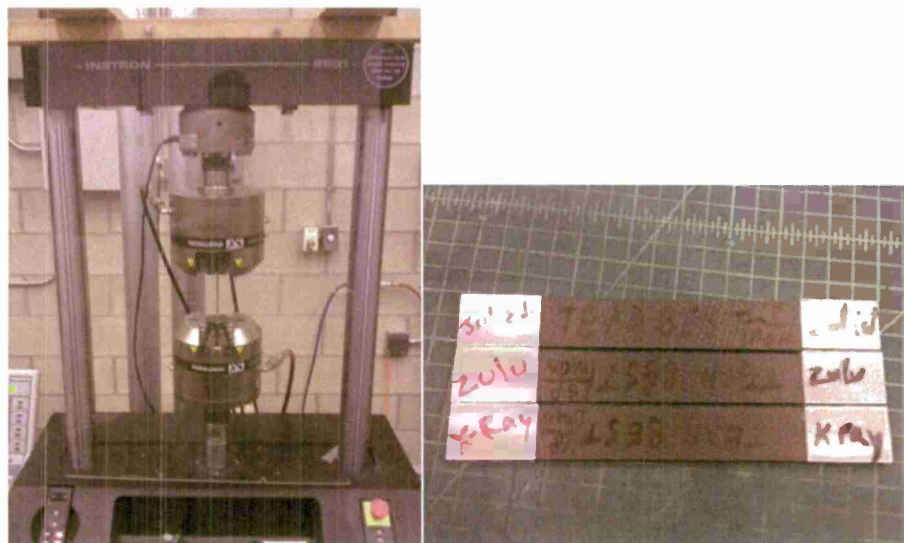
The material properties of the face sheet, LTM45 was tested and analyzed. The test apparatus can be seen in Figure 99 - Test Specimens for LTM45. The Elastic Modulus and the Poisson's Ratio of the material were calculated from the stress/strain curve of the test specimens. The Poisson's Ratio was calculated by adding a strain gage on the horizontal direction to calculate the value. The results can be seen in Table 10.



**Table 10 - Material Characteristics of LTM45**

|                      | Compressive Strength (psi) | Percent Difference (-) | Elastic Modulus (psi) | Percent Difference (-) | Poisson's Ratio (-) | Percent Difference (-) |
|----------------------|----------------------------|------------------------|-----------------------|------------------------|---------------------|------------------------|
| Manufacturer         | 214,000                    | -35.0%                 | 17,260,000            | -58.6%                 | (N/A)               | N/A                    |
| Experimental Testing | 130,000                    |                        | 7,149,000             |                        | 0.11                |                        |

The material properties of LTM45 was obtained from the manufacturer and tested to validate the data. From the table, the material properties of the material decreased by 35.0% for the compressive strength and about 58.6% for the elastic modulus of the material. This decrease in material property can be due to the degradation of the material. The material was donated by Boeing over three years ago and was stored in a freezer that barely meets the cooling standards of the carbon. When the material was donated from Boeing, it was considered by the FAA to not meet its specifications, but it is still suitable for research usage. The values obtained from experimental testing shows that the material properties of the LTM45 is still adequate for the research because compared to the foam the material is infinitely stiff a can handle the objectives of the thesis. Just like the foam, the experimental results of LTM45 will be used for the material characteristics for the FEM.

**Figure 99 - Test Specimens for LTM45**

The next material property that was tested was the overall Elastic Modulus and the Poisson's Ratio of the whole composite sandwich panel; the results can be seen in Figure 100 - Stress/Strain of Test Specimens without Notches. The specimens plotted show the stress/strain curve of the specimens manufactured from 3.1 Monotonic and Cyclic Loading. The results show that stress/strain curve of the specimens are only the linear

part of the curve to be able to calculate the true Elastic Modulus of the overall composite sandwich panel without any notches (holes). The results can be seen in Table 11.

The theoretical results of the Elastic Modulus were calculated using the equations from Chapter 5- Numerical Analysis. The typical failure of the test specimens, which can be seen in Figure 101 - Failure of overall material property specimens, happens in the wood part of the core. The wood section of the core starts to fracture and it propagates into the foam section of the core which is then transferred to the face sheets. When the fracture reaches the face sheets, it starts to delaminate from the core.

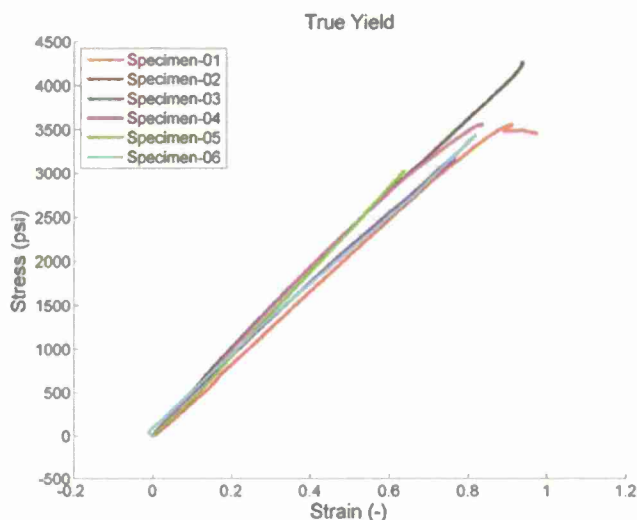


**Figure 100** - Stress/Strain of Test Specimens without Notches



**Figure 101** - Failure of overall material property specimens

**Table 11** - Elastic Modulus of Composite Sandwich panel

|                      | Elastic Modulus (psi) | Percent Difference (-) | Poisson's Ratio (-) | Percent Difference (-) |
|----------------------|-----------------------|------------------------|---------------------|------------------------|
| Theoretical          | 62,650                | 33.6%                  | 0.30                | 28.7%                  |
| Experimental Testing | 41,600                |                        | 0.214               |                        |

The result shows that the theoretical Elastic Modulus of the composite sandwich panel was 62,650 psi. This was calculated by assuming a Poisson's Ratio of 0.3 in the equations because the calculations from the equations gave a singular matrix. The experimental testing gave an Elastic Modulus of 41,600 psi and a Poisson's Ratio of 0.214. The theoretical results over predicted the material properties of the composite sandwich panel. This over prediction is due to the calculations are for laminates and not composite sandwich panels, but it can be assumed that the core can act as part of the laminate.

### Strain Rate/Control Group Results

The strain rate for the static testing needed to be investigated first before investigating the effects of the DADs on the composite sandwich panel. The strain rates that were investigated were between the rates of 0.5 mm/min to 1.5 mm/min with a spacing of 0.25 mm/min. The results can be seen in Table 12. Five control group plates were manufactured and cut down to specimens. A random sampling from the five plates was chosen for each strain rate to make sure that the results would not be biased from testing the strain rate from the same plate. The results showed that all five strain rates had similar failure load varying from 926 lbs to 1,011 lbs and had similar elastic modulus varying from 37,530 psi to 48,940 psi. Variance in the failure load and the elastic modulus is due to the manufacturing defects in the specimens. The results show that the strain rate did not greatly affect the characteristics of the panel, but it did show a variance in standard deviation for each case.

**Table 12 - Strain Rate Selection Results**

| Rate     | P <sub>cr</sub> | Std Dev | E      | Std Dev |
|----------|-----------------|---------|--------|---------|
| (mm/min) | (lb)            | (-)     | (psi)  | (-)     |
| 0.5      | 1,011           | 4.91%   | 45,170 | 4.21%   |
| 0.75     | 983             | 9.54%   | 48,940 | 7.53%   |
| 1.0      | 934             | 36.51   | 37,530 | 51.92%  |
| 1.25     | 926             | 12.71%  | 45,010 | 9.51%   |
| 1.5      | 940             | 7.34%   | 46,270 | 5.03%   |

The table shows that the slowest rate, 0.5 mm/min had the lowest standard deviation for both failure load and elastic modulus. This rate would be used for all static testing because it gives the best standard deviations compared to the other rates translating a better accuracy to future tests; this can be seen in Figure 102 - Standard Deviation for 0.5 mm/min. The results show that five of the six test specimens are within one standard deviation from the mean, while the first test specimen is considered an outlier, this being represented with an X as a symbol.

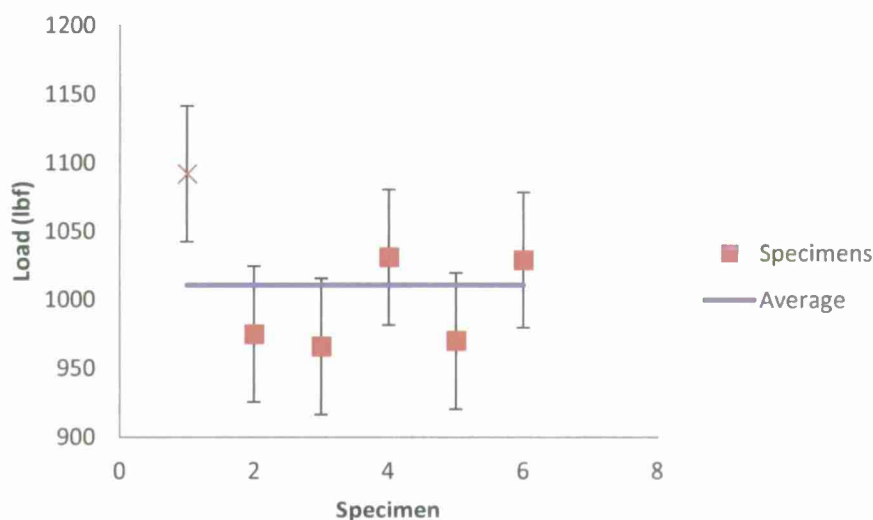


**Figure 102** - Standard Deviation for 0.5 mm/min

The results for the case, such as extension, stiffness, elastic modulus, and yield stress can be seen in Table 13. The outlier would be highlighted in yellow for the table. The table shows that the load, the yield stress, and the extension are within 5% with one other in standard deviation meaning that the specimens are failing similar to one another. This is very useful for fatigue testing because the yield stress or the first drop shows consistency to set the extension from experimental testing as the failure criterion for fatigue.

**Table 13** - Results for 0.5 mm/min Strain Rate

| Test #       | Test Sample | Load     | Yield Stress | Extension | K       | E       |
|--------------|-------------|----------|--------------|-----------|---------|---------|
| 1            | 0225-01     | 1091.5   | 954.84       | 0.0538    | 24598   | 43789   |
| 2            | 0225-06     | 974.0    | 853.71       | 0.0540    | 22920   | 40864   |
| 3            | 0226-01     | 967.0    | 855.31       | 0.0507    | 27390   | 49375   |
| 4            | 0226-06     | 1030.7   | 908.31       | 0.0527    | 22551   | 40441   |
| 5            | 0227-01     | 969.4    | 850.38       | 0.0585    | 30342   | 54194   |
| 6            | 0227-06     | 1027.6   | 893.31       | 0.0569    | 23909   | 42382   |
| Average Load |             | 1010.014 | 885.98       | 0.05443   | 25285.1 | 45174.2 |
| Std Dev      |             | 4.89%    | 4.67%        | 5.21%     | 11.92%  | 12.11%  |

For the rest of the strain rates that were tested, the standard deviations for the remaining strain rates can be seen in Figure 103, Figure 104, Figure 105, and Figure 106. The experimental results such as extension, stiffness, elastic modulus, and yield stress can be seen in Table 14, Table 15, Table 16, and Table 17. As before,

the figures show the outlier with an X marker and the specimens within one standard deviation have a square marker. The other strain rates have more outliers than the 0.5 mm/min by having as much as eight outliers and as least as four outliers. The worst of the strain rates was the 1.0 mm/min where eight of the nine test specimens are one standard deviation from the median. It also has the highest standard deviation for the ultimate failure load and the Elastic Modulus is the lowest of the five strain rates.

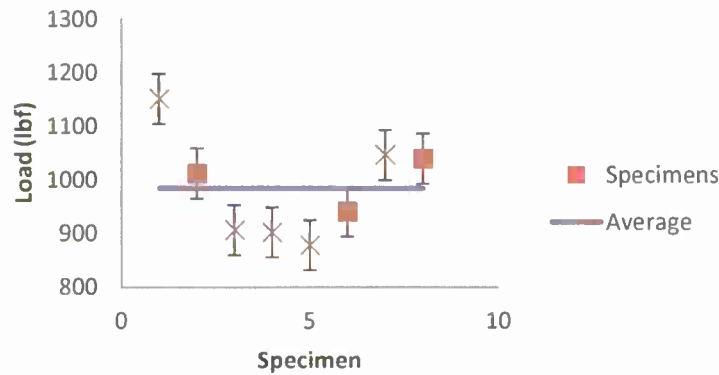


**Figure 103** - Standard Deviation for 0.75 mm/min

**Table 14** - Results for 0.75 mm/min Strain Rate

| Test #       | Test Sample | Load  | Yield Stress | K     | E     |
|--------------|-------------|-------|--------------|-------|-------|
| 1            | 0225-02     | 1149  | 1001         | 30300 | 53965 |
| 2            | 0225-07     | 1010  | 891          | 28829 | 52063 |
| 3            | 0226-02     | 905   | 801          | 28060 | 50670 |
| 4            | 0226-07     | 901   | 784          | 25921 | 45082 |
| 5            | 0227-02     | 877   | 765          | 24145 | 42984 |
| 6            | 0227-07     | 940   | 821          | 26416 | 47155 |
| 7            | 0305-01     | 1044  | 922          | 27133 | 48779 |
| 8            | 0305-02     | 1038  | 915          | 28800 | 50824 |
| Average Load |             | 983   | 862          | 27450 | 48940 |
| Std Dev      |             | 9.49% | 9.54%        | 7.11% | 7.53% |



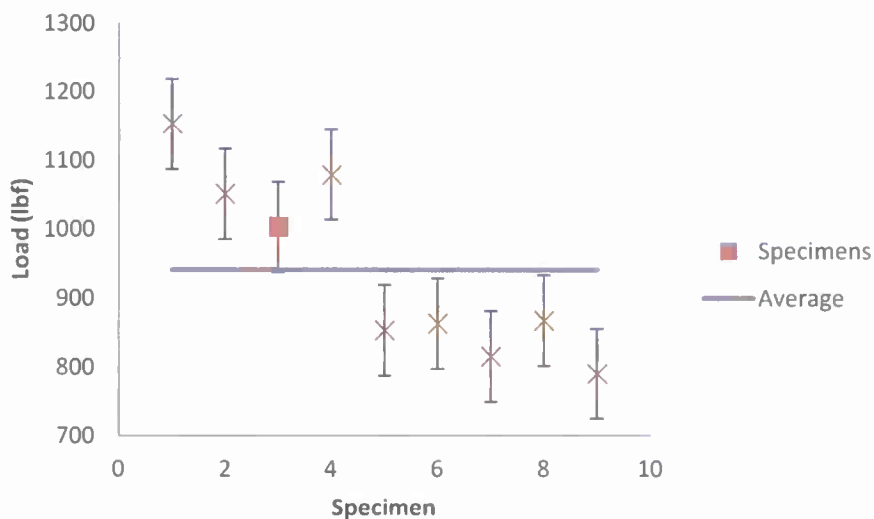


**Figure 104** - Standard Deviation for 1.0 mm/min

**Table 15** - Results for 1.0 mm/min Strain Rate

| Test #       | Test Sample | Load   | Yield Stress | K      | E      |
|--------------|-------------|--------|--------------|--------|--------|
| 1            | 0225-03     | 1153   | 1004         | 30549  | 54272  |
| 2            | 0225-08     | 1052   | 919          | 27990  | 49681  |
| 3            | 0226-03     | 1002   | 883          | 26295  | 47176  |
| 4            | 0226-08     | 1076   | 94           | 27533  | 4875   |
| 5            | 0227-03     | 853    | 748          | 28185  | 50366  |
| 6            | 0227-08     | 861    | 752          | 19646  | 34941  |
| 7            | 0305-03     | 796    | 692          | 24581  | 43640  |
| 8            | 0305-04     | 865    | 749          | 28030  | 48665  |
| 9            | 0305-07     | 751    | 670          | 22741  | 4113   |
| Average Load |             | 934    | 657          | 26172  | 37525  |
| Std Dev      |             | 14.93% | 36.15%       | 12.72% | 51.92% |

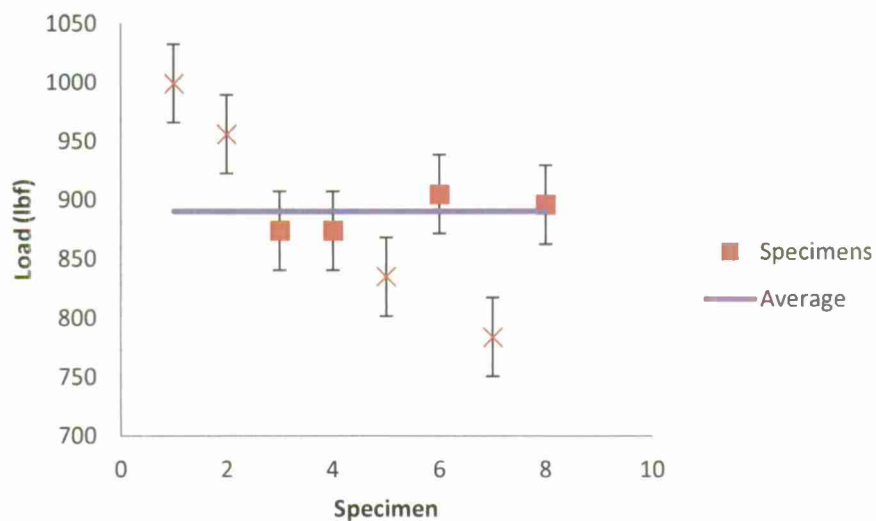


**Figure 105** - Standard Deviation for 1.25 mm/min

**Table 16** - Results for 1.25 mm/min Strain Rate

| Test #       | Test Sample | Load   | Yield Stress | K     | E     |
|--------------|-------------|--------|--------------|-------|-------|
| 1            | 0225-04     | 997    | 866          | 28798 | 51134 |
| 2            | 0225-09     | 954    | 832          | 22460 | 40020 |
| 3            | 0226-04     | 874    | 768          | 22835 | 40915 |
| 4            | 0226-09     | 1167   | 1017         | 28453 | 50613 |
| 5            | 0227-04     | 833    | 731          | 25978 | 46149 |
| 6            | 0227-09     | 904    | 794          | 26069 | 46526 |
| 7            | 0305-05     | 784    | 679          | 24287 | 42402 |
| 8            | 0305-06     | 896    | 796          | 23737 | 42331 |
| Average Load |             | 926    | 810          | 25327 | 45011 |
| Std Dev      |             | 12.71% | 12.51%       | 9.54% | 9.51% |

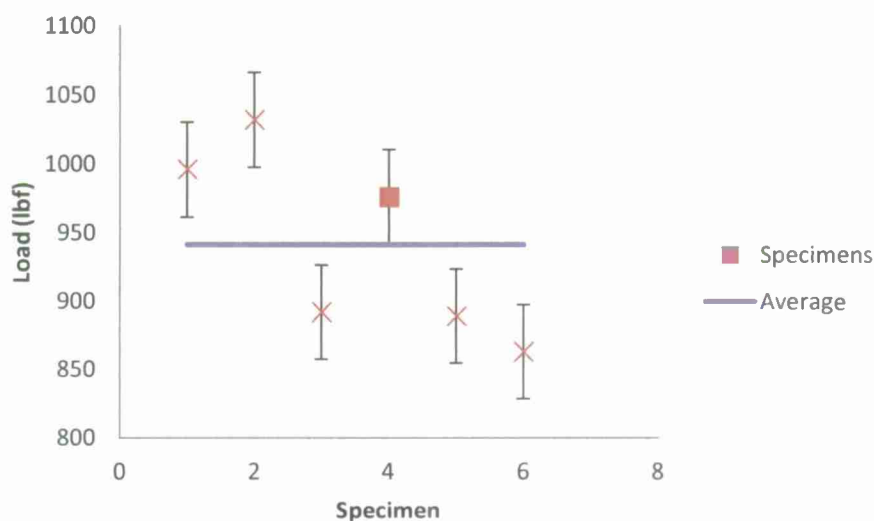


**Figure 106** - Standard Deviation for 1.5 mm/min

**Table 17** - Results for 1.5 mm/min Strain Rate

| Test #       | Test Sample | Load  | Yield Stress | K     | E     |
|--------------|-------------|-------|--------------|-------|-------|
| 1            | 0225-05     | 995   | 865          | 26856 | 47394 |
| 2            | 0225-10     | 1031  | 904          | 26181 | 46929 |
| 3            | 0226-05     | 892   | 786          | 23578 | 42446 |
| 4            | 0226-10     | 974   | 850          | 25942 | 46118 |
| 5            | 0227-05     | 887   | 782          | 27550 | 49404 |
| 6            | 0227-10     | 862   | 754          | 25291 | 45292 |
| Average Load |             | 940   | 823          | 25900 | 46264 |
| Std Dev      |             | 7.34% | 7.03%        | 5.32% | 5.03% |

The load/extension curves for the 0.5 mm/min case had the best testing results because it had the least amount of test specimens that had a drop in the load/extension curve and continued up after; this can be seen in Figure 107. The trend for the control group is that the specimen rises and then drops and rises again but drops at a lower load than before. This is due to the fastener slowly moving along the composite sandwich panel. The second rise in the curve is caused by the face sheet re-fracturing as the fastener moves along it. This is also known as micro buckling where the fibers break one at a time instead of it breaking at once. The leveling force seen at the end of the curve is when the fastener is “sawing” through the composite material with ease.

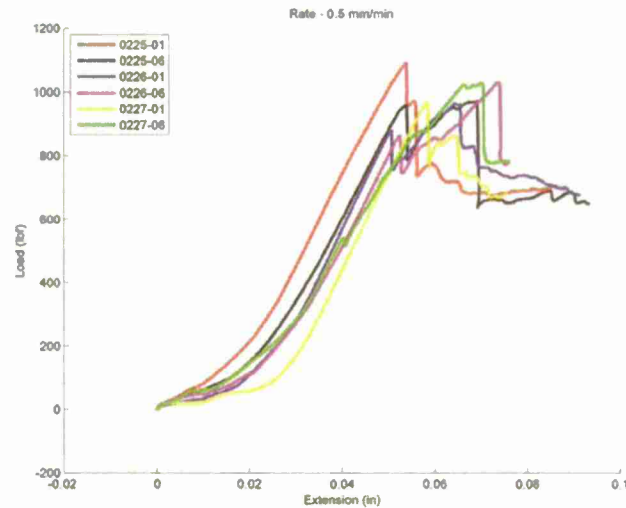


**Figure 107** - Load/Extension for 0.5 mm/min Rate

Load versus extension curves for the remaining strain rates can be seen in Figure 108. The four figures show that the remaining four strain rates have consistent test results by having similar slopes to one another. Just like the 0.5 mm/min strain rate, the test specimens for each strain rate group rises and then drops and rises again but drops at a lower load than before. This is due to the fastener slowly moving along the composite sandwich panel. The second rise in the curve is caused by the face sheet re-fracturing as the fastener moves along it. This is also known as micro buckling where the fibers break one at a time instead of it breaking at once. The leveling force seen at the end of the curve is when the fastener is “sawing” through the composite material with ease.

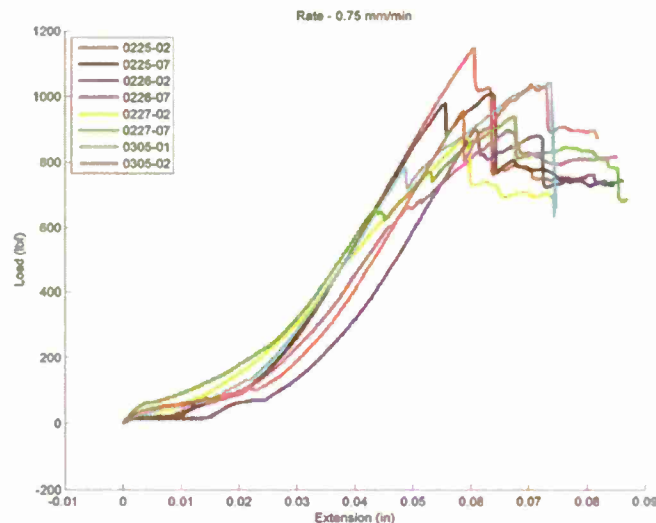


**Figure 108** - Load/Extension for 0.75 mm/min Rate

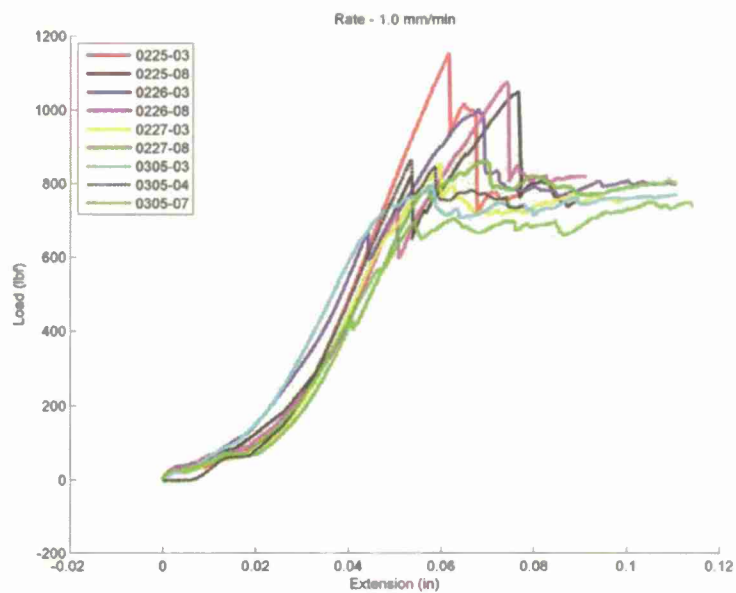


Figure 109 - Load/Extension for 1.0 mm/min Rate

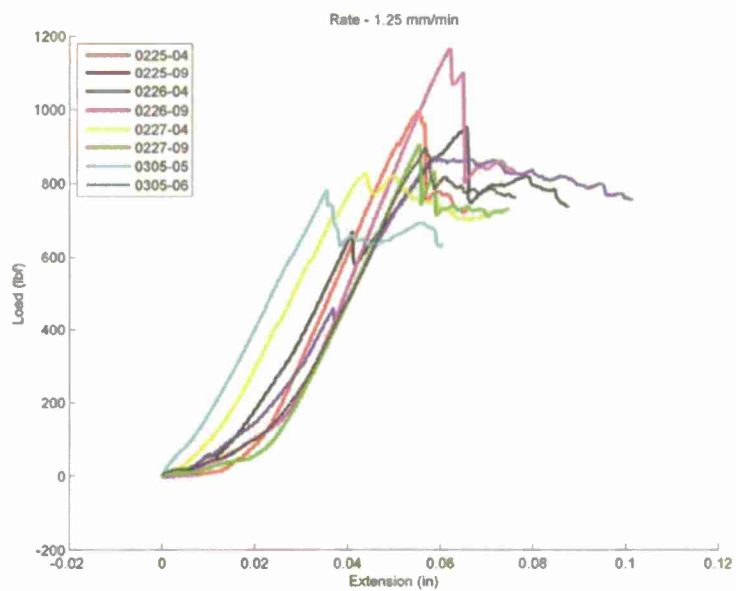


Figure 110 - Load/Extension for 1.25 mm/min Rate



## Chapter 5- Numerical Analysis

The following section is the numerical analysis results for the monotonic loading and fatigue case as well as for the damage arrestment device shear key.

### 5.1 Monotonic Loading and Fatigue

#### Model Geometry

During the model development it was determined that a 2-D finite element analysis (FEA) would be adequate for the preliminary analyses performed. A longitudinal view of the part was selected for the analysis because it would provide an adequate representation of the stress state longitudinal. The model geometry and coordinate system used for the analysis is shown in Figure 111. The upper and lower fiberglass skins were modeled as a single layer their material properties were determined experimentally. The y-axis runs vertically through the part and the x-axis runs horizontally along the length of the part. Key geometric properties for the analysis are shown in Table 18. A 3-D analysis was not selected because of the high computational cost associated with using solid elements. The delamination model was considered identical to model without delamination except that a seam was added to the region where the upper skin was not connected to the lower skin. The seam represents the piece of non-porous Teflon paper that separates the upper skin from the core.

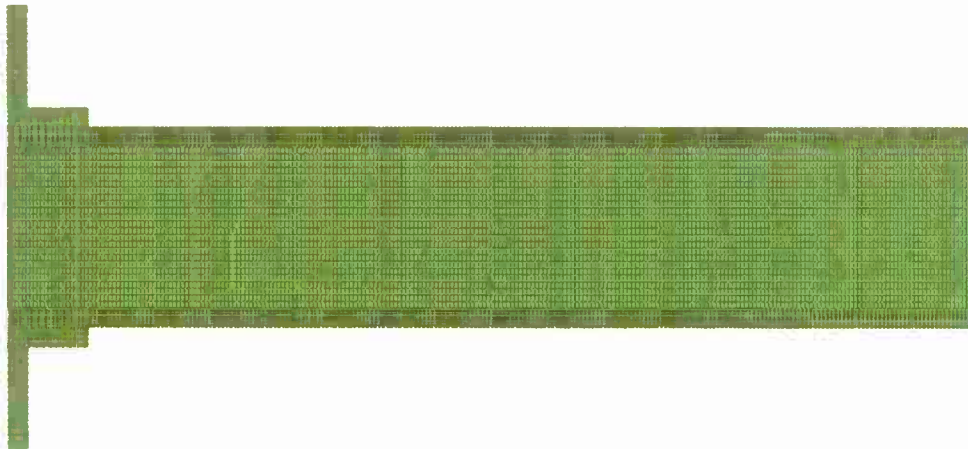


**Figure 111** - Finite element geometry for test specimen

**Table 18** - Sandwich structure geometry

|                         | Thickness<br>(inch) | Length<br>(inch) | Out of plane thickness<br>(inch) |
|-------------------------|---------------------|------------------|----------------------------------|
| Fiberglass skins (each) | 0.08                | 6.0              | 1.50                             |
| Foam                    | 0.787               |                  |                                  |

## Material Properties Development

Initially during the analysis it was assumed that the constitutive response for both the fiberglass skins and foam core was linearly elastic, homogeneous, and isotropic. In reality that is not the case because both materials are orthotropic and exhibit plastic characteristics. After looking at the initially linearly elastic results it was determined that the plasticity of the foam would need to be model to accurately capture the failure forces. The material properties for the Divinycell foam core were obtained from the manufactures' website<sup>23</sup> and the tensile (Figure 112) and compressive (Figure 113) stress strain curve were obtained during Dr. Mitra's initial shear key research<sup>4</sup>.

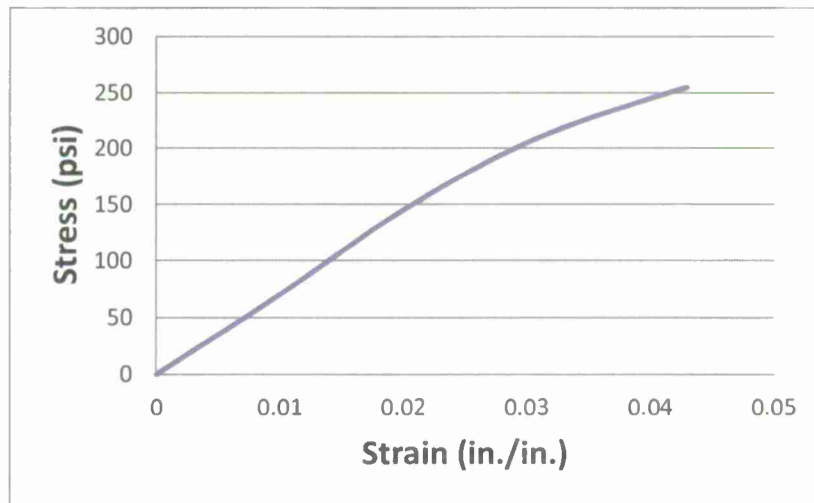


Figure 112 - Tensile response of Divinycell H100 foam<sup>4</sup>

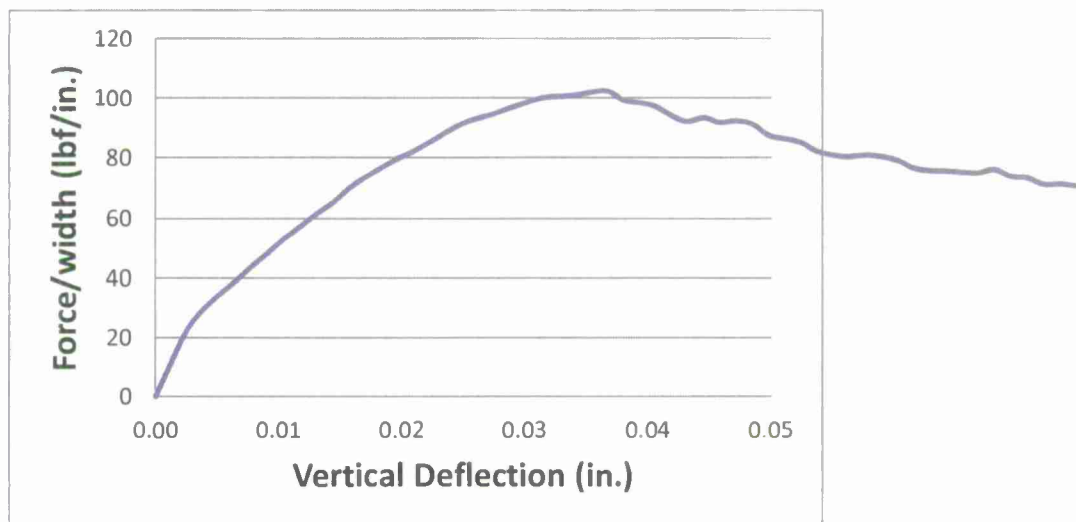
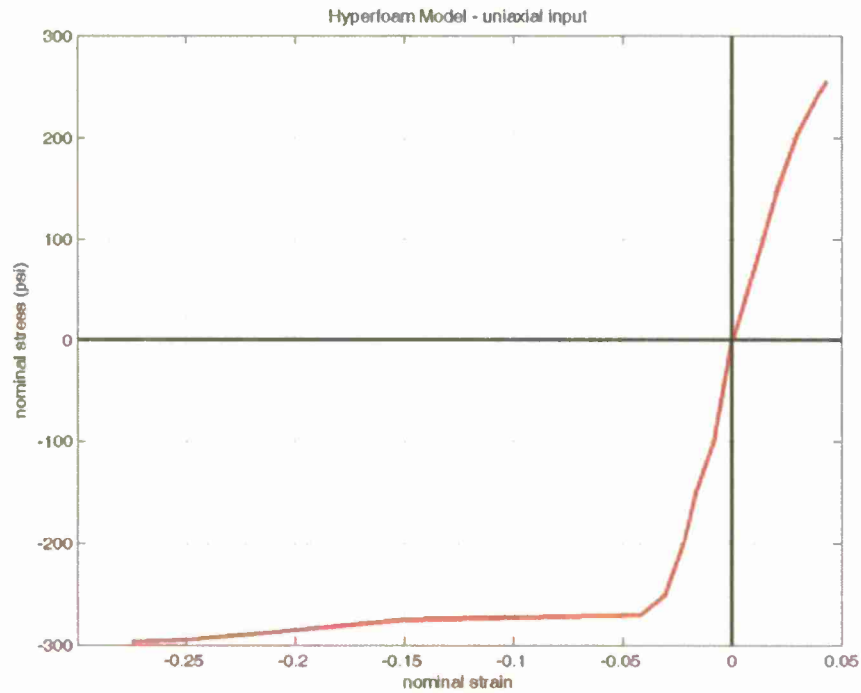


Figure 113 - Compressive response of Divinycell H100 foam<sup>4</sup>

Two different material models were used to represent the non-linear and plastic behavior of the foam after its yield strength was reached. Modeling the foam as a hyperelastic material was the first step in trying to more accurately capture the failure in the foam. A hyperelastic foam model was constructed for the foam by extrapolating data from the tensile and compressive tests for the Divinycell H100 foam. The hyperelastic foam curve used as an input into the material properties in Abaqus/CAE is shown in Figure 114.



**Figure 114 - Hyperelastic foam model**

The other foam model used was an expansion of the crushable foam model originally used by Dr. Nilanjan Mitra<sup>4</sup> during his shear loading research. The crushable foam hardening model used for the analysis is shown in Figure 115. Additional information regarding hyperelastic material properties could be found by consulting the Abaqus User's manual.

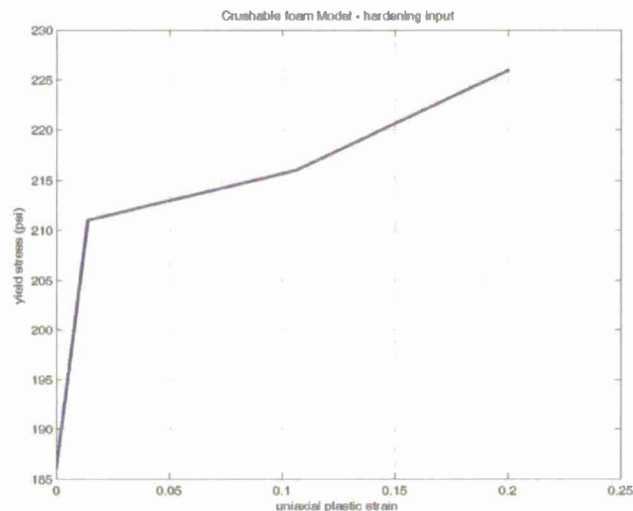


**Figure 115** - Crushable foam plasticity model

Material properties from the fiberglass manufacturers were not available so testing had to be performed to determine them. A 120 $\Omega$  linear strain gage with a gage factor of 2.1 was added near the middle of the test specimen and two holes were drilled near both the ends of the specimen. One hole was be used to constraint the specimen and the other hole was be used to hand weights off of. The strain gage was wired up in a quarter Wheatstone bridge configuration using the yellow strain gage box shown in Figure 116. Additional information regarding the crushable foam hardening could be found by consulting the Abaqus User's manual.

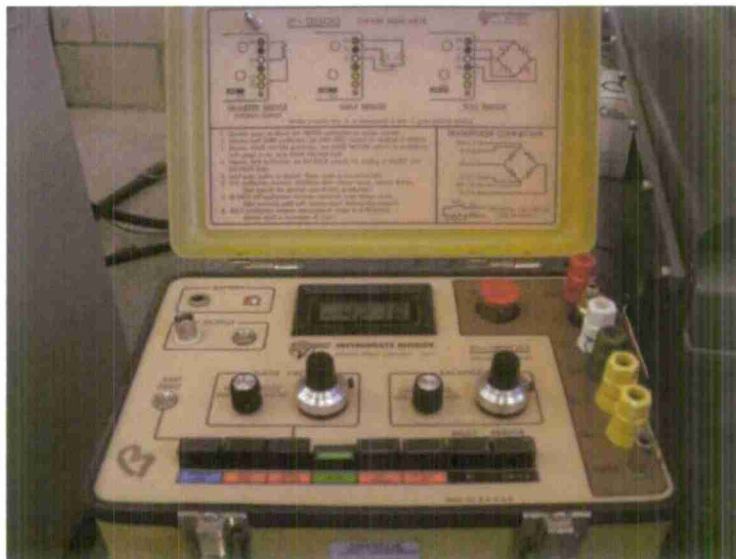


**Figure 116** - Yellow strain gage box with 1/4 bridge configuration

An aluminum test specimen was first used to ensure that the method used for the experiment was accurate because the material properties for aluminum were known. Figure 117 shows the aluminum test specimen with a strain gage as well as the boundary conditions used to fix the specimen. Figure 118 shows the jig used to hold the weights during the material calibration.

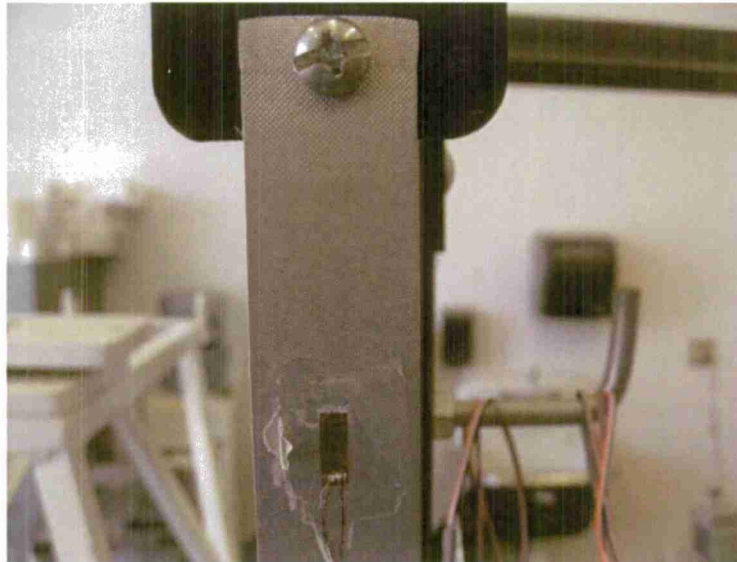


**Figure 117** - Aluminum test specimen under tensile load



**Figure 118** - Applied loading for material calibration

Before any weights or strain readings were recorded, the strain gage box was zeroed. Weights were then added in 10 lb increments and strain readings were recorded. Figure 119 shows the results obtained from the testing for the aluminum and fiberglass skin test specimens. Stress was plotted on the y-axis and strain was



plotted on the y-axis. Young's Modulus for the aluminum test specimen was experimentally determined to be  $9.6\text{e}6$  psi which was only 6% off the known Young's Modulus value of  $10\text{e}6$  psi. Young's Modulus for the fiberglass skin lay-up was determined to be  $5.7\text{e}6$  psi. There is also further confidence in the test because the slopes of the lines are straight and there were no jagged points, which generally represent incorrect strain readings.

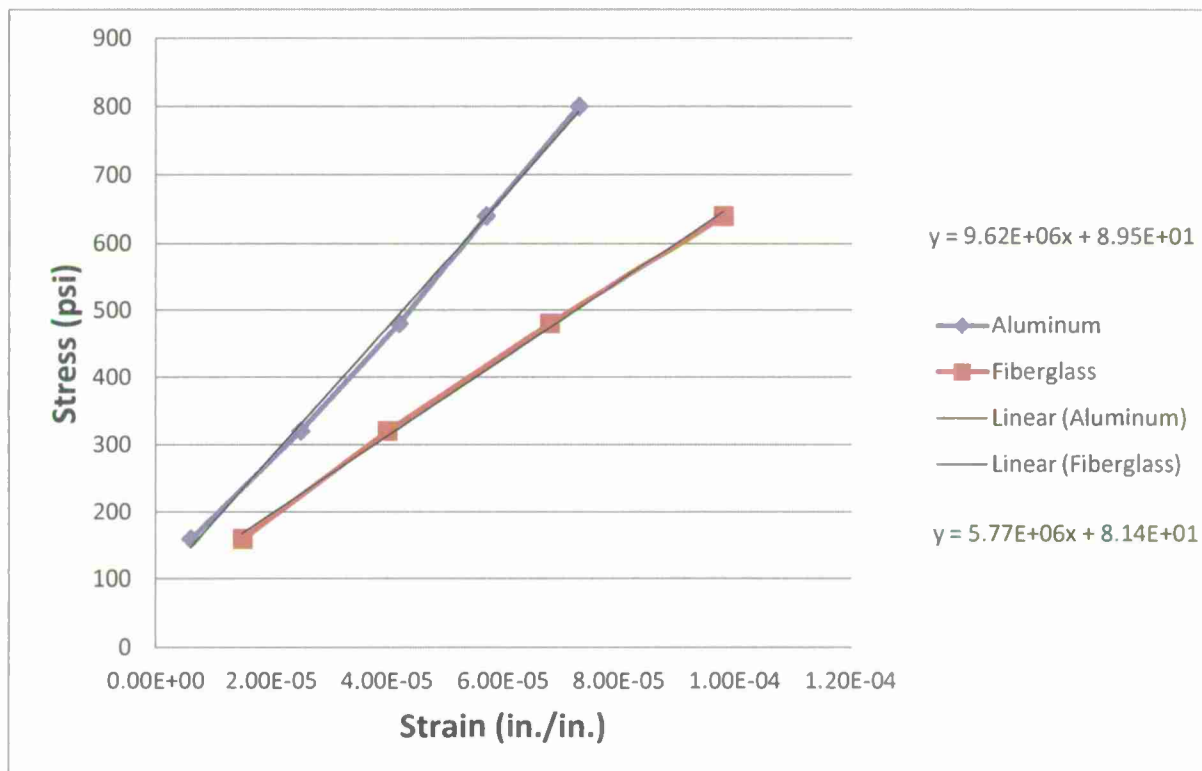


Figure 119 - Material calibration plot

### Loads/Boundary Conditions

The boundary conditions selected for the test specimens with no initial delamination and a 0.5 inch initial delamination analysis are shown in Figure 120. Displacement boundary conditions representing displacement test data were applied to the upper aluminum L-bracket. Both test specimens had the lower aluminum L-bracket fixed ( $U_1=U_2=0$ ). The back edge of the test specimens were also fixed using the jig which was fixed to the Instron machine. Figure 120 shows the loads and boundary conditions used for the models.

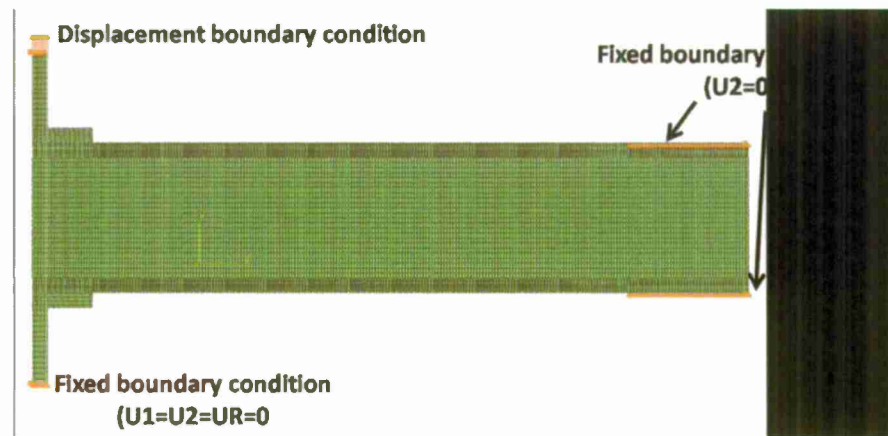


Figure 120 - FEM displacement boundary conditions

### Mesh Development

Shell elements were selected to represent the fiberglass skins and the foam core. The primary reason for choosing shell elements was because stress and displacement were expected to be the same throughout the entire depth of the test specimens. 3-D solid element was not selected because of the high computational costs associated with 3-D elements. The 2-D shell elements should provide a good approximation for the failure loads.

The 2-D shell elements were constructed in Abaqus/CAE by creating a 2-D shell. The skins were made by partitioning the 2-D rectangular shell using the thickness of the upper and lower skins. Additional partitions were added to represent the delaminated region where the force boundary conditions were applied.

Linear elements with reduced integration were selected to decrease computation time. It was deemed appropriate that linear elements with reduced integration could be used because the degree of confidence obtained through the mesh convergence study. A quadrilateral structured mesh was assigned to all regions of the test specimens. Plane stress elements were initially selected but modeling issues arose when plasticity was adding to the foam, which led to plane strain elements being used. Figure 121 shows the final mesh that was used for the analysis. Table 19 shows the mesh quality used for the numerical analysis.

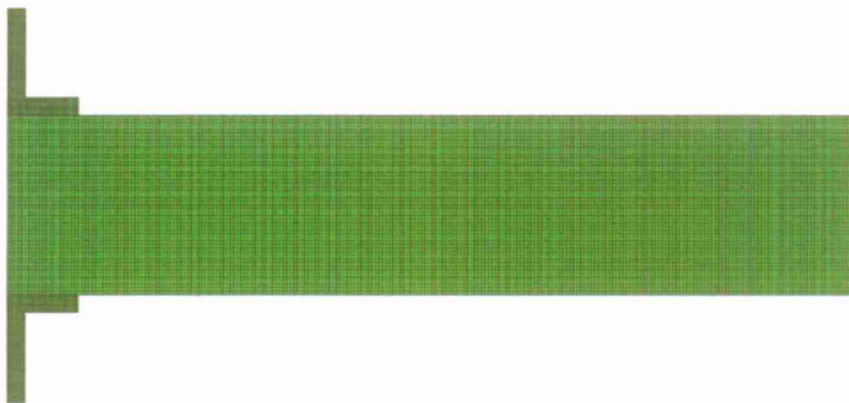


**Figure 121** - Final mesh used for analysis

**Table 19** - Mesh quality for final mesh

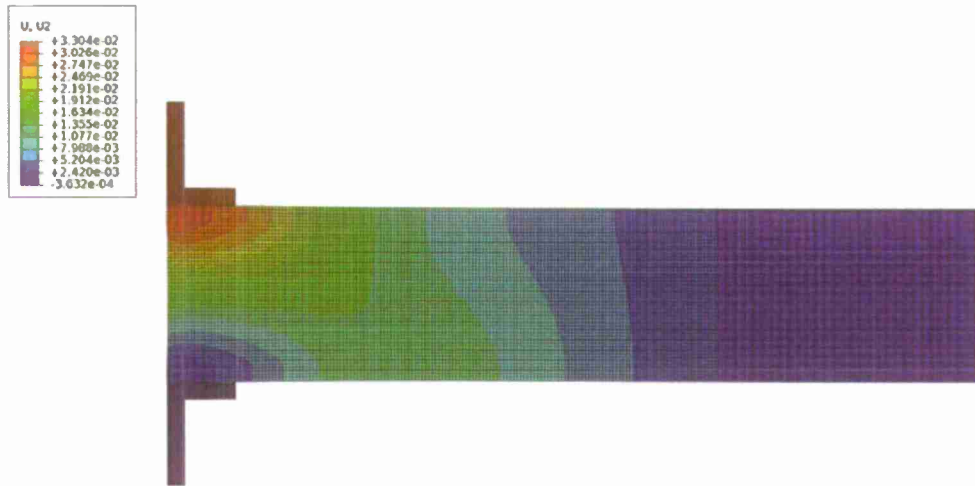
|                          | % Elems | # Elems | Average |
|--------------------------|---------|---------|---------|
| Face Corner Angle < 45°  | 0       | 0       | 90°     |
| Face Corner Angle > 135° | 0       | 0       | 90°     |
| AR > 5                   | 0       | 0       | 2.08    |

## Analysis

A non-linear static analysis was selected to simulate the monotonic loading conditions. A static analysis was selected because the monotonic loading conditions represented static testing. A linear static analysis was initially performed because plasticity was not modeled but the initial FEA analysis results needed plasticity to match the experimental data.

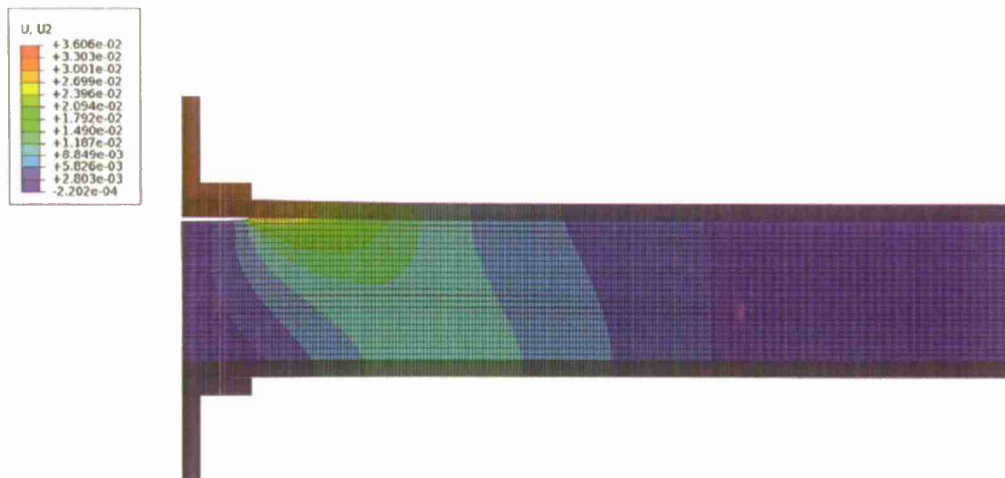
## Results

Figure 122 shows the vertical deflection (U2) contour for the test specimen with no initial delamination. The maximum vertical deflection of 0.03304 inch occurs at the top of the aluminum tab.



**Figure 122** - FEA vertical deflection for test specimen without initial delamination

Figure 123 shows a vertical deflection contour for the test specimen model containing an initial delamination of 0.5 inch. The maximum vertical deflection of 0.03606 inch is shown in Figure 123 at the upper edge of the aluminum tab. The 0.5 inch delamination deflection contour is very similar to the deflection contour in Figure 122 except that there is no seam in Figure 122.



**Figure 123** - FEA vertical deflection for test specimen with 0.5 inch initial delamination

## 5.2 Damage Arrestment Device

### Finite Element Modeling

For this chapter, the FEM analysis of the composite sandwich panels will be discussed. The creation of the model geometries and the mesh configurations for each model will be examined. The loading and boundary

conditions applied to the models will also be referenced. Lastly, the displacement and stress distributions results of each model will be discussed.

### Finite Element Model Geometry

The finite element model for the research will contain three different models for each the control group and the DAD group for the analysis. The software that will be used for the analysis is GeoStar or CosmosM, which is made by SolidWorks. The three different models will consist of just the test specimen, one with the test specimen and the bushing, and one with the test specimen, bushing and the fastener. The analysis will have a base model to work off, which refers to the test specimen because the other parts of the test will be added to the model. The base model can be seen in Figure 124.

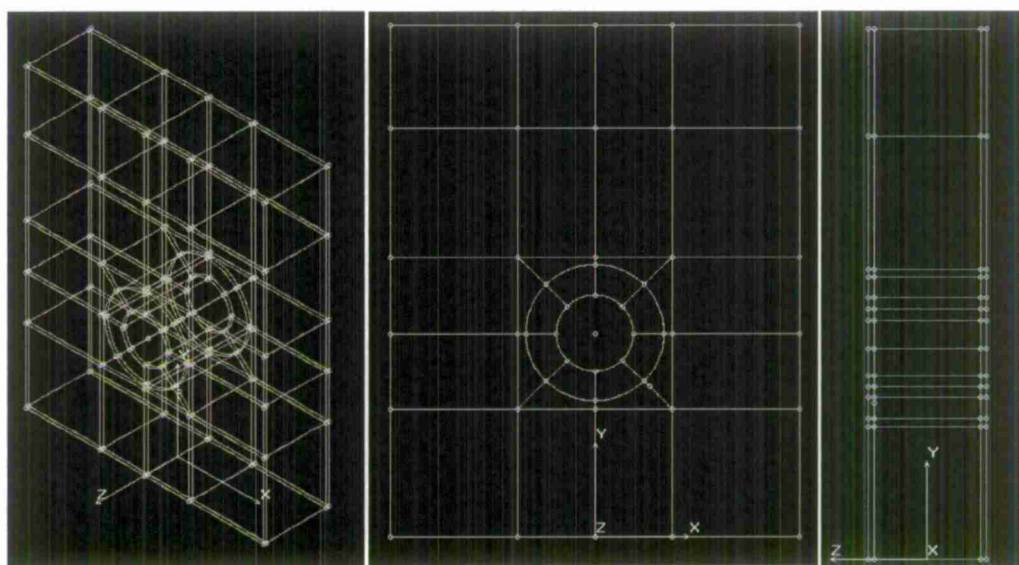


**Figure 124 - Base FEM Geometry**

The FEM base model is only half the model of the specimen, having only one hole rather than two, because of symmetry in the geometry. The geometry dimensions of the combined surfaces will be  $2.5 \times 2$ . The software accepts unitless values, allowing the operator to non-dimensionalize the data. The units have to be recorded for further analysis. The base geometry contains 32 surfaces that are extruded into volumes. The surfaces around the hole are segments of circles and outside of them are triangle shaped quadrilaterals. All surfaces are quadrilaterals because the maximum surfaces that can be created in the software are with four lines/curves. The radius of the circular surface around the hole will be 40% of the radius of the hole, which is 0.15". The purpose of this is to have a fine mesh of elements around the hole to capture the bearing failure and stresses from the fastener. The surfaces away from the hole are rectangles. The rectangular surfaces around the hole represent the DADs for later models. Using this method will greatly simplify the model and make it comparable to one another by having similar geometries and meshes. The 32 surfaces will then be extruded into three volumes to represent the test specimen. The three volumes will be the two face sheets and the core. The



surfaces will be extruded into the dimensions of each volume. The face sheet will have a depth of 0.026 and the core will have a depth of 0.5. The model geometry will then be ready to mesh.

The next model that was created was the base model with the bushing inside the hole. The bushing is being added to the FEM model to alleviate the pressure on the test specimen; this can be seen in Figure 125. The half model of the bushing will only be modeled. The bushing will have a radius of 0.0625" because the inner diameter of the bushing was 0.25" and the outer diameter of the bushing was 0.375".

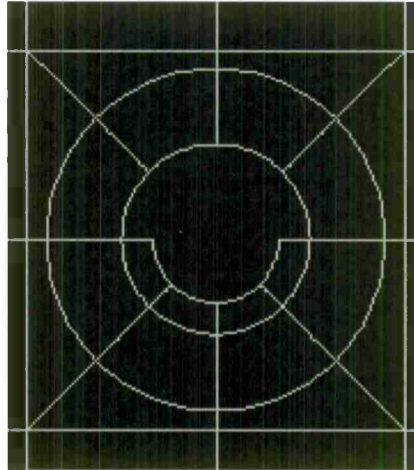


**Figure 125 - Base geometry with bushing**

The last model for the control group FEM was the base model with the bushing and the fastener; this can be seen in Figure 126. Just like the bushing, the fastener is added to the FEM model to simulate the true loading and geometry of the test specimens. The half model of the fastener would only be modeled. The fastener will have a radius of 0.125 because of the diameter of the fastener. The geometry will be created by using the three surface features to make each surface of the model.

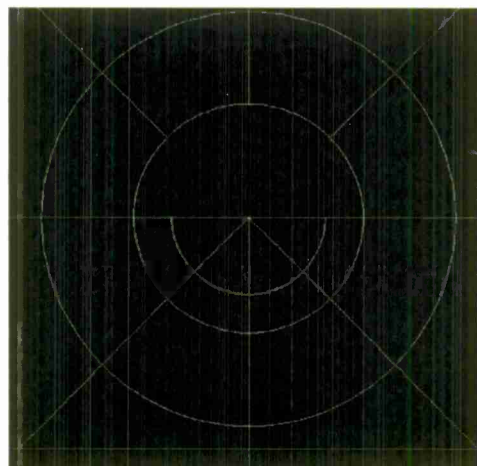


**Figure 126 - Base geometry with bushing and fastener**

The model for the DAD geometry is different than the base geometry. The planar geometry is the same as the base model by having the same number of surfaces; this can be seen in Figure 127. The geometry has the same dimensions of the overall sandwich composite panel, a dimension of 2.5 x 2. The difference in the geometry is in the Z direction, where the middle surfaces that represent the DAD are extruded into the core. The dimensions of the geometry were adjusted to accommodate the meshing of the elements. Since the thickness of each layer of LTM45 is 0.013", the thickness of the material for the FEM model would be a thickness of 0.02". This made the thickness of the face sheet become 0.04" and the thickness of the DAD became 0.06". This creates an even number of elements in the core to match the number of elements with the DAD and the face sheet. The thickness of the core remains the same. This geometry is the base model for the FEM of the DADs with the bushing and the fastener. The geometries for the DAD models with the bushing and the fastener are the same as the previous model. The bushing would be added on the lower part of the hole on the composite sandwich panel and the fastener is added on top of the bushing. The half models of the bushing and the fastener will be modeled.

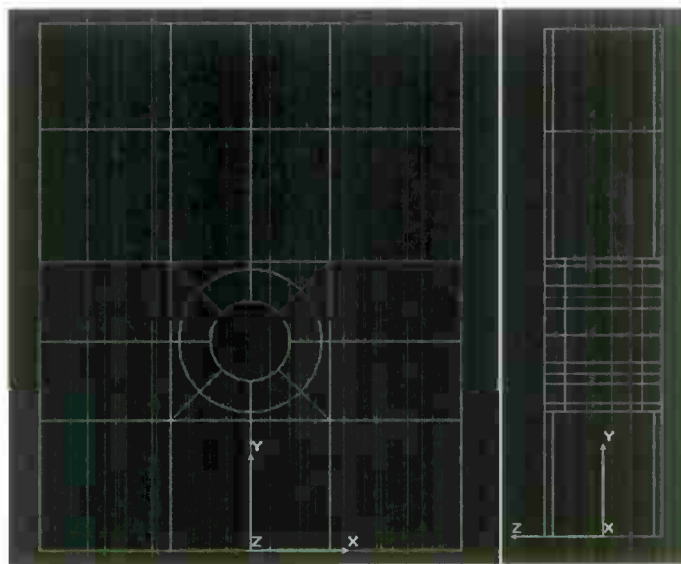


**Figure 127 - DAD geometry**

### ***Finite Element Model Meshing***

The base model uses a solid element to be able to calculate the strains and stresses inside the test geometry. The element mesh of the base model can be seen in Figure 128. All the elements for the model are quadrilateral elements. Two elements will make up the face sheet in the orthogonal direction of the plane. Each element will be represented as a layer of LTM45. Six elements make up the core in the orthogonal direction of the plane. Six elements were chosen because having too many would make the element count too high and too long to calculate; having fewer elements would decrease the accuracy of the analysis. The mesh will grow from a coarse mesh from the top edge to a fine mesh near the hole. A parametric mesh for each volume was created.

This means that the user defines the number of elements in the X, Y, and Z directions of the volume. The figure is divided into groups to make it easier to describe the mesh densities of each volume/surface. Group 1 will be the top horizontal surfaces. Group 2 will be the next horizontal surfaces below Group 1. Group 3 represents the rectangular surfaces on both sides of the hole. Group 4 represents the circular sections and the triangle shaped rectangular surfaces. Group 5 represents the bottom horizontal surfaces of the geometry. The material properties of the LTM45 and the FR-6710, the experimental results, are be used for the input for the elements for the face sheets and the core. The parametric meshing of each grouping can be seen in Table 20. The total element count for the whole geometry is 25,000 elements with 40,197 nodes. A majority of the elements are contained in Group 5 due to the fine mesh needed to capture the bearing failure around the hole.

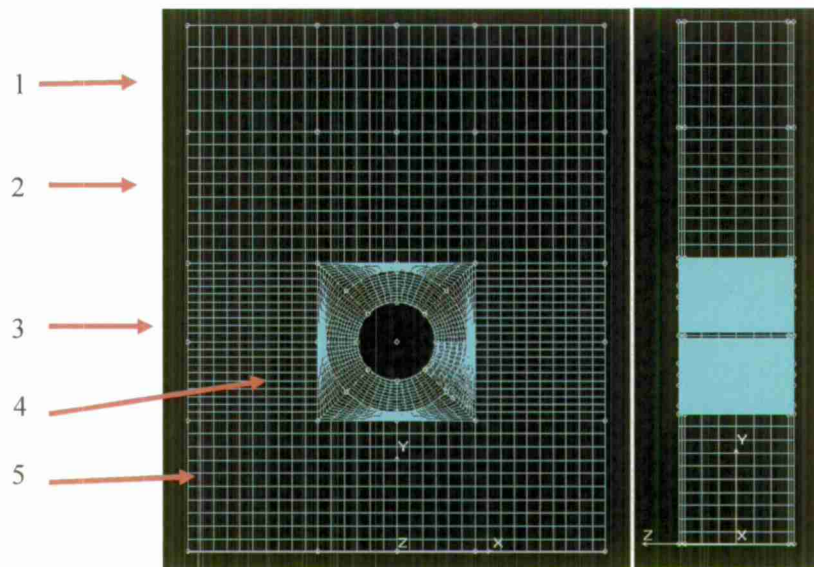


**Figure 128** - Base model element mesh

**Table 20** - Base Model Parametric Mesh

| Parametric Volume Meshing |    |    |                                 |
|---------------------------|----|----|---------------------------------|
|                           | X  | Y  | Z                               |
| Group 1                   | 32 | 5  | 2 for Face sheet and 6 for Core |
| Group 2                   | 32 | 10 |                                 |
| Group 3                   | 10 | 10 |                                 |
| Group 4                   | 12 | 10 |                                 |
| Group 5                   | 32 | 10 |                                 |

The base model with a bushing was meshed and can be seen in Figure 129. Everything but the bushing geometry has the same element mesh as before. The bushing material property that is used for the mesh is the bronze material property that is standard in the software. The two outside volumes, or the top volumes, have a

parametric mesh of ten elements in the X direction and a parametric mesh of ten elements in the Y direction. The two inside volumes, or the bottom volumes, have a parametric mesh of six elements in the X direction and ten elements in the Y direction. In the Z direction of the mesh, there are a total of 10 elements for the whole geometry. The mesh had a total of 28,800 elements, the bushing only adding 3,800 elements to the base model.

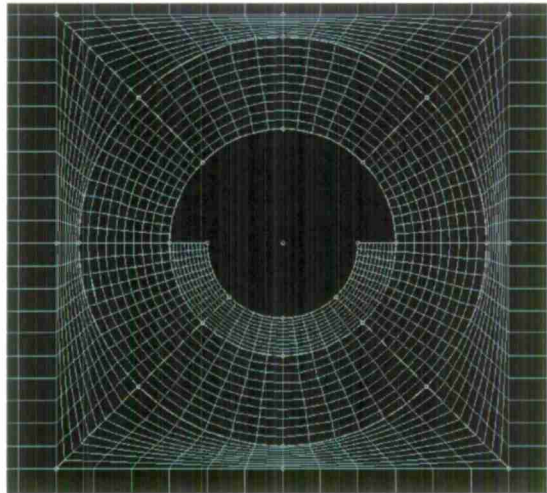


**Figure 129** - Base model with bushing element mesh

The base model with a bushing and a fastener was meshed, which can be seen in Figure 130. Everything but the fastener geometry has the same element mesh as in the previous cases. The fastener material property that is used for the mesh is the steel material property that is standard in the software. The two outside volumes, or the top volumes, has a parametric mesh of ten elements in the X direction and a parametric mesh of six elements in the Y direction. The two inside volumes, or the bottom volumes, has a parametric mesh of six elements in the X direction and ten elements in the Y direction. In the Z direction of the mesh, there are a total of 10 elements for the whole geometry. The mesh had a total of 30,000 elements, the bushing only adding 3,800 elements to the base model. The fastener added 1,200 elements to the model with the bushing and added 5,000 elements to the base model.

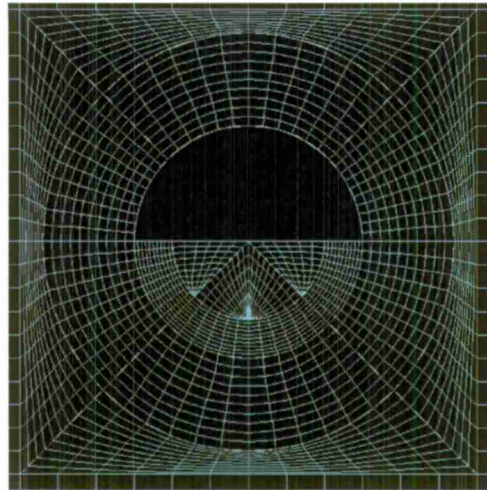


**Figure 130 - Base model with bushing and fastener**

The DAD models have the same mesh for the sandwich plane and the same reference axes previously mentioned. The only difference in the meshing between the DAD models and the base models is the number of elements in the Z direction; this can be seen in Figure 131. The number of elements for the face sheet in the Z direction remains the same with having two elements. The DADs sections have 3 elements in the Z direction. For the sections of the core that is between the face sheets without the DADS, the number of elements in the Z direction was changed to 25. For the sections of the core that is between the DADs have 19 elements in the Z direction. The sections of the core between the DADs have only 19 elements because the remaining six elements come from the DADs. Having four times the number of elements in the Z direction greatly increases the total element count of the model. The DAD model has a total of 73,420 elements for the whole model. This is a huge increase from the base model, which had a total of 25,000 elements. An increase of 48,420 elements is mostly in the core of the model. This increase of elements does not affect the results. Doing this procedure would actually make the analysis more accurate but it would take a lot longer to run the analysis than the base model. The main key for this analysis is that the same meshing method is used for the DAD models as with the bushing and fastener.



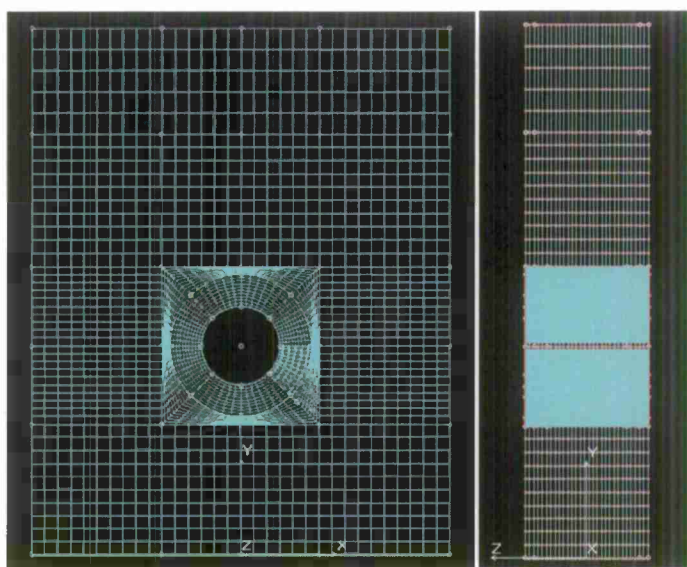


**Figure 131 - DAD model element mesh**

The element meshing scheme for the DAD models with the bushing and fastener would remain the same as before. The X and Y direction meshing scheme is the same except the Z direction differs by having more elements like the base DAD model. The DAD model with a bushing had a total of 81,200 elements. This is an increase of 7,780 elements with the addition of the bushing. The DAD model with the fastener had a total of 88,160 elements, which corresponds to an increase of 6,960 elements.

### **Finite Element Model Static Loading/Displacement**

The loading forces and the displacement constraints were added to the geometry. The displacement constraint was added on the bottom surface of the geometry to represent the symmetry of the specimen, which can be seen in Figure 132. Since the FEM geometry is a half model of the test specimen, it can be assumed that on the symmetry plane of the test specimen, the specimen will not move in the X, Y, Z directions and will have no moments acting on the faces. Displacement constraints are necessary so deformation displacements can be created from the loads applied on the test specimen. Without displacement constraints, the specimen would move as one piece and not deform. The displacement constraints are applied to all FEM models, including the models with and without DADs, at the bottom surface.

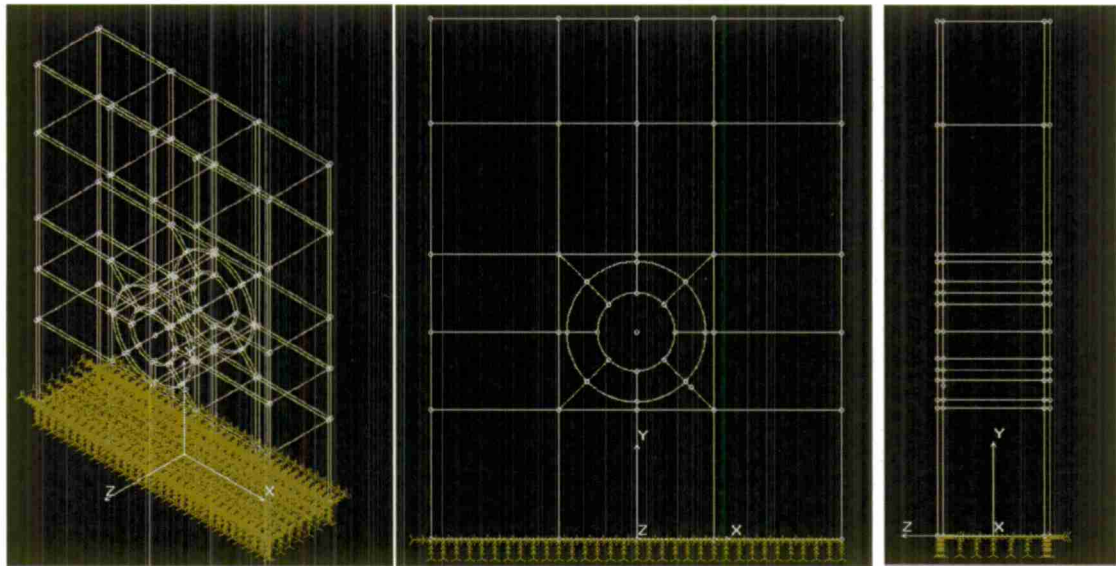


**Figure 132 - Base Model Displacements**

The loading on the specimens were then added to the model; this can be seen in **Error! Reference source not found.** The loading was applied on the bottom surfaces of the cut-out hole section of the test specimens. The loading applied is a pressure force, with a pressure of -2,891 psi, which corresponds to a monotonic load of -940 lbs. The loading for specimens with a DAD has a pressure force of -5081 psi, corresponding to a monotonic load of -1,652 lbs. This applied load is equivalent to the yield load found during experimental testing. The pressure is applied in the vertical or Y direction to try to capture the true loading seen on the test specimen. The overall displacement/extension of the FEM can then be compared to experimental results to see the accuracy of the model.

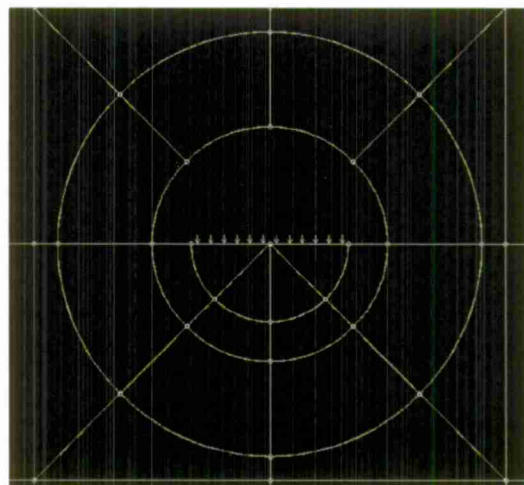


**Figure 133 - Base model with bushing and fastener**

From the results obtained for the pressure loading, the results for the bushing and fastener models gave very small displacement results from the experimental testing. The results obtained were all a power of ten

smaller than the experimental value; this will be discussed further in Finite Element Model Static Results. The decision that was made was to change the loading on each of the models from a pressure loading to a force loading. Instead of applying the loads along the bottom surface of the hole, the loads are applied to the center line of the hole; this can be seen in Figure 134. The force applied is the force obtained from experimental testing, which is -940 lbs for non-DAD models and -1652 lbs for DAD models. This loading is applied to the remaining models to see if there is any significant improvement in the results of the models.

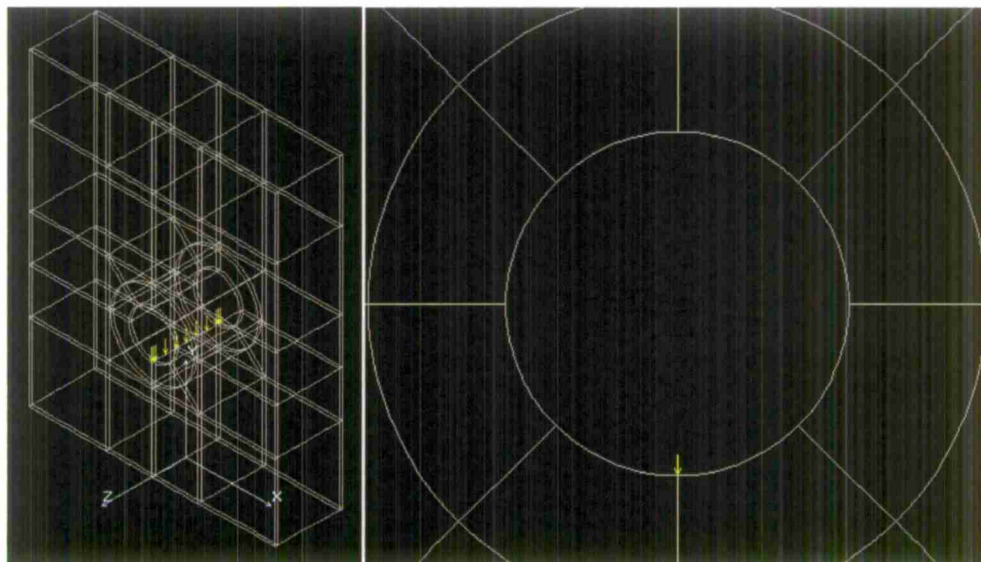


**Figure 134 - Force Loading on FEM Base Model**

### ***Finite Element Model Static Results***

The first analysis was the base FEM model for the control group. The displacement response of the model can be seen in Figure 135. The stress response of the model can be seen in Figure 136. The model shows that nothing is happening with the face sheets in both the displacement and stress figures. Most of the movement in the model is occurring in the foam. The foam is being displaced from the constant pressure and is pushing on the face sheet. This assumption can be backed up with the upward deformation of the foam seen in the displacement figure. The foam should be moving downward but instead is sliding up the face sheet. The foam cannot penetrate through the face sheet because it is a much stronger material than the core.



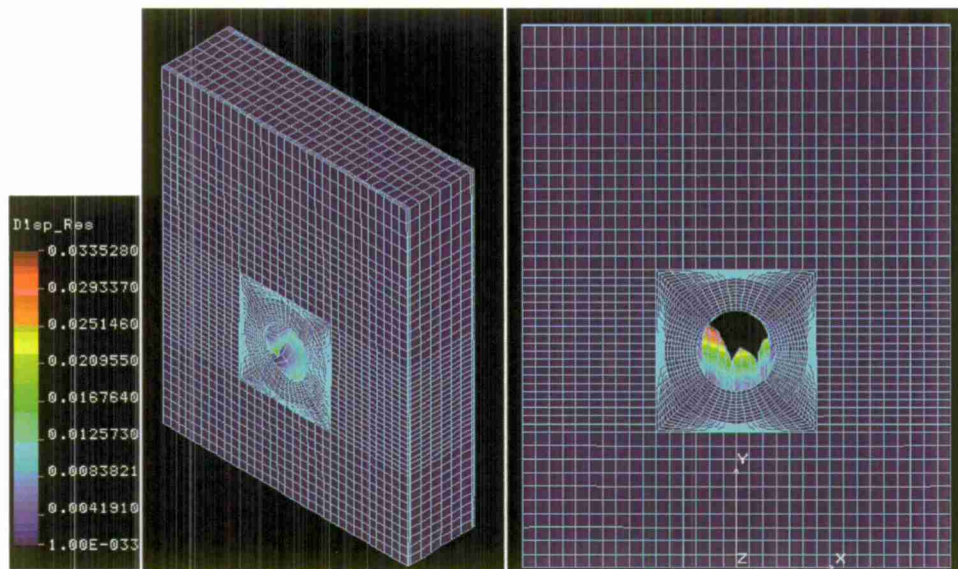


**Figure 135-** Displacement response of FEM base model with pressure loading

The stress distribution of the model shows that a circular stress concentration is seen at the bottom of the hole as well as around the hole. The stress distribution at the bottom of the hole could be from the stress of the core pushing out into the face sheet. An interesting stress concentration can be seen on the top corners of the meshing configuration on top of the hole. This could be due to how the mesh that was created around the hole. The elements might not be transferring the loads properly at that area. Another reason the stress concentration is appearing is that there is a counter reaction of the face sheets and the core from the pressure loading.

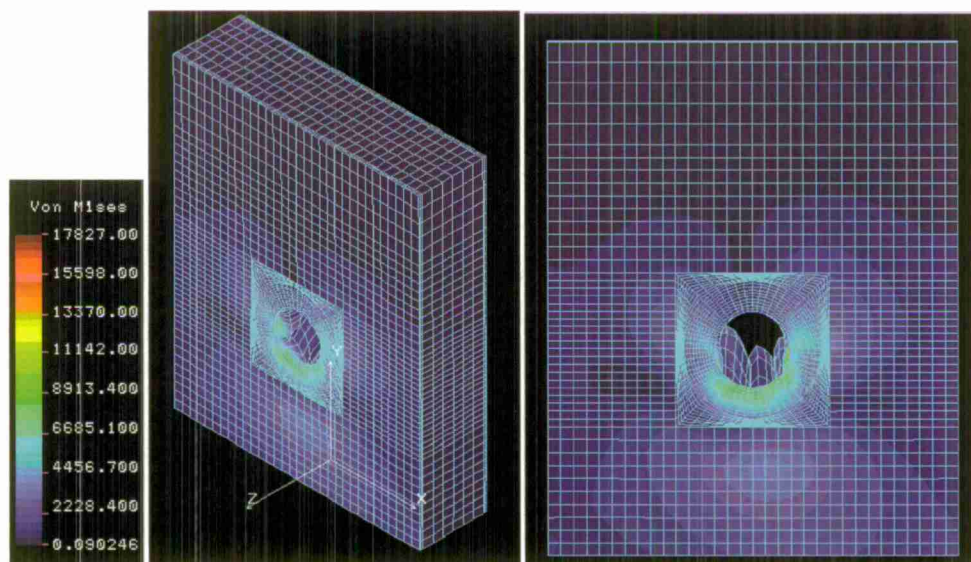


**Figure 136-** Stress response of FEM base model with pressure loading

The displacement response of the model can be seen in Figure 137. The stress response of the model can be seen in Figure 138. The displacement response of the model resembles more on what happened during

experimental testing. The section below the hole is actually displaced in the planar direction of the model, showing a bulge on the model. The bushing prevented the core from moving upward, like the previous model. Instead the core was forced to move downward and push out into the face sheet to create the bulge on the model. A semi-circular displacement distribution is also seen at the bottom of the hole from the loading seen from the bushing. The addition of the bushing severely affected the displacement of the model, even though the failure mode is similar to experimental results. The displacement contour bar shows that the maximum displacement seen in the model was 0.00278 in, which is a complete order of magnitude below the actual results. It seems that the bushing is dissipating too much of the loading seen on the model. The actual sandwich composite panel could be seeing a lot less force than what is applied.

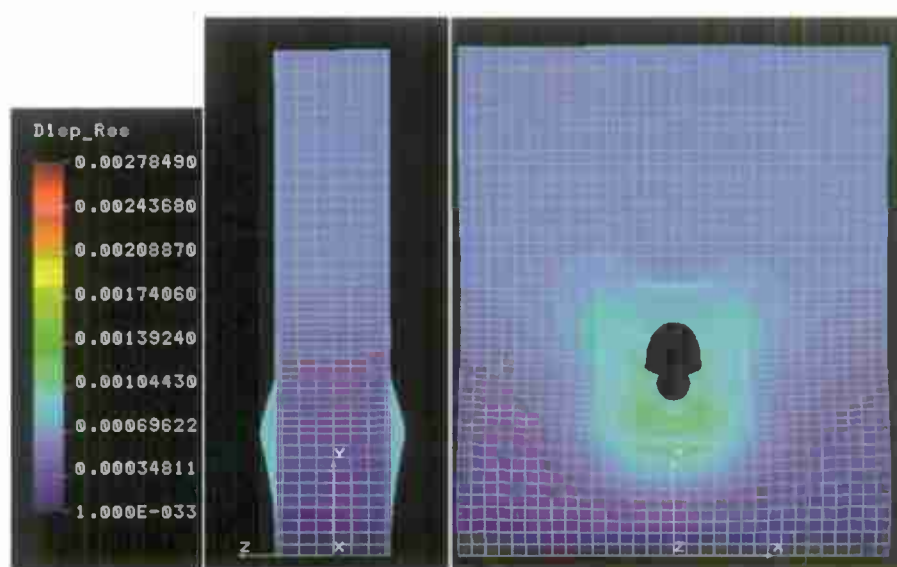


**Figure 137** - Displacement response of FEM base model with bushing and pressure loading

The stress distribution of the model with the bushing is similar to the base model. A more pronounced stress concentration is seen at the bottom of the hole than before. Instead of a circular shape, the stress concentration at the bottom of the hole stretches from the bushing all the way to the bottom of the model. This backs up the assumption made earlier that the core is pushing along the face sheet at the bottom of the hole. With the addition of the bushing, the stress concentration was actually able to push out onto the face sheet. The stress concentrations above the hole has disappeared, but new stress concentrations are seen at the tip of the bushing and the composite sandwich panel.



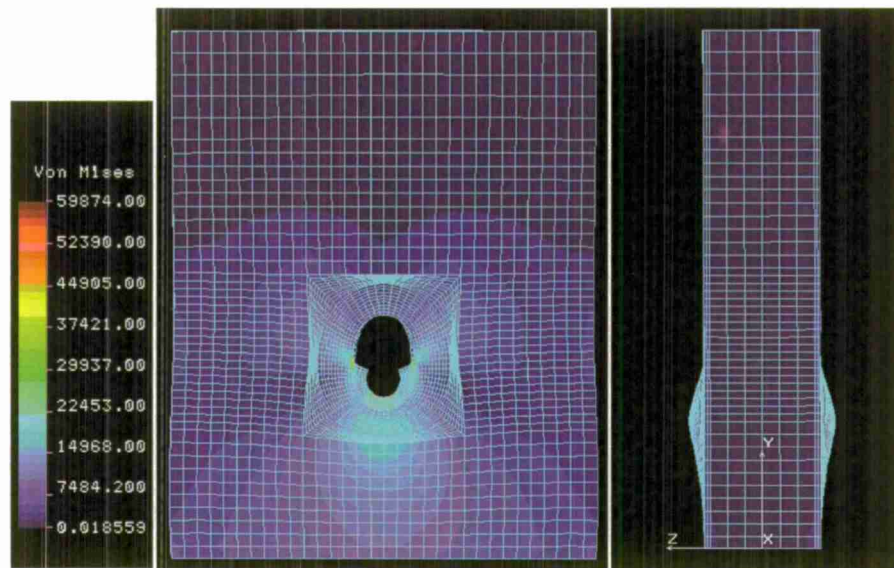


**Figure 138** - Stress response of FEM base model with bushing and pressure loading

The displacement and response of the model can be seen in Figure 139 and 142. The displacement response of the model is similar to the model with the bushing. The model has more of a pronounced displacement under the bushing and the fastener. The model also has a similar bulge at the bottom of the hole appearing on the face sheet. An interesting observation that was captured in the model was that the addition of the fastener only decreased the maximum displacement seen on the specimen by half compared to the model with the bushing. The maximum displacement from the model is still an order of magnitude below the experimental results showing that the fastener and the bushing are still dissipating the force seen on the composite sandwich panel.

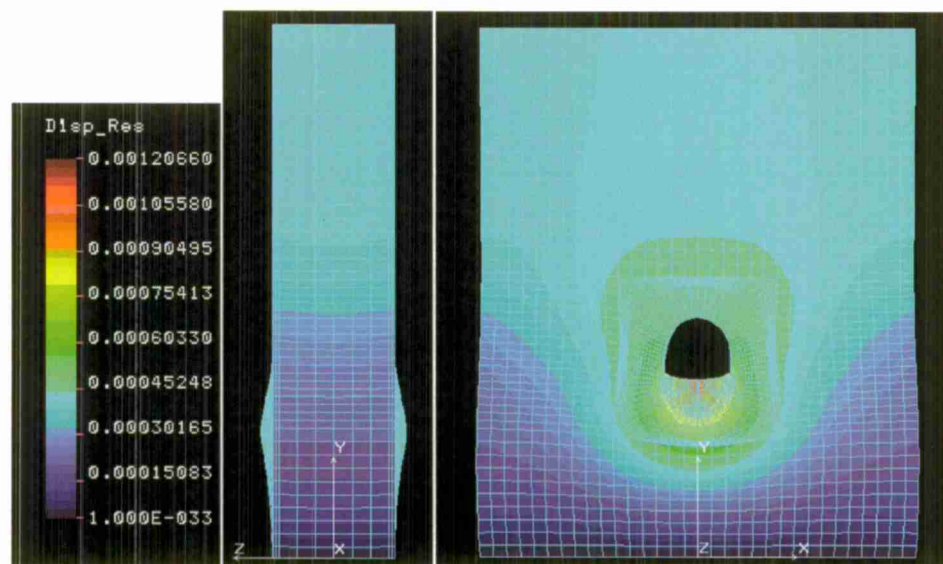


**Figure 139** - Displacement response of FEM base model with bushing, fastener and pressure loading

The stress distribution of the model with the bushing and fastener is similar to the bushing only model. The model still contains a more pronounced stress concentration as seen at the bottom of the hole. Instead of a circular shape, the stress concentration at the bottom of the hole stretches from the bushing all the way to the bottom of the model. These facts further back up the assumption made earlier that the core is pushing along the face sheet at the bottom of the hole. With the addition of the bushing and the fastener, the stress concentration was actually able push out onto the face sheet.

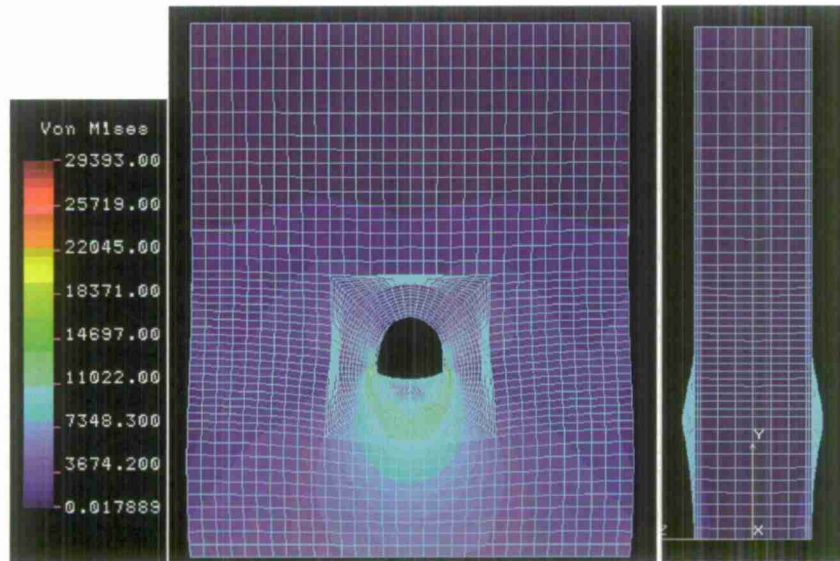


**Figure 140** - Stress response of FEM base model with bushing, fastener and pressure loading

The displacement and stress response of the model can be seen in Figure 141 and 144 respectively. The base model for the DADs shows less displacement along the face sheet of the composite sandwich panel. The model does show that there is an elongation of the core. The increase in force due to the increase in stiffness of the DADs creates a large effect on the core. Since the core is a lot weaker than the face sheet, the model shows that the core is being easily pushed down the panel, showing the elongation of the core in the model. The displacement contour bar shows that the maximum displacement is three times larger than the displacement observed from experimental testing. A little deformation is seen at the bottom of the hole, but is not as pronounced as the previous models. The little deformation could be due to the additional stiffness added from the DADs. This slightly resembles the failure results from the experimental testing.

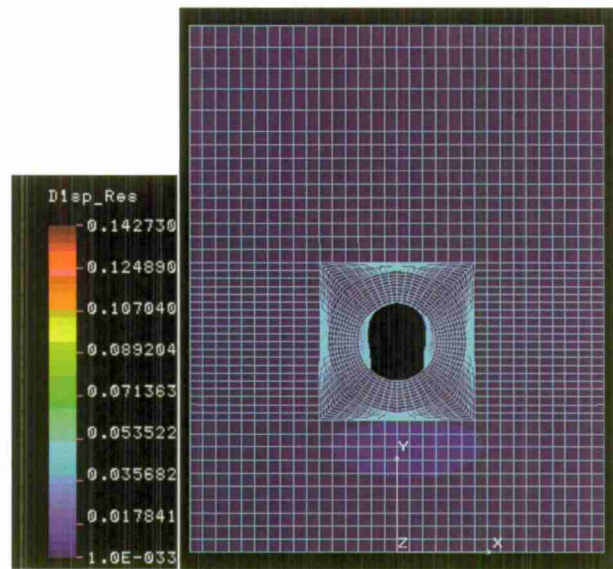


**Figure 141** - Displacement response of FEM DAD base model and pressure loading

The stress distribution of the model shows a far different distribution from the non-DAD models. The first significant difference is that the model shows a stress concentration all along the DAD, running along the width of the model. The whole DAD shows that stresses are seen along the body and that the stresses are higher where the DAD and the core meet. Another stress concentration is also seen at the bottom of the model. This attribute could be a counter reaction from the boundary conditions placed on the bottom of the model. This phenomenon can be attributed from the core being pushed down more than the previous models creating a high stress concentration.



**Figure 142** - Stress response of FEM DAD base model and pressure loading

The displacement response of the model can be seen in Figure 143. The stress response of the model can be seen in Figure 144. The displacement response shows a far different deformation from the base DAD model. The first significant difference is that the model has a more pronounced bulge at the bottom of the hole than all the other models. The side profile view shows that the model's deformation resembles of a vase with the thickness of the model gets smaller at the hole and becomes larger at the base. The largest displacement is seen right below the model, creating a circular shape displacement field. The maximum displacement from the model is still an order of magnitude below the experimental results showing that the bushing is still dissipating the force seen on the composite sandwich panel.

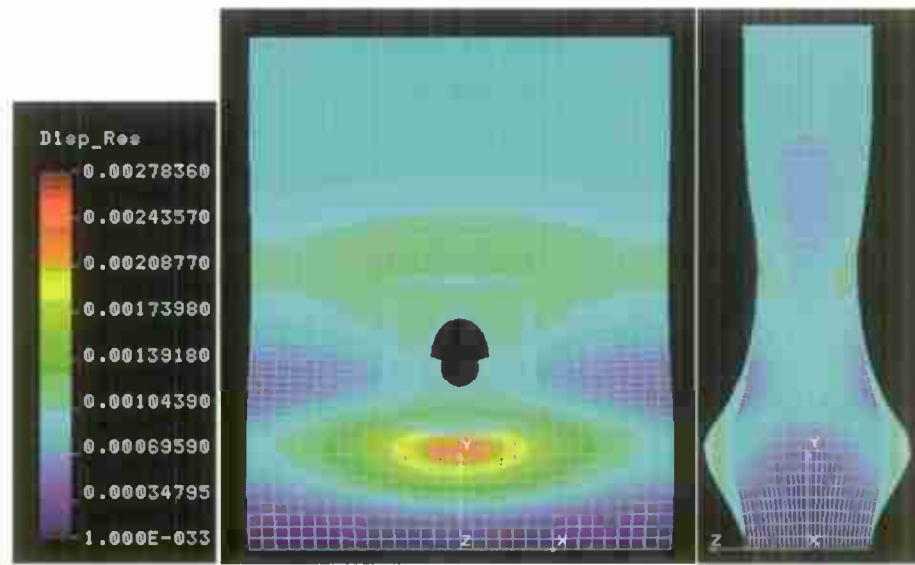


**Figure 143** - Displacement response of FEM DAD base model with bushing and pressure loading

The stress distribution of the model is more similar to the stress distribution of the non-DAD models but greatly differs from the base DAD model. The stress distribution shows a stress concentration seen along the bottom of the model. Like before, this could be a counter reaction from the boundary conditions placed on the bottom of the model. It is created from the core being pushed down more than the previous models creating a high stress concentration. The model also shows a stress concentration directly at the bottom of the hole but ends at the edge of the DAD. This is an interesting behavior because the figure shows that there is no stress transfer where the DAD and the core meet. This is far different from the previous model where stress concentrations are seen along the DAD.



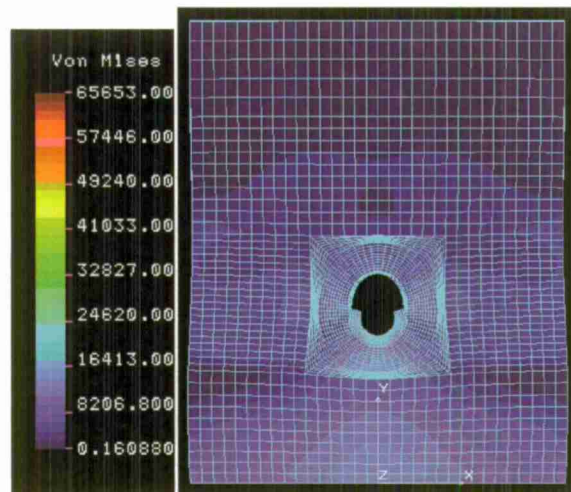


**Figure 144** - Stress response of FEM DAD base model with bushing and pressure loading

The displacement response shows a similar response to the DAD base model with a bushing. The model has a similar bulge at the bottom of the hole than all the other models. The side profile view shows that the model's deformation resembles of a vase with the thickness of the model gets smaller at the hole and becomes larger at the base. The largest displacement is seen right below the model, creating a circular shape displacement field. The displacement distribution extends vertically around the hole of the composite sandwich panel making a distorted anvil shape. The maximum displacement from the model is still an order of magnitude below the experimental results showing that the bushing and fastener is still dissipating the force seen on the composite sandwich panel. This model shows a similar trend from the non-DAD models where the maximum displacement is only half the displacement seen on the DAD model with a bushing.

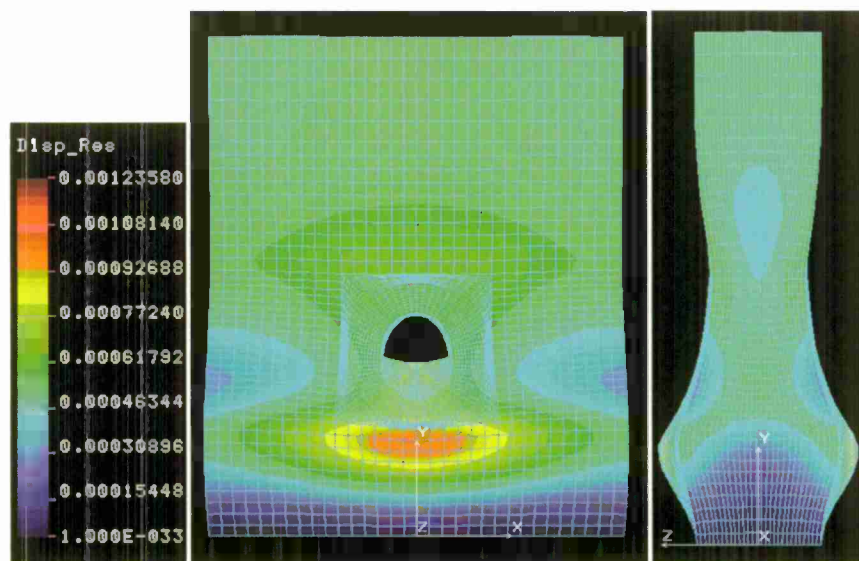


**Figure 145** - Displacement of FEM DAD base model with bushing, fastener and pressure loading



The stress distribution of the model resembles a similar distribution to the bushing model. The stress distribution shows a stress concentration seen along the bottom of the model. Like before, this could be a counter reaction from the boundary conditions placed on the bottom of the model. It can be mostly attributed to the core being pushed down more than the previous models creating a high stress concentration. The model also shows a stress concentration directly at the bottom of the hole and expands slowly to the edge of the DAD. Instead of the previous model, the stress concentration does not stop but expands all the way to the bottom of the model. This shows that the model needs a better mesh between the fine mesh around the hole and the DAD and a coarse mesh at the bottom. A better transition in the mesh would give a smoother stress concentration at the bottom of the hole.

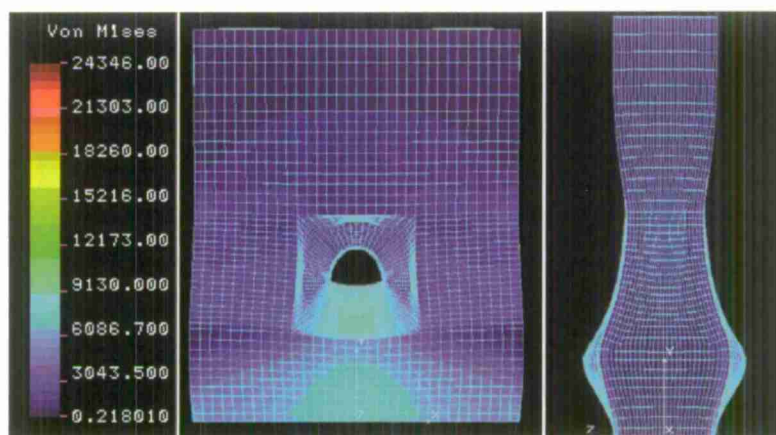


**Figure 146** - Stress response of FEM DAD base model with bushing, fastener and pressure loading

A summary of the displacement results for all six models with and without DADs can be seen in Table 21. The table shows that the base models for each group is in the same order of magnitude of numbers, while the base with the bushing and the base with the bushing and the fastener are one order of magnitude less than the base group. An interesting observation is that the base model with the bushing and the base model with the bushing and the fastener are the same for each group. This could be due to the dissipation seen in the metals where it contacts the composite sandwich panel. A more accurate loading must be applied for better results. The comparison between the FEM and the experimental results would be further discussed.

**Table 21** - FEM displacement results with pressure loading

|                        |                       | Extension (in) |
|------------------------|-----------------------|----------------|
| Control Group (No DAD) | Base                  | 0.0335         |
|                        | Base/Bushing          | 0.0028         |
|                        | Base/Bushing/Fastener | 0.0012         |
| DAD Group              | Base                  | 0.1473         |
|                        | Base/Bushing          | 0.0028         |
|                        | Base/Bushing/Fastener | 0.0012         |

To obtain better results, a force loading was applied on the center line of the hole. The first analysis that was conducted was the base model with no DADs with a force loading. The displacement response of the model can be seen in Figure 147. The stress response of the model can be seen in Figure 148. The displacement model shows that the displacement on the model is on an order of magnitude of seven, being nine whole orders above the experimental results. The displacement distribution also shows that parts of the core and face sheet have complete fractured and is hanging over the hole. This was totally unexpected and something happened during the analysis that would cause a complete failure of the specimen. This could be mainly due to the loading applied on the specimen. Instead of a pressure distribution which made sure that the yield loading was evenly distributed along the surface, the yield load was applied to each node along the center line. The displacement and stress distribution shows that there are no effects to the core or the face sheet. From the previous models, there was bulge present at the bottom of the hole or the core being distorted. The results for this case are be omitted for analysis due to the obscure and unexpected results.

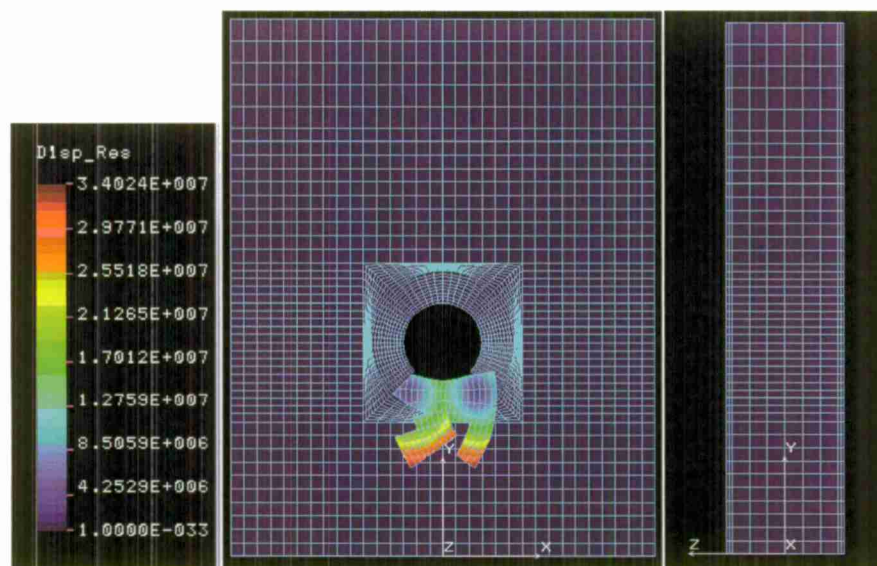


**Figure 147** - Displacement response of FEM base model with force loading

The stress distribution shows that there are not many stress concentrations seen on the face sheet of the composite sandwich panel. The stresses seen on the model could be coming more from the core than the face sheet. Since a direct force is applied on the core, the core must be deforming within the panel causing the failure in the model.

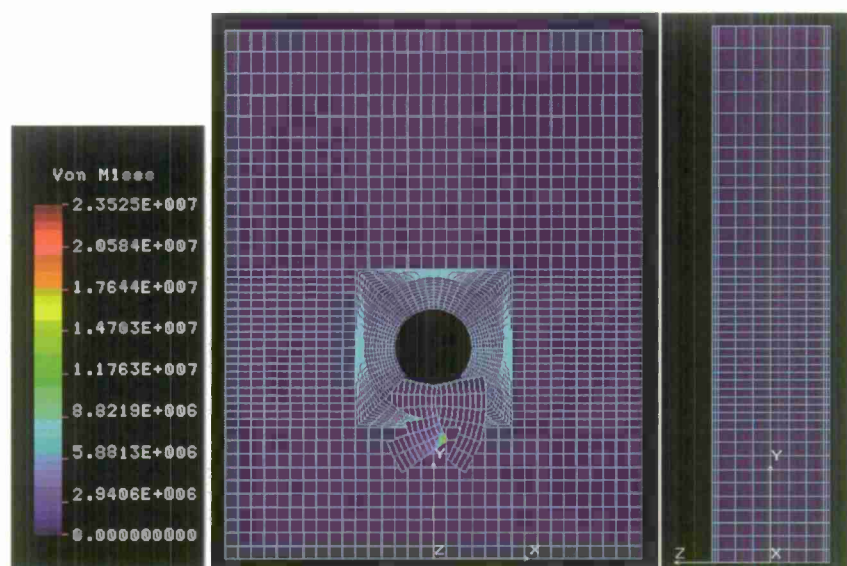


**Figure 148** - Stress response of base model with force loading

The displacement response of the model can be seen in Figure 149. The stress response of the model can be seen in Figure 150. The displacement model more closely resembles the base model with bushing with pressure loading. Both displacement models have similar contour curves on the model, showing that regardless of the loading, the bushing would apply a similar distribution on the specimen. The main difference between the two models is that there is a sharp indent on the bushing caused by the loading on the centerline of the hole. The model also has a similar bulge at the bottom of the hole. The great advantage to this model is that the maximum displacement of the specimen is in the same order of magnitude as the experimental results. The displacement distribution also shows that the maximum displacement of the model occurs in the core.

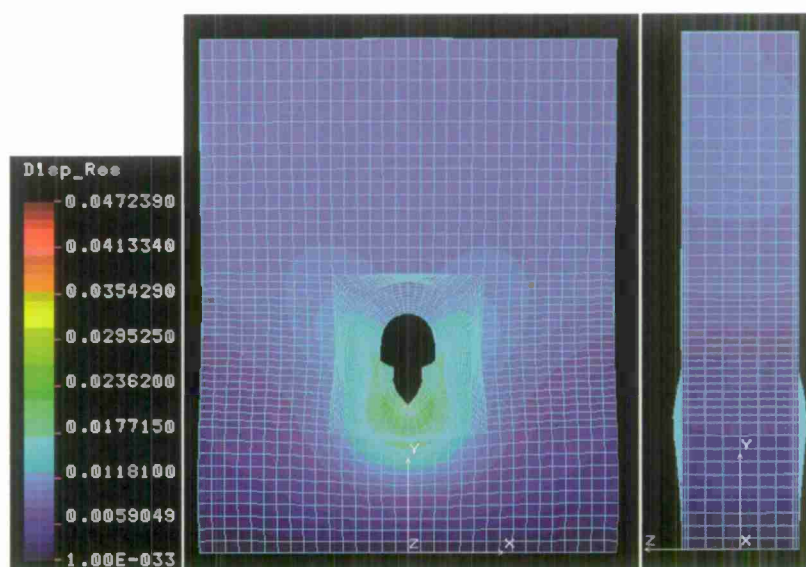


**Figure 149** - Displacement response of FEM base model with bushing and force loading



The stress distribution of the specimen shows that the use of force loading on the model does not create any stress concentrations on the face sheet. It looks like most of the stress concentrations occur on the foam at the hole. The model shows that there is an increase in stress around the hole compared to the rest of the outer surface of the model.

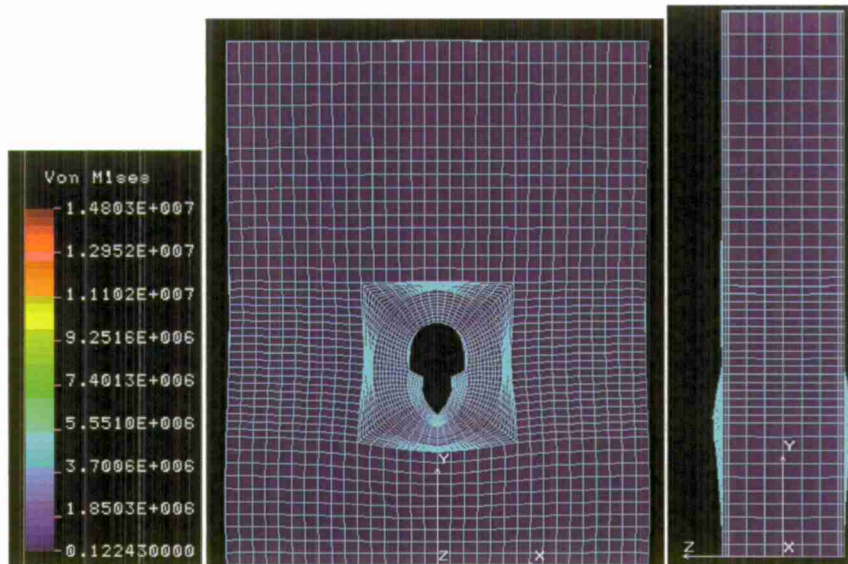


**Figure 150** - Stress response of FEM base model with bushing and force loading

The next analysis for the force loading was the base model with the bushing and the fastener. The displacement response of the model can be seen in Figure 151. The stress response of the model can be seen in Figure 152. The displacement model more closely resembles the base model with the bushing and the fastener and pressure loading. Both models have similar contour curves on the model, showing that regardless of the loading, the bushing and fastener would apply a similar distribution on the specimen. The main difference between the two models is that there is a sharp indent on the bushing caused by the loading on the centerline of the hole. The model also has a similar bulge at the bottom of the hole. The bulge is less pronounced than previous models. The great advantage to this model is that the maximum displacement of the specimen is in the same order of magnitude as the experimental results.

The stress distribution of the specimen shows that the use of force loading on the model does not create any stress concentrations on the face sheet. It looks like most of the stress concentrations would be occurring on the foam at the hole. The model shows that there is an increase in stress around the hole compared to the rest of the outer surface of the model.

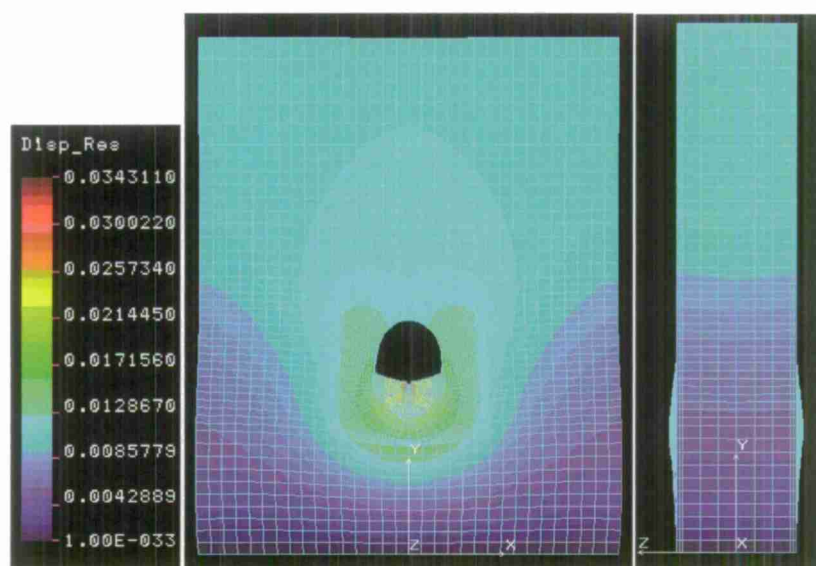


**Figure 151** - Displacement response of FEM base model with bushing, fastener and force loading

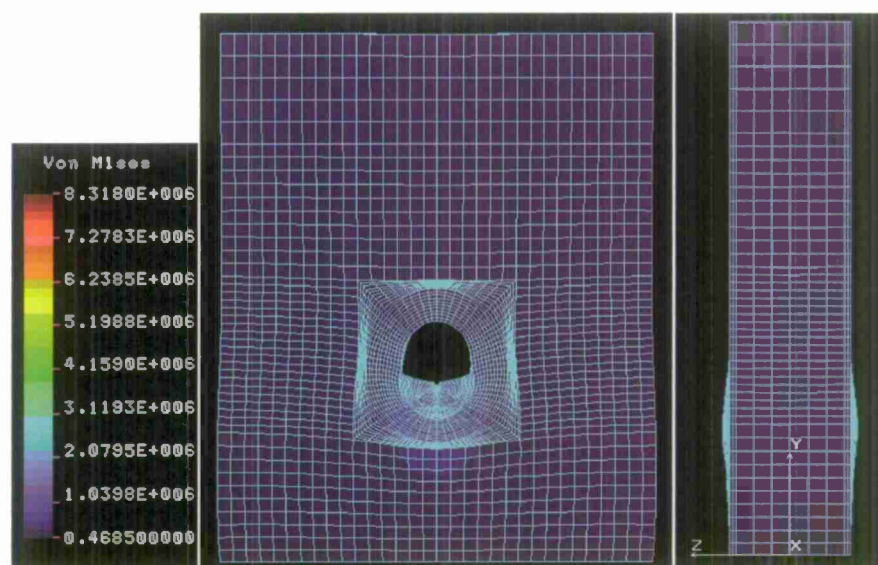


**Figure 152** - Stress response of FEM base model with bushing, fastener and force loading

The next analysis for the force loading was the base model with DADs. The displacement response of the model can be seen in Figure 153. The stress response of the model can be seen in Figure 154. Like the base model with no DADs with force loading, there is no significant displacement seen on the outer surface of the specimen. There is no bulge or any deformation seen on the model. This could be due to the addition of the DADS adding infinite stiffness to the model. The lack of deformation or displacement could be due to only having the loading on the centerline of the bottom hole surfaces. The maximum displacement contour bar shows that the maximum displacement seen on the specimen is three orders of magnitude higher than the experimental testing. This shows that the loading is affecting the model in an unusual and unexpected way. The results for this



model are omitted from any analysis due to the high displacement value and the lack of any distortion on the model.

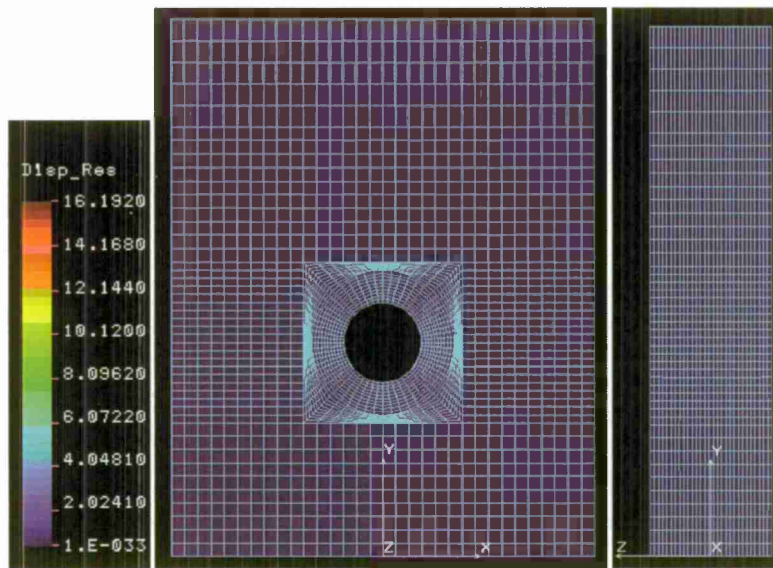


**Figure 153** - Displacement response of FEM DAD base model with force loading

The stress distribution of the model shows no high stress concentrations on the model. The distribution does show an increase stress at the bottom of the model and around the hole. The slight increase in stress resembles the shape of a mushroom cloud. This increase in stress could be due to the counter forces from the boundary conditions placed on the bottom of the model.

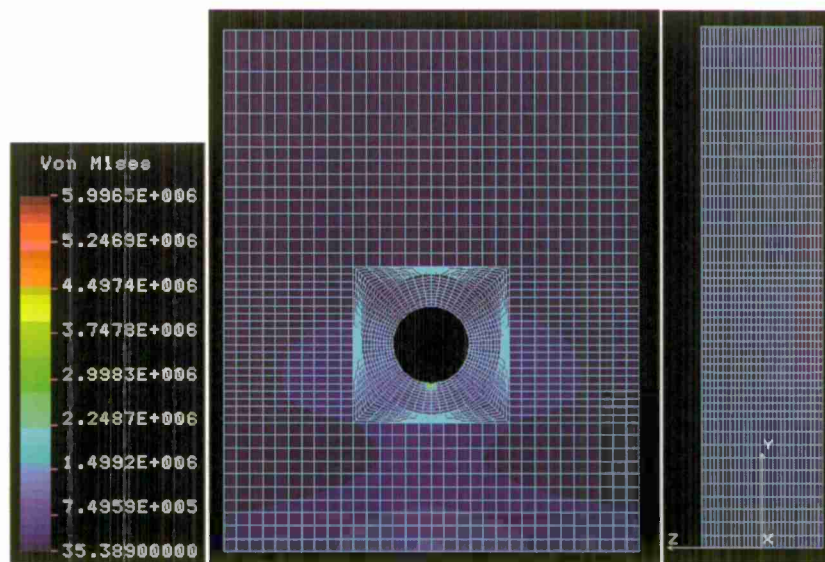


**Figure 154** - Stress response of FEM DAD base model with force loading

The next analysis with the force loading was the base model with DADs with a bushing and a fastener added to the model. The displacement response of the model can be seen in Figure 155. The stress response of

the model can be seen in Figure 156. The displacement response shows a similar response to the DAD base model with a bushing and force loading. The model has a similar bulge at the bottom of the hole than all the other models. The side profile view shows that the model's deformation resembles of a vase with the thickness of the model gets smaller at the hole and becomes larger at the base. The largest displacement is seen right below the model, creating a circular shape displacement field. The displacement distribution extends vertically around the hole of the composite sandwich panel making a distorted anvil shape. The maximum displacement from the model is an order of magnitude above the experimental results showing that the bushing and fastener is surprisingly not dissipating the loading compared to the previous loading analysis with this model.

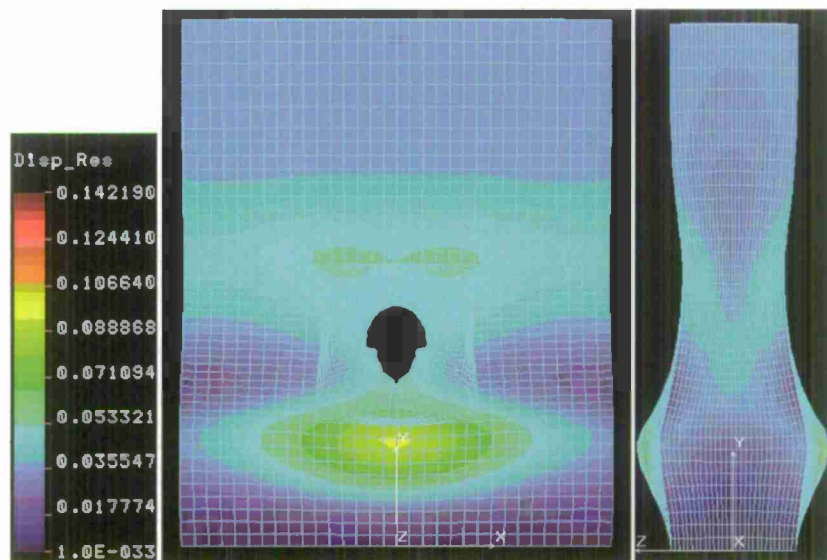


**Figure 155:** Displacement response of FEM DAD base model with bushing and force loading

The stress distribution of the models shows more of a stress concentration than previous models. The model has an increase stress concentration seen at the bottom of the panel. The slight increase in stress has a triangular shape with the tip of the triangle near where the DAD and the core meet.

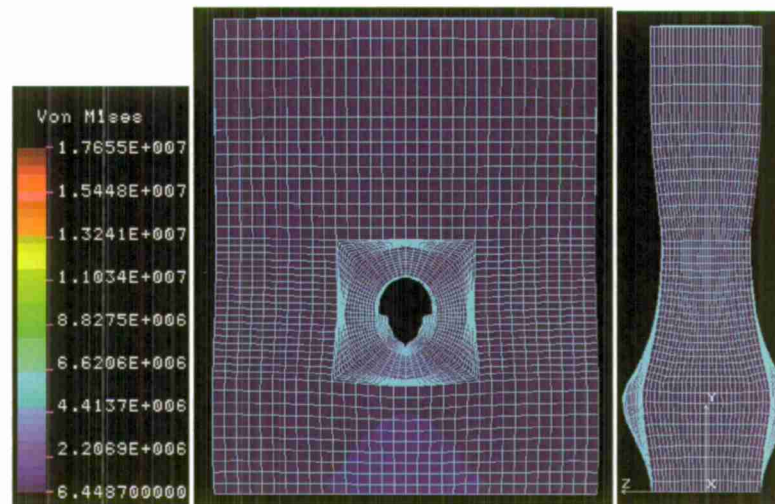


**Figure 156** - Stress response of FEM DAD base model with bushing and force loading

The last analysis with the force loading was the base model with DADs with a bushing and a fastener added to the model. The displacement response of the model can be seen in Figure 157. The stress response of the model can be seen in Figure 158. The displacement response shows a similar response to the DAD base model with a bushing. The model has a similar bulge at the bottom of the hole than all the other models. The side profile view shows that the model's deformation resembles of a vase with the thickness of the model gets smaller at the hole and becomes larger at the base. The largest displacement is seen right below the model, creating a circular shape displacement field. The displacement distribution extends vertically around the hole of the composite sandwich panel making a distorted anvil shape. The maximum displacement from the model is the same order of magnitude of the experimental results.

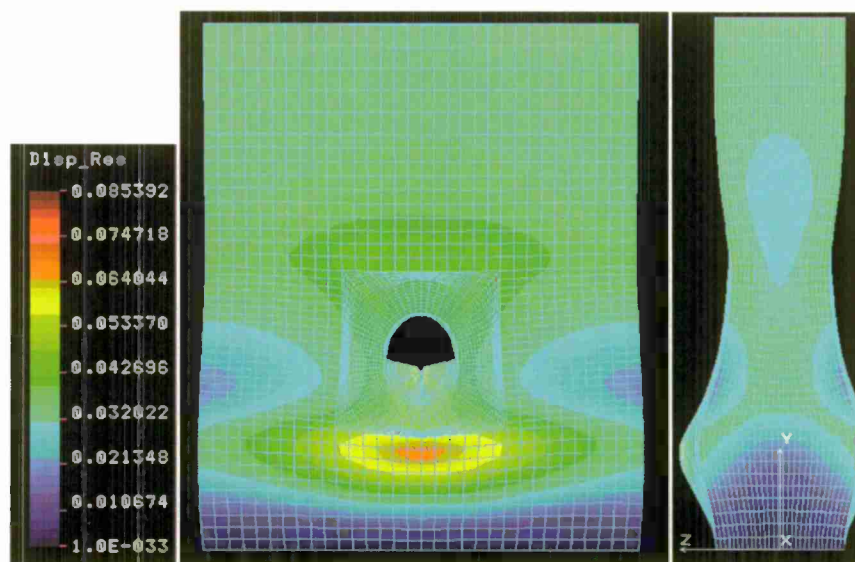


**Figure 157** - Displacement response of FEM DAD base model with bushing, fastener and force loading



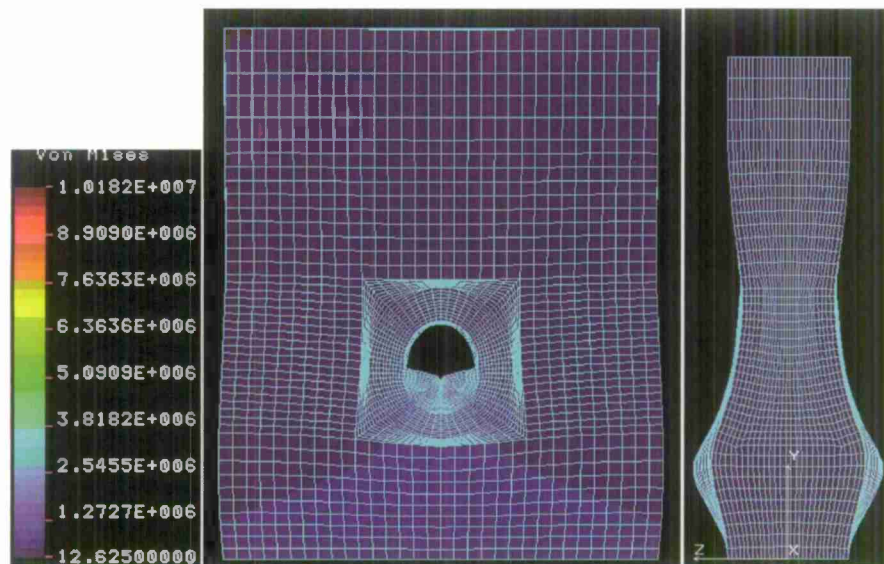


**Figure 158** - Stress response of FEM DAD base model with bushing, fastener and force loading

A summary of the displacement results for all six models with and without DADs can be seen in Table 22. The table shows that the base models for each group are omitted to having too high displacements due to the unexpected and obscure results. The use of the force loading made the results for both groups more in line with the experimental results. The control groups, models without DADs, are pretty close to one another showing that the addition of the fastener dissipated the force seen on the panel compared to the bushing alone. The DAD group shows the same trend by having a smaller displacement with the addition of the fastener. The comparison between the FEM and the experimental results are further discussed.

**Table 22** - FEM displacement results with force loading

|                        |                       | Extension |
|------------------------|-----------------------|-----------|
|                        |                       | (in)      |
| Control Group (No DAD) | Base                  | N/A       |
|                        | Base/Bushing          | 0.0472    |
|                        | Base/Bushing/Fastener | 0.0343    |
| DAD Group              | Base                  | N/A       |
|                        | Base/Bushing          | 0.1422    |
|                        | Base/Bushing/Fastener | 0.0854    |

## Chapter 6 Experimental and Numerical Comparison

### 6.1 Monotonic Loading Results

Figure 159 shows the failure stiffness (—) plotted against the vertical displacement from the experimental and numerical results for the test specimen without an initial delamination. The red curve plotted is the experimental data and the blue and green curves are numerical analysis results using two different material foam models. Both numerical modes closely follow the experimental results for displacements less than 0.015 inches but shortly afterwards the crushable foam models began to deviate from the experimental results and approach a stiffness value of approximately 175 — The hyperelastic foam model did a better job of following the experimental data but slowly deviates from the experimental data as the vertical displacement continues to increase. The hyperelastic foam model provided stiffness results within approximately 16.7% difference compared to the experimental results.

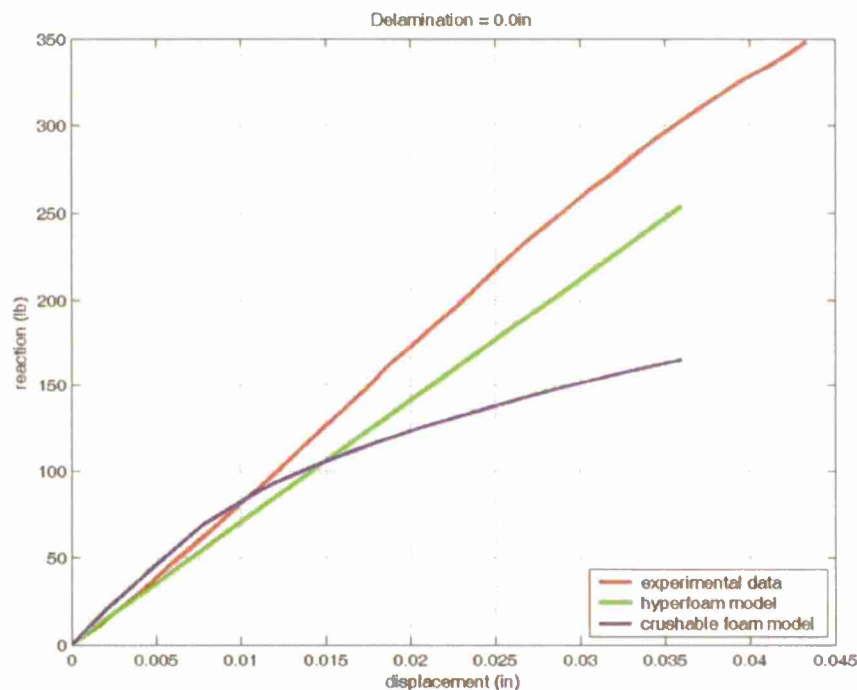


**Figure 159** - Experimental/Numerical Analysis comparison (No initial delamination)

Figure 160 shows the failure stiffness (—) plotted against the vertical displacement for the test specimens with an initial delamination of 0.5 inch. The red curve represents the experimental data and the blue and green curves represent the numerical analysis results. The green curve represents the hyper foam model which is almost a purely elastic curve. The hyper foam model provided good stiffness results for displacement



values less than 0.013 inches but afterwards over predicted the stiffness values. The crushable foam model yielded good results all the way up until the experimental results reach fracture. The crushable foam model provided stiffness values within approximately 5% compared to the experimental results.

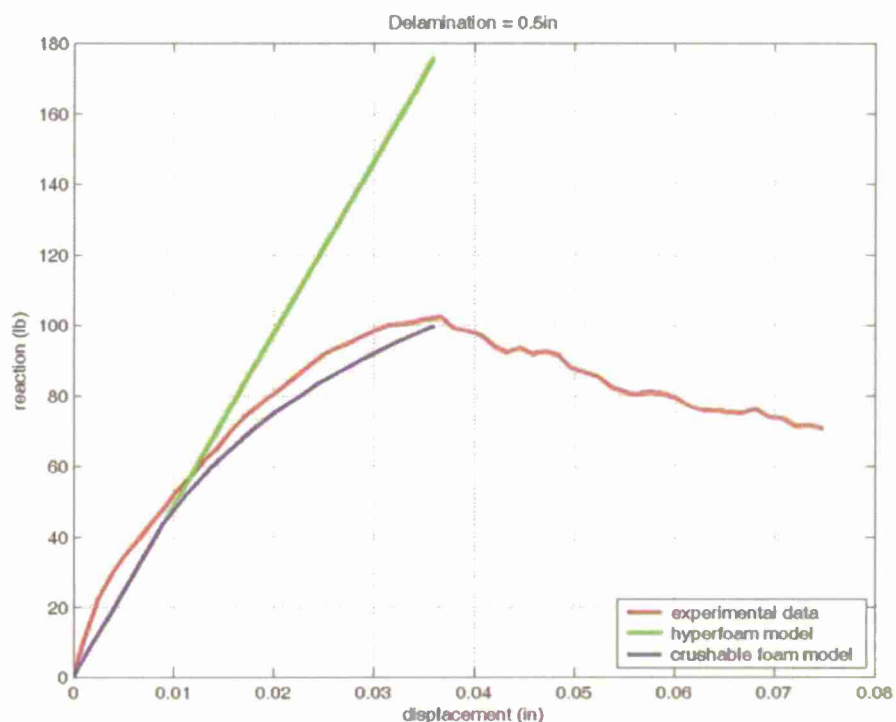


Figure 160 - Experimental/Numerical Analysis Comparison (0.5 inch initial delamination)

## 6.2 Damage Arrestment Device Results

A comparison of the maximum displacement or extension of the composite sandwich panel between the experimental testing and the FEMs was conducted. The comparison of results can be seen in Table 23. The table shows the results from both the pressure and force loading with and without DAD for the FEM models. The results highlighted with yellow represents the most accurate in extension/displacement for the FEM model compared to its respective group. For the control group, non-DAD models, the base model with a bushing and force loading was the most accurate by under predicting the experimental extension by 14.1% by having an extension of 0.0472 in. For the DAD group, the base model with a bushing, a fastener, and force loading was the most accurate by over predicting the experimental extension by 43.0% by having an extension of 0.0854 in.

**Table 23** - Comparison of maximum displacement between Experimental and FEM Results

|                  |                        |                       | Extension     | % Difference |
|------------------|------------------------|-----------------------|---------------|--------------|
|                  |                        |                       | (in)          | (-)          |
| Pressure Loading | Control Group (No DAD) | <b>Experimental</b>   | <b>0.0550</b> | -            |
|                  |                        | Base                  | 0.0335        | -39.1%       |
|                  |                        | Base/Bushing          | 0.0028        | -94.9%       |
|                  |                        | Base/Bushing/Fastener | 0.0012        | -97.8%       |
|                  | DAD Group              | <b>Experimental</b>   | <b>0.0597</b> | -            |
|                  |                        | Base                  | 0.1473        | 146.7%       |
|                  |                        | Base/Bushing          | 0.0028        | -95.3%       |
|                  |                        | Base/Bushing/Fastener | 0.0012        | -97.9%       |
| Force Loading    | Control Group (No DAD) | <b>Experimental</b>   | <b>0.0550</b> | -            |
|                  |                        | Base                  | N/A           | -            |
|                  |                        | Base/Bushing          | 0.0472        | -14.1%       |
|                  |                        | Base/Bushing/Fastener | 0.0343        | -37.6%       |
|                  | DAD Group              | <b>Experimental</b>   | <b>0.0597</b> | -            |
|                  |                        | Base                  | N/A           | -            |
|                  |                        | Base/Bushing          | 0.1422        | 138.2%       |
|                  |                        | Base/Bushing/Fastener | 0.0854        | 43.0%        |

Some interesting trends from the table is that for both groups with pressure loading, the base model with a bushing and the base model with both the bushing and the fastener are a complete order of magnitude below the experimental results. This is primarily due to how the loading is transferred to the composite sandwich panel by the metal inserts. On the other hand, the base models for both groups with pressure loading were in the same order of magnitude with the experimental results.

Another interesting trend from the table is that for both groups with force loading, the extension decrease as the models become more complex. Adding a fastener to both groups' models decreases the extension. This reinforces the assumption that adding the bushing or the fastener to the model would dissipate the load seen by the composite sandwich panel. The last interesting trend is that for the force loading models, the control group under predicted the experimental results and the DAD group over predicted the experimental results. This could be due to the addition of the DADs and shows that another type of loading must be applied to see if better results can be obtained for that group.

Changing the loading on the specimen from a pressure loading to a force loading along the centerline of the bottom surface of the hole significantly affected the overall extension of the specimen. It moved the results

from being one complete order of magnitude below the experimental results to within the same order of magnitude. The change to the new loading also gave better results, making the models ideal for future works.

### Comparison of load/extension curve and Elastic Modulus

A comparison of the load versus extension curve and the elastic modulus for the theoretical, experimental, and FEM results was conducted. The first comparison was the control group without any DADs for the load versus extension curve; this can be seen in Figure 161. The figure shows five curves: the theoretical curve, the experimental curve, the FEM with force loading on the base model with a bushing, the FEM with force loading on the base model with a bushing and a fastener, and the FEM with pressure loading on the base model. The three FEM were plotted because those were the only models that had the same order of magnitude to the experimental or theoretical results. The FEM curves were created changing the loading of the model to find its respective displacement. Five data points were taken for each FEM model to create the curve. The theoretical curve was obtained using the force spring equation and solved for displacement from stiffness and the yield force. The experimental curve was plotted using the test specimen that had the closest to the average elastic modulus from that test group.

The FEM results have a linear curve that end at the yield load and its respective yield extension because the FEM software assumes that the model is running in the elastic region and its assuming a linear failure model. A more advance analysis or software must be used to have a more non-linear curve.

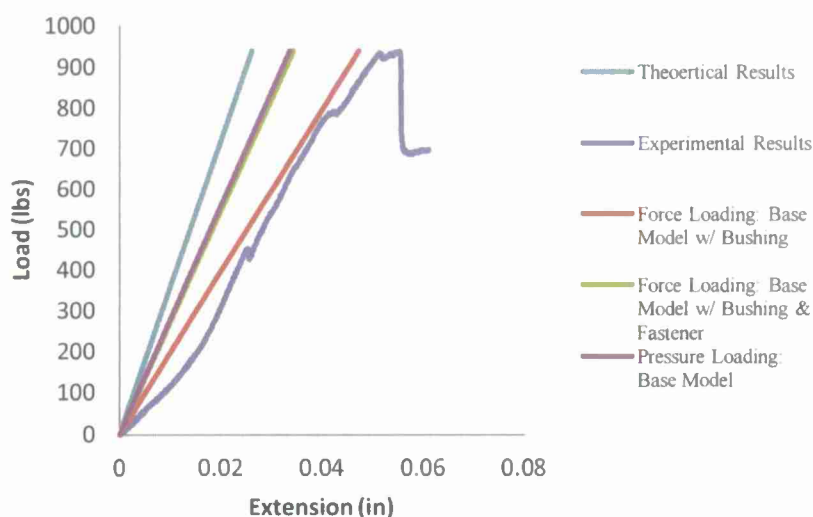


**Figure 161** - Load/Extension Comparison for Control Group

From the figure, it shows that the force loading on the base model with bushing and the pressure loading on the base model have similar slopes to the experimental results. The force loading on the base model with a bushing has the closest yield extension to the experimental results but it has more of a gradual slope than the experimental results. The figure shows that the steeper the slope of the curve, the lower the yield extension from

the experimental results. The elastic modulus of the curves can be seen in Table 24. The table shows that the theoretical elastic modulus of the composite sandwich panel is the highest. The elastic modulus was calculated by taking the slopes from the load versus extension curves, the slope is the stiffness (K), and is converted to elastic modulus by the geometry of the ideal test specimen. The FEM with force loading on the base model with a bushing has the lowest elastic modulus but is the closest in maximum displacement compared to the experimental results. The FEM with force loading on the base model with a bushing and a fastener and the FEM with pressure loading on the base model have similar elastic modulus and extension.

**Table 24** - Elastic Modulus Comparison for Control Group

|   | Elastic Modulus | % Difference from Theoretical | % Difference from Experimental |
|---|-----------------|-------------------------------|--------------------------------|
|   | (psi)           | (-)                           | (-)                            |
| Theoretical Results                             | 62,650          | -                             | -                              |
| Experimental Results                            | 45,174          | -27.9%                        | -                              |
| Force Loading: Base Model w/ Bushing            | 34,573          | -44.8%                        | -23.5%                         |
| Force Loading: Base Model w/ Bushing & Fastener | 47,578          | -24.1%                        | 5.3%                           |
| Pressure Loading: Base Model                    | 48,715          | -22.2%                        | 7.8%                           |

The first comparison was the control group with DADs for the load versus extension curve; this can be seen in Figure 162. The figure shows four curves: the theoretical curve, the experimental curve, the FEM with force loading on the base DAD model with a bushing, and the FEM with force loading on the base DAD model with a bushing and a fastener. The FEM, experimental and theoretical curves were created the same method as previously discussed.

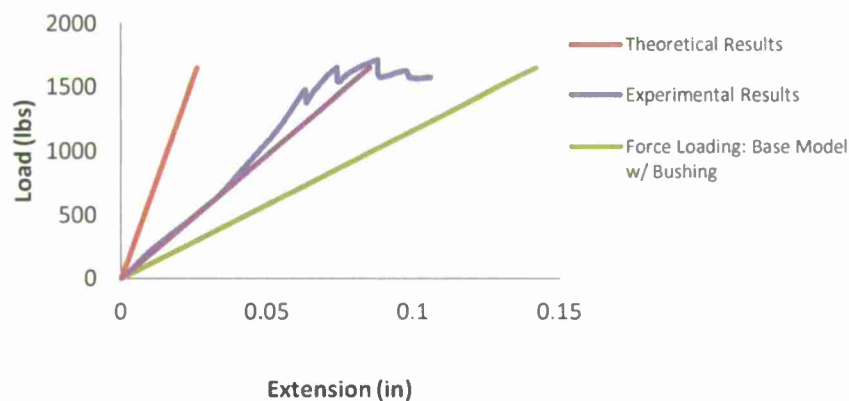


**Figure 162** - Load/Extension Comparison for DAD Group

The figure shows that the theoretical results over predict the elastic modulus of the experimental results and under predicts the extension of the specimen. The FEM with force loading on the base DAD model with a bushing under predicts the elastic modulus of the experimental results and over predicts the extension of the specimen. The most interesting curve is the FEM with the force loading on the base DAD model with a bushing and a fastener has a similar elastic modulus of the experimental testing by overlapping one another early on, but differs halfway through the experimental results. The model does over predict the extension compared to the experimental testing but is the closest of all FEM models. This is very surprising because the model captures the experimental results early on. The addition of a second linear curve to the model or a non-linear model would make the Fem more accurate to experimental results.

The elastic modulus of the curves can be seen in Table 25. The table shows a big contradiction to the curve by showing that the FEM with force loading on a base DAD model with a bushing and a fastener is 43% lower than the experimental values. This could be due to the elastic modulus of the experimental testing being calculated from the second slope of the curve rather than the first, where the FEM and the experimental results overlap one another. The two comparisons between the experimental and FEM results show that the FEMs need more refinement to be accurate to the experimental values.

**Table 25 - Elastic Modulus Comparison for DAD Group**

|  | Elastic<br>Modulus | % Difference from<br>Theoretical | % Difference from<br>Experimental |
|--|--------------------|----------------------------------|-----------------------------------|
|  | (psi)              | (-)                              | (-)                               |
| Theoretical Results                                    | 62,650             | -                                | -                                 |
| Experimental Results                                   | 59,340             | -5.3%                            | -                                 |
| Force Loading: Base DAD<br>Model w/ Bushing            | 20,168             | -67.8%                           | -66.0%                            |
| Force Loading: Base DAD<br>Model w/ Bushing & Fastener | 33,583             | -46.4%                           | -43.4%                            |



## Chapter 7 Conclusion

This research presents the experimental and numerical results for composite sandwich structures with an initial delamination. The effects of the initial delamination length were varied to see the effect an initial delamination had on decreasing the strength of the composite sandwich structures.

For the first application, fiberglass rods called shear keys were integrated into the initially delaminated sandwich structures with the intent of increasing the ultimate monotonic failure and fatigue life. The location of the shear keys with respect to the back edge of the delamination was varied to see the effect the shear keys had on the strength of the part. The fatigue life and fracture behavior was determined for sandwich structures with no initial delamination, 1 inch initial delamination, and 1 inch initial delamination with a shear key zero inches from the back edge of the delamination. A numerical analysis was performed using Abaqus/CAE and Cosmosm/M to verify the monotonic loading cases with no initial delamination and an initial delamination of 0.5 inches. Adding initial delaminations to the sandwich structure reduced the ultimate monotonic failure loads by approximately 70%. Increasing the delamination length had negligible effects on the ultimate monotonic failure load but a larger delamination corresponded to a larger yield force. This was attributed to the additional moment created from the Instron machine to the aluminum tabs. The shear key rods decreased the ultimate failure force of the sandwich structure compared to the test specimens with only an initial delamination. This was likely due to the stress concentration created by the shear key. The location of the shear key had a minimal effect on the overall strength of the composite sandwich structures. Shear keys located further away from the back of the delamination corresponded to a slightly weaker part than one with a shear key at the back edge of the delamination (0 inches). Test specimens with initial delaminations had a fatigue life approximately 75% less than test specimens with no initial delamination. The shear key test specimens had a fatigue life of approximately 80% less than the test specimens with no initial delamination. The numerical analysis was able to match the monotonic failure loads for the test specimens with no initial delamination to approximately 15% using a hyperelastic foam model. The numerical analysis was able to match the experimental failure loads for the test specimens with an initial delamination of 0.5 inches to within 5% using a crushable foam plasticity model.

For the second application of the buckling study, the results from the experimental testing of the composite sandwich showed following under buckling test.

Having a delamination arrestment key that spans the full anvil length and placed parallel to the load vector provides the best results where the majority of the overall failure load is maintained. For 1-inch delaminated 'SD' configuration test specimens, there is only an 11.8% drop in load capacity from a non-delaminated 'ND' composite sandwich structure and a 126% increase in load capacity from the 1-inch 'ID' configuration.

The failure modes of the experimental testing differ for the various configurations and delamination sizes. These failure modes range from localized buckling of the face sheet for the control 'ID' configuration to arrestment of the 1-inch delamination for the 'KD' configuration to point load concentrated failure for the 'PL' configurations. For the third application, this study presents the effect of damage arrestment devices to the failure mode around a hole in a composite sandwich panel. Seven different DAD thicknesses were tested under monotonic loading. Experimental and analytical tests were performed to determine the effects of varying the DAD thickness around the hole of a composite sandwich panel. Fatigue testing was also conducted on a control group without any DADs and a DAD group containing only a DAD thickness of three layers. The third experiment yielded results that showed that the introduction of a continuous arrestment key parallel to the in-plane loading and embedded into the composite sandwich structure provided a significant increase in loading and buckling capabilities. These results were compared to the control test specimens with and without an initial delamination and with no embedded key. The continuous key placed parallel to the load vector increased the structural strength with an increase of 126% from a 1-inch delaminated structure and only an 11% drop from non-delaminated structures. That is, 1-inch and 2-inch delaminated structures showed a 61% drop and 81% drop from non-delaminated structures respectively.

Numerical analysis was done using a finite element modeling software to predict the failure of the composite sandwich panels and was compared with experimental results. Three main models were created for specimens with and without DADs. The three models include the composite sandwich panel, a composite sandwich panel with a bushing, and a composite sandwich panel with a bushing and a fastener. Two types of loadings were applied on the six models to see which would produce the most accurate results compared to experimental testing. The key conclusion that was determined from experimental testing and numerical analysis is summarized:

- The failure mode of the experimental testing starts from a pure bearing stress on specimens with small or no DAD thicknesses to a buckling failure with the face sheet delaminating for specimens with thicker DADs.
- The fatigue testing showed that the specimens with or without a DAD have similar life cycle curves and fatigue endurance limits. This shows that the DADs only strengthen the composite sandwich panel and do not prolong the failure of the panels.

The numerical analysis shows that the type of loading on the model and the configuration of the model greatly affects the results. It was discovered that a force loading on the centerline of the specimen was ideal and that the addition of a bushing or a bushing and a fastener made the results more accurate. The addition of a bushing or a fastener helped dissipate the loading seen on the composite sandwich panel and gave it an even distribution. The numerical analysis needs more work because the model only captures the elastic or linear portion of the experimental results. Better modeling of the core and the interaction between the DADs and the core must be further investigated.

## Future Work

### Three-Point Bend Testing of Sandwich Carbon-Composite Panels

Low shear strength and delaminating effects of the skin from the core material have been known to cause significant problems to the design of sandwich composites. In effect, the preceding portions of this research focus on the mitigation of these two prominent disadvantages through the introduction of shear keys, while the following proposal will focus on the high energy absorption abilities of sandwich carbon-composite panels. Sandwich composite panels integrated with shear keys will be subjected to high and low-velocity localized impact testing, followed by three-point bend testing, in order to corroborate the energy absorption advantages of sandwich composite panels. Numerical analysis will substantiate all experimental data; the FEA program COSMOS will be used.

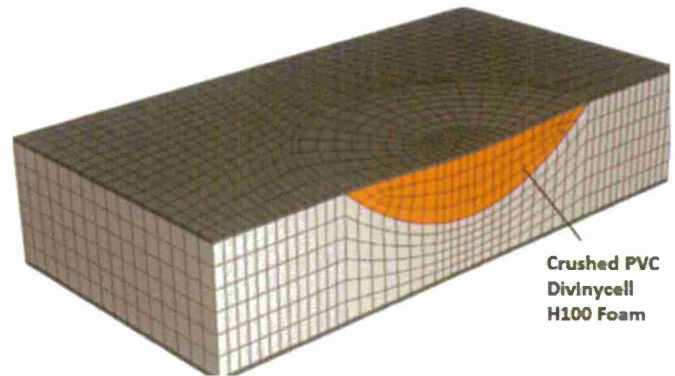


**Figure 163** - A finite element model of the sandwich Composite panel after impact loading

### Experimental/Numerical Testing

The sandwich composite panels will initially undergo a high and low velocity impact test. Seventy-five specimens will be subjected to the high velocity impact setting, and 75 specimens will be tested under the low velocity impact force. The skin is composed of resin pre-impregnated carbon fiber. The core material is composed of PVC Divinycell H100 foam.

After the impact loading, each sandwich composite panel will be subjected to a three point bend test, utilizing the servo-hydraulic machine in the Composites Laboratory at Cal Poly. Each specimen will be loaded until failure and the data will be recorded. Figure 164 delineates an experimental and finite element rendering of the three point bend test:

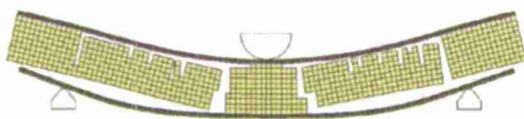


**Figure 164** - An experimental and finite element rendering of the three point bend test

The sandwich composite panel will be analyzed using the finite element software COSMOS prior to the experimental portion of this proposal.

## References

1. "Light Sandwich Constructions." CTiHuati Composites Co., Ltd. 2008.  
<http://www.ctihuatai.com/Products-sandwichEN.htm>
2. Hurwitz, Dr. Frances I., and Sullivan Dr. Roy M. "Multifunctional, Foam Core, Ceramic Matrix Composite Integrated Structures Development." NASA. 14 Dec. 2007.  
<http://www.grc.nasa.gov/WWW/RT/2006/RX/RX11C-hurwitz1.html>
3. Bigelow, Chaterine A. "Effects of Fatigue and Environment of Residual Strengths of Center-cracked Graphite/Epoxy Buffer Strip Panels." March 1989.
4. Mitra, Dr. Nilajan and Kasper, Dr. Eric. "A novel technique for preventing delamination of the composite skin from the core: Sandwich panels with shear keys." 2008. pg. 1-15.
5. Mitra, Dr. Nilajan, and Jacobson, Michael. "Sandwich Composite Report." 2008. pg. 1 – 15.
6. Davis, Richard; Engels, Nathaniel; Morham, Brett; Ung, Ryan. "Delamination of Fiberglass Sandwich Composites." 8 June 2009.
7. "Composites." NDT Resource Center. 2006. <http://www.ndt-ed.org/EducationResources/CommunityCollege/Materials/Graphics/Composites.jpg>
8. "Carbon Fiber Panel 12"x12"x0.015"/0.38mm, 2x2 Twill." Carbon & Fiberglass Sales. 2009.  
<http://carbonsales.com/images/P/%2361052-50.jpg>
9. Plastic World. 2001. <http://www.plasticworld.ca/fiberglass.jpg>
10. "Subaru Impreza 2.5 rs Kevlar/s-glass skid plate." Bar One Composites. 2008.  
<http://www.baronecomposites.com/images/Kevlar.jpg>
11. "Comparison of Theoretical and Experimental Analysis of Unidirectional and Cross-ply Composite Laminate Plates." 2007.
12. "Fibre-reinforced plastic." Wikipedia. 23 Oct. 2009. [http://en.wikipedia.org/wiki/Fibre-reinforced\\_plastic](http://en.wikipedia.org/wiki/Fibre-reinforced_plastic)
13. "Composite Material." Wikipedia. 24 Oct. 2009. [http://en.wikipedia.org/wiki/Composite\\_material](http://en.wikipedia.org/wiki/Composite_material)
14. "Fabrication Methods." Composites World. 8 Jan. 2009.  
[http://www.compositesworld.com/uploadedimages/Publications/CW/Articles/Internal/SB09\\_composites\\_thematerials\\_h.jpg](http://www.compositesworld.com/uploadedimages/Publications/CW/Articles/Internal/SB09_composites_thematerials_h.jpg)
15. "Vacuum Resin Transfer Molding (VARTM)." Kenway Corporation. 2009.  
<http://www.kenway.com/pictures/vardtr.jpg>
16. "Fatigue (material)." Wikipedia. 14 Oct. 2009. [http://en.wikipedia.org/wiki/Material\\_fatigue](http://en.wikipedia.org/wiki/Material_fatigue)
17. "Piston fracture." Hirth aircraft engine, diagnosing piston damage to your engine. 2006.  
<http://www.ultralightnews.com/hirth/images/piston7.jpg>

18. "Fatigue Testing." Stork Material Technology. 2009.  
<http://www.storksmt.com/images/TechnicalServices/SMT/Failure/FatigueFrac400.gif>
19. Pascoe, David. "Parallel Universe – Composite Troubles in Aircraft." Core and Structural Issues. 29 March 2005. [http://www.yachtsurvey.com/composite\\_rudder-2.JPG](http://www.yachtsurvey.com/composite_rudder-2.JPG)
20. Spiegel, Peter. "F-15 fleet grounded after a jet falls apart." LA Times. 6 Nov. 2007.  
<http://www.latimes.com/news/nationworld/nation/la-na-fl156nov06,1,6807945.story>
21. Kelly, Shawn. "Fatigue." Virginia Tech Materials Science Engineering. 4 May 1997.  
[http://www.sv.vt.edu/classes/MSE2094\\_NoteBook/97ClassProj/anal/kelly/fatigue.html#tworef](http://www.sv.vt.edu/classes/MSE2094_NoteBook/97ClassProj/anal/kelly/fatigue.html#tworef)
22. "Vacuum Infusion Guide." Composites World. 2009.  
[http://www.compositesworld.com/uploadedimages/Publications/CW/New\\_Product\\_Announcements/fibreglast-433.jpg](http://www.compositesworld.com/uploadedimages/Publications/CW/New_Product_Announcements/fibreglast-433.jpg)
23. "Vacuum Infusion - The Process of Resin Infusion." Vacuum Infusion Technology. 2008.  
[http://www.bladeoceancraft.com.au/assets/images/autogen/a\\_infusion-diagramAA.gif](http://www.bladeoceancraft.com.au/assets/images/autogen/a_infusion-diagramAA.gif)
24. "Divinycell H - High Performance Foam." DIAB Products. 2009.  
[http://www.diabgroup.com/americas/u\\_products/u\\_divinycell\\_h.html](http://www.diabgroup.com/americas/u_products/u_divinycell_h.html)



**Developing a Visual Tracking System for Small Marine Animal  
Research**

**Principal Investigators:**

**Pat M. Fidopiastis, Ph.D., Biological Sciences**

**Christopher M. Clark, Ph.D., Computer Science**

**Vladimir Prodanov, Ph.D., Electrical Engineering**

**California Polytechnic State University  
San Luis Obispo, CA**

## 1. Abstract

During the summer of 2011, Drs. Fidopiastis and Clark, and Cal Poly students Tim Peterson and Jia Chiang traveled to Hawaii to use Remotely Operated Vehicles (ROVs) to capture 50 gigabytes of video footage of the elusive, nocturnal, shallow water squid *Euprymna scolopes*. Our data was used to better understand squid behavior in terms of the motion patterns, velocities, acceleration and distance covered during two distinct behavioral modes, namely, escaping predators and feeding. To accomplish this, an ROV equipped with a video camera was used with a new LED beacon positioning system. Post-processing of the video data using standard image processing techniques and camera geometry has generated state estimates of various squid during these different behaviors. Squid movement relative to the LED beacons was then characterized through the use of off-line image processing and state estimation. Student Sam Yim used blob-tracking image processing techniques to detect and track squid in several of the videos, allowing the ability to calculate the squid state relative to the ROV. Combining this state information with absolute ROV state estimates obtained using optical flow techniques, the relative motion of the squid was determined. Results show typical trajectories of the squid during evasion and feeding. To our knowledge, this is the first ever attempt to observe and track these squid in their natural environment.

## 2. Project significance

The vast majority of animals are smaller than 5 cm and weigh less than 10 grams. When larval and juvenile forms of larger animals are considered, the proportion of smaller animals to larger ones is even greater. Not surprisingly, our knowledge of the population densities, migration patterns, dispersal, mortality, and effects of climate and other environmental factors on smaller animals, including economically significant ones such as crabs, shrimp, and squid is very limited. This lack of knowledge is due primarily to the limited availability of technology capable of tracking these animals *in situ*. Traditionally, the approaches to track smaller animals have almost entirely been indirect, such as tagging with an obvious marker followed by an attempt to recapture. For example, members of the National Institute for Fisheries Research and Development (in an on-going, as yet unpublished study) tagged 900 shrimp with a visible marking and released them off the coast of Argentina. Of these 900 shrimp, only 19 were recovered. While these 19 shrimp are providing data, the inefficiency of the approach is clear with respect to smaller animals. In fact, the technology to track animals reliably over their home ranges has only been rigorously demonstrated in larger animals (>300 gms) due to power and size constraints of modern tracking systems (reviewed in [1]). Recently, Steig and Greene (2006) were the first to successfully track individual shrimp *in situ* using acoustic tags. Acoustic tags are currently the smallest tags available and cost hundreds of dollars per unit. In our study, we plan to design, build and implement optical tags that are about one-third

the size and weight of acoustic tags. We anticipate that this will be possible using inexpensive surface-mount electronic components, resulting in a micro tag that costs a few dollars per unit. This approach will be designed to work synergistically with our developing system for visually tracking the small tropical squid *Euprymna scolopes* using remotely operated vehicles. The highly tractable symbiotic association between *V. fischeri* and its animal host *E. scolopes* has emerged as an important model system with strong biomedical implications (reviewed in [3]). In order to study this system, several labs are cooperating to produce, and share, sufficient numbers of squid for experiments. This has allowed us to make impressive gains in understanding the mechanisms used by *V. fischeri* to make light and colonize squid. A next step in our work is studies on the behavior of squid in the wild, including the role of bacterial-derived light in the biology of the squid. Squid behavior in the wild has never been documented; our knowledge is limited to anecdotal observations on the behavior of captive squid maintained under highly unnatural laboratory conditions [4] [5]. Furthermore, increased collaboration and the development of more tools have led to an increased demand for wild caught squid for our aquaculture programs. There is now an urgent need to develop the technology to locate new populations of squid, better understand their feeding and mating behaviors, mortality rates at different stages, and estimate our impact on wild populations.

While the development of tools for tracking and observing squid is substantial, it is notable that these tools will have a variety of applications to National Security and ONR Code 30 Science and Technology Program. In using ROVs with onboard monocular vision to track marine life, contributions will be made in the National Security areas of "remote sensing, optics, robotics, biosensing, and detection". The image processing system will have to detect an LED through thresholding of filtered images. Thus, our ability to develop a system capable of producing filtered measurements of moving marine life will have many applications in biosensing. For example, this work could support on-going Navy research on new methods for detection of fish, fish populations, and mapping of fish habitats. Under Code 30, this project is directly relevant to the "Command and Control" component, in particular, our integration of GPS into the system will allow for remote squid tracking. In addition, there are applications in the "Mine countermeasures" thrust area, such as shallow underwater imaging. The shallow water localization system and image processing techniques developed in this project and our previous work will have direct applications to detecting and mapping the location of mines and other obstacles that would threaten amphibious forces in shallow water and surf zone operating areas. The core technological advancements include 1) design and verification of a scanning sonar-based shallow water localization system, and 2) design of vision processing algorithms for tracking dynamic targets (e.g. squid with known and presumed evasion adaptations) within shallow beach environments. This research also falls in line with ONR's Code 30 thrust on "Intelligence, surveillance and reconnaissance" for its emphasis on "tagging, tracking, and locating." In developing a system for tagging, tracking and locating small marine species, our work will be also be

transferable to a wider variety of underwater state estimation applications (e.g. ship hull inspection, marine archeology, naval warfare, etc.).

### 3. Background/prior work

To date, *Euprymna scolopes* squid have been detected in only three coastal Oahu locations; each location is a shallow, sandy bottom bay (Fig. 1a). Adult squid (Fig. 1b, 1c) can be maintained in the laboratory for several months, but even slight perturbations (e.g. water chemistry, natural bacterial populations in seawater, etc) can severely limit their lifespan in captivity. Although we have had sufficient success at breeding adult animals, only one research group has reported limited success in raising hatchling squid to a sub-adult stage [5]. Typically, hatchlings from a single egg clutch will live about four days, which is just long enough to perform some of our experiments. Based on observations in the lab, this dynamic association begins when an adult female squid lays hundreds of eggs that will hatch synchronously at dusk after about 20 days of embryogenesis. Juvenile squid hatch without *V. fischeri* but acquire the cells within a few hours of exposure to their natural habitat. Cells of *V. fischeri* swim into the light organ, a specialized structure in the squid mantle cavity (reviewed in [6]). Once inside the light organ, the bacteria are fed nutrients in the form of peptides [7]. These bacteria then grow to a density sufficient to activate luminescence [8].

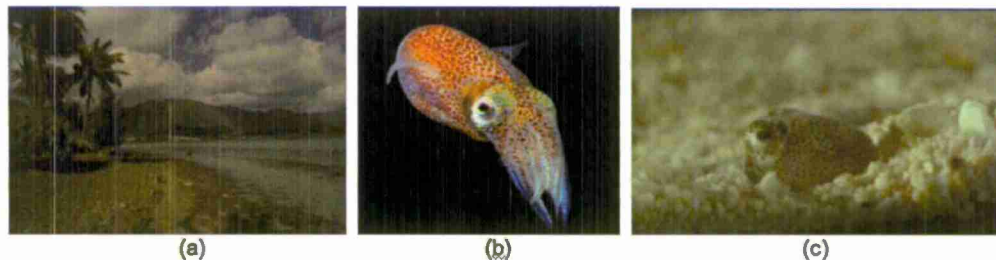


Figure 1. Kaneohe Bay, Oahu (a), one of three locations where squid are collected. In (b), an adult *E. scolopes* is shown displaying typical nocturnal swimming behavior. Adult squid displaying daytime burying behavior are shown in (c).

While the benefit of this association to the bacteria is being rigorously tested, the benefit to the squid is less certain. The prevailing hypothesis is that bacterial luminescence provides the host with counter-illumination on its ventral surface, apparently camouflaging and protecting it from predation. This behavior has been described in other marine animals [9] and is consistent with other camouflaging behaviors by the squid, such as changing color, burying in sand, and squirting ink. Interestingly, despite 20 years of detailed study and millions of dollars in research funding, this phenomenon has never been studied in nature, and there has only been one study to support this hypothesis using sensitive equipment in the laboratory [10]. Although the study did suggest counter-illumination was likely, removing the squid from its natural habitat and performing the experiment in a

highly artificial setting (i.e. in the absence of predators, ground cover, natural light, etc) strongly suggests that the conclusions are limited. Thus, the vast majority of support for this hypothesis is inferred from structural features of the squid.

Until recently, we did not have the tools to answer fundamental questions on the role of bacteria-derived light or the life history of the squid in its natural environment. We propose the use of inexpensive, micro scale optical tags to enhance our developing *in situ* tracking system that utilizes an Autonomously Operated Vehicle (ROV), or underwater robot, to observe the squid in its natural environment. An active tag is an electronic transmitter that is attached a specimen [11]. In theory, one could use tags that transmit radio frequency, infrared, acoustic, or optical signals. Radio frequency and infrared signals however do not propagate well in water [12]. Therefore, acoustic signaling and optical signaling are the only viable underwater alternatives. Acoustic transmitter tags are commercially available from several sources [13] [14] [15]. State-of-art acoustic transmitters are approximately 12-16 mm in length and 5-7 mm in diameter. The operating frequency is in the range of 200 kHz to 400 kHz, depending on the manufacturer. The typical pulse rate interval (PRI) is 2 to 10 sec. The life of the tag depends upon the PRI and the size of the battery, and ranges from one month to one year. The detection range is estimated at up to one kilometer, although achieving this range requires many microphones and is highly susceptible to acoustical interference. Perhaps the greatest limitation of these tags is their unit price, which is typically \$200-\$300. Nevertheless they have been used to track a variety of animals, including shrimp [16].

#### 4. Discussion of Results

The goal of this work is to develop a tracking system that can calculate the trajectory of the squid within its natural environment. The trajectory  $\chi_s$ , consisting of time parameterized squid states, is calculated with respect to an inertial coordinate frame attached to the environment.

$$\chi_s = \{(X_{s,t})I \mid t \in [0, t_{max}]\} \quad (1)$$

$$X_{s,t} = [x_{s,t} y_{s,t} z_{s,t}] \quad (2)$$

Water depth is shallow (0.2-1.0 meters) with reasonable visibility (1.0 meter minimum). The squid is nocturnal so natural light is minimal with the rare exception of a full moon on a cloudless night. As well, the path of the squid during tracking is limited (2.0 meters maximum). The proposed method uses an ROV equipped with a video camera with which images of the squid can be recorded. To accomplish ROV localization within an inertial coordinate frame, an LED beacon system was used. Several LED beacons were placed at known locations on the seafloor. Each beacon contained 4 LEDs that are all programmed to blink with a unique, easily identifiable pattern. To increase the likelihood of



identifying squid within video images, an LED tag was attached to squid. Fig. 2 illustrates a typical sampling scenario, in which a squid is swimming over the LED beacons. In this setup, the inertial coordinate system is anchored at the center of four LED beacons, which form a 1 m x 1 m square on the seafloor.

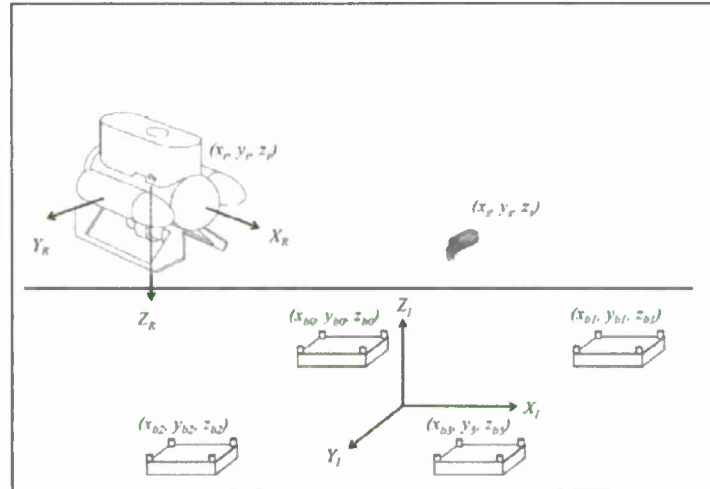


Fig. 2. The coordinate systems used to represent states of LED beacons, the squid, and the ROV.

### System Hardware

#### *ROV*

The VideoRay Pro III (Fig. 3) is a submersible vehicle remotely operated for underwater observation and exploration. It has a depth rating of 150 m, and is actuated with two forward thrusters and one vertical thruster. Its buoyancy and weighting tend to dampen out pitch and roll motion. The differential thrust configuration allows for rotation on the spot but no lateral motion. Its sensors include one forward-facing color video camera, one rearward-facing black and white video camera, a compass, and a depth sensor. Two forward facing lights are mounted in front of the thrusters. A tether connects the ROV to a surface control box, allowing control signals (e.g. joystick commands) be sent to the ROV and ROV sensor measurements (including video) be sent in real-time to the control box. Also, the control box can be interfaced with an external computer for customized software control and processing of sensor measurements.

#### *LED Positioning Beacons*

Student Jia Chiang developed 4 waterproof beacons, each consisting of four LEDs, battery pack, and microcontroller. Each microcontroller was programmed to blink LEDs in a distinct pattern to make it uniquely identifiable. LEDs were positioned at the four corners of the beacon, (Figs. 2 and 4a).



Figure 3. VideoRay Pro III ROV

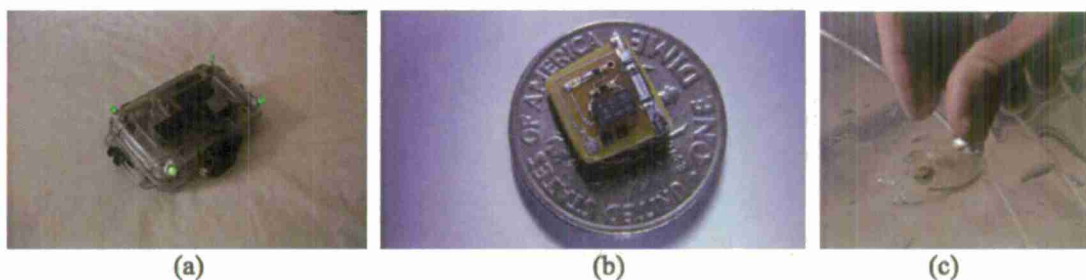


Figure 4. (a) The positioning beacon to be placed on the sea floor. (b) The LED tag to be fixed on the squid is shown on top of a dime to provide scale. The image in (c) shows a student affixing the tag to a squid.

#### *LED Tags*

A small tag built with battery, chip, and LED was designed and constructed. The LEDs were programmed to blink at frequency sufficient for tracking while maximizing battery duration. Fig. 4b shows the tag on a dime. Notably, this tag must be waterproofed before affixing it to the squid (Fig. 4c), thereby increasing its bulk.

#### *Software Development*

At the core of the software is an image-processing algorithm written in Matlab. The application uses blurring, blob tracking, Particle Filtering (PF), clustering, and camera calibration to best estimate the position of the squid in 3 dimensions.

#### *Data Acquisition*

The research team arrived in Oahu on June 20<sup>th</sup>, 2011 and left on June 29<sup>th</sup>, 2011. Attempts were made each night to find squid. Weather including wind and rain made it impossible to find squid on several nights, since such conditions stirred up shallow water and severely limited visibility below the surface. However, on those nights we were able to deploy the LED beacons and Table 1 provides an overview of data collected on a nightly basis.

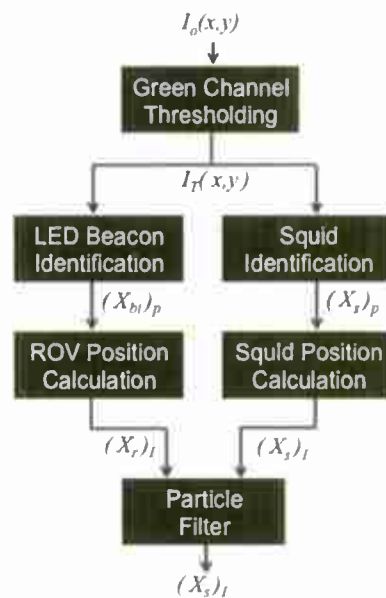


Figure 5. Block diagram illustrating the proposed flow of data through the image processing software. From an image  $I_0(x,y)$ , the absolute position of squid  $X_s$  is estimated.

Table 1: Data Collection Summary

| Date    | Location    | Conditions                  | Squid Observed /Video Data Collected |
|---------|-------------|-----------------------------|--------------------------------------|
| June 21 | Paiko Beach | Wind, waves, low visibility | No                                   |
| June 22 | "           | Wind, waves, low visibility | No                                   |
| June 23 | "           | Wind, waves, low visibility | No                                   |
| June 24 | "           | Clear conditions            | Yes/No Video                         |
| June 25 | "           | Clear conditions            | Yes                                  |
| June 26 | "           | Clear conditions            | Yes                                  |
| June 27 | "           | Clear conditions            | Yes                                  |
| June 28 | "           | Clear conditions            | Yes                                  |

Documented briefly are the results from tracking a simulated squid of known location in a swimming pool, and tracking an actual squid while it feeds in its natural environment.

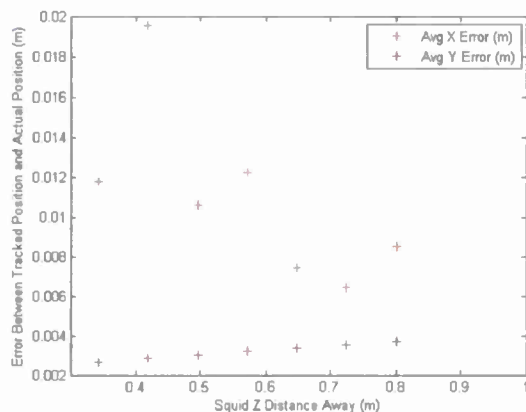
Fig. 5 shows the methodology used for image processing. Fig. 6 reveals some sample results from the simulated squid experiments that provide a measure of squid position estimation accuracy associated with the system developed. In Fig. 6a, an image of the simulated squid (green) as it is maneuvered over a grid with

known positions. The errors, i.e. difference between the actual positions of the simulated squid and those estimated using our camera/software system, are plotted in Figs. 6b and 6c. The results show centimeter accuracy in XY localization, with larger errors in range Z that grow with greater range. A new calibration routine is being explored to handle these errors.

(a)



(b)



(c)

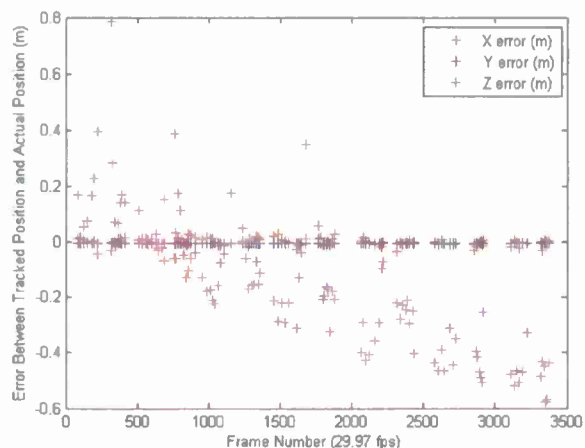


Figure 6. The squid object moved across a grid (a). (b) The difference between estimated and actual X,Y positions, i.e. errors on average as a function of range Z. (c) Error as a function of time.

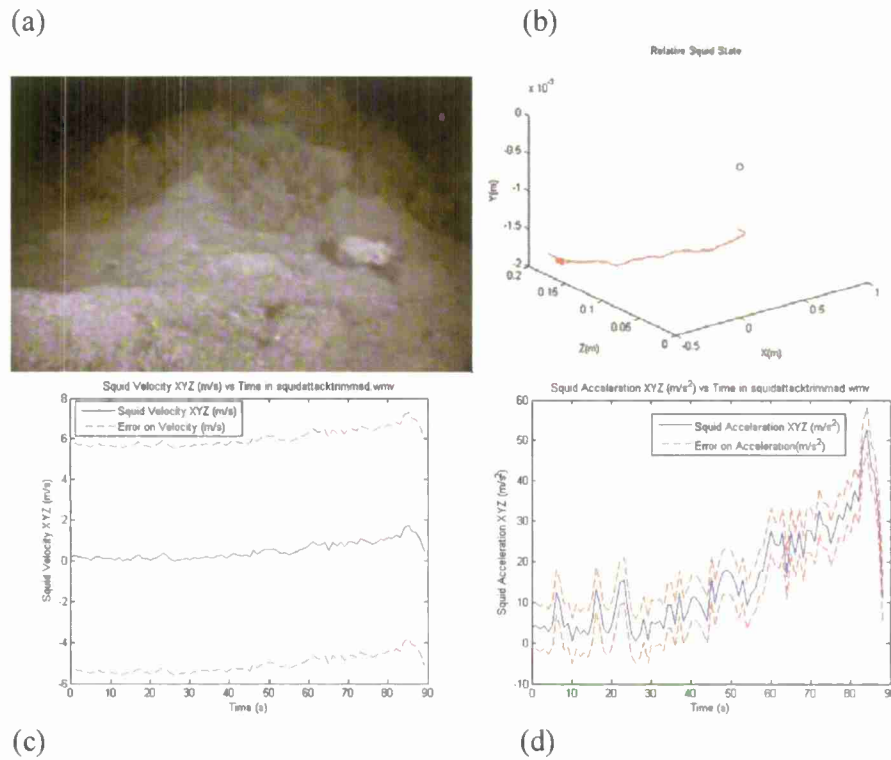


Figure 7. An image of the squid about to capture its prey is shown in (a). The path of this feeding is shown in (b), with associated plots of velocity and acceleration in (c) and (d) respectively.

In Fig 7, the tracking results from one experiment are shown for brevity. In Fig. 7a, an image of the squid about to capture its prey is shown. The red line in Fig. 7b illustrates the path of the squid en route to the capture. The velocity of the squid during this trajectory is shown in Fig. 7c. The acceleration is shown in Fig. 7d. Notably, until now, such state estimates of squid movement during such behaviors have never been calculated.



## 5. Future Work Planned

We plan to leverage our recent work that validates accurate squid state estimation in the X-Y plane, into improving estimation in range. To note, student Sam Yim continues to progress and improve the range estimation through better calibration and modification to the particle filter correction step. He plans to work on this until December of 2012. The algorithms that process images of squid for localization to the robot will be ported (ideally without much effort) to the task of localization of the beacons. Given that the beacons are at known locations within a global coordinate frame, the location of squid with respect to this frame can be estimated. Our future work will include determination of these global state estimates.

Contributions to the biological science side of this project will also be made in the future. There are several video clips of squid trajectories that have not been processed, for example, our footage of squid evading predation. Furthermore, the results of processing all videos of squid capturing prey could produce an idea of the distance traveled, duration, frequency, velocity, and acceleration of feeding trajectories. Furthermore, additional fieldwork could produce this data over an entire season, to determine long-term variations with weather and season. Ultimately, we envision the tools developed in this project to be applied to tracking and studying not just *Euprymna*, but also commercially important species of shrimp, squid, and fish.

We plan to present our findings at the OCEANS MTS/IEEE 2013 meeting in San Diego. We also expect to use our findings to support the re-submission of our proposal entitled "IDBR - Development of an Autonomous Hybrid ROV for Biological Sampling" to NSF.

## 6. References cited

- [1] Wikelski, M. et al. 2007. Going wild: what a global small-animal tracking system could do for experimental biologists. *J. Exp. Biol.* 210: 181-186
- [2] Steig, T.W. and C.H. Greene. 2006. Ocean Sciences Meeting. Personal communication.
- [3] Ruby, E.G. 1999. The *Euprymna scolopes-Vibrio fischeri* symbiosis: a biomedical model for the study of bacterial colonization of animal tissue. *J. Mol. Microbiol. Biotechnol.* 1:3-21
- [4] Singley, C. T. 1983. *Euprymna scolopes*, Cephalopod Life Cycles. 1:69-74. London: Academic Press.
- [5] Hanlon, R.T. et al. 1997. Laboratory culture of the sepiolid squid *Euprymna scolopes*: A model system for bacteria- animal symbiosis. *Biol. Bull.* 192: 364-374
- [6] Nyholm, S. V. and M. J. McFall-Ngai. 2004. The Winnowing: Establishing the Squid-Vibrio Symbiosis. *Nat. Rev. Microbiol.*, 2:632-42, 2004
- [7] Graf, J., and Ruby, E.G. 1998. Host-derived amino acids support the proliferation of symbiotic bacteria. *Proc. Natl. Acad. Sci. USA.* 95: 1818-1822

- [8] Visick, K.L. et al. 2000. *Vibrio fischeri lux* genes play an important role in colonization and development of the host light organ, J. Bacteriol, 182:4578-4586
- [9] Harper, R.D., and J.F. Case. 1999. Counterillumination and its anti-predatory value in the plainfin midshipman fish *Porichthys notatus*. Mar. Biol. 134:529-540
- [10] Jones, B.W., and M.K. Nishiguchi. 2004. Counterillumination in the Hawaiian bobtail squid, *Euprymna scolopes* Berry (Mollusca: Cephalopoda). Mar. Biol. 144:1151-1155
- [11] Electronic Tagging of Marine Animals," Publication of The Scientific Committee on Oceanic Research, [http://www.scor-int.org/Tech\\_Panel/SCOR-tagging.pdf](http://www.scor-int.org/Tech_Panel/SCOR-tagging.pdf)
- [12] Lanbo, L. et al. 2008. Prospects and Problems of Wireless Communication for Underwater Sensor Networks. Wireless Communications & Mobile Computing. 8: 977-994
- [13] Advanced Telemetry Systems, ATS Acoustic Micro Transmitter, <http://atstrack.com/pdfs/jsats.pdf>
- [14] Vemco, V6 Coded Transmitter, <http://www.vemco.com/pdf/v6coded.pdf>
- [15] Hydroacoustic Technology Inc., Model 795-Series A Acoustic Tags [http://www.htisonar.com/spec\\_sheets/M795\\_Acoustic\\_Tag\\_Specs\\_2010.pdf](http://www.htisonar.com/spec_sheets/M795_Acoustic_Tag_Specs_2010.pdf)
- [16] Bernardez, C. et al. 2003. Movements of juvenile and adult spidercrab (*Maja squinado*) in the Ría da Coruña (N-WSpain), Aquatic telemetry: advances and applications. Proceedings of the Fifth Conference on Fish Telemetry held in Europe. Ustica, Italy, 9-13 June 2003

## **Materials and Methods of Interconnections in LED Packaging**

Principal Investigator:

**John Pan, Ph.D. Industrial & Manufacturing Engineering**

California Polytechnic State University  
San Luis Obispo, CA

## 1. Abstract

Light-Emitting Diode (LED) lighting has potential to fundamentally alter lighting by replacing incandescent and fluorescent technologies because it offers significant energy saving, longer operational life, mercury-free materials, and many other advantages. Excellent thermal management and low-cost is vital for LED lighting to become the market standard for general lighting. The packaged LED is typically soldered to the metal-core printed circuit board (MCPCB). However, as the size of the packaged LED increases, voiding in solder joints becomes a major problem since voiding increases the thermal resistance. The research questions are: what is the effect of flux in solder paste and size of the package LED on the voiding? What is the relationship between the voiding and the thermal performance of the LED? In this study, a total of 72 packaged LEDs with three different sizes were assembled to MCPCBs using solder paste with two different types of fluxes. The voiding in solder joints was checked by X-Ray. The detailed void characteristics were analyzed. Each LED was calibrated and the k-factor was determined based on the diode's forward voltage junction temperature measurement method. Each LED's junction temperature was measured at the 350 mA and 680 mA current level. The relationship between the junction temperature and the void characteristics was established. The results show that flux in solder paste has significant effect on the voiding. There is 5% less voiding in solder joint on average when M500 flux was used compared to when M406 flux was used. The LED size has significant effect on the voiding as well. There is less voiding in the solder joint when the LED is smaller. As the size of LED increase to a certain level, the percentage of voiding to total area ratio won't increase, but the small voids will combine together into larger voids, which may be a concern for thermal performance since it could produce local overheating. The results indicate is that when the voiding percentage is less than 25%, the effect of voiding on the thermal performance is insignificance; when the voiding percentage is over 25%, there is weak positive correlation between the voiding and the thermal performance. Further study is needed to find out the effect of voiding that is over 50% of total area on the thermal performance of LED; to repeat this experiment with higher accuracy measurement equipment, to conduct thermal modeling of the voiding effect, and to investigate the effect of voiding on the transient junction temperature of LEDs.

## 2. Project significance

Thermal management is critical to LED packaging since the junction temperature of an LED strongly affects the reliability, energy efficiency, and color quality of the LED. Thus, proper thermal management is critical to achieving reliable, high light output, and consistent color quality LED luminaires.

The packaged LED is typically soldered to the metal-core printed circuit board (MCPCB). However, as the size of the packaged LED increases, voiding in solder joints becomes a major problem since voiding increases the thermal resistance. Thus, it is important to understand the effect of voiding on the thermal performance of LEDs. However, no study has been published on the relationship between the voiding in solder joints and the thermal performance of a LED.

The objective of this study is to answer the following research questions:

- 1) What is the effect of flux in solder paste and size of the package LED on the voiding?
- 2) What is the relationship between the voiding and the thermal performance of the LED?

The results of this study will be very useful for LED manufacturers to control the LED assembly quality.

### **3. Background/prior work**

The current standard lighting technologies are incandescent and fluorescent. However, both technologies have major drawbacks. The incandescent lighting is not energy efficient as evidenced by the fact that only 8% of the electrical energy is converted to lighting [1]. This inefficient lighting has led many nations to phase out the use of incandescent light bulbs by 2012 [2]. The main disadvantage of the fluorescent technology is that the fluorescent bulb contains mercury, a toxic material.

Light-Emitting Diode (LED) lighting has potential to fundamentally alter lighting in the future by replacing incandescent and fluorescent technologies because it offers significant energy saving, longer operational life, smaller package size, mercury-free materials, and many other advantages. The US Department of Energy (DOE) estimated that if just twelve niche markets such as traffic signals and retail displays switched to LEDs overnight, energy savings would be 180 TWh [3], or \$20 billion in electricity annually. Many LED lighting packages are rated for 60,000 hours of use, which is 6.8 years of continuous lighting, or 3 to 6 times more than a conventional fluorescent bulb.

Low-power LEDs have existed for several decades but the use of high-power high-brightness LEDs for general lighting is still relatively new. Excellent thermal management and low-cost is vital for LED lighting to become the mainstream for general lighting. The LED source could convert 50% energy into visible light theoretically. But at the current technological level, only about 15% - 25% of the electrical energy is converted into visible light and the remaining 75% - 85% energy is converted to heat [1]. If the heat in LED package is not dissipated quickly, the high junction temperature in the LED die will significantly decrease the operational life of the LED and affect LED performance such as reduction in light output (lumen per watt) and color shifting due to emitting different wavelengths of the light. Thus, good thermal management is critical to ensuring that high energy-efficient (lumen per watt), consistent color quality, and long life of LEDs are achievable. Cost is another issue. A LED bulb such as PAR-38 or MR-16 costs from \$40 to \$120 each compared with less than \$1 for an incandescent bulb.

Thermal management is critical to LED packaging. Firstly, the reliability or the operational life of a LED is mainly dominated by the junction temperature [4-5]. Figure 1 shows the useful life of two identical LEDs operated at the same current but with different junction temperatures. It shows the useful life as defined as 70% lumen maintenance decreased from about 37,000 hours to about 16,000 hours when the junction



temperature is 11°C higher. Secondly, high junction temperature can cause a reduction in energy efficiency in lumens per watt by 20 or 30% [6]. Thirdly, the color quality of an LED is directly dependent on the junction temperature [4, 7]. Thus, proper thermal management is critical to achieving reliable, high light output, and consistent color quality LED luminaires.

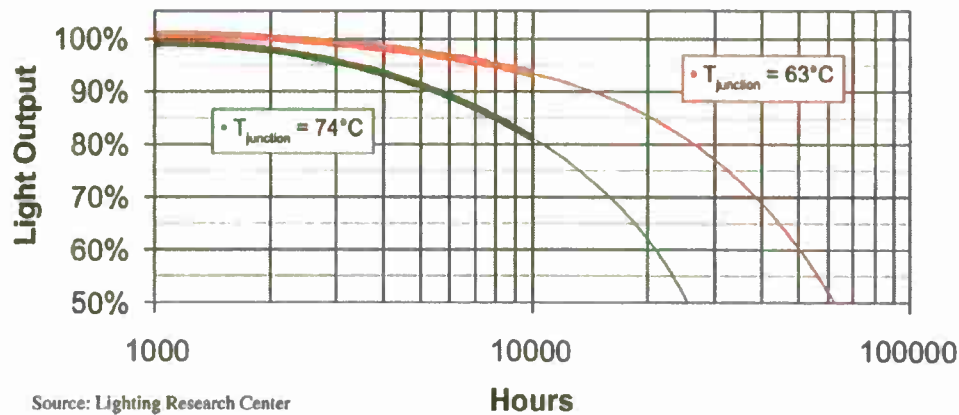


Figure 1. Useful life of LEDs at different junction temperatures

Some research has been done in LED thermal management. For example, Luo, et al. [8] analyzed thermal performance of an 80W Light-Emitting Diode Street Lamp. Jang and Shin [9] presented a thermal analysis of LED arrays for automotive headlamps. Chen et al. [10] presented a package design of high-power LEDs. However, no research has been done on the effect of materials and methods of interconnections on the thermal performance of LED luminaires.

The key in LED thermal management is to reduce the thermal resistance between the LED die and the ambient. The bottlenecks of the thermal path between the LED die and the ambient are three interconnections in LED packaging: LED die to package, the packaged LED to a MCPCB, and the MCPCB to the heat sink. The LED die is typically attached to the package substrate through a soldering process or a flip-chip process. The packaged LED is typically soldered to the MCPCB. The MCPCB is then mechanically attached to a heat sink using one or more screws. There is voiding in solder joints in level 1 and level 2 interconnections, which increases the thermal resistance. In this study, the focus is on the interconnections between the packaged LED and the MCPCB. As the size of the packaged LED increases, voiding in solder joints becomes a major problem. The research questions are: what is the effect of flux in solder paste and size of the package LED on the voiding? What is the relationship between the voiding and the thermal performance of the LED?

The key to lower the junction temperature of an LED is to reduce the thermal resistance between the LED die and the ambient. There are three levels of thermal interconnections in a typical LED lighting system as shown in Figure 2: LED die to package (level 1), the packaged LED to a metal-core printed circuit board (MCPCB) (level 2), and the MCPCB to the heat sink (level 3). The 2<sup>nd</sup> level interconnection is typically achieved using a lead-

free solder and the 3<sup>rd</sup> level interconnection is done using one or more screws. Figure 3 shows a similar structure.

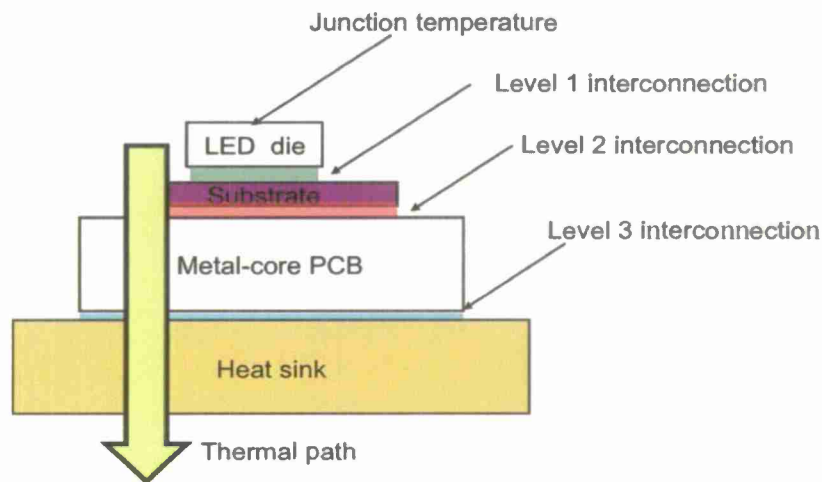


Figure 2. A schematic of interconnections and thermal paths in a typical LED system

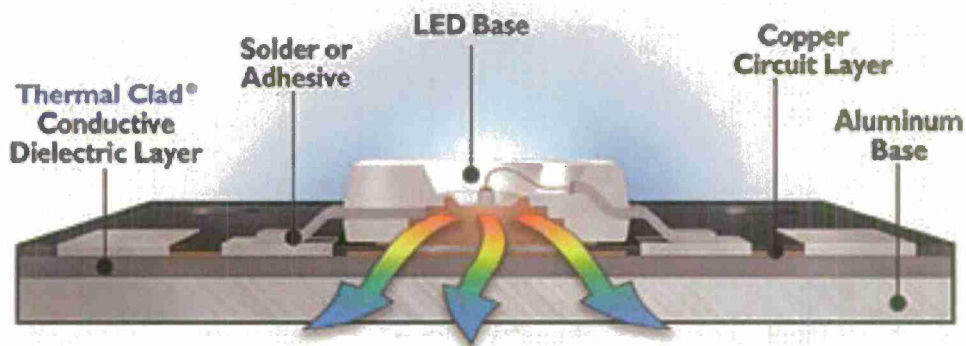


Figure 3. A schematic of the thermal path in a typical LED system [11]

In order to characterize thermal performance of an LED, it is important to be able to measure the junction temperature of the LED. There are several measurement methods reported, but no standard exists for LED testing [4]. Table 1 summarizes four methods for measuring junction temperature.

Table 1. Summary of Junction Temperature Measurement Methods

| Method                      | Accuracy            | Comments   | References      |
|-----------------------------|---------------------|--|-----------------|
| Forward Voltage             | +/- 3°C             | <ul style="list-style-type: none"> <li>• The most widely used method in industry</li> <li>• Requires a long process of calibration</li> </ul>                                | [4, 7, 12, 16]  |
| IR Thermography             | Depends on package  | <ul style="list-style-type: none"> <li>• Easy to operate</li> <li>• Sensitive to the material emissivity</li> <li>• Difficult to measure IR-transparent materials</li> </ul> | [4, 12]         |
| Spectral-based              | +/- 25°C            | <ul style="list-style-type: none"> <li>• Sensitive to temperature</li> <li>• Low accuracy</li> </ul>   | [4, 13, 15, 16] |
| Liquid Crystal Thermography | Depends on crystals | <ul style="list-style-type: none"> <li>• Maximum surface temperature used to approximate the junction temperature</li> </ul>   | [14]            |

Among these four methods, the forward voltage method is the most widely used. The method is based on the Shockley ideal diode equation. There is a linear relationship between the changes in junction temperature of a diode and the changes in forward voltage. When a constant current at low level is applied to a diode, the forward voltage across the diode will decrease or increase at a constant rate as the junction temperature is increased or decreased. The slope of the linear relationship between the forward voltage and the junction temperature at a given current level is called k-factor, typically measured in mV/°C.

It is important to note that the measurement current ( $I_m$ ) must be small enough not to cause significant self-heating by the LED and large enough to obtain a reliable forward voltage reading [17]. If the measurement current is too small, the difference among forward voltage changes could be in the voltage measurement error, and the forward voltage reading could also be affected by surface leakage of the LED [17]. A typical measurement current is in 1 mA.

The relationship can be determined by k-factor calibration as described in Equation 1.

(1)

where  $\Delta V_f$  is the changes in forward voltage and  $\Delta T_j$  is the changes in junction temperature. The calibration procedures are as follows: 1) place an LED in an oven at a fixed temperature and wait for the LED to reach the equilibrium temperature at the set temperature. Apply a measurement current  $I_M$  and measure the voltage across the LED; 2) Adjust the oven temperature and repeat step 1). The temperature and forward voltage across the LED is measured and recorded. Though a “two-temperature point” is enough for determining the K-factor, a common practice is to set 4 to 6 different temperatures and measure the resulting forward voltage to minimize temperature and voltage measurement errors.

The junction temperature of an LED can be calculated using Equation 2.

$$T_j = T_{ref} + R_{j-ref} P \quad (2)$$

where

$T_j$ : Junction temperature of a LED, in °C

$T_{ref}$ : Reference temperature, in °C

$R_{j-ref}$ : thermal resistance from the junction of an LED to the reference environment, in °C/W

$P$ : power dissipated in the LED, in W

Thus, to decrease the junction temperature of an LED, it can be achieved by reducing the LED's surrounding ambient temperature, the power dissipated by the LED, and the thermal resistance between the LED junction and the surrounding ambient. Since the power dissipated by the LED and the surrounding ambient temperature are typically unable to be reduced, it is clear that the best way to reduce the junction temperature of the LED is to reduce the thermal resistance between the junction of the LED and the reference environment.

#### 4. Discussion of Results

The objective of this study is to investigate the effect of flux in solder paste and size of the package LED on the voiding and find out the relationship between the voiding and the thermal performance of the LED. A two-factor factorial experimental design was selected. The input variables are the flux types and the size of the LED. Table 1 lists the two flux types and three different sizes of LED.

##### 4.1 Experimental Design

The solder paste used in this study was lead-free solder SAC305 (Sn96.5Ag3.0Cu0.5). There are two types of flux, S3X58-M406, an anti-pillow-defect solder paste, and S3X58-M500, a low-void and anti-pillow-defect solder paste, both from the Koki Company.

The three LEDs used in this study were Cree's XLamp XP-E, XLamp MT-G EasyWhite, and XLamp MP-L EasyWhite. The size of XP-E is 3.45 x 3.45 mm; the size of MT-G is 8.90 x 8.90 mm; and the size of MP-L is 12.15 x 13.15 mm. Figure 4 shows these three LEDs.

Table 1. Experiment Matrix

| Factors  | Levels                       |                               |                                |
|----------|------------------------------|-------------------------------|--------------------------------|
| Flux     | Traditional (S3X58-M406)     |                               | Low-void (S3X58-M500)          |
| LED Size | Small (XP-E), 3.45 x 3.45 mm | Medium (MT-G), 8.90 x 8.90 mm | Large (MP-L), 12.15 x 13.15 mm |

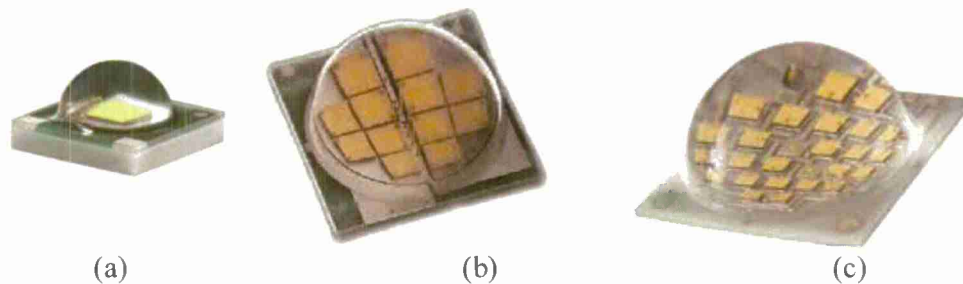


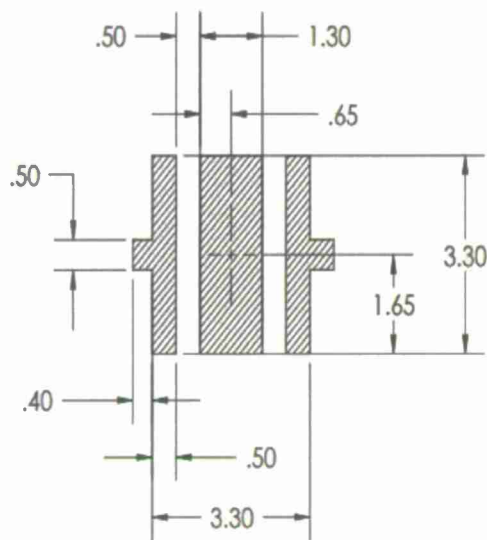
Figure 4. LEDs used in this study (a) Cree's XLamp XP-E, (b) Cree's XLamp MT-G EasyWhite, (c) Cree's XLamp MP-L EasyWhite

#### 4.2 Process Development

The voiding in solder joint is not only influenced by the flux of solder paste, but also affected by the stencil design, reflow profile, and the metallization of the substrate and the component. Thus, the stencil pattern should be carefully designed and the reflow profile should be carefully developed.

In this study, a 5 mil (1.25 mm) thick, laser-cut, stainless steel stencil was used. Cree recommended stencil pattern design for XP-E is shown in Figure 5 and for MT-G is shown in Figure 6. In this study, stencil design for XP-E is a 2 x 5 array with 18 mils x 18 mils square aperture openings. Stencil design for MT-G is an array with a diameter of 30 mils aperture openings. The MCPCBs with printed solder paste using stencil designed for this study are shown in Figure 7. The purpose of these designs is to minimize the voiding formed during the reflow process. The voids are formed by gasses created from the flux reaction with the solder paste particles during the reflow process. Due to the geometry of the component solder joint, these voids are not completely removed from the solder joint during the reflow process. The stencil design for MP-L is a 7 x 7 array with a diameter of 50 mils aperture openings. The MCPCBs with LEDs placed are shown in Figure 8.





RECOMMENDED PCB SOLDER PAD

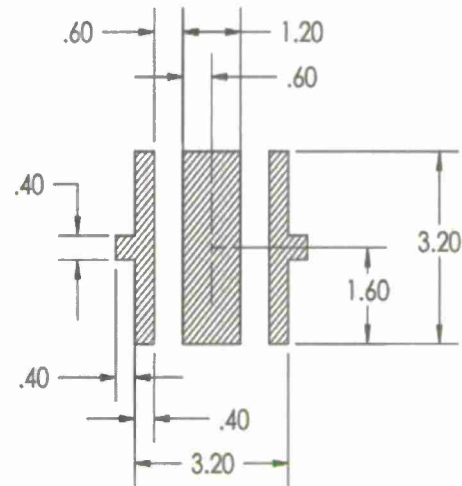
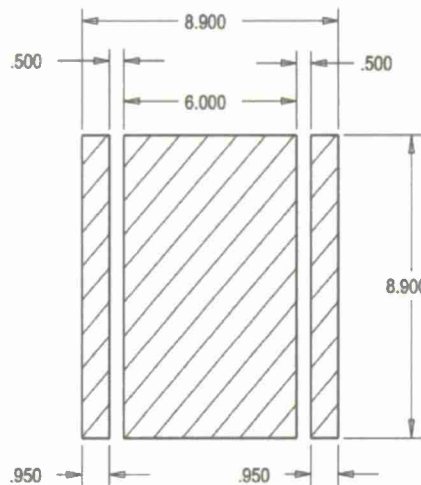
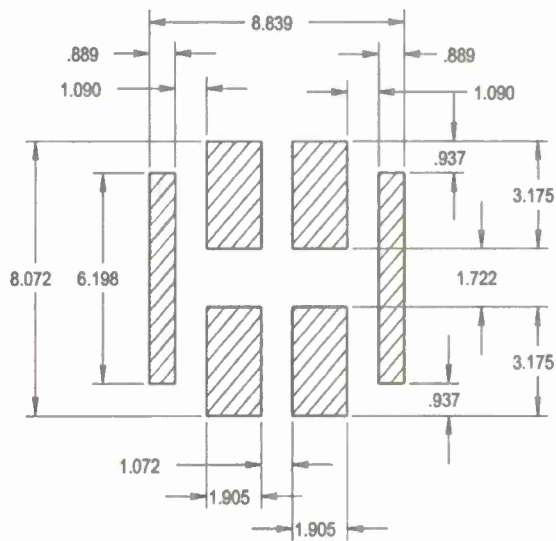
RECOMMENDED STENCIL PATTERN  
(HATCHED AREA IS OPENING)

Figure 5. Cree recommended stencil pattern design for XP-E.



RECOMMENDED PC BOARD SOLDER PAD



RECOMMENDED STENCIL PATTERN

Figure 6. Cree recommended stencil pattern design for MT-G.

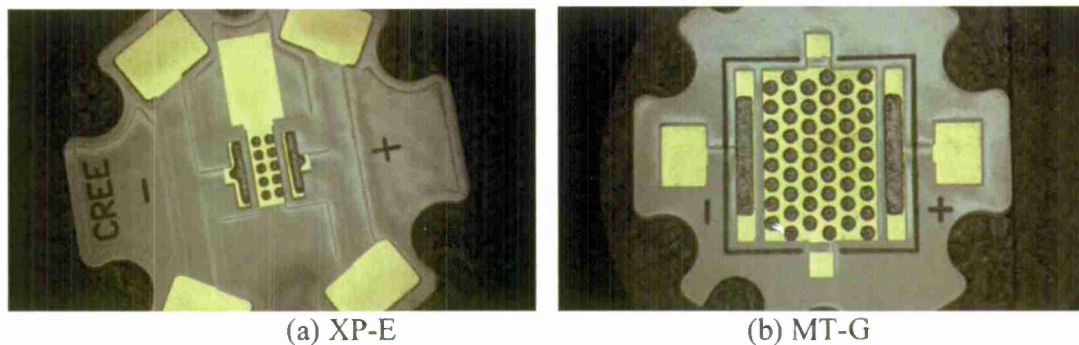


Figure 7. MCPCB with printed solder paste with stencil designed for this study

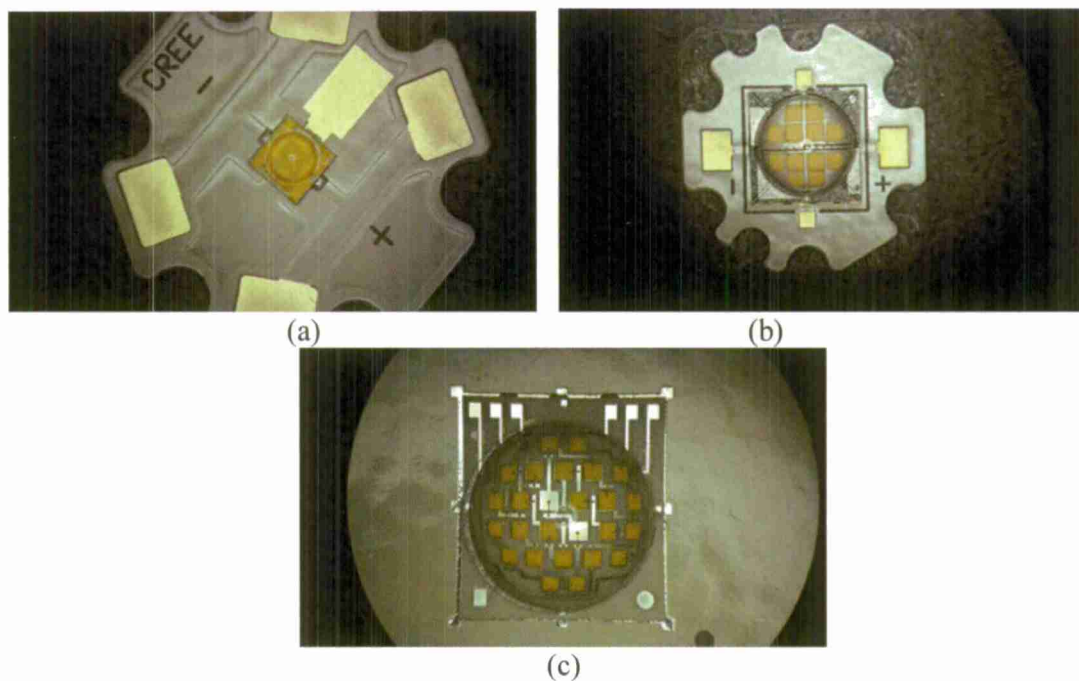


Figure 8. MCPCB with LED placed. (a) XP-E, (b) MT-G, (c) MP-L

Reflow profile has significant effect in controlling voiding as well. After reviewing the solder paste supplier recommendations, the desired characteristics of the reflow profile are summarized in Table 2. Figure 9 shows the recommended reflow profiles for two solder pastes. A Heller 5-zone reflow oven 1500EXLMS was used in this study. Figure 10 shows the developed reflow profiles for the three LEDs.

Table 2. Desired Characteristics of the Reflow Profile

| Reflow Profile Parameters                  | Desired range   | Target value |
|--|-----------------|--------------|
| Peak temperature                           | 230 °C ~ 250 °C | 240 °C       |
| Time above liquidus (217 °C)               | 60 ~ 90 sec.    | 75 sec.      |
| Duration at soak zone (150 °C ~ 217 °C)    | 120 ~ 180 sec.  | 150 sec.     |
| Duration at ramp-up zone (110 °C ~ 190 °C) | 90 ~ 120 sec.   |              |
| Maximum ramp-up rate                       | < 3°C/sec.      |              |

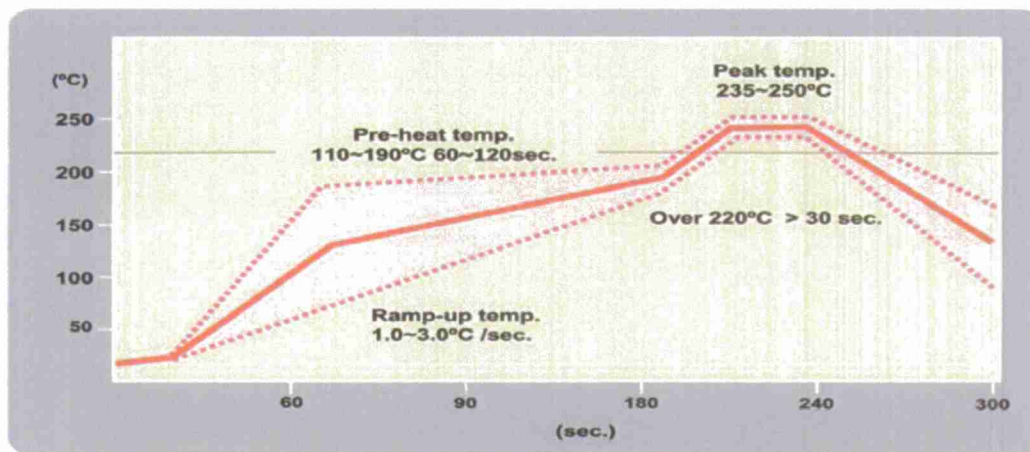
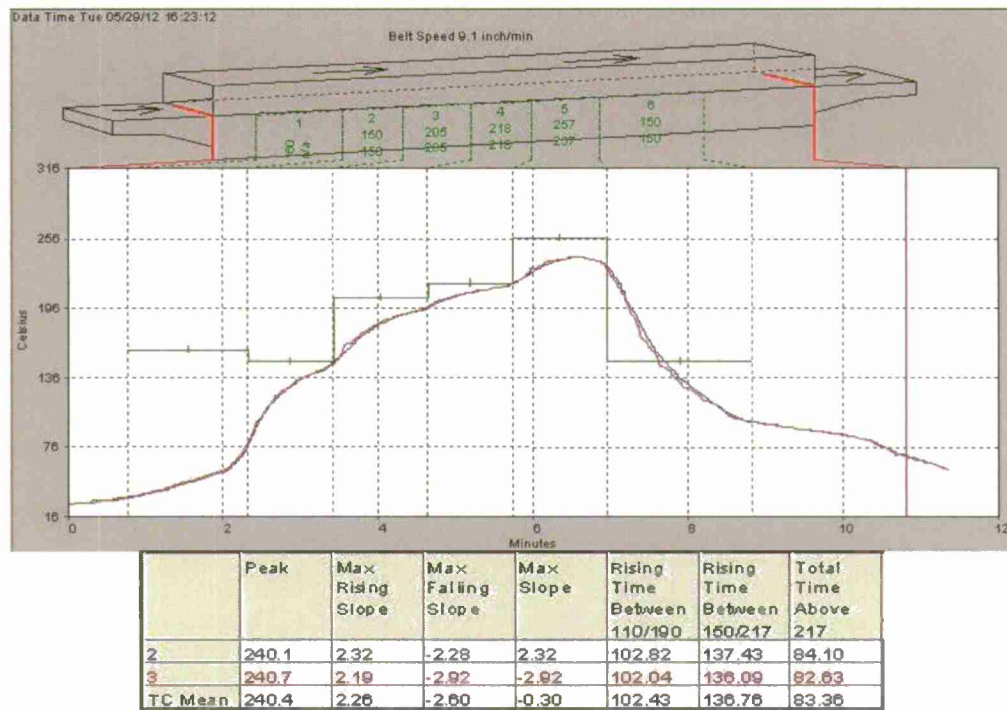


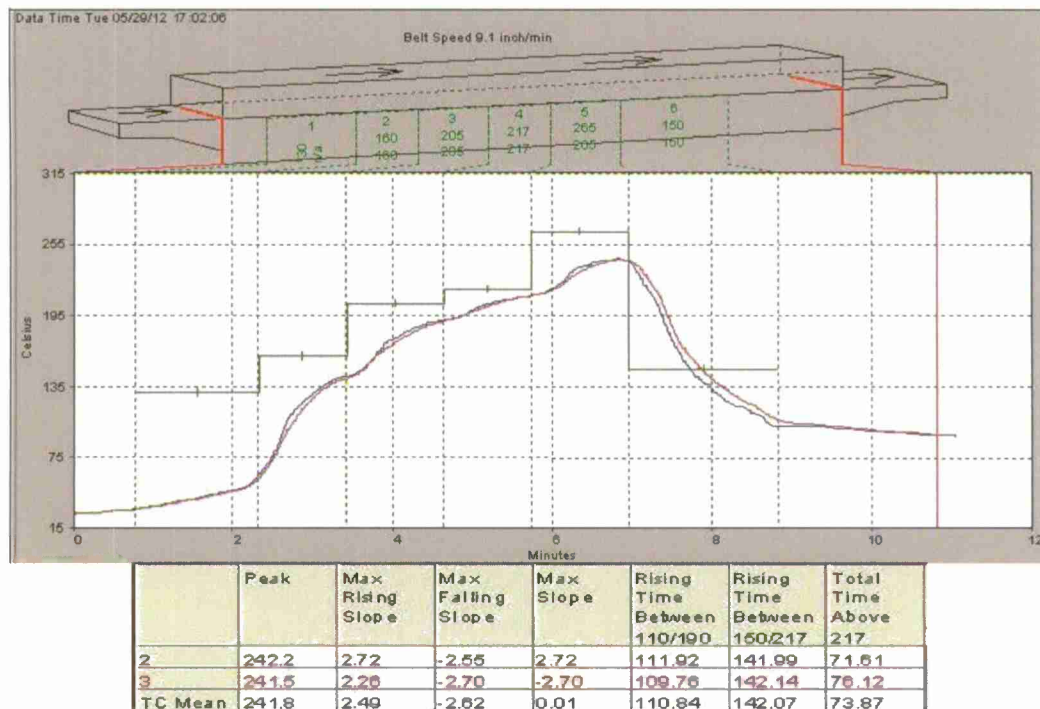
Figure 9. Recommended Reflow Profile for both Koki S3X58-M406 and S3X58-M500 solder pastes.



(a) Reflow Profile for Cree XLamp XP-E



(b) Reflow Profile Cree XLamp MT-G EasyWhite



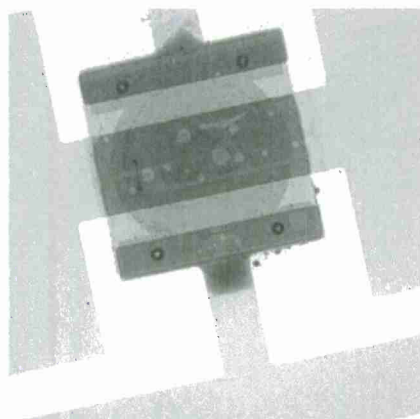
(c) Reflow Profile for Cree XLamp MP-L

Figure 10. Developed Reflow Profiles (a) XP-E, (b) MT-G, (c) MP-L

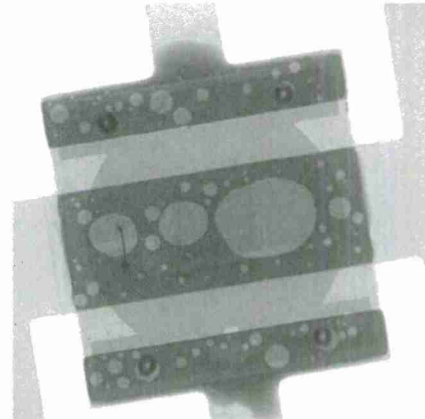


#### 4.3 Void Measurement and Analysis

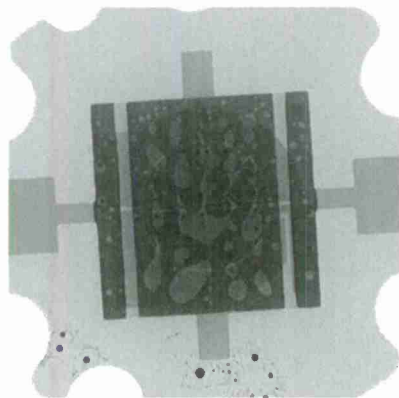
The voiding in every solder joint was checked by X-Ray. Figure 11 shows some examples of low voiding and high voiding images. The detailed voids characteristics were analyzed using software ImageJ. The characteristics include total void to total area ratio, percentage of voids with size over 2% of the total area to total area ratio, percentage of voids with size between 1% and 2% of the total area to total area ratio, and percentage of voids with size between 0.1% and 1% of the total area to total area ratio.



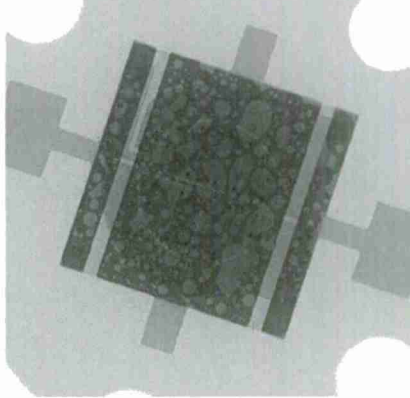
(a) XP-E low voiding (5%) (M500-14)



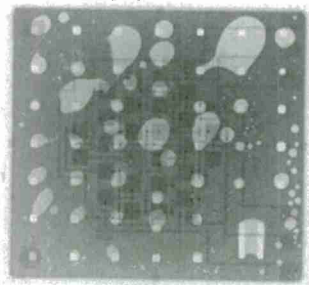
(b) XP-E high voiding (27%)(M406-31)



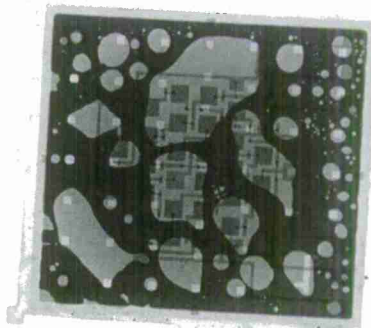
(c) MT-G low voiding (19%) (M500-3)



(d) MT-G high voiding (44%) (M406-36)



(e) MP-L low voiding (19%) (M406-1)



(f) MP-L high voiding (40%) (M406-34)

Figure 11. Examples of voiding in solder joints



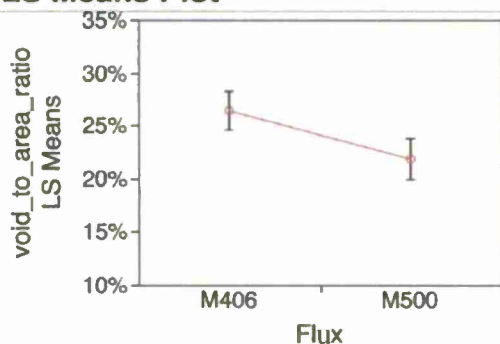
Table 3 summarizes the average void to area ratio. Figure 12 shows the least-square means plot for the effect of flux and effect of LED size on the void to area ratio. It is clear that there is 5% less voiding in solder joint on average when M500 flux was used compared to when M406 flux was used.

LED size has significant effect on the voiding as well. There is less voiding in the solder joint when the LED is smaller, such as in the XP-E case. When the size of LED reaches a certain level, the percentage of voiding to total area ratio won't increase. However, as the LED size increases, the small voids will combine together into larger voids as shown in Figure 11 (f). The larger void could be a concern for thermal performance since it could produce local overheating.

Table 3. Average void to area ratio

| LED Type/Size | Flux | % of void to total area ratio | % of voids with size over 2% of total area to total area ratio | % of voids with size between 1% ~ 2% of total area to total area ratio | % of voids with size between 0.1% ~ 1% of total area to total area ratio |
|---------------|------|-------------------------------|--|--|--|
| MP-L (Large)  | M406 | 26.5%                         | 6.5%   | 6.0%   | 11.6%  |
| MP-L (Large)  | M500 | 23.9%                         | 5.5%   | 4.4%   | 11.9%  |
| MT-G (Medium) | M406 | 33.0%                         | 7.3%   | 4.1%   | 13.9%  |
| MT-G (Medium) | M500 | 27.2%                         | 3.1%   | 3.2%   | 13.1%  |
| XP-E (Small)  | M406 | 19.7%                         | 7.6%   | 2.8%   | 6.5%   |
| XP-E (Small)  | M500 | 14.7%                         | 5.2%   | 2.2%   | 5.6%   |

LS Means Plot



LS Means Plot

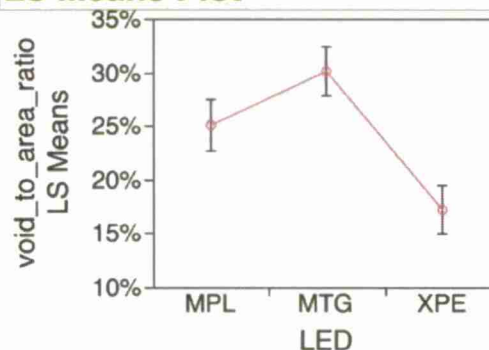


Figure 12. Effect of Flux and LED size on the void-to-area ratio

#### 4.4 LED K-factor Calibration

In order to measure the junction temperature of a LED using the forward voltage method, the K-factor for each LED must be calibrated first. The equipment used in this calibration includes a breadboard, programmable DC power supply (TENMA 72-6630), Omega thermocouple data logger (HH147U), Fluke 117 true RMS multi-meter, Type K thermocouple, 150K Ohm resistors, and an oven.

The calibration circuit schematic is shown in Figure 13 and the equipment setup is shown in Figure 14. As described in Section 3, the measurement current ( $I_m$ ) must be small enough not to cause significant self-heating by the LED and large enough to obtain a reliable forward voltage reading. In this study, 150K $\Omega$  resistor is fixed in the calibration circuit and 15 V was used for XP-E LED and MT-G LED and 25 V was used for MP-L LED. The threshold voltage for XP-E, MT-G, and MP-L is 2.4 V, 4.55 V, and 19 V, respectively. Thus, the resulting current for XP-E was 84  $\mu$ A, for MT-G was 70  $\mu$ A, and for MP-L was about 40  $\mu$ A.

To get the accurate K-factor, both temperature and voltage measurement must be accurate. In this study, we placed 3 T-type thermocouples (about 1°C accuracy) inside the oven to monitor the temperature; one near the LED, one on the top of the MCPCB, and the third on the bottom of the MCPCB directly below the LED. The voltage measurement has an accuracy of 1 mV.

The K-factor calibration procedures are as follows:

- 1) Set up circuit as shown in Figures 13 & 14;
- 2) At room temperature, record temperature and LED forward voltage;
- 3) Increase oven temperature by 20°C and wait at least 15 minutes or as long as it takes for the thermocouples on the top and bottom of the LED to be within 1°C for five minutes; Take a measurement and record both temperature and voltage;
- 4) Repeat step 3 until 5 data points are taken or the temperature reaches about 110°C.

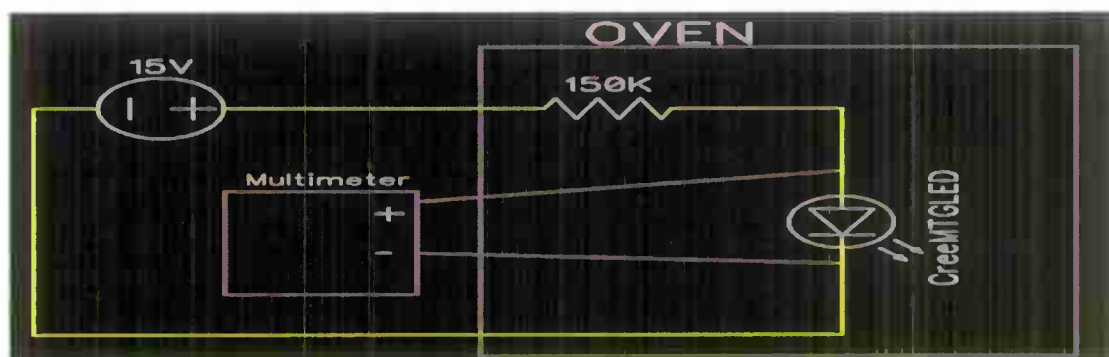


Figure 13. Calibration circuit schematic

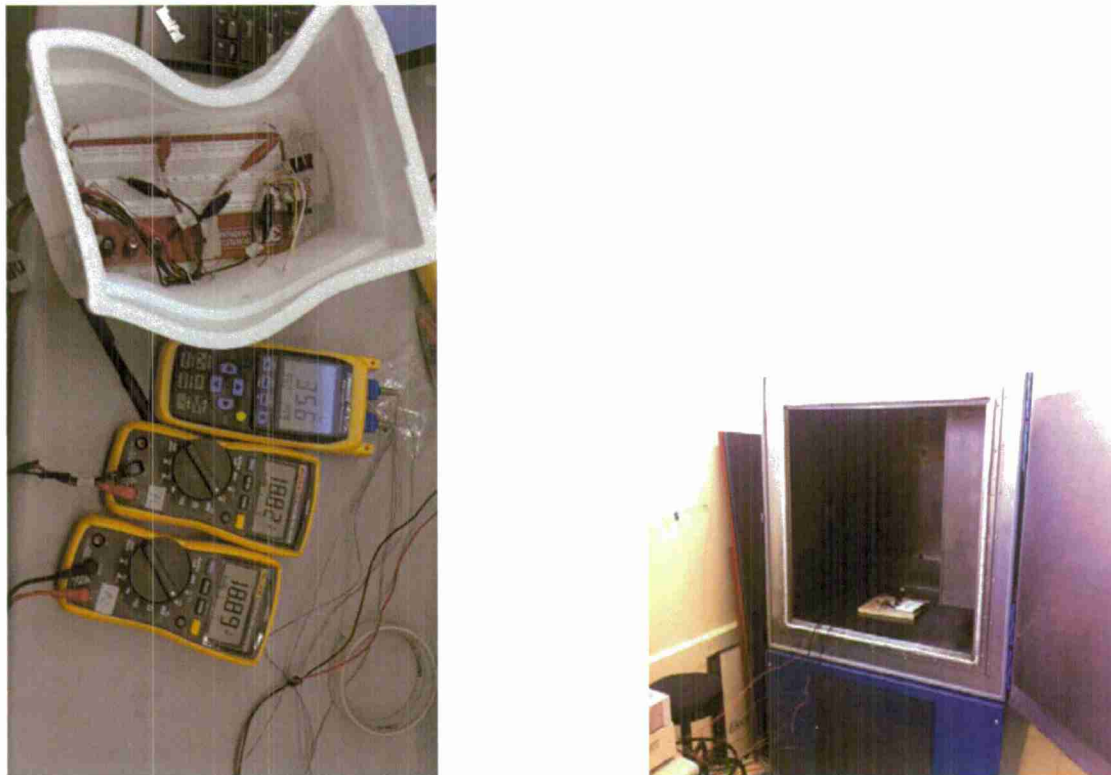


Figure 14. Equipment setup for K-factor calibration

An example of data recording is shown in Table 4. An example of K-factor calculation is shown in Figure 15. The summary of k factor calibration results is shown in Tables 5 to 9. Since both the ratio of the standard deviation to the average of both XP-E and MT-G LEDs are over 3%, according to EIA/JEDEC standard 51-1 [17], the K-factor of each LED needs to be calibrated individually.

Table 4. An example of data recorded in the LED K-factor calibration

| Time of cal | Date of cal | LED  | Flux | Assembly | LED Number | K (mV/°C) | Vsource (V) | V <sub>f</sub> (V) | I <sub>f</sub> forward (μA) | Femp. Interval (°C) | T <sub>com of MCP</sub> (°C) | T <sub>2(ambient)</sub> (°C) | LED Voltage (V) |
|-------------|-------------|------|------|----------|------------|-----------|-------------|--------------------|-----------------------------|---------------------|------------------------------|------------------------------|-----------------|
| 6pm         | 7/5/12      | MT-G | MS00 | 2        | LED 2-500  | -4.96     | 15          | 4.55               | 70                          | 30                  | 27.8                         | 27.5                         | 4.463           |
|             |             |      |      |          |            |           |             |                    |                             | 50                  | 47                           | 47                           | 4.376           |
|             |             |      |      |          |            |           |             |                    |                             | 70                  | 65.1                         | 65.3                         | 4.287           |
|             |             |      |      |          |            |           |             |                    |                             | 90                  | 84.7                         | 84.7                         | 4.188           |
|             |             |      |      |          |            |           |             |                    |                             | 110                 | 102.2                        | 102.3                        | 4.094           |

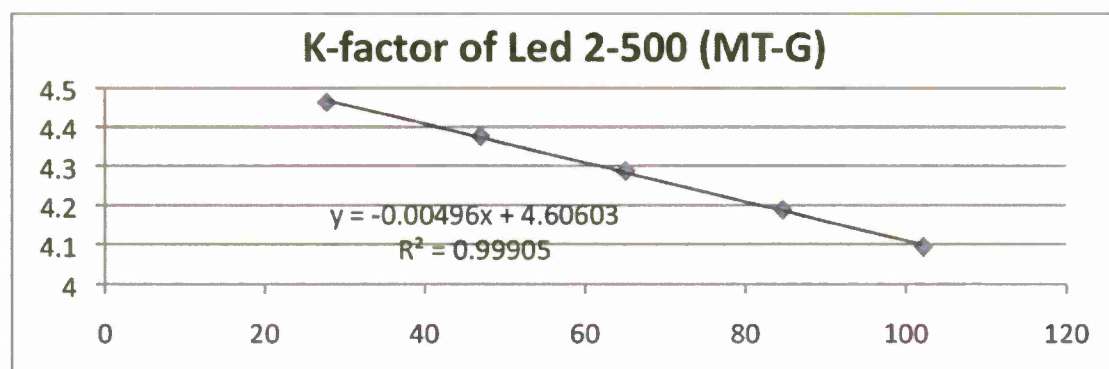


Figure 15. An Example of K-factor calculation

Table 5. Summary of K-factor calibration results for XP-E LED when  $I_m$  at 84  $\mu A$ .

| LED                | Flux | Assembly sequence | LED Number | K (mV/ $^{\circ}C$ ) | V <sub>source</sub> (V) | V <sub>f</sub> (V) | I <sub>forward</sub> ( $\mu A$ ) |
|--------------------|------|-------------------|------------|----------------------|-------------------------|--------------------|----------------------------------|
| XP-E               | M500 | 6                 | LED 6-500  | -1.86                | 15                      | 2.4                | 84                               |
| XP-E               | M500 | 31                | LED 31-500 | -2.13                | 15                      | 2.4                | 84                               |
| XP-E               | M406 | 19                | LED 19-406 | -1.58                | 15                      | 2.4                | 84                               |
| XP-E               | M406 | 28                | LED 28-406 | -1.58                | 15                      | 2.4                | 84                               |
| XP-E               | M406 | 33                | LED 33-406 | -1.48                | 15                      | 2.4                | 84                               |
| XP-E               | M406 | 31                | LED 31-406 | -1.59                | 15                      | 2.4                | 84                               |
| XP-E               | M406 | 18                | LED 18-406 | -1.61                | 15                      | 2.4                | 84                               |
| XP-E               | M406 | 9                 | LED 9-406  | -1.65                | 15                      | 2.4                | 84                               |
| XP-E               | M406 | 22                | LED 22-406 | -1.62                | 15                      | 2.4                | 84                               |
| XP-E               | M406 | 23                | LED 22-406 | -1.6                 | 15                      | 2.4                | 84                               |
| Average            |      |                   |            | -1.67                |                         |                    |                                  |
| Standard deviation |      |                   |            | 0.19                 |                         |                    |                                  |

Table 6. Summary of K-factor calibration results for MT-G LED when  $I_m$  at 70  $\mu A$ .

| LED                | Flux | Assembly sequence | LED Number | K (mV/ $^{\circ}C$ ) | V <sub>source</sub> (V) | V <sub>f</sub> (V) | I <sub>forward</sub> ( $\mu A$ ) |
|--------------------|------|-------------------|------------|----------------------|-------------------------|--------------------|----------------------------------|
| MT-G               | M500 | 2                 | LED 2-500  | -4.96                | 15                      | 4.55               | 70                               |
| MT-G               | M500 | 9                 | LED 9-500  | -4.42                | 15                      | 4.55               | 70                               |
| MT-G               | M500 | 7                 | LED 7-500  | -4.74                | 15                      | 4.55               | 70                               |
| MT-G               | M500 | 17                | LED 17-500 | -4.52                | 15                      | 4.55               | 70                               |
| MT-G               | M500 | 3                 | LED 3-500  | -5.12                | 15                      | 4.55               | 70                               |
| MT-G               | M500 | 22                | LED 22-500 | -4.31                | 15                      | 4.55               | 70                               |
| MT-G               | M500 | 19                | LED 19-500 | -4.86                | 15                      | 4.55               | 70                               |
| MT-G               | M500 | 29                | LED 29-500 | -4.38                | 15                      | 4.55               | 70                               |
| Average            |      |                   |            | -4.66                |                         |                    |                                  |
| Standard deviation |      |                   |            | 0.30                 |                         |                    |                                  |

Table 7. Summary of K-factor calibration results for MP-L LED when  $I_m$  at 40  $\mu A$ .

| LED                | Flux | Assembly sequence | LED Number | K (mV/°C) | Vsource (V) | V f (V) | I forward ( $\mu A$ ) |
|--------------------|------|-------------------|------------|-----------|-------------|---------|-----------------------|
| MP-L               | M406 | 1                 | LED 1-406  | -17.15    | 25          | 19      | 40                    |
| MP-L               | M406 | 2                 | LED 2-406  | -16.41    | 25          | 19      | 40                    |
| MP-L               | M406 | 34                | LED 34-406 | -15.78    | 25          | 19      | 40                    |
| MP-L               | M406 | 35                | LED 35-406 | -15.97    | 25          | 19      | 40                    |
| MP-L               | M500 | 28                | LED 31-500 | -16.11    | 25          | 19      | 40                    |
| MP-L               | M500 | 36                | LED 9-500  | -16.23    | 25          | 19      | 40                    |
| MP-L               | M500 | 33                | LED 33-500 | -16.39    | 25          | 19      | 40                    |
| MP-L               | M500 | 21                | LED 21-500 | -16.29    | 25          | 19      | 40                    |
| Average            |      |                   |            | -16.29    |             |         |                       |
| Standard deviation |      |                   |            | 0.41      |             |         |                       |

Table 8. Summary of K-factor calibration results for XP-E LED when  $I_m$  at 1000  $\mu A$ .

| LED     | Flux | Assembly sequence | LED Number | K (mV/°C) | I_forward ( $\mu A$ ) |
|---------|------|-------------------|------------|-----------|-----------------------|
| XP-E    | M500 | 1                 | LED 1-500  | 1.39      | 1000                  |
| XP-E    | M406 | 33                | LED 33-406 | 1.38      | 1000                  |
| XP-E    | M406 | 17                | LED 17-406 | 1.37      | 1000                  |
| XP-E    | M406 | 18                | LED 18-406 | 1.45      | 1000                  |
| XP-E    | M406 | 21                | LED 21-406 | 1.73      | 1000                  |
| XP-E    | M406 | 22                | LED 22-406 | 1.46      | 1000                  |
| Average |      |                   |            | 1.46      |                       |
| stdev   |      |                   |            | 0.14      |                       |

Table 9. Summary of K-factor calibration results for MT-G LED when  $I_m$  at 1000  $\mu A$ .

| LED     | Flux | Assembly sequence | LED Number | K (mV/°C) | I_forward ( $\mu A$ ) |
|---------|------|-------------------|------------|-----------|-----------------------|
| MT-G    | M500 | 30                | LED 30-500 | 3.58      | 1000                  |
| MT-G    | M500 | 25                | LED 25-500 | 3.45      | 1000                  |
| MT-G    | M406 | 27                | LED 27-406 | 3.75      | 1000                  |
| MT-G    | M406 | 25                | LED 25-406 | 3.70      | 1000                  |
| MT-G    | M500 | 7                 | LED 7-500  | 3.61      | 1000                  |
| MT-G    | M500 | 22                | LED 22-500 | 3.49      | 1000                  |
| MT-G    | M500 | 19                | LED 19-500 | 3.85      | 1000                  |
| MT-G    | M406 | 20                | LED 20-406 | 3.51      | 1000                  |
| MT-G    | M406 | 16                | LED 16-406 | 3.69      | 1000                  |
| MT-G    | M406 | 11                | LED 11-406 | 3.52      | 1000                  |
| Average |      |                   |            | 3.62      |                       |
| stdev   |      |                   |            | 0.13      |                       |



#### 4.5 Junction Temperature Measurements and Thermal Resistance Calculation

The thermal resistance can be calculated using the following equation:

$$R_{jX} = \frac{T_j - T_X}{P_H} = \frac{\Delta T_{jX}}{P_H} \quad (3)$$

where  $R_{jX}$  thermal resistance between the junction to the environment X

$T_j$  Junction temperature

$T_X$  Environment temperature where X could be the board or the heat sink

$P_H$  Heat dissipated by the device

$\Delta T_{jX}$  change in junction temperature due to heated power

Due to the difference in the environment temperature between the measurement stage and the heating stage, the change in junction temperature due to heated power can be calculated as follows:

$$\Delta T_{jX} = K \Delta V - (T_{jH} - T_{jM})$$

where  $K = k$  - factor

$\Delta V$  is the change in voltage due to junction temperature change

$T_{jH}$  Environment temperature at the heating stage

$T_{jM}$  Environment temperature at the measurement stage (no heating)

Here environment could be the board or the heatsink.

It should be noted that the K-factor is current dependent. Thus, the K-factor must be calibrated at the same current as the measurement current. In this study, we used measurement current at 1 mA.

The junction temperature of LEDs was measured using Cree's junction measurement test set. The data are summarized in Tables 10 and 11. The relationship between the thermal resistance and the voiding for MT-G and XP-E is shown in Figures 16 and 17, respectively. In the MT-G case, it seems that there is a positive correlation between the thermal resistance from the junction to the MCPCB and the voiding in the solder joint. However, the correlation is weak as indicated the R-square value of 4%. In the XP-E case, there is no correlation between the thermal resistance from the junction to the MCPCB and voiding in the solder joint. The results may indicate is that when the voiding percentage is less than 25%, the effect of voiding on the thermal performance is insignificant; when the voiding percentage is over 25%, there is weak positive correlation between the voiding and the thermal performance.

Table 10. Thermal Resistance of MT-G LEDs.

| LED Type                 | MT-G   | MT-G   | MT-G   | MT-G   | MT-G   | MT-G   | MT-G   | MT-G   | MT-G   | MT-G   |
|--------------------------|--------|--------|--------|--------|--------|--------|--------|--------|--------|--------|
| LED #                    | 406-20 | 406-11 | 406-27 | 406-16 | 406-25 | 500-30 | 500-25 | 500-7  | 500-22 | 500-19 |
| Voiding %                | 19.4   | 35.9   | 35.8   | 34.4   | 26.6   | 35.1   | 28.6   | 23.8   | 26.7   | 30     |
| V @I=0.99mA @T=24 C      | 4.7505 | 4.7817 | 4.8108 | 4.801  | 4.8108 | 4.7942 | 4.7836 | 4.7832 | 4.7561 | 4.794  |
| T at measurement (C)     | 24     | 24     | 24     | 24     | 24     | 24     | 24     | 24     | 24     | 24     |
| K-factor at I=1mA (mV/C) | 3.51   | 3.52   | 3.75   | 3.69   | 3.7    | 3.58   | 3.45   | 3.61   | 3.49   | 3.85   |
| I_forward in mA          | 350    | 350    | 350    | 350    | 350    | 350    | 350    | 350    | 350    | 350    |
| Vh @I=350mA              | 5.4752 | 5.4665 | 5.4773 | 5.5026 | 5.4887 | 5.4716 | 5.4769 | 5.5118 | 5.4696 | 5.4975 |
| Vj @I=0.99mA             | 4.7152 | 4.7425 | 4.7433 | 4.7566 | 4.7567 | 4.7416 | 4.7369 | 4.7578 | 4.6989 | 4.7595 |
| T_board @I=350mA         | 29.9   | 33     | 34.2   | 34.6   | 34.3   | 33.9   | 32.7   | 30     | 32.5   | 30.6   |
| delta T (Tj-Tb)          | 4.16   | 2.14   | 7.80   | 1.43   | 4.32   | 4.79   | 4.84   | 1.04   | 7.89   | 2.36   |
| R_jb                     | 2.17   | 1.12   | 4.07   | 0.74   | 2.25   | 2.50   | 2.52   | 0.54   | 4.12   | 1.23   |
| T_heatsink @I=350mA      | 28.7   | 31     | 31.9   | 32.1   | 32.4   | 32.7   | 30     | 27.2   | 30.7   | 28.6   |
| delta T (Tj-Th)          | 5.36   | 4.14   | 10.10  | 3.93   | 6.22   | 5.99   | 7.54   | 3.84   | 9.69   | 4.36   |
| R_jh                     | 2.80   | 2.16   | 5.27   | 2.04   | 3.24   | 3.13   | 3.93   | 1.99   | 5.06   | 2.27   |
| I_forward in mA          | 680    | 680    | 680    | 680    | 680    | 680    | 680    | 680    | 680    | 680    |
| Vh @I=680mA              | 5.6763 | 5.6498 | 5.6648 | 5.693  | 5.6775 | 5.6683 | 5.6605 | 5.7152 | 5.6589 | 5.6906 |
| Vj @I=0.99mA, Ih=680mA   | 4.6943 | 4.7178 | 4.7108 | 4.725  | 4.7275 | 4.7203 | 4.7065 | 4.7312 | 4.6989 | 4.7346 |
| T_board @I=680mA         | 32.5   | 35.9   | 37.5   | 37.9   | 37.1   | 35.9   | 35.9   | 33     | 34.7   | 34.6   |
| delta T (Tj-Tb)          | 7.51   | 6.25   | 13.17  | 6.70   | 9.41   | 8.74   | 10.45  | 5.40   | 5.69   | 4.83   |
| R_jb                     | 1.95   | 1.63   | 3.42   | 1.73   | 2.44   | 2.27   | 2.71   | 1.39   | 1.48   | 1.25   |
| T_heatsink @I=680mA      | 30.1   | 32.2   | 33     | 32.8   | 33.6   | 33.4   | 30.5   | 28     | 31     | 30.5   |
| delta T (Tj-Th)          | 9.91   | 9.95   | 17.67  | 11.80  | 12.91  | 11.24  | 15.85  | 10.40  | 9.39   | 8.93   |
| R_jh                     | 2.57   | 2.59   | 4.59   | 3.05   | 3.34   | 2.92   | 4.12   | 2.68   | 2.44   | 2.31   |

Table 11. Thermal Resistance of XP-E LEDs.

| LED Type                 | XP-E   | XP-E   | XP-E   | XP-E   | XP-E   | XP-E   |
|--------------------------|--------|--------|--------|--------|--------|--------|
| LED #                    | 500-1  | 406-33 | 406-17 | 406-18 | 406-22 | 406-21 |
| Voiding %                | 11.1   | 13.2   | 14.4   | 24.1   | 25.1   | 21     |
| V @I=0.99mA @T=24 C      | 2.5188 | 2.5191 | 2.512  | 2.5126 | 2.5137 | 2.4947 |
| T at measurement (C)     | 24     | 24     | 24     | 24     | 24     | 24     |
| K-factor at I=1mA (mV/C) | 1.39   | 1.38   | 1.37   | 1.45   | 1.46   | 1.73   |
| I_forward in mA          | 350    | 350    | 350    | 350    | 350    | 350    |
| Vh @I=350mA              | 3.0053 | 3.0322 | 3.0138 | 3.0329 | 3.0421 | 3.0646 |
| Vj @I=0.99mA             | 2.5013 | 2.5082 | 2.4978 | 2.4949 | 2.4981 | 2.4826 |
| T_board @I=350mA         | 31.8   | 25.9   | 29.6   | 29     | 28.2   | 26.1   |
| delta T (Tj-Tb)          | 4.79   | 6.00   | 4.76   | 7.21   | 6.48   | 4.89   |
| R_jb                     | 4.55   | 5.65   | 4.52   | 6.79   | 6.09   | 4.56   |
| T_heatsink @I=350mA      | 28.9   | 25     | 26.4   | 27.7   | 27     | 23.4   |
| delta T (Tj-Th)          | 7.69   | 6.90   | 7.96   | 8.51   | 7.68   | 7.59   |
| R_jh                     | 7.31   | 6.50   | 7.55   | 8.01   | 7.22   | 7.08   |
| I_forward in mA          | 680    | 680    | 680    | 680    | 680    | 680    |
| Vh @I=680mA              | 3.2029 | 3.2242 | 3.2189 | 3.2403 | 3.2446 | 3.2761 |
| Vj @I=0.99mA, Ih=680mA   | 2.4819 | 2.4962 | 2.4829 | 2.4773 | 2.4826 | 2.4601 |
| T_board @I=680mA         | 35.1   | 29.7   | 33.4   | 30.9   | 30.3   | 29.9   |
| delta T (Tj-Tb)          | 15.45  | 10.89  | 11.84  | 17.44  | 15.00  | 14.10  |
| R_jb                     | 7.09   | 4.97   | 5.41   | 7.92   | 6.80   | 6.33   |
| T_heatsink @I=680mA      | 28.9   | 27.7   | 26.7   | 28.1   | 27.4   | 23.8   |
| delta T (Tj-Th)          | 21.65  | 12.89  | 18.54  | 20.24  | 17.90  | 20.20  |
| R_jh                     | 9.94   | 5.88   | 8.47   | 9.19   | 8.11   | 9.07   |

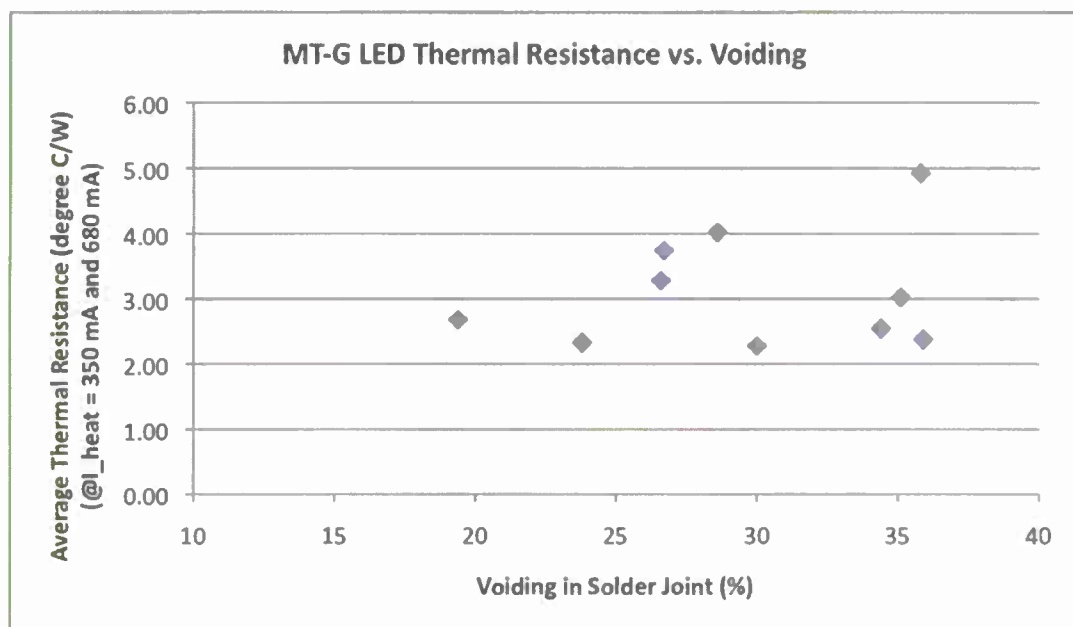


Figure 16. Relationship between MT-G LED Thermal Resistance and Voiding

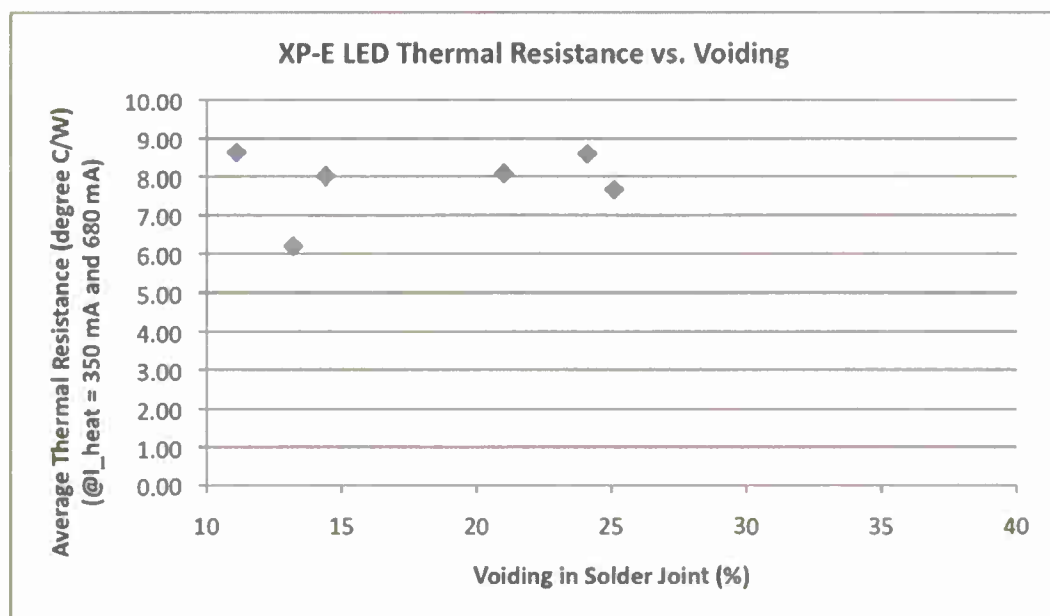


Figure 17. Relationship between XP-E LED Thermal Resistance and Voiding

#### 4.6 Summary

A study on the effect of flux in solder paste and size of LED package on the voiding and on the relationship between the voiding and the thermal performance of the LED has been done.

The results show that flux in solder paste has significant effect on the voiding. There is 5% less voiding in solder joint on average when M500 flux was used compared to when M406 flux was used.

The LED size has significant effect on the voiding as well. There is less voiding in the solder joint when the LED is smaller. As the size of LED increase to a certain level, the percentage of voiding to total area ratio won't increase, but the small voids will combine together into larger voids, which may be a concern for thermal performance since it could produce local overheating.

The results may indicate is that when the voiding percentage is less than 25%, the effect of voiding on the thermal performance is insignificance; when the voiding percentage is over 25%, there is weak positive correlation between the voiding and the thermal performance.

### **5. Future Work Planned**

It would be interesting to find out the effect of voiding that is over 50% of total area on the thermal performance of LED. In this study, the maximum voiding is less than 40%. That was achieved by reflow profiles and stencil patterns purposefully designed to minimize voiding.

We would like to find out why there is no strong correlation between the LED thermal resistance and the voiding in the solder joint when the voiding is less than 40%. One possible reason is that the variation in the thermal resistance from the junction to the solder joint among different LEDs is too large compared to the effect of voiding on the thermal resistance. Note that the thermal resistance from the junction to the board includes the thermal resistance from the junction to the solder joint and the thermal resistance from the solder joint to the board. The second possible reason is that the variation in k-factor calibration and junction temperature measurement is too large. We are designing a new junction temperature measurement setup and k-factor calibration system with a much better accuracy. A repeated experiment with higher accuracy test equipment will be conducted and the results will be compared.

A thermal model will be developed in the next study that can explain the experimental results.

It will be interesting to find out whether the transient thermal resistance is correlated to the voiding percentage. In this study, the temperature measurement was done at the steady state. We also plan to find out the differences in the K-factor differs at different measurement current. We plan to check solder joint quality through cross-section and SEM/EDX.

The results of this project are planned to be presented at the Department of Energy (DOE) Solid State Lighting (SSL) LED reliability consortium in Long Beach, CA on January 30, 2013. A technical paper is also planned to be submitted for publication at one IEEE conference in 2013. At the 2013 DOE SSL R&D workshop on January 2013, the PI plans to solicit continuing support from industry.

### Acknowledgements

The PI would like to acknowledge the research funding by the Department of the Navy, Office of Naval Research, under Award # N00014-11-1-0359. The PI would like to acknowledge support from Cree (Goleta, CA) for sponsoring LEDs, Koki (Japan) for sponsoring solder paste, Fine line Stencil (San Jose, CA) for sponsoring stencils, Advanced Tooling Design (San Jose, CA) for sponsoring fixtures, and Western Digital (Irvine, CA) for providing X-Ray service. The PI would like to thank Dr. James Ibbetson, Dr. Ted Lowes, and Ms. Yejin He of Cree for technical support, Jasbir Bath of Bath and Associates Consultancy LLC for technical support, Vicki Hamada of Advanced Tooling Design for support in stencil and fixture design, David Zueck and Keith Larsen of Western Digital for assistance in X-Ray inspection, Martin Koch at Cal Poly for technical support in assembly, Travis J. Malmgren at Cal Poly for developing reflow profiles, Vincent Khougaz and Buddy Bump at Cal Poly for calibrating LEDs.

### 6. References cited

- [1] US Department of Energy, "Solid-State Lighting: Comparison of Power Conversion of White Light Sources," Jan. 2009. Available at [http://www1.eere.energy.gov/buildings/ssl/comparing\\_lights.html](http://www1.eere.energy.gov/buildings/ssl/comparing_lights.html).
- [2] K. Gajewski. "Nations set goals to phase out the use and sale of incandescent light bulbs." *The Humanist*, July 2007.
- [3] Navigant Consulting Inc., "Energy Savings Estimates of Light Emitting Diodes in Niche Lighting Applications," Department of Energy report, October 2008, available at [http://apps1.eere.energy.gov/buildings/publications/pdfs/ssl/nichefinalreport\\_october2008.pdf](http://apps1.eere.energy.gov/buildings/publications/pdfs/ssl/nichefinalreport_october2008.pdf)
- [4] Li Zhang and Theo Treurniet, "On the Challenges of Thermal Characterization of High-Power, High-Brightness LED Packages," *Electronics Cooling*, May 2008.
- [5] Theo Treurniet, "Thermal Challenges in LED Systems," presentation at the 8th International Business and Technology Summit, Natick, MA, August 20-21, 2008.
- [6] The Institute for Energy Efficiency at UC Santa Barbara, "Fast-Tracking widespread adoption of LED lighting," White Paper of a one-day workshop, May 2010.
- [7] Y. Xi and E. Schubert, "Junction-Temperature Measurement in GaN Ultraviolet Light-Emitting Diodes using Diode Forward Voltage Method," *Applied Physics Letters*, Vol. 85, No. 12, Sep 2004.
- [8] X. Luo, T. Cheng, W. Xiong, Z. Gan, S. Liu, "Thermal Analysis of an 80W Light-Emitting Diode Street Lamp", *IET Optoelectronics*, Vol. 1, Issue 5, Oct 2007, pp. 191-196.
- [9] S. Jang and M. Shin, "Thermal Analysis of LED Arrays for Automotive Headlamp with a Novel Cooling System", *IEEE Transactions on Device and Materials Reliability*, Vol. 8, No. 3, Sep 2008, pp. 561-564.



- [10] K. Chen, Y. Su, C. Lin, Y. Lu, and W. Li, "Thermal Management and Novel Package Design of High Power Light-Emitting Diodes", Proceedings of IEEE Electronic Components and Technology Conference, May 2008, pp. 795-797.
- [11] Bergquist webpage at [http://www.bergquistcompany.com/thermal\\_substrates/LEDs/intro.html](http://www.bergquistcompany.com/thermal_substrates/LEDs/intro.html), accessed on Nov. 2012.
- [12] J. Cheng, C. Liu, Y. Chao, and R. Tain. "Cooling Performance of Silicon-Based Thermoelectric Device on High Power LED." Proceedings of International Conference on Thermoelectronics, 2005.
- [13] E. Hong and N. Narendran. "A Method for Projecting Useful Life of LED Lighting Systems." Proceedings of the 3<sup>rd</sup> International Conference on Solid State Lighting, 2004.
- [14] C. Lee, "Temperature Measurement of Visible Light-Emitting Diodes Using Nematic Liquid Crystal Thermography with Laser Illumination." *IEEE Photonics Technology Letters*, Vol.16, 2004.
- [15] C. Chen, Y. Wang, C. Tseng, and Y. Yang. "Determination of Junction Temperature in AlGaInP/GaAs Light Emitting Diodes by Self-Excited Photoluminescence Signal." *Applied Physics Letters*, Vol. 89, 2006.
- [16] Y. Xi, J. Xi, T. Gessmann, J. Shah, J. Kim, E. Schubert, A. Fischer, M. Crawford, K. Bogart, and A. Allerman. "Junction and Carrier Temperature Measurements in Deep-Ultraviolet Light-Emitting Diodes Using Three Different Methods." *Applied Physics Letters*, Vol.86, 2005.
- [17] EIA/JEDEC Standard 51-1, Integrated Circuits Thermal Measurement Method – Electrical Test Method (Single Semiconductor Device), December 1995, Electronic Industries Association.

## **Linear RF Amplifiers**

Principal Investigator:

**Vladimir I. Prodanov, Ph.D., Electrical Engineering**

California Polytechnic State University  
San Luis Obispo, CA

## 1. Abstract

Over the last decade, the number of mobile wireless devices has increased substantially. New “multi-carrier” modulation schemes, such as OFDM, WCDMA, and LTE, have been deployed to accommodate the demand for higher data rates. These modulation schemes create signals with high peak-to-average power ratios (PAPR). To process high-PAPR signals without causing an unacceptable level of distortion, RF power amplifiers, in mobile devices, must operate under an input power backed-off. Such an operation results in poor power efficiency; i.e. most of the energy drawn from the battery is converted into heat as opposed to being converted into RF energy.

This C<sup>3</sup>RP project deals with power amplifier architectures with improved efficiency under back-off. Two topologies were investigated. The first topology is a “load modulation” architecture related to the well-known Doherty amplifier. Unlike the Doherty amplifier, this two-transistor architecture uses partial positive feedback and it does not require an input power splitter. Hence, it could achieve a larger (by at least 3dB) power gain. Extensive simulations were performed and low-frequency “demonstrator” was implemented. The collected results suggest that the proposed architecture might be a viable alternative to the Doherty amplifier. The second architecture is a linear Class-C amplifier. The linearity is achieved using dynamic biasing. Unlike other such structures, the reported one is a pseudo close-loop implementation. It leverages scaled-down “replica” devices in a servo loop arrangement and it is appropriate for IC implementation.

This work has yielded two MS Reports and three Senior Design Reports. The work might be of interest to anyone involved in the design of fully-integrated RF transceivers.

## 2. Project significance

This project deals with the power efficiency of amplifiers intended for modern “multi-carrier” wireless communications.

Power efficiency is a “hot” research topic and its importance will continue to grow in the future. In the last two decades we have witnessed a revolution in wireless connectivity. A clear attribute to this revolution is the dramatic increase of functionality for a given device size/volume. Currently, the size of many portable devices is determined by the size of the battery and/or heat dissipation constraints. Decreasing the energy required for a given task both reduces battery size and alleviates heat dissipation. Hence, improvement of the power efficiency of electronic sub-systems is paramount to future progress.

The performance of RF Power Amplifiers impacts both battery size and data rates. Radio-frequency power amplifiers convert the energy of the source (battery) into high-frequency energy supplied to the antenna; hence, they are integral part of any wireless communication device. In practice only a portion of the supplied energy is converted while the rest is “lost” in a form of heat. Power amplifiers intended for processing of “multi-carrier” communication signals must be linear. Deviation from linearity, called “distortion”, reduces the amount of useful information that one could transmit or received within a given time interval and/or allocated frequency bandwidth.

High data rate RF communications demand power amplifiers with high linearity; such amplifiers can be very wasteful of power. New “multi-carrier” modulation schemes,

such as OFDM, WCDMA, and LTE, have been developed to accommodate the increasing number of users and the demand for larger data rates within the limited commercial frequency spectrum. These complex modulation schemes create signals with high peak-to-average power ratios (PAPR), exhibiting rapid changes in the signal magnitude. To accommodate these high-PAPR signals, RF power amplifiers in mobile devices must operate under backed-off gain conditions, resulting in poor power efficiency.

All RF power amplifiers are subject to linearity-efficiency tradeoff. Linearity and efficiency appear to be contradictory requirements, i.e. very good efficiency can be achieved if large amount of distortion is allowed. Similarly, excellent linearity is achievable if low level of efficiency (say sub-10%) is allowed. Note that efficiency of 10% implies that 90% of consumed energy is wasted!

### 3. Background/prior work

Many solutions to the linearity-efficiency tradeoff of power amplifiers have been presented over the years. They can be classified as: 1) load modulation; 2) dynamic transistor biasing; 3) supply adaptation techniques; 4) envelope elimination and restoration techniques [1, 2]. The first three are the most common. *The strategies that we investigated fall in those three categories.*

#### Architectures that use Load Modulation

The so-called Doherty Amplifier is the earliest and most popular amplifier topology. This circuit consists of two amplifying devices. One device is used to transmit at the average power level. The second device turns-on when peak power needs to be delivered. The ingenious power combining strategy ensures that the linearity of the overall topology is determined (mostly) by the first device. The circuit was first described in 1936 and after couple of decades of intense use in AM transmitters was all but forgotten [2, 3]. Its demise is attributed to the predominant use of frequency modulation (FM) broadcasting. FM signals allow for the use of highly-efficient (non-linear) power amplifiers. Because of the proliferation of OFDM and other multi-channel systems, the Doherty Amplifier has been “resurrected” [4, 5]. In the last 10 years more than 300 IEEE papers, having “Doherty Amplifier” in their title, have been published.

Another amplifier topology that falls into the load modulation category was introduced by the author [6] and an implementation was attempted by C. Neslen in 2010 [7]. The conceptual schematic of a negative conductance power amplifier is shown in Fig. 1. This is also a 2-transistor architecture where one of the transistors implements the “PA” and the other one implements the “Negative Conductance Load”.

The theory of operation and one possible design strategy can be found in [7]. The negative conductance power amplifier is akin to a Doherty amplifier because it uses two amplifying devices and an impedance inverter. The difference is that the “helper” transistor is driven by the output signal rather than the input one. As a result, no power splitter is used at the input. In theory, this would yield increase of power gain and potentially improved linearity.

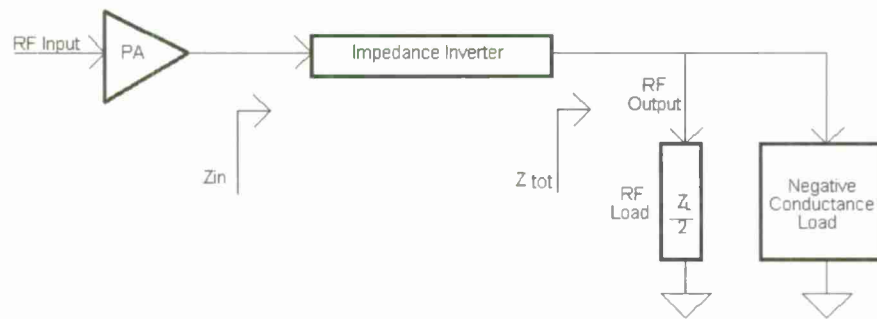


Figure 1- Conceptual Schematic of a "Negative Conductance" Amplifier [7]

The simulations confirmed the expectations of "Doherty-like" effect and the improved power gain. The implementation however was not successful, most likely due to the use of cascaded phase-shifting and voltage scaling networks which were highly sensitive to component variation and non-idealities, as well as the absence of harmonic termination. *One of the goals of this project was to find a more robust implementation.*

#### Class-C Amplifiers with Dynamic Biasing

Traditionally, class C operation has been avoided due to its inherent nonlinearity. However, the required wide-range of power control in modern wireless communications (especially for CDMA [2]) have renewed the interest in class C operation. To overcome the problems of nonlinearity, several dynamic biasing schemes have been proposed [8-10]. The major issue in these topologies is their open-loop approach to dynamic biasing. As the input drive increases, a power detector senses this increase and lowers the gate/base bias depending upon the magnitude. The actual level of the output of the PA is not sensed. Since the output may vary due to thermal conditions, the results seen in [8-10] may differ considerably in practical implementations.

Recently, a new dynamic biasing scheme was proposed by the author and it was investigated by G. LaCaille [11]. This scheme recognizes the fact that a Class-C amplifier can be "linearized" by ensuring constant conduction angle irrespective of signal strength. Maintaining a constant conduction angle means only allowing a predetermined constant fraction of the input signal to be presented on the output.

Conceptual schematic of the proposed "constant conduction angle" biasing scheme is shown in Figure 2. The approach uses two small-size "replica" devices,  $M_1$  and  $M_2$ , to implement a "servo loop". As the magnitude of the input AC signal increases, the servo loop lowers the DC biasing of the "power device"  $M$ , therefore ensuring nearly-constant conduction angle and resulting in linear operation.

The operation of the circuit has been verified using extensive transistor-level computer simulations. LaCaille also identified one severe shortcoming of the proposed approach – the operation of both the class-AB sensing and the class-C controlled device cannot be simultaneously optimized. *For the proposed approach to be viable, this issue had to be resolved; hence, the efforts described in "Discussion of Results".*



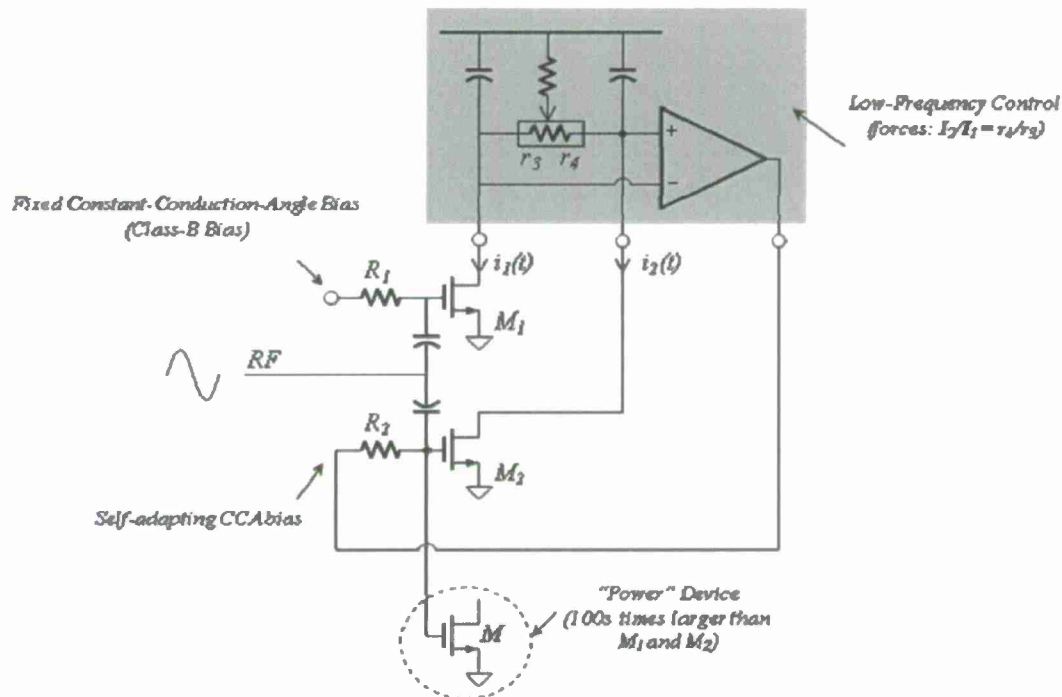


Figure 2 - Conceptual Schematic of the "Constant Conduction Angle" Biasing Scheme

#### 4. Discussion of Results

As stated in the previous section, the work supported by this C<sup>3</sup>RP grant stems from previous efforts and more specifically from the MS thesis work of Neslen and LaCaille.

##### Achieving Doherty Effect using Transformer Feedback

A new method for implementing a negative conductance power amplifier was identified. This method makes use of pair of magnetically-coupled coils. The first coil is inserted in series with one of the legs of the L-C-L impedance inverter. The second coil is used to provide both DC bias and AC drive to the transistor implementing the negative conductance stage. This topology is shown in Figure 3 and under the advisement of the author, was investigated by M. King [12].

Important feature of this topology is that the required (coupled) inductors have small value relative to that of inductors implementing the impedance inverter stage. Therefore, their physical size, when implemented on an integrated circuit will also be small.

##### Resolving LaCaille's Issue and Demonstrating Linear Class-C Amplifier

The original approach described by in [11] was generalized. It was shown that class-C operation with constant conduction angle can be achieved in two distinctly different ways:

- 1) By supplying equal drive and enforcing different DC currents in the two replica devices  $M_1$  and  $M_2$ . This is the original approach (see Fig. 2)
- 2) By supplying different drives to the devices and enforcing equal DC currents.

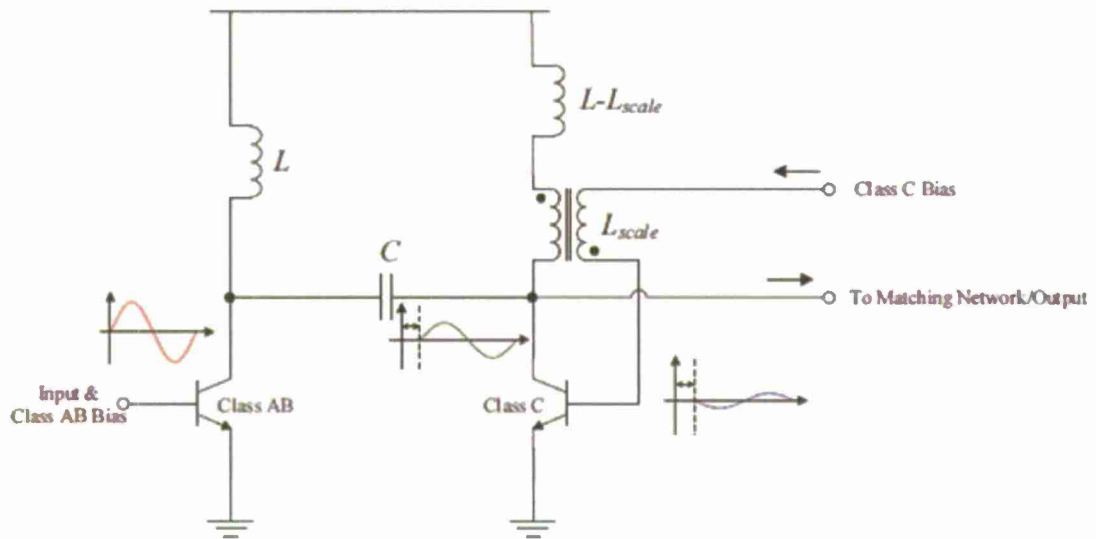


Figure 4 – Conceptual Schematic of a Negative Conductance Power Amplifier using transformer feedback. [12]

Under the supervision of the author, S. Garber demonstrated (using computer simulations) that there are in fact infinitely many practical solutions that fall in-between the above-stated two cases [13]. Those we refer to as “hybrids”. One such hybrid was implemented by M. Spahn [14]. This low-frequency (1MHz) implementation successfully demonstrated the concept but it exhibited unexpected signal artifacts.

Further progress was made with the help of another student - G. Rai. We showed that there is an optimum hybrid solution that resolves the issue identified by LaCaille. Also, artifacts observed by Spahn were shown to be the result of a poorly compensated servo-loop. Detailed description of this investigation can be found in [15].

#### Developing High-PAR Signaling Capability

The work completed so far is based upon computer simulations and low-frequency “demonstrators”. Cal Poly currently lacks capability to produce. Such equipment is extremely expensive. Cal Poly, through an existing relationship with Texas Instruments (TI) was able to utilize TI equipment for this task. The equipment comprised of two recently-developed evaluation boards. When connected together, and programmed by a PC, these two boards implement a multi-GHz generator capable of synthesizing the type of communication signals. The capability of this two-board solution was verified as a part of another power amplifier project [16].

### **5. Future Work Planned**

#### Architectures that use Load Modulation

- 1) Fix existing board error in transformer-feedback architecture and taking measurements.

In King's experimental set up there was a technical issue that prevented us from experimentally characterizing the topology [12]. This issue is believed associated with the use of transistor arrays (as opposed to single discrete components).

2) Write two patent disclosures

We believe that the transformer-feedback implementation might be patentable because the original patent did not disclose any such implementation [6] and the solution is not obvious.

#### Linearized Class-C Amplifier

1) Submitting the work to Electronics Letters

The paper has already been written [16].

2) Write patent disclosure on the possibility of frequency-doubling linear power amplifiers

The ability to keep the conduction angle of a Power amplifier constant opens the possibility of implementing a power amplifier with frequency doubling. Such a power amplifier might be useful in fully-integrated transmitters because it will eliminate the so-called "LO-pulling" effect.

#### Developing High-PAR Signaling Capability

1) Explore possibilities for an "equipment grant" that will allow us to purchase 8 more such 2-board set-ups for EE Microwave lab.

Currently our communication courses only use AM and FM signaling. It will be beneficial to both students and faculty to have OFDM-capable signal generators.

#### **6. References cited**

1. S.C. Cripps, RF Power Amplifiers for Wireless Communications. Norwood, MA: Artech House, 1999.
2. V. Prodanov and M. Banu, "Power Amplifier Principles and Modern Design Techniques", Wireless Technologies: Circuits, Systems, and Devices, CRC Press, 2008.
3. W.H. Doherty, "A new high efficiency power amplifier for modulated waves," Proc. IRE, vol. 24, no. 9, pp. 1163-1182, 1936.
4. "The Doherty Amplifier: New After 70 Years," by Freescale Semiconductor, RF Division, Microwave Product Digest, Aug. 2007
5. J. Kim et al, "A highly-integrated Doherty amplifier for CDMA handset applications using an active phase splitter," IEEE Microwave and Wireless Components Letters, pp. 333-335, May 2005.
6. US # 7,135,931, "Negative Conductance Power Amplifier," V. Prodanov
7. Cody Neslen, "Negative Conductance Load Modulation RF Power Amplifier," MS Thesis, Cal Poly, June 2010

8. G. Grillo, D. Cristaudo, "Adaptive Biasing for UMTS Power Amplifiers," IEEE BCTM, pp. 188-1991, 2004.
9. S. Reed, Y. Wang, F. Huin, and S. Toutain, "HBT Power Amplifier With Dynamic Base Biasing for 3G Handset Applications," IEEE Microwave and Wireless Components Letters, vol. 14, pp. 380-382, Aug. 2004.
10. V. Leung, J. Deng, P. Gudem, and L. Larson, "Analysis of Envelope Signal Injection for Improvement of RF Amplifier Intermodulation Distortion," IEEE Journal of Solid State Circuits, vol. 40, pp. 1888-1894, Sept. 2005.
11. Greg LaCaille, "A Constant Conduction Angle Biased Amplifier for Improved Linearization in Class C Operation," MS Thesis, Cal Poly, June 2010
12. Matthew E. King, "Linear Power-Efficient RF Amplifier with Partial Positive Feedback," MS Thesis, Cal Poly, June 2012
13. Stephen Garber, "Constant Conduction Angle Bias Generation for Monolithic RF Power Amplifiers," Senior Design Project, Cal Poly, June 2011
14. Michael Spahn, "Constant Conduction Angle Bias Experimental Generation for RF Power Amplifiers," Senior Design Project, Cal Poly, Aug. 2011
15. Gursewak Singh Rai, "A Constant Conduction Angle Biasing for Class-C Monolithic RF Power Amplifiers," MS Thesis, Cal Poly, Nov. 2012
16. Kevin Maulhardt and Kevin Haskett, "Pulsed Class-G RF Amplifier System," Senior Design Project, Cal Poly, June 2012
17. G.S. Rai, V.I. Prodanov and S.Garber, "Linearized class C power amplifiers by virtue of constant conduction angle biasing," to be submitted to Electronic Letters

## **Structural Origami Based Deployable Disaster Relief Shelter**

Principal Investigator:

**Dr. Satwant Rihal, Professor Emeritus  
Architectural Engineering Department  
College of Architecture and Environmental Design**

California Polytechnic State University  
San Luis Obispo, CA  
October 2012



## 1. Abstract

Feasibility of the application of the art of origami has been explored for developing a temporary disaster shelter for areas affected by disasters e.g. earthquakes. The application of sustainable materials e.g. corrugated boards, commonly used in the packaging industry has been explored for an origami disaster relief shelter concept. Innovative structural forms, based on the art of origami folding have been developed for applications to a temporary disaster shelter. Hands-on experimental methods, including digital fabrication and load testing have been used for developing an origami disaster shelter concept. The fundamental origami folding patterns were identified and analyzed for potential applications in a temporary disaster relief shelter. The structural origami forms for the temporary shelter were identified as arched frames / vaults and domes. Mock-ups of origami frames and arch/vault forms of increasing scale, and varying densities of folding were designed and built using digital fabrication techniques, and load tested to failure. Preliminary test results, including load-deflection behavior and modes of failure for each of the origami form mock-ups, were obtained. Based on the results of the load testing of the small scale mock-ups of disaster shelter concepts, a half-scale mock-up of our origami disaster shelter, was designed and fabricated using two layers of corrugated polypropylene sheets; including end enclosures and access door opening, and attached to an OSB base platform. The folding pattern was a diamond module with natural geometry extension. The structural form of the half-scale origami disaster shelter may be described as a hybrid symmetrical vault with natural geometry extensions. The inner and outer layers of the origami disaster shelter were attached together using pop-rivets, and innovative tab joints in the inner polypropylene layer and overlap joints in the outer polypropylene layer, that were developed for fabrication and realization of the half-scale origami shelter mock-up. Our half-scale mock-up of the origami disaster shelter was then subjected to simulated wind loads using an innovative load-testing scheme developed for this project. Results of this wind load testing include lateral load behavior and plots of lateral load vs. lateral deflection; as well as the effect of the wind loads on the geometry and form of our origami disaster shelter. The viability of the origami vault form for our disaster shelter was thus established. Finally a full-scale mock-up of our origami disaster shelter was designed and fabricated using two layers of white polypropylene sheets, using tabbed joints in the inner layer and overlap joints in the outer layer, and pop-riveted together at the joints, and attached to an OSB base platform as in the case of the half-scale shelter mock-up. The end enclosures and their attachments to the main origami vault were especially designed considering the effects of scale, need for stiffening, ease of attachment, and door access. The full-scale origami disaster shelter mock-up has been assembled and installed in the Simpson Strong-Tie Materials Demonstration Laboratory of the Construction Innovations Center at Cal Poly. The results of this research provide innovative ideas for meeting needs of temporary shelters following disasters such as earthquakes not only for naval facilities but also for civilian facilities around the globe. The full text for this investigation is found in the Appendix to this final report.

**Keywords:** *origami; folded forms; emergency shelters; digital fabrication; corrugated boards.*

## 2. Project significance

The world faces significant shortage of temporary shelter for the affected population following major disasters e.g. earthquakes, etc. The significance of this project is that

innovative ideas for meeting the needs for temporary human shelters following disasters have been explored. An innovative and collaborative design process has been established for developing a temporary deployable disaster shelter based on the art of origami, using sustainable materials such as those used in the packaging industry. Structural vault forms based on the patterns of origami folding, that are suitable for a temporary disaster shelter have been established. Using sustainable materials e.g. polypropylene sheets and digital fabrication techniques, a half-scale as well as a full-scale mock-up of a proposed temporary disaster shelter were designed, fabricated and installed in our laboratory. A unique double-layer vault design of the origami disaster shelter, using polypropylene sheets has been developed. Innovative connection designs consisting of tabbed as well as overlap joints, have been developed for the polypropylene sheets, and load tested for validation of the two connection types. A unique and practical wind load testing method was developed and implemented for the lateral load testing of the half-scale origami disaster shelter mock-up, and quantitative results of load vs. deflection behavior have been obtained. The significant project outcomes include not only the design and testing processes for developing temporary disaster shelters based on the ancient art of origami, but also quantitative results for validation of design concepts for full-scale realization of origami form disaster shelters. The results of this research provide innovative solutions for meeting needs of temporary shelters following disasters such as earthquakes, not only for naval facilities but also for civilian facilities around the globe.



Figure 1. Half-Scale Origami Disaster Shelter Mock-Up, Simulated Wind Load Testing Set-Up (Ref. 19, page 142).

### 3. Background/prior work

An attempt to develop a cardboard shelter for the homeless was presented by Hovesejian as Cardborigami [14]. A study of transitional shelter case-studies for Haiti, following the 2010 earthquake was presented by Architects for Humanity / Habitat for Humanity [15]. A project that applied cardboard while addressing environmental concerns was the Westborough School in Essex, UK [16]. The team used folded cardboard panels with timber framing and a concrete foundation to hold up the structure. A paper tube emergency shelter has been developed by architect Shigeru Ban in Japan [17].

### 4. Discussion of Results

1. For a given origami vault form (e.g. arched vault), polypropylene sheets exhibited a more consistent and ductile like behavior, compared to double wall (BC flutes) and single wall (C flute) corrugated boards. Even though the double wall corrugated board was the most successful in the applied gravity load test, this material is more expensive when compared to the relative cost of the polypropylene or single wall corrugated board. In addition, the polypropylene board is a plastic material—it is inherently waterproof unlike the fibrous double wall and single wall materials. The polypropylene board, when analyzing the material's lifecycle, may out-perform the double-wall corrugated material. [ORIG 5, ORIG 6, ORIG 7]<sup>1</sup>
2. An origami structural form that uses folds that are more acute and deeper is found to be noticeably stronger. If the structure is made with more obtuse fold angles, the repeating origami pattern is flatter overall and does not seem to provide as good a resistance to the vertical load it is subjected to. [ORIG 13, ORIG 14]<sup>1</sup>
3. Based on the results of testing of asymmetrical vaults, we are able to conclude that a smaller number of bays is more effective in asymmetrical design of vaults. Moreover, a design with less asymmetry is more successful. [ORIG 8, ORIG 12]<sup>1</sup>
4. Based on the results of testing of hybrid vaults (with natural geometry extension), with 4, 5 and 6 bays, we can conclude that a higher number of bays benefitted the design. Unlike the asymmetrical designs, having a higher number of bays resulted in a higher load bearing capacity. [ORIG 11, ORIG 13, ORIG 14]<sup>1</sup>
5. Within the symmetrical and asymmetrical designs, it is evident that vertical walls are not as efficient as the natural geometry extensions; the vertical walls tend to buckle easily under the thrust caused by the applied gravity load. [ORIG 09, ORIG 08, ORIG 12]<sup>1</sup>
6. Based on the preliminary testing of the vault configurations with and without extensions under gravity and lateral loads, it can be concluded that the enclosure extension provides stiffening and lateral resistance for the vault. The single layer configuration with extensions and tab joints performed significantly better than the

---

<sup>1</sup> Items in parenthesis refer to list of specimen in Table 5.1-1, Ref. [19]

double layer configurations without extensions and tab/overlap joints. [ORIG 16, ORIG 17, ORIG 18]<sup>1</sup>

7. For a given origami vault form fabricated from polypropylene sheets, tab joints and overlap joints have comparable resistance. Tab joints provide greater lateral resistance and stiffness under gravity and lateral loads. However, overlap joints provide a greater resistance to uplift movement imposed by gravity and lateral loads. [ORIG 19, ORIG 20, ORIG 21]<sup>1</sup>

## 5. Future Work Planned

1. Further research on the shelter base connections and materials would improve the origami disaster shelter's ability to adapt to different site conditions. So far, we focused mainly on attaching the polypropylene vault structure to a flat OSB base/platform, using screws. A more integrated base design that could be shipped in folded / compressed sheet form, along with the disaster shelter components, would improve the convenience of distribution and assembly.
2. Due to the restrictions of material and sheet size, we utilized only 4 ft. x 8 ft. corrugated polypropylene sheets 4 mm. in thickness. The stiffness of a single sheet of 4 mm polypropylene required us to develop a double-layer design for our origami disaster shelter. To minimize fabrication costs, it would be beneficial to experiment with 6 mm polypropylene sheets for our disaster shelter. This could result in reduced number of pop-rivet overlap or tab joints that were required for stiffening our origami vault structure.
3. The development of the full-scale origami disaster shelter considered mostly structural and spatial issues. Further development of design for better ventilation is required to create airflow in the disaster shelter for a comfortable living environment. Design details concerning sealing and weatherproofing the joints are also essential in the environmental conditions under which disaster shelters have to function.
4. As we have experienced in many disaster-shelter communities, structures that are intended to be temporary become semi-permanent. Considering and predicting long-term effects of polypropylene, connections, and other details could potentially necessitate design revisions. Different layers of sustainable materials could be placed or adhered to the structure to increase the life span and structural benefits of the disaster shelter.

## 5. References cited

- [1] "Special Issue on the 2010 Haiti Earthquake", *Earthquake Spectra*, EERI, Oakland, CA, Vol. 27, No. 1, 2011.
- [2] Tachi T, "Cellular Origami from Foldable Tubes", *Structural Morphology Group Seminar*, London, September 2011.



- [3] Tachi T, "One – DOF Foldable Structures from Space Curves", IABSE – IASS Conference, London, 20-23 September 2011.
- [4] Buri H, and Weinand Y., *Origami – Folded Plate Structures*, EPFL, Lusanne, Switzerland, 2010.
- [5] Trautz M, and Herkrath R., "The Application of Folded Plate Principles on Spatial Structures with Regular, Irregular and Free-Form Geometries", *Proc. of The International Association for Shell and Spatial Structures (IASS) Symposium*, Valencia, Spain, 2009.
- [6] Trautz M, and Ciernack S., "Folds and Fold Plate Structures in Architecture and Engineering", *Structural Morphology Group Seminar*, London, September 2011.
- [7] Schenk M, and Guest S., "Origami Folding: A Structural Engineering Approach", *Fifth International Meeting of Origami Science Mathematics and Education*, September 2010.
- [8] Falk A, and Von Buelow P., "Form Exploration of Folded Plate Timber Structures based on Performance Criteria", *IABSE-IASS Symposium*, London, 2011.
- [9] Mahadevan L, and Rica S., "Leaf Origami", Wyss Institute, Harvard University, Cambridge, Massachusetts, 2005.
- [10] Moussavi F, and Lopez D., *The Function of Form*, Actar and Harvard University School of Design, 2009.
- [11] Engel H, *Structure Systems*, Praeger, New York, 1968.
- [12] Saha K, and Kisch R., "Fundamentals of Corrugated Boards in Packaging", Personal Communication, IT Department, Cal Poly State University, San Luis Obispo, June 2011.
- [13] Speidel E, "Plastics in Construction", Personal Communication, Construction Management Department, Cal Poly State University, San Luis Obispo, June 2011.
- [14] Hovsepian T, *Cardborigami*. Web: <<http://www.cardborigami.org>>, 2010.
- [15] Transitional Shelter Case-Studies, *Architecture for Humanity / Habitat for Humanity*, 2010.
- [16] Cripps A, "Cardboard as a Construction Material: A Case Study", *Building Research and Information*, United Kingdom, Vol. 32, No. 3, 2004, pp. 207-219.
- [17] Goodier R, "Ten Great Emergency Shelter Designs", *Engineering for Change*, Web: <[https://www.engineeringforchange.org/news/2011/10/30/ten\\_great\\_emergency\\_shelter\\_designs.html](https://www.engineeringforchange.org/news/2011/10/30/ten_great_emergency_shelter_designs.html)>, October 2010.
- [18] *Rhinoceros*, Version 5.0, Web: <<http://www.rhino3d.com/>>, McNeel North America Corporation, 2010.
- [19] Rihal, Satwant, et. al., "Structural Origami Based Deployable Disaster Shelter", Architectural Engineering Department, College of Architecture and Environmental Design, Cal Poly State University, San Luis Obispo, California, Final Technical Report, October 2012. Final Technical Report, submitted to the Department of the Navy, Office of Naval Research, October 2012.



## **Rapidly Assembled Emergency Shelters, Phase II**

Principal Investigators:

**Robert Arens, AIA, Architecture**  
**Edmond Saliklis, Ph.D., P.E., Architectural Engineering**

California Polytechnic State University  
San Luis Obispo, CA

## 1. Abstract

An interdisciplinary design team of architects and engineers investigated the development of an efficient, economical, and environmentally responsible emergency shelter. A team of faculty and students worked collaboratively to design a shelter, the process by which it would be produced, erected and delivered. Design innovations of the shelter include the fact that it is constructed by hand with no special tools and no scaffolding. When complete it can shelter several people. The premise of the design is a mix of short-term disposable materials, as well as long term more durable materials. The durable materials could later be used in wider reconstruction efforts. A major design innovation is the combination of precise friction joints that are cut using a digitally controlled cutter, in conjunction with zip ties that are secured by hand. Our research established not only the role of shelters within the larger context of disaster relief, but also the methodology of using full-scale prototypes in actual materials. Full-scale prototyping made with the help of digital fabrication techniques allowed for optimization efforts to reduce weight and enabled simplification of both fabrication and construction. A provisional patent on the shelter was filed and six publications resulted from the Phase II research effort. Nine paid Cal Poly student research assistants were used in the project providing them with a unique opportunity to learn by doing.

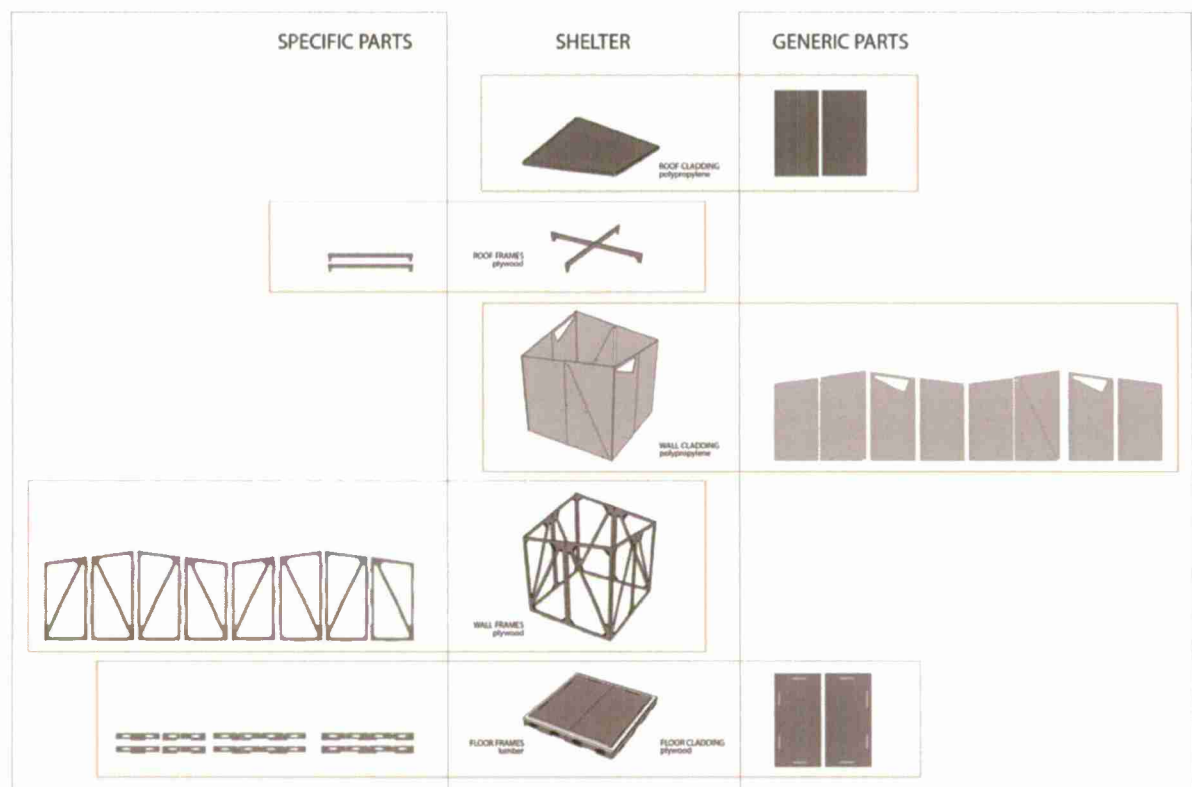


Figure 1: Diagram of the shelter components, highlighting the level of shaping and therefore the likelihood of their re-purposing in future rebuilding efforts.

## 2. Project significance

National and international headlines regularly point to the alarming frequency of natural disasters. Even a cursory glance at statistics compiled by international agencies reveals the extreme costs in human life and the enormous social and economic toll of these disasters. Recent data indicate that of the 245 disasters reported in 2009, 224 were weather-related and these accounted for 55 million people affected, 7000 killed, and US\$15 billion in economic damages. Worse yet, the frequency of natural disasters has spiked dramatically in the 20th century, a trend that is very likely to continue considering global weather changes. [1] Our research goal was to develop the prototype for an emergency shelter that could be mass-produced inexpensively and rapidly deployed to disaster relief sites. A seeming simple project wrapped in multiple shrouds of complexity, the project demanded that we not only design an object, but also devise the process for its production, determine how it would be constructed and sourced, identify the most efficient assembly sequence, and outline a strategy for the shelters' distribution. The faculty-student team built five full-scale prototypes that have contributed to a clearer definition of the demands of a rapidly-deployed emergency shelter design and with each generation of development lead us closer to a viable solution in terms of material use, production methods, shipping procedures, and constructability.



Figure 2: Views of earlier prototypes 3 (left) and 3X. These utilized plywood for the superstructure and resulted in more complexity and weight than desired; cardboard became the focus in prototype 4.

## 3. Background/prior work

The pressing National Security need for post-disaster sheltering of distressed populations has called our design team into action. Earthquakes, tsunamis and hurricanes regularly destroy thousands of homes and the need for emergency shelter is real and enormous. Funds from C3RP Phase I supported this project. Five different prototypes were constructed in Phase I and seven scholarly attainments were published.

In Phase II we clarified the design of the shelter to four essential components:

- 1) a series of paperboard walls that are digitally cut to create precise friction joints,
- 2) thin, recycled polypropylene sheets that form a weather barrier on the walls and roof,
- 3) zip ties, secured by hand, that connect elements of the structure and skin, and

4) a plywood floor that serves as a clamshell packaging case for delivery.

The novelty is that a stiff and stable structure can be created by hand with no scaffolding or cranes required. The shelter is not a house, it is an affordable shelter that provides several types of materials, namely short term disposable materials for the walls and the roof and longer term materials in the cladding and floor/crate that can be used again in wider reconstruction efforts. The shelter can be assembled in an hours and can provide emergency shelter for several people in a disaster relief setting.

As background, it is important to position emergency shelters within the larger context of disaster relief. Disaster and relief officials, such as the Federal Emergency Management Agency in the United States (FEMA), view post-disaster housing in three ways: sheltering, interim housing and permanent housing. Sheltering refers to basic protection employed for short periods of time until the disaster subsides and the displaced population can return to their permanent dwellings. Interim housing refers to situations where permanent dwellings have been destroyed or rendered uninhabitable by serious disasters thereby necessitating temporary structures for displaced populations to occupy for extended periods (generally up to 18 months). Permanent housing refers to long-term structures used as permanent residences following natural disasters; these may be habitable or repairable existing structures that displaced populations return to, or may be replacement housing meant to take the place of structures rendered permanently uninhabitable. 2] Due to complex and overlapping factors, the line between these three types of housing is often indistinct. Major factors such as the severity of many disasters and the shortage of resources (funding, labor, materials, etc.) contribute to secondary factors such as extended clean up periods and the inability to repair or replace damaged housing stock. Consequently, sheltering constructed of temporary materials is often pressed into service for much longer periods than intended and is forced to function as interim housing inhabited for years not months. Worse yet, most sheltering, if forced to function as interim housing, reaches the end of its useful life before permanent housing can be provided. Although this situation presents a great challenge, we felt it was absolutely necessary to design a shelter that would address rather than ignore this troubling reality.



Figure 3: Prototype 4, the results of our work in Phase 2. Simplification of the roof plus the use of cardboard resulted in a lighter structure with connections that led to the use of zip ties.

#### **4. Discussion of Results**

The design team crafted the following set of six goals for the shelter design: efficiency, lightness, pack-ability, constructability, adaptability and re-usability. The first five address the short-term considerations of producing and providing a viable emergency shelter. The last goal, reusability, was a response to the harsh reality of sheltering, namely that short-term shelters often become interim housing in settings where the resources to replace it with permanent housing are limited. In other words, unless temporary shelters can contribute to the future rebuilding effort in some measure, they are a solution of limited value. Our design direction was to avoid highly specialized components of short-life materials where possible and include components of durable materials left in near-generic form. This hybrid approach called for a combination of short-life components that are easily recycled and more durable components that are easily repurposed as building materials for bona fide interim or replacement housing. Our goal was to contribute to both short-term and long-term housing needs at disaster relief sites. Regardless of whether the components were intended as short or long term, however, they would still have to meet our other five goals. In order to achieve this, we sought to optimize their constructability and pack-ability while making them as efficient, light and adaptable as possible.

The success of our research can be measured by several metrics. One is that the design is fairly mature and sophisticated now. We have full-scale prototype to prove the validity of our design. The second is that outside peer review has looked favorably on our research, resulting in a series of papers presented at International Conferences, National Conferences and Regional Meetings. Finally, it is worth noting that we had an enthusiastic and varied team of student assistants, some undergraduate and some graduate students from both the Architecture Department and from the Architectural Engineering Department. Their participation was critical to the success of the project and we are certain that they had a rewarding and unique intellectual opportunity to grow as students, designers and researchers.

##### **4A. List of Attainments:**

###### **International Presentations/Publications:**

“Optimizing a Disaster Relief Shelter with Prototypes”  
International Association for Shell and Spatial Structures  
Seoul, South Korea; 21-24 May 2012



“The Image of a Rapidly Assembled Emergency Shelter”  
 Third International Conference on the Image  
 Poznan Poland; 14-16 September 2012



Figure 4: Digital fabrication techniques allowed the wood and cardboard elements to be quickly and precisely manufactured. Through design and fabrication advances, the structure became very light and easy to construct.

“Versioning: Full-Scale Prototyping as a Prototype for Design Education?” (accepted)  
 Second International Conference for Design Education Researchers  
 Oslo, Norway; 14-17 May 2013

“Fold Here: Optimizing a Disaster Relief Shelter with Prototypes” (accepted)  
 Second International Conference on Structures and Architecture  
 Guimaraes, Portugal; 24-26 July 2013

#### **National Presentations/Publications:**

“Zip Lock: Taking a Longer View on Temporary Disaster Relief Shelters,” (pending)  
 101st Annual Meeting of the Association of Collegiate Schools of Architecture  
 San Francisco, CA; 21-24 March 2013

“Versioning: Design and Fabrication of a Flat Pack Emergency Shelter”  
 2011 Conference of the Building Technology Educators Society  
 Toronto, Canada; 4-6 August 2011

#### **Regional Presentations:**

“Pleats: Taking the Long View on Temporary Shelters for Disaster Relief”  
 West Regional Meeting of the Engineers Without Borders  
 San Luis Obispo, CA; 19-21 October 2013

#### **Provisional Patent:**

Emergency Shelter, Arens, R. and Saliklis, E.  
 US Patent Application (Provisional) Attorney Docket No. 8015-12

#### 4B. Student Research Assistants:

Akin-Zimmerman, Kristin ARCH Undergraduate  
 Bateman, Eric ARCE Graduate  
 Bermudez, Gustavo ARCH Undergraduate  
 Chan, Rockwell ARCH Undergraduate  
 Gree, Daniel ARCE Undergraduate  
 Hait-Campbell, Benjamin ARCH Undergraduate  
 Kao, Kathlyn ARCH Undergraduate  
 Schwaller, Nicklaus ARCH Undergraduate  
 Shayo, Tadei CEE Graduate

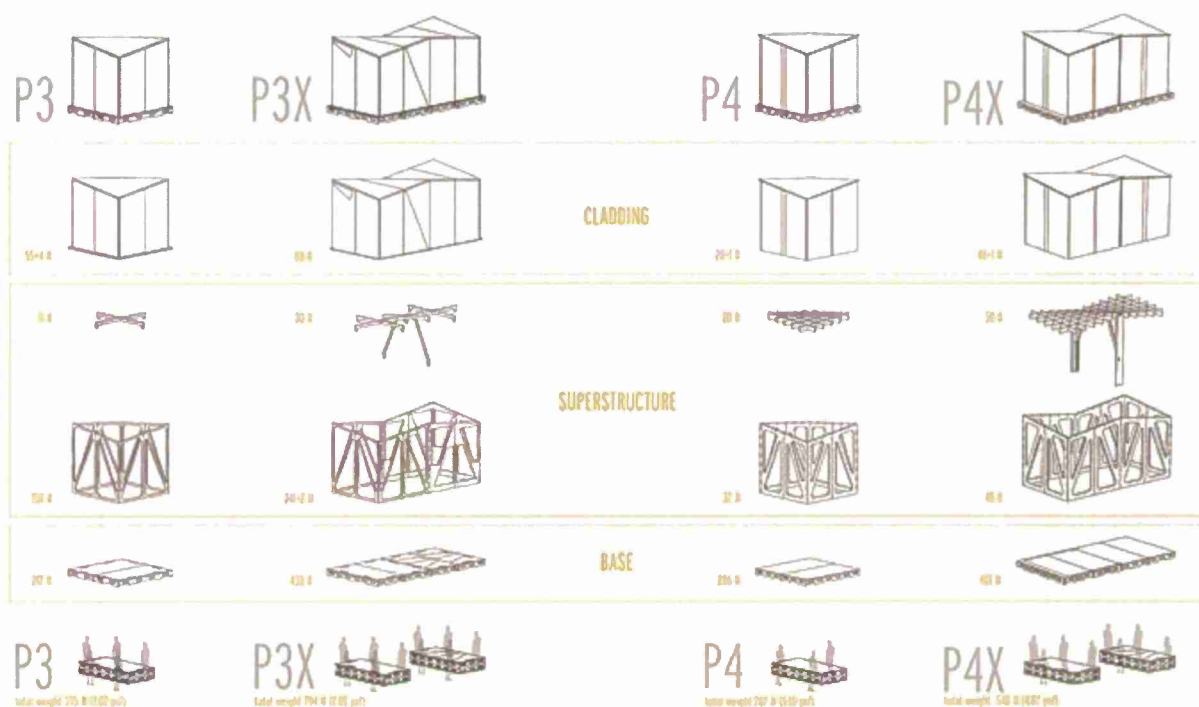


Figure 5: Optimization of materials and methods in Phase 2 led to improvements in fabrication and construction, as well as weight-savings of 31% (3X vs 4X).

#### 5. Future Work Planned

Through the iterative process, the design team was able to distill the project down to three simple materials that are either left close to their original state (plywood floor panels and polypropylene wall cladding) or are shaped using digital fabrication (crate edges and superstructure panels). Our hope is that the narrow palette of inexpensive and simple materials facilitates their distribution and that digital fabrication facilitates their production and sets the stage for a number of potential production/distribution models. An obvious approach would be to produce and distribute the shelters from a single location where materials and crated shelters could be warehoused until a disaster occurs and shipment is necessary. A more intriguing and cost beneficial model would be

to stockpile a far fewer number of shelters and produce/distribute them on-demand from countless hubs located around the globe. In the case of the latter, partners with CNC capabilities and suppliers of materials would be identified in strategic locations and engaged as part of a global network of shelter-providers ready and able to provide shelters from the closest point and hopefully quickest way possible. On its most immediate level, this project provided an opportunity for our team of faculty and students from the disciplines of architecture, structural engineering, and materials engineering to work collaboratively to develop a lightweight, rapidly-deployed emergency structure. Given the need for efficiency, lightness, mass-production and constructability, we found that adopting full scale prototyping with actual materials, a design process more common to product or packaging design, helped us optimize and test our outcomes. Our latest generation of prototypes have been developed to utilize the optimum combination of specific short-life components and generic long-life components; this approach may provide a solution to the vexing problem of housing disaster-stressed populations in the short term while providing materials for repurposing in long-term building efforts.

Although the scale of global disaster relief is overwhelming (and trending alarmingly higher), the design of a short-term shelter that could be mass-produced was a challenge well suited to our combined disciplines of architecture and engineering. We recognize that emergency shelters have recently been the focus of many talented designers and that numerous innovative approaches have resulted from their efforts. In the spirit of design intelligence we see ourselves as part of this movement and hope to contribute to this expanding body of work.

## **6. References cited**

- [1] See the United Nations International Strategy for Disaster Relief at [www.unisdr.org](http://www.unisdr.org).
- [2] FEMA, 2008 Disaster Housing Plan.

## **Implementation of the switchable grating concept**

Principal Investigator:

**John Sharpe, Ph.D. Physics**

California Polytechnic State University  
San Luis Obispo, CA

### **1. Abstract**

The purpose of this project is to implement an idea whereby an optical grating moves and creates a phase or frequency shift on the light which is diffracted from it. In order to accomplish this we investigated two approaches. The first approach is to use a liquid crystal cell containing fast switching ferroelectric liquid crystal (FLC). Such a cell was designed, manufactured and undergone preliminary testing where we have demonstrated that the FLC has good optical contrast and should be capable of switching at rates  $> 1$  kHz. At the time of writing we are still waiting on delivery of an electronic component which we need to generate voltage signals with the correct timing to drive the device. The other approach we considered was to use a Texas instruments Digital light projector which should be capable of similar frequency shifts but we have as yet been unable to demonstrate these capabilities.

### **2. Project significance**

In many areas of science and engineering there is a requirement for an accurately known frequency shift to be placed on an optical beam. This includes frequency shifts for laser Doppler velocimetry [1] and laser Doppler imaging systems [2], as well as other applications including optical microscopy [3]. Common methods for producing these shifts include mirrors and gratings that are mounted on piezo-electric stages. These approaches are typically slow, being limited to a few tens of hertz. Acousto-Optic modulators (AOM) are also used and are much faster but are bulky and expensive. The significance of this project is that we should be able to create a low-cost, high speed system for frequency shifts with shifts in the region of kilohertz.

### **3. Background/prior work**

This work is based on work we published in [4]. What we recognized was that while most other methods for producing frequency shifts rely on what is essentially a continuously moving periodic disturbance (for example, an acoustic wave); a similar effect could be achieved using a quantized movement.

One of the technologies we considered was fast-switching ferroelectric liquid crystal (FLC). The dynamics and optical response of FLC is well known [5] and can show switching times of  $\sim 1$  microsecond when held at elevated temperatures. At room temperature several kHz are quite possible. We had planned to use a mixture called SCE9, developed by the corporation BDH which was later bought by Merck. However, we found that Merck no longer made this product so we approached Kingston Chemicals (Hull, UK) to make a FLC mixture with similar characteristics. An electrode structure was then designed and fabricated in transparent indium tin oxide (ITO) on a glass substrate to define a set of electrodes which could be used to apply fields across the FLC and cause it to switch from opaque to transparent states and back again. A schematic of the structure is shown in Figure 1. In order to fabricate the final device we needed to position the electrode structure over a glass slide which had been uniformly coated with ITO and would provide the other side of the FLC "cell" and then introduce the FLC in the gap. Although we originally envisioned gapping and filling the grating structure



ourselves, we decided to take advantage of the expertise of a commercial foundry. In September 2012 we arranged with Boulder Nonlinear Systems (BNS) (Lafayette, CO) to have the structure gapped and filled with the FLC at a gap width of 1.75 microns. This thickness, with this particular FLC, gives a nominal half-wave structure at  $\sim 630$  nm.

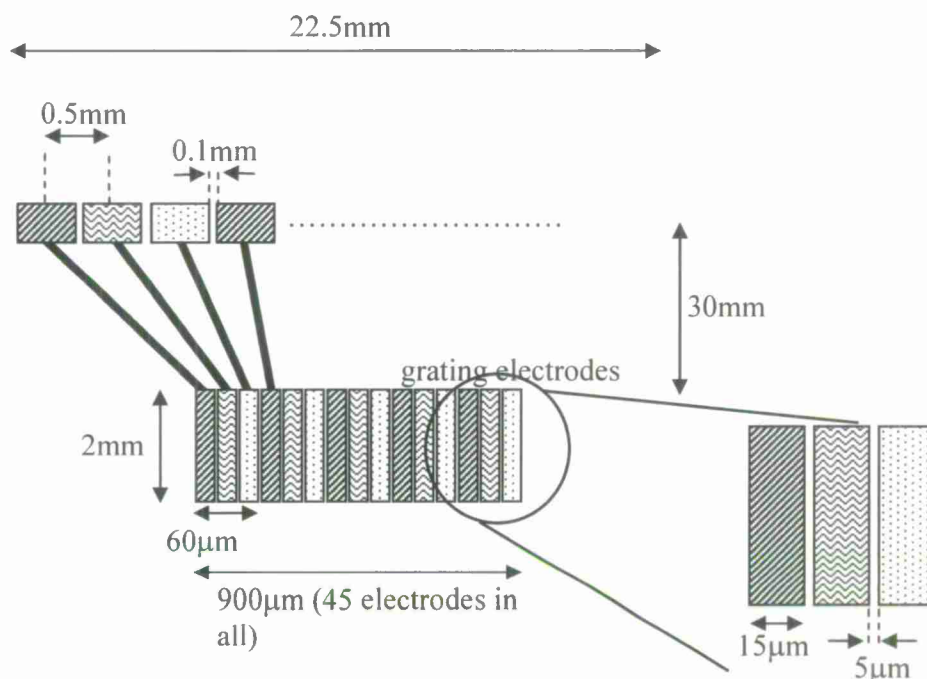
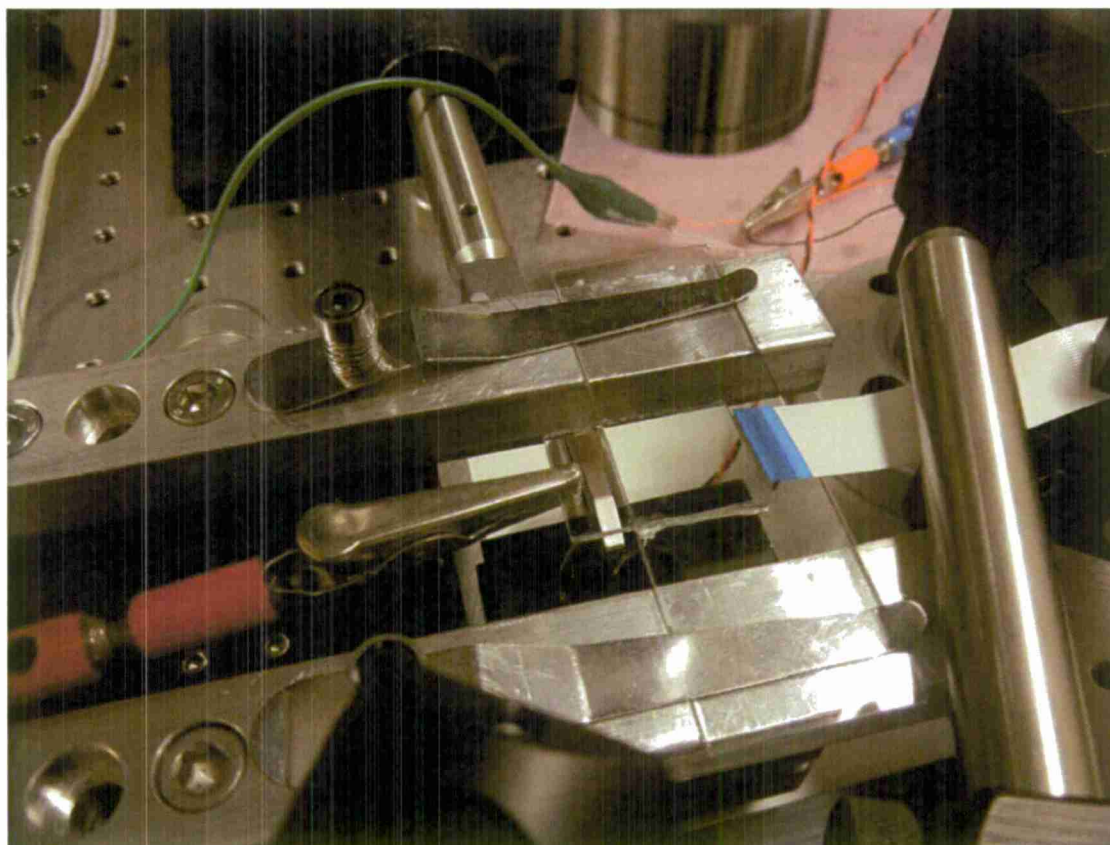


FIGURE 1. Schematic of the electrode structure to be used for addressing the FLC

A picture of the completed cell mounted in a test rig is shown in Figure 2



*FIGURE 2. The completed FLC device is seen here mounted on a test stage. An alligator clip at the left provides electrical contact to the uniform ITO-coated glass cover. The end of the ribbon cable (blue) for making contact to the individual pads of the electrode structure is at the right. No details of the electrode structure can be seen in this photograph.*

#### **4. Discussion of Results**

In order to assess the completed device we constructed the test-rig shown in Figure 3. Here polarized light is incident on the device from below and is either transmitted or blocked by a polarizer on the top depending on the state of the FLC. Transmitted light can be either intercepted using the camera – to form an image of the grating – or directed to a photodetector to make high speed measurements. One of the most severe problems we currently face is how to make electrical contact to the individual ITO pads that connect to the electrodes. Soldering to the ITO pads is not really feasible since they are too small and at the minute we just clamp a Molex ribbon cable in the region of the pads. In the future we will probably use an elastomeric connector. However, we are still able to make sufficient contact so that we can assess two parameters. These are the contrast ratio and the speed of FLC switching. An image of the grating taken through the camera is shown in Figure 4. We measured the contrast ratio (the ratio of the light through the FLC device in its “on” state to the light intensity in the “off” state) using laser light illumination and found it to be  $\sim 10:1$ . This is quite sufficient for our application.

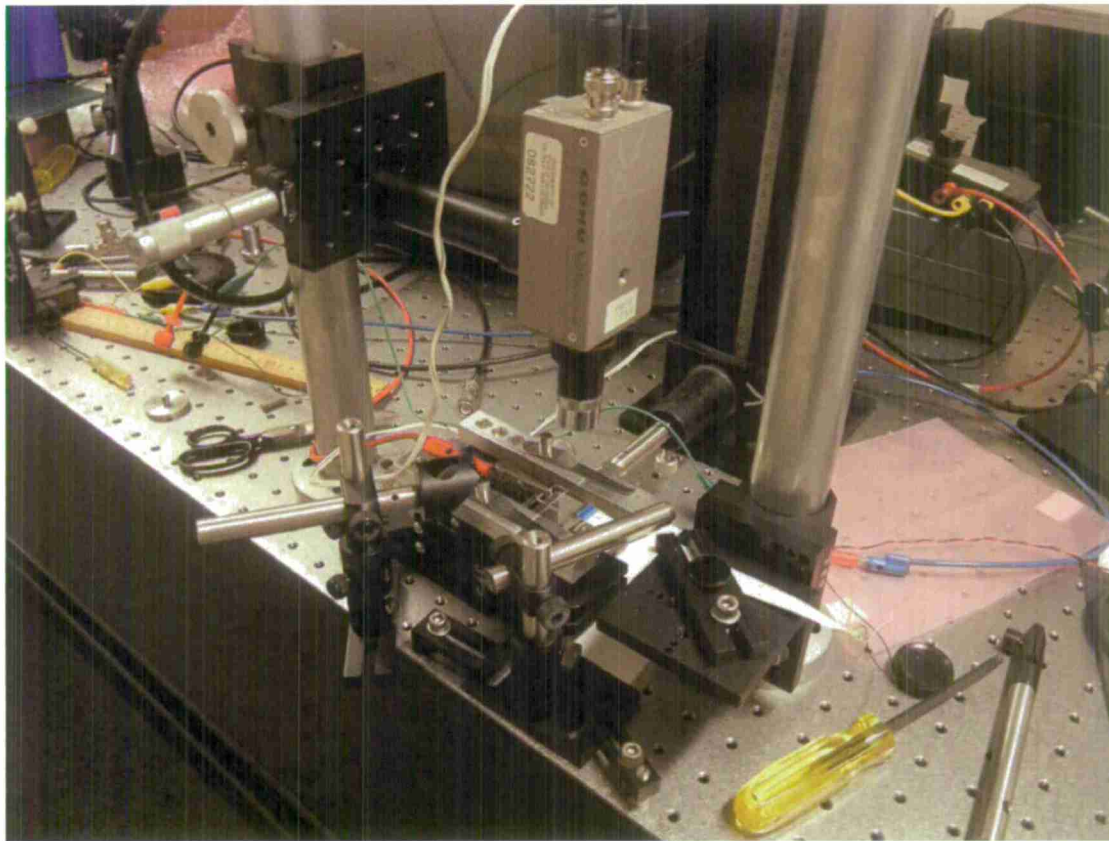


*FIGURE 3. Setup for testing the device. A laser diode is mounted underneath the test cell. Above the cell one can see a camera to image the grating.*

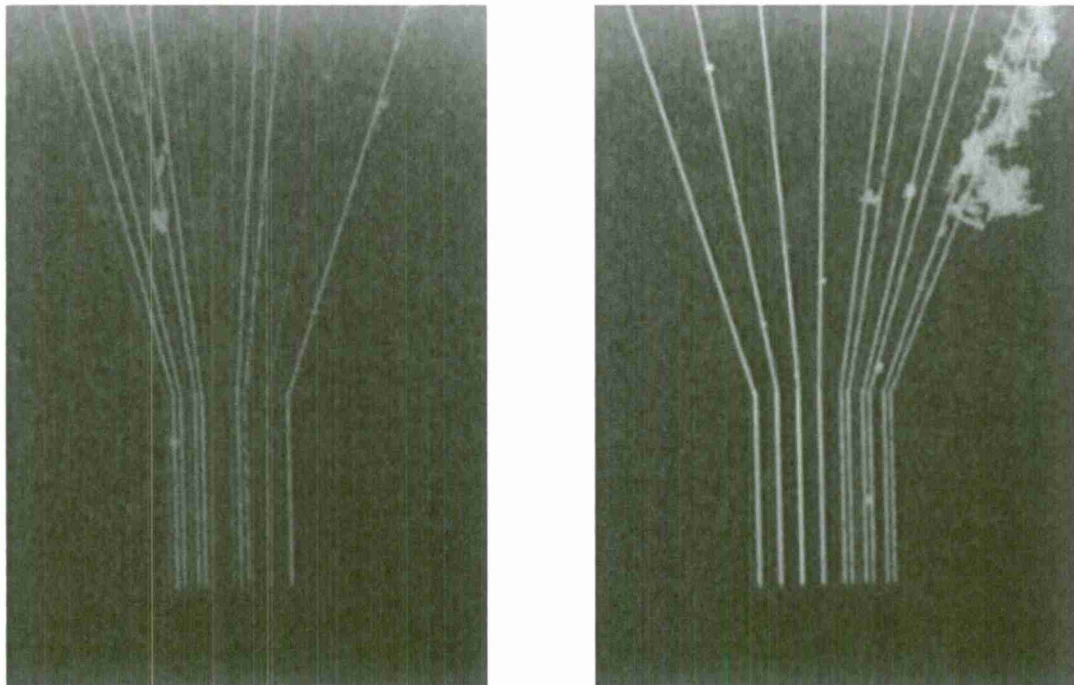


*FIGURE 4. These two photographs show how the state of the device changes when we drive it with a 5V pk-pk square wave at a low frequency (in this case 1 Hz). On the left the device is nominally “off” though there is still some transmission through the grating. To the right one can see several lines of the grating that are clearly in the “on” state.*

A critical feature of the final device is the speed at which it can switch. To assess this we illuminated the grating structure with light at  $\lambda = 633$  nm and directed the transmitted light to a photomultiplier tube. We drove the device with a 0 V offset square wave, varying both the amplitude and the frequency of driving. In order to characterize the switching of the liquid crystal we measure the response as the difference between the intensity in the “off” state and the intensity in the “on” state. Figure 5 shows a graph of the modulation as a function of the driving frequency. One can see that for fixed amplitude of the driving voltage the modulation decreases as the frequency increases. In order to make a useful device we believe that we would need to be able to get a reasonable modulation at frequencies in the order of 10 kHz. From the graph this appears to be achievable for switching voltages of around 20 V peak-to-peak.



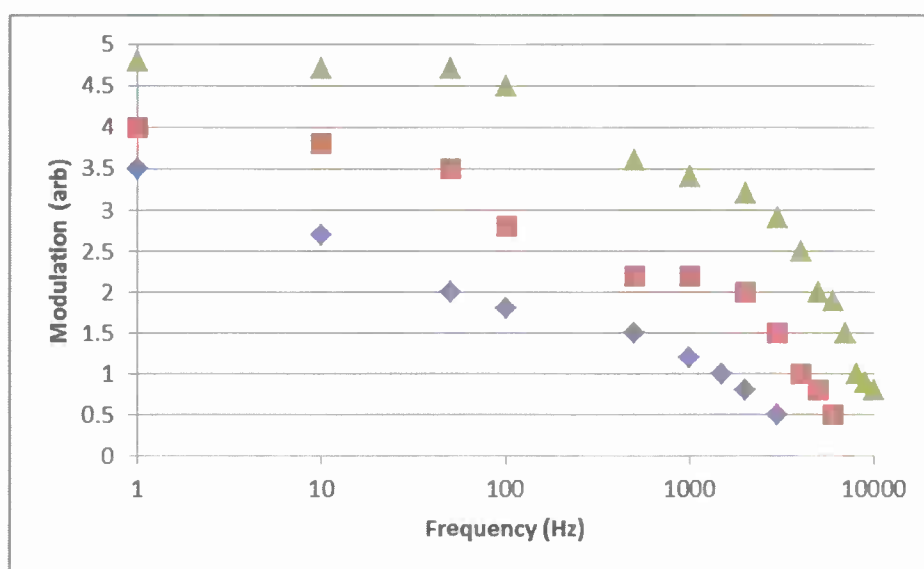


FIGURE 5: Response of the FLC device as a function of the driving frequency. The response of the FLC is characterized by the modulation which we define as the difference in the output from the phototube between the on and off states. (Since we are not imaging a specific line of the grating this number is not comparable to the contrast ratio). The data represents driving with a zero-offset square wave with peak-peak voltages of 5V (diamonds), 10V (squares) and 20V (triangles)

## 5. Future Work Planned

At this time (Nov/30/12) we are waiting for a computer board so we can generate the signals required to step the grating between its three different phase positions. Once we do this, and are able to make the necessary electrical contacts, we intend to demonstrate the use of the device in the context of laser Doppler imaging. The reason for picking this application is that laser Doppler imaging finds application in the relatively slow flows associated with, for example, blood circulation and thus is compatible with the relatively small frequency shifts obtainable with our FLC device.

As mentioned in the abstract we also looked into using a Texas Instruments DLP device for the switchable grating. We obtained a Pico Development kit which contains a DLP device along with associated control electronics and we bought a board-level computer for driving the device. So far we have been able to generate moving gratings but only at a speed of 10 Hz. It should be possible to display gratings at several kHz, but we have not been able to do that yet.

## 6. References cited

- [1] Drain, L. E. "The laser Doppler Technique" Wiley (1980)
- [2] Atlan, M and M. Gross. "Laser Doppler imaging, revisited." Rev. Sci. Inst. 77, 116103 (2006)
- [3] Zeiss Apotome for Optical Sectioning.



<http://zeisscampus.magnet.fsu.edu/tutorials/opticalsectioning/apotomemechanics/index.html>

[4] Sharpe, J. P. "A phase stepped grating technique for frequency shifting in laser Doppler velocimetry." Opt. Las. Engng 45, 1067 (2007)

[5] Elston, S. J. "The optics of ferroelectric liquid crystals" J. Mod. Opt. 42, 19 (1995)

**Scientific Visualization of Massive Underwater Science Data Acquired from  
Underwater Robots**

Principal Investigator:

**Zoë Wood, Computer Science**

California Polytechnic State University  
San Luis Obispo, CA

## **1. Abstract**

We present our research and results for developing scientific visualization computer applications for the purpose of visualizing underwater science and map data acquired from underwater robot deployments. Using computer graphics to create visualizations, the systems allows for real-time rendering of mission data, including science data as glyphs or volumes and the relevant contextual data, namely the underwater terrain from bathymetry and GIS data and the robot and mission path, in addition significant development focused on the reconstruction of geometric data (i.e. the underwater environment) from sensor data (namely sonar and stereo pairs). Working with colleagues in the fields of robotics, biology, and archeology, this project produced several systems for visualizing science data and map data collected by underwater robots. The PI and students working on the project have explored and researched the data representation and visualization of large terrain data-sets, visualization of science data, including scalar, volumetric, image and sonar data. The systems can be used by biologists and archeologists to explore their data and by robotics researchers to help plan future robot missions. The system has the potential for a broader impact for understanding, navigating and manipulating the ocean environment in general. Potential applications include biological sampling, shallow underwater imaging, oil spill investigation, underwater archeology, and search and rescue operations. Additionally, this project has made research contributions in science data visualization in an under water setting.

## **2. Project significance**

Oceans cover 70% of the earth's surface and are an important focus of scientific study and exploration. Oceans are a significant source of food for a large part of the planet. Due to the impact of global warming oceans are central to predicting how our climate will change in the future. To understand the ocean, scientists need a sense of not just physical characteristics, such as temperature and currents, but chemical, biological, and even geological parameters [10].

Scientific visualization computer applications generate visual representations of large and complex sets of science data. These types of applications allow scientists to gain greater knowledge and insight into their data. For example, the visualization of environmental data, such as currents and temperature, is of particular interest to biologists when trying to understand how complex variables interact. Modern robotics and sensors expand the ability to collect environmental data, thus, the size and variety of these data sets have likewise grown. The collected data are deposited into files and databases where they sit in their separate and unique formats. Without easy to use visualization tools, it is difficult to understand and interpret the information within these data sets. Additionally, marine archeologists wishing to study historical water systems rely on underwater robot deployments to gather data and map environments that can be dangerous for humans to explore.

Working with colleagues in the fields of robotics, biology and archeology, this project has focused on creating several systems to create interactive visualizations of underwater data gathered by underwater robots, such as, Autonomous Underwater Vehicles (AUVs), Remotely Operated Vehicles (ROVs) and gliders. The building of these systems required the implementation of various methods taken from scientific visualization, real-time rendering, scattered data interpolation, surface reconstruction and uncertainty visualization. As underwater robots are equipped with more and more sensors, they can generate large amounts of data and information about the underwater environments on our planet. In order to make this data useful, scientific visualization can be employed to help scientists visualize and explore this acquired data.

The PI and students have worked with robotics researcher, Dr. Chris Clark (Harvey Mudd College), marine biologist Kasper Henke (University of Southern Denmark (SDU)) and Marine Archeologist Professor Timothy Gambin (University of Malta). These systems are under use to explore science data (oxygen diffusion) and to visualize water system maps (geometric data). The systems have the potential for broader impact for understanding, and conveying educational information about the ocean environment. Potential applications include biological sampling, shallow underwater imaging, oil spill investigation through visualization, and underwater archeology. Three research publications related to the visualization of underwater data have been published during this research and three others are under review or under preparation.

### **3. Background/prior work**

An initial scientific visualization system was built and used for one particular underwater robot, the Slocum Glider, in conjunction with NORUS, the North America-Norway educational program. This existing application was developed under the supervision of the PI, with a Cal Poly master's student, Daniel Medina [1]. This computer application allowed for real time visualizations of the underwater environment, the robot and the science data acquired from the glider missions. The system developed, addresses the problem of creating an interactive underwater visualization system capable of handling very large and diverse sets of science data collected by underwater robots such as the Slocum Glider. The system also provides configurability for individual visualization, such as choosing which specific types of science data the user would like to see at a given time. During this research period, this work was documented, published and presented at the International Offshore and Polar Engineering Conference, [17]. This earlier work has greatly been enhanced by current work detailed below.

Prior to this project, the PI has worked on several scientific visualization research projects, which inform this research project. Notably, at UC Santa Cruz, the PI worked on a very large environmental visualization project in the Monterey Bay, REINAS, which included massive science data, from both the land and sea. This work is summarized in the paper, "Integrated Visualization of Real-time Environmental Data" [2]. The PI's work on REINAS included exposure to numerous different environmental data types and visualizations, coming from numerous sensors, such as wind velocities, water and air

temperature, all of which are displayed as glyphs on the terrain.

In addition, the PI has worked on several visualization systems at Cal Poly related to archeological applications. These applications addressed the need to compute the cost of traveling a given terrain on foot and then creatively visualized relevant paths across the terrain or geographical regions of interest [3], [4], and [5]. These systems included the visualizations of the relevant GIS terrain. Of note, one of these projects [4], addressed the problem of computing foot paths across massive terrain data, including the GIS for the entire Continental United States, a data set containing over 19 billion data points [4]. This work utilized a combination of multi-threading, multi-resolution terrain representations and terrain caching in order to compute paths and visualize the terrain and paths across this massive GIS dataset.

Additional, work by the PI in scientific visualization includes work on visualizing force coloring on physically based animations in order to assist the user to select appropriate material and force parameters [6]. This work includes intelligent histogram quantification in order to best map the force ranges to the color range. This kind of algorithm is needed in any scientific visualization work in order to best highlight the regions of interest for the user. Finally, the PI has several related projects in real-time rendering applications for both scientific and entertainment applications [7] [8], and [9]. This work can help inform some of the trade-offs and options when designing our scientific visualizations to be both realistic in terms of light transport and real-time rendering while dealing with massive amounts of science data. This work includes work on large volumetric datasets [8]. Related work by other researchers includes a few specific marine visualization systems [11-16].

#### **4. Discussion of Results**

This project has broadly focused on underwater data visualization from data acquired from robot deployments in the underwater setting. This work has included the reconstruction of geometry from robot sensors (sonar and stereo pairs), scientific visualizations of science data measured from sensors (including terrain to contextualize the visualizations). This work includes explorations of surface reconstruction that includes a model of the uncertainty of the reconstruction, the novel application of geometric details using stereo pairs, explorations of the data representation (in terms of scale) for terrain data and the exploration of efficient real-time techniques to visualize volume data (of interpolated science data) (including exploration into lighting algorithms for volumetric data). This project has allowed for the development of new scientific visualization algorithms, the education of students in research related to scientific visualization and benefited marine science, marine archeologists and robotics faculty. This project has resulted in three peer-review conference publications (published and presented), in addition to three current publications (one which was recently accepted for publication, one under review and one under development). Two master's students have completed thesis work related to this project and a third is scheduled to defend and graduate in Winter quarter 2013 in addition, four undergraduate students have actively worked on research for this project.



### Objectives for this project have included:

- The creation of a compelling, efficient, and easy to use interactive systems for visualizing large sets of science data collected by underwater robots. Including:
  - The visualization of terrain data. In order to visualize terrain data, first high quality terrain data must be readily available. As there is limited resolution GIS and bathymetry data available, a system was developed to create height maps (which can be visualized as 3D data) from 2D topography maps. For example, for a particular robotic mission at Hopavågen Bay, Norway in which oxygen diffusion data was acquired via AUV deployment, only limited GIS data was available. A system was developed that could read in 2D topographic maps, segment the data and then produce a height field which could then be rendered as 3D terrain including coloring from satellite images. See Figure 2, for example of the stages of the algorithm and out put.
  - Integration of real-time rendering techniques to enhance the visual output of the system. For example, integrating satellite data into the rendering of the terrain to further cue the user to understand the environment (Figure 1 and 2), and real-time rendering of interpolated underwater data as a volume (not only as glyphs) (See Figure 3)
  - Enhancements of the visualization of isosurfaces of scalar data to allow for transparency to show all surfaces with similar scalar values. Figure 4 shows a comparison of isosurface visualizations using the prior system and the current system. As the science data in the underwater setting tends to form in sheets that can be nested, the visualization must account for this nesting. We have explored transparency and real-time volume rendering techniques to better expose the sheets of self-similar science data within a given region. A master's student also researched using offline volume rendering to enhance volumetric visualization of non-homogenous data [21].

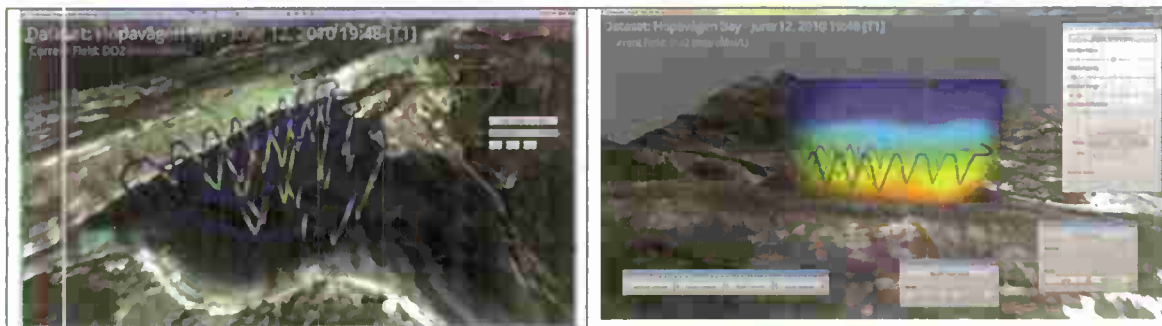


Figure 1 – New visualizations of oxygen diffusion data from Hopavågen Bay, including both the surrounding terrain and glyphs showing the science data acquired from an AUV deployment.

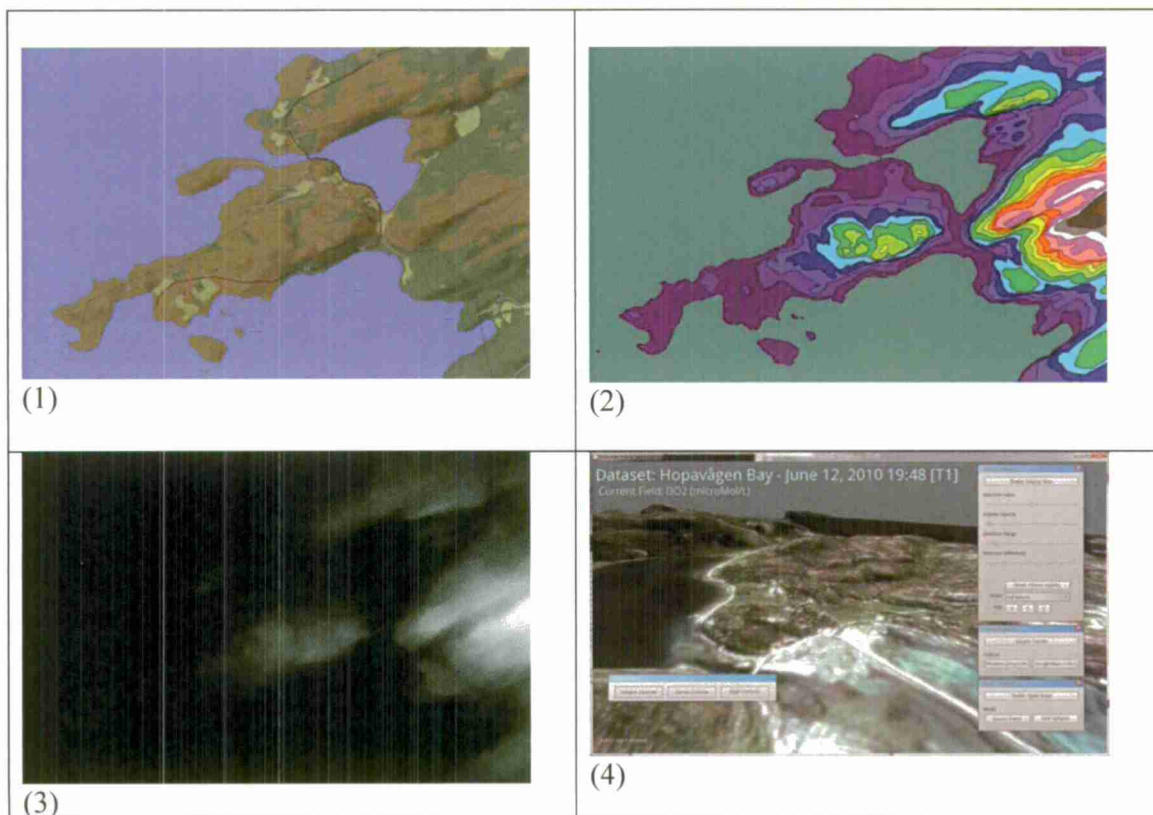
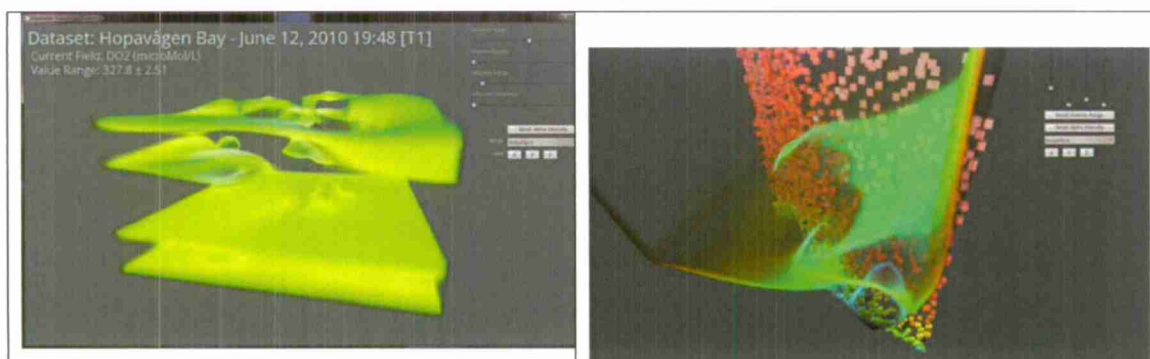


Figure 2 – Creating terrain contour data from a 2D topological map with limited user input. (1) Original source map (2) Posterized image: the program is fed a list of color values and associated height values. The image is cleaned so that only pixels of these colors and the dividing (contour) color remain in the image. The main purpose of this step is to remove anti-aliasing, which will interfere with further stages. (note, initial re-coloring done manually in Photoshop) (3) Final height map is generated pixel by pixel, interpolating based on the distance between next lowest and next highest contours. (4) 3D rendering of height map and with satellite image determining the color



|     |     |
|-----|-----|
| (a) | (b) |
|-----|-----|

- Figure 3 – New visualizations of oxygen diffusion data from Hopavågen Bay, including real-time visualizations of volume data (a) and volume data and glyphs (b).
- Investigation and development of algorithms to handle data acquired from new sensors on the underwater robots including:
  - Reconstruction of geometric models from sonar [18, 19] and stereo image pairs. As geometric data acquired via a scanning process can suffer from holes due to errors in the acquisition process, noise, or challenges in merging multiple inputs together into a unified map, we developed a straightforward algorithm to fill holes in incomplete evidence grids representing acquired geometric data. In addition, we developed methods to apply learning in order to statistically evaluate the proposed hole filling algorithm. This analysis validates our proposed method for hole filling and additionally enables the construction of a probability distribution function to represent the accuracy of the filled data per model. During surface reconstruction, this function can be used to visualize the certainty of the filled geometry via transparency and coloring giving the user an understanding of the data's accuracy. See Figure 5 for an example of the results of this work.
  - Although effective, sonar has a limited resolution and omits many fine geometric details. We also have developed a preliminary solution towards the reconstruction of fine details of organic underwater shapes using stereovision. These fine details can be integrated into 3D models reconstructed from sonar to create a more visually accurate model. We present initial results, shown in Figure 6 of a reconstruction of fine level geometry from stereo image pairs.
  - Creating animated visualizations of a shark's path (acquired from acoustic sensors on an AUV). See Figure 7 for an example of an image from the animation. This work is a part of a master's student's thesis (expected graduation Winter 2013).
- Investigation and development of algorithms to handle the visualization of large terrain/bathymetry data. Work using images for terrain at a large distance from the camera (image imposters) was completed as a part of a student's master's thesis [20] and an undergraduate student continues work on exploring multi-resolution terrain representations.

|  |  |
|--|--|
|  |  |
|--|--|

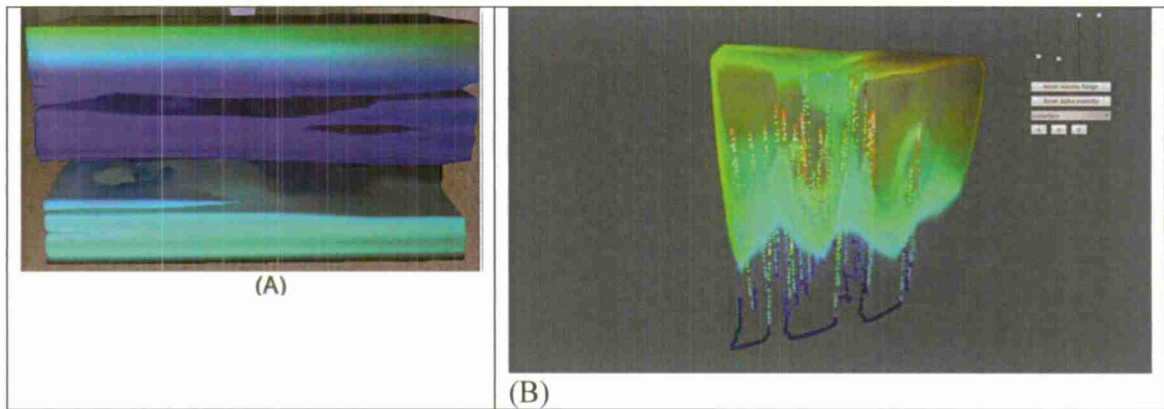


Figure 4 – Example visualizations created with the system as the start of the grant period. On the left is a similar visualization with the current system, which uses real-time volume visualization methods allowing for a transparent view more conducive for underwater data visualizations.

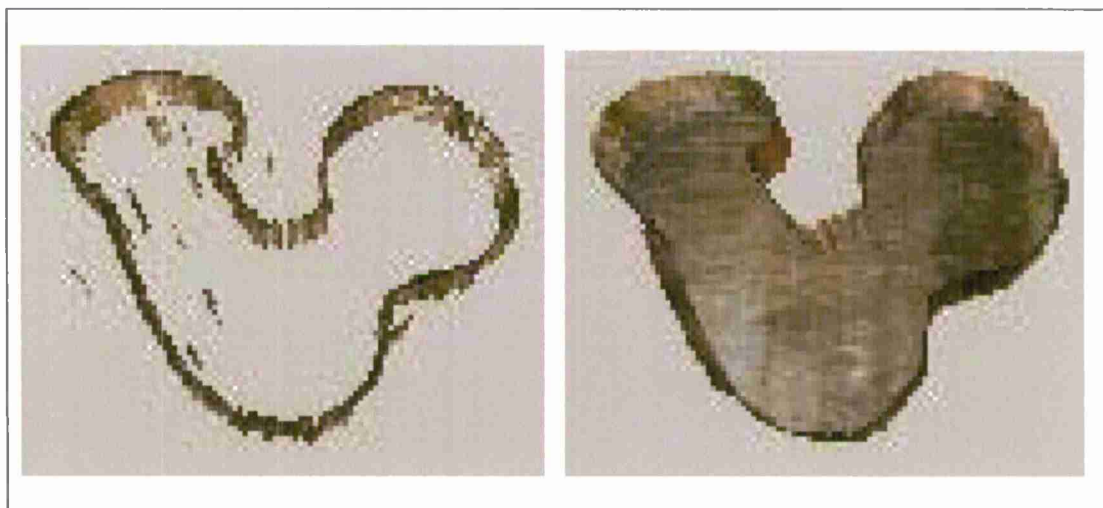


Figure 5 – Surface reconstruction from sonar data of an ancient underwater storage system, on the left is the reconstruction without the application of our systems hole filling. The right shows the final model, including uncertainty visualization for the filled regions with uncertainty derived from our algorithm's application of statistical learning and the construction of a probability distribution function to represent the accuracy of the filled data per model.



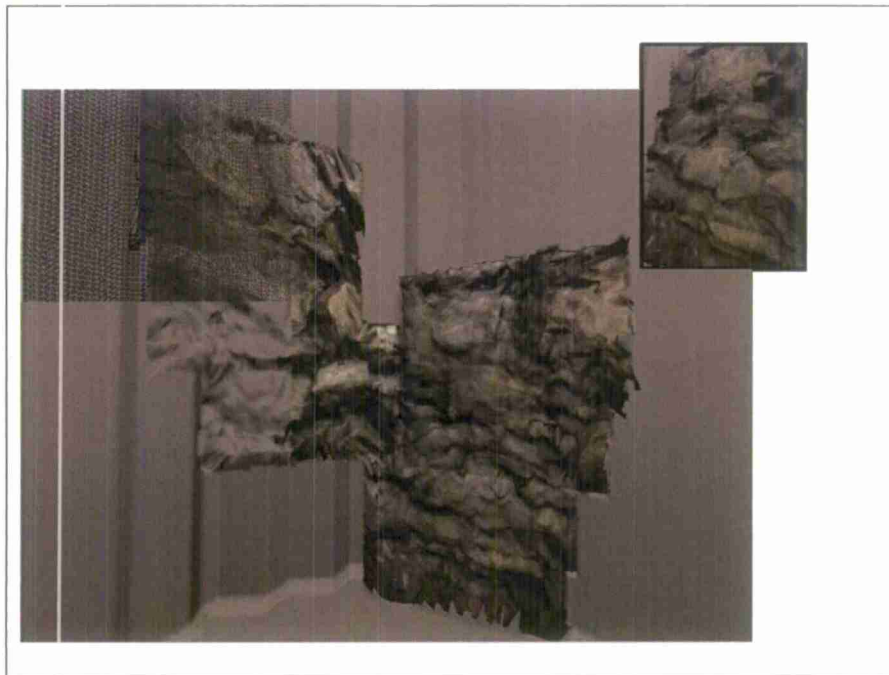


Figure 6 – Surface reconstruction from sonar data with the integration of fine detailed geometry acquired from stereo pair disparities.

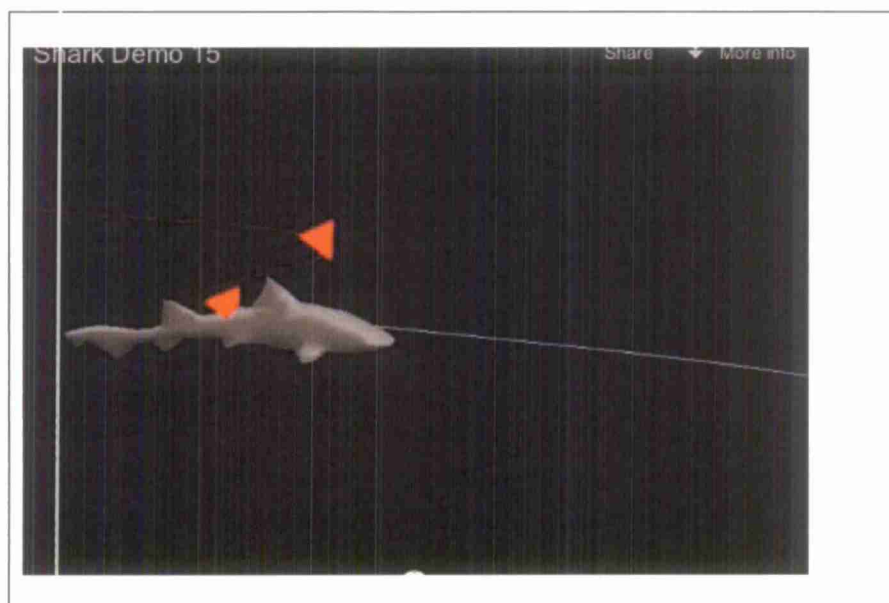


Figure 7 – View from the animation system to visualize data of a shark swimming, where the path data was acquired from acoustic sensors on an AUV tracking the shark's path in an open ocean environment.



Publications, which were accepted and presented at peer-reviewed conferences related to this research work, include:

- “Real-Time Visualizations of Ocean Data Collected By The NORUS Glider in Svalbard, Norway”, Daniel Medina, Mark Moline, Christopher Clark, and Zoë J. Wood, Proceedings of the Twenty-first (2011) International Offshore and Polar Engineering Conference Maui, Hawaii, USA, June 19-24, 2011
- “Surface Reconstruction of Maltese Cisterns Using ROV Sonar Data for Archeological Study”, C. Forney, J. Forrester, B. Bagley, W. McVicker, J. White, T. Smith, J. Batryn, A. Gonzlaez, J. Lehr, T. Gambin, C. Clark and Z. Wood Proceedings of the 7th International Symposium on Visual Computing (Published in Advances in Visual Computing: Lecture Notes in Computer Science)
- “Mapping and Visualizing Ancient Water Storage Systems with an ROV: An Approach Based on Fusing Stationary Scans within a Particle Filter”, McVicker, W., Forrester, J., Gambin, T., Lehr, J., Wood, Z.J., and Clark, C.M., Proc. of the IEEE International Conference on Robotics and Biomimetics (ROBIO2012), China, Dec. 14-18, 2012.

In addition, three other papers related to this work are in various stages of preparation and review, (one was just accepted for publication, one was just submitted for review, and yet another is under preparation).

Two students completed master's thesis work related to this project and a third is finalizing their thesis, graduating Winter 2013:

- “An Approach to Point Based Approximate Color Bleeding with Volumes”, Chris Gibson
- “Terrain Impostors”, William Hess
- “Shark Sim: A Procedural Method of Animating Leopard Shark Triakis Semifasciata Based on Location Data”, Katherine Blizzard (expected January 2013)

In addition, four undergraduate students have actively worked on the various systems associated with this project, Jeffrey Forrester, Erik Nelson, Timothy Peters, and Ian Dunn.

## **5. Future Work Planned**

The research started in this C3RP proposal is actively being pursued as follows:

- Continued work on 3D surface reconstruction of underwater geometry (using sensors such as sonar, laser scanner, and stereo pair data). In particular, for the 3D setting, underwater data typically suffers from poor resolution, noise and large gaps in the data. We are actively exploring

using level set methods to address these challenges and we wish to develop ways to integrate uncertainty computations into the level-set reconstructions to best convey uncertainty to the end user. In addition, the use of small, reasonably priced underwater cameras such as goPro cameras offers an exciting way to enhance the resolution of sonar data for underwater geometry reconstruction, however, such cameras and the underwater setting create a challenge for feature matching for disparity map generation. We are actively exploring enhancements (such as color space shifts and varying lighting to enhance the disparity maps generated from such cameras. Related to the use of disparity maps, is the challenge of then integrating this high resolution geometry with the lower resolution geometry from the sonar maps. We intend to explore the integration of these various resolution data in addition to exploring the application of learning and probabilistic modeling to generate high resolution displacements from a small input sample data (where applicable).

- Continued work on visualization of science data acquired via robot deployments (especially related to using real-time methods to produce compelling interactive visualizations of terrain and volume data in conjunction). We are exploring the challenge of comparing data from multi-deployments in order for the biologists to better see how the science data changes over time. This requires careful localization of the various data sets to guarantee that the spatial comparison is accurate.
- Continued work on the scale of the acquired data and the application of data mining to visualize the data of highest importance.

## 6. References cited

- 1) D. Medina, "Real-Time Visualizations of Ocean Data Collected by the NORUS Glider", Cal Poly Master's Theses and Project Reports (MS #1365), June 2010, <http://digitalcommons.calpoly.edu>
- 2) E. Saxon, Z. Wood, M. O'Neil, C. Oates, J. Story, S. Djurcilov and A. Pang, "Integrated Visualization of Realtime Environmental Data", Proceedings of the Spring Conference on Computer Graphics, 1997, Slovakia
- 3) B. Wood and Z. Wood, "Energetically Optimal Travel across Terrain: Visualizations and a New Metric of Geographic Distance with Archaeological Applications", Proceedings of SPIE Electronic Imaging, San Jose, January 2006
- 4) A. Tsui and Z. Wood, "Energetic Path Finding Across Massive Terrain Data", Proceedings of ISVC, 2009
- 5) Z. Wood, G. Hoffman, and M. Wazny, "Finding Good Paths: Applications of Least Cost Caloric Path Computations", Proceedings of CATA, 2010
- 6) J. Skorupski, Z. Wood and A. Pang, "Interactive Thin Shells - A Model Interface for the Analysis of Physically-based Animation", Proceedings of CAINE, San Francisco,

CA, November 2007

- 7) Z. Wood, H. Hoppe, M. Desbrun and P. Schröder, "An Out-of-core Algorithm for Isosurface Topology Simplification", ACM TOG, April 2004
- 8) M. Barry and Z. Wood, "Direct Extraction of Normal Mapped Meshes from Volume Data", Proceedings of ISVC, 2008 and Lecture Notes in Computer Science (Advances in Visual Computing), Springer Verlag, 2007
- 9) H. McKenzie Chapter, "Textured Hierarchical Precomputed Radiance Transfer" Cal Poly Master's Theses and Project Reports, June 2010, <http://digitalcommons.calpoly.edu>
- 10) J. G. Bellingham and M. Godin. Exploring ocean data. SIGMOD Rec., 37(2):78–82, 2008
- 11) D. P. Brutzman. "A virtual world for an autonomous underwater vehicle". PhD thesis, Naval Postgraduate School, December 1994
- 12) P. Chapman, D. Wills, P. Stevens, and G. Brookes. "Whole field modelling (case study): effective real-time and post-survey visualization of underwater pipelines", In VIS '99: Proceedings of the conference on Visualization '99, pages 445–448, Los Alamitos, CA, USA, 1999. IEEE Computer Society Press.
- 13) P. Chapman, D. Wills, P. Stevens, and G. Brookes. "Real-time visualization of the clear-up of a former U.S. naval base", In VIS '00: Proceedings of the conference on Visualization '00, pages 505–508, Los Alamitos, CA, USA, 2000. IEEE Computer Society Press.
- 14) K. Grochow. "Cove: a visual environment for multidisciplinary science collaboration", In GROUP '09: Proceedings of the ACM 2009 international conference on Supporting group work, pages 377–378, New York, NY, USA, 2009. ACM.
- 15) M. P. McCann. "Creating 3d oceanographic data visualizations for the web", In Web3D '02: Proceedings of the seventh international conference on 3D Web technology, pages 179–184, New York, NY, USA, 2002. ACM.
- 16) M. P. McCann. "Using geovrml for 3d oceanographic data visualizations", In Web3D '04: Proceedings of the ninth international conference on 3D Web technology, pages 15–21, New York, NY, USA, 2004. ACM.
- 17) Daniel Medina, Mark Moline, Christopher Clark, and Zoë J. Wood, "Real-Time Visualizations of Ocean Data Collected By The NORUS Glider in Svalbard, Norway", Proceedings of the Twenty-first (2011) International Offshore and Polar Engineering Conference Maui, Hawaii, USA, June 19-24, 2011

- 18) C. Forney, J. Forrester, B. Bagley, W. McVicker, J. White, T. Smith, J. Batryn, A. Gonzlaez, J. Lehr, T. Gambin, C. Clark and Z. Wood , "Surface Reconstruction of Maltese Cisterns Using ROV Sonar Data for Archeological Study", Proceedings of the 7th International Symposium on Visual Computing (Published in Advances in Visual Computing: Lecture Notes in Computer Science)
- 19) McVicker, W., Forrester, J., Gambin, T., Lehr, J., Wood, Z.J., and Clark, C.M., "Mapping and Visualizing Ancient Water Storage Systems with an ROV: An Approach Based on Fusing Stationary Scans within a Particle Filter", Proc. of the IEEE International Conference on Robotics and Biomimetics (ROBIO2012), China, Dec. 14-18, 2012.
- 20) C. Gibson, " An Approach to Point Based Approximate Color Bleeding with Volumes ", Cal Poly Master's Theses and Project Reports, [http://digitalcommons.calpoly.edu/csse\\_fac/196/](http://digitalcommons.calpoly.edu/csse_fac/196/)
- 21) W. Hess, "Terrain Imposters" Cal Poly Master's Theses and Project Reports, <http://digitalcommons.calpoly.edu/theses/453/>

**Facile covalent surface functionalization of multiwalled carbon nanotubes with poly (2-hydroxyethyl methacrylate) and interface related studies when incorporated into epoxy composites**

Principal Investigator:

**Keith Vorst Ph.D., Industrial Technology**

California Polytechnic State University  
San Luis Obispo, CA

Co-Investigators:

**Greg Curtzwiler and Andreas Plagge**

School of Polymers and High Performance Materials, University of Southern Mississippi

**John Story**

Cameron School of Business, University of St. Thomas



## Abstract

Carbon nanotubes (CNTs) have seen increased interest from manufacturers as a nano fiber filler for the enhancement of various physical and mechanical properties. A major drawback for widespread commercial use has been the cost associated with growing, functionalizing, and incorporating CNTs into commercially available polymeric matrices. Accordingly, the main objective of this study was to investigate the effects of adding commercially viable functionalized multiwalled carbon nanotubes (MWCNT) to a commercially available epoxy matrix. The mechanical behavior of the nanocomposites was investigated by mechanical testing in tensile mode and fractures were examined by scanning electron microscopy (SEM). The thermal behavior was investigated by differential scanning calorimetry (DSC) and thermogravimetric analysis (TGA). Molecular composition was analyzed by attenuated total reflectance Fourier transform infrared spectroscopy (ATR-FTIR). Mechanical testing of the epoxy/functionalized-MWCNT indicated that the 0.15 wt% functionalized MWCNT composite possessed the highest engineering stress and toughness out of the systems evaluated without affecting the Young's Modulus of the material.

## Introduction

The addition of carbon nanotubes (CNTs) to polymer matrices to increase the thermal, mechanical, and electrical properties of the resulting composite has been well documented. [1-16] For CNTs to effectively enhance the properties of a composite, the CNTs must be deagglomerated, well dispersed, and have sufficient interfacial interaction with the host matrix [3, 4, 8-10, 13, 15, 17-23]. Both theoretical and experimental studies indicate that optimizing the polymer-CNT interface is essential to maximize substrate properties [3, 4, 18, 24]. The most useful approach to increase interfacial interaction is chemical modification of the CNT to create functionality that has the potential to crosslink into the host matrix [3, 4, 25, 26]. A CNT functionalization of only 1% of the surface's carbon atoms covalently linked into the host matrix can increase interfacial shear strength by over an order of magnitude without significantly decreasing CNT stiffness due to disruption of conjugation [4, 27]. Several approaches have been employed to overcome the obstacles associated with CNT dispersion and deagglomeration with promising results [3, 4, 8, 19, 28-30].

However, many of the processes developed to incorporate CNTs into high performance composites have difficulties when producing in commercial amounts due to the problems associated with incorporating CNTs into polymers. Carbon nanotubes have high aspect ratios and surface areas (over 1000 m<sup>2</sup> per gram) and the high polarizability of the extended  $\pi$ -electron cloud yields large van der Waals forces (estimated to be 500 eV/micron of tube length) causing agglomeration thereby making complete exfoliation of bundled nanotubes a difficult challenge.[3, 4, 6, 10, 13, 15, 19, 22, 31] ENREF 1. This tendency leads to a decrease of most of the critical properties of well-distributed CNTs. To form stable suspensions of CNTs in polymeric systems, the CNTs must be isolated, followed by a surface modification to inhibit re-agglomeration and increase interactions with the host media for the application of interest [3, 4, 19, 28, 32, 33]. The deagglomeration process is labor intensive and time consuming, hence the ongoing inability to practically apply the potential of CNTs to commercial reality, even on a relatively small scale.

Many studies have indicated that chemical functionalization of the carbon nanotube sidewalls can significantly increase the interactions with the host matrix resulting in increased levels of dispersion [1, 4, 7, 8, 13, 15, 19, 21, 24, 27-30, 32-36]. For example, the addition of amino groups to double walled-carbon nanotubes (DWCNTs) increased dispersion over non-functionalized DWCNTs and increased fracture toughness over neat epoxy resin at loadings of approximately 1% [4]. Several labs have developed methods to achieve useful CNT material. However, the time consuming process of functionalization and preparation in a way that make production systems practical or economically viable, except in the most specialized applications, has yet to be realized. For example, Nguyen et al and Wu et al fabricated isocyanate functionalized MWCNTs and polystyrene functionalized MWCNTs that required 48 hr and 4 hr, respectively, considering experimental setup, processing, and purification steps [29, 30]. This setup and process time is still considered too costly for full production scale by many manufacturers.

The high aspect ratio, high strength, low density, and high stiffness are especially attractive attributes when considering use of CNT for polymer additives [3, 4, 8, 13, 15, 16, 18, 19, 21]. The potential mechanisms for mechanical enhancement include CNT pull-out (matrix debonding), CNT bridging, and crack deflection [3, 24, 25, 28]. CNT bridging, in particular, causes the most enhancement in mechanical properties as a result of the high mechanical properties of the CNT. As the crack propagates through the polymer matrix, it approaches a CNT and transfers the load which dissipates energy and inhibits propagation [24, 28]. For the CNT-bridging mechanism to dominate during a fracture event, the length of the CNT must be above a critical length as well as have sufficient interaction with the matrix and a high degree of dispersion [24]. Below these critical parameters, the dominating mechanism will probably be CNT pull-out. Above different critical conditions, the dominating mechanism will be a combination of CNT pull-out and rupture [24].

The surface morphology of fractured, brittle materials, such as crosslinked epoxy networks, can be related to the macroscopically measured fracture properties as the released elastic energy can be equated to the surface energy for creating new crack surfaces [16, 37, 38]. In general, tougher materials possess rougher fractured surfaces; this correlates to requiring more work to propagate the crack [16, 26, 37-39]. The correlation between a fractured surface morphology and measured macroscopic properties of more ductile materials may be more complex due to plastic deformation as the work related to plastic deformation is much higher than the surface energy of the newly formed surface [37]. When a material is less prone to fracture, it will exhibit more variation within the microstructure compared to a surface that contains more smooth planes [16, 17, 38]. Perez et al reported significantly rougher surfaces for tougher CNT based composites when compared to the neat epoxy [18]. Rougher surfaces have also been attributed to a good adhesion between the host matrix and the nano-particle [17, 26, 33].

Previous research has suggested that coating MWCNTs with polymeric hydroxyethyl methacrylate increased the interactions between MWCNTs and a polyurethane matrix, which was realized via a commercially viable process [32]. Accordingly, the main objective of this study was to investigate the effects of adding commercially viable functionalized MWCNTs to a commercially available epoxy matrix for employment according to the manufacturer's cure schedule. The authors believe the functionalization process described in the current research to be more commercially viable than those described in the literature due to reduced

functionalization time, reduced cost of starting materials, facile methodology, and ease of scale up manufacturing. The functionalization methodology has also allowed for the realization of enhanced mechanical and thermal properties and reduced carbon nanotube concentrations than those observed in the literature. The mechanical properties were determined by electromechanical testing in tensile mode and crack propagation was studied post-fracture by scanning electron microscopy (SEM). The thermal transitions and thermal decomposition behavior were determined by differential scanning calorimetry (DSC) and thermogravimetric analysis (TGA), respectively. The molecular composition of the surface was investigated by attenuated total reflectance Fourier-transform infrared spectroscopy (ATR-FTIR).

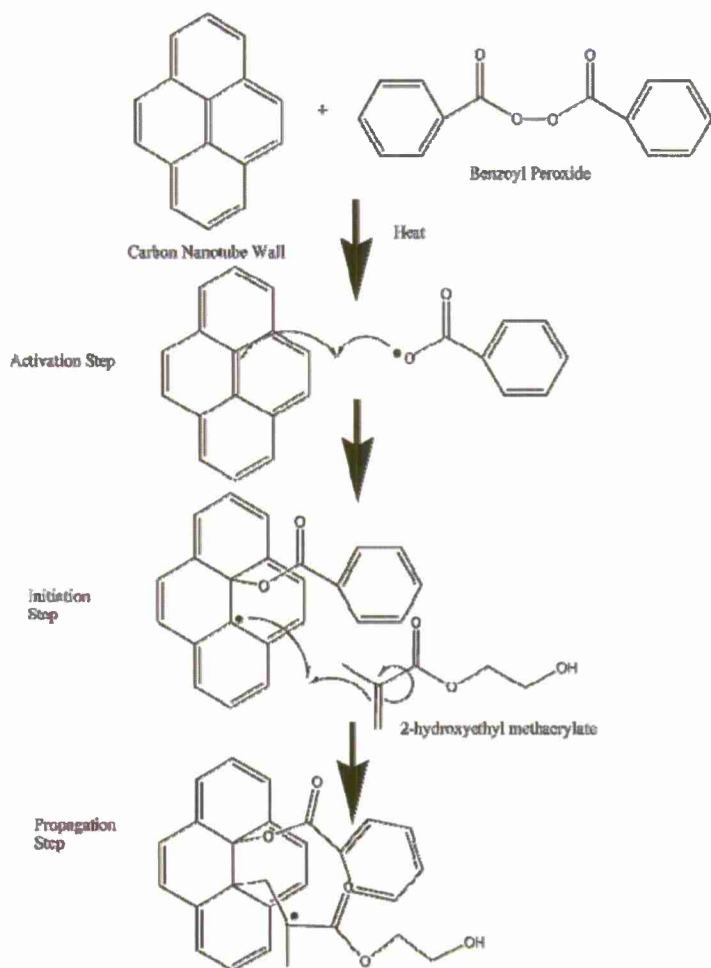
## Methods and Materials

### *Materials*

Purified, unbundled, multi-walled carbon nanotubes (MWCNT) were used as received from Ahwahnee Technology (San Jose, CA). The epoxy resin was EPON 8111 (Resolution Performance Products, Pueblo, CO) and had an epoxy equivalent weight (EEW) of 300-320 g/eq and a viscosity of 800-1100 cP at 25 °C. The curing agent was Ancamine triethylene tetramine (TETA) (Air Products, Allentown, PA) and had active hydrogen equivalent weight of 27 g/eq and a viscosity of 20 cP at 25 °C. All other items were used as received from commercially available sources and used without further purification.

### *Fabrication of Poly (hydroxyethyl methacrylate) Coated Multi-Walled Carbon Nanotubes*

A 25 mL round bottom flask was loaded with MWCNT (380 mg), 2-hydroxyethyl methacrylate (HEMA) (10.0 g), tetrahydrofuran (THF) (10.0 g), ethyl acetate (10.0 g), and a magnetic stir bar. A 0.25 inch diameter, tapered tip sonication horn was submerged in the liquid. The mixture was sonicated with a Misonix Microson XL 2000 (Farmingdale, NY) equipped with a 0.25 inch tapered tip at 20 watts for 5 min. Benzoyl peroxide (BPO) (100 mg) was dissolved in THF (1.0 g) and added to the reaction flask after the solution was allowed to cool to room temperature. The system was purged with nitrogen for 15 min, and then placed in an oil bath at 80 °C for 10 min. No control experiments were performed as previous research has indicated that under the conditions employed in this study, the polymer is covalently attached to the MWCNT surface as according to the proposed mechanism in Scheme 1 [32].



Scheme 1. Proposal of mechanism for surface initiated polymerization of hydroxyethyl methacrylate from multiwalled carbon nanotube.

The highly viscous liquid was washed with a 50 vol% of THF/ethyl acetate solution three times. A wash cycle consisted of sonicating at 20 watts for 30 seconds in the washing solvent followed by 10 min of centrifugation at 4000 rpm. The supernatant was decanted off into a glass bottle and the pellet was re-suspended in fresh solvent via tip sonication at 20 watts for 30 seconds. The poly (HEMA) coated MWCNTs were determined to have a functionality of 30 wt% by TGA.

*Fabrication of Poly (hydroxyethyl methacrylate) Coated Multi-Walled Carbon Nanotube/ Epoxy Plaques*

The functionalized MWCNTs from the pellet were sonicated in Ancamine TETA for 3 min at 20 watts such that plaques could be made containing 0.15 wt% and 1.0 wt% poly (HEMA) MWCNTS when cured. The poly (HEMA)-MWCNT functionalized TETA was mixed with EPON 8111 epoxy resin at the manufacturer's recommended stoichiometry for 1 min in a Thinky planetary mixer (model AR-100, Tokyo, Japan) followed by 30 s of defoaming then poured into a 8 in by 8 in polished aluminum mold and allowed to gel at room temperature. After the system gelled, it was placed into an oven at 100 °C for 2 hours.

### *Mechanical Analysis*

The plaques were cut into rectangular strips that were approximately 200 mm long and 12.7 mm  $\pm$  0.1 mm wide via waterjet (Motive Systems, Paso Robles, CA). The strips were allowed to condition at 23 °C and 50% relative humidity for 24 hours prior to testing. The mechanical analysis was performed at 23 °C and 50% relative humidity with a Testometric Universal Testing Machine (Model M350-5kN, Lancashire, UK) equipped with a 500 kgf load cell in tensile mode. The machine had a capacity of 5 kN with an accuracy of  $\pm$  0.5%. The rate of grip separation was 50.0 mm/min with a gauge length of 76.2 mm (3.0 in). The stress and strain at the proportional limit (FL), yield stress and strain, elastic modulus, and toughness were calculated from the force-deformation curves obtained from 5 specimens per epoxy plaque type. The toughness was estimated utilizing the trapezoidal rule.

### *Hardness*

The hardness of each plaque was examined using a Vogel Measurements Shore D durometer at 20 °C and 60% relative humidity according to ASTM D 2240. Each system was tested 10 times in random locations to ensure proper representation of the bulk properties.

### *Thermal Gravimetric Analysis*

The thermal stability of each epoxy type was determined through TGA and is defined as the temperature at which the relative weight loss is two percent. The derivative of the relative weight loss curve with respect to temperature at a heat rate of 20 °C per minute was utilized to observe the onset of major thermal decomposition steps. The peak of the derivative with respect to temperature was utilized to determine the temperature at which the maximum rate of thermal decomposition was observed.

Samples were obtained of each poly (HEMA)-MWCNT/epoxy composite and analyzed for the temperatures associated with the 2% weight loss, 5% weight loss, and the maximum peak derivative of the signal utilizing a Q500 TGA analyzer (TA Instruments, DE) and TA Universal Analysis software 4.5A for evaluation. The flow rate of the nitrogen (industrial grade, Air Gas, San Luis Obispo, CA) purge gas was 20 mL/min and the furnace was set to increase the temperature at a rate of 20 °C/min.

### *Differential Scanning Calorimetry*

DSC experiments were performed to determine first and second order thermal transitions of the poly (HEMA)-MWCNT/ epoxy composites between -70 °C and 150 °C. Samples obtained from the prepared epoxy/ poly-HEMA-MWCNT containing 0, 0.15, and 1.0 wt% MWCNT were placed in separate aluminum pans and non-hermetically sealed. Thermal transitions were evaluated on a TA Instruments Calorimeter model DSC Q2000 (TA Instruments, DE). The poly (HEMA)-MWCNT experiments consisted of a heat/cool/heat cycle between -70 and 150 °C at a rate of 20 °C/min in accordance with ASTM D3418-03 [40]. The nitrogen flow rate inside the calorimeter cell was set to 50 mL/min and was supplied by a nitrogen generator (Domnick Hunter, model G5010W, Birtley, U.K.) with a purity of 99.999% N<sub>2</sub>.



### *Attenuated Total Reflectance-Fourier Transform Infrared Spectroscopy*

The molecular composition of the surfaces was examined using ATR-FTIR spectroscopy. Each scan consisted of measurements between 4000 and 650  $\text{cm}^{-1}$  into a ZnSe based ATR crystal with dimensions 80x10x4 mm and 45° face angle. Each spectrum consisted of 100 scans and was rationed versus a background spectrum. The latter was obtained prior to analyzing the samples and consisted of 100 scans. The spectra were obtained from the cast plaque comprised of poly (HEMA)-MWCNT /epoxy composites utilized for mechanical testing. A Pike Horizontal Attenuated Total Reflectance assembly, model 8224, was attached to a Digilab FT-IR FTS 2000 spectrometer. To avoid atmospheric contaminants a constant purge flow with dried nitrogen and flow rate of 30 ml/min was applied during the analyses. All obtained final spectra were corrected for baseline and for optical distortions using Digilab software Win IR-pro 3.6.

### *Scanning Electron Microscopy*

The surface characteristics of the fractured surface of the plaques were investigated utilizing an FEI Quanta 200 scanning electron microscope at an electron acceleration voltage of 20 kV. The surface of the fractured plaques was sputter-coated with a ca. 10nm thick gold coating using an Emitech K550X sputter coater and Ar as process gas. All images were obtained with the electron beam normal to the fractured surface.

## **Results**

### *Attenuated Total Reflectance-Fourier Transform Infrared Spectroscopy*

ATR-FTIR spectroscopy experiments were conducted to determine the molecular composition of the surface of the carbon nanotube raw material, functionalized MWCNTs, and epoxy composites.

Figure 1 illustrates ATR-FTIR spectra I for raw MWCNT, and II for poly (HEMA) modified MWCNT and transmission IR spectrum III of neat poly (HEMA) as a reference material. As can be seen when comparing the IR fingerprint region between 1300 – 1000  $\text{cm}^{-1}$  in Figure 1, ATR-FTIR spectrum II and IR transmission spectrum III are complimentary and the relative intensity was determined by integration of bands. In this fingerprint region, band intensities A through D follows sequence  $B > C > A > D$  for both IR spectra II and III. In contrast, IR spectrum I (raw MWCNT), as illustrated in Figure 1a does not reveal this characteristic 4-band pattern. This indicates that the surface chemistry of modified MWCNT is defined by presence of OH-containing poly (HEMA) polymer which is expected to govern interface related chemistry.

It can also be seen in Figure 1 that IR spectrum I of raw MWCNT indicates a relative complex surface chemistry (with possibly oxygen related functional groups present). Because of the latter evaluation of an additional IR spectral range was necessary to specifically reveal OH content at raw versus modified MWCNT type.

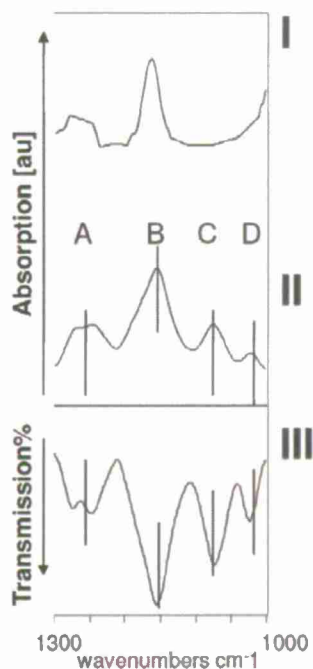


Figure 1. Comparison of IR fingerprint region between 1300 – 1000  $\text{cm}^{-1}$  ATR-FTIR spectra of raw MWCNT (I) and poly (HEMA) modified MWCNT (II). Transmission FT-IR spectrum of neat poly (HEMA) (III).

This approach is seen in ATR-FTIR spectra of Figure 2. Hydroxyl content is illustrated by band at approximately 3415  $\text{cm}^{-1}$  (OH stretch) where trace I describes raw MWCNTs and IR trace II modified MWCNTs. Integration of OH band area at about 3415  $\text{cm}^{-1}$  was done for both IR traces I and II and each value was rationed versus integrated band area for alkyl related band (between approximately 3050-2770  $\text{cm}^{-1}$ ) present in each trace I and II of Figure 2. Such a procedure enables semi-quantitative conclusions on OH content change for raw MWCNTs where a complex surface chemistry is indicated in IR spectra. The calculated ratio for modified MWCNTs was 2.2 versus 0.1 for raw MWCNT proving that the OH content in modified MWCNTs has significantly increased after poly (HEMA) was attached. Hydroxyl enriched surfaces on the modified MWCNTs should govern its interface chemistry.

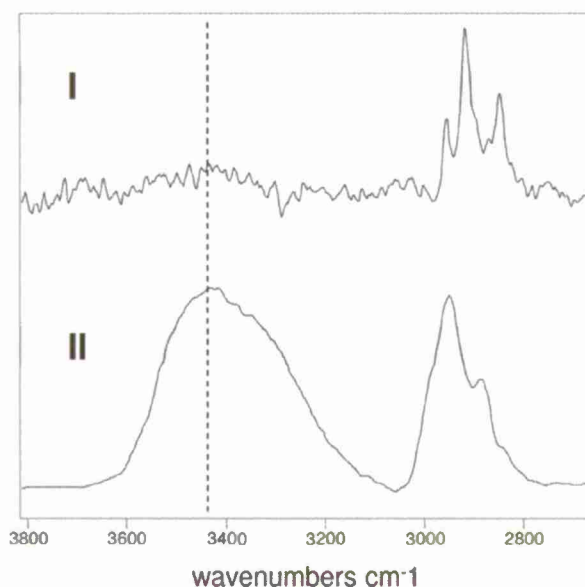


Figure 2. ATR spectra of raw MWCNT (I) and poly (HEMA) modified MWCNT (II).

The chemical effects of incorporating poly (HEMA) modified MWCNT in different amounts in epoxy as additive is illustrated by compositional ATR-FTIR analysis in Figure 3, focusing on spectral range between  $1800\text{ cm}^{-1}$  –  $750\text{ cm}^{-1}$ . For this IR study, protocols described by O'Brien/Hartman [41], Dannenberg/Harp [42] and Fountain [43] were used for band assignments and definition of functional groups typically present in crosslinked epoxy networks. [ENREF 1](#) As seen in IR trace I of Figure 3 composition and band pattern of composite with low concentration (0.15 wt%) poly (HEMA)/MWCNT is in close resemblance to neat epoxy, seen in trace III of Figure 3. However, the band pattern of the latter appears to be slightly different when compared to IR spectral pattern obtained from the higher 1 wt% poly (HEMA)/MWCNT concentration, seen in IR trace II of Figure 3.

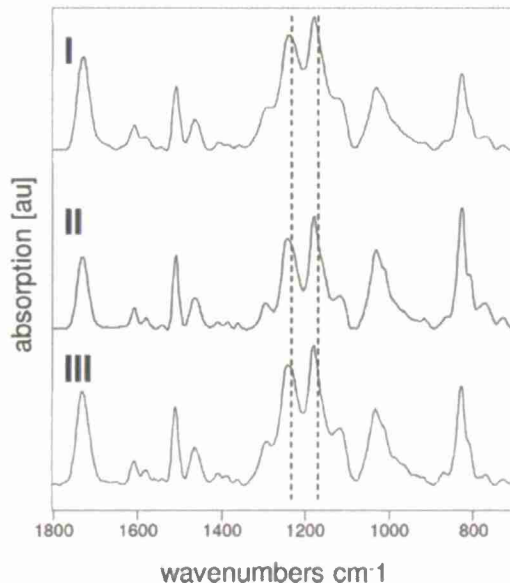


Figure 3. ATR-FTIR spectra of poly (HEMA)/MWCNT containing epoxy composites with 0.15 wt% (I) and 1 wt% (II). Trace III illustrates neat epoxy film.

In an approach to more precisely analyze how the modified MWCNT interface affects conversion in epoxy-composites when the polymer network is formed, a closer look at important IR spectral regions was investigated (Figures 4a and 4b). In Figure 4a, traces IA through IIIA of ATR-FTIR spectra illustrate overall concentration of OH groups in two epoxy composites and neat epoxy while IR traces IB through IIIB illustrate remaining oxirane concentration in crosslinked setups and are used to compare overall cure in epoxy, following [42].

ATR-FTIR spectra in Figure 3a were used to semi-quantify OH group concentration in epoxy composite networks. Standard procedure was to integrate the band of OH stretch at approximately  $3360\text{ cm}^{-1}$  (highlighted in Figure 4a) and ratio versus integrated alkyl group band (between  $3005 - 2800\text{ cm}^{-1}$ ). These data are summarized in Table 1. The calculation leads to a sequence where OH group concentration of neat epoxy  $\gg 1\text{ wt\%} > 0.15\text{ wt\%}$ . Evaluation indicates the highest OH group concentration for neat epoxy, seen at trace IIIA of Figure 4a and lowest OH group concentration for composite with 0.15 wt%, seen in IR trace IA of Figure 4a. Observation is supported by literature and that epoxy curing reaction between oxirane functional group and amine based hardener – seen in reaction scheme 2a - results in higher number of OH functional groups compared to curing reaction where oxirane groups react with OH groups as reactive specimen [41]. In latter curing scenario overall OH group concentration remains unchanged, illustrated by reaction scheme 2b.



Scheme 2. Potential reactions between oxirane groups and amines (a) and hydroxyls (b) [41].

Both curing reactions are simplified: for this reason, used multifunctional amine curing agent is illustrated with one amine group only in Scheme 2a. Polyfunctional poly (HEMA) modified MWCNT is illustrated with single OH group in Scheme 2b. The observation that final OH group concentration in crosslinked poly (HEMA)/MWCNT networks is smaller than for neat epoxy supports that modified and OH rich MWCNT interface successfully takes part in epoxy crosslinking reaction and becomes chemically attached to the epoxy network. Again, this can be concluded from ATR-FTIR spectra of Figure 4a and traces IA and IIA where relative intensity of OH bands is lower when compared to neat epoxy setup at IR trace IIIA.



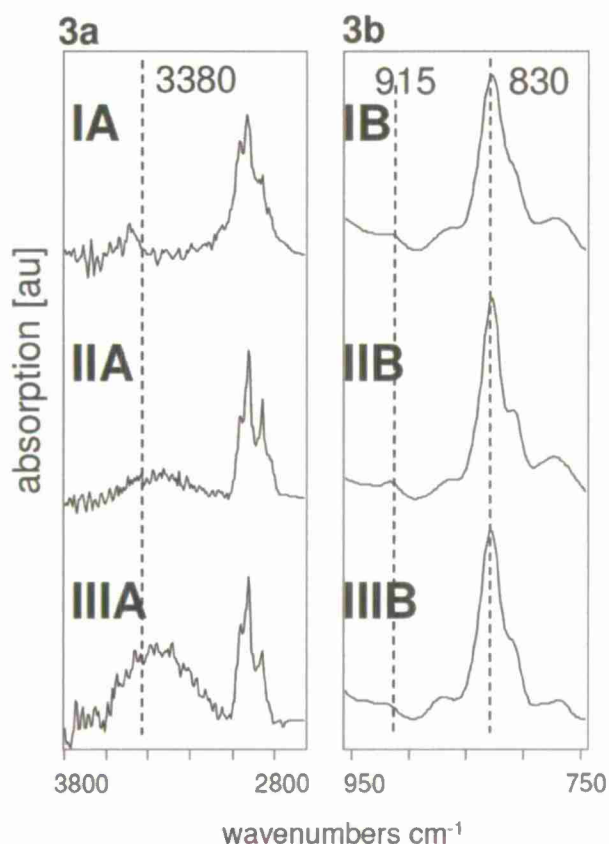


Figure 4. ATR-FTIR spectra of poly (HEMA)/MWCNT containing epoxy composites with 0.15 wt% (I) and with 1 wt% (II) compared with neat epoxy (III). Traces “A” illustrate OH functional group and “B” oxirane functional group content in epoxy/composites.

An additional effort to determine how interface chemistry and presence of modified MWCNT affects curing rate in epoxy final content of oxirane group after crosslinking was analyzed and is illustrated by ATR-FTIR spectra of Figure 4b and traces 1B through 111B. To semi-quantify data, the band area for oxirane ring deformation at  $915\text{ cm}^{-1}$  was determined by integration (and normalized to out of plane bending vibration of para substituted benzene ring at  $830\text{ cm}^{-1}$ ). This approach follows evaluation suggested in literature to determine general cure rate of epoxy thermosets [42, 43]; numerical data from this procedure are summarized in Table 1. Integration of the oxirane band at  $915\text{ cm}^{-1}$  for ATR-FTIR traces 1B through 111B of Figure 4b followed the sequence 111B > 1B ~ 111B. This sequence indicated that the highest remaining oxirane group concentration was observed for the composite with 1 wt% poly (HEMA)/MWCNT concentration while lowest for 0.15 wt% content which was equivalent for neat epoxy.

ATR-FTIR experiments indicated that crosslink formation and crosslink structures are different for epoxy composite setups when oxirane group conversion is used as qualitative measure. Because 1 wt% poly (HEMA) MWCNT composites indicated the lowest conversion (and highest remaining oxirane content), curing appears to be reduced for elevated concentration of modified MWCNT; therefore, reduced concentrations of this additive type employed in potential technical composites appear to be favorable.

Table 1. Integrated Bands for Evaluation of Conversion Reaction/Crosslink Formation for Epoxy Composites

| Epoxy composite type       | Integrated OH                      | Integrated oxirane group          |
|----------------------------|------------------------------------|-----------------------------------|
|                            | band at 3380 cm <sup>-1</sup> [au] | band at 915 cm <sup>-1</sup> [au] |
| 0.15 wt% poly (HEMA)/MWCNT | 0.10                               | 0.02                              |
| 1 wt% poly (HEMA)/MWCNT    | 0.42                               | 0.05                              |
| Neat epoxy                 | 1.21                               | 0.02                              |

*Mechanical Analysis*

The cast poly (HEMA)-MWCNT/epoxy plaques containing 0, 0.15, and 1.0 wt% poly (HEMA) coated MWCNTs were evaluated for mechanical strength. The force-deformation curves were obtained from 5 specimens per loading of poly (HEMA)-MWCNT (0, 0.15, and 1.0 wt%) and characterized for properties relating to the proportional limit, yield point, and toughness (Table 2).

Table 2. Mechanical Properties of Poly (hydroxyethyl methacrylate) Coated Multiwalled Carbon Nanotube-Epoxy Composites

|                 | Stress<br>@ PL<br>(MPa) | Strain<br>@ PL<br>(mm/mm) | Max<br>Stress<br>(MPa) | Max<br>Strain<br>(mm/mm) | Young's<br>Modulus<br>(MPa) | Toughness<br>(MJ/m <sup>3</sup> ) |
|-----------------|-------------------------|---------------------------|------------------------|--------------------------|-----------------------------|-----------------------------------|
| <b>Neat</b>     |                         |                           |                        |                          |                             |                                   |
| Ave             | 54.8                    | 0.053                     | 54.8                   | 0.053                    | 1036.9                      | 1.8                               |
| Stdev           | 4.4                     | 0.005                     | 4.4                    | 0.005                    | 44.7                        | 0.3                               |
| <b>0.15 wt%</b> |                         |                           |                        |                          |                             |                                   |
| Ave             | 62.3                    | 0.061                     | 63.2                   | 0.062                    | 1028.4                      | 2.3                               |
| Stdev           | 4.8                     | 0.005                     | 4.7                    | 0.005                    | 45.3                        | 0.4                               |
| <b>1.0 wt%</b>  |                         |                           |                        |                          |                             |                                   |
| Ave             | 56.1                    | 0.054                     | 56.1                   | 0.054                    | 1033.8                      | 1.6                               |
| Stdev           | 1.6                     | 0.001                     | 1.6                    | 0.001                    | 29.1                        | 0.3                               |

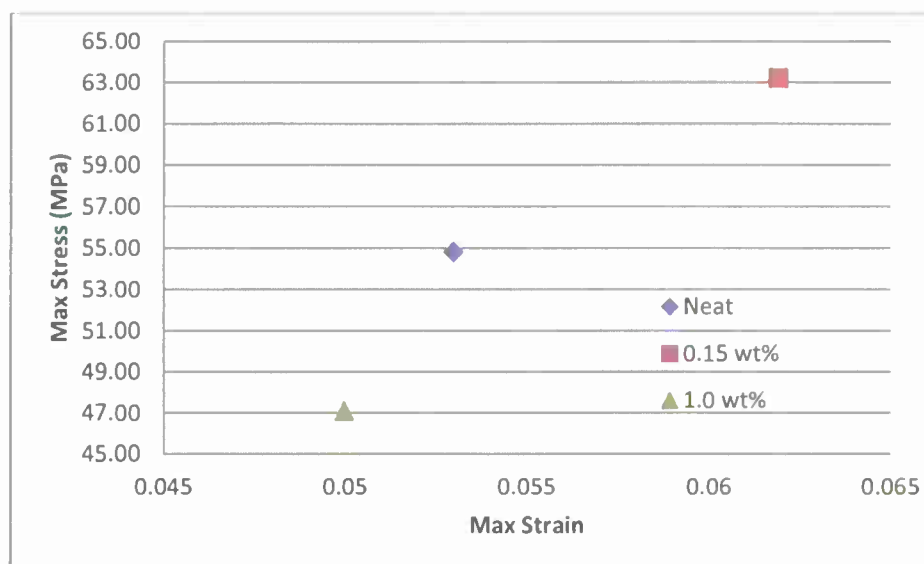


Figure 5. Stress and strain values at break for epoxy matrix containing 0, 0.15, and 1.0 wt% poly (HEMA)-MWCNT.

Mechanical analysis indicated that the poly (HEMA)-MWCNT/epoxy composite containing 0.15 wt% possessed the highest mechanical properties for stress and strain at the proportional limit (PL) and maximum stress and strain for the systems evaluated in this study (Figure 5). However, the Young's Modulus of the composite of both the poly (HEMA)-MWCNT and the neat system were within approximately 2%. Although a major objective of carbon nanotube studies are to enhance the Young's Modulus of a system, increasing the ultimate tensile strength of a composite while retaining similar stiffness properties enables CNT modified systems to be utilized in the same applications as intended with higher performance. Mechanical analysis indicated that the epoxy composites did not undergo plastic deformation under the conditions employed indicating that the increase in toughness observed was induced by a different mechanism. The increase in toughness can then be attributed to an increase in load transfer from the matrix to the MWCNT. These results indicate that more research should be performed for MWCNT concentrations near 0.15 wt% for determination of the optimal carbon nanotube loading.

#### *Hardness*

The hardness of each system was measured with a Shore D durometer to observe the effect incorporating functionalized MWCNTs (Table 3). Each measurement was obtained from a specimen of the plaques used for mechanical analysis to ensure that the substrate did not influence the results. The hardness of each system behaved similarly to the mechanical properties observed above; the 0.15 wt% functionalized MWCNT had the highest hardness and the neat and 1.0 wt% composite types had similar values (Table 3).

---

Table 3. Shore D Hardness of Poly (hydroxyethyl methacrylate) Coated Multiwalled Carbon Nanotube-Epoxy Composites

---

| Epoxy Composite Type | Shore D Hardness | Std Deviation |
|----------------------|------------------|---------------|
| Neat                 | 82               | 5             |
| 0.15                 | 87               | 5             |
| 1%                   | 83               | 15            |

---

*Thermal Gravimetric Analysis*

Characterization of the functionalized MWCNTs indicated that they are comprised of approximately 30 wt% poly (HEMA).

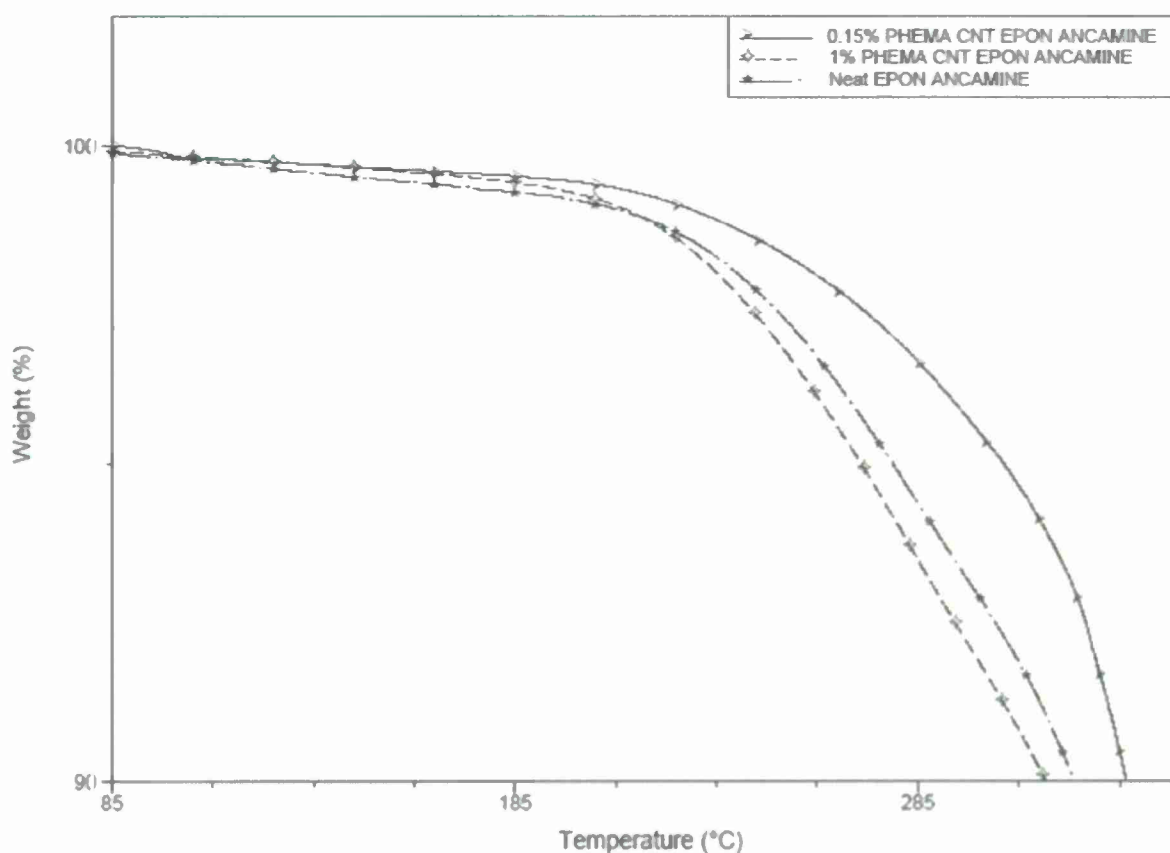


Figure 6. Representative thermograms of EPON 8111/TETA epoxy samples that were functionalized by poly (HEMA)-multiwalled carbon nanotubes at 0, 0.15, and 1.0 wt%.

The addition of poly (HEMA)-MWCNTs at 0.15 wt% will increase thermal stability of the system as observed in Figure 4 (Table 4) using thermogravimetric analysis. At a 1.0 wt% loading of the poly (HEMA)-MWCNTs, thermal stability of the system decreased compared to the neat epoxy system; this behavior was also observed when investigating the mechanical properties (Table 2) and can be attributed to stoichiometric imbalance caused by the increased concentration of hydroxyl groups from the functionalized MWCNTs or incomplete conversion of the crosslinking system due to steric hindrance of the poly (HEMA) coated MWCNT during the cure.



Table 4. Thermogravimetric Measurements of Poly (HEMA)-MWCNT/epoxy Nanocomposites at Various Heating Rates

| Sample                 | 2%<br>Weight Loss | 5%<br>Weight Loss | 10%<br>Weight Loss | Derivative<br>Onset 1 | Derivative<br>Onset 2 | Derivative<br>Peak |
|------------------------|-------------------|-------------------|--------------------|-----------------------|-----------------------|--------------------|
| <b><u>20°C/min</u></b> |                   |                   |                    |                       |                       |                    |
| <b>Neat</b>            |                   |                   |                    |                       |                       |                    |
| Average                | 238               | 278               | 318                | 200                   | 325                   | 369                |
| St Dev                 | 11                | 14                | 10                 | 5                     | 7                     | 3                  |
| <b>0.15 wt %</b>       |                   |                   |                    |                       |                       |                    |
| Average                | 245               | 287               | 326                | 206                   | 327                   | 372                |
| St Dev                 | 10                | 15                | 9                  | 5                     | 3                     | 8                  |
| <b>1.0 wt %</b>        |                   |                   |                    |                       |                       |                    |
| Average                | 232               | 269               | 312                | 201                   | 328                   | 371                |
| St Dev                 | 8                 | 13                | 19                 | 3                     | 3                     | 2                  |

#### *Differential Scanning Calorimetry*

The DSC scans indicated that none of the specimens analyzed were fully cured despite utilizing the manufacturers' cure schedule. As a result, an increase in the glass transition was observed upon the second heating scan when compared to the peak signal of the physical aging peak due to increased cure. However, the main objective of this research was to incorporate commercially viable functionalized MWCNTs into a commercially available system according to the recommended cure schedule; thus, the systems studied here should accurately replicate the physical properties when employed in real world applications. The maximum signal, glass transition temperature from the cooling cycle, and glass transition from the heating cycle are found in Table 5.

Table 5. Thermal Transitions of Poly (hydroxyethyl methacrylate) Functionalized Multiwalled Carbon Nanotube-Epoxy Composites

| <b>Sample</b>   | <b>Endotherm Peak</b> | <b>T<sub>g</sub> cool</b> | <b>T<sub>g</sub></b> |
|-----------------|-----------------------|---------------------------|----------------------|
| <b>Neat</b>     |                       |                           |                      |
| Average         | 58.53                 | 57.87                     | 62.36                |
| Std Dev         | 0.22                  | 0.79                      | 1.13                 |
| <b>0.15 wt%</b> |                       |                           |                      |
| Average         | 58.49                 | 57.68                     | 62.16                |
| Std Dev         | 0.60                  | 1.45                      | 1.32                 |
| <b>1.0 wt%</b>  |                       |                           |                      |
| Average         | 55.79                 | 53.73                     | 58.48                |
| Std Dev         | 0.49                  | 0.57                      | 0.85                 |

The glass transition temperature of a thermosetting polymer is directly dependent on the crosslink density, number of free chain ends, and rigidity of polymeric segments and has been the subject of previous research [44, 45]. The poly (HEMA)-MWCNTs introduced to the epoxy system leads to an increase in chain ends and free volume in the system, from poly (HEMA), unreacted TETA and the epoxy resin, which should alter the glass transition temperature. However, differential scanning calorimetry indicated no observable change in the glass transition temperature of the resin system utilized in this study when incorporating poly (HEMA)-MWCNTs at a concentration of 0.15 wt%. The composite that contained 1.0 wt% poly (HEMA)-MWCNTs was observed to have a lower  $T_g$  and physical aging peak when compared to neat resin; this may be attributed to an increased amount of free chain ends and stoichiometry imbalance of the additional functional groups of the poly (HEMA)-MWCNTs.

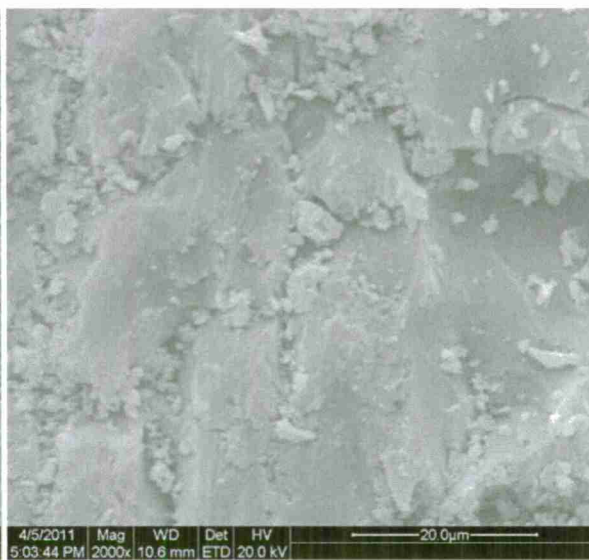
#### *Scanning Electron Microscopy*

The surface roughness of a fracture material can bring insight into the mechanism of crack propagation through the material. In general, the rougher the surface, the more tortuous path the crack must propagate during the fracture event [16-18, 26, 39]. When a crack initiates, propagation occurs along the plane of least resistance (typically matrix defects) until a portion of the matrix has sufficient energy to stop or deflect propagation.

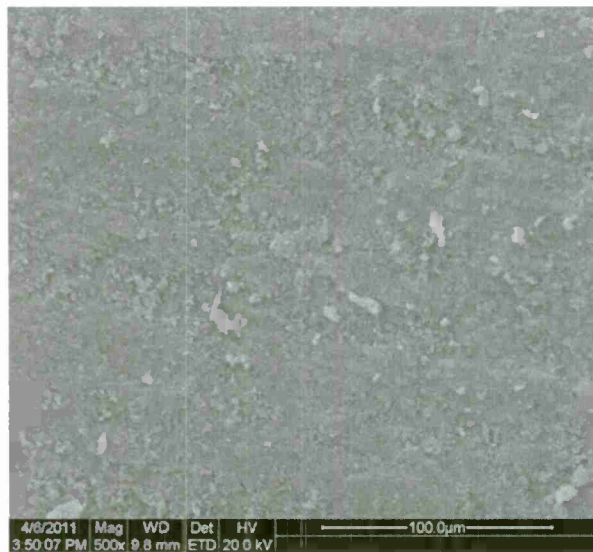
The moieties that alter crack propagation in the system used in this study can be either chemical bonds or functionalized MWCNT (if present in the matrix). To observe crack propagation during the fracture event, the fractured surfaces were investigated using SEM at 500 and 2000x magnification (Figure 7).



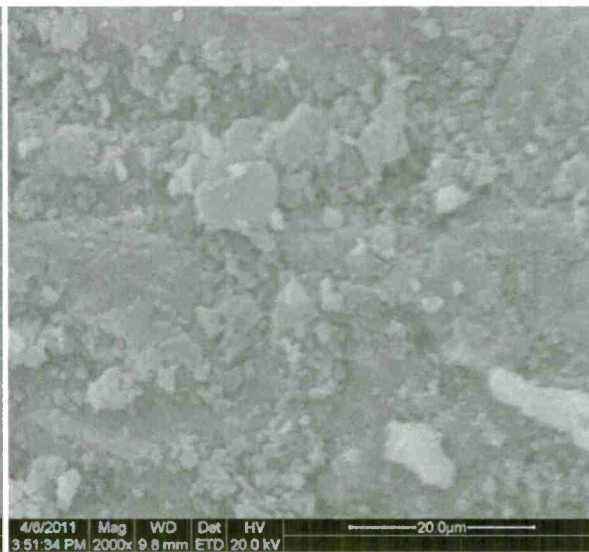
a



b



c



d

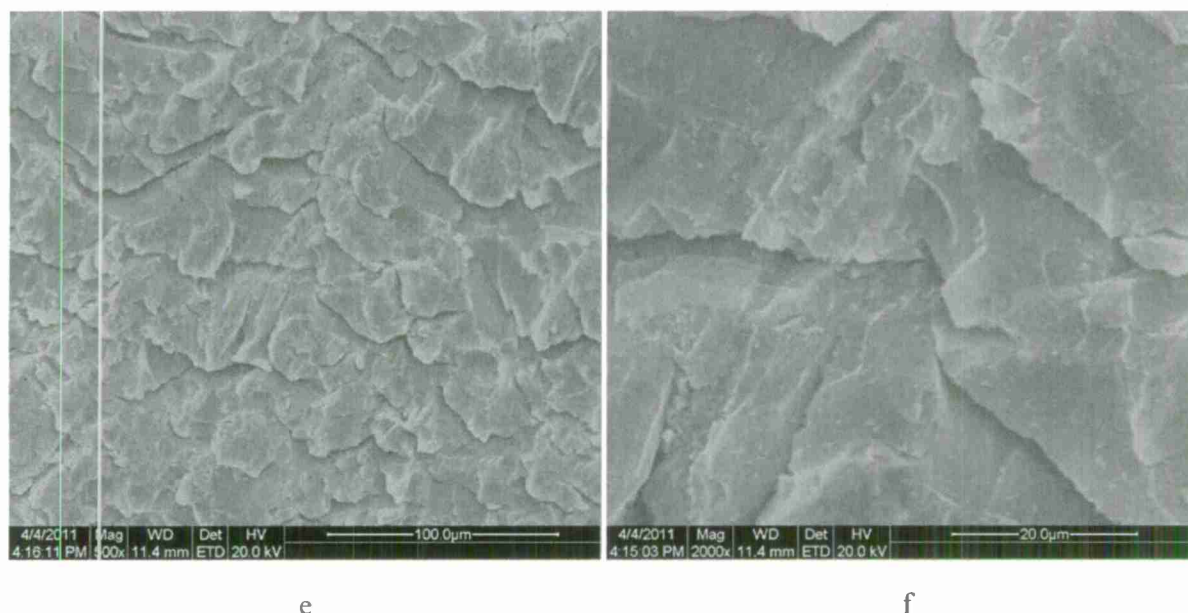


Figure 7. SEM image of neat epoxy at 500x (a) and 2000x (b), 0.15 wt% at 500x (c) and 2000x (d), and 1.0 wt% at 500x (e) and 2000x (f).

The surface morphology of the neat epoxy after fracture had several smooth structures when observed at 2000x (Figure 7b). These structures appear throughout the fractured surface as shown by the images obtained at 500x (Figure 7a); the presence of these structures indicates that there were several planes where the crack was relatively free to propagate. The poly (HEMA)-MWCNT/epoxy composite at 0.15 wt% loading qualitatively contained much smaller and more numerous smooth sections on the fractured surface when compared to the neat epoxy. This can be attributed to crack propagation being either stopped or deflected due to the presence of well dispersed MWCNTs with enhanced interaction with the epoxy matrix. This behavior of crack propagation in the 0.15 wt% poly (HEMA)-MWCNT/epoxy system follows the mechanical properties as described above. The surface morphology of the 1.0 wt% poly (HEMA)-MWCNT/epoxy composite is very different from those observed in the neat and 0.15 wt% poly (HEMA)-MWCNT/epoxy systems. This can be attributed to agglomeration of the MWCNTs due to higher MWCNT concentration within the matrix or an increase of free volume due to more chain ends within the polymer matrix.

### Conclusions:

Purified multiwalled carbon nanotubes were chemically functionalized by a surface initiated polymerization of 2-hydroxyethyl methacrylate using benzoyl peroxide. The poly (HEMA)-MWCNTs were incorporated into a commercially available epoxy resin and the thermal and mechanical properties were investigated. Strips of poly (HEMA)-MWCNTs/ epoxy were cut via waterjet from cast plaques. Mechanical analysis indicated an ultimate tensile strength approximately 30% higher at a poly (HEMA)-MWCNT loading of 0.15 wt% when compared to the neat resin, yet a similar Young's Modulus. The fractured surfaces of the tensile experiments were examined by scanning electron microscopy; the surface of the 0.15 wt% was found to possess a rougher surface when compared to the neat and 1.0 wt% specimens. These results



indicate that the poly (HEMA) coated MWCNTs have good interfacial interaction with the epoxy resin. The glass transition temperature of the 0.15 wt% was found to be nearly the same as the neat epoxy polymer whereas the  $T_g$  of the 1.0 wt% was slightly lower compared to the neat epoxy. The effects of varying functionalization parameters (i.e. initiator concentration, sonication time, polymerization time, monomer composition) and carbon nanotube concentrations must be better understood to synthesize functionalized MWCNTs for optimal properties for various applications.

### Acknowledgements:

The authors would like to thank the California Central Coast Research Partnership (C<sup>3</sup>RP) California Polytechnic State University, San Luis Obispo and the Office of Naval Research under grant N00014-11-1-0359 for providing funding to complete the project, and the University of Southern Mississippi and Dr. William Jarrett for instrumentation advice.

### References:

1. Coleman, J.N., et al., *Small but strong: A review of the mechanical properties of carbon nanotube-polymer composites*. Carbon, 2006. **44**(9): p. 1624-1652.
2. Ugur, S., O. Yargi, and O. Pekcan, *Percolation and film formation behaviors of MWNT/PS nanocomposites*. Procedia Eng., 2011. **10**(Copyright (C) 2012 American Chemical Society (ACS). All Rights Reserved.): p. 1709-1717.
3. Chou, T.-W., et al., *An assessment of the science and technology of carbon nanotube-based fibers and composites*. Composites Science and Technology, 2010. **70**(1): p. 1-19.
4. Gojny, F.H., et al., *Carbon nanotube-reinforced epoxy-composites: enhanced stiffness and fracture toughness at low nanotube content*. Composites Science and Technology, 2004. **64**(15): p. 2363-2371.
5. Kim, Y.S., et al., *Influence of Stabilizer Concentration on Transport Behavior and Thermopower of CNT-Filled Latex-Based Composites*. Macromol. Mater. Eng., 2010. **295**(Copyright (C) 2012 American Chemical Society (ACS). All Rights Reserved.): p. 431-436.
6. Jurewicz, I., et al., *Locking Carbon Nanotubes in Confined Lattice Geometries - A Route to Low Percolation in Conducting Composites*. J. Phys. Chem. B, 2011. **115**(Copyright (C) 2012 American Chemical Society (ACS). All Rights Reserved.): p. 6395-6400.
7. Burghard, M., *Electronic and vibrational properties of chemically modified single-wall carbon nanotubes*. Surface Science Reports, 2005. **58**(1-4): p. 1-109.
8. Spitalsky, Z., et al., *Carbon nanotube-polymer composites: Chemistry, processing, mechanical and electrical properties*. Progress in Polymer Science, 2010. **35**(3): p. 357-401.
9. Li, X., et al., *Non-covalent functionalization of multiwalled carbon nanotubes and their application for conductive composites*. Carbon, 2008. **46**(Copyright (C) 2012 American Chemical Society (ACS). All Rights Reserved.): p. 829-831.
10. Xia, H., G. Qiu, and Q. Wang, *Polymer/carbon nanotube composite emulsion prepared through ultrasonically assisted in situ emulsion polymerization*. J. Appl. Polym. Sci., 2006. **100**(Copyright (C) 2012 American Chemical Society (ACS). All Rights Reserved.): p. 3123-3130.
11. Lu, J., et al., *Chemo-sensitivity of latex-based films containing segregated networks of carbon nanotubes*. Sens. Actuators, B, 2011. **B155**(Copyright (C) 2012 American Chemical Society (ACS). All Rights Reserved.): p. 28-36.
12. Kyrlyuk, A.V., et al., *Controlling electrical percolation in multicomponent carbon nanotube dispersions*. Nat. Nanotechnol., 2011. **6**(Copyright (C) 2012 American Chemical Society (ACS). All Rights Reserved.): p. 364-369.



13. Grossiord, N., et al., *Toolbox for Dispersing Carbon Nanotubes into Polymers To Get Conductive Nanocomposites*. Chem. Mater., 2006. **18**(Copyright (C) 2012 American Chemical Society (ACS). All Rights Reserved.): p. 1089-1099.
14. Bose, S., et al., *Tuning the dispersion of multiwall carbon nanotubes in co-continuous polymer blends: A generic approach*. Nanotechnology, 2008. **19**(Copyright (C) 2012 American Chemical Society (ACS). All Rights Reserved.): p. 335704/1-335704/8.
15. Bose, S., R.A. Khare, and P. Moldenaers, *Assessing the strengths and weaknesses of various types of pre-treatments of carbon nanotubes on the properties of polymer/carbon nanotubes composites: A critical review*. Polymer, 2010. **51**(5): p. 975-993.
16. Ayatollahi, M.R., et al., *Effect of multi-walled carbon nanotube aspect ratio on mechanical and electrical properties of epoxy-based nanocomposites*. Polymer Testing, 2011. **30**(5): p. 548-556.
17. Sun, L., et al., *Energy absorption capability of nanocomposites: A review*. Composites Science and Technology, 2009. **69**(14): p. 2392-2409.
18. Hernández-Pérez, A., et al., *Effective properties of multiwalled carbon nanotube/epoxy composites using two different tubes*. Composites Science and Technology, 2008. **68**(6): p. 1422-1431.
19. Ma, P.-C., et al., *Dispersion and functionalization of carbon nanotubes for polymer-based nanocomposites: A review*. Composites Part A: Applied Science and Manufacturing, 2010. **41**(10): p. 1345-1367.
20. Xie, X.-L., Y.-W. Mai, and X.-P. Zhou, *Dispersion and alignment of carbon nanotubes in polymer matrix: A review*. Materials Science and Engineering: R: Reports, 2005. **49**(4): p. 89-112.
21. Sahoo, N.G., et al., *Polymer nanocomposites based on functionalized carbon nanotubes*. Progress in Polymer Science, 2010. **35**(7): p. 837-867.
22. Grossiord, N., et al., *Time-Dependent Study of the Exfoliation Process of Carbon Nanotubes in Aqueous Dispersions by Using UV-Visible Spectroscopy*. Anal. Chem., 2005. **77**(Copyright (C) 2012 American Chemical Society (ACS). All Rights Reserved.): p. 5135-5139.
23. Grossiord, N., et al., *Determination of the Surface Coverage of Exfoliated Carbon Nanotubes by Surfactant Molecules in Aqueous Solution*. Langmuir, 2007. **23**(Copyright (C) 2012 American Chemical Society (ACS). All Rights Reserved.): p. 3646-3653.
24. Mirjalili, V. and P. Hubert, *Modelling of the carbon nanotube bridging effect on the toughening of polymers and experimental verification*. Composites Science and Technology, 2010. **70**(10): p. 1537-1543.
25. Kostopoulos, V., et al., *Impact and after-impact properties of carbon fibre reinforced composites enhanced with multi-wall carbon nanotubes*. Composites Science and Technology, 2010. **70**(4): p. 553-563.
26. Gojny, F.H., et al., *Influence of different carbon nanotubes on the mechanical properties of epoxy matrix composites – A comparative study*. Composites Science and Technology, 2005. **65**(15-16): p. 2300-2313.
27. Gojny, F.H., et al., *Surface modified multi-walled carbon nanotubes in CNT/epoxy-composites*. Chemical Physics Letters, 2003. **370**(5-6): p. 820-824.
28. Zhang, W., R.C. Picu, and N. Koratkar, *The effect of carbon nanotube dimensions and dispersion on the fatigue behavior of epoxy nanocomposites*. Nanotechnology, 2008. **19**(28): p. 285709.
29. Granier, A., et al. *A novel method to covalently functionalize carbon nanotubes with isocyanate for polyurethane nanocomposite coatings*. 2007: Federation of Societies for Coatings Technology.
30. Wu, H.-X., et al., *Functionalization of multiwalled carbon nanotubes with polystyrene under atom transfer radical polymerization conditions*. Carbon, 2007. **45**(1): p. 152-159.
31. Grossiord, N., et al., *Conductive carbon-nanotube/polymer composites: spectroscopic monitoring of the exfoliation process in water*. Compos. Sci. Technol., 2007. **67**(Copyright (C) 2012 American Chemical Society (ACS). All Rights Reserved.): p. 778-782.

32. Curtzwiler, G., et al., *Thermal-initiated hydroxyethyl methacrylate functionalization of multiwalled carbon nanotubes*. Journal of Applied Polymer Science, 2011. **121**(2): p. 964-969.
33. Sun, L., et al., *Mechanical properties of surface-functionalized SWCNT/epoxy composites*. Carbon, 2008. **46**(2): p. 320-328.
34. Ganguli, S., et al., *Effect of loading and surface modification of MWCNTs on the fracture behavior of epoxy nanocomposites*. J. Reinf. Plast. Compos., 2006. **25**(Copyright (C) 2012 American Chemical Society (ACS). All Rights Reserved.): p. 175-188.
35. Yaping, Z., et al., *Functionalized effect on carbon nanotube/epoxy nano-composites*. Materials Science and Engineering: A, 2006. **435-436**(0): p. 145-149.
36. Qian, H., et al., *Mapping local microstructure and mechanical performance around carbon nanotube grafted silica fibres: methodologies for hierarchical composites*. Nanoscale, 2011. **3**(Copyright (C) 2012 American Chemical Society (ACS). All Rights Reserved.): p. 4759-4767.
37. Haris, A., T. Adachi, and W. Araki, *Nano-scale characterization of fracture surfaces of blended epoxy resins related to fracture properties*. Materials Science and Engineering: A, 2008. **496**(1-2): p. 337-344.
38. Ayatollahi, M.R., S. Shadlou, and M.M. Shokrieh, *Mixed mode brittle fracture in epoxy/multi-walled carbon nanotube nanocomposites*. Engineering Fracture Mechanics, 2011. **78**(14): p. 2620-2632.
39. Ganguli, S., et al., *Effect of multi-walled carbon nanotube reinforcement on the fracture behavior of a tetrafunctional epoxy*. Journal of Materials Science, 2005. **40**(13): p. 3593-3595.
40. D3418-03, A.S., *Standard Test Method for Transition Temperatures and Enthalpies of Fusion and Crystallization of Polymers by Differential Scanning Calorimetry*. 2003, ASTM International: West Conshohocken, PA.
41. O'Brien, R.N. and K. Hartman, *Air infrared spectroscopy study of the epoxy-cellulose interface*. Journal of Polymer Science Part C: Polymer Symposia, 1971. **34**(1): p. 293-301.
42. Dannenberg, H. and W.R. Harp, *Determination of Cure and Analysis of Cured Epoxy Resins*. Analytical Chemistry, 1956. **28**(1): p. 86-90.
43. Fountain, R., *Characterization and control of a structural epoxy adhesive*. Polymer Engineering & Science, 1974. **14**(9): p. 597-603.
44. van, E.P.J., *Handbook of Thermal Analysis and Calorimetry Vol. 3, Applications to Polymers and Plastics*, Stephen Z.D. Cheng (Ed.), Patrick K. Gallagher (Series Ed.), Elsevier, Amsterdam, 2002. Thermochim. Acta, 2003. **407**(Copyright (C) 2012 American Chemical Society (ACS). All Rights Reserved.): p. 121-123.
45. Hiemenz, P. and T. Lodge, *Glass Transition*, in *Polymer Chemistry*. 2007, Taylor and Francis Group: Boca Raton, FL.

## **Appendix A**

### High – Tech Breakfast Forum Agenda



CALIFORNIA CENTRAL COAST  
RESEARCH PARTNERSHIP

## High-Tech Industry Breakfast Forum *Technology Serving Humanity*

**Date:** February 11, 2011

**Time:** 7:30 am - 9:00 am

**Location:** Cal Poly Technology Park - BLDG 83 - (Free parking is available at the Park)

You are invited to participate in our on-going breakfast forum for the local high-tech industry, hosted by Susan Opava, Cal Poly's Dean of Research and Graduate Programs, and Jim Dunning, C<sup>3</sup>RP Program Manager. The purpose of the forum is to bring principals from high-tech companies in the region to campus on a regular basis, to foster a mutually beneficial relationship between Cal Poly and this important local industry sector. We are pleased to host this event for the first time at the new Technology Park.

**7:30 am**

Continental Breakfast - Small group discussions & networking

**7:50 am**

Introductions

**8:00 am**

Adobe / Mud Brick Solutions.

Dr. Craig Baltimore - Associate Professor  
Architectural Engineering

**8:15 am**

Portable Water Treatment.

Dr. Tryg Lundquist - Assistant Professor  
Civil & Environmental Engineering

**8:30 am**

Rapidly Assembled Emergency Shelters

Dr. Ed Saliklis - Associate Professor  
Architectural Engineering

**8:45 am**

Electrochlorinator Project

Kevin Gallagher - Military Affairs Manager  
Cascade Designs, Inc.

**9:00 am**

Adjourn

# High-Tech Industry Breakfast Forum

## *Robots, Mobile Applications & Gaming*

**Date:** May 27, 2011  
**Time:** 7:30 am - 9:00 am  
**Location:** Cal Poly Technology Park - BLD 83 Cal Poly - (Parking will be provided)

You are invited to participate in our on-going breakfast forum for the local high-tech industry, hosted by Susan Opava, Cal Poly's Dean of Research and Graduate Programs, and Jim Dunning, C<sup>3</sup>RP Program Manager. The purpose of this forum is to bring principals from high-tech companies in the region to campus on a regular basis, to foster a mutually beneficial relationship between the university and this important local industry sector.

|                |  |   |
|----------------|--|---|
| <b>7:30 am</b> | Continental Breakfast - Small group discussions & networking |   |
| <b>7:50 am</b> | Introductions  |   |
| <b>8:00 am</b> | Autonomous underwater vehicles (AUVs)                        | Dr. Chris Clark - Assistant Professor<br>Department of Computer Science           |
| <b>8:15 am</b> | Mobile application development                               | Dr. David Janzen - Associate Professor<br>Department of Computer Science          |
| <b>8:30 am</b> | Human Computer Interaction                                   | Dr. Lynne Slivovsky - Associate Professor<br>Department of Electrical Engineering |
| <b>8:45 am</b> | Mobile gaming development                                    | Joy C. Montoya<br>GOGII   |
| <b>9:00 am</b> | Adjourn  |   |

RSVP # of participants to: Dejana Lubura 805-756-4733 or [dlubura@calpoly.edu](mailto:dlubura@calpoly.edu) by **May 20, 2011**





CALIFORNIA CENTRAL COAST  
RESEARCH PARTNERSHIP

## High-Tech Industry Breakfast Forum

### *Highlighting University - Industry R&D Partnerships*

**Date:** December 09, 2011

**Time:** 7:30 am - 9:00 am

**Location:** Cal Poly Technology Park - BLDG 83 (Free Parking)

You are invited to participate in our on-going breakfast forum for the local high-tech industry, hosted by Susan Opava, Cal Poly's Dean of Research and Graduate Programs, and Jim Dunning, C<sup>3</sup>RP Program Manager. The purpose of this forum is to bring principals from high-tech companies in the region to campus on a regular basis, to foster a mutually beneficial relationship between the university and this important local industry sector.

**7:30 am** Continental Breakfast - Small group discussions, networking and introductions

**8:00 am** Biotechnology - Applied Biotechnology Institute

Dr. John Howard - President & CEO  
Dr. Rafael Jimenez-Flores - Professor  
Dairy Sciences Department

**8:25 am** Packaging - V Laboratories

Dr. Keith Vorst - Associate Professor  
Industrial Technology - College of  
Business & Department of Horticulture  
and Crop Science

**8:45am** Cal Poly Fee-for-Service Opportunities

Jim Dunning - Program Manager  
California Central Coast Research  
Partnership (C<sup>3</sup>RP)

**9:00 am** Adjourn

# High-Tech Industry Breakfast Forum

*Communication Technologies -*

*Development tools, enabling technologies, and new applications*

**February 24, 2012 - 7:30 - 9:00 am - Cal Poly Technology Park - BLDG 83 (Free Parking)**

You are invited to participate in our on-going breakfast forum for the local high-tech industry, hosted by Susan Opava, Cal Poly's Dean of Research and Graduate Programs, and Jim Dunning, C<sup>3</sup>RP Program Manager. The purpose of this forum is to bring principals from high-tech companies in the region to campus on a regular basis, to foster a mutually beneficial relationship between the university and this important local industry sector.

**7:30 am** Continental Breakfast - Small group discussions, networking and introductions

**8:00 am** Cal Poly's Anechoic Chamber - Tool for wireless communications, RF/microwave, and antenna developers  
Dr. Dean Arakaki - Associate Professor  
Electrical Engineering

**8:15 am** High efficiency linear RF amplifiers for mobile device applications  
Dr. Vladimir Prodanov - Assistant Professor  
Electrical Engineering

**8:30 am** Transportation Systems, Data, & Applications  
Dr. Anurag Pande - Assistant Professor  
Civil & Environmental Engineering

**8:45 am** Mentor eData LLC - Technology-based solutions that improve driver performance and safety using a suite of on-board and web-based tools  
Stephen Lakowske - President Mentor  
eData Arroyo Grande, CA

**9:00 am** Adjourn

RSVP # of participants to: [Dejana.Lubura.805.756.458@calpoly.edu](mailto:Dejana.Lubura.805.756.458@calpoly.edu) or [dlubura@calpoly.edu](mailto:dlubura@calpoly.edu) by **February 17, 2012**

## High-Tech Industry Breakfast Forum

*The Million Dollar Club*

*Highlighting Cal Poly sponsored projects near or exceeding \$1.0M*

**June 01, 2012 - 7:30 - 9:00 am - Cal Poly Technology Park - BLDG 83 (Free Parking)**

You are invited to participate in our on-going breakfast forum for the local high-tech industry, hosted by Susan Opava, Cal Poly's Dean of Research and Graduate Programs, and Jim Dunning, C<sup>3</sup>RP Program Manager. The purpose of this forum is to bring principals from high-tech companies in the region to campus on a regular basis, to foster a mutually beneficial relationship between the university and this important local industry sector.

- |                |   |  |
|----------------|---|--|
| <b>7:30 am</b> | Continental Breakfast - Small group discussions, networking and introductions   |  |
| <b>8:00 am</b> | An advanced extensible parametric geometry engine for multi-fidelity and multi-physics analysis in conceptual design            | Dr. Robert McDonald - Associate Professor Aerospace Engineering                |
| <b>8:15 am</b> | Investigation and testing of compressed air foam systems for structural firefighting  | Dr. Thomas Korman PE - Associate Professor Fire Protection Engineering Program |
| <b>8:30 am</b> | Prevention of postpartum weight retention in low income WIC women & Preventing excessive gestational weight gain in obese women | Dr. Suzanne Phelan - Associate Professor Kinesiology                           |
| <b>8:45 am</b> | TriActive America - TriActive Fitness™ Products and Projects  | James P. Sargen - Founder Grover Beach, CA                                     |
| <b>9:00 am</b> | Adjourn   |  |



## High-Tech Industry Breakfast Forum

### California Central Coast Research Partnership (C<sup>3</sup>RP)

#### Program Highlights & Select Research Projects

**December 14, 2012 - 7:30 - 9:00 am - Cal Poly Technology Park - BLDG 83 (Free Parking)**

You are invited to participate in our on-going breakfast forum for the local high-tech industry, hosted by Susan Opava, Cal Poly's Dean of Research and Graduate Programs, and Jim Dunning, C<sup>3</sup>RP Program Manager. The purpose of this forum is to bring principals from high-tech companies in the region to campus on a regular basis, to foster a mutually beneficial relationship between the university and this important local industry sector.

|                |  |  |
|----------------|--|--|
| <b>7:30 am</b> | Continental Breakfast - Small group discussions, networking and introductions  |  |
| <b>8:00 am</b> | Overview of the California Central Coast Research Partnership (C <sup>3</sup> RP)  | Dr. Susan C. Opava - Dean, Research & Graduate Programs                          |
| <b>8:15 am</b> | Use of Un-stiffened Steel Plates to Prevent Progressive Collapse of Existing Steel Building Frames with Simple Beam-to-Column Connection | Dr. Bing Qu PE -Assistant Professor<br>Civil & Environmental Engineering         |
| <b>8:30 am</b> | Overcoming Barriers to Affordable Algae Biofuels: Phase 2  | Dr. Tryg Lundquist - Associate<br>Professor Civil & Environmental<br>Engineering |
| <b>8:45 am</b> | Materials and Methods of Interconnections in LED Packaging   | Dr. John Pan - Professor Industrial<br>and Manufacturing Engineering             |
| <b>9:00 am</b> | Adjourn  |  |

